AD-A023 511

PROCEEDINGS OF THE CONFERENCE ON THE NUMERICAL
SIMULATION OF PLASMAS (4TH), HELD AT THE NAVAL
RESEARCH LABORATORY, WASHINGTON, D. C.,
ON 2, 3 NOVEMBER 1970

Naval Research Laboratory
Washington, D. C.

19 July 1971

Proceedings

Fourth Conference
on
NUMERICAL SIMULATION OF PLASMAS

1970

NAVAL RESEARCH LABORATORY
DEPARTMENT OF THE NAVY
Washington, D.C.

Proceedings

Fourth Conference

on

NUMERICAL SIMULATION OF PLASMAS

Edited by

Jay P. Boris and Ramy A. Shanny
Plasma Physics Division
Naval Research Laboratory

Sponsored and Hosted by

Naval Research Laboratory

In Cooperation with

Office of Naval Research

November 2, 3, 1970

NAVAL RESEARCH LABORATORY
Washington, D.C.

PREFACE

This book contains the Proceedings of the Fourth Conference on the Numerical Simulation of Plasmas held at the Naval Research Laboratory, Washington, D.C. on the 2nd and 3rd of November 1970. The conferences on the Numerical Simulation of Plasmas were used in the past to disseminate progress in the state-of-the-art of plasma simulation and specific applications of computer experiments to plasma physics. The first conference was held in 1967 at the College of William and Mary; the second was held in 1968 at the Los Alamos Scientific Laboratory and the third at Stanford University in 1969. At the time of the Fourth Conference, the field reached a highly sophisticated degree of maturity and won the acceptance of the general Plasma Physics Community. The number of presentations related to plasma simulation at APS Meetings of the Plasma Physics Division has been exponential since 1963. Eight percent of the total papers presented at the 1970 APS Meeting were in the field of numerical simulation. Most of these papers were oriented toward the application of numerical methods to the solution and understanding of physical phenomena. Therefore, the decision was taken at the Third Simulation Conference at Stanford to restrict the papers presented at the Fourth Conference to numerical techniques rather than the application of such techniques to plasma physics. It was further decided that the papers should be more comprehensive even though this would reduce the number of papers which could be presented orally at a two-day conference. The selection of papers for oral presentation at the Conference was based on the detailed, extended abstracts submitted by the authors. These extended abstracts provided the basis for evaluating proposed presentations in light of the two objectives of the Conference. The ultimate objective of the Conference was to present the state-of-the-art to which plasma simulation has evolved. An auxiliary goal was to make available to the general community a set of proceedings encompassing all aspects of the field and providing the researcher with a working reference and the graduate student with guidelines in this area of research.

The Conference was comprised of four sessions. The first session was composed of advanced numerical models and programming methods for computer representation of plasmas. The second session, designated computational sciences, was comprised entirely of invited papers which dealt with numerical techniques in fields other than plasma physics. The third session dealt with numerical methods for the solution of plasma models other than particle simulation. The fourth session included the theory of particle simulation as well as detailed optimization techniques.

It is felt that this Proceedings provides a reasonably complete and detailed exposition of the current state of numerical plasma simulation and will be useful to both the novice in the field and the professional.

We wish to extend our thank, to the authors and participants who made the 1970 Conference a success. We are grateful to Professors C. K. Birdsall and J. M. Dawson for their assistance in selecting the format of the Conference. We would like to acknowledge the help and assistance provided by the Management of the Naval Research Laboratory in the hosting of this Conference, and especially, the superb efforts of the Technical Information Division in the preparation of these Proceedings. In addition, we would like to acknowledge the help and assistance of Mrs. Tena M. Mason and Mrs. Melba O. Dubrosky in organizing the Conference without which the Conference could not have been held, as well as their efforts in prodding the editors in the preparation of manuscripts.

<div style="text-align:right">

JAY P. BORIS, EDITOR
RAMY A SHANNY, EDITOR

</div>

July 19, 1971
Naval Research Laboratory
Washington, D. C.

CONTENTS

iii

v

Monday, November 2, 1970

Session I

Chairman: R. A. Shanny

Naval Research Laboratory
Washington, D.C.

Relativistic Plasma Simulation—Optimization of a Hybrid Code

J. P. Boris
Naval Research Laboratory
Washington, D.C.

I.   INTRODUCTION

This paper contains the description of a plasma-simulation program,
CYLRAD, for two-dimensional systems of charged, fully relativistic particles
with fully retarded, self-consistent electric and magnetic fields. The geometry
of the basic physical system is r-z cylindrical, so the elemental charges are
azimuthally symmetric rings, but the methods generalize to other geometries
and to three dimensions quite easily. Two and three dimensional calculations
on such a complete plasma model would have been rather impractical on the small,
slow computers of previous generations; therefore, only recently has the pro-
blem of finding efficient, accurate, numerical models for solving this problem
been much more than an academic exercise. The larger and faster machines
presently available make these calculations possible today, however, and the

3

soaring costs of high-technology plasma experiments make them necessary. Thus, the author hopes that CYLRAD will be of interest.

Many important problems in astrophysics, plasma physics, high energy accelerator physics and electronics can be approached computationally by following the orbits of a great number of representative simulation particles under the interactions of their self-consistent electrostatic and electromagnetic forces. These self-consistent fields are often augmented in real problems by additional forces caused by charges and currents which are external to the domain of interest. Electrostatic calculations in plasma codes with time independent applied electric and magnetic fields have been used,[1,2,3] for example, to study electrostatic streaming instabilities and magnetic containment problems. It has long been realized that self-consistent magnetic fields would have to be calculated, as well as the electrostatic fields, to have an adequate description of many important plasma physics problems. Although the self-consistent electrostatic forces dominate in some non-charge-neutral systems, there exist many regimes where self-consistent electromagnetic effects cannot be ignored.

Two rather different circumstances can occur in plasma problems which are essentially charge neutral. In one class of problems fairly large, approximately divergence-free currents are present; the magnetic fields and induction electric fields which arise can then be comparable to or larger than the residual electrostatic fields caused by deviations from charge neutrality in the plasma.[4,5]

In another class of charge-neutral problems there need be no large plasma currents and yet electromagnetic effects contribute significantly to the plasma behavior, for example, through radiation effects or anisotropy instabilities.[6,7,8] In many cases the approach of non-equilibrium plasma to thermal equilibrium is determined predominantly by relatively weak electromagnetic effects rather than the stronger electrostatic phenomena simply because non-equilibrium plasmas,

4

which are electrostatically stable, are often unstable to one of the electro-
magnetic modes. Problems of these two types are often those in which induction
electric fields are important but where the transverse displacement current is
not the dominating term in Ampere's Law. This induction model, where the magnetic
vector potential satisfies the Poisson Equation, $\nabla^2 \underline{A} = \frac{4\pi}{c} \underline{J}$, is usually called
Darwin's model.[9] Electromagnetic radiation is not present but the induction
electric field is retained so that low-frequency electromagnetic plasma phenomena
such as Alfven waves will be properly described.[10,11]

In a third class of problems, the particles are fully relativistic. The
magnetic and electric energies are then comparable, even in non-charge-neutral
systems. In this class of problems the self-consistent electromagnetic radiation
can also be important. Although there are many problems where the particles are
relativistic but where radiation can be neglected, and many problems where radia-
tion interactions are important but where the particles are non-relativistic,
the usefulness of a plasma simulation program which handles both relativistic
particle effects and a fully time-dependent electromagnetic field is assured.
Intended applications for CYLRAD are relativistic-electron-beam generation and
propagation, electron-ring-accelerator design, transmission line transformer
design, and basic plasma studies.

In CYLRAD all three components of the electric field and all three
components of the magnetic field are advanced forward in time from the evolvant
Maxwell Equations,

$$\frac{\partial E}{\partial t} = c \, \underline{\nabla} \times \underline{B} - 4\pi \, \underline{J} , \tag{1a}$$

$$\frac{\partial B}{\partial t} = -c \, \underline{\nabla} \times \underline{E} , \tag{1b}$$

5

using a fully reversible algorithm which ensures that the constitutive Maxwell Equations,

$$\underline{\nabla} \cdot \underline{E} = 4\pi \rho \text{ , and} \tag{2a}$$

$$\underline{\nabla} \cdot \underline{B} = 0 \text{ ,} \tag{2b}$$

are satisfied to computer round-off accuracy at each timestep. Here $\underline{E}$ and $\underline{B}$ are the vector electric and magnetic fields respectively, $\underline{J}$ and ρ are the current and charge densities, and c is the velocity of light. Azimuthal symmetry gives simple conditions on $\underline{E}$, $\underline{B}$, $\underline{J}$ and ρ at the axis and perfectly-conducting metallic boundary conditions are presently being applied at a finite radius $R_{max} = (NR + \frac{1}{2}) * \delta r$ to give a tractable, bounded system. The system is periodic in the Z direction with a replication length of $Z_{max} = NZ * \delta Z$.

The relativistic Newton Equation for each particle using the Lorentz force in the laboratory frame of reference,

$$\frac{dP}{dt} = \frac{qE}{m_0} + \frac{qV}{m_0 c} \times \underline{B} \text{ ,} \tag{3a}$$

completes the specification of the system. Here q and m_0 are the particle charge and rest mass and the velocity $\underline{V}$ is related to $\underline{P}$, by

$$\underline{V} = \underline{P} / \sqrt{1 + p^2/c^2} \text{ .} \tag{3b}$$

Notice that the rest mass has been extracted from the definition of $\underline{P}$. An accurate, reversible single-pass method for integrating these particle equations is presented which gives the correct particle orbits in the simple limits. This algorithm takes special account of the cylindrical geometry so that orbits passing through the axis can be integrated without loss of accuracy.

6

Relativistic Plasma Simulation

The algorithm described here is more flexible than those given pre-
viously[12,4,6] and reduces to previous algorithms in special cases. This algorithm
retains the advantageous property of being fully reversible while decoupling the
prescriptions for current and charge-density apportionment. Thus, an electro-
static calculation can be recovered by setting c and $\underline{J}$ to zero in Eqs. (1a-1b)
and various charge and current algorithms can be tested to optimize the playoff
between accuracy and running-speed. The method is computationally fast because
expensive divergence-conservative current[12,6] algorithms can be bypassed. Further,
several timesteps of the electromagnetic field quantities can be performed, for
each particle timestep, without destroying the reversibility of the algorithm.
Thus, particle pushing, which is at best an expensive process, need only be done
once every few timesteps when the particles satisfy $V_{th} \ll c$ and $\omega_{pe} \ll c/\delta x$.

In this paper the main emphasis has been placed on numerical techniques
with the aim of showing how the various aspects of program optimization can be
balanced in constructing a fairly general plasma simulation code. The CYLRAD
program falls into the category of a hybrid code, one which contains features of
both fluid and particle calculations. In CYLRAD the partial differential Maxwell
Equations are solved by finite difference techniques while the particle equations
of motion are integrated using techniques specially devised for performing fast
particle trajectory calculations.

The discussion of the methods breaks similarly into two parts, the
solution of the Maxwell Equations with arbitrary sources $\underline{J}$ and ρ, and the integra-
tion of the particle equations of motion with arbitrary forcing fields. In
Section II, the details of the Maxwell-Equation integration are given and analyzed.
Appendices A, B, and C discuss important side issues related to solving the
Maxwell Equations. Poisson-solver programs are discussed briefly in Appendix A.
In Appendix B, generalizations to other geometries, to three-dimensions, and to
implicit difference schemes are considered. Appendix C generalizes the discussion

7

to cover the case where the dielectric constant of the medium $\epsilon(z,r)$, is not constant and where the boundary conditions are complicated. Section III describes the details of the fully reversible particle integration. Section IV contains a discussion of merging these two major parts of the code. A method is presented for integrating the particles over a much longer timestep than is possible for the electromagnetic fields while keeping the overall algorithm fully time reversible. Section V describes of a few simple test calculations performed to test the code and to point out the various computational properties of the method.

II. SOLUTION OF THE MAXWELL EQUATIONS WITH ARBITRARY SOURCES

In this section the particular staggered-leapfrog integration of the Maxwell
Equations (1a-2b) used in CYLRAD is described in detail assuming that the charge
density ρ (r,z,t) and the three components of the current $\underline{J}$ (r,z,t) are arbitrary
but given functions. These sources need not satisfy the charge-conservation
condition, Eq. (4), exactly. The CYLRAD algorithm corrects for any discrepancy
between ρ and $\underline{J}$ as related by Eq. (4) so we are considering, for the moment, just
a general purpose Maxwell-Equation solver. The algorithm given here decouples
the charge-and-current-apportionment prescriptions for added efficiency, con-
venience, and flexibility. The discussion concerned with relating these source
terms to the particles is deferred until Section IV.

Professor O. Buneman of Stanford has pointed out the computational advan-
tages of employing a reversible, fully-causal formulation for the electromagnetic
field equations.[12,13] He argues that the digital computer is basically a causal
device, processing information in a deterministic way, and one will find com-
putational physics an easier discipline if this is kept in mind. He further
argues that reversible algorithms which mirror the reversibility properties of
the classical manybody problem should be used in the numerical calculations.
Whatever other misbehaviors may be present, certain types of instability and
other systematic inaccuracies will be absent. Modern computers are specially
suited to simple, very fast calculations so it is easier and usually more
profitable to use simple, clean, low-order algorithms and a highly refined mesh
rather than complicated high-order schemes and coarser meshes. The former
course conforms more closely to the "mentality" of modern computers than the
latter and considerably shortens the lead time to results. In other words it is
often better to use brute force subtly in computational physics rather than to
try to be brutal in the use of subtlety since the essence of high-speed computers
is brute force.[24]

9

The numerical algorithm suggested by Buneman for solving the Maxwell
Equations in three-dimensional Cartesian coordinates automatically ensured the
consistency condition

$$\frac{\delta \rho}{\delta t} + \underline{\nabla} \cdot \underline{J} = 0 \tag{4}$$

by carefully choosing a current-accumulation algorithm to complement the NGP[14,15,16]
charge-interpolation algorithm. Professor Buneman further suggested a relatistic
particle-pushing algorithm to ensure that $\underline{V}$ for the simulation particles could never
exceed $\underline{c}$, the velocity of propagation of waves in the Maxwell Equatios. Although
Buneman realized that this algorithm would be useful for solving problems where
electromagnetic modes interact strongly with plasma, he also pointed out that an
artificially small value of c could be used to bring the various time and length
scales in the plasma closer together for computational convenience. This is much
in the spirit of choosing a 100:1 mass ratio, for instance, in electrostatic
calculations.

A recent application of these ideas[6,] has generalized the charge apportion-
ment to bilinear interpolation and specialized the calculation to two dimensions.
The CYLRAD code solves the Maxwell Equations in a 2-D azimuthally symmetric,
perfectly-conducting, metalic cylinder but the basic algorithm is applicaole
for three dimensions and for other geometries.

A staggered-leapfrog scheme[23,39] is used to advance $\underline{B}$ and $\underline{E}$ causally in a
fully space- and time-centered way. Figure 1 shows the entire time line for
CYLRAD with the electromagnetic field integration and the particle integration
separated. We are primarily interested in the field integration here, the upper
portion of the figure. The electric and magnetic fields are specified at different
times to ensure time centering and the currents are assumed to be known at the
magnetic field times. The electric field is integrated forward from t = -3δt to

**CYLRAD TIME INTEGRATION
CENTERED AND REVERSIBLE**
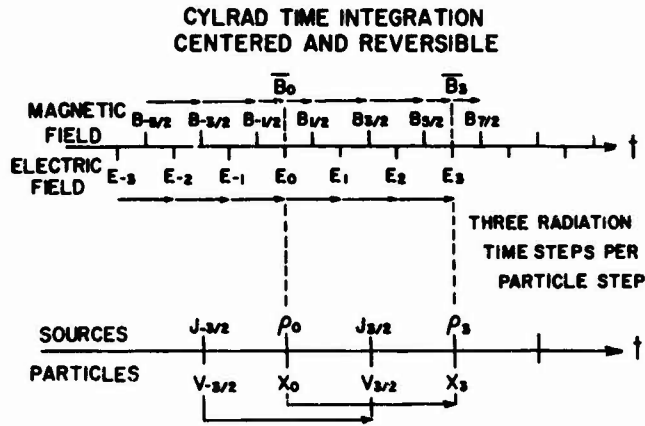
Figure 1. Time centering in CYLRAD. The field and particle variables are specified at times such that the temporal integration is fully reversible, centered, and second-order accurate.

CYLRAD GRIDS
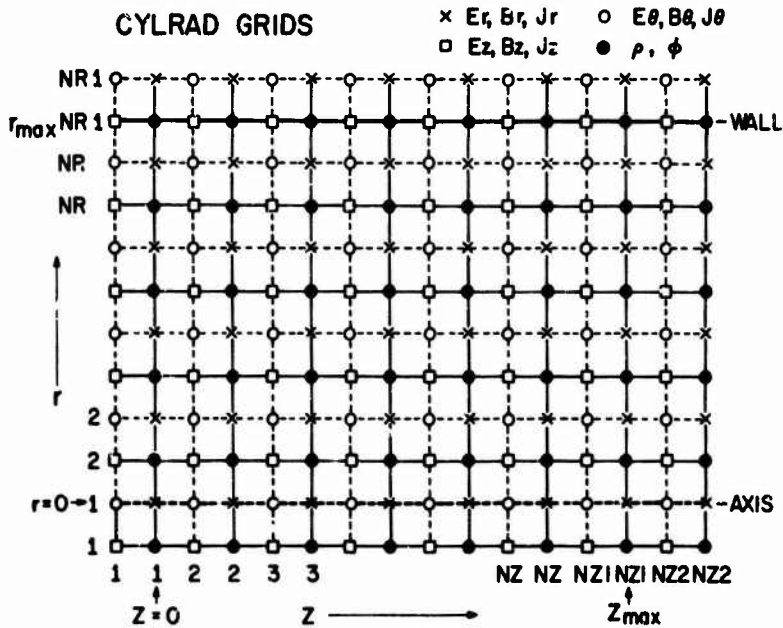
Figure 2. The four interlaced meshes in CYLRAD. By fully centering the meshes consistent definitions of the finite-difference operators allow full second-order accuracy (except near the axis).

11

t = -2δt using the magnetic field and current specified at t = -5/2δt to compute the right hand side of Eq. (1a). The magnetic field is then integrated forward one timestep from t = -5/2δt to t = -3/2δt using $\underline{E}_{-2}$ to compute the right hand side of Eq. (1b). This leapfrogging of $\underline{E}$ and $\underline{B}$ can then be repeated indefinitely to give the numerically-computed time evolution of the electric and magnetic fields. Since $\underline{E}$ and $\underline{B}$ are both needed at the same time for energy diagnostics on the fields and for particle pushing, $\underline{\overline{B}}_{0}$ is computed at t = 0, for example, in a fully centered way by averaging $\underline{B}$ (t + 1/2δt) and $\underline{B}$ (t - 1/2δt). This is done by integrating $\underline{B}$ forward only half a step on exit from the field-integration subroutine when t = 0 in the figure. $\underline{B}$ is then integrated forward another half step on entry to this routine prior to performing the leapfrog integration for the next few timesteps. This reduces the storage required since $\underline{\overline{B}}$ and $\underline{B}$ can reside in the same matrices in the computer memory.

Figure 2 shows the four staggered spatial meshes used in the CYLRAD program. Staggering the meshes in this way ensures that spatial centering, and thus second-order accuracy, is maintained throughout the bulk of the mesh. This, coupled with complete time centering, ensures that full reversibility is also retained. The meshes extend from 1Z = 1 to NR1. The allowed region for the particles extends from z = 0 to Z_{max} and from r = 0 (the axis) to r = R_{max} (the wall) as marked in the figure. The r and θ fields (x and 0) meshes) have IR = 1 at the axis and IR = NR1 half a cell outside the wall of the metallic cylinder. The Z and scalar fields (□ and 0 mesh points) have IR = 1 half a cell past the axis and IR = NR1 right at the outer metal wall. The boundary conditions at the axis are then

$$E_r(1,j) = 0 = B_r(1,j),\qquad(5a)$$

$$E_\theta(1,j) = 0 = B_\theta(1,j),$$

$$\rho(1,j) = \rho(2,j),$$

$$\delta\phi(1,j) = \delta\phi(2,j),$$
$$B_z(1,j) = B_z(2,j), \quad \text{and} \tag{5a}$$
$$E_z(1,j) = E_z(2,j).$$

At the outer limits of the mesh (the radial factors are defined by Eq. (8))

$$\rho(NR1,j) = \text{irrelevant},$$
$$\delta\phi(NR1,j) = 0, \tag{5b}$$
$$E_z(NR1,j) = 0,$$
$$B_z(NR1,j) = \text{computed normally},$$
$$E_r(NR1,j) = E_r(NR,j) * r^-/r^+ ,$$
$$B_r(NR1,j) = -B_r(NR,j) ,$$
$$E_\theta(NR1,j) = -E_\theta(NR,j), \quad \text{and}$$
$$B_\theta(NR1,j) = B_\theta(NR,j) * r^-/r^+ .$$

The significance of $\delta\phi$ will be brought out shortly.

Periodic boundary conditions on z are assumed (see Appendices A,B,C) so columns IZ = 1 and IZ = NZ2 are replicated from columns IZ = NZ1 and IZ = 2 respectively. These extra columns are used as guardlines, a technique also used on the MRHYDE staggered leapfrog mesh[26], to simplify the calculation throughout the interior of the mesh. The value of NZ = NZ2-2 must be a power of 2 in CYLRAD to satisfy the fast-Fourier transform Poisson solver but NR1 is arbitrary. The mesh spacing is uniform in both r and z but the mesh intervals δr and δz are arbitrary.

Figure 2 could apply equally well to a Cartesian grid but the boundary conditions at the axis, Equations (5a), would have to be replaced by some other set appropriate to say a metal wall. In Cartesian coordinates it is easy to show that the usual centered difference operators defined on the mesh of Fig. 2 satisfy the usual vector differential relations

$$\underline{\nabla}_D \cdot \underline{\nabla}_D \times \underline{A} = 0, \tag{6}$$

13

$$\underline{\nabla}_D \times \underline{\nabla}_D \phi \equiv 0 , \quad \text{and}$$

$$\nabla_D^2 \phi \equiv \underline{\nabla} \cdot \underline{\nabla}_D \phi .$$

(6)

The maintenance of these relations in the difference analogues of the differential operators is essential if the distinction between transverse and longitudinal fields, vital to the solution of Maxwell's equations, is to hold properly in the numerical solutions. This separation is used throughout CYLRAD.

Since we do not wish to have divergence of $\underline{B}$ deviate from zero, for instance, if initially set to zero, the divergence of the curl operator, $\underline{\nabla}_D \times$, must be identically zero in Faraday's law, Eq. (2a). This condition, when satisfied, has the further consequence that the transverse and longitudinal parts of the electromagnetic field can be decoupled in the difference as well as the differential Maxwell Equations when the dielectric matrix ϵ = constant. That is, the $\underline{\nabla}_D \times \underline{B}$ term in Ampere's Law, Eq. (1a) cannot contribute to the longitudinal part of $\underline{E}$ either. To insure this, the divergence operator $\underline{\nabla}_D$ has been chosen in a difference form to ensure that $\underline{\nabla}_D \cdot (\underline{\nabla}_D \times \underline{A})$ is identically zero for any vector field $\underline{A}$ whatsoever.

To ensure these relations in cylindrical coordinates, I have defined

$$(\underline{\nabla}_D \phi)_r (i,j) \equiv \frac{\phi(i+1,j) - \phi(i,j)}{\delta r} ,$$

(7a)

$$(\underline{\nabla}_D \phi)_z (i,j) \equiv \frac{\phi(i,j) - \phi(i,j-1)}{\delta z} ,$$

(7b)

$$(\underline{\nabla}_D \times \underline{A})_r (i,j) \equiv - \frac{A_\theta(i,j+1) - A_\theta(i,j)}{\delta z} ,$$

(7c)

$$(\underline{\nabla}_D \times \underline{A})_\theta (i,j) \equiv \frac{A_r(i,j) - A_r(i,j-1)}{\delta z}$$

(7d)

$$- \frac{A_z(i+1,j) - A_z(i,j)}{\delta r} ,$$

14

$$(\underline{\nabla}_D \times \underline{A})_z(i,j) \equiv \frac{r_i^+ A_\theta(i,j) - r_i^- A_\theta(i-1,j)}{r_i \delta r} , \tag{7e}$$

$$(\underline{\nabla}_D \cdot \underline{A})(i,j) \equiv \frac{r_i^+ A_r(i,j) - r_i^- A_r(i-1,j)}{r_i \delta r}$$

$$+ \frac{A_z(i,j+1) - A_z(i,j)}{\delta z} . \tag{7f}$$

The subscript D refers to "difference" operator. Throughout the rest of this paper the indices i and j will be used for IR and IZ respectively. These variables will be indexed as on their respective grids in Fig. 2. The indices on the radial factors r_i, r_i^+ and r_i^- have the following meaning:

$$r_i \equiv (i-3/2)\delta r,$$
$$r_i^+ \equiv r_i + \delta r/2, \text{ and} \tag{8}$$
$$r_i^- \equiv r_i - \delta r/2 .$$

It is an easy matter to verify relations (6) using Eqs. (7) and (8). This of course, requires the definition,

$$\nabla_D^2 \phi(i,j) \equiv \frac{r_i^+ \phi(i+1,j) - 2r_i \phi(i,j) + r_i^- \phi(i-1,j)}{r_i \delta r^2}$$

$$+ \frac{\phi(i,j+1) - 2\phi(i,j) + \phi(i,j-1)}{\delta z^2} \tag{9}$$

The step-by-step leapfrog integration of the Maxwell Equations can thus be written symbolically as

$$\underline{E}(i,j,t = \delta t) = \underline{E}(i,j,t = 0) + c\delta t \left[\underline{\nabla}_D \times \underline{B}(t = \delta t/2) \right](i,j)$$

$$-4\pi \underline{J}(i,j,t = \delta t/2) , \text{ and} \tag{10}$$

$$\underline{B}(i,j,t = 3/2 \delta t) = \underline{B}(i,j,t = \delta t/2) - c\delta t \left[\underline{\nabla}_D \times \underline{E} (t = \delta t) \right](i,j) . \tag{11}$$

15

This basic integration scheme has been tested thoroughly in Symbolic Algol[27,28,29] and discussed elsewhere.[23,39] It has the following dispersion relation (in Cartesian coordinates),

$$\sin^2 \frac{\omega \delta t}{2} = \frac{c^2 \delta t^2}{\delta x^2} \sin^2 \frac{k_x \delta x}{2} + \frac{c^2 \delta t^2}{\delta y^2} \sin^2 \frac{k_y \delta y}{2} , \qquad (12)$$

and thus the stability condition,

$$\delta t^2 \leq \frac{\delta x^2}{c^2} / (1 + \frac{\delta x^2}{\delta y^2}), \qquad (13)$$

because it is an explicit algorithm. Long wavelength modes propagate effectively at c but there is a numerical dispersion of modes due to the finite-difference approximations used. The shortest mode which can be represent on the mesh has wavelength 2 cells. Here $k_x \delta x = \pi$, for instance, and the dispersion, as shown in Fig. 3, for one dimension, is a maximum. The short wavelength modes are slowed down below the speed of light artificially. In one dimension, with $c \delta t / \delta x = 1$, this dispersion can be minimized but in two dimensions, there are always badly dispersed short wavelength modes. In all (stable) cases, however, the modes are non-diffusive so the mode amplitudes remain unchanged in time. The electromagnetic part of the CYLRAD code is therefore completely energy conservative in this sense.

Appendix B considers extensions of the CYLRAD electromagnetic field integrator to other geometries, to three dimensions, and to other difference schemes. In Appendix C the inclusion of a spatially varying dielectric matrix is discussed. By including a matrix $(1/\epsilon)(i,j)$ defined on the θ mesh (and averaged onto the other 3 meshes, much more general problems including Cerenkov radiation and metal boundaries can be included with a minimum of effort because the ϵ-metal boundaries are computed exactly as all other points. The causal, conservative formulation of the Maxwell Equations employed here makes this especially easy and ensures that the boundary conditions are satisfied for all time.

The question of the current source terms in Eqs. (1a) and (10) must be settled

now. In physical problems the continuity equation,

$$\frac{\partial \rho}{\partial t} + \underline{\nabla} \cdot \underline{J} = 0, \tag{14}$$

must always be satisfied. This ensures that every charge in the system
has come from somewhere physically and will be going somewhere physically. It
seems sensible, therefore, to ensure this condition in our finite-difference model
for Maxwell's Equations. Since our divergence operator has already been specified,
Eq. (14) gives a numerical consistency condition between ρ and $\underline{J}$. We have no
reason to suspect that $\rho(r,z,t)$ and the longitudinal part of $\underline{J}(r,z,t)$ satisfy
this numerical condition since we are treating these sources as arbitrary inputs,
suitably discretized, to a field integration algorithm. In practical plasma
applications where ρ and $\underline{J}$ come from particles[12,6], this condition can be enforced
at some computational expense by considering current fluxes through space-time
cell boundaries. In the general case, where boundary conditions may be compli-
cated however, the continuity equation must be used specifically to correct the
input sources. This frees the input to allow vector fields of ρ and the longi-
tudinal current $\underline{J}_\ell$ which are only approximately consistent. In pure Maxwell-
Equation calculations for instance, analytic forms for ρ and $\underline{J}$ can be used with-
out worrisome consideration of consistency. In plasma calculations the current
and charge-apportionment algorithms can be completely decoupled for simplicity,
generality, and computational efficiency. This allows one to greatly speed the
calculation of particle trajectories, by far the slowest part of the relativistic
plasma simulation.

Of course extra work must be performed elsewhere to ensure Eq. (14) but
this loss is small compared to the gains realized. To enforce consistency, either
the charge density or the current must be modified. Since only the currents

17

NUMERICAL DISPERSION
CURVES FOR CYLRAD
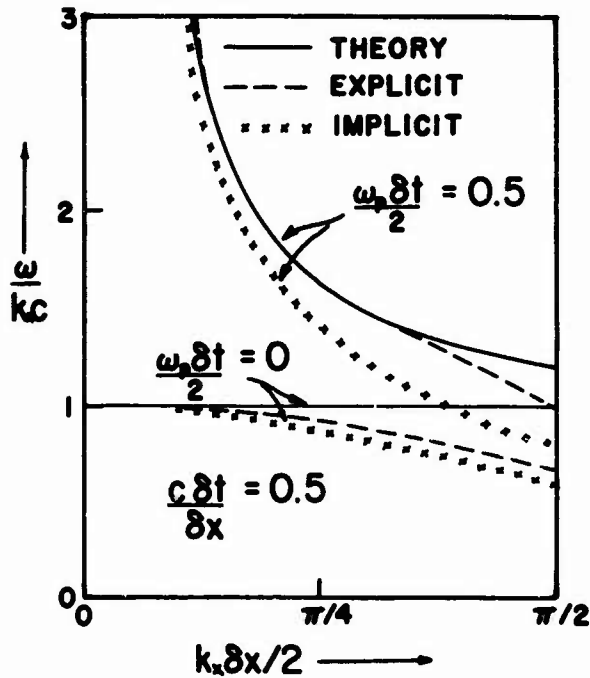
Figure 3. Dispersion relations for explicit
and implicit integration of Maxwell's Eq-
uat ns with fluid-like plasma represented
by a constant ωp. The theoretical modes
are shown for comparison.

appear in the dynamical Maxwell Equations and since the charge density is a zeroth moment while $\underline{J}$ is a first moment, it is natural and physically sensible to modify the longitudinal current to be consistent with the given charge density. This is done through the Poisson Equation,

$$\underline{\nabla} \cdot \underline{E} = 4\pi\rho \tag{15}$$

rather than through the continuity equation. The given currents give rise to an electric field via the leapfrog scheme, which has both a transverse and a longitudinal part. Thus

$$\underline{E}_\ell(t+\delta t) - \underline{E}_\ell(t) = -4\pi\delta t \ \underline{J}_\ell(t+\delta t/2) \tag{16}$$

can be solved for $\underline{E}_\ell(t+\delta t)$, actually calculated simultaneously with a transverse part. If we call this field $\underline{E}^*$, for the moment,

$$\underline{\nabla}_D \cdot \underline{E}^* = 4\pi\rho^* \neq 4\pi\rho \tag{17}$$

because of the assumed inaccuracies in $\underline{J}_\ell$. The corrected field $\underline{E}$ is found by subtracting the difference gradient of a correction potential $\delta\phi$ from $\underline{E}^*$. Thus

$$\underline{E} = \underline{E}^* - \underline{\nabla}_D \ \delta\phi \ . \tag{18}$$

It is easily seen that

$$-\underline{\nabla}_D^2 \ \delta\phi = 4\pi\rho - \underline{\nabla}_D \cdot \underline{E}^* \tag{19}$$

forces

$$\underline{\nabla}_D \cdot \underline{E} = 4\pi\rho \ .$$

It must be stressed the $\delta\phi(i,j)$ is only a correction potential, not the full electrostatic potential. The major portion of the longitudinal part of $\underline{E}$ is found from integrating Ampere's Law; only discrepancies between $\underline{J}$ and $\frac{\delta\rho}{\delta t}$ appear in $\delta\phi$. The boundary conditions on $\delta\phi$, which are implied by Eq. (19), depend on the boundary conditions satisfied by $\underline{E}^*$. In CYLRAD, E_z^* is zero on the metallic wall at $r = R_{MAX}$ and therefore $\delta\phi = 0$ at the wall is both simple and correct. If,

19

as is possible using complicated current algorithms, the continuity equation in difference form is automatically satisfied, $\delta\phi$ is zero throughout the system. If on the other hand, the deviations from consistency are of the order of truncation errors in the finite difference scheme, as will be the case for the fairly efficient current-charge algorithm used for the particles in CYLRAD, small, acausal longitudinal correction fields will be felt throughout the system. These fields propagate with infinite speed across the system but are generally bery srall.

The Maxwell Equation solver described here, even without self-consistent particle orbits promises to be very useful in transformer, waveguide, and antenna calculations. Analytic or empirical current fields can be specified and the radiation fields can be found. Appendix C, as mentioned earlier, allows extension of these field calculations to much more complicated geometrics where the dielectric constant is an arbitrary function of position. The program is completed when equations for the plasma particles have been added to the system. The next section treats integration of the relativistic equations of motion of charged particles in given $\underline{E}$ and $\underline{B}$ fields. These particles will then be totalled on the mesh to get self-consistent current components and charge densities, used as sources in the solution of Maxwell's equations.

III.   THE CYLRAD PARTICLE PUSHER

The relativistic equations of motion for a point particle of rest mass m_o and charge q in a given electric and magnetic field are

$$\frac{d\underline{P}(t)}{dt} = \frac{q}{m_o} \underline{E}(\underline{X}(t),t) + \frac{q}{m_o c} \sqrt{\frac{\underline{P}(t) \times \underline{B}(\underline{X}(t),t)}{1+P^2(t)/c^2}} \qquad (20)$$

$$\frac{d\underline{X}(t)}{dt} = \underline{V}(t), \qquad (21)$$

where $\underline{P} \equiv \underline{V}/(1-V^2/c^2)^{\frac{1}{2}}$. This definition of $\underline{P}$ will be noted to differ from the usual relativistic particle momentum by the factor of m_o which has been extracted so that $\underline{P}$ reduces to $\underline{V}$ in the Galilean limit. A finite difference algorithm to integrate these equations should satisfy three basic criteria:

1) accuracy,

2) speed,

3) simplicity.

Several algorithms for the non-relativistic case with arbitrary $\underline{E}$ and $\underline{B}$ fields have been used previously; a comparison of these has been performed by Carl Wagner of NRL.[30] The most used of these is the reversible, so-called "implicit" algorithm where $\underline{E}$ and $\underline{B}$ are given at t, when the particle position $\underline{X}$ is specified, and where $\underline{V}$ is integrated forward one timestep from $\underline{V}_O$ at $t-\delta t/2$ to $\underline{V}_N$ at $t+\delta t/2$. The new velocity is found by solving the 3 x 3 system of equations

$$(\underline{V}_N - \underline{V}_O)/\delta t = \frac{q}{m} \underline{E} + \frac{q}{2mc} (\underline{V}_N + \underline{V}_O) \times \underline{B}. \qquad (22)$$

Here O and N have the mnemonic meaning "old" and "new" respectively. This method is characterized by the time-centered $\underline{V} \times \underline{B}$ term using the average of the new and old velocities. The name "implicit" arises because $\underline{V}_N$ is involved implicitly in the right-hand side.

This method has several nice properties which make it quite attractive:

1) The algorithm is reversible. The particle trajectory can, in

21

principle, be retraced if time is reversed in the code. This neglects of course, computer round-off errors.

2) The usual electrostatic leapfrog algorithm is recaptured when $\underline{B} = 0$.

3) When $\underline{E} = 0$, the particle moves in a non-drifting circle and the radius of the orbit is constant. By dotting (3) with $(\underline{V_N} + \underline{V_0})\,\delta t$ one finds

$$V_N^2 - V_0^2 = \frac{q}{m}\,\delta t\underline{E}\cdot(\underline{V_N} + \underline{V_0}), \tag{23}$$

showing that $|V_N| = |V_0|$ in the absence of an electric field.

4) The energy gain, by (4), is just $\underline{E}\cdot\overline{\underline{V}}$, as would be expected on physical grounds.

5) The frequency of the finite timestep cyclotron gyration can be corrected by the standard $\tan\alpha/\alpha$ correction[31] so that the particles themselves execute the classical orbits at precisely the correct gyrofrequency.

An additional criterion which can be satisfied is:

6) Simplicity and hence speed. The implicit algorithm can be made acceptably fast if programmed carefully. Solving Eq. (22) by a 3 x 3 matrix inversion is not the fastest way, as shown shortly.

The orbits generated by the implicit algorithm even in the case of constant $\underline{E}$ and $\underline{B}$ are not exact but can be improved to give the correct $\underline{E} \times \underline{B}$ drift by modifying the electric field vector, as well as the magnetic field, to include corrections for the finite-difference features of the algorithm. This can be done in another, simpler, way. As long as $|\underline{E} \times \underline{B}| < B^2$, these exists a frame of reference in which the electric field is zero. By subtracting the velocity $\underline{V_E} = c\,\underline{E} \times \underline{B}\,/\,B^2$ where $\underline{E}$ and $\underline{B}$ are evaluated at the current particle position, we get the following "E xB" algorithm for advancing the velocity.

$$\underline{V_1} = \underline{V_0} - \underline{V_E}, \tag{24}$$

$$\underline{V}_2 = \underline{V}_1 + \frac{q \delta t}{2mc} (\underline{V}_2 + \underline{V}_1) \times \underline{B} \text{ (plus } \tan \alpha/\alpha), \qquad (24)$$

$$\underline{V}_N = \underline{V}_2 + \underline{V}_E .$$

The advantages of the $\underline{E} \times \underline{B}$ over the implicit algorithm are that exact cycloidal orbits, without modifications to the electric field can be obtained in the limit where $\underline{E}$ and $\underline{B}$ are constant. Furthermore, $\underline{V}_E$ can be precomputed as a cell quantity and so (24) can be made somewhat faster than (22). The method (24), for all its physical appeal, suffers a serious defect. When $|\underline{E} \times \underline{B}| > B^2$ there is no frame of reference where $\underline{E}$ is zero but $\underline{B}$ can be transformed away. Thus a wholly different algorithm is needed when $\underline{V}_E > c$. Still a third algorithm would be required when $\underline{V}_E = c$. These problems arise in practice when the magnetic field is zero and thus pose serious problems, for instance, when configurations with neutral points, lines, or planes are being considered.

There exists a third variation of the implicit particle pushing algorithm which possesses advantages of both the implicit and $\underline{E} \times \underline{B}$ methods and can be made somewhat faster than either. In addition, it generalizes conveniently to the fully relativistic equations (1) whereas direct solution of Eq. (22) in the implicit algorithm does not. The algorithm is basically three-step in nature:

$$\underline{V}_1 = \underline{V}_0 + \frac{q \delta t}{2m} \underline{E} ,$$

$$\underline{V}_3 = \underline{V}_1 + \frac{q \delta t}{2mc} (\underline{V}_3 + \underline{V}_1) \times \underline{B} \text{ (using } \tan \alpha/\alpha), \qquad (25)$$

$$\underline{V}_N = \underline{V}_3 + \frac{q \delta t}{2m} \underline{E}.$$

By applying half the electric field before the magnetic field rotation and half afterward, the algorithm becomes fully reversible and yet the magnetic interaction can be treated in the absence of an electric field. This latter fact is very important when one generalizes to the relativistic Eq. (20). When the algorithm in (25) is used, it is easy to show that the implicit result

is recovered. When the magnetic field $\underline{B}$ is zero, the usual electrostatic leap-frog method is recovered so that $V_N{}^2 - V_0{}^2 = (\underline{V_N} + \underline{V_0}) \cdot \frac{q\delta t}{m} \underline{E}$.

Since the correct cyclotron frequency can be achieved by corrections to $\underline{B}$, the solution arising from Eqs. (25) must be judged somewhat superior to the other methods mentioned because it is faster. It is made fast using the two-step rotation procedure given above, rather than the usual 3 x 3 linear-equation reduction, to solve for $\underline{V_3}$ given $\underline{V_1}$ (with $\underline{E}$ absent). This is done by setting

$$\underline{V_2} = \underline{V_1} + f_1 \underline{V_1} \times \underline{B} ,$$

$$\underline{V_3} = \underline{V_1} + f_2 \underline{V_2} \times \underline{B} \qquad (26)$$

where $\qquad f_1 = \dfrac{\tan \frac{q\delta t}{2mc} |B|}{|B|}$ and $f_2 = 2f_1/(1 + f_1^2 B^2)$.

In practice f_1 is expanded up through fourth order and evaluated very efficiently giving roughly single-precision round-off-sized truncation errors on the IBM 360/91 where 6 to 7 digits can be kept through most calculations.

Figure 4 shows the geometric interpretation of this method in the plane perpendicular to $\underline{B}$. The pure magnetic push over timestep δt with constant $\underline{B}$ is really a rotation of $\underline{V_2}$ in the velocity space by the angle $\beta = \omega_c \delta t = \frac{q\delta t}{mc} |B|$. The correction factor f_1 ensures that $\underline{V_2}$ is displaced an angle of exactly $\beta/2$ from $\underline{V_1}$ even though $\underline{V_2}$ does not lie on the orbit circle beacuse it has the wrong magnitude. $\underline{V_2} \times \underline{B}$ does point from $\underline{V_1}$ through $\underline{V_3}$ because the angle has been bisected, however, so the magnitude correction f_2 ensures that $f_2 \underline{V_2} \times \underline{B}$ stops exactly on $\underline{V_3}$. It should be fairly clear that the amount of work involved computationally is much less than required to solve Eq. (22) directly even with $\underline{E} = 0$. The two-step "half $\underline{E}$" algorithm, which is shown in Eq. (25) requires in fact about 35% fewer operations than the implicit push.

$$\beta = \delta t \, qB/mc$$
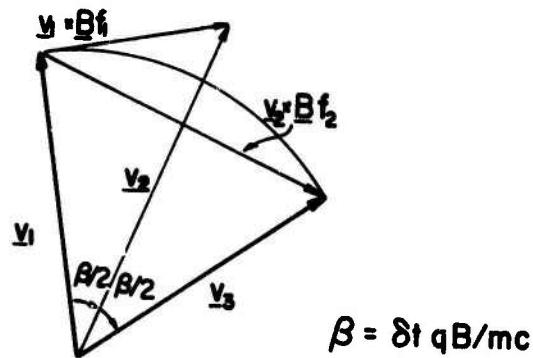
VELOCITY SPACE ROTATION

$$r_2 = \delta t \sqrt{(v_r + r_1/\delta t)^2 + v_\theta^2}$$

$$\sin \alpha = \frac{v_\theta \delta t}{r}$$

$$\cos \alpha = \frac{(r_1 + v_r \delta t)}{r_2}$$
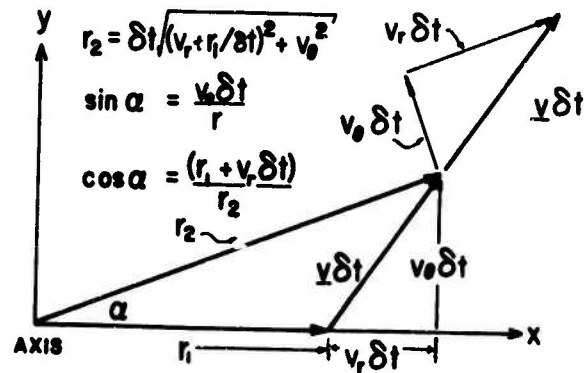
CONFIGURATION SPACE ROTATION

Figure 4. Geometric interpretations of the particle pushing algorithm. Both the configuration space and velocity space portions of the algorithm contain energy conserving rotations.

When the relativistic equations are being solved, the relativistic mass must be used in expressing the factor f_1. Thus, $\frac{q\delta t}{m_0 c}\sqrt{\frac{c^2}{c^2 + P^2}}$ where $\underline{P}$ is the relativistic momentum (over m_0) replaces $\underline{V}$ in the previous arguments. Provided that P^2 is constant, therefore, the relativity merely amounts to a renormalization of the magnetic field. This is the great advantage of the "half $\underline{E}$" algorithm. By separating the electric and magnetic interactions in the relativistic generalization of Eqs. (25), $P_3^2 = P_1^2$ has been assured and thus P^2 inside the square root,

$$\sqrt{\frac{c^2}{c^2 + P^2}} \, ,$$

which is used in the magnetic field renormalization, can be treated as constant over the timestep and evaluated explicitly. Except for this square root factor, the relativistic and classical integrations are the same.

Actually, in the course of updating the particle position as well as its velocity, three more square roots must be taken, one to retrieve the laboratory velocity from $\underline{P}$ and two to correct for cylindrical coordinates, a problem discussed below. To handle these four square roots in the optimized code (they take about 15% of the particle-pushing time in the Fortran version of the code), a special hand-coded PL360 program has been written which requires no power series expansions to start. A table look-up process on the floating point exponent and the floating point fraction is used to get a very good starting value for a simple iteration which doubles the number of significant figures every cycle. This routine requires ~ 3 µsec per square root and thus uses only 40% of the time taken by the system square root. One pays for this with a table of over 1000 words, a fairly small price on the IBM 360/91.

The integration of $\underline{P}$ from $t - \frac{\delta t}{2}$ to $t + \frac{\delta t}{2}$ constitutes only half of the particle-pushing algorithm. Integration of $\underline{X}$ from t to $t + \delta t$ is accomplished

26

as follows in Cartesian codes:

$$\underline{X}(t + \delta t) = \underline{X}(t) + \delta t\underline{V}(t + \frac{\delta t}{2}) . \tag{27}$$

In the relativistic case $\underline{V}(t + \frac{\delta t}{2})$ is determined, as mentioned above by taking a square root, an annoying but not prohibitive procedure. What is more constricting is the cylindrical coordinate system in which we must operate. In Cartesian coordinates $\underline{X}$ executes circular motion in constant $\underline{B}$ with zero $\underline{E}$ and moves with the proper parabolic motion when $\underline{E}$ is constant and $\underline{B}$ zero. Great difficulties arise from the angular momentum accelerations of the charged rings in the r-θ plane of a cylindrical system. At the axis, for instance, there is a cubic singularity L^2/r^3 when the angular momentum is nonzero. Furthermore, we would like to preserve helical orbits (circular in the r-θ plane) for single particles in a constant axial magnetic field. The algorithm given below accomplishes this in a very simple and therefore efficient way by focusing on the Cartesian-cylindrical transformations. Therefore singularity and circularity problems are completely bypassed.

We need only consider the perpendicular plane and are given V_r and V_θ, defined at $t + \frac{\delta t}{2}$, with which we must advance r and θ. Since the basic enzatz is azimuthal symmetry, however, only the radius r of the charge rings is given as no θ variation is permitted. We are free, therefore, to focus on the ring element at $\theta = 0$, as shown in Figure 4b. The particle traverses the straight line element $\underline{V} \delta t$ from $\underline{r_1}$ to $\underline{r_2}$. At the starting point $V_x = V_r$ and $V_y = V_\theta$. Since these velocities continue constant throughout the time interval δt, we have:

$$X_2 = r_1 + V_r\delta t ,$$

$$Y_2 = V_\theta\delta t . \tag{28}$$

27

The initial radius is r_1. The final radius r_2 is given by

$$r_2 \equiv \sqrt{X_2^2 + Y_2^2}$$

(29)

The optimized square root is used of course. During the next timestep r_2 becomes r_1 and is again assumed to lie along the x axis. The matter does not end here. Since $\underline{r}$ has rotated an angle α, the resolution of $\underline{V}$ along $\hat{r}$ and $\hat{\theta}$ must be changed at the end of the timestep even though the actual velocity of each ring element is constant over the entire interval δt. The transformation used is simple,

$$V_{r_2} = V_{r_1} \cos \alpha + V_{\theta_1} \sin \alpha ,$$

$$V_{\theta_2} = -V_{r_1} \sin \alpha + V_{\theta_1} \cos \alpha ,$$

(30)

where $\sin \alpha = Y_2/r_2$, $\cos \alpha = X_1/r_2$. The only problem arises when a "particle" stops exactly on the axis. In this case, we can arbitrarily set $\cos \alpha = 1$ and $\sin \alpha = 0$. This makes all momentum radial which it would have to be for a particle to stop on the axis.

Stringent tests of this entire technique have been performed. Energy is conserved exceedingly well when $\underline{E}$ is zero because the particles execute perfect circular motion about a constant axial magnetic field. It is obvious, in this respect, that transformation (30) is energy conserving. It is also clear that the algorithm is fully reversible, a property generally considered good in particle pushers.

The data format of the coordinates and velocities for each ring is floating point although the positions are treated in fixed-point insofar as area weighting is concerned. The DIC method of area weighting is used,[16] a fixed-point technique particularly well suited for use when the multiple-mesh feature of the field definitions is taken into account. Normal bilinear area weighting of $\underline{E}$, $\underline{B}$, $\underline{J}$ and ρ is used but four distinct meshes and hence four distinct sets of

weights are needed. (The currents are also being treated NGP, as discussed elsewhere.) By using DIC, these weights are precomputed for a finite set of $M_z \times M_r$ subcells with each computational cell. M_z and M_r are powers of 2 so that the subcell numbers are represented as $\log_2 M_z$ and $\log_2 M_r$ sequential bits in the fixed-point representations of z and r respectively.

In actual use, of course, the accuracy of the particle-equation integrations is not perfect. The method is fully second order, due to the time centering and reversibility and thus the well established guidelines for particle pushers must hold as discussed in Section IV. Thus δt should be chosen sufficiently small that $\omega_c \delta t$ and $\omega_p \delta t$ are considerably less than unity. One also expects[33,34,35] that the code will misbehave when λ_D and c/ω_{pe} are lengths considerably less than one cell. From preliminary runs, as discussed in Section V, the greatest errors seem to arise from interpolating particle wource terms and field quantities to and from the cylindrical mesh.

The initial Fortran version of the particle pusher used 145 μsec of computer time per particle on the 360/91. A highly optimized PL360 version has been written which is computationally identical but which requires only 95 μsec per particle. The savings result from special computational techniques[15,16,24,25] which can be written effectively only in machine code. Shifts, rather than fix and float operations, can be used to sort out the cell and subcell numbers for instance. It is felt that even greater improvements can be made by increased use of fixed-point operations.

Although the PL360 version is highly machine dependent, similar techniques would be profitable on other machines with a greatly different structure. Of particular importance in particle pushers is the one-pass aspect of the overall algorithm. An entire timestep can be performed with only a single reference to

29

the particle tables. If external mass storage is being used for the particle table, the relatively expensive transfer times to and from disc, say, need only be paid once per timestep. In the present example, magnetic disc transfer times per particle are about 65 μsec for reading and writing, quite comparable to the particle-integration time. Since these transfers can be overlapped with each other and with the one-pass integration of particles in the CPU as well, optimal use is being made of the computer. Even when direct core residence time is not being charged as CPU time for I/O transfers, as is the case on the IBM 360/91, total program residence time must be considered. If, for example, overlapping were not possible, the running of a 1 hour CPU job would require roughly 3 hours of wall time. If the program filled core (as these jobs often do), nonoverlapping (or a poor compute-transfer balance, could mean that two thirds or more of the CPU computing power was being wasted. Since computer centers are also aware of this possibility, it is not surprising to see that most charging algorithms charge by the core request as well as the CPU time used. Thus jobs which fill core usually pay for the whole machine since fractional utilization of the CPU is no longer a factor.

IV. MERGING THE FIELD INTEGRATION WITH THE PARTICLE INTEGRATION

In Section II a rather general algorithm was given for numerically integrating the Maxwell Equations forward in time to determine the three components of $\underline{E}$ and the three components of $\underline{B}$ on the two-dimensional r-z mesh with all values being specified at the same point in time. In Section III an optimized, efficient algorithm is given for integrating the relativistic charged-particle equations of motion given $\underline{E}$ and $\underline{B}$ fields on a uniformily spaced r-z mesh. To complete specification of the entire CYLRAD algorithm, the prescription for merging these two phases of the calculation is now discussed in more detail.

Interpolating $\underline{E}$ and $\underline{B}$ from the mesh to the particle position is carried through according to the usual area-weighting, or bilinear interpolation algorithm.[32,38] Although the mesh is basically cylindrical, this part of the calculation is carried out as if the mesh were Cartesian. At the axis, where problems with the metric will be most severe, E_r, E_θ, B_r, and B_θ vary linearly anyway so the calculation will be accurate. The z components of $\underline{E}$ and $\underline{B}$ typically vary quadricatically away from the axis so the straight area weighting will only be accurate to zero order in these two cases.

The calculation of the sources is currently being carried out in the usual charge-and current-sharing approximation as on a Cartesian grid but several extra degrees of freedom are permitted the physicist here. Even though the charge and current densities are required in Maxwell's Equations, the CYLRAD particle pusher gives the total charge and total currents in each cell. Presently this total charge and current is being divided by the exact cell volume but this part of the calculation can be modified in many ways. Averaging over several adjacent cells could reduce spurious fluctuations, for example.

In area weighting to determine the fields and sources, the geometric interpretation is that of an azimuthally symmetric ring with rectangular cross-section

31

expanding and shrinking as it moves on the mesh. The ring extends from
$r - \delta r/2$ to $r + \delta r/2$ in radius and from $z - \delta z/2$ to $z + \delta z/2$ along the axis. Although
more than half of the ring's charge, if of uniform density, lies outside r, the
simple area weighting prescription does not take this into account. To treat
this properly, the radius r_c used in computing the sources must be somewhat
larger than r in order that simple charge sharing have no systematic error.
It is easy to show that

$$r_c = \sqrt{r^2 + \tfrac{1}{4}} \tag{31}$$

forces the usual charge sharing to allocate the correct proportion of charge
inside and outside of the particle radius r since r_c is the center-of-charge
radius of the extended ring (The improved square root routine is used here).

One also has the possibility of employing k-space smoothing[15,16] of ρ and $\underline{J}$ by
Fouier analyzing in the z direction. This would not improve the radial varia-
tion at all but would be helpful where the radial variation is smoothed by
other means. Thus finite-sized particles[36] could be used easily in Cartesian
codes. Perhaps then the NGP algorithm for charges and currents could be used
with sufficient accuracy.

It has been mentioned that the DIC,[16,25,37] or Discretized Interpolation
in Cells, method has been used for all the bilinear interpolations and charge
sharing. In this program each cell is thought of as subdivided into an array
of 16x16 subcells. For each subcell the four weights for the cell corners are
precalculated as if the particle were at the center of the subcell. Thus the
particles are effectively calculated Nearest Grid Point in the subcells rather
than the major cells. These weights are stored in a table and "looked up"
when needed by a very fast algorithm rather than recalculated each time.

32

DIC is particularly useful in CYLRAD where four distinct meshes must be treated so that the same set of weights cannot be reused for all the components of $\underline{E}$ and $\underline{B}$ or $\underline{J}$ and ρ. A table of weights is calculated for each mesh and all can be referenced by locating the particle on one of the meshes. The present particle pusher, in optimized form, takes 95 μsec/particle of which about 30% is area weighting. If direct recalculation of all of the weights were performed, approximately four times as much work would be done on the area weighting thus doubling the CPU time required per particle.

A glance at Figure 1 shows that the current $\underline{J}$ is specified at the velocity time, half way between the two position times at the beginning and the end of the timestep. To ensure centering, therefore, the current must be area weighted twice; half of the current is apportioned before the position is updated (but using the new velocity) and half of the current, using the same velocities, is apportioned to the new position at the end of the timestep. In addition to centering $\underline{J}$ and thus keeping the algorithm fully reversible, a sort of averaging is being performed which will help greatly in smoothing fluctuations which are highly enhanced in this numerical plasma due to the paucity of particles in a Debye sphere relative to most real plasmas.

Figure 1 shows the entire timeline for CYLRAD with particle as well as field times indicated for a case where 3 radiation steps are performed for every particle timestep. The current $\underline{J}_{3/2}$ is used in each of the 3 radiation steps integrating $\underline{E}_{-3}$, $\overline{\underline{B}}_{-3}$ to $\underline{E}_0$, $\overline{\underline{B}}_0$. These latter fields are then perfectly centered to integrate $\underline{V}_{-3/2}$ to $\underline{V}_{3/2}$ and hence X from $\underline{X}_0$ to $\underline{X}_e$. The ability to perform fully reversible multiple field timesteps for each particle timestep is very important to the optimization. In Section II the stability criterion for the field integration was given. This means, in practice, that light can traverse only half a cell or less per timestep. Even for extremely relativistic particles, two or three radiation steps could elapse between particle steps thus speeding up the code by a factor of two or three. In

33

non-relativistic plasmas the situation is even worse and decoupled timesteps are even more necessary. An average particle traveling at 0.1c would need 20 timesteps or so just to cross a single cell regardless of λ_d or ω_{pe}.

When the presence of the particles are included in the stability analysis in a simple way, one finds the dispersion relation,

$$\sin^2 \frac{\omega \delta t}{2} = \frac{c^2 \delta t^2}{\delta x^2} \sin^2\left(\frac{k_x \delta x}{2}\right) \tag{32a}$$

$$+ \frac{c^2 \delta t^2}{\delta y^2} \sin^2\left(\frac{k_y \delta x}{2}\right) + \frac{\omega_{pe}^2 \delta t^2}{4}$$

for the case of one particle step for each radiation step. Eq. (32a), in the long wavelength limit, reduces to the correct physical dispersion relation,

$$\omega^2 = \omega_{pe}^2 + k^2 c^2 . \tag{32b}$$

Since $\sin^2 \left(\frac{\omega \delta t}{2}\right)$ cannot exceed unity for a numerically stable mode, we now have a much more stringent stability condition on δt,

$$\frac{1}{\delta t^2} \geq \frac{c^2}{\delta x^2} + \frac{c^2}{\delta y^2} + \frac{\omega_{pe}^2}{4} . \tag{33}$$

In dense plasmas ω_{pe}^2 will dominate. Then $\delta t < \frac{2}{\omega_{pe}}$ for stability. When the density is very low, we approach the previous result. In all cases, however, the presence of plasma acts to require a shorter timestep for stability and hence makes multiple timestepping more attractive.

Empirically, multiple timestepping has been found stable and otherwise numerically well behaved. There is some evidence, although not conclusive, from early runs that multiple timestepping reduces the emission of bremsstrahlung from particle collisions. This is very much to be desired in a numerical model where collision frequencies are too large anyway due to the relatively small number of particles which can be followed. Dispersion relations can be found

34

analytically but they are extremely complicated even in the case of only 2 or 3 radiation steps per particle step. In some of the simpler limits, however, the dispersion relation has been solved with the result that the algorithm is numerically stable as expected.

The data structure of CYLRAD follows that of P POWER[25] closely. The grid quantities, 11 in number (3 E's, 3 B's, 3 J's, ρ, and $1/\epsilon$), are all kept in fast core storage as single precision floating point numbers. Given 330K words, certainly available on an IBM 360/91, we have 30K words/matrix. This is 120 x 256 in resolution. The particles are stored in an arbitrary number of records of fixed length which can reside either in core or on an external I/O device. The program is transparent to the actual mode of the record storage so the program runs identically on small in-core systems and large out-of-core systems.

Figure 5 a. shows the structure of each record. The first 16 words of each record contain pertinent information about the particles in the record such as charge, mass, the speed of light, δt, δr, δz, etc. The first word of the record heading contains the number of particles in the record. All records have the same number of particles, NPART.

Following the heading are NPART disposition bytes, one for each particle in the record. The disposition byte can have any one of 256 values, each in principle specifying a different specific action to be taken for the corresponding particle. At present 0 means the particle is to be integrated normally and any other value means that the particle is to be ignored. Some particles could be integrated for a while without contributing to the sources. Others could have their charge varied slowly, for example.

Following the disposition bytes, actually held in NPART/4 words, are 5 * NPART words containing the positions and velocities for each particle.
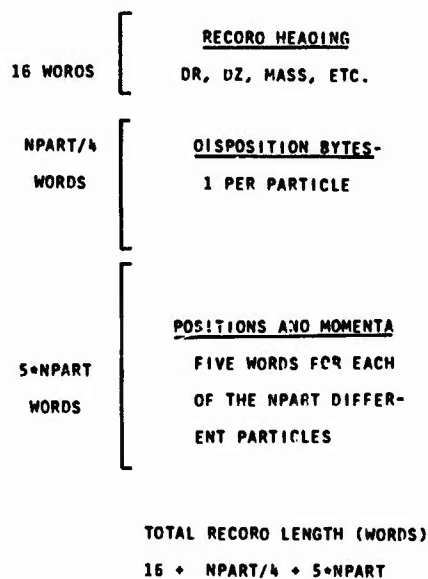
5a. DATA STRUCTURE　　　5b. INITIALIZATION
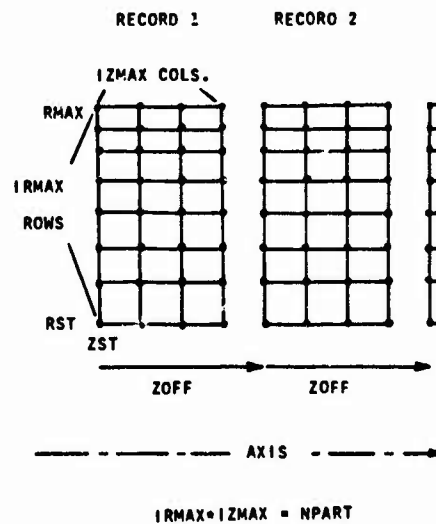
Figure 5. Record data structure of CYLRAD. (a) The organization of each record with heading, disposition bytes, and particle coordinates and momenta. (b) Record initialization of particle locations. Uniform density cylinders, slugs, and tubes can be initialized.

Relativistic Plasma Simulation

The order is z, r, P_r, P_θ, P_z for each particle. The momenta (divided by rest mass) are in real physical units but the positions are carried in cell units to aid in locating the particles on the grid in fixed point.

The records of particles can be grouped into larger units called classes. The classes could comprise different species of say n records each but their use is somewhat more general. It is convenient to consider electrons in oppositely directed beams as being in different classes, for example, since the kinetic energy and momenta of each class are printed out as well as the total kinetic energy and the total momenta of the system. Different classes could also have different q values but the same q/m_0 value in order to pack rather finely certain important regions of phase space.[40,41]

In initializing the positions and velocities of the particles, the record-class structure is also useful. All records in a class, using the present initializer, are given the same drift and thermal velocities, these six numbers being specified as data for each class. The positions of the particles within a class are initialized as shown in Fig. 5b. The charge density arising from each record is nearly constant over a cylinder extending from RST to RMAX and from ZST to ZST+IZMAX*DZ where IZMAX is an integer factor of NPART. The number of particles distributed radially from RST to RMAX for each value of IZ is IRMAX $\equiv$ NPART/IZMAX. After each record in the class, ZST (Z start) is incremented by ZOFF (Z offset). Thus continuous cylinders, hollow cylinders, full tubes of plasmas, slugs, and point blobs can all be initialized with the same program. This capability covers most of the simple configurations of interest including homogeneous plasmas, streaming instabilities, E layers, and electron beam drift tubes and thus helps to optimize a programmer's time by minimizing reprogramming.

37

V. TESTS OF CYLRAD

Several of the test problems used to check out various facets of the CYLRAD program are described in this section and the results are given. The tests performed to date have been quite comprehensive but the testing phase is still incomplete. Simulation with plasma in the system has only recently been achieved and much remains to be done with diagnostics, radiation levels, and stability. The tests chosen for discussion here will be described in chronological order.

The first part of the program written was the main program with data structure, loop logic, and provision for data buffering. This framework was largely copied from the PPOWER program[25] and thus has been thoroughly tested and used extensively. To this framework was added the Maxwell Equation integrator without provision for source terms. Figure 6 shows selected computer output of the Transverse Magnetic cavity modes from one of the test runs. The system was initialized at t = 0 by setting all fields to zero except for E_θ and B_θ. These two components were made nonzero only in a small torus as shown in the first picture for B_θ.

As noted in Appendix B, TE and TM radiation separates conveniently in the code as well as in real wave-guides. Thus the field components (E_θ, B_r, B_z) and (B_θ, E_r, E_z) remain totally decoupled in the code. The code was run with only E_θ nonzero and then with only B_θ nonzero proving that TE and TM are actually decoupled in the code.

In Fig. 6, the initially localized radiation spreads out at velocity c until it fills the cavity. The eigenmodes excited then continue to oscillate independently. Since Maxwell's Equations are linear, perhaps the most important tests of this phase of the calculation were the energy and divergence checks. Without sources $\underline{\nabla} \cdot \underline{E}$ and $\underline{\nabla} \cdot \underline{B}$ are both zero to computer roundoff as they should be, for runs lasting thousands of timesteps. The energy in the system is conserved to about 0.03 % over the same length of time with no observable

38

CYLRAD -TM RADIATION   7/25/70

R₀=13.75 Z₀=38.4

C = 2.0   dt = 0.05
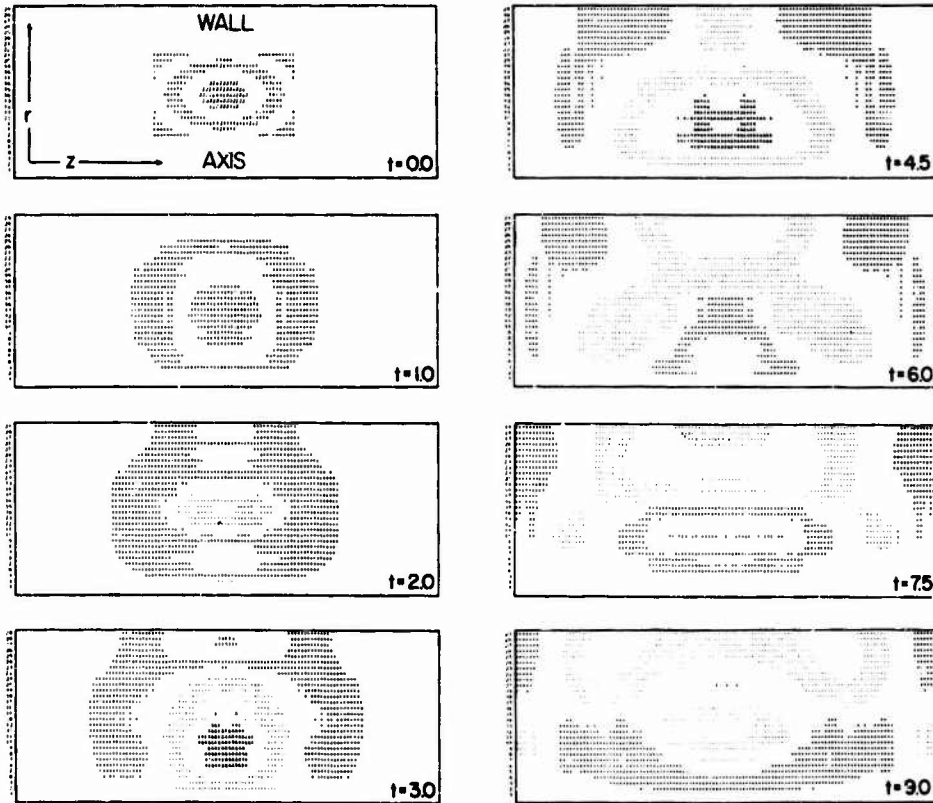
Figure 6. Transverse magnetic cavity modes. An initially localized distribution of $B_\theta(r,z,t=0)$ (all other fields zero) was released and followed in time. Energy conservation holds to a few hundredths of a percent with an infinite conductivity metallic wall.

39

systematic trends. This is reasonable because the staggered leapfrog scheme is marginally stable and because the wave equations are linear and the eigenmodes of the cavity are orthogonal numerically as well as physically. The small fluctuations observed are due, in fact, to the small incompatibilities between the energy-calculating algorithm and the actual conserved amplitudes of the modes. The energies of TE and TM fields are conserved separately as expected.

The Poisson solver is described in Appendix A. Several severe tests were conducted separately and then the subroutine was inserted into CYLRAD. The most severe test performed in CYLRAD had $\underline{J}$ set by a random number generator and ρ set to zero at each time step. The divergence of $\underline{E}$ was printed out before and after the Poisson solve. Since CYLRAD forces the longitudinal part of $\underline{E}$ to be consistent with ρ, $\underline{\nabla} \cdot \underline{E}$ should be zero after the Poisson solve in this test. In the runs, the magnitude $|\underline{\nabla} \cdot \underline{E}|$ dropped by roughly 5 orders of magnitude. This is about the best one could expect taking the roundoff-error figures for the Poisson-solver accuracy into account.

The particle pusher was then written and tested separately in a number of simple applied fields. Figure 7 shows the radius versus time curves for four particles in a constant axial magnetic field. The electric field is zero in this case. Each particle had identically the same axial and perpendicular energy but the particles were started at different radii. As can be seen in the figure, all particles have exactly the same frequency. This frequency, furthermore, is given correctly by

$$\omega_c = \frac{qB}{m_o c} \sqrt{\frac{c^2}{p^2 + c^2}} \qquad (34)$$

to roughly machine roundoff because of the $\frac{\tan\beta/2}{\beta}$ correction described in Section III. The particles were initialized so that each started at a different radius or in a different direction. One of the particles looped around the axis so that its radial excursion apparently differs from that of the other

40

CYLRAD PARTICLE ORBITS
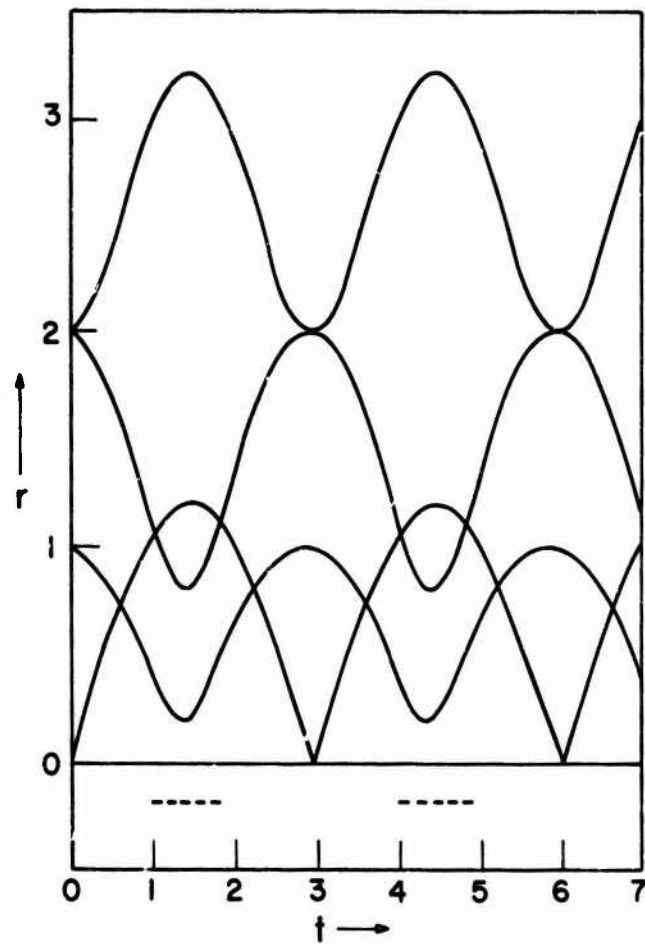
Figure 7. Radius versus time for four particles at fixed momentum in a constant axial field. The electric field was chosen zero. The diameter and period of the four orbits are identical. The particles are executing off-axis circular orbits as theoretically predicted.

41

particles but this is not actually the case. If the effective negative r position is marked, as shown by the dashed lines in the figure, all particles can be seen to have orbits with the same diameter.

One of the particles passes through the axis during each orbit. The two components of the perpendicular momenta are shown in Figure 8 for this particle. The radial momentum changes discontinuously (drawn linearly) over one timestep and the azimuthal momentum has a cusp. Even for this particle the energy is conserved out to machine roundoff in the absence of electric fields. The ability to treat orbits accurately near the axis for beam problems was one of the reasons for choosing to solve the momentum equation directly rather than to utilize conservation of angular momentum[38] to get V_θ from A_θ.

A radial, linearly increasing electric field was applied to this particle and the test performed again. Energy is not conserved exactly in this case because the electric field was not self-consistent, but the orbit was periodic and did return to the initial energy when the particle returned to the axis. The main feature of this test was the presence of an azimuthal $\underline{E} \times \underline{B}$ precession of the orbit which appeared as expected. During these various particle tests, the source matrices calculated were printed out and checked in detail to ensure that the area-weighting algorithm works properly.

The particle pusher was then inserted into the CYLRAD code and the entire program was tested on the increasing-current run whose results are shown in Fig. 9. A column of charge was initialized along the full length of the axis extending out to a finite radius less than the tube radius and then accelerated slowly along the axis by an applied non-electromagnetic force. Initially only the radial electrostatic electric fields were present plus a low level of cavity modes included to tickle any instabilities, if present. In this problem the acceleration was sufficiently slow that a quasi-static azimuthal magnetic field could be expected to develop where B_θ varies as r inside the

42

PARTICLE MOMENTA VS TIME

$C = 2.0$ $\quad$ $P_\perp^2 = 0.2$ $\quad$ ———— P_r

$2\pi\omega_c^{-1} \simeq 2.99$ $\quad$ $P_z^2 = 4.0$ $\quad$ — — — — P_θ
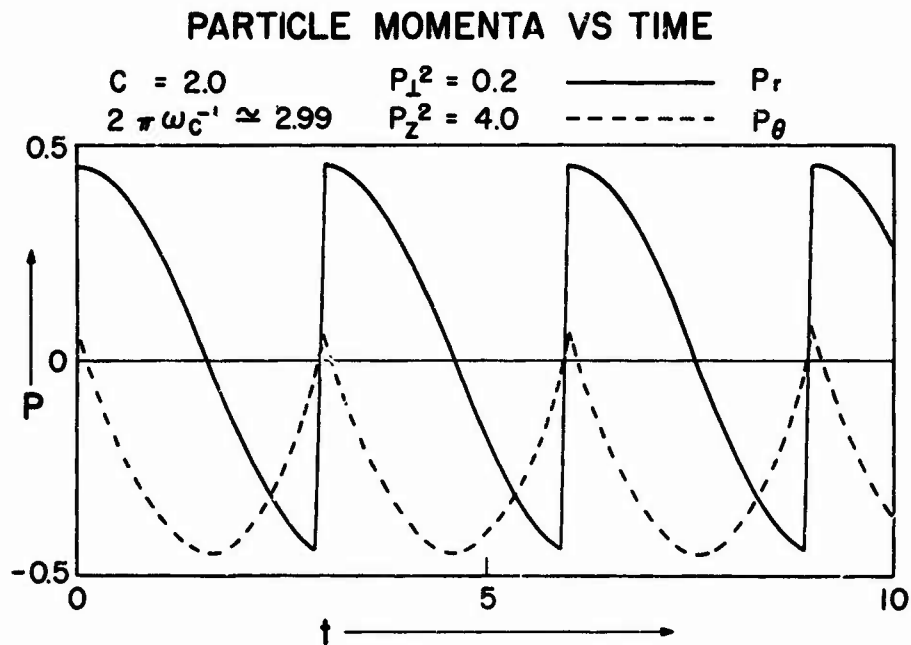
Figure 8. Radial and Azimuthal Momenta for a particle passing through the axis of the cylinder. The orbit is exactly periodic and energy conserving even though P_r reverses discontinuously as the particle passes through the axis.

charged cylinder and drops off as 1/r outside the cylinder. The mass of the
particles in the charge cylinder was taken so large that no appreciable radial
expansion took place from the radial electrostatic field during the course of
the run.

In the figure, $rB_\theta(r)$ is plotted at three equally spaced times after the
beginning of the run. The quantity $rB_\theta(r)$ should vary quadratically out to the
beam radius and then should be constant outside this radius. The theoretical
curve is shown for the particle current at t = 150. The numerical data from one
29-point radial line is also shown for comparison. The agreement is excellent.
The levels of $rB_\theta(r)$ seem to be getting closer together as time goes on. This
occurs because of the relativistic saturation of $\underline{V}$ at c; only the quantity
$\underline{V}/\sqrt{1-V^2/c^2}$ is being accelerated uniformly.

Two other features of this particular test will be of interest. The radia-
tion fields generated when the charged beam is accelerated would normally rattle
about in the cylinder forever were it not for the radiation-absorbing layer
included in the calculation. This layer extends over two cells in radius, shown
cross hatched in Fig. 9, and along the full length of the system. The electric
fields in this region are knocked down at each timestep as they would be in a
resistive medium. Thus the radiation energy which develops does not continue
indefinitely. During the course of the run the transverse electric energy, which
does not interact with the beam at all, decreases by two orders of magnitude due
to the absorption.

The second feature of the calculation is the presence of an ϵ-metal wall two
cells inside the real wall of the cylinder. Appendix C discusses the inclusion
of a spatially varying dielectric constant in CYLRAD. This allows more complicated
physical problems to be handled where the radiation propagates through a spatially-

44
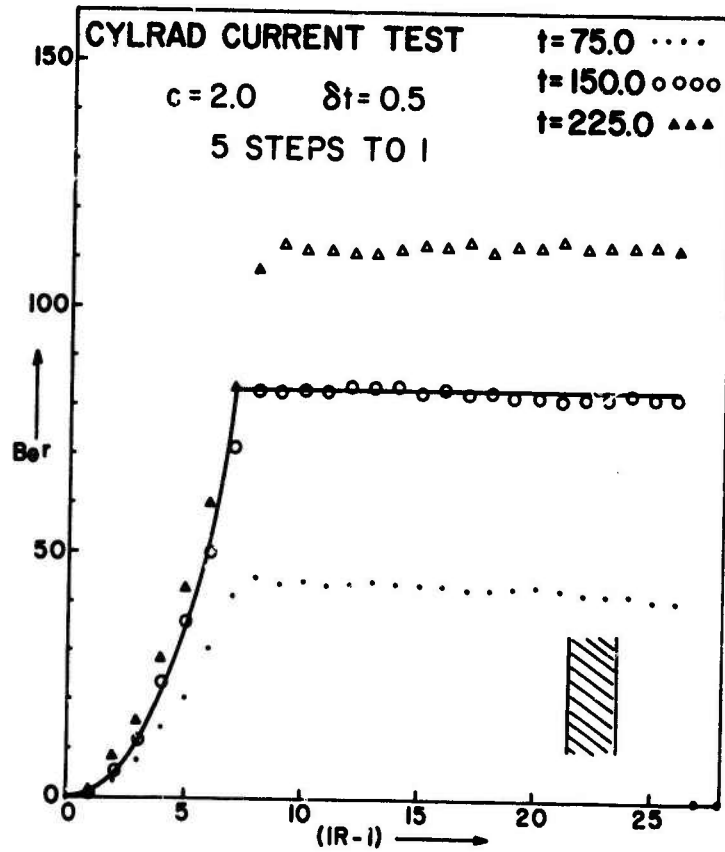
Figure 9. Azimuthal magnetic field of a slowly accelerated charged cylinder. The solid line shows the theoretical magneto-static field which would prevail at t = 150.0 if the charged cylinder were moving at constant velocity.

varying, frequency independent dielectric medium (Cherenkov radiation could be treated for instance). An important use for this flexibility is the case for $\epsilon \to \infty$, which is really treated as $1/\epsilon = 0$. As noted in the appendix, the code treats this as a metallic, perfectly-conducting boundary condition. Thus complicated metal boundarys can be included quite easily by reducing the valves in the $1/\epsilon$ matrix from 1.0 to 0.0 in regions which are supposed to be metal.

In the test shown by Fig. 9, the outer wall of the calculation was taken to be two cells of this ϵ-metal, explaining the two points at zero near the outer radius. This ϵ-metal conserves energy properly and does not contribute to the divergence of $\underline{E}$ or the divergence of $\underline{B}$. These convenient properties are all made possible by the fully causal treatment of the Maxwell Equations embodied in the code.

A final series of tests are being conducted in which the cylinder is filled uniformly with electrons and with a smeared out ion background. The particle distribution is initially random in velocity with all fields zero except the electrostatic field caused by initial discrepancies from charge neutrality. These tests were designed to check overall energy conservation and the bremsstrahlung radiated from the particle collisions. The plasma temperature was low, taken so that $n\lambda_D^2 \sim 15$, and the particles were initialized so that there were only 2 per cell on average. These conditions give fairly high collision times and fluctuation and therefore fairly fast bremsstrahlung thermalization. Furthermore, because the fluctuation levels are high, conservation of total energy in the code should be all the more difficult to achieve. In typical runs the energy was conserved to better than 1% over 400 ω_p^{-1} when area weighting was used on all fields and sources. When NGP was used on the currents, however, with all other quantities area weighted, the energy conservation disappeared entirely. Errors of 300% were recorded for the same length run. The large NGP error

46

is explained when one realizes that no k-space smoothing to the sources or fields is being applied as in electrostatic simulations.[25]

Electromagnetic collision (thermalization) times go roughly like $(\omega/\omega_p)^2$ times the corresponding electrostatic times. In simulation plasmas, $10n\lambda_D^2$ is a rule-of-thumb electrostatic collision time. In the present case, therefore, $150\omega_p^{-1}$ is a good estimate of the Coulomb collision time. Since there are at most a few modes in the system tested (dimensions 16 cells x 29 cells), the very shortest wavelengths, which are the slowest modes to thermalize have $(\omega/\omega_p)^2 \leqslant 10$. Thus $400\omega_p^{-1}$ is a reasonable estimate for the bremsstrahlung thermalization time, in good agreement with the computer simulation.

When several timesteps for the fields are taken for each particle timestep, the bremsstrahlung radiation rate became considerably slower. Thus the ability to take multiple timesteps was found to improve the physical properties of the simulation as well as the computational properties. This effect clearly results because radiation arises from orbit deflections. When the orbits suffer fewer deflections, even though of larger amplitudes, the radiation at short wavelengths will saturate more slowly.

The field energy saturation levels are also fairly well explained for these tests. In the case of NGP currents one would expect roughly $\frac{1}{2}k\overline{T}$ of energy for each field component at each grid point. Here $\overline{T}$ is the temperature at equilibrium. One also expects $\frac{3}{2}k\overline{T}$ energy in kinetic motion for each particle. Since there are 2 particles per cell in these runs, the NGP field energy at saturation should be roughly twice the kinetic energy. The actual ratio observed was about 3. When area weighting is used, wavelengths shorter than about 4 cells are strongly supressed; that is, three fourths of the modes are largely inoperative. This means that kinetic energy should be twice the field energy, a ratio close to the 30% number given by Fig. 1C.

47
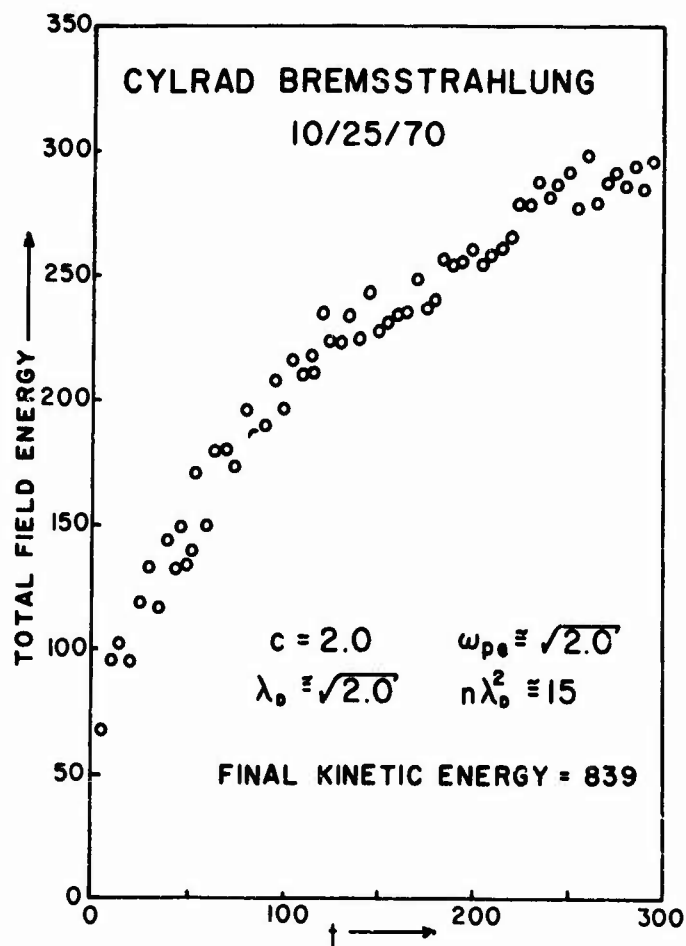
Figure 10. Radiation of Bremsstrahlung by
a non-equilibrium plasma in CYLRAD. The
electromagnetic field (initially zero) ap-
proaches equilibrium, as estimated by equi-
partition arguments, as $\omega_{pe}t$ approaches 450.

48

VI. CONCLUSIONS

The two dimensional relativistic plasma simulation program CYLRAD has been described in some detail. Two main modules have been developed, the general purpose r-z cylindrical Maxwell-Equation solver, and the relativistic particle pusher. The overall algorithm is fully time reversible. In several instances, alternative algorithms have been mentioned and the reasons for each choice given. General criteria of simplicity, flexibility, accuracy, and efficiency have been balanced in each of the algorithm choices. The paper has stressed the numerical aspects of the CYLRAD program in order to show first, how such a program can be constructed to be both flexible and efficient, and second, how the interplay between partial differential finite-difference techniques (fluid codes) and particle techniques can be merged in the development of a hybrid code. These techniques will find application throughout computational physics. In incompressible flow the vorticity can be discretized, for example. Or in the study of galactic evolution, the gas clouds could be followed in an MHD approximation while the stars could be followed as particles.

Several of the ideas presented here may be of special interest.

1) Separation of the longitudinal and transverse contributions of the currents to the electromagnetic fields has been previously recognized.[33] The method given in Section II and Appendix A is both flexible and efficient.

2) A spatially varying dielectric matrix is allowed. The correct boundary conditions are automatically satisfied everywhere even when $\epsilon \rightarrow \infty$, thus quasi-metallic or dielectric obstacles and walls can be placed arbitrarily in the cavity.

3) A method for accurate integration of the particle orbits near the axis of symmetry is given. Thus axis crossings can be handled smoothly without singularity.

49

4) The relativistic mass correction is performed in a simple, reversible, energy-conserving manner. This integration method is to be contrasted with algorithms where $\underline{V}$ and $\underline{\gamma}$ are advanced independently.

5) The completed plasma-simulation algorithm, including the solution of the Maxwell Equations and the relativistic particle pusher, allows the fields to be advanced on a shorter timescale than the particles. This increased freedom has been found to reduce collisional effects as well as improve program efficiency.

6) The completed plasma simulation algorithm is fully space-centered and fully time-reversible. Thus a host of problems, which might otherwise occur, can be avoided.

Proposed calculations on the IBM 360/91 computer ($\sim$ 400K words of 32 bits each of useable fast core memory) can be performed on a 50 x 512 mesh at less than 2.0 seconds per 3 radiation steps plus Poisson solve. Using 11 grids, then, of 25K points each still leaves plenty of core for program, diagnostics matrices, and particle buffers. By stretching the computational cells 3:1 in the axial direction, systems with a 30:1 aspect ratio can be treated easily. The running time for this problem, assuming 4 particles per spatial grid point is 12 seconds (100K particles x 100 μsec/particle + 2 seconds for fields). In physical units this is about one ω_p^{-1} of real time per minute of CPU time.

Relativistic Plasma Simulation

Appendix A - Poisson Solvers

In this paper, the constitutive Maxwell Equation,

$$\underline{\nabla} \cdot \underline{E} = 4\pi\rho , \qquad (A-1)$$

is ensured by an auxiliary calculation rather than by choosing one of the conservative charge-current algorithms.[6,12] The many advantages of this are discussed in Section II. One disadvantage is that a Poisson equation must be solved. This Poisson equation,

$$\nabla^2 \delta\phi = \underline{\nabla} \cdot \underline{E} - 4\pi\rho , \qquad (A-2)$$

generates a correction potential $\delta\phi(r,z)$, whose gradient is subtracted from $\underline{E}^*$ to ensure that

$$\underline{E} = \underline{E}^* - \underline{\nabla}\delta\phi \qquad (A-3)$$

satisfies Eq. (A-1). Calling the right hand side of Eq. (A-2) $S(i,j)$, consistency of the difference analogues to the differential operators necessitates using the 5-point Poisson approximation (r_i^+, r_i, r_i^- are defined in Section II),

$$\frac{r_i^+ \delta\phi(i+1,j) - 2r_i \delta\phi(i,j) + r_i^- \delta\phi(i-1,j)}{r_i \delta r^2}$$

$$+ \frac{\delta\phi(i,j+1) - 2\delta\phi(i,j) + \delta\phi(i,j-1)}{\delta z^2} = S(i,j) , \qquad (A-4)$$

for $i = 2,3 \ldots, NR$ and $j = 2,3 \ldots, NZ1$. Here we again use i as the radial index IR and j as the axial index IZ. The boundary conditions on $\delta\phi$ are $\delta\phi(1,j) = \delta\phi(2,j)$ from azimuthal symmetry and $\delta\phi(NR1,j) = 0$ because the outer wall is considered to be perfectly conducting. This second condition is true only because E_z^*, the electric field from the staggered leapfrog integration of Maxwell's Equations, satisfies $E_z^*(NR1,j) = 0$ already.

It is clear from Eq. (A-4) that $S(1,j)$ are not used. Thus ρ is effectively discarded at these points even though the charge-sharing algorithm does attribute

51

some charge to these cells. At the axis all of this charge is used, however, in going from a charge matrix to a charge density matrix. At the wall, the charge lost can be attributed to a numerical indeterminacy principle which states that all charge within half a cell, $\delta r/2$, of the wall connot be distinguished from the cancelling image charges in the wall, which also lie in the same computational cell. Thus this charge can have no effect on the longitudinal fields in the system.

In CYLRAD, Eq. (A-4) is solved directly without iteration by a combination fast Fourier-transform reduction in the z direction and a double sweep matrix inversion of the tridiagonal equations for the resultant Fourier harmonics. After Fourier transforming each row of S in the z direction, we need only consider individual harmonic terms of the form $\delta\phi_K$ (i) exp $(2\pi\ iKj/NZ)$. Substituting into (A-4) gives

$$\frac{1}{\delta r^2} \times \left[\frac{r_i^+}{r_i}\ \delta\phi_K\ (i+1)\ -\ 2\delta\phi_K(i)\ +\ \frac{r_i^-}{r_i}\ \delta\phi_K(i-1) \right]$$

$$-4\ \frac{\sin^2\ \pi K/NZ}{\delta z^2}\ \delta\phi_K(i) = S_K(\ ).$$

(A-5)

Solving the tridiagonal system of Eqs. (A-5) for $i = 2,3\ ...,$ NR gives a matrix of $\delta\phi_K$ to overwrite S_K. These harmonics are then Fourier synthesized to give the final result, $\delta\phi(i,j)$.

The fast-Fourier-transform method was developed by the author at Culham[15] and has been in use for over a year at NRL in the PPOWER electrostic simulation code[24,25]. Every effort has been made to make the code efficient and accurate. With the FFT subroutine in assembly language and the tridiagonal solver in Fortran, a 128 by 128 system can be Poisson solved in cylindrical coordinates in .48 seconds on the 390/91. The tridiagonal solver is presently being coded

in PL360, a symbolic assembly language for 360 computers, and is being
modified to solve two harmonic equations simultaneously. The estimated Poisson-
solving time for the 128 by 128 system will then be about .35 sec. For compar-
ison, a single radiation timestep leapfrogging $\underline{E}$ and $\underline{B}$ forward takes about .20
sec. in Fortran. Thus the field integration part of the CYLRAD code will be
slowed by about 50% if 3 radiation steps are performed for every particle step
(Poisson solve). This 50% slow down of the field integration is small, however,
when particle integration times are considered as well. With only 2 particles
per cell, we have over 30,000 particles to integrate every timestep. This is 3
seconds per timestep for particles, .6 second for fields, and .35 second for a
Poisson solve. Thus the Poisson solve costs at most 10% of the cycle time. By
contrast, the conservative charge-current algorithm, except for possibly knotty
problems at the boundaries, would allow us to do away with the Poisson solve
entirely but would roughly double the particle integration time. Thus the
Poisson solve method saves a factor of about 2 overall.

As a special case, the conservative charge-current prescription could be
used in the CYLRAD algorithm resulting in $\delta\phi(i,j) = 0$ to computer roundoff error
everywhere in the region of calculation. Since single precision is only 6 figures
or so on the 360 computers, however, it seems quite likely that some form of
"divergence cleaning" would still be necessary every 1000 timesteps or so. The
divergence of $\underline{B}$ in CYLRAD is zero to only about 4 or 5 places, for example, since
roundoff errors accumulate over a few thousand timesteps of the radiation fields.
Thus it may be necessary to use such a divergence-cleaning routine for $\underline{B}$ as well.

It is advantageous to calculate in single precision as much as possible
since the useable core storage is then effectively doubled. Therefore close
error checks on the Poisson solver have been performed. The test cases were on
small 16 x 29 systems and on larger 128 x 128 systems. In the former case

$\nabla^2 \, \delta\phi \; = S$ to about 5 figure accuracy; in the latter case, to about 4 figures. As $\underline{\nabla} \, \delta\phi$ is typically only a few percent relative to $\underline{E}^*$, however, the actual error in the physical fields, in the worst cases would only be a few parts per million.

Other methods of Poisson solving would suffice for this problem, of course, since the consistency conditions for the difference analogues of the vector differential operations prevent the use of Poisson coefficient smoothing[15,16] immediately. Buneman[18], Hockney[19,20], Golub and Nielson[21] all have direct methods for Poisson solving which may be adapted to this problem. In addition, the classical iteration methods[22], could also be applied but at a large expense. The Fourier method seems more flexible than these methods and is of comparable speed and so has been used here. The Fourier method also generalizes conveniently to other geometries and to three dimensions since harmonic analysis in the θ direction (or X, Y, Z) as well as the Z direction is allowed.

Relativistic Plasma Simulation

Appendix B - Generalizations of the Maxwell Equation Solver

Since the particle-pushing algorithm treats one particle at a time and only five coupled ordinary differential equations must be solved, generalization of the algorithms given or suggested here to different geometries or to three dimensions will be quite straight forward. Modification of the Maxwell-Equation algorithms including the Poisson Solver used here presents a far more difficult problem from a practical viewpoint. This Appendix considers Maxwell-Equation Solvers in other than r-z cylindrical coordinates and gives variations on the staggered leapfrog integration algorithm which have special properties for various applications. I consider first the integration of the Maxwell Equations using an implicit rather than an explicit formulation of the partial differential equations.

An implicit difference equation is one in which the time derivative terms include the quantity being solved for at the new time. For the Maxwell Equations we write, in analogy with Eqs. (10-11),

$$\underline{E}(t+\delta t) = \underline{E}(t) + \frac{c\delta t}{2}\left[\nabla_{\underline{D}} \times \underline{B}(t) + \nabla_{\underline{D}} \times \underline{B}(t+\delta t)\right]$$
$$-4\pi\delta t \ \underline{J}(t+\delta t/2),$$
$$\tag{B-1}$$

$$\underline{B}(t+\delta t) = \underline{B}(t) - \frac{c\delta t}{2}\left[\nabla_{\underline{D}} \times \underline{E}(t) + \nabla_{\underline{D}} \times \underline{E}(t+\delta t)\right].\tag{B-2}$$

In these vector equations the desired fields $\underline{E}(t+\delta t)$ and $\underline{B}(t+\delta t)$ appear explicitly on the left hand side and implicitly on the right. When the finite difference operators ∇_D are expanded, a complicated coupled system of equations is obtained which must be solved either directly or iteratively. These equations can be decoupled into 2 three-component sets in either of two manners. Equation (B-1) can be substituted into the right side of (B-2) and (B-2) into the right side of (B-1) to obtain second-order spatial equations for $\underline{E}(t+\delta t)$ and $\underline{B}(t+\delta t)$ separately.

Alternatively, the Transverse Electric $(E_\theta B_r B_z$ in r-z cylindrical and Transverse Magnetic $(B_\theta E_r E_z$ in r-z cylindrical) modes can be decoupled in solving (B-1) and (B-2). This decoupling is both convenient and physically reasonable in 2D systems. In testing the present version of CYLRAD the distinction between TE and TM radiation has been rigorously maintained and each set of cavity modes has been checked for energy conservation and numerical stability independently.

The dispersion relation for Equations (B-1) and (B-2), when the spatial derivatives are all fully staggered in Cartesian coordinates, is

$$\tan^2 \omega \delta t/2 = \frac{c^2 \delta t^2}{\delta x^2} \sin^2 k_x \delta x/2 + \frac{c^2 \delta t^2}{\delta y^2} \sin^2 k_y \delta y/2 + \frac{\omega_p^2 \delta t^2}{4} . \tag{B-3}$$

This dispersion relation differs from that found earlier, Eq.(32a), by the conversion of the $\sin^2$ term to $\tan^2$ with no other change. This means that the stability condition found earlier, because the right side of Eq. (32a) could not exceed unity for any wave vector, can be relaxed. In the fully implicit algorithm under discussion here, marginally stable oscillatory solutions exist for any δt because $\tan^2$ ranges from zero to infinity. The dispersion properties of this method are as bad as for the explicit algorithm, however, as can be seen in Figure 3 for a one-dimensional case with low plasma density. Thus the implicit algorithm, if used with substantially longer timesteps than allowed by the explicit stability condition, will suffer unacceptably large numerical dispersion in physically interesting wavelengths.

The more appropriate regime for use of the implicit formulation is in coordinate systems having a singularity. Polar cylindrical coordinates is a good example and will be considered briefly. The method also generalizes easily to r-θ-z systems since the z coordinate is particularly easy to treat and Cartesian systems, x-y and x-y-z, are even simpler. Figure 11 shows an appropriate r-θ grid whose major difference from Fig. 2 is the non-staggering of meshes in θ.

56

A MESH FOR POLAR COORDINATES
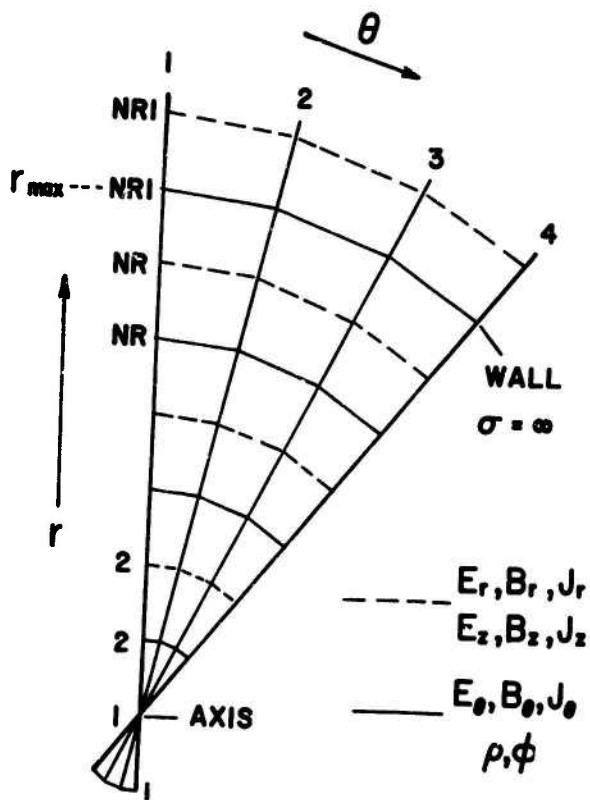
Figure 11. An r-θ mesh for the implicit integration of Maxwell's Equations. Notice the interchange of θ and z coordinates radially relative to the CYLRAD Mesh.

This added complication is removed because a fast Fourier transform of (B-1) and (B-2) in θ is to be performed to decouple the radial variation from the azimuthal variation. This transform allows derivatives in θ to be taken analytically in m-space and does not couple adjacent m values. The TE (E_z, B_r, B_θ) and TM (B_z, E_r, E_θ) equations therefore become tridiagonal systems in r for each θ harmonic labelled by m.

To pursue this in greater detail, consider the following difference-operator definitions (assuming their use in m-space for θ variations):

$$(\underline{\nabla}_D \Psi)_r(i,m) = \hat{r} \frac{\Psi(i+1) - \Psi(i)}{\delta r} , \tag{B-4}$$

$$(\underline{\nabla}_D \Psi)_\theta(i,m) = \hat{\theta} \frac{im \Psi(i)}{r_i} \tag{B-5}$$

$$(\underline{\nabla}_D \cdot \underline{A})(i,m) = \frac{1}{r_i} \frac{(r_i^+ A_r(i) - r_i^- A_r(i-1))}{\delta r} + \frac{im}{r_i} A_\theta(i), \tag{B-6}$$

$$(\underline{\nabla}_D \times \underline{A})_r(i,m) = \hat{r} \frac{im}{r_i^+} A_z(i), \tag{B-7}$$

$$(\underline{\nabla}_D \times \underline{A})_\theta(i,m) = -\hat{\theta} \frac{(A_z(i) - A_z(i-1))}{\delta r} , \tag{B-8}$$

$$(\underline{\nabla}_D \times \underline{A})_z(i,m) = \hat{z}\left[\frac{1}{r_i^+} \frac{(r_{i+1} A_\theta(i+1) - r_i A_\theta(i))}{\delta r} - \frac{im}{r_i^+} A_r(i) \right], \tag{B-9}$$

$$\nabla_D^2 \Psi(i,m) = \frac{1}{r_i}\left[\frac{r_i^+ \Psi(i+1) - 2r_i \Psi(i) + r_i^- \Psi(i-1)}{\delta r^2} \right] - \frac{m^2}{r_i^2} \Psi(i) . \tag{B-10}$$

where the radial factors are defined as

$$r_i^+ \equiv (i-1) \delta r$$

$$r_i \equiv (i-3/2) \delta r , \tag{B-11}$$

$$r_i^- \equiv (i-2) \delta r .$$

58

Here "m" can be replaced by any particular finite difference analogue, say $\frac{\sin m\,\delta\theta}{\delta\theta}$, for the θ derivative if desired.

When these definitions are substituted into (B-1) and (B-2), the following two systems of tridiagonal finite-difference equations are obtained

$$B_r(t+\delta t,i) = \left[B_r(t,i) - \frac{c\,\delta t}{2}\left(\underline{\nabla}_D \times \underline{E}(t)\right)_r(i)\right] - \frac{imc\,\delta t}{2r_i^+}\,E_z(t+\delta t,i),$$

$$B_\theta(t+\delta t,i) = \left[B_\theta(t,i) - \frac{c\,\delta t}{2}\left(\underline{\nabla}_D \times \underline{E}(t)\right)_\theta(i)\right]$$

$$+ \frac{c\,\delta t}{2\delta r}\left(E_z(t+\delta t,i) - E_z(t+\delta t,i-1)\right),$$

$$E_z(t+\delta t,i) = \left[E_z(t,i) + \frac{c\,\delta t}{2}\left(\underline{\nabla}_D \times \underline{B}(t)\right)_z(i) - 4\pi\delta t J_z\right]$$

$$+ \frac{c\,\delta t}{2r_i^+}\left[\frac{r_{i+1}\,B_\theta(t+\delta t,i+1) - r_i\,B_\theta(t+\delta t,i)}{\delta r}\right] \tag{B-12}$$

$$- \frac{c\,\delta t}{2r_i^+}\,imB_r(t+\delta t,i)$$

for Transverse Electric modes and

$$E_r(t+\delta t,i) = \left[E_r(t,i) + \frac{c\,\delta t}{2}\left(\underline{\nabla}_D \times \underline{B}(t)\right)_r(i) - 4\pi\delta t J_r\right]$$

$$+ \frac{c\,\delta t}{2r_i^+}\,im\,B_z(t+\delta t,i),$$

$$\tag{B-13}$$

$$E_\theta(t+\delta t,i) = \left[E_\theta(t,i) + \frac{c\,\delta t}{2}\left(\underline{\nabla}_D \times \underline{B}(t)\right)_\theta(i) - 4\pi\delta t J_\theta\right]$$

$$- \frac{c\,\delta t}{2\delta r}\left[B_z(t+\delta t,i) - B_z(t+\delta t,i-1)\right],$$

$$B_z(t+\delta t, i) = \left[B_z(t,i) - \frac{c\delta t}{2} \left(\underline{\nabla}_D \times \underline{E}(t) \right)_z(i) \right]$$

$$- \frac{c\delta t}{2r_i^{\nabla}} \left[\frac{r_{i+1} E_\theta(t+\delta t, i+1) - r_i E_\theta(t+\delta t, i)}{\delta r} \right] \qquad (B-13)$$

$$+ \frac{c\delta t}{2r_i^{\nabla}} \; imE_r(t+\delta t, i)$$

for Transverse Magnetic modes. In both the TE and the TM cases the equations to be solved can be reduced to a single scalar tridiagonal system. For example, in Eqs. (B-12) for TE radiation, the equations for $B_r(t+\delta t, i)$ and $B_\theta(t+\delta t, i)$ can be substituted into the equation for $E_z(t+\delta t, i)$. Once the resultant scalar equation is solved, $B_r(t+\delta t, i)$ and $B_\theta(t+\delta t, i)$ can be found explicitly by substitution. This algorithm has the disadvantage of requiring Fourier transforms, in θ, of all the field variables. Longer time steps can be taken, however. This algorithm also suffers in that the dielectric matrix technique mentioned earlier and discussed in Appendix C can only be used in axially symmetric configurations. There is the compensation that Fourier smoothing techniques can be applied in θ and somewhat coarser θ resolutions can be allowed than would be possible using an unsmoothed finite-difference approach.

In 3D cylindrical and in 2D and 3D Cartesian coordinates similar equations are obtained. In each case the implicit equations can be solved directly without iteration by Fourier transforming in all but one of the dimensions and then solving the resultant scalar tridiagonal equation by a two-sweep Gaussian reduction as used in the CYLRAD Poisson solver.

The Fourier harmonics labelled by k in the z direction and by m in the θ direction can be treated "exactly" in the following sense: The $\sin^2$ terms on the right hand side of Eq. (B-3) get replaced by the corresponding analytic derivatives. Thus, if Fourier analysis were used for both the x and the y derivatives in Eq. (B-3), one would have (for Cartesian coordinates)

Relativistic Plasma Simulation

$$\frac{\tan^2 \omega \delta t/2}{\delta t^2/4} = c^2(k_x^2 + k_y^2) + \omega_p^2 . \tag{B-14}$$

The only dispersion remaining arises from the finite timestep used in the integration. This result suggests a fully dispersionless integration of the Maxwell Equations in Cartesian systems where Fourier analysis is possible in all directions. Rather than using a finite difference integration in time, giving rise to a dispersion relation like Eq. (B-14), the correct dispersion relation

$$\omega^2 = c^2(k_x^2 + k_y^2) \tag{B-15}$$

can be used to advance the phase of each of the Fourier harmonics analytically. When this is done, no numerical dispersion is present, only the aliasing which occurs because a finite discrete representation of an essentially continuous system cannot be avoided. This method of dispersionless integration would allow much more accurate treatment of short wavelengths and would permit much longer runs with strong phase coherence of waves in systems where (B-15) applies.

The treatment of the plasma sources would be somewhat more complicated than indicated above in Eq. (B-15) and would involve the charge-current considerations mentioned earlier in connection with the CYLRAD algorithm. These problems are all handled quite easily and accurately in k-space however. One such problem arises in the form of a numerical inaccuracy because the source $\underline{J}(t+\delta t/2)$ will be assumed constant over a timestep when advancing the amplitude and phase of the (k_x, k_y) mode. The (k_x, k_y) component of $\underline{J}$ must actually be reduced by about $\dfrac{\sin\left[\omega(k_x, k_y) \, \delta t/2\right]}{\omega(k_x, k_y) \, \delta t/2}$ to reduce this inaccuracy. This is just the factor by which $\dfrac{1}{\delta t}\displaystyle\int_0^{\delta t} \underline{J}_o \, e^{-i\omega t} dt$ differs from $\underline{J}_o \cdot e^{-i\omega \delta t/2}$, the value of the current at the center of the timestep.

61

Appendix C - Spatially Varying Dielectrics

The general purpose Maxwell Equation solver discussed in Section II can be generalized very simply to include the presence of a spatially varying dielectric. The properties of this dielectric medium are assumed to be time and frequency independent. The pertinent Maxwell Equations become

$$\frac{\partial \underline{D}^*}{\partial t} = c \, \underline{\nabla}_D \times \underline{B} - 4\pi \underline{J} \, , \tag{C-1}$$

$$\frac{\partial \underline{B}}{\partial t} = -c \, \underline{\nabla}_D \times [\, \underline{D}/\epsilon \,] \, , \quad \text{and} \tag{C-2}$$

$$\underline{\nabla}_D \cdot \underline{D} = 4\pi\rho \, . \tag{C-3}$$

The superscript * in Eq. (C-1) indicates that the $\underline{D}^*$ contains, in principle, error components in the longitudinal field due to discrepancies between ρ and $\underline{J}$ as discussed in detail in Sections II, IV, and in Appendix A. These error components can still be eliminated using the Poisson Equation arising from (C-3), as before, with simple boundary conditions on $\delta\phi$, regardless of the spatial distribution of dielectric, $\epsilon(r,z)$. In CYLRAD the quantity $1/\epsilon(r,z)$ is stored in a matrix defined at the θ mesh of Fig. 2. The values of $\frac{1}{\epsilon}$ on the other meshes are found by interpolation from the stored values when needed.

The term $\underline{D}/\epsilon$ is found by a multiply inside the difference operator $\underline{\nabla}_D \times$ and thus $\underline{\nabla}_D \cdot \underline{B} = 0$ is still assured. Furthermore $\underline{D}_\ell$ (longitudinal) arises only from $\underline{J}_\ell$, as required by physics although $\underline{D}_t$ (transverse) can arise in part from $\underline{J}_\ell$ through coupling caused by the $1/\epsilon$ term in Eq. (C-2). The usual boundary conditions $\underline{E}_\parallel$ continuous, $\underline{D}_\perp$ continuous, at a dielectric interface with no surface charge are also preserved in the staggered leapfrog solution of the finite-difference Maxwell Equations. Thus a very complicated elliptic boundary

62

value problem is solved in an essentially simple manner by solving the causal, hyperbolic, time-dependent physical equations.

The quantity D/ϵ is the electric field, of course. When $E_{\parallel}$ is not continuous across a dielectric interface, the curl of E is also non-zero so a burst of radiation is emitted through time variation of the magnetic field. This source of $\partial B/\partial t$ turns off when the boundary condition is satisfied. The method is sufficiently flexible to allow perfectly-conducting metallic boundary conditions to be simulated. By setting $1/\epsilon = 0$ in some region, the electric fields in that region are brought to zero. The longitudinal displacement D does not even see these complicated ϵ-metal regions, however, so a very simple set of boundary conditions is retained for the Poisson Equation and the difference-formula integration. The importance of being able to solve the wave equations with arbitrary dielectric media in the calculation cannot be overstated. Very complicated problems become easily tractable. Cherenkov radiation of particles traveling through dielectric media at velocities faster than the light velocity in the medium can be studied in a detailed way for quite general dielectric-particle configurations. Complicated dielectric wave guide and transformer problems become tractable. Most important of all is the ability to treat radiation and plasma in fairly arbitrary metallic containers.

When ϵ approaches infinity in a dielectric, the medium imitates metallic behavior because the polarization charge becomes almost totally free to move and therefore moves as would the equivalent conduction charges in a metal. If a point charge is imbedded in an ϵ-metal, for instance, the "metal" polarizes and all the charge from the point particle appears at the surface of the ϵ-metal region since E is zero inside. Further, since the equilibrium $E_{\parallel}$ must be continuous across the ϵ-metal bounding surface, and since E is zero inside, the

63

electric field leaving the ϵ-metal will become perpendicular to the surface when all the radiation fields from initial transients have been damped away. This means that very complex electrostatic problems, as well as time-dependent electromagnetic problems can be solved quite trivially by CYLRAD.

The equations can undoubtedly also be generalized to treat problems where a spatially varying $\mu(r,z)$, the permeability, is included. In many cases it may be necessary, in fact, to run the entire problem with a false value of μ in order to scale the electric and magnetic fields in a convenient way so that the scale length c/ω_{pe} and $\lambda_{D_e} \equiv V_{th}/\omega_{pe}$ will not be too disparate. An equivalent way of looking at this is to rescale c or to decouple the electrostatic and electromagnetic masses of the particle.

REFERENCES

1. J. A. Byers and M. Grewal, "Perpendicularly Propagating Plasma Cyclotron Instabilities Simulated With a One-Dimensional Computer Model," *Physics of Fluids* 13 (7), 1819-1831, July 1970.

2. R. N. Carlile, "Quasi Three-Dimensional Particle Code for Simulating an Anisotropic Plasma," *Fourth Conference on the Numerical Simulation of Plasmas*, proceedings, Naval Research Laboratory, Washington, D. C., 2-3 November 1970.

3. J. P. Boris, J. H. Orens, J. M. Dawson and K. V. Roberts, "Computations on Anomalous Resistance," *Phys. Rev. Letters* 25 (11), p. 706 (1970).

4. R. D. Burn, "Computer Experiments on Sheet Pinch Stability," *Plasma Physics* 12, pp 331-339 (1970).

5. R. C. Davidson, I. Haber, D. A. Hammer, and C. E. Wagner, *Bull. Am. Phys. Soc.* 15, 1436 (1970); also D. A. Hammer, J. P. Boris, R. C. Davidson, J. M. Dawson, I. Haber, and C. E. Wagner, *Bull. Am. Phys. Soc.* 15, 1436 (1970).

6. R. L. Morse and C. W. Nielson, "Numerical Simulation of the Weibel Instability in One and Two Dimensions," Los Alamos Report LA-4482, July 1970.

7. R. C. Davidson, I. Haber, D. A. Hammer, "Transverse Electromagnetic Instabilities in Collisionless Plasmas," to be published.

8. E. W. Weibel, *Phys. Rev. Letters* 2, 83 (1959).

9. C. G. Darwin, *Phil. Mag.* 39, 537 (1920). See also Landau and Lifshitz, *Classical Theory of Fields*, § 65, or J. D. Jackson, *Classical Electrodynamics*, § 12.6.

10. I. Haber, C. E. Wagner, J. P. Boris, and J. M. Dawson, "A Self-Consistent Electromagnetic Particle Code," *Fourth Conference on Numerical Simulation of Plasmas*, proceedings, Naval Research Laboratory, Washington, D. C., 2-3 November 1970.

11. A. G. Kulikovskiy and G. A. Lyubimov, *Magnetohydrodynamics*, Addison-Wesley Publishing Company, Inc., Palo Alto, (1965).

12. O. Buneman, "Fast Numerical Procedures for Computer Experiments on Relativistic Plasmas," in *Relativistic Plasmas - The Coral Gables Conference*, University of Miami, 1968, ed. O. Buneman & W. Pardo, (W. A. Benjamin, N. Y., 1968).

13. O. Buneman, *Journal of Computational Physics* 1, 517 (1967).

14. R. W. Hockney, *Journal of the Association for Computing Machinery*, 12 (1), pp 95-113 (1965).

15. J. P. Boris and K. V. Roberts, "The Optimization of Particle Calculations in 2 and 3 Dimensions," *J. Comp. Phys.* 4 (4), (Dec, 1969).

16. J. P. Boris, "The Acceleration Calculation from a Scalar Potential," Princeton Plasma Physics Laboratory Report MATT-769, (March 1970).

65

17. K. H. Sinz, "Formulation of Self-Consistent 2- and $2\frac{1}{2}$- Dimensional Electromagnetic and Relativistic Simulations," <u>Fourth Conference on the Numerical Simulation of Plasmas</u>, proceedings, Naval Research Laboratory, Washington, D. C., 2-3 November 1970.

18. O. Buneman, "A Compact Non-Iterative Poisson Solver," Stanford University Institute for Plasma Research Report 294, (May 1969).

19. R. W. Hockney, "The Potential Calculation," Proc. APS Topical Conference on Numerical Simulation of Plasma, Los Alamos, IA-3990, paper D6 (1968).

20. R. W. Hockney, "The Potential Calculation and Some Applications," Chapter in <u>Methods in Computational Physics</u>, vol. 9, ed. B. Alder, S. Fernbach, and Manuel Rotenberg (Academic Press, New York 1970).

21. B. L. Buzbee, G. H. Golub, and C. W. Nielson, Technical Report No. CS 128, Computer Science Department, Stanford University, April 1969.

22. R. S. Varga, <u>Matrix Iterative Analysis</u>, Prentice Hall, Englewood Cliffs, New Jersey 1926.

23. G. J. Haltiner, "Numerical Weather Prediction," Navy Weather Research Facility 30--768-142, (July 1968).

24. J. P. Boris and J. H. Orens, "Topics in Optimization for Computational Plasma Physics," to be published.

25. J. H. Orens, J. P. Boris, and I. Haber, "Optimization Techniques for Particle Codes," <u>Fourth Conference on the Numerical Simulation of Plasmas</u>, proceedings, Naval Research Laboratory, Washington, D. C., 2-3 November 1970.

26. J. P. Boris, "Three-Dimensional Magnetohydrodynamics - Optimization of a Fluid Code," to be published.

27. J. P. Boris, "The Solution of Partial Differential Equations Using a Symbolic Style of Algol," NRL Memorandum Report 2168, Naval Research Laboratory, Washington, D. C., 1970.

28. N. K. Winsor and E. Bowers, "Choice of Grids in Low β Fluid Computations," <u>Fourth Conference on the Numerical Simulation of Plasmas</u>, proceedings, Naval Research Laboratory, Washington, D. C., 2-3 November 1970.

29. K. V. Roberts and J. P. Boris, "The Solution of Partial Differential Equations Using a Symbolic Style of Algol," to be published in <u>Journal of Computational Physics.</u>

30. C. E. Wagner (private communications, Jan. - April 1970).

31. C. K. Birdsall, D. Fuss, and A. B. Langdon (private communications, Plasma Simulation Users Conference, Livermore, California 1968).

32. C. K. Birdsall and D. Fuss, <u>Journal of Computational Physics</u> 3, pp 494-511 (1969).

33. A. B. Langdon and J. M. Dawson, "Investigations of A Sheet Model for a Bounded Plasma with Magnetic Field and Radiation," Memorandum ERL-M-257, Electronics Research Laboratory, University of California, Berkeley, January 1969; also Bull. Am. Phys. Soc. 12 (15), 806 (1966).

34. A. B. Langdon and C. K. Birdsall, "Theory of Plasma Simulation Using Finite Size-Particles," Physics of Fluids 13 (8), p. 2115-2123, August 1970.

35. H. Okuda, "Non-Physical Instabilities in Plasma Simulation due to Small $\lambda_D / \Delta X$," Fourth Conference on the Numerical Simulation of Plasmas, proceedings, Naval Research Laboratory, Washington, D. C., 2-3 November 1970.

36. G. Hsi, J. M. Dawson, J. P. Boris, and W. Kruer, Bull. Am. Phys. Soc. 13, 1555 (1968).

37. J. P. Boris and A. B. Langdon, "The Acceleration Calculation in Numerical Simulation," to be published.

38. R. L. Morse, "Multidimensional Plasma Simulation by the Particle-in-Cell Method," Chapter in Methods in Computational Physics, vol. 9, ed. B. Alder, S. Fernbach, and Manuel Rotenberg (Academic Press, New York 1970).

39. K. V. Roberts and D. E. Potter, "Magnetohydrodynamic Calculations," Chapter in Methods in Computational Physics, vol. 9, ed. B. Alder, S. Fernbach, and Manuel Rotenberg (Academic Press, New York, 1970).

40. J. Byers, "Noise Suppression Techniques in Macroparticle Models of Collisionless Plasmas," Fourth Conference on the Numerical Simulation of Plasmas, proceedings, Naval Research Laboratory, Washington, D. C., 2-3 November 1970.

41. J. Denavit, "Numerical Solutions of the Vlasov Equation," Fourth Conference on the Numerical Simulation of Plasmas, proceedings, Naval Research Laboratory, Washington, D. C., 2-3 November 1970.

67

Bit-Pushing and Distribution-Pushing Techniques
for the Solution of the Vlasov Equation*

K. R. Symon, D. Marshall, and K. W. Li
Department of Physics
University of Wisconsin
Madison, Wisconsin

ABSTRACT

In a bit-pushing program a plasma is simulated by manipulating a pattern
of bits in the computer memory representing the pattern of particles in phase
space. The method is analyzed and compared with conventional particle-
pushing techniques. In a distribution-pushing program the particle distribu-
tion function is modified according to the leap-frog equations of motion for
the particles. Algorithms are developed for accuracy and efficiency. Sample
results of both kinds of programs are presented. Results are presented from
a one and one half dimensional distribution pushing program simulating a plasma
beam emerging from a circular hole.

Techniques for Solution of Vlasov Equation

I. INTRODUCTION

In this paper we present two approaches to the computer simulation of plasmas which have been investigated as ways of economizing on memory storage space and time required for the solution. In order to illustrate the method, we will consider primarily one dimensional problems. Programs utilizing these methods for one and one half and two dimensional problems are under development.

We wish to find the behavior of a system of particles of a single species moving according to the equations:

$$\dot{x}_j = v_j, \quad \dot{v}_j = a(x_j), \tag{1}$$

where x_j, v_j are the coordinate and velocity of the jth particle and the acceleration is given by

$$a(x_j) = a_e(x_j) + \sum_{i \neq j} K(x_j - x_i), \tag{2}$$

where $K(x)$ is the force (per unit mass) between two particles a distance x apart, and where $a_e(x)$ is the acceleration due to the externally applied force, if any, on a particle at position x. The force kernel $K(x)$ may have various forms depending upon the particular problem to be simulated. Typical examples are shown in Fig. 1. For the case of a Coulomb force between plane
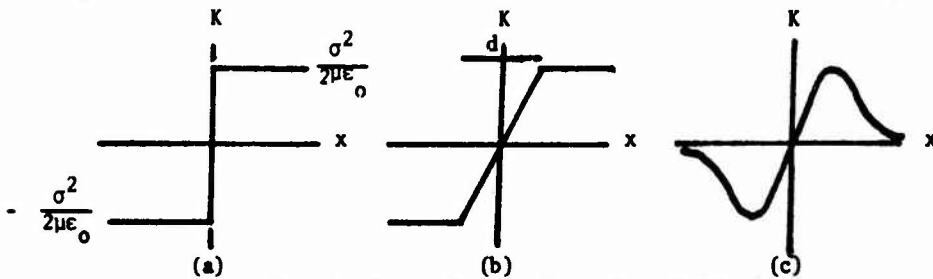
Fig. 1. Forms for the force kernel $K(x)$.

69

charged sheets, the kernel has the form shown in Fig. 1(a), where σ is the charge density per unit area and μ is the mass density per unit area. If we take the charged sheets to have a finite thickness d, then the abrupt step becomes modified as shown in Fig. 1(b); this is also the form for the force kernel associated with the cloud in cell model in one dimension. If we are dealing with a beam of particles of finite cross-section, the kernel will have the form shown in Fig. 1(c), where the force falls off at large distances as $1/x^2$ if the beam is in empty space, and falls off exponentially if the beam is confined between conducting walls. We will assume that the plasma is contained within a length L along the x-axis, $-\tfrac{1}{2}L < x \leq \tfrac{1}{2}L$. We will take periodic boundary conditions, that is we will assume that for every particle in this interval there is an identical particle at the same relative point in every other interval of length L along the x-axis. For this reason it will usually be convenient to choose a kernel of the form 1(c) for which the force between two particles falls to zero before they reach a distance L apart.

The energy integral for the above equations is

$$E = \sum_j \tfrac{1}{2}v_j^2 + \sum_j V_e(x_j) + \sum_{\text{all pairs } i,j} V_p(x_j - x_i) \tag{3}$$

where the external and pair potential energies are given by

$$V_e(x) = -\int^x a_e(x)\, dx, \tag{4}$$

$$V_p(x) = -\int^x K(x)\, dx. \tag{5}$$

If we use the coulomb kernel 1(a) for a large number of charge sheets distributed with a density $\kappa(x)$ per unit length, then the electric field is given by

$$\mathcal{E}(x) = \frac{\mu}{\sigma} \int K(x-x') \; \kappa(x') \; dx', \tag{6}$$

and we can show that the third term on the right in Eq. (3) reduces to the usual formula for the electrostatic potential energy:

$$\frac{1}{2} \iint \kappa(x)\kappa(x') \; V_p(x-x') \; dxdx' = \int \frac{1}{2}\epsilon_0 \mathcal{E}^2(x) \; dx \tag{7}$$

The Vlasov equation corresponding to this problem is

$$\frac{\partial f}{\partial t} + v \frac{\partial f}{\partial x} + a(x) \frac{\partial f}{\partial v} = 0, \tag{8}$$

$$a(x) = a_e(x) + \iint K(x-x') \; f(x',v') \; dx'dv'. \tag{9}$$

The linear dispersion relation for waves of wave number k, frequency ω is readily shown to be

$$1 + \frac{\omega_k^2}{k} \int \frac{\partial g/\partial v}{\omega - kv} \; dv = 0, \tag{10}$$

where $g(v)$ is the unperturbed velocity distribution,

$$f_{unperturbed}(v) = \kappa g(v), \quad \int g(v)dv = 1, \tag{11}$$

where κ is the number of particles per unit length along x, and where

$$\omega_k^2 = LkK_k. \tag{12}$$

We have assumed that the kernel $K(x)$ is an odd function of x and have expanded it in a Fourier series:

$$K(x) = \sum_{k=2\pi n/L} 2K_k \sin kx . \tag{13}$$

For the coulomb kernel 1(a) for plain sheets, kK_k has the constant value

$$kK_k = \sigma^2/L\mu\epsilon_0. \tag{14}$$

71

and ω_k is independent of k and is just equal to the plasma frequency

$$\omega_k^2 = \omega_p^2 = \kappa\sigma^2/\mu\epsilon_0 = ne^2/m\epsilon_0. \tag{15}$$

For finite thickness sheets, the Fourier coefficients of the kernel have the value (14) for long wavelengths, but approach zero for wave lengths shorter than the thickness d. For the kernel 1(c), the quantity kK_k falls to zero for both long and short wavelengths; we may in this case define the plasma frequency by the formula (12) for the value of k for which kK_k is a maximum.

Throughout this paper we will assume that the motion of the particles may be computed by using the standard leap-frog algorithm. We divide the time axis into intervals τ according to

$$t_n = n\tau. \tag{16}$$

The positions x are to be calculated at integer time points t_n, and the velocities v at half integer time points. The leap-frog advancement algorithm is then

$$v_{j,n+\frac{1}{2}} = v_{j,n-\frac{1}{2}} + a(x_{jn})\tau,$$
$$\tag{17}$$
$$x_{j,n+1} = x_{jn} + v_{j,n+\frac{1}{2}}\tau.$$

II. BIT-PUSHING PROGRAMS

Let us divide the fundamental period L along the x axis into J intervals each of length h, (L = Jh). Let us likewise choose a maximum and minimum velocity v_{max}, v_{min} which are relevant to a particular problem, and let us divide the interval $(v_{max} - v_{min})$ into I intervals each of length g, $(v_{max} - v_{min} = Ig)$. The intervals h and g are to be chosen sufficiently small so that they represent the maximum precision with which we care to

specify the positions and velocities of the particles. The phase space for the problem is now divided up into IJ cells. We may locate any particle by specifying the cell in which its position and velocity are located. Conversely, we may describe the particle distribution by specifying the cells which are occupied by particles.

In a bit-pushing program, a rectangular array of IJ bits is reserved in the memory, each bit correlated with a cell in the rectangular phase space. A cell which is occupied by a particle is denoted by a one bit. A zero bit denotes an unoccupied cell. This pattern of bits is then pushed according to the leap-frog algorithm (17). At a half-integer time step, each row corresponding to a particular velocity is advanced in the x direction by an appropriate increment vτ. At an integer time step, each column corresponding to a particular position is advanced in the velocity direction by an increment aτ. Some time can be saved in the computation by utilizing the fact that at a given time step all bits in a given row or column are advanced at the same time and by the same number of intervals. Even more time could be saved in a computer whose logic is well suited to pattern manipulation. Since the same J intervals along the x-axis are used in calculating the acceleration field, no interpolation or area weighting is required.

We have found it convenient to align words in the phase-space memory bank along the velocity direction. That is, a complete word corresponds to a group of phase cells having different velocities at a single position x. The velocity increments at an integer time step can then be accomplished simply by a series of shifts. Pushing a row in the x direction at a half-integer time step requires an individual examination and manipulation of each bit on present computers. Such an examination is in any case required to

perform the sum appearing in Eq. (2) for the self field. In order to facilitate the calculation of this sum, we store in a linear array of J words the number of particles in each x interval (the density). When a row is to be shifted at the half-integer time step, we scan along the row, noting those points at which there is a change from a zero to a one or from a one to a zero bit. The appropriate succeeding bits are corrected and at the same time the corresponding densities are corrected. Thus if we encounter a sequence of empty or full cells we need make no changes until we come to the end of the sequence. At each half-integer or integer time step the increment $v\tau$ or $a\tau$ is calculated according to the algorithm (17) and rounded off to the nearest integer number of position intervals h or velocity intervals g, for each row to be moved. If the round is unbiased and if the remainder is discarded, a random error of $h/\sqrt{6}$ or $g/\sqrt{6}$ (rms) is made in the position or velocity at each half-integer or integer time step. This error can be reduced by accumulating the rounded off remainders for each row and column and adding the accumulated remainders to the calculated increments at the next time step. A particle which stays in a given row at a particular velocity then suffers no net position error during successive position increments until it is shifted to another velocity row, whereupon it suffers an rms position increment $h/\sqrt{6}$. This procedure reduces the round-off error considerably in those cases where increments in position or velocity per time step are of the order of or less than one interval h or g. There is little improvement when the increments are many intervals per time step.

A similar scheme has been used by Miller and Prendergast[1] in the simulation of many-body problems in galactic astronomy. Miller and Prendergast avoid the round-off error by choosing position, velocity, and time increments so that

$g\tau$ = h. All position increments are then integral multiples of h. Miller and Prendergast quantize the forces so that $a\tau$ is always an integer multiple of $\cdot$g. The round-off error then effectively appears only in the quantization of the force. This procedure seems to place very severe restrictions on the choice of parameters unless a very large number of phase cells is used.

A little reflection will show that the following theorem is true:

Theorem. A bit-pushing program with $J = 2^j$ position intervals and $I = 2^i$ velocity intervals is precisely equivalent and will give identical results to a conventional particle-pushing program in which the positions and velocities of the particles are stored as fixed-point numbers of i and j bits respectively. If the same round-off procedures are used in both cases for the position and velocity increments, then the round-off errors will also be the same.

If floating point numbers are used for the positions and velocities in the particle-pushing code then the equivalence is not precise, but it is still very close if the numbers of significant bits in the position and velocity are j and i. If we assume that the precisions j and i in position and velocity may be freely chosen, then once they are chosen and once the number of particles has been chosen, it is entirely a matter of economy in memory space and in computing time whether we choose to push bits or to push particles.

The number of memory bits required to store the particle distribution in a bit-pushing program is

$$N_{bp} = 2^{i+j}. \tag{18}$$

The number required to store the same information in the corresponding particle-pushing program is

$$N_{pp} = N_p (i+j), \tag{19}$$

75

where N_p is the number of particles. So far as memory space is concerned, the bit-pushing program will be more economical then the particle-pushing program when the ratio

$$\frac{N_{pp}}{N_{bp}} = (i+j) \frac{N_p}{2^{i+j}} \tag{20}$$

is greater than one. Bit-pushing programs are generally run with a mean particle density per phase cell $N/2^{i+j}$ of the order of 1/3 or 1/4, and with $i + j$ of the order of 15 to 20. Under these conditions, the bit-pushing program is evidently more efficient, as might be expected. Conversely, particle-pushing programs are normally run with $i + j$ of the order of 50 and with N of the order 2^{12} or more. Under these conditions, the particle-pushing program is more efficient, and a bit-pushing program would be out of the question.

We are also interested in comparing the economy of time. The relative computing time for the two programs depends rather sensitively upon the computer which is used, and in particular upon the machine-language vocabulary which is available. One might imagine an ideally flexible computer in which computing time would be strictly proportional to the number of bits to be manipulated. Although this ideal is not very closely approximated with existing computers, we will confine our comparison of the two programs to the number of memory bits which must be reserved in each case, and assume that the computing times required will be at least roughly proportional.

Let us imagine an ideal computer in which the word length is entirely flexible. For a given total storage capacity N_{pp} in a particle-pushing program, we are then free to trade off the word lengths i and j against the number N_p of particles to be followed. In most computers this trade off can in fact to a considerable extent be made by using word packing techniques. We may then ask the question, for a particular problem to be simulated, what is

the optimum trade-off among these parameters. If we could answer this question, we could then compare the numbers N_{pp} and N_{bp} to determine for the optimum case whether a bit-pushing or a particle-pushing program would be more efficient. Unfortunately, we do not as yet have any satisfactory answer to this question. The following paragraph presents a preliminary approach.

Let us consider a problem in which the relevant phase space is divided up into 2^{i+j} cells, (see Fig. 2). Let us assume that the smallest relevant phase element for the problem to be simulated, that is the size of the smallest bundle of particles to be distinguished, is a rectangle of dimensions $\xi\nu$. Let the entire phase rectangle be divided into $k\ell$ elements of area $\xi\nu$, where

$$L = \ell\xi, \quad v_{max} - v_{min} = k\nu. \tag{21}$$

Let the total time period during which the system is to be followed be $T = n\tau$. If an unbiased round is used for the position and velocity increments and if the remainders are discarded, the rms error in position and velocity of a particle at the end of the calculation due to round-off errors will be

$$\sigma_x = hn^{\frac{1}{2}}/\sqrt{6}, \quad \sigma_v = gn^{\frac{1}{2}}/\sqrt{6}. \tag{22}$$
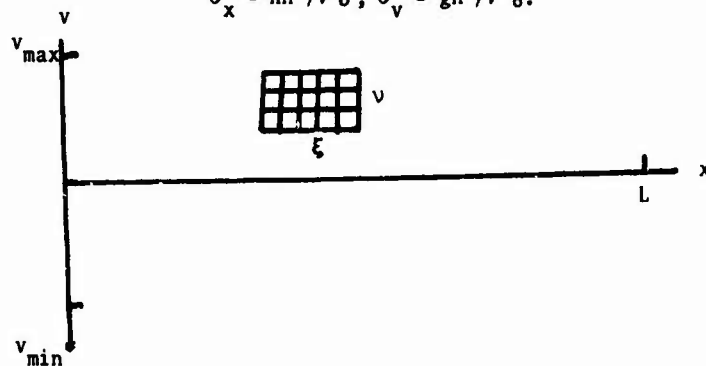
Fig. 2. Relevant element in phase space.

77

The number of bits in the phase element $\xi\nu$ must then be at least

$$\xi\nu/hg \geq n/6, \tag{23}$$

if round-off is not to carry a particle out of the element $\xi\nu$. If the minimum relevant particle density is f_{min}, and if we wish to determine this density to within an rms fractional error $\cdot$, then the minimum number of particles in the phase element must be

$$\xi\nu f_{min} = 1/p^2. \tag{24}$$

Let the ratio of the mean overall phase density $\bar{f}$ to the minimum phase density be

$$R_1 = \bar{f}/f_{min}. \tag{25}$$

The minimum number of particles which must be followed is then

$$N_p = k\ell\, R_1/p^2. \tag{26}$$

If the ratio of the maximum to the mean phase density is

$$R_2 = f_{max}/\bar{f}, \tag{27}$$

then the maximum number of phase cells in a phase element $\xi\nu$ must be at least

$$\xi\nu/hg \geq \xi\nu f_{max} = R_1 R_2/p^2. \tag{28}$$

We have then for the required number of phase cells, depending upon whether we take the limit given by equation (23) or (28) (whichever is greater),

$$2^{i+j} = \begin{cases} k\ell n/6, & \text{for (23), or} \\ k\ell R_1 R_2/p^2, & \text{for (28).} \end{cases} \tag{29}$$

Correspondingly, the ratio (20) is given by

$$\frac{N_{pp}}{N_{bp}} = \begin{cases} \frac{6}{np^2} R \, l \ln_2 \left(k l n / 6 \right), & \text{for (23), or} \\ \frac{1}{R_2} \ln_2 \left(k l R_1 R_2 / p^2 \right), & \text{for (28).} \end{cases} \tag{30}$$

If for example we choose $p = 1/8$, $R_1 = R_2 = 2$, $k = l = 8$, $n = 256$, then Eq. (28) is the appropriate limit, and we find $N_{pp}/N_{bp} = 7$, so that the bit pushing algorithm would appear to be more efficient in this case. For these parameters, we find $\xi \nu / hg = 256$, $2^{i+j} = 16,384$, $i = j = 7$, $N_p = 8,192$. As the number of time steps to be computed increases, the limit (23) will eventually prevail, and we can then see from formula (30) that for a sufficiently large number of time steps the particle-pushing program eventually wins out. The reader may enter his own numbers and juggle the formulas.

Some preliminary observations of the two stream instability have been made with the bit pusher.[2] The Coulomb kernel (Fig. 1a) was used. The phase space was 216 x 216 bits square, for a length of 38 λ_D. A total of 15,500 particles, approximately one third of the number of cells, were used. The length of the runs was 9.6 T_p, where $T_p = 2\pi \omega_p^{-1}$. In Fig. 3a, b, and c we show total and potential energy vs time for three different time steps, approximately 0.1 T_p, 0.05 T_p, and 0.025 T_p. These runs were made on a univac 1108, using approximately one, one and one half, and two minutes of computing time, respectively, not including time to output results.

Initially all phase cells in velocity rows ±19 to ±54 were filled, to give two uniform rectangular beams, and rows ±18 were half filled randomly to provide a spatial density perturbation of 1.3%. For the large time step, note the oscillation in total energy. This has an amplitude of ~1% of the total energy, or ~20% of the variations in potential energy. The oscillation
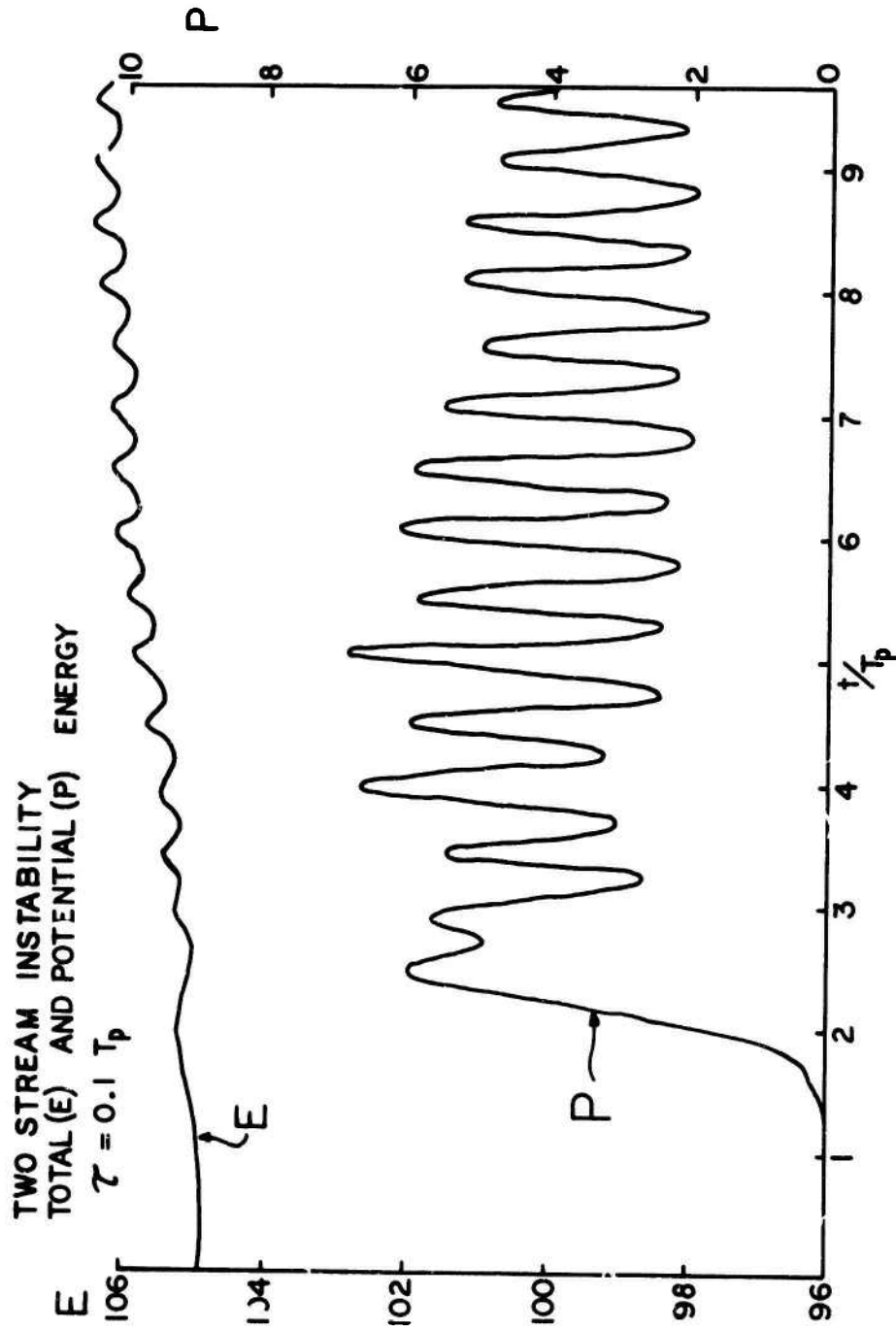
FIGURE 3a.   TWO STREAM INSTABILITY

TWO STREAM INSTABILITY
TOTAL (E) AND POTENTIAL (P) ENERGY
$\tau = 0.05\, T_p$
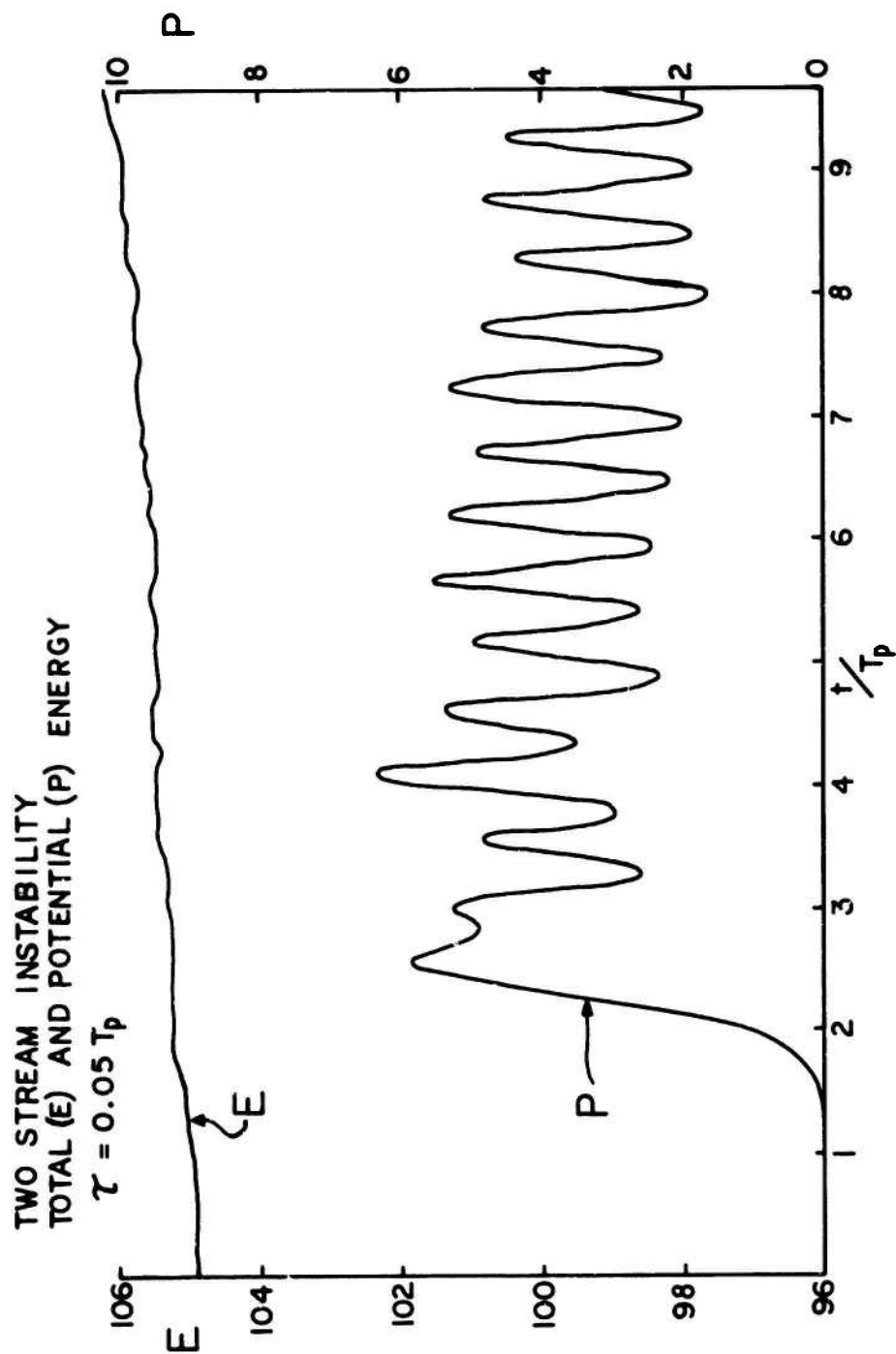
FIGURE 3b. TWO STREAM INSTABILITY

81

TWO STREAM INSTABILITY
TOTAL (E) AND POTENTIAL (P) ENERGY
$\tau = 0.025\ T_p$
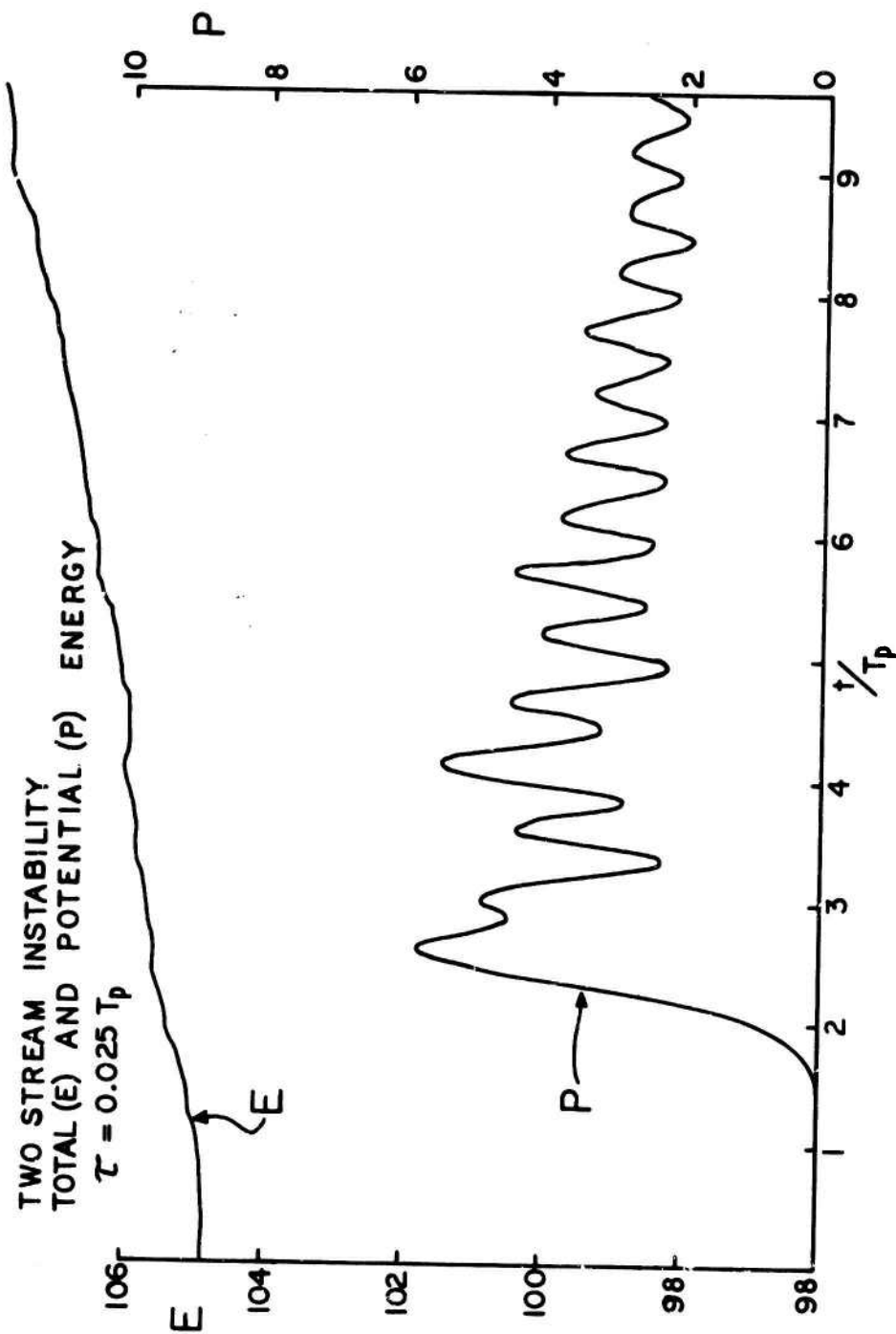
FIGURE 3c. TWO STREAM INSTABILITY

is caused by truncation error, and its amplitude is proportional to τ^2. As
the time step is reduced, he oscillation disappears and a steady growth in
total energy appears. This growth is due to increasing round-off errors,
and is proportional to the number of time steps. The round-off also causes
an apparent damping of the nonlinear oscillations, for the smallest time step.
As the round-off errors accumulate, the potential energy is reduced due to a
"smearing" of the density. At the same time, "smearing" in velocity space
causes the kinetic energy to increase. The sum of these two effects appears
as a growth in total energy. The time step $0.05\ T_p$ represents the best compro-
mise between truncation and round-off errors.

Methods of removing the order τ^2 truncation error are now being investi-
gated. If this error were removed, a larger time step could be used,
resulting in further reduction of round-off errors.

111. DISTRIBUTION-PUSHING ALGORITHMS

Let us assume that for a particular problem to be simulated, the leap-
frog algorithm (17) with an appropriately chosen time step has adequate accuracy.
Let us then replace the actual system of particles moving according to Eqs. (1)
by a system of leap-frogging particles moving according to Eqs. (17). The
Vlasov equations describing the behavior of a system of leap-frogging particles
are

$$f_{n+\frac{1}{2}}(x,v) = f_n(x,v-a_n(x)\tau),$$

$$f_{n+1}(x,v) = f_{n+\frac{1}{2}}(x-v\tau,v),$$

(31)

where $a(x)$ is given by Eq. (9) and the subscript refers to the time (Eq. (16)).

83

We have now separated the problem of discretizing the time, a problem which is presumably reasonably in hand and need receive no further consideration in the present treatment from the problem of following a very large number of particles which is still with us in Eqs. (31) and which is by no means so well in hand. We assume then that if we can find a satisfactory way of solving Eqs. (31), the result will be a satisfactory solution of the Vlasov Eq. (8) corresponding to the differential equations (1).

In order to find a computer simulation method for Eqs. (31), we must first choose a way of specifying the distribution function $f(x,v)$ by means of some finite set of numbers which can be stored in the computer. We assume that a set of parameters has been chosen suited to the problem to be simulated, the number of parameters being large enough to specify in adequate detail the distribution function $f(x,v)$, and small enough to be stored in the computer memory (10^4 words for example). We assume further that a rule is given whereby to any particular set of values of these parameters, there corresponds a specified function $f(x,v)$. As an example, a suitable set of basis functions may be chosen in terms of which to expand the function $f(x,v)$, and the coefficients of perhaps 10^4 terms in this expansion may be taken as the parameters to be stored. Since a complete set will contain an infinite number of basis functions, in order to specify uniquely the function $f(x,v)$, it will be necessary in addition to give some termination rule whereby from the 10^4 given coefficients the remaining coefficients in the expansion may be determined. A common rule, though not a necessary one, is simply to truncate the series, that is, to specify that the remaining coefficients are to be taken as zero. A second method of choosing the parameters is to set up a grid of perhaps 10^4 points in the x,v phase space and to choose as the parameters to be specified

84

the values of the function f at these grid points. Again the function $f(x,v)$
is not uniquely specified by these values until we have given an interpolation
rule which specifies the function at all points in the phase space. Note that
we are requiring that a specific function $f(x,v)$ be uniquely specified by a
particular set of values of the parameters chosen. Since there are only a
finite number of parameters, the set of functions which may be so specified
will by no means include all possible functions, or even all continuous or
analytic functions, but will be instead a particular family of functions
specifiable by the given finite set of parameters according to the given rule.
A function belonging to this set we will call a <u>representable</u> <u>function</u>.
Although not every possible distribution function is representable, if the
method of representation has been well chosen, then presumably for any dis-
tribution function $f(x,v)$ which might occur in the problem to be simulated
there is a representable function which is sufficiently close to it, in the
sense that the two functions would lead to the same present and future behavior
of the system so far as the phenomena to be studied are concerned and within
the required accuracy. It is in this sense that we have required that the
representation method chosen be suitable to the problem to be simulated.

Since a satisfactory experiment must produce repeatable results, and
since the number of parameters which would need to be controlled in an experi-
mental situation in order to repeat the experiment is probably considerably
less than the information storage capacity of a modern computer, we may at
least hope that suitable methods of representation in the above sense can
indeed be found. This plausibility argument is not an existence proof; it
might for example turn out that in order to know whether two distribution
functions are sufficiently close to be represented by the same representable

85

function, we would need already to have solved the simulation problem. In any case it would seem that the method we are suggesting provides a very great degree of flexibility. It even includes the particle-pushing methods, since one possible choice of parameters would be to choose, either at random or otherwise, a finite sample of the particles in the system to be followed and to specify the positions and velocities of this set of particles. The distribution function could then be defined by regarding these at any given moment as a random (or otherwise) sample in the set of all particles. From this point of view, particle-pushing does not appear to be very efficient, since because of statistical fluctuations the precision with which we can define the distribution function is considerably less than if we used the same number of parameters in an expansion scheme or an interpolation scheme between grid points.

Let us assume that at a particular time t_n we have stored the values of a set of parameters which specify then a particular distribution function $f_n(x,v)$. The first of Eqs. (31) then specifies uniquely the distribution function which follows at time $t_{n+\frac{1}{2}}$. Unfortunately, if $f_n(x,v)$ is a representable function, then in general $f_{n+\frac{1}{2}}(x,v)$ is not necessarily also representable. It is possible to find representation schemes in which the second of Eqs. (31) leads from one representable function to another, but it is almost certainly impossible to find a representation scheme in which each of these equations leads from one representable function to another. We do not know of a proof of this impossibility, 'ut it is clear that if such a representation scheme exists, then we can find exact solutions of Eqs. (31) valid for all times, an unlikely piece of good luck except for very specialized problems. We are faced therefore with the problem of choosing a suitable

86

representable function with which to replace the function given at any particular time step by the formulas (31). If the representation we have chosen is suitable in the sense defined above, then it should be possible to find a suitable replacement rule. Either of Eqs. (31), together with a replacement rule, will lead to an advancement algorithm for converting the parameter values at a given time to the parameter values at a time t_n later. The best replacement rule will be some sort of compromise between the requirements of accuracy and speed of computation.

It is just in the replacement rule that an approximation enters into the distribution-pushing schemes. (Recall that we have already disposed of the approximation involved in the leap-frog algorithm itself). Note however that the approximation is one which is completely within our control. Equation (31) tells us precisely what the new distribution function should be. The replacement rule tells us with precisely what function we have replaced it. We therefore know at each time step precisely what error we have made in the distribution function. If, for example, we require that the replacement rule be such that it at least preserves the total number of particles, then the representable replacement distribution may be obtained from the correct distribution given by Eq. (31) by moving each particle from its position in the latter distribution to its position in the former. (The set of particle displacements required is of course not uniquely determined, but there is presumably a set of displacements for which the rms displacement is a minimum.) We may then say that the particles in the distribution-pushing algorithm move according to the Eqs. (31) but in addition suffer at each time step a small error displacement. The characteristics of the error displacements can be determined by

studying the replacement rule. One might try to minimize the rms error displacement in choosing the replacement rules, although this goal seems to lead .n practice to rather formidable algebraic problems. Alternatively, one may place certain plausible physical requirements and certain convenient computational requirements on the replacement rule, sufficient to determine the advancement algorithm.

It has been the authors' admittedly somewhat limited experience that the numerical analytic methods of developing difference equations for approximating the Vlasov equation (8) lead to errors whose physical nature and consequences are often difficult to determine, although of course the magnitude of the errors at any given time step is known. In contrast, our experience with the development of algorithms following the distribution-pushing philosophy has been that one usually has considerable physical insight into the nature of the approximations being made. We have indeed had very few surprises; methods which we predicted in advance would have unacceptable errors indeed turned out to have such errors, and more important, methods in which these errors were supposed to have been removed indeed turned out to produce satisfactory results. A study of the replacement problem, or of the representation problem which preceeds it, usually leads to an insight into the nature of the errors involved in any given procedure and into ways in which these errors can be reduced. We will give an example below.

It can be shown t it the grid interpolation schemes and series expansion schemes are essentially the same in the following sense. Given on the one hand any set of N grid points in the phase plane and an interpolation rule which defines the function $f(x,v)$ everywhere in terms of its values at these N grid points, and given on the other hand a set of basis functions in terms of which

.

a function $f(x,v)$ can be expanded, we can find a corresponding termination rule which tells us, given N coefficients in the series, how to find the remaining coefficients. The correspondence is such that the set of representable functions is the same in both cases. The choice between the two methods is then a matter of mathematical and computational convenience. In this paper we will confine ourselves primarily to grid interpolation representation schemes. Although more general grid arrangements are under study and have advantages for many kinds of problems, we will confine ourselves here to rectangular grids of points. Let us take a rectangular array of $N=IJ$ grid points located at the positions given by all combinations of the following values

$$x_j = jh, \; j = 1, \ldots, J,$$

$$v_i = v_{min} + ig, \; i = 1, \ldots, I, \tag{32}$$

$$v_{max} = v_{min} + (I + 1)g \; .$$

We will take the system to be periodic in x with period $L = Jh$, and we will assume that the distribution function vanishes for $v > v_{max}$ and for $v < v_{min}$.

We now show that it is possible to treat separately the interpolation problem for x and for v, and still achieve a fairly high degree of accuracy. Let us assume that we have an interpolation rule in x which defines the function $f(x,ig)$ on the horizontal grid lines in the phase space. (See Fig. 4).
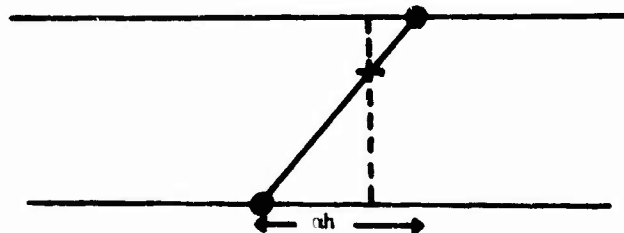
Fig. 4. Advancement shears the phase space.

89

Let us further assume that we have found a suitable advancement algorithm for the second of Eqs. (31) on the horizontal grid lines, so that we can represent precisely, or at any rate with sufficient accuracy for our purpose, the function $f(x - ih\tau, ih)$ for any value of i. Let us further assume that we are interpolating linearly in v between the horizontal grid lines. The effect of the second of Eqs. (31) is to produce a linear horizontal shear in the phase space. The points marked o in Fig. 4 which were initially in the same vertical line, one at $v = ig$, the other one at $v = (i + 1)g$, will after the shear be on the same horizontal line but displaced in x by an amount αh, where

$$\alpha = g\tau/h. \tag{33}$$

Consider now the point marked + in Fig. 4 on the line joining the two points o at $v = (i + \beta)g$. The correct value of f at this point after the shear is to be linearly interpolated between the values f_{i+1} and f_i at the two points o. This value will be replaced by a value linearly interpolated between the points directly above and below the point + on the two horizontal grid lines. The error in this process is readily calculated to be

$$\Delta f = f_{corr} - f_{repl} \doteq \alpha\beta(1 - \beta)h \frac{\partial}{\partial x}(f_{i+1} - f_i), \tag{34}$$

where we have kept only the linear term in a Taylor series for $f(x)$ along the two horizontal grid lines about the points o. If we average the above result assuming that β is equally likely to be any where between zero and one, we find

$$\langle\Delta f\rangle \doteq \frac{\alpha h}{12} \frac{\partial}{\partial x} (f_{i+1} - f_i) \doteq \frac{\alpha hg}{12} \frac{\partial^2 f}{\partial x \partial v}. \tag{35}$$

If α is not too large, say $\alpha < \frac{1}{2}$, then the error is less than or of the order of 5% of the difference between the function values at adjacent grid points and

is therefore presumably of the same order of magnitude as the error involved in replacing a physical distribution function by a linearly interpolated function, a replacement which we have assumed above is suitable. It is furthermore worth noting that the error (35) vanishes if integrated horizontally along any horizontal line or if integrated vertically along a vertical line in the phase space. Therefore the distribution in x, $(\int f(x,v)dv)$, and the distribution in v, $(\int f(x,v)dx)$, are not affected by the error. In particular, neither the kinetic energy nor the acceleration fields nor the potential energy are affected by this error. Although the above result was derived assuming a linear interpolation in v, it is presumably correct in order of magnitude for any reasonable interpolation rule in v. A similar argument applies to the replacement problem associated with the first of Eqs. (31). We therefore direct our attention to the problem of finding suitable replacement algorithms for functions of a single variable x or v. We should keep in mind however that the Taylor series in x used in the derivation of Eq. (34) is not generally valid for typical interpolation rules on x, so that the result expressed by Eq. (35) is only an estimate of the error. Furthermore the difference between this estimate and the true error will not in general have the property that its integral along a line parallel to either the x- or the v-axis vanishes.

Let the period L along the x-axis be divided into sub-intervals of length h according to the first of Eqs. (32). Let an interpolation rule be given for finding a function $f(x)$ when its values at the grid points are given. We define the interpolation function $G(x)$ as the function obtained from the given interpolation rule when the function values are specified to be $f_j = \delta_{jo}$. As
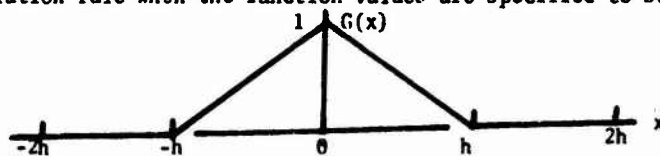
Fig. 5. Interpolation function for linear interpolation.

91

an example, we show in Fig. 5 the interpolation function for linear interpolation. Any interpolated function $f(x)$ can be written in the form

$$f(x) = \sum_{j=1}^{J} f_j G(x - jh).$$ (36)

If $f(x)$ passes through the values f_j at the grid points, the function $G(x)$ will have to have the property

$$G(jh) = \delta_{jo}.$$ (37)

It is usually desirable that the interpolation procedure be such that it yields a horizontal straight line when all the function values f_j are equal. This entails the condition

$$\sum_{j=1}^{J} G(x - jh) = 1.$$ (38)

In view of the periodicity requirement, the function f may be Fourier analyzed:

$$f(x) = \sum_{\ell=-\infty}^{\infty} \tilde{F}_\ell \, e^{\frac{2\pi i \ell x}{Jh}}.$$ (39)

The Fourier coefficients are given by

$$\tilde{F}_\ell = \frac{1}{Jh} \int_0^{Jh} f(x) e^{-\frac{2\pi i \ell x}{Jh}} dx = F_{(\ell)} G_\ell,$$ (40)

where G_ℓ is the Fourier coefficient of $G(x)$ defined by

$$G_\ell = \frac{1}{h} \int_{-\frac{1}{2}Jh}^{\frac{1}{2}Jh} G(x) e^{-\frac{2\pi i \ell x}{Jh}} dx,$$ (41)

and F_ℓ is the Fourier point transform of the function values f_j:

$$F_\ell = \frac{1}{J} \sum_{j=1}^{J} f_j \, e^{\frac{2\pi i \ell j}{J}},$$ (42)

$$f_j = \sum_{\ell=-(\frac{1}{2}J)}^{(\frac{1}{2}J)} F_\ell e^{\frac{2\pi i \ell j}{J}} \tag{43}$$

The function F_ℓ is periodic in ℓ with period J, so that we may restrict the values of ℓ to lie within a single period, say from $-\frac{1}{2}J+1$ to $\frac{1}{2}J$ if J is even, and from $-\frac{1}{2}J+\frac{1}{2}$ to $\frac{1}{2}J-\frac{1}{2}$ if J is odd. This is the meaning of the parentheses around $\frac{1}{2}J$ in Eq. (43). The parentheses around the subscript ℓ in Eq. (40) remind us that the coefficient $F_{(\ell)}$ is periodic in ℓ, although the coefficient G_ℓ is not. We see that instead of defining the function $f(x)$ by giving its J values at the grid points and interpolating between using the function $G(x)$, we could alternatively define $f(x)$ by giving J of its Fourier coefficients $\tilde{F}_\ell$, and then using Eq. (40) to provide all of the remaining Fourier coefficients. We thus see that any interpolation rule on a mesh is equivalent to a rule (40) for terminating a Fourier series, in the sense that both yield the same set of representable functions.

The moments

$$f^{(n)} = \oint x^n f(x) dx \tag{44}$$

of an interpolated $f(x)$ are given by the formula

$$f^{(n)} = \sum_{k=0}^{n} \frac{n!}{k!(n-k)!} G^{(n-k)} \sum_j (jh)^k f_j, \tag{45}$$

where $G^{(n)}$ is the nth moment of the interpolation function, defined also as in Eq. (44). It will be useful to record here the moments of the interpolation function for linear interpolation shown in Fig. 5:

$$G^{(o)} = h, \quad G^{(1)} = 0, \quad G^{(2)} = h^2/6. \tag{46}$$

93

For purposes of illustration, let us consider the simplest possible approach to the replacement problem. Let us assume that we are using linear interpolation and that we wish to find a replacement rule for the function

$$f_c(x) = f(x - \alpha h), \tag{47}$$

where we may assume $|\alpha| < \frac{1}{2}$, since if α is an integer, we may make the replacement exactly, simply by setting

$$f_{cj} = f_{j-\alpha}. \tag{48}$$

A simple way to obtain a replacement rule would be to set

$$f_{rj} = f_c(jh) = f(jh - \alpha h), \tag{49}$$

so that the interpolated replacement function $f_r(x)$ coincides at the grid points with the correct function $f_c(x)$ which it is supposed to replace. It is a simple matter to calculate f_{rj} from Eq. (49). If α is positive, the result is

$$f_{rj} = (1-\alpha)f_j + \alpha f_{j-1}. \tag{50}$$

The function $f_r(x)$ is certainly not equal to the function $f_c(x)$ which it replaces. For example, we show in Fig. 6 a sketch of the situation for the case when $f(x) = G(x)$ and $\alpha = 1/3$. One can readily verify that the
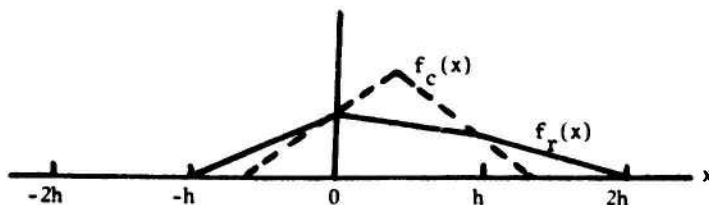
Fig. 6. Spreading of $f(x)$ with two-point advancement algorism.

zeroth and first moments of the function $f_r(x)$ agree with those of $f_c(x)$, so that the total number of particles and their mean positions in the two distributions are the same. The second moments are however

$$f_c^{(2)} = \oint x^2 f(x-\alpha h)dx = \oint (x+\alpha h)^2 f(x)dx$$

$$= f^{(2)} + 2\alpha h f^{(1)} + \alpha^2 h^2 f^{(0)} \tag{51}$$

$$= h^3 [(\alpha^2 + \tfrac{1}{6}) \sum_j f_j + 2\alpha \sum_j j f_j + \sum_j j^2 f_j],$$

$$f_r^{(2)} = h^3 [\tfrac{1}{6} \sum_j f_{rj} \cdot \sum_j j^2 f_{rj}]$$

$$= h^3 [(\alpha + \tfrac{1}{6}) \sum_j f_j + 2\alpha \sum_j j f_j + \sum_j j^2 f_j]. \tag{52}$$

The difference is

$$\Delta f^{(2)} = f_r^{(2)} - f_c^{(2)} = \alpha(1-\alpha)h^3. \tag{53}$$

If we assume α is equally likely to have any value between 0 and $\tfrac{1}{2}$, the average difference is

$$\langle \Delta f^{(2)} \rangle = h^3/12 . \tag{54}$$

Since the difference is positive the replacement distribution is more spread out than the correct distribution $f_c(x)$, as is also evident from Fig. 6.

According to our previous discussion, the distribution-pushing advancement algorithm for the second of Eqs. (31) requires us to displace horizontally the function $f(x,ig)$ along each horizontal grid line by an amount $\alpha h = v\tau = ig\tau$. For each grid line, we use the rule (48) to displace the function by an amount equal to the nearest integer to α, and then use the replacement rule (50) to displace the function by the fractional part of α. We follow a similar

procedure to obtain the algorithm for the first of Eqs. (31) by displacing
the distribution function along the vertical grid lines. Equation (54) then
tells us that the resulting algorithm is equivalent to moving each particle
according to the leap-frog equations and subjecting it in addition to a
random walk at each time step of rms step $h/\sqrt{12}$ in the x direction and $g/\sqrt{12}$
in the v direction. Such a random walk leads to an unacceptable spreading
of the distribution function for a reasonable number of time steps unless the
grid spacings are taken unreasonably small.

Since the effect results from the way we are solving the Vlasov equations
(31), and not from the self-field calculation (Eq. (9)), we may study it by
studying a system of particles subject only to an external force field a_e,
without any interaction between them. As an example, we have used the above
described advancement algorithm to find the distribution function for an
ensemble of harmonic oscillators.[3] A grid of $IJ = 91 \times 91$ mesh points was
taken. The numbers were so chosen that the orbits in phase space are circles,
with 60 time steps required for one complete cycle. The initial distribution
function at $t = 0$ was taken to be zero at every grid point except the point
$x = 0$, $v = 30$ g. where it had the value 42 (per cell gh). The results after
15, 30 and 60 time steps are shown in Figs. 7a, 7b and 7c. At each grid point,
we print the nearest integer value to f_{ij}, except that if $f_{ij} < 0.1$, we do not
print anything. As predicted, the distribution function spreads out rapidly.
Already after 15 time steps the maximum value has dropped from 42 to 3. The
distribution after that continues to spread, but more slowly, in proportion
to the square root of the time. The center of mass of the distribution moves
correctly around the circle. We offer our apologies for the fact that the
function values are printed sideways on the graphs. It is perhaps too severe
a test to start with a single non zero function value f_{ij}; in Fig. 8 we show

96
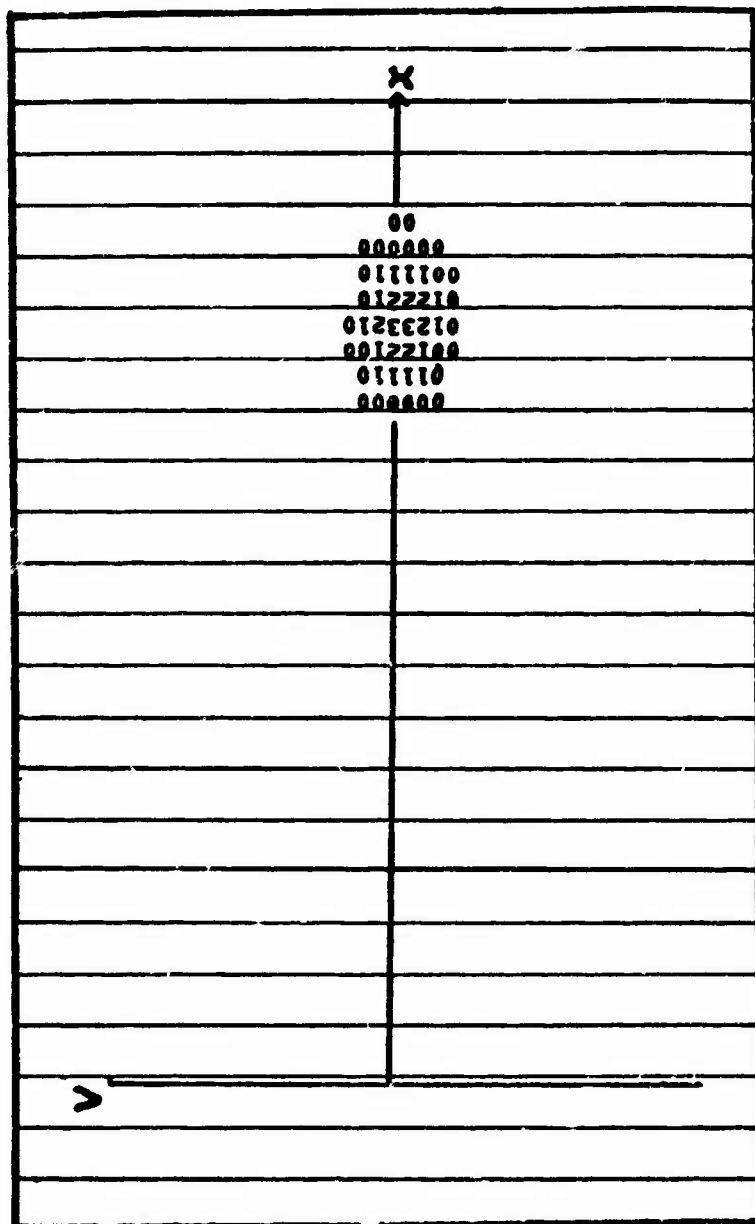
Fig. 7a. Phase density for harmonic oscillators with two-point advancement algorithm. After 15 time steps.
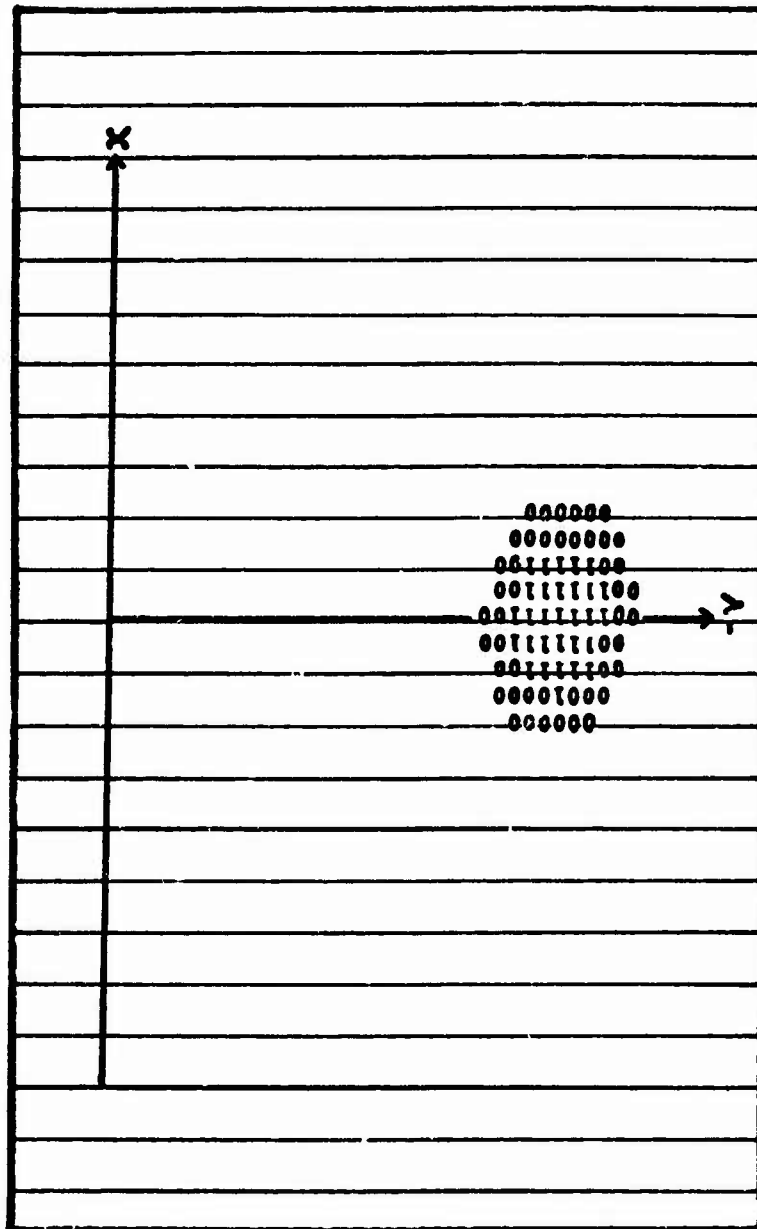
Fig. 7b. Phase density after 30 time steps.
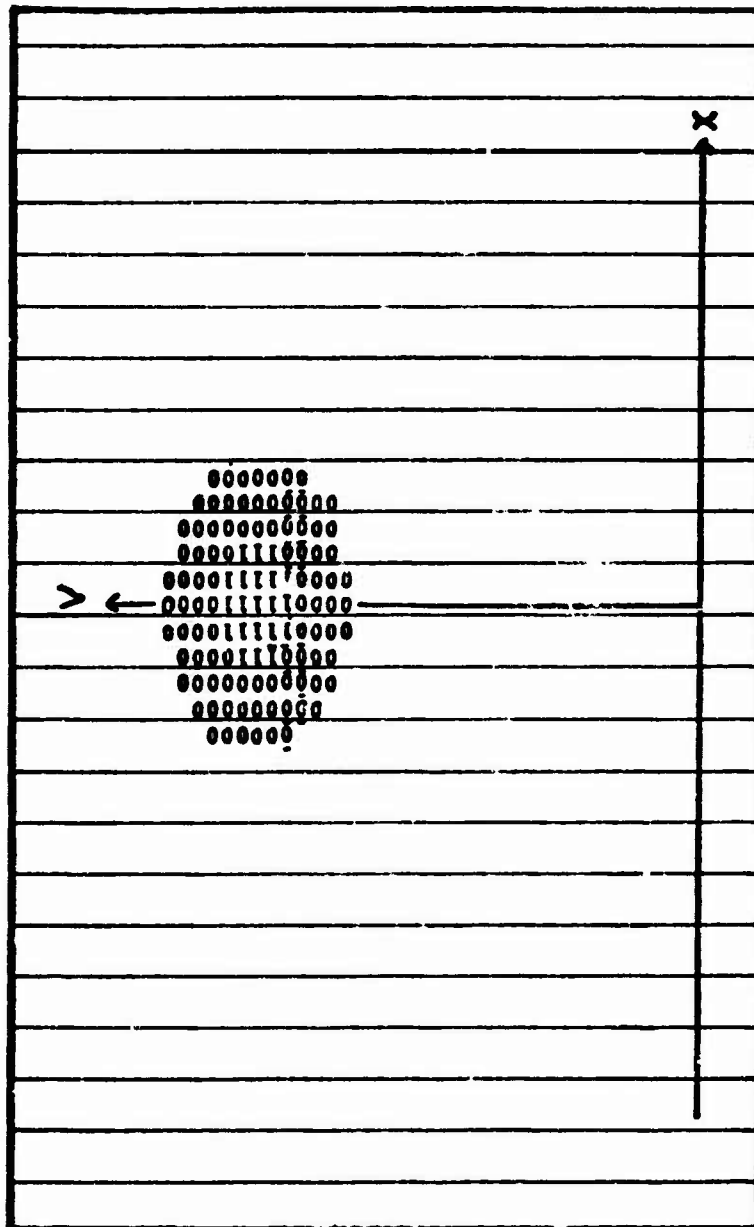
Fig. 7c. Phase density after 60 time steps.

99
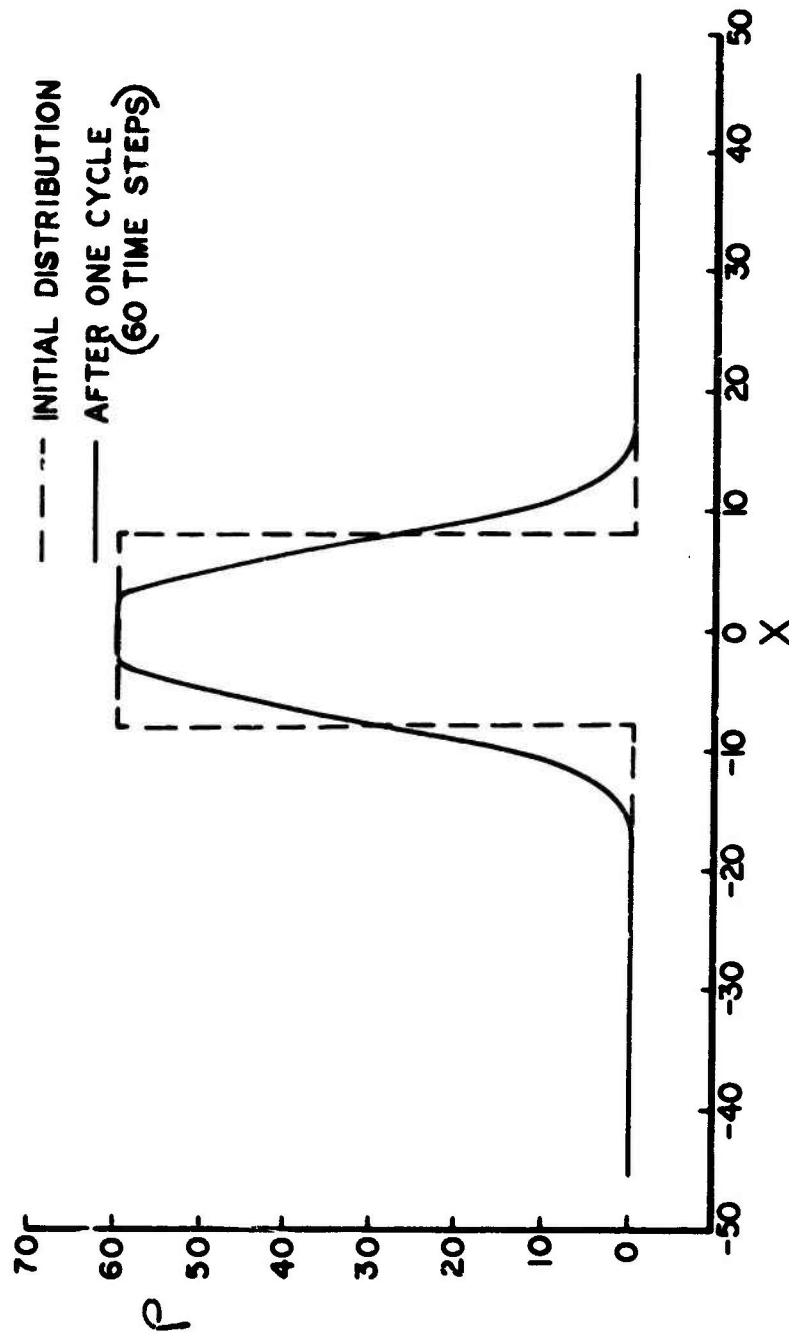
Fig. 8. Spatial density distributions for two point advancement algorithm.

the initial and final distribution in spatial density after a complete cycle for an initial distribution dist.ibuted uniformly over a rectangle in the phase space of area 17 h x 5 g. The spreading is still unacceptably large.

In order to reduce the spreading, let us seek a replacement rule for the function $f_c(x)$ in Eq. (47) which preserves also the second moment. We will also generalize the interpolation scheme by requiring only that

$$G^{(0)} = h, \; G^{(1)} = 0, \; G^{(2)} = \sigma^2 h^3 \tag{55}$$

where σ^2 is some number, which for linear interpolation is 1/6. Let the replacement rule be

$$f_{rj} = \sum_\ell a_\ell f_{j-\ell}, \tag{56}$$

where the sum over ℓ must contain at least 3 terms if we are to preserve 3 moments. The condition that the zeroth and first moments be preserved in the replacement is readily shown to be

$$\Sigma_\ell a_\ell = 1, \tag{57}$$

$$\Sigma_\ell \ell a_\ell = \alpha. \tag{58}$$

These conditions are evidently satisfied by the simple replacement rule (50). The second moments are calculated in a manner similar to those in Eqs. (51) and (52), and are

$$f_c^{(2)} = h^3 [(\alpha^2 + \sigma^2) \underset{j}{\Sigma} f_j + 2\alpha \underset{j}{\Sigma} j f_j + \underset{j}{\Sigma} j^2 f_j], \tag{59}$$

$$
\begin{aligned}
f_r^{(2)} &= h^3 [(\sigma^2 \underset{\ell}{\Sigma} a_\ell + \underset{\ell}{\Sigma} \ell^2 a_\ell) \underset{j}{\Sigma} f_j + 2\underset{\ell}{\Sigma} \ell a_\ell \underset{j}{\Sigma} j f_j + \underset{\ell}{\Sigma} a_\ell \underset{j}{\Sigma} j^2 f_j] \\
&= h^3 [(\sigma^2 + \underset{\ell}{\Sigma} \ell^2 a_\ell) \underset{j}{\Sigma} f_j + 2\alpha \underset{j}{\Sigma} j f_j + \underset{j}{\Sigma} j^2 f_j],
\end{aligned}
\tag{60}
$$

where in the last line we have used Eqs. (57) and (58). The condition that Eqs. (59) and (60) agree is that

$$\sum_{\ell} \ell^2 a_\ell = \alpha^2. \tag{61}$$

Note that this condition is independent of the choice of interpolation function! An algorithm satisfying Eqs. (57), (58) and (61) will preserve the moments of the distribution function through the second regardless of the interpolation scheme used. If a non-uniform spacing of grid points is used, then it is no longer true that the advancement algorithm is independent of the interpolation rule. A small term depending on the interpolation rule also appears if we take into account both the x and v dependence of $f(x,v)$ in working out the advancement algorithm.

A similar result applies if we require that higher moments be preserved. It does not appear to us however that there is any particular advantage in preserving the higher moments. Rather it seems to us that it is desirable to use as few terms as possible in the replacement rule (56). This not only shortens the computations, but it means that changes in the distribution function at a certain point are affected only by its nearest neighbors at any given time step. If our only object is economy in memory space (and time), then it would seem that we would want to use as large a grid spacing as possible. This means that the grid spacing will be of the order of or perhaps somewhat smaller than the smallest identifiable group of particles in the phase space. With such a large grid spacing, it does not seem plausible that either the interpolation scheme or the advancement algorithm near a given grid point should reach very far from that grid point. If we then keep only the three terms $\ell = -1, 0, 1$, Eqs. (57), (58) and (61) have the solutions

$$a_0 = 1 - \alpha^2,$$

$$a_1 = \tfrac{1}{2}\alpha(1 + \alpha), \tag{62}$$

$$a_{-1} = -\tfrac{1}{2}\alpha(1 - \alpha).$$

Note that the replacement rule given by Eqs. (62) guarantees the pre-servation of the moments of the distribution function through the second no matter what the values of f_j may be. This means that this advancement rule, starting from any interpolated distribution function $f(x)$ in Eq. (47), does very much more than simply preserve the first three moments of $f_c(x)$. For we may resolve the original function $f(x)$ in any fashion into a sum of component interpolated functions, and our advancement rule guarantees that the component replacement functions each have the proper first three moments. In this sense, we may say that this replacement rule preserves the number of particles, the mean position, and the rms spread of every component part of the distribution $f_c(x)$. If we develop an advancement algorithm for the Vlasov equations (31) based on the replacement coefficients (62), then whatever the errors introduced in the distribution in each time step, they cannot corres-pond to an independent random walk of each particle in the distribution, since the rms steps in such a walk would have to be zero. Instead, the error displacements of the particles at each step are correlated in such a way that although the new distribution is not quite the same as the old, its mean and standard deviation, and indeed the means and standard deviations of each component part, are preserved.

It is evident from Eqs. (62) that except in the special cases $\alpha = 0$, ± 1, at least one of the three coefficients will be negative. This means that it is possible, starting from positive values of all x_j, to arrive at

103

negative values of some of the f_{rj}. The function $f_r(x)$ will then not be a
true distribution function. This is perhaps not surprising, since we have
legislated that the second moment shall not increase under the replacement,
and in fact shall remain constant even under repeated displacements. Yet
it is evident that if we start from a distribution function which has only
one nonzero f_j, then unless the advancement algorithm (56) contains only one
term, the replacement functions obtained by repeated application of the rule
(56) will contain a region of nonzero values which increases in size linearly
with the number of repetitions of the advancement. In the case of the rule
(62), the distribution of nonzero values spreads out one interval h in each
direction at each advancement. The replacement algorithm (62) neatly avoids
increasing the second moment of the distribution by inserting negative values
f_{rj} on the wings of the distribution. The negative values occur only on the
edges of the distribution function and are small except when there are abrupt
changes in the function $f(x)$. The appearance of negative values can be
avoided altogether if certain restrictions can be placed on the initial dis-
tribution function. In particular it is sufficient, though by no means
necessary, to require that the function values f_j at neighboring grid points
never differ by a factor more than e. (The factor could be as large as 5.8).
There is of course no guarantee that if we start with a distribution function
which meets this requirement, the advancement algorithm will never lead to a
function for which it fails. In practice we have found with a program using
a three point advancement algorithm for the Vlasov Eqs. (31) based on the
replacement rule (62) (with always $|\alpha| < \frac{1}{2}$), that if we start with such a
distribution then only a few very small negative values f_{ij} ever arise.

Techniques for Solution of Vlasov Equation

It is interesting to note that if we use parabolic interpolation, then the above replacement rule leads to a function $f_r(x)$ which coincides with the correct function $f_c(x)$ at the grid points. In parabolic interpolation, we interpolate the function out to h on either side of a given grid point by passing a parabola through that grid point and the two neighboring points. The resulting function is in general discontinuous at the rid points. The interpolation function is shown in Fig. 9. Figure 9 makes it clear why the above replacement algorithm can give negative values for f_{rj}, since with parabolic interpolation the original interpolated $f(x)$ itself can have negative values even though none of the function values f_j is negative. It is not difficult to determine conditions on the function values f_j so that parabolic interpolation does not lead to negative values. It is in this way that we arrived at the conditions under which the replacement rule (62) does not lead to negative values. We emphasize again that we may use the replacement rule (62) with any interpolation procedure.
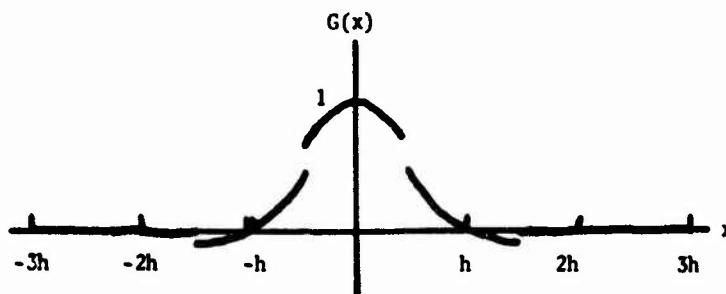
Fig. 9. Interpolation function for parabolic interpolation.

105

In Figs. 10a, b, c, and d we show the results of a calculation for the motion of an ensemble of harmonic oscillators using a distribution-pushing advancement algorithm based on the replacement rule (62). The problem is the same as that shown in Fig. 7 except that the initial distribution shown in Fig. 10a is tapered exponentially away from the central grid point at $x = 0$, $v = 30$ g, where it has its maximum value 9. Figures 10b, c, and d then show the resulting distributions after 15, 30, and 60 time steps. It will be seen that the spread in the distribution is very slight. The dots in the figure represent negative function values between -0.1 and -0.5. (For larger negative values, our program prints a minus sign.) Figure 11 shows a comparison of the initial and final distributions in x after one complete cycle, for a rectangular distribution similar to that shown in Fig. 8, except that the distribution at the edges is tapered down exponentially. We conclude from these results that this three-point distribution-pushing algorithm can give satisfactory results.

Encouraged by these results, we set up a program of this type to solve the Vlasov equation with an acceleration field kernel of the form shown in Fig. 1c. We chose the opposite sign to that shown in Fig. 1c so as to provide an attractive force to simulate the negative mass instability. The usual stability conditions, linear growth rates, and nonlinear bunching now are observed. Contour plots of the density in phase space are shown in Fig. 12. Figure 12a shows the initial distribution in the phase space consisting in a beam with a sinusoidal density perturbation. Figures 12b, c, d, and e show the results after 10, 20, 30 and 50 time steps. A striking feature, particularly of the later plots, to one who is used to seeing results from particle-pushing programs, is the uniformity of the three vortices which develop. The initial
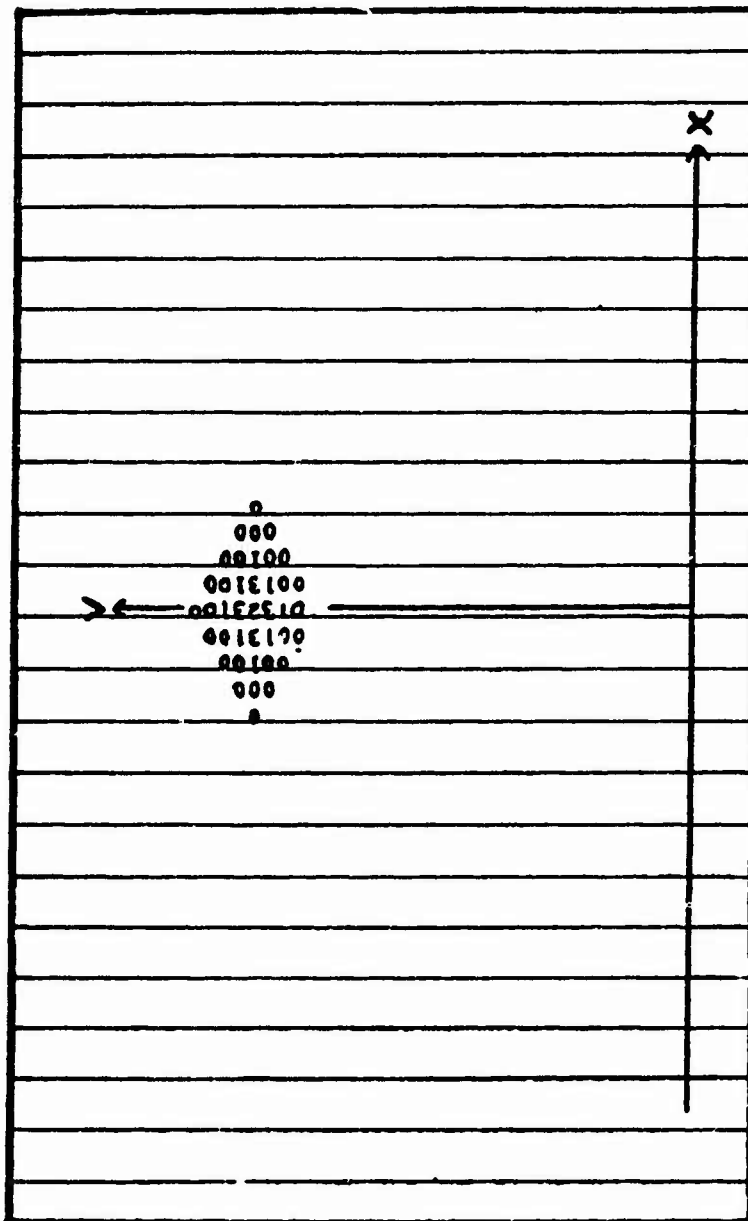
Fig. 10a. Phase density for harmonic oscillators with three-point advancement algorithm. Initial distribution.
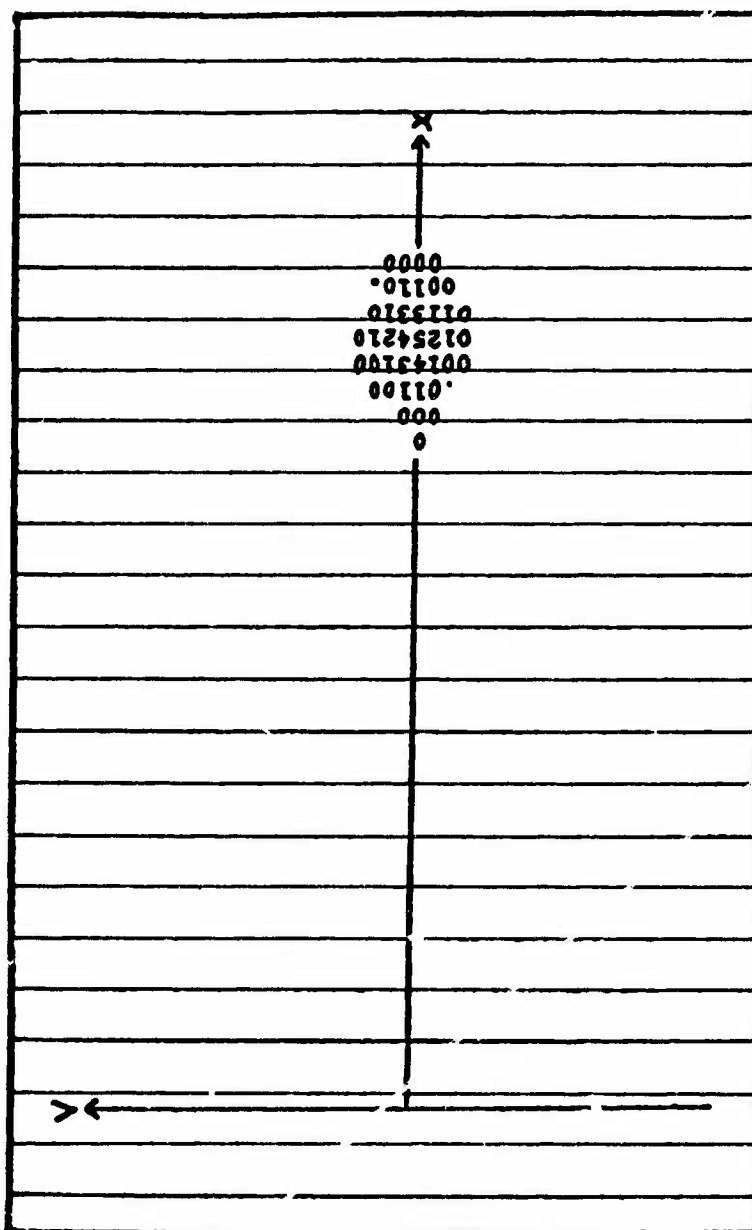
Fig. 10b. Phase density after 15 time steps.
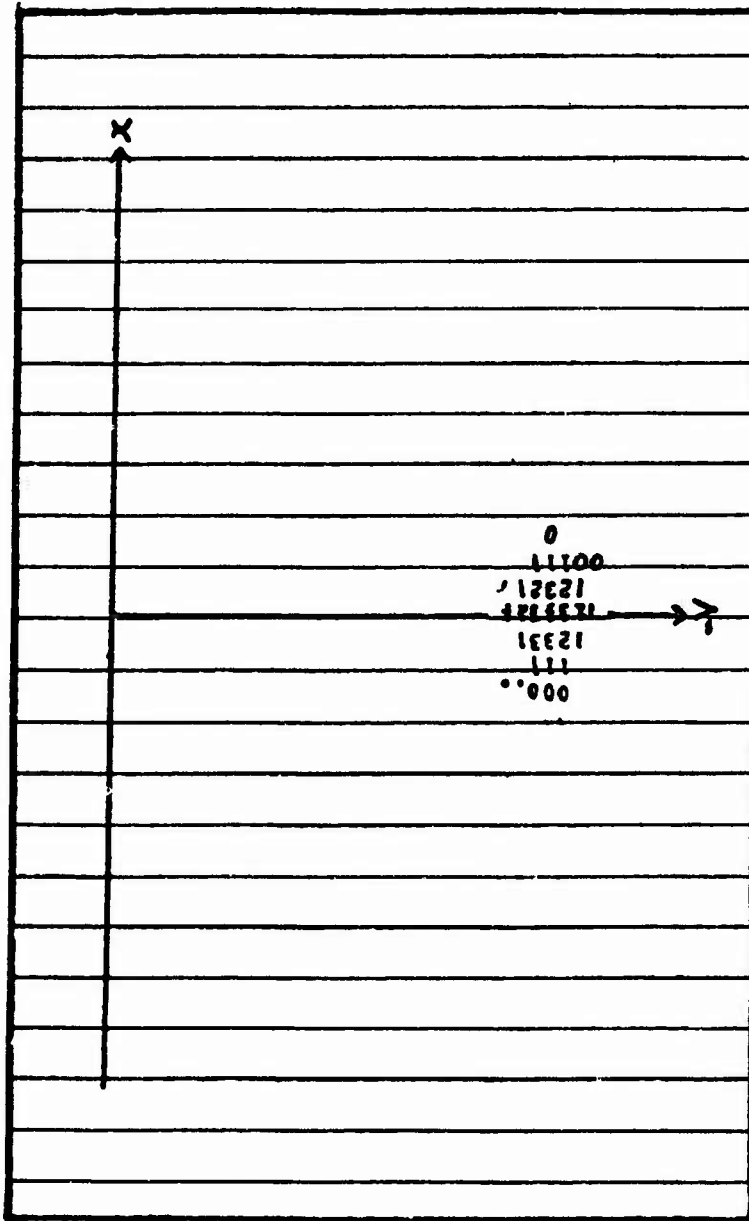
Fig. 10c. Phase density after 30 time steps.
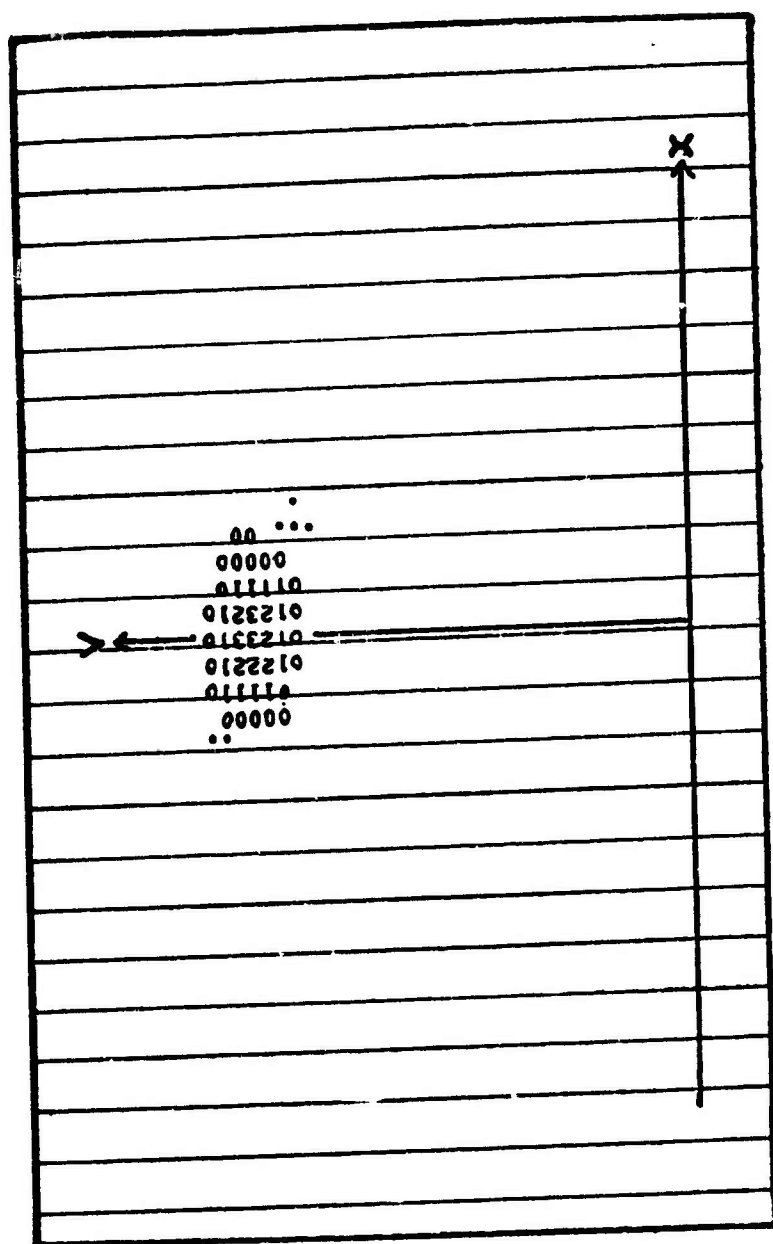
Fig. 10d.   Phase density after 60 time steps.
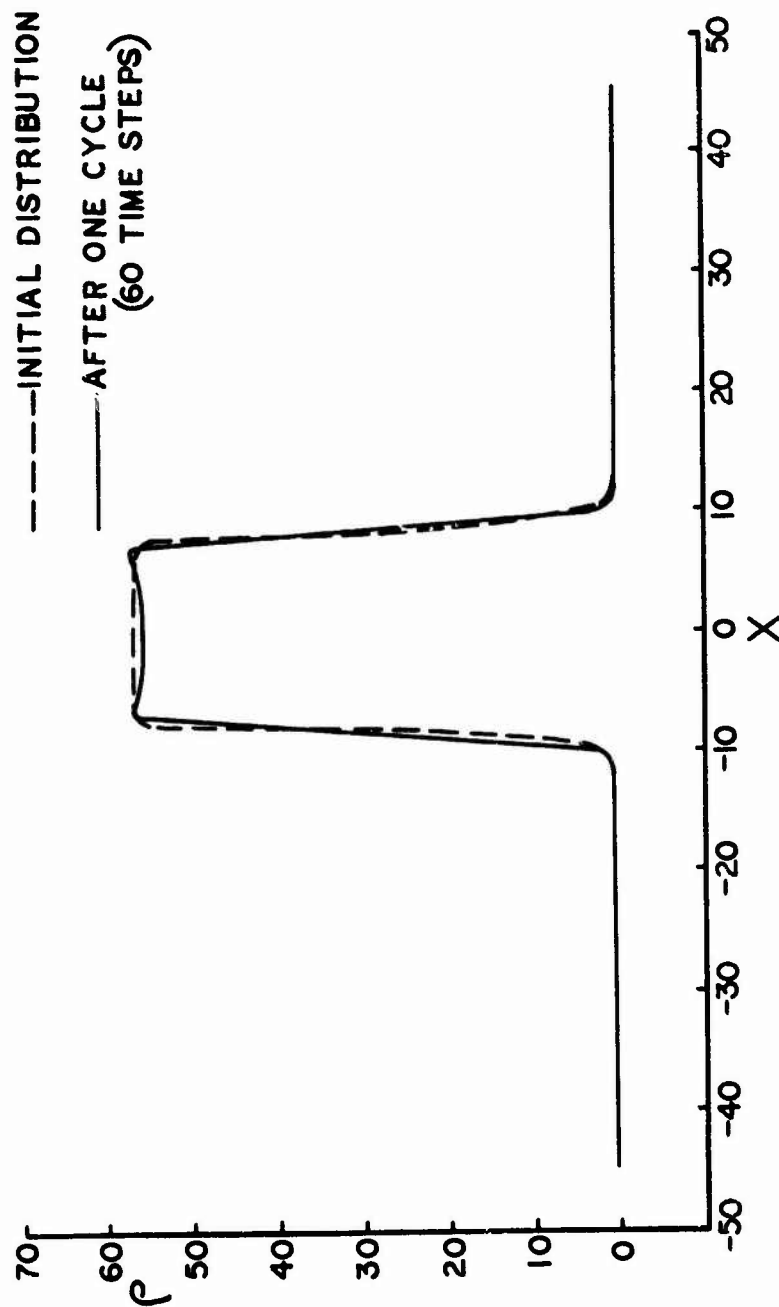
Fig. 11. Spatial density distributions for three point advancement algorithm.

111
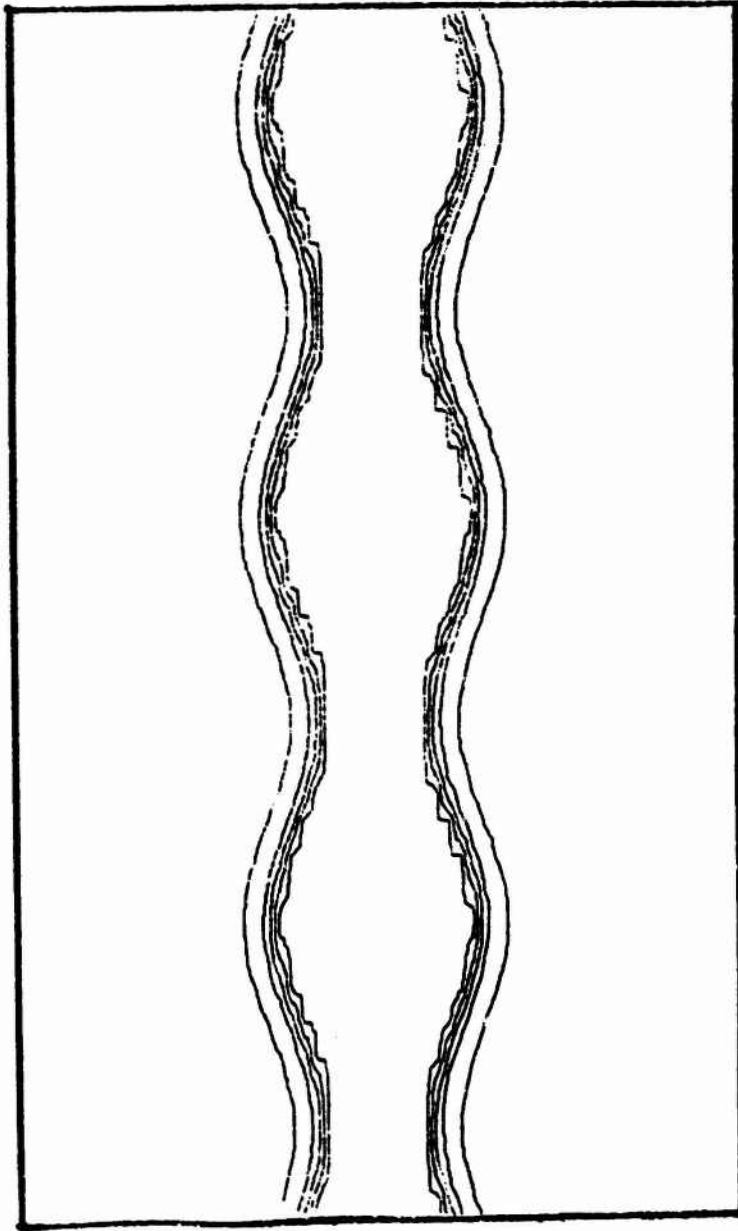
Fig. 12a. Density contours in phase space for negative mass instability. Initial distribution.
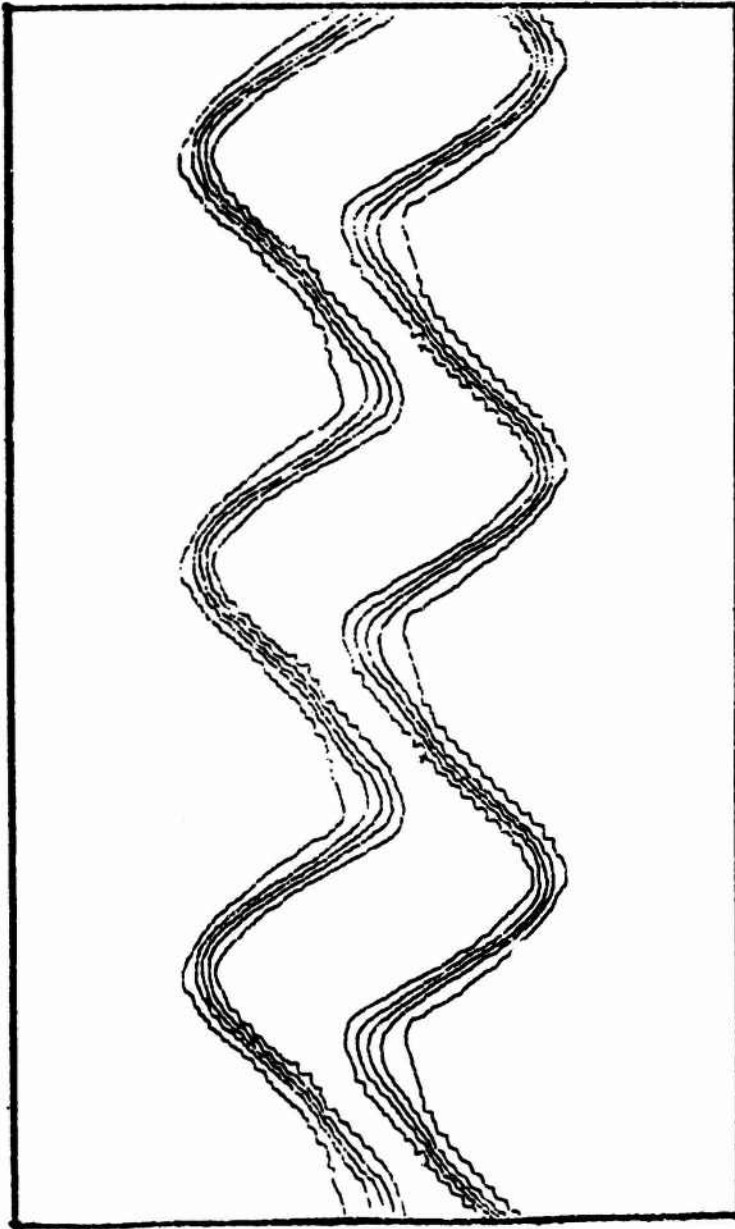
Fig. 12b. Density after 10 time steps.
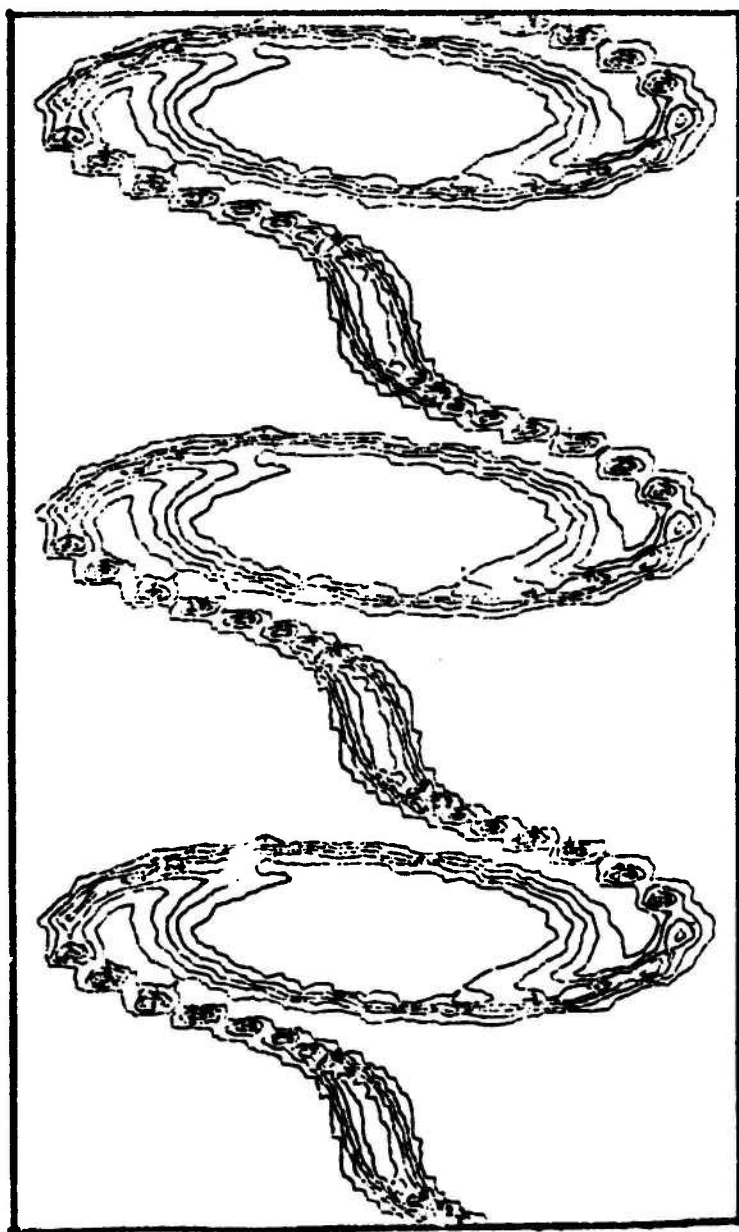
Fig. 12c. Density after 20 time steps.

114
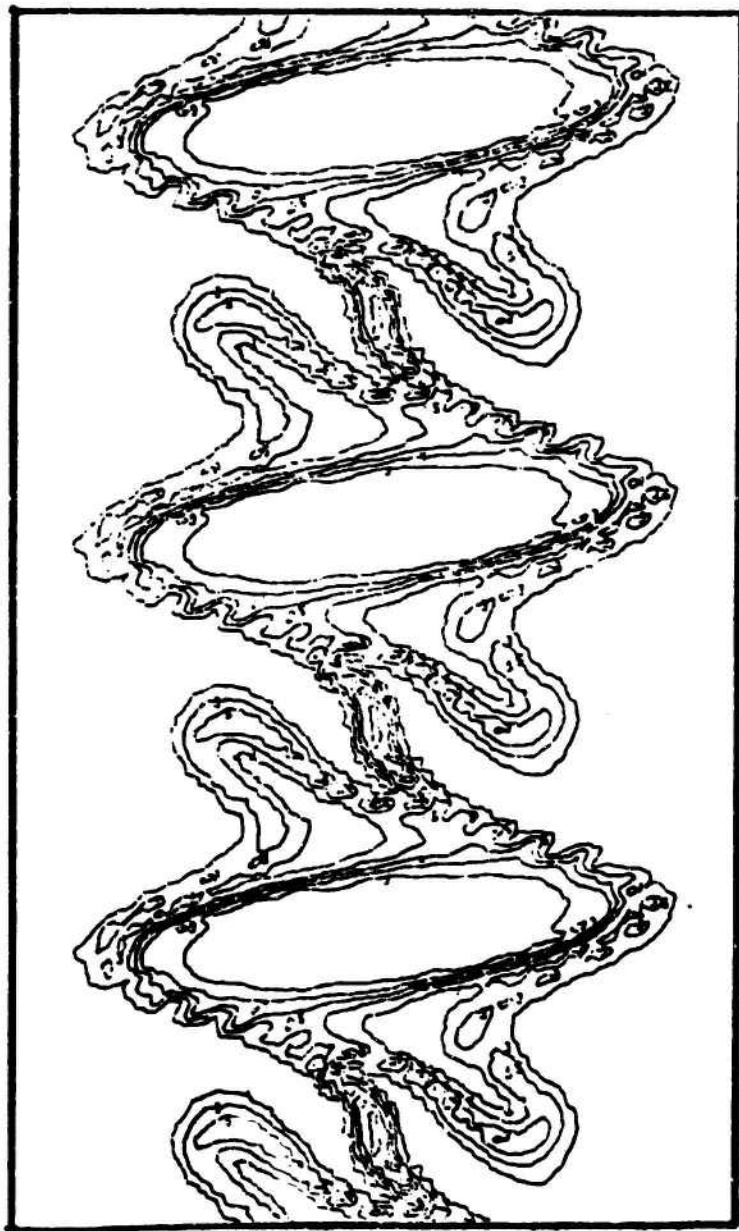
Fig. 12d. Density after 30 time steps.
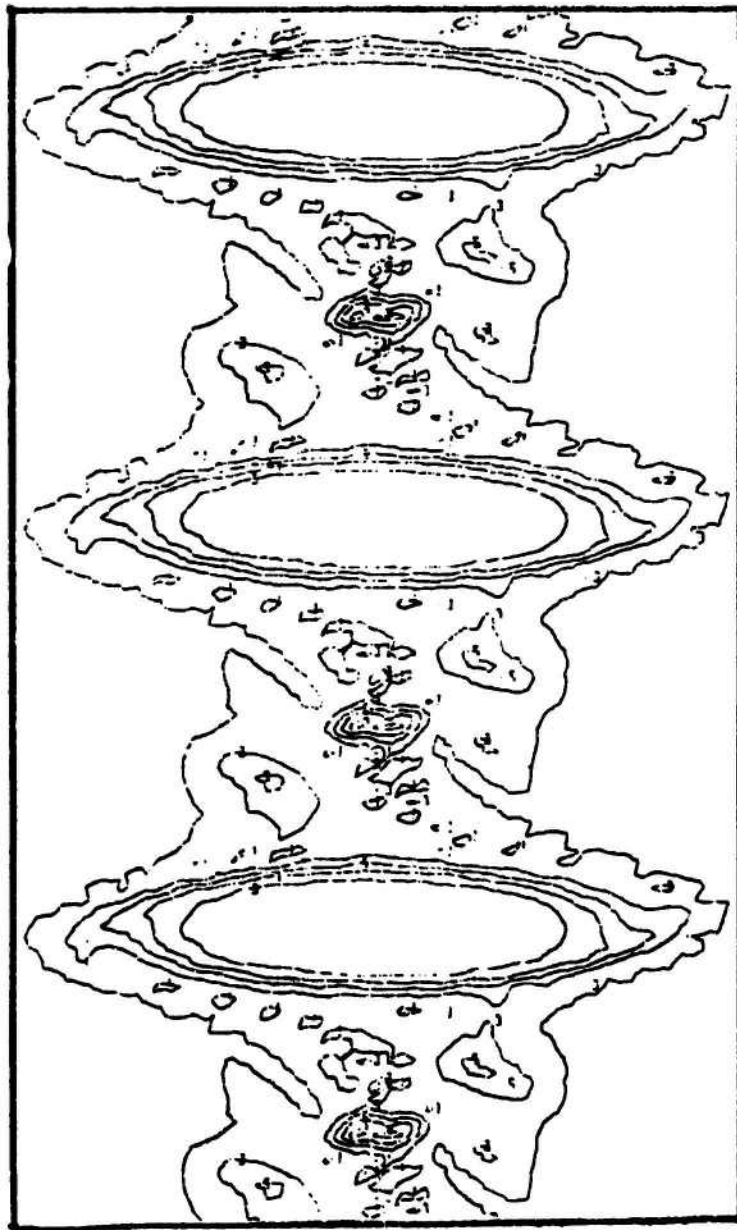
Fig. 12e. Density after 50 time steps.

perturbation is purely sinusoidal and contains three periods in the length L.
The result after 50 time steps shows three well developed identical vortices.
The identity of these vortices even down to the finest details is a symptom
of the lack of statistical noise in a distribution-pushing program in con-
trast to that which results from a particle-pushing program.

The mesh used in this calculation was 61 velocity grid points by 100
position grid points. The time step was such that $g\tau/h = 0.1$. The beam has
a rectangular velocity distribution with tapered edges, of width equal to 12
mesh units in the velocity direction plus a sinusoidal perturbation of
amplitude 2 mesh units. The total time to do the calculations shown was
three minutes on a CDC 3600, or about 1/3 of the time required by a bit-
pushing program to do the same problem (with essentially the same results).

It is of interest to ask whether an interpolation rule exists for which
the translated function $f_c(x)$ in Eq. (47) is itself representable. This
question is easily answered if we go to a representation by Fourier series.
If $f(x)$ is given by Eq. (39), then the Fourier coefficients of the translated
function (47) are

$$\tilde{F}_{c\ell} = \tilde{F}_\ell \, e^{-\frac{2\pi i \ell \alpha}{J}} \, .$$

If J coefficients $\tilde{F}_\ell$ are given, (say $-\tfrac{1}{2}J < \ell \leq \tfrac{1}{2}J$) and a termination rule is
given which determines the rest, we require that the same rule determine also
the remaining coefficients $\tilde{F}_{c\ell}$. This can be true for all α only if the rule
is that all the other coefficients vanish (except for $\ell = -\tfrac{1}{2}J$ if J is even).
The set of functions whose Fourier transform has only J non-vanishing coef-
ficients goes over into itself under the translation (47). We see from
Eq. (40) that the transform G_ℓ of the corresponding interpolation function
has exactly J non-vanishing coefficients. Any such function $G(x)$ inserted in

117

Eq. (36) defines the same set of representable functions. If we require that $f(jh) = f_j$, then Eqs. (39) and (43) show that $\tilde{F}_\ell = F_\ell$ and

$$G_\ell = 1 \text{ if } |\ell| \leq \tfrac{1}{2} J, \qquad G_\ell = 0 \text{ otherwise}$$

The required interpolation function is therefore

$$G(x) = \frac{\sin(\pi x/h)}{J \sin(\pi x/Jh)} \cdot$$

For an infinite period, $Jh \to \infty$, this approaches the familiar function

$$G(x) = \frac{\sin(\pi x/h)}{\pi x/h},$$

which provides an interpolation rule on an infinite interval which gives a set of representable functions which goes into itself under translations. We have experimented with the use of this kind of interpolation rule, but it does not seem to offer any decided advantages.

IV. A ONE AND ONE-HALF DIMENSIONAL PROBLEM

As a final example, we present briefly the results of a simulation of a $1\tfrac{1}{2}$ dimensional problem using the distribution-pushing algorithm described in the previous section.[4] The problem was suggested by an experiment conducted by C. Stallings.[5] In the experiment a beam of plasma is shot from a gun through a hole in a plate as shown in Fig. 13. The electrostatic potential is measured as a function of the radius r from the axis, and the distance z from the hole. Rather complicated oscillations in potential are observed as a function of z and of r. In order to simulate this problem, we assume that ions coming out of the hole form a fixed uniform positive charge density in a cylinder of radius R (the hole radius). We assume that the electrons all

113
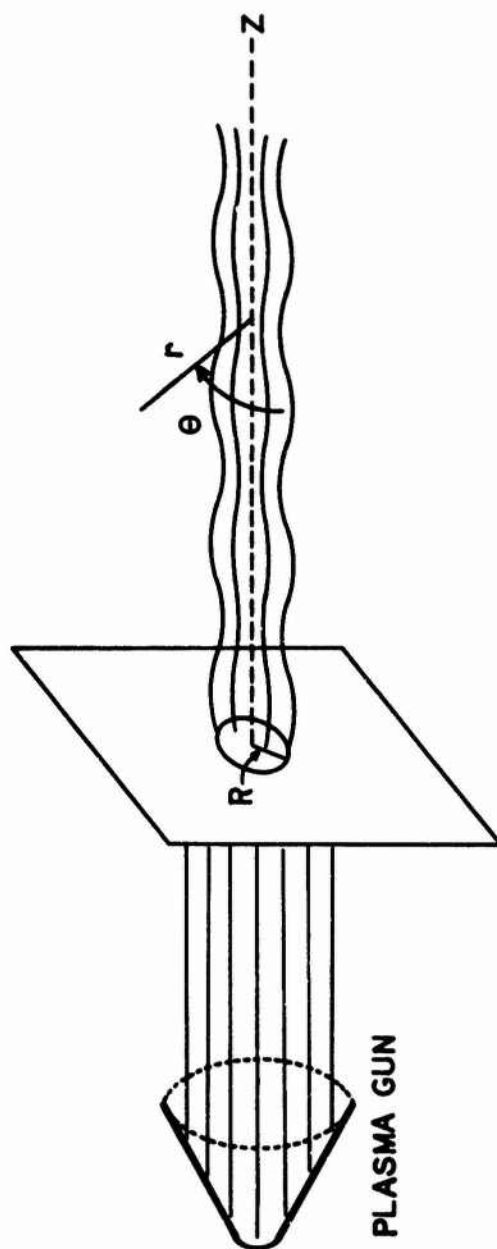
Fig. 13. Stallings' experiments

have the same z-component of velocity, so that $z = v_z t$ and we may use either z or t as independent variable. We assume also that the wave lengths of oscillations in the z direction are much greater than R, so that the potential can be calculated as for a uniform infinitely long cylinder. Each electron is then described by four coordinates and momenta r, $\dot{r}$, θ, p_θ, which are functions of the time t, or alternatively of the coordinate z. If we assume circular symmetry, then the distribution function $f(r, \dot{r}, p_\theta)$ will be independent of θ and the angular momentum p_θ is a constant of the motion.

We choose M fixed values of the angular momentum. (In our case M = 9). For each angular momentum, we write the appropriate Vlasov Eqs. (31) in the r, $\dot{r}$ space using the correct equations of motion for the radius r corresponding to that particular angular momentum. The charge density as a function of r is then calculated by integrating numerically over $\dot{r}$ and p_θ. From the densities the electric fields can be calculated which go into the equations of motion, as well as the electrostatic potential for purposes of comparison with measured values.

We start initially with a uniform spatial density of electrons out to the radius R of the hole, and with a Maxwellian distribution in velocity space:

$$f_0(r, \dot{r}, p_\theta) = \frac{2\pi n_0}{kT} e^{-\frac{m\dot{r}^2}{2kT}} e^{-\frac{p_\theta^2}{2mkTr^2}}, \; r < R, \tag{63}$$

where n_0 is the initial electron density per unit volume within the cylinder and we have normalized the distribution so that the number of particles per unit length is

$$\int_0^R f_0(r, \dot{r}, p_\theta) \, dr \, d\dot{r} \, dp_\theta = \pi R^2 n_0. \tag{64}$$

120

After the beam travels away from the hole in the plate it will oscillate in radius and the velocity distributions may not remain Maxwellian. An examination of the distribution (63) will show that if we desire to choose a minimum number M of values of p_θ, then the choice of values must be very carefully made, if we are to be able to represent reasonably well the Maxwellian form over a significant range of radii. The solution to this problem is perhaps of some interest and we will therefore give the details in the next paragraph.

Let us assume that we wish to choose a sequence of values of p_θ so that we can represent the final exponential factor in Eq. (63) about equally well at all radii. At a given radius r_0 a typical value of p_θ which is important in the exponent is

$$p_0 = r_0 (2mkT)^{\frac{1}{2}}. \tag{65}$$

For values of p_θ much smaller than p_0 the exponential function is essentially unity, and for values of p_θ much larger than p_0 the exponential function is very small. It is evident that the detail with which we can represent the Maxwellian function for this particular value $r = r_0$ is determined by the relative spacings $\Delta p_\theta / p_0$ of the values of p_θ in the neighborhood of p_0. In order to represent the distribution equally well at all values of r, we should therefore choose a geometrical progression of values for p_θ:

$$p_j = \eta^j p_0, \tag{66}$$

where p_j are the chosen sequence of values for p_θ, η is a numerical factor, and j is an integer which for the moment we allow to range over all positive and negative values. In practice we found that we could choose $\eta = 2$ and still represent the Maxwellian distribution with sufficient accuracy so that integrals over p_θ calculated by the algorithm we are about to develop are

121

accurate to about 0.1%. In order to develop an algorithm for integrating a distribution function over p_θ, let us put

$$p_\theta = p_0 e^{\beta y}, \tag{67}$$

where

$$\eta = e^\beta, \tag{68}$$

so that

$$p_j = p_0 e^{\beta j}. \tag{69}$$

If $f(p_\theta)$ is a distribution function, then we have

$$\int_0^\infty f(p_\theta) dp_\theta = \int_{-\infty}^\infty f(p_0 e^{\beta y}) \beta p_0 e^{\beta y} dy. \tag{70}$$

Now the integrand on the right is known at integer values of y, as we see by comparing Eqs. (67) and (69). It can be shown that the best possible integration formula for integrals extending over the entire y-axis where the integrand is known at equally spaced values of y, and provided nothing else is known about the integrand, is no better than a simple summation of the values of the integrand at the given points. We therefore have the following algorithm for the desired integral:

$$\int_0^\infty f(p_\theta) dp_\theta = p_0 \ln \eta \sum_{-\infty}^\infty \eta^j f_j \tag{71}$$

Since the initial distribution extends out only to $r = R$, the values f_j will be negligibly small for values of j for which p_j is larger than about twice the value given by Eq. (65) for $r_0 = R$. We may therefore set the upper limit of the sum at this value of j. We choose for p_0 a value given

122

by Eq. (65) with r_o about one half the smallest value of r of interest. We assume that the function $f(p_\theta)$ for $p_\theta < p_o$ can be fitted with sufficient accuracy by a parabola passing through the values f_o and f_1 at p_o and p_1. This assumption allows us to calculate the values f_j for j negative. The sum over negative j in Eq. (71) can then be evaluated. The resulting formula is

$$\int_0^\infty f(p_\theta) dp_\theta = p_o \ln \eta \ \frac{\eta^4 f_o - \eta f_1}{(\eta-1)(\eta^3-1)} + \sum_0^{M-1} \eta^j f_j \ . \tag{72}$$

We have found that with $\eta = 2$ and with $M = 9$, and with the Gaussian distribution (63), the formula (72) gives results accurate to about 0.1%.

The simulation program was run for 300 time steps of 2×10^{-9} sec each. The initial electron density was 4×10^{12} m^{-3} giving a plasma frequency $\omega_p = 1.124 \times 10^8$ sec^{-1}. The temperature was 2 eV, giving a Debye length 0.44 cm. The hole radius $R = 1.25$ cm. We show in Fig. 14a and b the calculated charged densities as functions of time at two different positions and in Fig. 14c the potential as a function of time at one radial position. The potential variations are of the same order and roughly similar to those measured, except that the measured variations are not so regularly sinusoidal. The measured frequency of the oscillations in density in Fig. 14a is 0.53% less than the plasma frequency! The amplitude of the oscillations in radius of the electron beam is about 2 Debye lengths.

The calculations were carried out with a grid of 100 x 31 grid points in each of the nine r, $\dot{r}$ phase spaces. The time required for the computation of 300 time steps as shown in Fig. 14 was 22 minutes on a UNIVAC 1108.
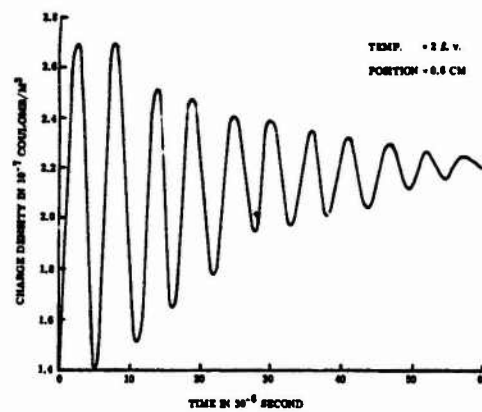
Fig. 14a.   Charge density in cylindrical beam at 0.6 cm radius.
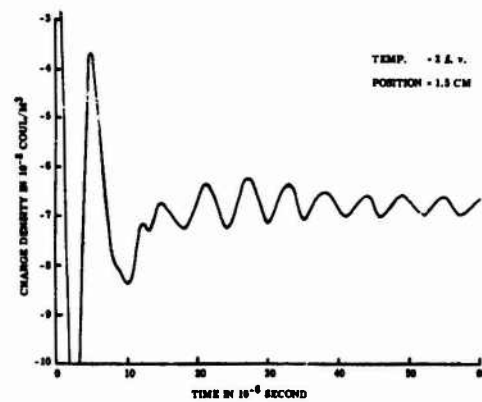
Fig. 14b.   Charge density at 1.5 cm radius.
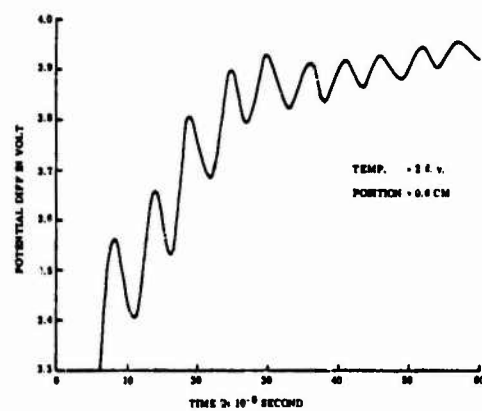
Fig. 14c.   Potential at 0.6 cm radius.

Techniques for Solution of Vlasov Equation

References

1. R. H. Miller and K. H. Prendergast, Astrophys. Jour, 151, 699 (1968).

2. D. Marshall, A Bit-Pushing Algorithm for one Dimensional Plasma Simulation. Report PLP 319[*] (Univ. of Wisconsin), Nov. 1969.

3. K. W. Li, Simulation of a One Dimensional Plasma by Interpolation of Distribution Function. Report PLP 360[*] (Univ. of Wisconsin), Nov. 1969.

4. K. W. Li, Simulation of a Laboratory Plasma with Cylindrical Symmetry. Report 361[*] (Univ. of Wisconsin), May 1970.

5. C. H. Stallings, An Electron Beam as a Method of Finding the Potential Distribution in a Cylindrically Symmetric Plasma. Report PLP 331[*] (Univ. of Wisconsin), Feb. 1970.

[*] These PLP reports are informal preliminary reports which may be obtained on request to the Plasma Physics Group, University of Wisconsin, Madison, Wisconsin 53706.

A Self-Consistent Electromagnetic Particle Code

I. Haber, C. E. Wagner, J. P. Boris, and J. M. Dawson
Naval Research Laboratory
Washington, D.C.

I. INTRODUCTION

In computer simulations of plasmas, difficulties often arise in properly modeling physical problems. Plasmas in the physical world have large system sizes with large numbers of particles having disparate masses. Here many phenomena are assumed decoupled due to the widely differing time and length scales characteristic of these physical parameters. In a simulation model, due to the finite size and speed of present-day computers, it is often necessary to choose time and length scales which are not as widely varied as those encountered in the physical world. However, our understanding of the physics is greatly facilitated if all of the physically decoupled phenomena under investigation remain decoupled in our computer model.

In particular for particles of differing masses moving in the presence of electromagnetic fields, the electrostatic phenomena tend to scale as

the square root of mass ratio while the magnetic phenomena scale directly
as the mass ratio. It is, therefore, often desirable in a computer code
to follow ion trajectories in the electrostatic approximation (large ion
Larmor radius) while following the detailed electron behavior due to the
electric and magnetic fields. This can be accomplished by decoupling the
electrostatic and electromagnetic mass of the ions. The Lorentz law
equation of motion,

$$\frac{d\overline{V}}{dt} = \frac{q\overline{E}}{m_e} + \frac{q\overline{V} \times \overline{B}}{m_m c}$$

can be solved with the magnetic mass $m_m \gg m_e$. The limit $m_m \to \infty$ is
particularly interesting, for example.

A similar circumstance exists when the magnetic pressure becomes
comparable to the particle pressure $(\beta \approx 1)$. We would like to follow
the effects of the self-consistent magnetic fields. However, for system
parameters amenable to computer simulations, the presence of the radiation
fields causes unnecessary complications. For reasonable numerical ratios
of electrostatic to electromagnetic energies, one finds an unphysical
buildup of the radiation fields via bremsstrahlung. In a periodic code
the radiation eventually reaches an energy balance with the particle
kinetic energies.

The code described here follows the orbits of simulation particles in
their self-consistent electric and magnetic fields, but neglects the trans-
verse displacement current term of Ampere's Law. The ratio of

127

electromagnetic to electrostatic fields may then be adjusted by changing
the constant c in Maxwell's equations without a corresponding change in
the radiated fields. By making c small, a large number of magnetic Debye
lengths $(c/\omega_{p\,e})$ can fit into a reasonable length system and the code can
be used to examine, from a particle viewpoint, problems such as Alfven
and magnetocoustic interactions which are often vie ed as essentially
fluid in character. The code can therefore be used to examine the effects
of particle behavior in problems such as the electromagnetic collisionless
shock.

This model of the electromagnetic-particle interaction has been
treated theoretically for a long time and is often called Darwin's model.[1]
Because the complicated retardation effects of the electromagnetic fields
are absent, the model is naturally attractive for plasma simulation. Pre-
vious computational approaches have been applied to the sheet model[2] and
to simplified configuations[3] where the canonical momentum[4] is strictly
conserved. The present paper extends the Darwin model to a one-dimensional,
finite-sized particle model where external magnetic fields destroy the con-
servation of the canonical momenta. A priori it would seem more physical
and therefore advantageous, to solve the particle equations of motion
directly. It can be show by arguments of numerical analysis, however,
that direct solution of the momentum equation by the usual methods leads
to violent numerical instabilities. These numerical instabilities have
their root in the physical fact that retardation exists in reality. The

removal of retardation adds extra constraints to the motion because the degrees of freedom in the electromagnetic field have been removed. When the transverse displacement current is retained,[5] it can be shown by numerical analysis that the same algorithm, generalized, is stable.

The algorithms presented here integrate the Darwin model by solving an evolution equation for the no-longer-constant canonical momenta. This method involves the solution of a relatively complicated, implicit, coupled Helmholtz equation for the components of the vector potential. In this way the pathology of an unstable initial-value problem in time is converted to a two-point boundary-value problem with pathologies of its own. These problems are resolved, however, by relatively standard techniques.

II. DEFINING EQUATIONS

Introducing the standard vector and scalar potentials[6] and invoking the Coulomb Gage,

$$\nabla \cdot \bar{A} = 0, \tag{1}$$

Maxwell's equations may be written (in Gaussian Units)

$$\nabla^2 \phi = -4\pi\rho , \tag{2}$$

$$\nabla^2 \bar{A} - \frac{1}{c^2} \frac{\partial \bar{A}}{\partial t^2} = -\frac{4\pi}{c} \bar{J}_t \tag{3}$$

129

where $\bar{J}_t$ is the transverse current whose divergence is zero. The actual field quantities are then derived from the potentials as:

$$\bar{B} = \nabla \times \bar{A} + \bar{B}_{ext} \tag{4}$$

$$\bar{E} = -\nabla \phi - \frac{1}{c} \frac{\partial \bar{A}}{\partial t} \tag{5}$$

where the externally applied magnetic field has been separated for convenience.

In a one-dimensional system $(\frac{\partial}{\partial y} = \frac{\partial}{\partial z} = 0)$, neglecting the $\frac{\partial^2 \bar{A}}{\partial t^2}$ term in Eq. 3, the equations to be solved are then:

$$\frac{\partial^2 \phi}{\partial x^2} = -4\pi\rho , \tag{6}$$

and

$$\frac{\partial^2 \bar{A}}{\partial x^2} = \frac{-4\pi\bar{J}_\perp}{c} \tag{7}$$

The equation of motion of the i'th particle is:

$$\frac{d\bar{V}_i}{dt} = \frac{q_i}{m_i} (\bar{E} + \frac{\bar{V}_i}{c} \times \bar{B}) \tag{8}$$

Since the system is one dimensional, it is convenient to treat the x-direction and the transverse (y,z) directions differently. This equation of motion may be written in terms of the potentials as:

$$\frac{d\overline{V}_{xi}}{dt} = \frac{-q_i}{m_i} \frac{\partial \phi}{\partial x} \hat{x} + \frac{q_i}{m_i c} \overline{V}_{\perp i} \times \overline{B}_{\perp ext} - \frac{q_i}{m_i c} \overline{V}_{\perp i} \cdot \frac{\partial \overline{A}_\perp}{\partial x} \hat{x} \quad (9)$$

and

$$\frac{d\overline{V}_{\perp i}}{dt} = -\frac{q_i}{m_i c} \overline{V}_{\perp i} \times \overline{B}_{x_{ext}} + \frac{q_i}{m_i c} \overline{V}_{xi} \times \overline{B}_{\perp ext} - \frac{q_i}{m_i c} (\overline{V}_{xi} \cdot \nabla) \overline{A}_\perp \quad (10)$$

If we define the canonical momentum of the i'th particle in the transverse direction,

$$\overline{P}_{\perp i} = m_i \overline{V}_{\perp i} + \frac{q_i}{c} \overline{A}_\perp \ ,$$

them

$$\frac{d\overline{P}_{\perp i}}{dt} = \frac{q_i}{m_i c} \frac{d\overline{V}_{\perp i}}{dt} + \frac{q_i}{c} \frac{\partial \overline{A}_\perp}{\partial t} + \frac{q_i}{c} (\overline{V}_{xi} \cdot \nabla) \overline{A}_\perp \quad (11)$$

and Eq. (10) may be rewritten as:

$$\frac{d\overline{P}_{\perp i}}{dt} = \frac{q_i}{c} (\overline{V}_{\perp i} \times \overline{B}_{x_{ext}} + \overline{V}_{x_i} \times \overline{B}_{\perp_{ext}}) \quad (12)$$

The external perpendicular field, $\overline{B}_{\perp_{ext}}$, could be included in the vector potential, if desired, but since the total convective derivative of $\overline{P}_{\perp i}$ vanishes when the external magnetic fields are zero it is more convenient not to do so. Second, notice that the canonical momenta in y and z are coupled by the externally applied field $\overline{B}_{x_{ext}}$ because $\overline{V}_{\perp i} = \frac{\overline{P}_{\perp i}}{m_i} - \frac{q_i \overline{A}_{\perp i}}{m_i c}$ by Eq. (11).

131

III. NUMERICAL ALGORITHM

Figure 1 diagrams the time advancement of the various quantities. All particle and field quantities are defined at integral time steps except for the x-components of the particle velocities which are defined at staggered, half-integral, time. If we assume that all quantities prior to and including t_0 are known, the advancement of the particles proceeds as follows: Using the accelerating fields at t_0 we may leapfrog $V_{x_{-\frac{1}{2}}}$ to $V_{x_{+\frac{1}{2}}}$ This enables us to advance the particles to their new positions at t_1. The scalar potential at t_1 may now be found directly by accumulating the charge density of the particles and then solving Poisson's equation. However, finding the vector potential at t_1 is somewhat more involved. Since both the new velocities and new momenta are unknown, it requires an implicit solution for the particle momenta and the current at the new time t_1.

Let us write the time evolution of momentum Eq. (12) in a finite difference form using the time definitions illustrated in Figure 1.

$$
\begin{aligned}
\overline{P}_{\perp i_1} &= \overline{P}_{\perp i_0} + \frac{q_i \nabla t}{c} \left[\frac{\left(\overline{V}_{\perp i_1} + \overline{V}_{\perp i_0}\right)}{2} \times \overline{B}_{xext} + \overline{V}_{xi_{\frac{1}{2}}} \times \overline{B}_{\perp ext} \right] \\
&= \overline{P}_{\perp i_0} + \frac{q_i \nabla t}{c} \left[\left(\frac{\overline{P}_{\perp i_1}}{2m_i} - \frac{q_i \overline{A}_{\perp i_1}}{2m_i c}\right) \times \overline{B}_{xext} \right. \\
&\quad + \left. \frac{\overline{V}_{\perp i_0}}{2} \times \overline{B}_{xext} + \overline{V}_{xi_{\frac{1}{2}}} \times \overline{B}_{\perp ext} \right]
\end{aligned} \tag{13}
$$

Equation (13) can be summed over all particles in the system and solved for $\overline{P}_{\perp i_1}$, and $\overline{A}_1$, in terms of the known quantities $\overline{P}_{i_0}$, $\overline{V}_{x_{\frac{1}{2}}}$, $\overline{A}_0$, $\overline{B}_{ext}$.
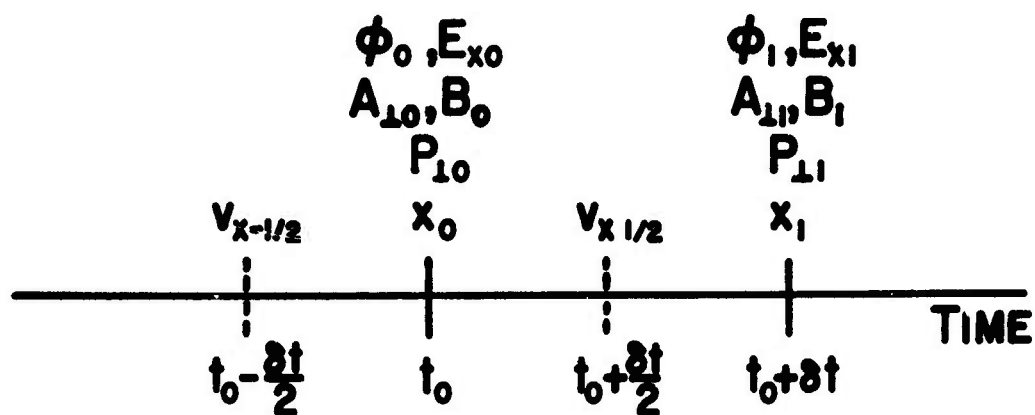
Fig. 1 - Time advancement of field and particle quantities

For illustration let us consider first the simple case where $B_{xext} = 0$. Here the momenta in the y and z directions uncouple and we are left with two scalar equations rather than a vector one. In this case equation (13) reduces to

$$\overline{P}_{\perp i_1} = \overline{P}_{\perp i_0} + \frac{q_i \Delta t}{c} \ \overline{V}_{xi_{\frac{1}{2}}} \times \overline{B}_{\perp ext} \tag{14}$$

Multiplying (14) by $\frac{q_i}{m_i}$ and recalling the definition of $\overline{P}_i$ (Eq. 11) we obtain

$$\sum_i q_i V_{\perp i_1} + \sum_i \frac{q_i^2}{m_i c} A_{\perp i_1} = \sum_i \frac{q_i}{m_i} P_{\perp i_0} + \sum_i \frac{q_i^2 \Delta t}{m_i c} V_{xi_{\frac{1}{2}}} \times B_{\perp ext} \tag{15}$$

The right side of (15) now contains only known terms.

Making use of $\nabla^2 \overline{A} = -\frac{4\pi \overline{J}_\perp}{c}$,

we obtain

$$\frac{\partial A_{\perp_1}}{\partial x^2} - \sum_i \frac{4\pi q_i^2}{m_i c^2} A_{\perp_1} = -\sum_i \frac{4\pi q_i}{m_i c} P_{\perp i_0} - \sum_i \frac{4\pi q_i^2 \Delta t}{m_i c^2} V_{xi_{\frac{1}{2}}} \times B_{\perp ext} \tag{16}$$

which is of the form.

$$\frac{\partial^2 A(x)}{\partial x^2} - K^2(x) A(x) = S(x) \tag{16a}$$

where the definitions of $K^2(x)$ and $S(x)$ may be seen from (16). The numerical method used in solving (16a) is explained in detail in Section V.

When $B_{xext} \neq 0$ by again summing over the particles we obtain an equation analogous to Eq. (16) of the form.

$$\frac{\partial^2 \bar{A}_{\perp_1}}{\partial x^2} - \sum_i \frac{4\pi q_i^2 \bar{A}_{\perp_1}}{m_i c^2 \left[1 + \left(\frac{q_i \bar{B}_{xext} \Delta t}{2 m_i c}\right)\right]^2} - \sum_i \frac{4\pi q_i \left(\frac{q_i \Delta t}{2 m_i c}\right)\left(\bar{B}_{x_{ext}} \times \bar{A}_{\perp_1}\right)}{m_i c^2 \left[1 + \left(\frac{q_i B_{x_{ext}}}{2 m_i c}\right)\right]^2} =$$

$$\frac{\sum_i \frac{q_i \bar{P}_{\perp i_0}}{m_i} - \sum_i \frac{q_i^2 \Delta t}{m_i c} \left(\bar{V}_{x_i} \times \bar{B}_{\perp ext}\right) - \sum_i \frac{q_i \Delta t}{2 m_i c} \left\{\bar{B}_{x_{ext}} \times \left[\frac{q_i \bar{P}_{\perp i_0}}{m_i}\right]\right.}{\left[\frac{c}{4\pi}\left(1 + \frac{q_i B_{xext}}{2 m_i c}\right)\right]^2} \quad (17)$$

$$\frac{\left. + q_i \bar{V}_{\perp i_0} + \frac{q_i^2 \Delta t}{m_i c}\left(\bar{V}_x \times \bar{B}_{\perp ext}\right)\right\} + \sum_i \left(\frac{q_i \Delta t \, B_{xext}}{2 m_i c}\right)^2 q_i \bar{V}_{\perp i_0}}{}$$

This equation is of the form.

$$\frac{\partial^2 \bar{A}(x)}{\partial x^2} - k^2(x) \bar{A}(x) - \bar{T}(x) \times \bar{A}(x) = \bar{S}(x)$$

where now

$$k^2(x) = \sum_{\text{species}} \frac{\omega_{ps}^2(x)}{c^2 (1 + \Omega_s^2)}$$

135

$$\overline{T}(x) = \sum_{species} \frac{\omega_{ps}^2 (x) \, \Omega_s}{c^2 \, (1 + \Omega_s^2)}$$

where $\Omega_s = \dfrac{q_s B_x \Delta t}{2m_s c}$, $\omega_{ps}^2 = \dfrac{4\pi \, m_s q_s^2}{m_s}$, and $S(x)$ is the right side of
Equation (17) which contains known quantities only. The quantities $K^2(x)$,
$T(x)$, and $S(x)$ are all computed from known cell quantities which are accumu-
lated during a pass through the particle table. Boundary conditions and the
numerical solution of this vector equations are discussed in the next sections.

Once the vector potential is determined at the new time t_1, the magnetic
fields may be determined from it by fast-Fourier transforms or simply from
the numerical derivative of the vector potential.

To complete the loop the individual particle momenta may now be updated
by solving Equation (12) implicitly for $P_{\perp i_1}$ since $V_{\perp i_1}$ may be written in
terms of $P_{\perp i_1}$ and $A_{\perp i_1}$ which is now known.

The full calculation may be seen schematically in Figure 2. Starting
with an initial ensemble of positions and momenta, the velocities are accumu-
lated to give a current matrix and equation (7) is solved to find the vector
potential. From the velocities and vector potentials, the cannonical momenta
are calculated and all the quantities are now known prior to entering the loop
which advances the system in time.

By accumulating the particle densities and velocities over a matrix of
cells, assigning each quantity to the nearest grid point, the density and
current in each species and the quantities needed for the dipole approximation
solution to the electric fields are obtained.

136
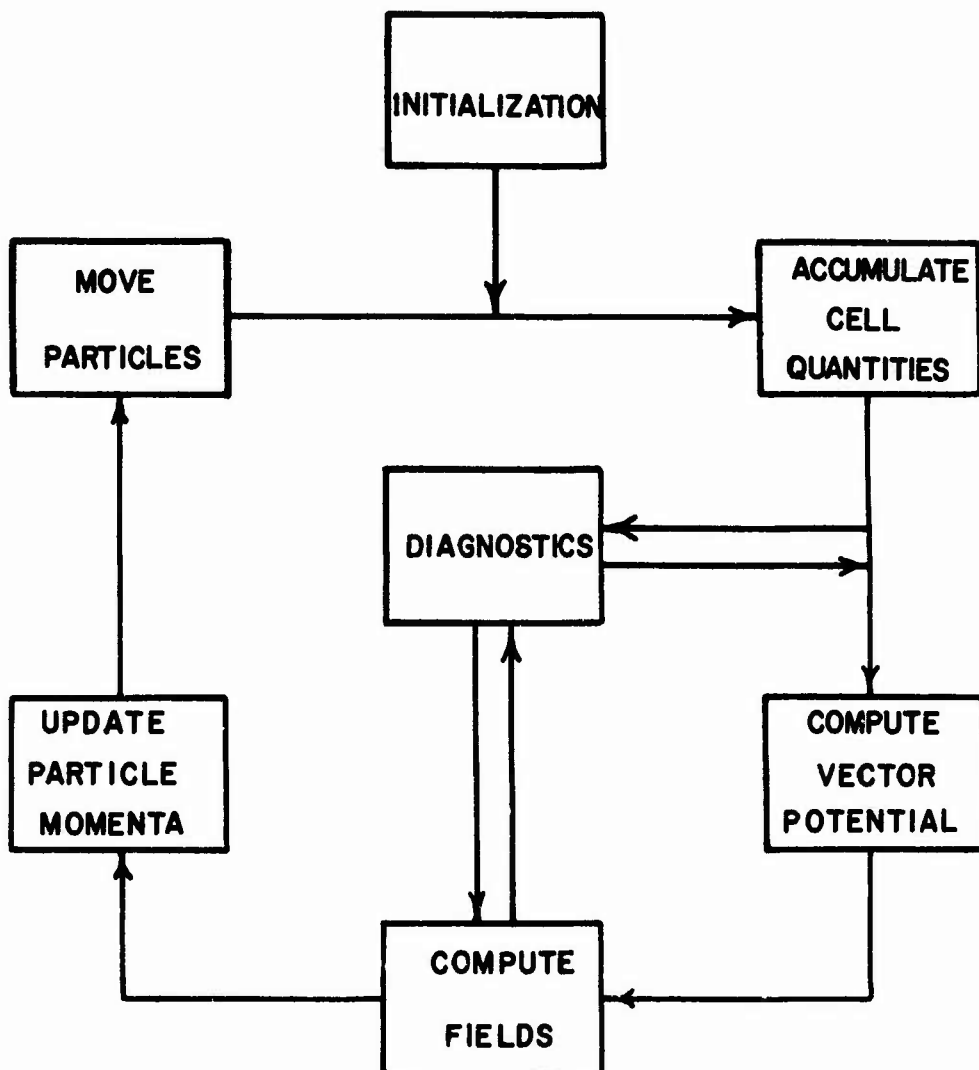
Fig. 2 - Flow diagram

The vector potential is found from the accumulated quantities in the transverse direction by the method discussed in Section V and the magnetic field $\overline{B}$ is found from the numerical derivative of the vector potential. The electric field is calculated from the dipole approximation of the charge density using fast Fourier transforms. The transformed fields are multiplied by a form factor to give Gaussian shaped particles and thereby reduce the collision frequency and anomalous heating.[7]

Though we have used an implicit algorithm to find the vector potential from the particle momenta, the actual particle momenta have not yet been changed. Using the known fields Equation (13) can now be used to find the new momenta.

The particle x-velocities are then updated using the calculated electric and magnetic fields and the new positions are calculated to close the loop.

It is important to note that though the momentum updating, particle moving, and cell quantity accumulations are shown as three separate steps all three can be performed on each particle sequentially. That is, all the particle quantities can be calculated in one loop. This means that if the particles are stored on a slow external device, only one pass through the particles is required, and efficient use can be made of whatever fast storage is available to store the field quantities. Furthermore, it is worth noting that the code is fully time centered and reversible.

IV. BOUNDARY CONDITIONS

When applying the algorithm presented to a physical problem, it is necessary to specify a well-posed set of boundary conditions on both the scalar and vector potentials. The effect of these boundary conditions on the physics under investigation should be recognized and understood.

For many problems of physical interest, i.e., those having no net charge buildup, no net momentum, and no net transverse current, it is often reasonable to impose periodic boundary conditions. However, if the system develops a net transverse current or charge, naive imposition of a particular boundary condition can lead to non-physical behavior.

For example, if a net transverse current develops, imposition of periodicity at system ends amounts to providing a return current at the ends. There is an ambiguity about specification of the return current. Even if it is decided to provide a return current at the ends of the system, the magnetic field is only specified to within a constant.

Consider the fields due to one sheet of current. The jump in magnetic field across the charge is the only thing specified. If the current sheet were between conducting walls at the ends of the system, the fields would depend on the end distance from each wall. If the simulation of an infinite system is desired, however, this same approach would be undesirable. As the charge moves toward either wall, the field would be compressed; that is, the system is not translation invariant as one would desire in an infinite system.

We can, therefore, consider the behavior imposed on a sheet charge in an invariant system as shown in Figure 4.
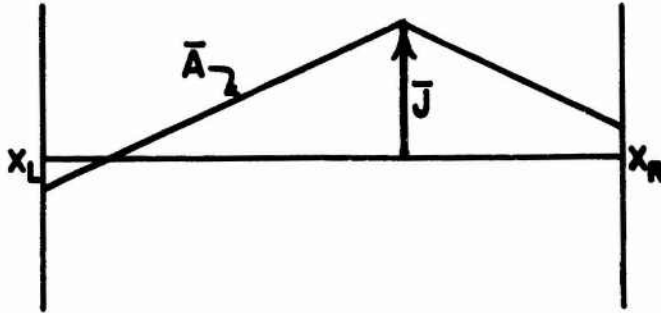
Figure 3

As $\nabla^2 \overline{A} = -4\pi\overline{J}/c$ is second order, two constraints are needed to specify the potential. The value of the indeterminate constant may be reasonably chosen, such that the fields on opposite sides of the current sheet are equal and opposite. Thus one condition is

$$\frac{\partial \overline{A}}{\partial x}(x_L) + \frac{\partial \overline{A}}{\partial x}(x_R) = 0 . \tag{18}$$

If the current element is moved from side to side, it can be seen that $A(x_R) + A(x_L) =$ constant. If $A(\infty)$ is chosen to be zero in the absence of transverse current, the second condition becomes

$$\begin{aligned}
\overline{A}(x_R) + \overline{A}(x_L) &= -\int_{x_L}^{x_R} \frac{4\pi\overline{J}}{c}\, dx \\
&= \frac{\partial \overline{A}(x_L)}{\partial x} - \frac{\partial \overline{A}(x_R)}{\partial x}
\end{aligned} \tag{19}$$

140
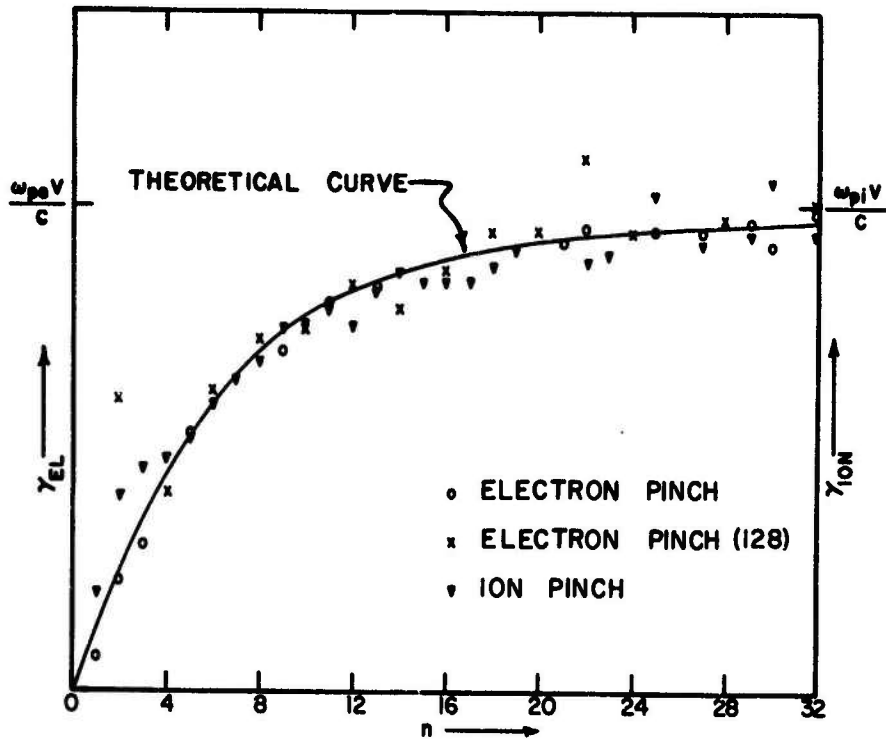
GROWTH RATE vs. WAVE NUMBER, $k = \dfrac{10 \pi n \omega_{pe}}{256 c}$

THEORETICAL GROWTH RATES:

$$\gamma_{EL} = \frac{\omega_{pe} V}{c\left(1 + \dfrac{\omega_{pe}^2}{k^2 c^2}\right)^{1/2}} \qquad \gamma_{ION} = \frac{\omega_{pi} V}{c\left(1 + \dfrac{\omega_{pe}^2 + \omega_{pi}^2}{k^2 c^2}\right)^{1/2}}$$

Figure 4

As a plasma is a superimposition of such current sheets, Equations (18) and (19) provide a way of simulating an infinite system without it being influenced by the return current.

In a uniform periodic system, it may not be desirable to specify any "end" and a uniform return current may be appropriate. Or, in the simulation of a shock problem, it may be appropriate to specify constancy of the upstream magnetic field. However, some insensitivity to the boundary conditions occurs when a plasma is present since the effect of a return current at the ends is usually shielded within a few magnetic Debye lengths.

In any system where ends are imposed, one must also consider what happens as particles move off the end. They can be reflected or reintroduced with the same or a new set of velocities at the other end. In such systems care must be taken so that the energy change of the algorithm is properly monitored if the code is to conserve energy.

There are certainly other well-posed sets of boundary conditions. The brief discussion here is not intended to be exhaustive. It does indicate, however, the nature of the problems which must be considered in some of the more important classes of problems and that care is sometimes in order.

V. SOLUTION OF THE VECTOR POTENTIAL EQUATION

When the x-component of the magnetic field is zero, the equations to
be solved for the y- and z- components decouple, each being of the form
(Equation 14)

$$\frac{\partial^2 A(x)}{\partial x^2} - K^2(x) \; A(x) = S(x). \tag{20}$$

where the source term $S(x)$ in the present application has been shown to
be a sum over particle momenta and the non-negative coefficient $K^2(x)$ is
essentially the plasma density. Problems arise in integrating this equation
because the two homogeneous solutions of Equation (20) are of an exponential
character, one right growing $(R(x))$ and the other left growing $(L(x))$. These
two homogeneous solutions, furthermore, do not satisfy the periodic boundary
conditions required of the complete solution $A(x)$ in an important class of
problems.

The exponential problem [8,9] becomes serious precisely in the many
magnetic Debye length case when $\langle K \rangle x_{max} \gg 1$ for then both $R(x)$ and $L(x)$ will
exponentiate many times in traversing the system from $x = 0$ to $x = x_{max}$.
(where $\langle K \rangle$ is an average value of k across the system). Since any truncation
or round-off error in integrating Equation (20) numerically toward either the
left or the right can be represented as a linear combination of R and L,
this numerical error will grow by many orders of magnitude compared to the
actual solution sought when $\langle K \rangle x_{max} \gg 1$. Thus extremely long word length and
very accurate algorithms would be necessary to permit even a moderate accuracy
in the desired solution after integrating Equation (20) from $x = 0$ to $x = x_{max}$.

The exponential problem here is further compounded by the fact that $S(x)$ are given as mesh functions, that is $\left\{S_i\right\}$ for $i = 1, 2, \ldots, N+1$, where $S_1 = S_{n+1}$ and similarly for $K^2(x)$. What is clearly required is a simple, quick, low-order algorithm which can be used a 1000 to 10,000 times without consuming undue computer time. Furthermore, this algorithm must give a uniformly accurate solution across the entire grid. The "partial Wronskian" method[8] described here gives a way of solving ordinary differential equations which exhibit an exponential problem irrespective of integration technique. In the present application, a second-order difference equation for $\left\{A_i\right\}$ is solved given $\left\{K_i^2\right\}$ and $\left\{S_i\right\}$ for $i = 1, 2, \ldots, N + 1$ such that $A_1 = A_{n+1}$ and $A_1' = A_{n+1}'$.

We write (with $\delta x = 1$)

$$A_{i-1} - (2 + K_i^2) A_i + A_{i+1} = S_i \quad (i=1, 2, \ldots, N) \tag{20a}$$

as the set of N difference equations to be solved for the N unknowns $\left\{A_i\right\}$. This is just the usual tridiagonal matrix equation where two additional elements in the matrix corners are non-zero due to periodicity. If $\left\{K_i^2\right\}$ were constant or of certain prescribed forms, a cyclic reduction technique could be used to solve (20a) both efficiently and accurately. In the present case a direct solution by the direct two-sweep elimination method[10] is possible when fixed boundary conditions on $\left\{A_i\right\}$ are given (say $A_1 = A_{n+1} = 0$ to eliminate the corner elements). The periodic solution can be recovered by adding to this particular inhomogeneous solution $\left\{A_{pi}\right\}$ a linear combination of the exponential (non-periodic) solutions which insure periodicity of the derivative (i.e., $A_1 = A_{n+1}$) as well as of the function itself. These

inhomogeneous solutions $\left\{\begin{matrix} R \\ 1 \end{matrix}\right\}$ and $\left\{\begin{matrix} L \\ 1 \end{matrix}\right\}$ can be found by integrating the Equation (20a) to the right and to the left respectively to minimize the accumulation of round-off error from the exponential problem.

The proposed partial Wronskian method has two advantages, however, over the direct two-sweep method. The partial Wronskian method does not propagate information concerning the particular solution across the entire system and this reduces error accumulation. The operation count is also better than for the direct solution of the tridiagonal matrix equation and no divides are required. Thus both speed and accuracy are superior. Furthermore, the method generalizes quite readily to the fourth-order set of coupled second-order equations for the transverse components of the vector potential which replaces Equation (20) when the x-component of the magnetic field is non-zero. This problem will be discussed shortly.

First consider the homogeneous solutions of Equation (20), $R(x)$ and $L(x)$. We can write a Wronskian for these two solutions from the differential equation

$$W_{RL}(x) = R(x)L(x) - R(x)L(x) = 1. \tag{21}$$

This Wronskian plays the role of the quantum mechanical orthonormality condition in the following analysis for, given an arbitrary set of two numbers as $(A(x), A'(x))$ at some x, we can use Equation (21) and the known solutions $R(x)$ and $L(x)$ to find the composition of (A, A') in terms of R and L. Thus

$$A = a R + bL \tag{22}$$

where $a \equiv W_{AL}$ and $b \equiv W_{RA}$. From (21) one can see that $W_{LL} = W_{RR} \equiv 0$.

Equation (21) is furthermore a global relation in the sense that the Wronskian between these two solutions has the value 1 for all x, independent of the function $K^2(x)$.

The global condition (21) can be used to eliminate the divides required by the two-sweep method while eliminating error propagation. Consider the following algorithm for solving Equation (20). The result will be equivalent to solving the standard difference formulation Equation (20a). The homogeneous solutions can be determined by integrating (20a) starting with R_1 and $R_{\frac{1}{2}}$ chosen to approximate the right-growing analytic solution. Then, using a standard leapfrog integration moving to the right,

$$R'_{i+\frac{1}{2}} = R'_{i-\frac{1}{2}} + K_i^2 R_i,$$

$$R_{i+1} = R_i + R'_{i+\frac{1}{2}}.$$

(23)

R_i is an exact solution of the homogeneous difference equation (20a without S) for which the round-off error accumulation is negligible. $\left\{ L_i \right\}$ can be found to the same accuracy by using the same leapfrog algorithm but integrating from right to left. We define

$$W_i(R,L) = R_i L'_{i-\frac{1}{2}} - R'_{i-\frac{1}{2}} L_i$$

(24)

Then, using (24) to advance both $\left\{ R_i \right\}$ and $\left\{ L_i \right\}$ it is easy to show that $W_{i+1} = W_i$. Thus the Wronskian is a conserved quantity of the difference as well as the

146

differential equations. Defining $A'_{i+\frac{1}{2}} \equiv A_{i+1} - A_i$ as for the solutions R_i

and L_i, the difference equation (20a) becomes

$$A'_{i+\frac{1}{2}} - A'_{i-\frac{1}{2}} = S_i + K_i^2 A_i \qquad (25)$$

Now define A as a linear combination of the left and right-growing solutions
between the grid points. Thus

$$A_{i+} = a_{i+\frac{1}{2}} R_i + b_{i+\frac{1}{2}} L_i,$$

$$A_{i-} = a_{i-\frac{1}{2}} R_i + b_{i-\frac{1}{2}} L_i$$

hold for $i \leq x \leq i+1$ and $i-1 \leq x \leq i$ respectively. Since we must have
$A_{i+} = A_{i-}$ at the grid point i,

$$(a_{i+\frac{1}{2}} - a_{i-\frac{1}{2}}) R_i = - (b_{i+\frac{1}{2}} - b_{i-\frac{1}{2}}) L_i. \qquad (26)$$

Using the above expansions in Equation (26) gives

$$(a_{i+\frac{1}{2}} - a_{i-\frac{1}{2}}) R'_{i-\frac{1}{2}} = - (b_{i+\frac{1}{2}} - b_{i-\frac{1}{2}}) L'_{i-\frac{1}{2}} + S_i. \qquad (27)$$

The terms in K_i^2 cancel when $(R'_{i+\frac{1}{2}}, L'_{i+\frac{1}{2}})$ is written in terms of $(R'_{i-\frac{1}{2}}, L'_{i-\frac{1}{2}})$.

Solving (27) and (28) gives

$$(a_{i+\frac{1}{2}} - a_{i-\frac{1}{2}}) = - S_i L_i / W_i,$$

$$(b_{i+\frac{1}{2}} - b_{i-\frac{1}{2}}) = S_i R_i / W_i. \qquad (28)$$

Note that $W_i \approx 1$ under a suitable normalization of L_{n+1}. Because the
expansion of A in terms of R and L for one cell can be found from those in a
neighboring cell by applying Equation (29), a particular solution $\{A_i\}$ can be
accumulated in two extremely simple sweeps, one from the right to the left

147

accumulating the contribution of R and one from the left to the right for
the contribution of L. These two sweeps are accomplished as follows:

Set $B_{\frac{1}{2}} = c$, $A_1 = o$, then accumulate using

$$b_{i+\frac{1}{2}} = b_{i-\frac{1}{2}} + S_i R_i,$$

$$A_{i+1} = b_{i+\frac{1}{2}} L_{i+1}.$$

(29a)

Set $a_{N+\frac{1}{2}} = o$, A_{N+1} given from previous sweep. Then accumulate using

$$a_{i-\frac{1}{2}} = a_{i+\frac{1}{2}} + S_i L_i,$$

$$A_{i-1} = A_i + a_{i-\frac{1}{2}} R_{i-1}.$$

(29b)

The periodic boundary conditions are satisfied by adding the appropriate
linear combination of $\left\{R_i\right\}$ and $\left\{L_i\right\}$ to the particular solution $\left\{A_i\right\}$ determined
as above. Similarly some other set of well-posed boundary conditions could be
so satisfied.

The extreme simplicity of (29a) and (29b), using as they do the additional
knowledge that the Wronskian is constant, provide the great speed of the method.
The symmetry of the method, treating right and left directions equivalently and
only accumulating the particular solution by sweeping in the direction of
decrease of the homogeneous solutions provides the accuracy. The contributions
to the round-off error of the overall solution decay exponentially away in
both directions using this method. Thus, accumulation of error can occur over
only a single magnetic Debye length rather than across the entire system.

This method has an additional advantage. It generalizes quite readily
to the coupled set of second-order equations for $(A_y(x), A_z(x))$ which arise

148

when the externally applied B_x field is non-zero. This coupled equation is of the form

$$\frac{d^2\bar{A}(x)}{dx^2} - K^2(x)\,\bar{A}(x) + \bar{T}(x) \times \bar{A} = \bar{S}(x) . \tag{30}$$

Here $\bar{T}(x)$ can be an arbitrary function of x but actually has the same functional form as K^2 in the problem being solved here. We seek a solution, in the present circumstances, to the finite difference analogue of (30),

$$\bar{A}_{i-1} - a\bar{A}_i + \bar{A}_{i+1} - K_i^2\,\bar{A}_i + \bar{T}_i \times \bar{A}_i = \bar{S}_i \tag{30a}$$

The usual double-sweep method now requires solution as 2 x 2 matrix operations for each grid point.

The solution of (30a) is begun by finding the four independent solutions of the homogeneous difference-equation system. There are now two right-growing and left-growing solutions which we shall label as $\left\{\bar{R}_{1_i}\right\}$ $\left\{\bar{R}_{2_i}\right\}$, $\left\{\bar{L}_{1_i}\right\}$, and $\left\{\bar{L}_{2_i}\right\}$. These, of course, are found by a leapfrog generalization of Equation (23) where the integration is performed in the direction of growth for each of the solutions. Actually only two integrations are necessary, one from each side, because $\bar{R}_2$ can be found from $\bar{R}_1$ as follows:

$$\bar{R}_{2_y} = \bar{R}_{1_z} , \quad \bar{R}_{2_z} = -\bar{R}_{1_y} . \tag{31}$$

and similarly for $\bar{L}_2$.

The partial Wronskian is derived from the quantity W_i formed in analogy with Equation (24). Suppose $\bar{H}_1$ and $\bar{H}_2$ are two solutions of the homogeneous difference equation (30a) (i.e., any linear combinations of $\bar{R}_1$, $\bar{R}_2$, $\bar{L}_1$ and $\bar{L}_2$).

Then, by dotting (30a) with $(H_{2y} - H_{2z})$ and with $(H_{1y} - H_{1z})$, the following partial Wronskian relation can be derived:

$$W_i(\overline{H}_1, \overline{H}_2) \equiv (H_{1_{yi}} H'_{2_{yi-\frac{1}{2}}} - H'_{1_{yi-\frac{1}{2}}} H_{2_{yi}})$$

$$- (H_{1_{zi}} H'_{2_{zi-\frac{1}{2}}} - H'_{1_{zi-\frac{1}{2}}} H_{2_{zi}}) = \text{constant.} \tag{32}$$

This somewhat more complicated "partial Wronskian" takes the place of the uncoupled-equation result, Equation (24). It is clear then

$$W_i(\overline{H}_a, \overline{H}_a) \equiv 0 \tag{32a}$$

where $\overline{H}_a$ is any homogeneous solution. From Equations (31) it is also clear then

$$W_i(\overline{R}_1, \overline{R}_2) \equiv W_i(\overline{L}_1, \overline{L}_2) \equiv 0. \tag{32b}$$

Furthermore, we can choose $\overline{L}_1$ initially so that $W_i(\overline{R}_2, \overline{L}_1) \equiv 0$. This is so because we have the freedom to "rotate" the left-growing solutions, determined by a single integration and application of Equation (31), and the second half of (32b) will still hold true. A simple normalization of $\overline{L}_1$ then insures that

$$W_i(\overline{R}_1, \overline{L}_1) = 1, \quad W_i(\overline{R}_2, \overline{L}_1) = 0. \tag{32c}$$

It is then easy to show, that $W_i(\overline{R}_1, \overline{L}_2) = 0$ and $W_i(\overline{R}_2, \overline{L}_2) = -1$. These relations then again operate as orthormality conditions. Equations analogous to (26) and (27) can be written and accumulations sweeping to the right and to the left can be taken to minimize error. Then, still in analogy with the solution of Equation (20), the correct linear combination of the four homogeneous solutions can be added to the particular solution to correctly satisfy the four boundary conditions.

150

An even greater speed improvement is found for the coupled case because the divides of the usual tridiagonal matrix reduction become 2 x 2 matrix inversions in the coupled case. These inversions are effectively absent in the partial Wronskian method because W_i is constant and can be judiciously made either 0 or 1.

VI.   CONCLUSION

The preceding sections have discussed the details of a simulation code which follows the particle orbits in their self-constant electric and magnetic fields. At this time, some experience has been compiled already running the code. Using a non-optimized Fortran version with 40 thousand particles in a 1024 system, approximately 3 seconds is required per time step on a 360/91.

The code has been tested by running a number of transverse pinch experiments. Figure 3 is a plot of the growth rates experimentally observed. The two electron pinches were run with counterstreaming cold electron beams and a heavy neutralizing background. The experimental points are shown for experiments on a 128 cell system and a 256 cell system. Also shown is a set of points for an ion pinch experiment (mass ratio 16) with cold counterstreaming ions in a cold electron background.

Since the code presently uses a nearest grid point approximation for the magnetic field, it has generally been found that wavelengths of only a few cells are not handled accurately. This can account for the experimental scatter on the high wavenumber end. Since the higher wavenumber modes grow more rapidly than the lower ones, saturation occurs in just a few growth time for the lowest modes shown. The experimental scatter on the low end is because of the lack of enough time before saturation to get an accurate slope.

151

Physically meaningful results have also been obtained in more complex situations, such as counterstreaming inhomogeneous beams but here the theory is not complete enough for easy comparison to experiment. However, the code has yielded valuable physical insight into complex physical situations.

REFERENCES

1. C. G. Darwin, Phil. Mag. 39, 537 (1920). See also Landau and Lifshitz, Classical Theory of Fields, §65, or J. D. Jackson, Classical Electrodynamics, § 12.6.

2. A. Hasegawa and H. Okuda, "One-Dimensional Plasma Model in the Presence of a Magnetic Field," Physics of Fluids 11, p. 1995 (1968).

3. D. O. Dickman, R. L. Morse, and C. W. Nielson, "Numerical Simulation of Axisymmetric, Collisionless, Finite-β Plasma," Physics of Fluids, 12, p. 1708 (1969).

4. H. Goldstein, "Classical Mechanics," Addison-Wesley Pub. Co., Mass., p. 209.

5. J. P. Boris, "Relativistic Plasma Simulation - Optimization of a Hybrid Code," Fourth Conference on Numerical Simulation of Plasmas, proceedings, Naval Research Laboratory, Washington, D. C., 2-3 Nov., 1970.

6. Jackson, op cit., p. 181.

7. B. Rosen and W. Kruer, "Suds - A Faster Version of the Dipole Expansion," Fourth Conference on the Numerical Simulation of Plasmas, proceedings, Naval Research Laboratory, Washington, D. C., 2-3 Nov., 1970. See also references to the original dipole method (finite-sized particles), G. Hsi, J. M. Dawson, J. P. Boris, and W. L. Kruer, Bulletin of the American Physical Society, 13, 1555 (1968).

8. J. P. Boris and J. M. Greene, "Determination of Subdominant Solutions Using a Partial Wronskian," Journal of Computational Physics 4, p. 30 (1969).

9. B. Coppi, J. M. Greene, and J. L. Johnson, Nuclear Fusion 6, p. 101, (1966).

10. R. D. Richtmyer and K. W. Morten, Difference Methods for Initial-Valve Problems, 2nd Edition, Interscience, New York (1967).

Formulation of Self-Consistent 2- and 2-1/2-Dimensional Electromagnetic and Relativistic Simulations*

K. H. Sinz
Lawrence Radiation Laboratory
University of California
Livermore, California

ABSTRACT

A formulation for self-consistent 2- and 2 1/2-dimensional electromagnetic and relativistic particle simulations is presented. The particles are infinitely long charged rods that move under the influence of their self-consistent fields. The numerical algorithms that numerically solve the appropriate Maxwell's equations and the Lorentz force law in a first order central difference scheme are given. The principal results are also applicable to simulations in one or three dimensions.

153

I.   INTRODUCTION

Over the past few years considerable efforts have been made in the study of relativistic electron beams in plasmas. The approach has usually been the use of fluid type equations in which for example the background is approximated as an Ohmic medium.[1] To make a study of the nonlinear aspects of the hose mode and the tearing mode in relativistic beams which avoids such approximations, we have developed a self-consistent relativistic and electromagnetic particle simulation. Since the effects of interest seem to depend primarily on only two linearly independent wave vectors — one parallel and one perpendicular to the direction of beam propagation — we restrict ourselves to two dimensions. A description of such a model is given in Sec. II. The numerical scheme employed is a first order central difference scheme. The numerical algorithms are developed in Sec. III. It is interesting to note that with the exception of the constants the result for the Lorentz force is also applicable to a three-dimensional model.

II.   PHYSICAL DESCRIPTION

In a two-dimensional model the particles are taken to be thin uniformly charged rods of infinite length that always remain parallel to one another. A plasma consisting of such rods is inhomogeneous in x and y, which are taken to be the directions perpendicular to the rods and homogeneous in z — the direction along the rods. If the rods move only in the x and y directions the model is considered to be simply 2-D. Motion of the rods along the infinite dimension constitutes infinite-line currents with the associated x and y magnetic fields and the z electric field. If this latter motion is incorporated in the model it is for

154

convenience referred to as 2 1/2-D. In both the 2-D and 2 1/2-D models gradients with respect to z are absent. The boundaries are taken to be perfectly conducting walls that are infinite in z and that form a rectangle in x and y.

Initial conditions can be determined in several ways. In our case we will be interested among other things in phenomena associated with the beam head. We therefore need a beam injection mechanism. This is simulated by "peeling" charge rods off the wall and letting them proceed at the desired initial velocity into the cavity formed by the conducting walls. This can be thought of as a charged particle entering an experimental tank of some sort through a conducting foil. The background plasma can be thought of as a pre-existing but very cold plasma. It is particularly convenient to let the initial background be a perfectly cold and perfectly neutralized "gas" with no fields which is then "ionized" by the beam. The initial conditions and the boundary conditions obtained in this way are all self-consistent and allow us to treat transient phenomena associated with the beam head.

The equations that are solved numerically to advance the particles in time are Maxwell's equations together with the Lorentz force law. This approach was adopted because the required differentiation when using the vector and scalar potentials proved unfeasible for numerical reasons. In order to put these equations in finite difference form the notion of finite size particles is used. This means that the charged rods above are not infinitely thin line charges but have a finite cross section. The interpolation schemes of Birdsall and Fuss[2]

are used to assign currents to points in the grid which is constructed in x and y, and to determine the forces on the particles. The differencing scheme is a first order central difference scheme in space and in time. A 1 1/2-D code written to test the methods gave satisfactory results. The same conclusion is born out by preliminary results from a 2 1/2-D code.
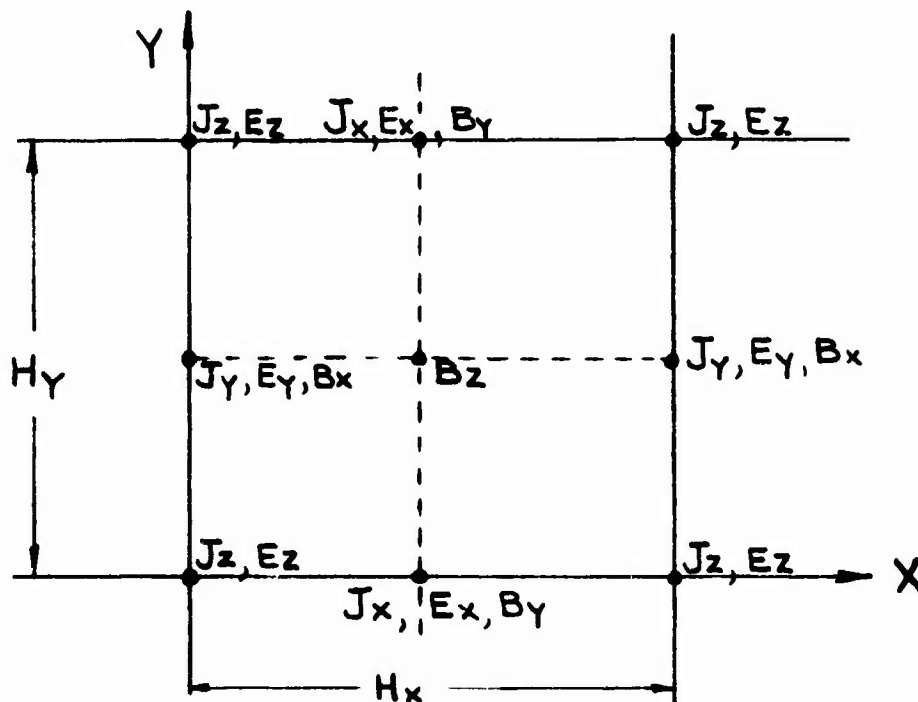
Fig. 1. One grid cell showing the relative positions of the points for which the various quantities are calculated.

III. NUMERICAL PROCEDURE

In order to simulate a plasma including electromagnetic and relativistic effects we need to solve

$$\nabla \times \hat{B} = \frac{4\pi}{c} \hat{J} + \frac{1}{c} \frac{\partial \hat{E}}{\partial t}$$

$$\nabla \times \hat{E} + \frac{1}{c} \frac{\partial \hat{B}}{\partial t} = 0$$

$$\frac{d}{dt} (\gamma \hat{v}) = \frac{e}{m} (\hat{E} + \frac{\hat{v} \times \hat{B}}{c}).$$

$\nabla \cdot \hat{B} = 0$ is satisfied if we start with zero field and $\nabla \cdot \hat{E} = 4\pi\rho$ is accounted for by the first equation and the continuity guaranteed by the Lorentz force. The latter two equations can be used to determine initial conditions and to check consistency of the computation.

We shall restrict ourselves to cases where $\frac{\partial}{\partial z} = 0$. It is convenient to make these equations dimensionless according to

$$\hat{v} = \hat{u} \frac{c}{\gamma}$$

$$t = t' \frac{\lambda}{c}$$

$$q = q' Q$$

$$x = x' \lambda$$

$$y = y' \lambda$$

$$E = E' \frac{4\pi Q}{\lambda}$$

$$B = B' \frac{4\pi Q}{\lambda}$$

157

where

> Q = charge/length
>
> λ = some typical length
>
> c = speed of light.

In component form the dimensionless equations that need to be solved are:

(1) $\dfrac{\partial B_z}{\partial y} = J_x + \dfrac{\partial E_x}{\partial t}$

(2) $-\dfrac{\partial B_z}{\partial x} = J_y + \dfrac{\partial E_y}{\partial t}$

(3) $\dfrac{\partial B_y}{\partial x} - \dfrac{\partial B_x}{\partial y} = J_z + \dfrac{\partial E_z}{\partial t}$

(4) $\dfrac{\partial E_z}{\partial y} + \dfrac{\partial B_x}{\partial t} = 0$

(5) $-\dfrac{\partial E_z}{\partial x} + \dfrac{\partial B_y}{\partial t} = 0$

(6) $\dfrac{\partial E_y}{\partial x} - \dfrac{\partial E_x}{\partial y} + \dfrac{\partial B_z}{\partial t} = 0,$

along with

(7) $\dfrac{d\hat{u}}{dt} = q \left(\dfrac{4\pi Q^2}{mc^2} \right) \left[\hat{E} + \dfrac{\hat{u} \times \hat{B}}{\gamma} \right]$

where

$$\hat{J} = \Sigma_k \; q_k \; \dfrac{\hat{u}_k}{\gamma_k} \; \delta(x - x_k) \; \delta(y - y_k)$$

and

$$\gamma_k = \sqrt{1 + (u_{xk})^2 + (u_{yk})^2 + (u_{zk})^2}$$

(NOTE: $\left(\dfrac{4\pi Q^2}{mc^2} \right)$ is dimensionless)

158

Electromagnetic and Relativistic Simulations

Inspection of Eqs. (1)(2) and (6) shows that they form a complete set of equations for a 2-D system with J_x and J_y as the driving terms. Equations (3), (4) and (5) are the additional equations to make the system $2\frac{1}{2}$-D. We will put the above equations in finite difference form using the central difference scheme:

$$\frac{dA}{d\omega}\bigg|_{\omega_{\ell+\frac{1}{2}}} = \frac{A_{\ell+1} - A_\ell}{H\omega}$$

where $H\omega$ is the step size. We use a rectangular grid.

Numbering x,y,t steps i,j,n respectively (and denoting particles by k) we find it convenient to use the following quantities for a 2-D computation:

$$E^n_{x_{i+\frac{1}{2},j}} \qquad E^n_{y_{i,\ j+\frac{1}{2}}} \qquad B^{n+\frac{1}{2}}_{z_{i+\frac{1}{2},j+\frac{1}{2}}}.$$

For a $2\frac{1}{2}$-D computation we also need

$$E^n_{z_{i,j}} \qquad B^{n+\frac{1}{2}}_{x_{i,j+\frac{1}{2}}} \qquad B^{n+\frac{1}{2}}_{y_{i+\frac{1}{2},j}}.$$

We shall be concerned mostly with rectangular systems with perfectly conducting boundaries. If the boundaries are chosen to be at $i = 0$, $i = L$, $j = 0$, $j = W$, where L and W are integers, then we see that the above choice of field quantities is just right to make the fields that are known from the boundary conditions fall exactly on the boundaries rather than an half grid space from them. That is to say $\hat{n} \times \hat{E} = 0$ and $\hat{n} \cdot \hat{B} = 0$ imply

$$E^n_{x_{i+\frac{1}{2},j=0_W}} = 0 \qquad\qquad E^n_{y_{i=0_L,j+\frac{1}{2}}} = 0 \qquad\qquad \text{for 2-D}$$

and

$$E^n_{z_{i=0_L,j}} = 0 \qquad\qquad E^n_{z_{i,j=0_W}} = 0$$

$$\left.\begin{array}{l} \\ \\ \\ B^{n+\frac{1}{2}}_{x_{i=0_L,j}} = 0 \qquad\qquad B^{n+\frac{1}{2}}_{y_{i+\frac{1}{2},j}} = 0 \end{array}\right\} \text{ for } 2\tfrac{1}{2}\text{-D}$$

where the choice of integral and half steps agrees to satisfy these boundary conditions exactly.

The algorithms that give the fields are for 2-D

$$E^n_{x_{i+\frac{1}{2},j}} = -Ht\cdot J^{n-\frac{1}{2}}_{x_{i+\frac{1}{2},j}} + E^{n-1}_{x_{i+\frac{1}{2},j}} + \left(\frac{Ht}{Hy}\right)\left(B^{n-\frac{1}{2}}_{z_{i+\frac{1}{2},j+\frac{1}{2}}} - B^{n-\frac{1}{2}}_{z_{i+\frac{1}{2},j-\frac{1}{2}}}\right)$$

$$E^n_{y_{i,j+\frac{1}{2}}} = -Ht\cdot J^{n-\frac{1}{2}}_{y_{i,j+\frac{1}{2}}} + E^{n-1}_{y_{i,j+\frac{1}{2}}} - \left(\frac{Ht}{Hx}\right)\left(B^{n-\frac{1}{2}}_{z_{i+\frac{1}{2},j+\frac{1}{2}}} - B^{n-\frac{1}{2}}_{z_{i-\frac{1}{2},j+\frac{1}{2}}}\right)$$

$$B^{n+\frac{1}{2}}_{z_{i+\frac{1}{2},j+\frac{1}{2}}} = B^{n-\frac{1}{2}}_{z_{i+\frac{1}{2},j+\frac{1}{2}}} - \left(\frac{Ht}{Hx}\right)\left(E^n_{y_{i+1,j+\frac{1}{2}}} - E^n_{y_{i,j+\frac{1}{2}}}\right)$$
$$+ \left(\frac{Ht}{Hy}\right)\left(E^n_{x_{i+\frac{1}{2},j+1}} - E^n_{x_{i+\frac{1}{2},j}}\right)$$

and additionally for $2\tfrac{1}{2}$-D

$$E^n_{z_{i,j}} = -Ht\cdot J^{n-\frac{1}{2}}_{z_{i,j}} + E^{n-1}_{z_{i,j}} + \left(\frac{Ht}{Hx}\right)\left(B^{n-\frac{1}{2}}_{y_{i+\frac{1}{2},j}} - B^{n-\frac{1}{2}}_{y_{i-\frac{1}{2},j}}\right)$$
$$- \left(\frac{Ht}{Hy}\right)\left(B^{n-\frac{1}{2}}_{x_{i,j+\frac{1}{2}}} - B^{n-\frac{1}{2}}_{x_{i,j-\frac{1}{2}}}\right)$$

$$B_{x_{i,j+\frac{1}{2}}}^{n+\frac{1}{2}} = B_{x_{i,j+\frac{1}{2}}}^{n-\frac{1}{2}} - \left(\frac{Ht}{Hy}\right)\left(E_{z_{i,j+1}}^{n} - E_{z_{i,j}}^{n}\right)$$

$$B_{y_{i+\frac{1}{2},j}}^{n+\frac{1}{2}} = B_{y_{i+\frac{1}{2},j}}^{n-\frac{1}{2}} + \left(\frac{Ht}{Hx}\right)\left(E_{z_{i+1,j}}^{n} - E_{z_{i,j}}^{n}\right)$$

where we have made allowance for using a rectangular rather than a square grid.

We now turn to the Lorentz force. In difference form it is

$$\frac{\hat{u}^{n+\frac{1}{2}} - \hat{u}^{n-\frac{1}{2}}}{Ht} = q\,\frac{4\pi Q^2}{mc^2}\left[\hat{E}^n + \frac{\hat{u}^n \times \hat{B}^n}{\gamma^n}\right].$$

If we use $\dfrac{\hat{u}^{n+\frac{1}{2}} + \hat{u}^{n-\frac{1}{2}}}{2}$ in the expression for γ we then in practice have a set of three coupled fourth-order algebraic equations for the components of $\hat{u}^{n+\frac{1}{2}}$. Let us find a different way to solve these equations. To this end we realize that for large u, γ varies nearly linearly with u. If we assume that changes in $\overset{\wedge\;\bullet}{u}$ in one time step are small, we can then expand $\dfrac{\hat{u}^n}{\gamma^n}$ in powers of $(\hat{u}^{n+\frac{1}{2}} - \hat{u}^{n-\frac{1}{2}})$. The result is

$$\frac{\hat{u}^n}{\gamma^n} = \frac{\hat{u}^{n-\frac{1}{2}}}{\gamma^{n-\frac{1}{2}}} + \frac{\hat{u}^{n+\frac{1}{2}} - \hat{u}^{n-\frac{1}{2}}}{2\gamma^{n-\frac{1}{2}}} + \hat{u}^{n-\frac{1}{2}}\left[-\frac{(\hat{u}^{n+\frac{1}{2}} - \hat{u}^{n-\frac{1}{2}})\cdot\hat{u}^{n-\frac{1}{2}}}{2(\gamma^{n-\frac{1}{2}})^3}\right]$$

Substitution of this expression in the Lorentz force gives a linear vector equation in $\hat{u}^{n+\frac{1}{2}}$. We have dropped a $(\hat{u}^{n+\frac{1}{2}} - \hat{u}^{n-\frac{1}{2}})^2$ term which contributes to $\hat{u}^{n+\frac{1}{2}}$ only in the second order. Using the following notation:

161

$$\hat{B} = \hat{B}^n \; Ht \; q \; \frac{4\pi Q^2}{mc^2} \qquad \Big| \qquad \hat{u}^+ = \hat{u}^{n+\frac{1}{2}}$$

$$\hat{E} = \hat{E}^n \; Ht \; q \; \frac{4\pi Q^2}{mc^2} \qquad \Big| \qquad \hat{u} = \hat{u}^{n-\frac{1}{2}}$$

$$\gamma = \gamma^{n-\frac{1}{2}}$$

the Lorentz force becomes

$$(\hat{u}^+ - \hat{u}) - \frac{(\hat{u}^+ - \hat{u}) \times \hat{B}}{2\gamma} + \frac{1}{2}\left[(\hat{u}^+ - \hat{u}) \cdot \frac{\hat{u}}{\gamma^3}\right]\hat{u} \times \hat{B} = \hat{E} + \frac{\hat{u}}{\gamma} \times \hat{B}$$

This can be solved to yield

$$\hat{u}^+ - \hat{u} = \left\{ \hat{E} + \hat{B}\frac{(\hat{E}\cdot\hat{B})}{4\gamma^2} + \left\{ \hat{B}\left(\frac{\hat{B}\cdot\hat{u}}{2\gamma^2}\right) - \hat{u}\frac{\hat{B}^2}{2\gamma^2} + \frac{\hat{u} \times \hat{B}}{\gamma} \right\} \right.$$
$$\left.\left[1 - \frac{\hat{u}\cdot(\hat{u}^+ - \hat{u})}{2\gamma^2}\right] + \frac{\hat{E} \times \hat{B}}{2\gamma} \right\}\left(1 + \frac{B^2}{4\gamma^2}\right)^{-1}$$

where

$$\hat{u}\cdot(\hat{u}^+ - \hat{u}) = \frac{\hat{u}\cdot\hat{E} + \frac{(\hat{u}\cdot\hat{B})(\hat{E}\cdot\hat{B})}{4\gamma^2} - \frac{\hat{u}}{2\gamma}\cdot\left(\hat{B} \times \hat{E} + \frac{\hat{u}B^2 - \hat{B}(\hat{u}\cdot\hat{B})}{\gamma}\right)}{1 + \frac{B^2}{4\gamma^4} + \frac{(\hat{u}\cdot\hat{B})^2}{4\gamma^4}}$$

This is an explicit solution for $\hat{u}^+$. It is also the general solution in three dimensions.

The new positions are given by

$$\hat{x}^{n+1} = \hat{x}^n + Ht \; \frac{\hat{u}^{n+\frac{1}{2}}}{\gamma^{n+\frac{1}{2}}}.$$

It is clear that in a 2-D system no forces can ever arise to make the system $2\frac{1}{2}$-D. Also we see that e-m waves polarized in the x-y plane can

162

exist in the 2-D system. In the 2½-D system all polarizations are possible. In all cases the wave fronts have to be cylindrical.

Because of the frequent occurrence of γ and the square-rooting involved it is desirable to find a way to calculate this quantity in some other way to save time. This is particularly true in our system of units because during the nth time step the value of γ at $n-\frac{1}{2}$ is needed in the Lorentz force and the value of γ at $n+\frac{1}{2}$ is needed to calculate the new $\hat{J}$ and the new $\hat{x}$.

However, we could use

$$\gamma^{n+\frac{1}{2}} = \gamma^{n-\frac{1}{2}} + (\hat{u}^{n+\frac{1}{2}} - \hat{u}^{n-\frac{1}{2}}) \cdot \frac{\hat{u}^{n-\frac{1}{2}}}{\gamma^{n-\frac{1}{2}}} + \ldots \ldots$$

This approximation is not completely consistent with our other approximations, but for large u, γ varies very nearly linearly with u, so that this is not a serious matter. For example using $u_x^{n-\frac{1}{2}} = .1$, $u_y^{n-\frac{1}{2}} = .1$, $u_z^{n-\frac{1}{2}} = .1$ and $u_x^{n+\frac{1}{2}} = .15$, $u_y^{n+\frac{1}{2}} = .15$, $u_z^{n+\frac{1}{2}} = .15$ gives $\gamma^{n+\frac{1}{2}} = 1.030$ compared to the exact $\gamma^{n+\frac{1}{2}} \sim 1.033$. In practice we do not expect velocity jumps of 50%. Even at that, however, for larger u the agreement of approximate and exact γ values becomes outstanding for the same relative size jump.

In connection with the evaluation of the new $\hat{J}$'s we remark parenthetically that the assignment of $\hat{J}$ values to the grid space requires an interpolation in $\hat{x}$ at half time steps. However, $\hat{x}$ is calculated only at integral time steps. The apparent need for two $\hat{x}$ arrays can be avoided by calculating each particle's contribution to the $\hat{J}$ array as its velocity and position are updated. Also, the interpolations that are associated with the

aforementioned finite size of the particles are the same as those of Birdsall and Fuss[2].

The methods above have already been used in a 1 1/2-D code. The results were satisfactory and no reason was found to modify the approach. Preliminary runs of a 2 1/2-D code also indicate that the present methods are adequate.

References

1. S. Weinberg, J. of Math. Phys., 8, 614 (1967).

2. C. K. Birdsall and D. Fuss, J. of Comp. Phys., 3, 494 (1969).

Symbolic Programming for Plasma Physicists

K. V. Roberts and R. S. Peckover
Culham Laboratory
Abingdon, Berks., England

1.   Introduction

The details of computing are one of the burdens that must be
borne by the physicist who believes in a particular case that only
by a complex calculation will he be able to substantiate his theory
or establish the intricacies of a real experimental situation.
Nevertheless, it seems to us that the simulation of plasma behaviour,
to take an example, is at present made a more difficult task than it
need be partly because of the limitations of existing programming
languages, and partly because each worker in the field usually constructs
his own input, output and control facilities, and often does not develop
his program in a systematic way. However, a common structure can
be adopted for a wide class of time-dependent fluid flow problems.

To help the computational plasma physicist to keep closer to
his problem, the symbolic use of Algol has been developed[1,2,3].
Further a system has been devised which enables computer programs
to be built quickly out of a set of standard prefabricated modules,
with the addition of a few further modules peculiar to the problem.
The style enables all details of mathematics and logic to be hidden
at a lower level.   The discussion will be based on the use of
Symbolic Algol, see section II, but the remarks about the need for

a good adaptable program structure hold true also in Fortran (see
Appendix).

The prefabricated general purpose modules deal with output,
vector algebra, vector analysis, program control etc., act as a
library, and provide the physicist with a program which has a logical
structure and with the mathematical tools with which he is familiar.

Many programs in plasma simulation share the same superficial
structure - a set of differential equations are solved as a function
of time - and this superficial structure can be made the same in a
suite of computer programs, and only the sections describing the
actual physics need be different from case to case. Symbolic Algol

programs can moreover be written in a machine-independent way, so that
they will run quickly on any computer system, and with careful design
they can be made to execute with high efficiency.

To construct worthwhile programs rapidly, modules with well-defined
interfaces and dependable characteristics must be available - this
can be achieved using tiny testbed programs the results of which are
available as guarantees of confidence. The "standard empty program"
DUMMYRUN described in section III was tested in just this way before
being used as the skeleton on which to hang more substantial programs.
Such programs as FOLLS (a 2D program for studying enclosed convection)
and TRINITY (a 3D MHD program) have been tested this way and provide
good illustrations of the way in which initial conditions and boundary
conditions (see section VI) can be set up easily in Symbolic Algol I.
These were initially programs using leapfrog schemes but the modular
structure is flexible enough for other schemes both explicit and
implicit to be incorporated without major surgery. Such flexibility
is illustrated in Section VII.

166

2.   Symbolic Algol I

Let us first recall how symbolic Algol techniques can be used
to express programs that solve sets of partial differential
equations. These techniques were briefly reported at Culham (1)
and a more complete account can be seen in papers to be published
soon (2,3).

For mathematical text books, a fairly standard notation has
been adopted for such topics as vector algebra, and analysis. This
notation is highly compressed and can be co-ordinate-free. For
example, the vector magnetic field is written tersely as $\underline{B}$ instead
of in the expanded form $(B_x(x,y,z),\ B_y(x,y,z),\ B_z(x,y,z))$ and such
expressions as $(\text{curl } \underline{P}) \wedge \underline{B}$ are independent of both the particular
co-ordinate system used and the effective number of dimensions.

Consider the equation of charge conservation

$$\frac{\partial q}{\partial t} + \text{div } \underline{j} = 0. \tag{1}$$

Using an explicit difference scheme we may express this in Algol 60
as:-

$$AQ[O] := Q - DT * DIV(J); \tag{2}$$

where:

> AQ is an array holding the charge;
>
> O is the local origin of the difference scheme;
>
> Q is the value of the charge at the 'old' time;
>
> DT is the effective time increment;
>
> J is the current vector;
>
> DIV is a finite difference operator.

Here Q, J, and possibly DT are real parameterless procedures. i.e.
they depend only on implicit   s which represent the chosen

vector component end lattice point in terms of the geometry of the problem and do not depend on any explicitly exhibited variable.

The differential operator "div" is defined in mathematical physics for a cartesian co-ordinate system by

$$\text{div } \underline{F} = \sum_{i=1}^{3} \frac{\partial F_i}{\partial x_i} \qquad (3)$$

In Symbolic Algol I it is represented by the quite analogous real procedure DIV which has a declaration of the form

real procedure DIV (A); real A; DIV: = SIGMA(DEL(A)); (4)

The procedure DIV here has an explicit argument, as div does in vector analysis.

A second example of the compactness of Symbolic Algol notation is in the difference form for the Vlasov equation. For a continuous distribution function f we may write the Vlasov equation in ordinary mathematical notation as

$$\frac{\partial f}{\partial t} + (v.\nabla)f + (\underline{a}. \frac{\partial}{\partial \underline{v}})f = 0 \qquad (5)$$

without needing to say explicitly that f is a function of (x,y,z,u,v,w,t) wherever it is mentioned.

In Algol 60 this can be written

AF [0] : = F - DT * (DOT(V,DEL(F)) + DOT (A,DELV(F))); (6)

Because procedures can be parameterless in Algol (unlike Fortran) we can express the distribution function as F, its current value, through the definition:

real procedure F : F = AF(0); (7)

where 0 is a matrix subscript and represents the current position on the lattice.

The real procedure DOT is the finite difference analogue of the inner vector product i.e.

$$\underline{a} \cdot \underline{b} \;\rightarrow\; DOT(A,B) \tag{8}$$

To show the way in which Symbolic Algol I is able to build up new procedures from older ones in a hierarchic fashion, the nested structure of DEL can be exhibited. The abbreviation RP will be used for real procedure and IP for integer procedure

$$\left.\begin{array}{l}
\underline{RP}\ DEL(F);\quad \underline{real}\ F;\quad DEL = (EP(F)-EM(F))/(2^{*}DS); \\[4pt]
\underline{RP}\ EM(F);\quad \underline{real}\ F;\ \underline{begin}\ 0 : = 0 - DO;\ EM:=F;0:=0 + DO\ \underline{end} \\[4pt]
\underline{RP}\ EP(F);\quad \underline{real}\ F;\quad \underline{begin}\ 0 : = 0 + DO;\ EP:=F;\ 0:= 0-DO;\ \underline{end} \\[4pt]
\underline{IP}\ DO; \\[4pt]
DO:=\ \underline{if}\ C\ \underline{eq}\ 1\ \underline{then}\ 1\ \underline{else}\ \underline{if}\ C\ \underline{eq}\ 2\ \underline{then}\ PI\ \underline{else}\ PI^{*}PJ
\end{array}\right\} \tag{9}$$

0 is the current lattice point. C is the index specifying the direction.

If C = 1, DO corresponds to the length PA, and the statement 0:= 0 + DO moves the current origin from P to A. If C = 2 the origin is moved to B, but if C = 3 it is moved in the z-direction.

This may be compared with the mathematical hierachy

$$\nabla_h \psi \equiv \frac{1}{2h}\ (E^{+} - E^{-})\psi \tag{10}$$

where

$$\begin{aligned}
E^{+}\psi(\underline{r}) &= \psi(\underline{r}+\underline{dr}) \\
E^{-}\psi(\underline{r}) &= \psi(\underline{r}-\underline{dr})
\end{aligned} \tag{11}$$

and

$$\left.\begin{array}{l}
\underline{dr} = dx\ (x\ component) \\
\quad or\ dy\ (y\ component) \\
\quad or\ dz\ (z\ component)
\end{array}\right\} \tag{12}$$

169

With so many nested procedure calls Symbolic Algol I usually executes slowly, but it is very clear what the program is doing. Such an approach enables clear programming in the initial stages. Subsequently DEL could be made faster by introducing a vector DR with 3 elements containing 1, PI, and PI * PJ respectively. The procedure definition for DEL could then be compacted to

$$
\begin{aligned}
&\underline{RP}\ DEL\ (F);\ \underline{real}\ F;\ \underline{begin}\ \underline{real}\ F1 \\
&\underline{integer}\ DO; \\
&DO:\ =\ DR(C);\ \ O:\ =\ O\ +\ DO;\ F1:\ =\ F; \\
&\qquad O:\ =\ O\ -\ 2\ *\ DO;\ DEL:\ =\ (F1\ -\ F)/(2\ *\ DS); \\
&\qquad O:\ =\ O\ +\ DO;\ \underline{end}
\end{aligned}
\qquad (13)
$$

A deeper level of optimisation is to replace the r.h.s. of equation (6) by an explicit linear form in AF $[0 + e]$ for a sum of terms in o. For example when C = 1,

$$
DEL(F)\ =\ (AF[O\ +\ 1]\ -\ AF\ [O\ -\ 1])/(2\ *\ DS); \qquad (14)
$$

Optimisations of this kind can be carried out automatically and are discussed in detail elsewhere[2].

Converter programs exist[14] which enable equations to be converted automatically into an optimized code for any desired combination of output language, co-ordinate system, and difference scheme. Languages implemented so far have been Algol, Fortran, KDF9 Usercode and IBM 360 assembly language. The optimized module is then used, in conjunction with the remainder of the original Symbolic Algol 1 program, to carry out the production runs.

3. Standard Modular Structure

Consider two programs that solve two sets of different time-dependent fluid equations. Evidently these programs could be designed to have a lot in common; everything, in fact, except the physics. We

have developed a series of Algol modules which deal with standard tasks
such as output, vector algebra and analysis, program control and so on,
and which fit together to enable a wide range of physics programs to be
constructed quickly. Some of these prefabricated modules have been put
together to form a skeletal program DUMMYRUN which has the general
structure of a program that simulates time-dependent particle and fluid
flows, although it actually does <u>no</u> physics. It is a "standard empty
program" which with little effort can be converted into a running
program for a real physical problem.

DUMMYRUN consists of a set of modules which are available as on-line
files and has the following structure:

DUMMYHEAD

OUTALGOL

ALGEBRA

CARTESIAN

UTILITIES

DUMMY PREDATA

MAIN CONTROL

DUMMY PHYSICS

DUMMY CONTROL

TAIL

Fig. 1

Let us build the program up piece by piece:

(a) An Algol program needs job control cards, and a <u>begin</u> } HEAD
for the outer block.

(b) It needs an <u>end</u> for both the outer block and the inner } TAIL
problem-oriented block.

(c) In order to output anything, an output channel must be } OUTALGOL
specified and output procedures provided.

171

(d) The type of physics problems in which we are interested uses vector algebra, difference schemes in Cartesian geometry, with various sorts of array output.

ALGEBRA
CARTESIAN
UTILITIES

(e) Clearly other standard library modules could be inserted, to generate on-line graphical display or to use cylindrical co-ordinates, for example.

(f) Prior to entering the inner (physics) block, dynamic array bounds must be set and the various modules activated.

PREDATA

(g) Most fluid simulation programs seem to require much the same elements, as we find by perusing programs written in the past both by ourselves and by others. These have been formalized into a standard control structure . MAIN CONTROL consists of a series of parameterless procedures whose names describe their functions (Fig. 2). This provides a compact way of stating clearly what each section of the program does . Each of the procedures called by MAIN CONTROL must be defined and a series of modules are created to do this. Initially we need only two: CONTROL and PHYSICS.

MAIN CONTROL

(h) CONTROL provides the procedures which control the progress of the calculation, i.e. which label the run, clear the core store, initialize the run, output when required, and tie up the loose ends after the run is complete.

CONTROL

172

```
┌─'COMMENT'──────────────────────────────────────────────────
│  ┌──────────────────────────────────────────────────────────┐
│  │        S-FILE*MAIN CONTROL.CPIP'  (STANDARD MAIN PPOGRAM);│
│  │                                                          │
│  │ 'PROCEDURE'MAIN CONTROL;'BEGIN'                          │
│  │     LABEL THE RUN;                      REPORT(1,1);     │
│  │     CLEAR VARIABLES AND ARRAYS;         REPORT(1,2);     │
│  │     SET DEFAULT VALUES;                 REPORT(1,3);     │
│  │     DEFINE DATA SPECIFIC TO RUN;        REPORT(1,4);     │
│  │     SET AUXILIARY VALUES;               REPORT(1,5);     │
│  │     DEFINE INITIAL CONDITIONS;          REPORT(1,6);     │
│  │     INITIAL OUTPUT;                     REPORT(1,7);     │
│  │                                                          │
│  │ 'FOR' N=NSTART'STEP'1'UNTIL'NSTOP'DO'                    │
│  │     'BEGIN'MAIN COMPUTATION CYCLE'.' T=T+DELTAT;        │
│  │     ADVANCE ONE TIMESTEP; OUTPUT IF REQUIRED;           │
│  │     'END' OF MAIN CYCLE;                REPORT(1,8);     │
│  │                                                          │
│  │     N=NSTOP; FINAL OUTPUT;TERMINATE THE RUN; REPORT(1,9);│
│  │ 'END'                                                    │
│  └──────────────────────────────────────────────────────────┘
```

Fig.2

(i) PHYSICS provides a slot where the real physics is to be

inserted. Initially it contains only a dummy procedure: (Fig.3)

Fig.3

```
┌─────────────────────────────────────────────────────────┐
│                  FILE*DUMMY PHYSICS*                     │
│ 'PROCEDURE'ADVANCE ONE TIMESTEP;'BEGIN'LINE              │
│     TEXT(' '**WE**HAVE**ADVANCED**ONE**TIMESTEP**' ')    │
│ LINE;'END';                                             │
└─────────────────────────────────────────────────────────┘
```

PHYSICS

PHYSICS can be augmented, if required, by procedures which

solve Poisson's equation or which deal with standard

boundary conditions, for example.

(j) Through the module OUTALGOL, mentioned earlier in DUMMYRUN,

is funnelled all input and output. This makes the program

portable, since the changes required to run on a different

machine are all concentrated into one place.

DUMMYRUN

4. Acceptance Tests

Each module is part of an assembly, and as with any engineering

component that is to be used without constant attention, it is

sensible to put the module through a proper set of acceptance tests

to guarantee that each element of the module performs properly. Every module must be completely dependable. Further, by making the tests generally available, the authors of the program raise confidence levels, and allow the user to see for himself any restrictions which may apply.

Let us introduce the concept of a "testbed". This is a special small program written for the new module which uses and tests out all its features in as thorough but economical a way as possible. A testbed program consists of:

(a) The pre-tested modules required in order to use the new module, or to perform the tests.

(b) The new module itself.

(c) A specially written TRIAL module, which is the part of the program that runs through all the procedures in the module which is being tested.

For example, the TESTBED of the module "ALGEBRA" which is used in DUMMYRUN consists of 4 modules:- HEAD (which contains the job control cards); OUTALGOL (through which is funnelled all output); ALGEBRA itself, and its associated TRIAL module (see figure 4).
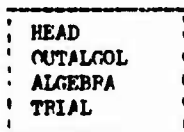
```
HEAD
OUTALGOL
ALGEBRA
TRIAL
```
Fig.4

HEAD and OUTALGOL are modules which have been put through just such tests previously. The results of this test are made available as part of the documentation for the module, and this facilitates conversion to other computer systems.

For further illustration let us consider the module CARTESIAN. It consists of procedures which are the finite difference analogues

174

Symbolic Programming

of DIV, GRAD, CURL. Of course these have different forms depending on difference scheme and geometry; the forms in CARTESIAN are appropriate for 3-D Cartesian geometry in which the operators are defined in terms of central difference formulae.

Analytically

$$\left\{ curl(\underline{u}) \right\}_i \equiv \epsilon_{ijk} \frac{\partial u_j}{\partial x_k} \tag{15}$$

In 3 dimensions, it is convenient to think of the dimensions (x,y,z) as (x_1, x_2, x_3) which can be written as $\left\{ (x_{i-1}, x_i, x_{i+1}) \ / \text{ modulo } 3 \right\}$. In terms of these we may write

$$\left\{ curl(\underline{u}) \right\}_i = \frac{\partial u_{i-1}}{\partial x_{i+1}} - \frac{\partial u_{i+1}}{\partial x_{i-1}} \tag{16}$$

$$\text{i.e. } \left\{ curl(\underline{u}) \right\}_i = \frac{\partial u_{i+2}}{\partial x_{i+1}} - \frac{\partial u_{i-2}}{\partial x_{i-1}} \quad \text{(modulo 3 again)}$$

The Algol procedure CURL is defined by

$$CURL(U) = RP(DEL(RP(U))) - PM(DEL(RM(U))); \tag{17}$$

in Symbolic Algol I. The procedure RP effectively increases the index by unity, and RM decreases it by unity. DEL is the analog of ∇ (see equation 9 above).

A test for CURL could be as follows:- Let f_1, f_2, f_3, φ be any scalar functions of x,y,z. Construct a general vector $\underline{A}$ s.t.

$$\underline{A} = curl (f_1 \, \hat{x} + f_2 \, \hat{y} + f_3 \, \hat{z}) + \nabla \varphi \tag{18}$$

Then for the differential operators, the following 2 identities hold:-

$$\text{div curl } \underline{A} \equiv 0 \tag{19}$$

and

$$\text{curl grad } f_1 \equiv 0 \tag{20}$$

If the finite difference operators DIV, CURL, GRAD are defined in terms of central differences on a Cartesian mesh, these identities

175

still hold. For a TESTBED for these, a TRIAL module would then contain:

'RP' F1; F1:= (user's choice: e.g. $x^4 + y^4 + z^4$);

'RP' F2; F2:= (user's choice: e.g. 3xyz);

'RP' F3; F3:= (user's choice: e.g. $x^3 + y^3 + z$);

'RP' G; G:=   (user's choice: e.g. e^{x+y+z});

'RP' A; A:=

CURL(F1*E1 + F2*E2 + F3*E3) + GRAD(G);

and the printing PROCEDURES

PRINT VECTOR (CURL(GRAD(F1));

PRINT SCALAR(DIV(CURL(A));

The output is of course

0.0   0.0   0.0

and

0.0

The procedures E1, E2, E3 come from the module "ALGEBRA", and are defined thus:-

'RP' E1; E1:= <u>if</u> C <u>eq</u> 1 <u>then</u> 1 <u>else</u> 0;

'RP' E2; E2:= <u>if</u> C <u>eq</u> 2 <u>then</u> 1 <u>else</u> 0;

'RP' E3; E3:= <u>if</u> C <u>eq</u> 3 <u>then</u> 1 <u>else</u> 0;

where C is an index indicating which component - x, y or z - is under consideration. E1, E2, E3 are in fact the unit vectors in the x, y, and z directions respectively.

The modules of which the skeleton program DUMMYRUN is composed have each been tested using the TESTBED approach. The progressive way in which such tests can be carried out is illustrated in figure 5.
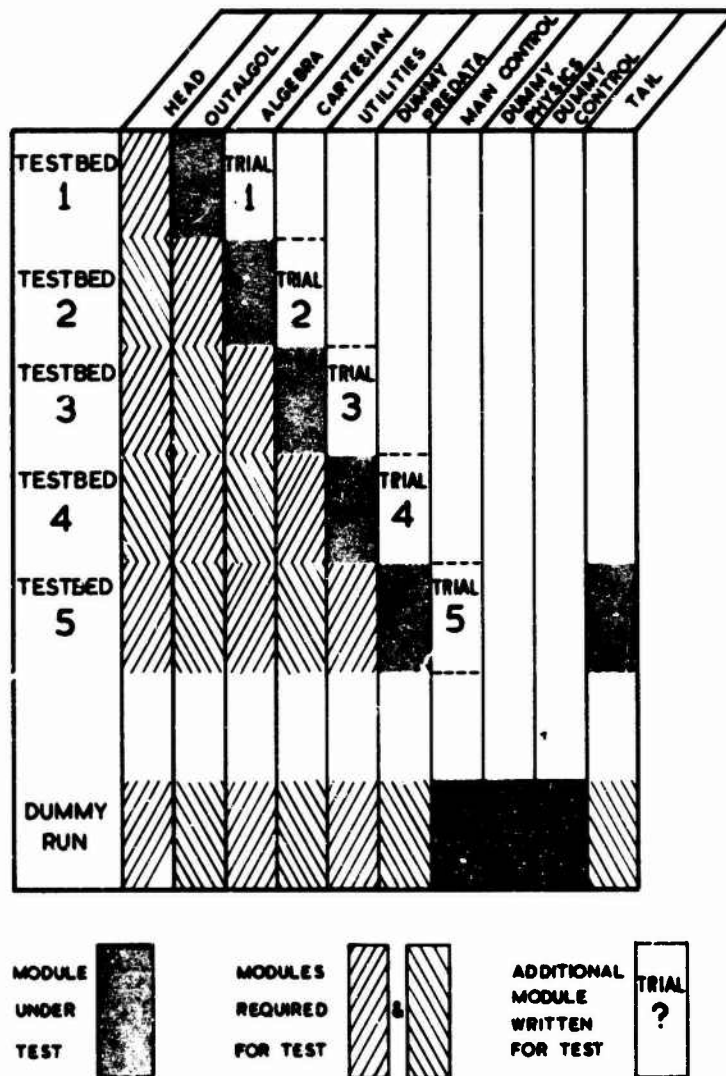
Figure 5: Listed along the top are the modules of which DUMMYRUN
is constructed. The staircase shows the systematic
way in which modules must be tested. For example
TESTBED4 requires 4 pre-tested modules (DUMMYHEAD,
OUTALGOL, ALGEBRA, CARTESIAN) in order to test
UTILITIES. TRIAL4 is the specially written module
containing the test material.

177

5. Portability

Collaboration between the staff of different laboratories can often make desirable the running of the same computer program on different machines. The transfer from one machine to another can be made more quickly.if the changes which must be made are localised into regions where such changes can be flagged.

A program can be made more portable in 3 separate areas:-

i)   By carefully avoiding, in the early mark numbers of a program , exploitation of the advanced features and quirks peculiar to a machine (we are of course discussing programs which in the past have taken at least 1 man year to get into production). In Fortran this might imply for example restricting oneself at this time to Fortran IV. In Algol, one avoids Jensen's device for example. In later versions, some pieces of program can be replaced by code tailored for a particular machine and by fast assembler subroutines.

ii)   Input and output should be localised and flagged. If I/O is restricted (for example) in Fortran to particular subroutines it enables the more sophisticated I/O packages available on some machines to be introduced easily into the program on transfer to these machines.

iii) Every machine might well as a matter of course have available a series of tiny programs or macros which will change the character codes, (and in the case of Algol alter the representation of the Algol Basic Symbols) from that used on one machine to that for another. For the job control languages, while the variety of different machines continues, there seems no better way of grafting a program onto an unfamiliar machine than having the aid of someone with local knowledge.

Thus, at the Culham Laboratory we are deliberately writing our Fortran programs in ASA Fortran IV, which enables a program to be

178

portable, and incidentally to be publishable and open to the criticism of other computational physicists. For example, since the name-list facility is not implemented on all big machines, it is not used, even though it is very convenient. In Algol, calls by value are avoided since some compilers do not have this feature. Again, since only the first six letters of an identifier are significant on an IBM machine, the long identifiers are chosen with care to ensure the distinct identity of each to the compiler.

For input and output, and the program transfer macros, we restrict our attention at this point to Algol; further comments on Fortran are found in the appendix.

The Algol module OUTALGOL (see also section 3 above) has been written to contain the high level procedure calls required to make simple-minded input and output requests, some of these are shown in Figure 6 as they are implemented on the KDF9 at Culham. The intention is to hide detail, irrelevant in more physical contexts. The advocacy of the use of such procedures, independent of implementation, is not new, see for example Michie, et al[5]. We report that their systematic use is worth the additional care in design initially. For the implementation on an IBM 360 see Figure 7. Similar OUTALGOL modules have been written for CDC 6600, the ICL 1900 series and GE 235.

To effect transfer from one machine to another the character code must be altered, and the Algol Basic symbols correctly represented. For this purpose the CACTUS package has been developed at Culham. On the Culham KDF9, the COTAN on-line system, contains among its commands the facility for generating a "macro" command - i.e. a command which blocks together a   series of commands in a file and activates them with a single command[15]. Macros have been written which change

```
'PROCEDURE' OUTALGOL;
    'BEGIN' DECIMAL=LAYOUT('['S-NDDD.DD']');
    NTEGER=LAYOUT('['S-NDDD']');OUT=10;'END';
'INTEGER' DECIMAL,NTEGER,OUT;

'PROCEDURE' BLANK;SPACE(OUT,1);
'PROCEDURE' INTVAR(N);'INTEGER'N;WRITE(OUT,NTEGER,N);
'PROCEDURE' IVAR(NAME,N);'STRING'NAME;'INTEGER'N;
    'BEGIN' TEXT(NAME);BLANK;TEXT('['='']');INTVAR(N);'END';
'PROCEDURE' LINE;NEWLIN(OUT,1);
'PROCEDURE' PAGE;GAP(OUT,1);
'PROCEDURE' TEXT(T);'STRING'T;WRITET(OUT,T);
```

Figure 6:   The module *OUTALGOL* includes such procedures as the

                 above. REALVAR and RVAR are similar to INTVAR and IVAR.


```
'PROCEDURE' OUTALGOL.,
 'BEGIN' OUT .= 1.,  'END'.,
'INTEGER' OUT.,

'PROCEDURE' BLANK., OUTSTRING(OUT,'(' ')').,
'PROCEDURE' INTVAR(N).,'INTEGER'N., OUTINTEGER(OUT,N).,
'PROCEDURE' IVAR(NAME,N).,'STRING'NAME.,'INTEGER'N.,
    'BEGIN'TEXT(NAME).,BLANK.,TEXT('('=')').,INTVAR(N).,'END'.,
'PROCEDURE' LINE.,  SYSACT(OUT,14,1).,
'PROCEDURE' PAGE.,  SYSACT(OUT,15,1).,
'PROCEDURE' TEXT(T)., 'STRING' T., OUTSTRING(OUT,T).,
```

Figure 7:   Some OUTALGOL procedures used on an IBM 360.

180

the representation of Algol basic symbols on the disc in such a way
that it comes to a Data Dynamics teletype in the form suitable for
whichever machine is to be recipient. It is stored on the disc as
"Wheteg Algol" which is a subset of the representation acceptable to
the Whetatone compiler for instant execution and which is also accept-
able to our Egdon compiler for batch processing. This flexibility
enables the KDF9 to be used reasonably efficiently (viewed as a
man+machine entity).

Given an Algol program in "Wheteg", it can be automatically
translated into the forms required for use on a CDC 6600, IBM 360,
ICL 1900 or GE 235, though still stored in an on-line file. The actual
transfer can occur in a very simple fashion: the ISO paper tape code
used by teletypes interfaces with all machines which can use teletypes.
Thus a paper tape can be produced for an Algol program which is then
read back to another teletype (or the same one) connected up to a
different machine. Thus the existence of different card codes on the
various machines can be circumvented. The development of a program
on a machine with a fast compiler and good debugging facilities, and
the subsequent transfer to a machine with fast running times and a big
core seems an attractive method of computing effectively.

6. Initial Conditions and Boundary Conditions

The setting of initial conditions and boundary conditions is, in
a substantial computer program, a nuisance. It takes up, in coding
terms, far more statements and involves more intricate devices than
the body of the calculation in which most of the time of the computation
is spent.

This need not be so, and we describe in this section some of the
tools with which we have provided ourselves. Some of these could be

produced in Fortran, but there is no doubt that the availability of parameterless procedures in Algol is a boon.

For example it is convenient to be able to set the values of an array in a simple fashion. Consider the triplet of Algol statements:-

    TWO D;

    FULL REGION;

    SET SCALAR(PHI,SIN(2*PIE*X)*SIN(2*PIE*Y));

This sets the potential of ϕ over the whole region of interest in a two-dimensional calculation, to be $\sin(2\pi x)\sin(2\pi y)$. Of course the setting of parameters and general spadework needs to be done somewhere, but not at this point where we are only concerned with the mathematical formulation of the physics of the problem. Further assignment of values is not a clumsy matter but can be done tersely, as can best be made clear by setting down the contents of the above procedures.

<u>procedure</u> TWO D; <u>begin</u> NDIM:= 2; I:= J:= 0; K:= -1; NK:= 0; <u>end</u>;

    (the problem is declared to be 2D, the values of I and J are

    cleared, and the k-direction is cut out).

<u>procedure</u> FULL REGION; <u>begin</u> IP1:= JP1:= KP1:= 0; IP2:= NI; JP2:= NJ;

    KP2:= NK; <u>end</u>;

    (the upper and lower bounds for the array indexes are set in

    terms of the array sizes).

<u>procedure</u> SET SCALAR (A,F); <u>array</u> A; <u>real</u> F;

    <u>begin</u> <u>procedure</u> SETS2(K); <u>integer</u> K;

        <u>for</u> J:= JP1 <u>step</u> 1 <u>until</u> JP2 <u>do</u>

        <u>for</u> I:= IP1 <u>step</u> 1 <u>until</u> IP2 <u>do</u>

        <u>begin</u> 0:= 1 + (I + 1) + PI*(J + 1) + PI*PJ*(K + 1);

            A[0]:= F; <u>end</u> ;

    <u>if</u> NDIM <u>eq</u> 2 <u>then</u> SET S2(-1);

else for K:= KP1 step 1 until KP2 do SET S2 (K);

(the array A is set to have the function value F evaluated at

the relevant point on the lattice).

To set the value in 3 dimensions of the magnetic field $\underline{B}$ for each

of its components B_x, B_y, B_z in the interior of the region of interest

we may write

THREED;

INTERIOR REGION;

SET VECTOR (AB, Z*Z*E1 + 0.5*X*Z*E2 + X*E3);

This sets the magnetic field to be

$$\underline{B} = (Z^2, \tfrac{1}{2}ZX, X)$$

E1, E2, E3 are the unit vectors defined earlier (in section 4);

AB(C,0) is an array with 2 arguments: C (which determines the component

x,y,z) and 0 (which determines the current lattice point).

The declaration

real procedure B; B:= AB(C,0);

enables B to be used in equations for the magnetic field as vector $\underline{B}$

would be.

An alternative approach is to use 3 component arrays

$$BX[0], \quad BY[0], \quad BZ[0]$$

rather than the single array AB(C,0). Obviously a powerful technique

should not be tied to a decision on how to store the information about the

magnetic field.

In terms of these 3 arrays, we could set up $\underline{B}$ with the procedure calls

THREE D;

INTERIOR REGION;

SET SCALAR (BX, Z*Z);

SET SCALAR (BY, 0.5*X*Z);

SET SCALAR (BZ, X);

Another set of useful procedures involves setting values on lines and surfaces inside the region of interest. These are all tiny proc dures, where the purpose of defining them is to remove the mechanics of the computing from the focus of attention. For example

procedure SET XLINE (A, JJ, KK, F); array A; real F; integer JJ, KK;

begin J:= JJ; K:= KK;

for 1:= 1P1 step 1 until 1P2 do

begin DEFINE 0; A[0]:= F; end end

This sets the elements of the array A, corresponding to points on the line $y = y_j$ $Z = z_k$ (i.e. J = JJ; K = KK) to have the functional values F.

This ruled line provides a simple way of setting values on a plane surface parallel to an axis. Thus

procedure SET YZ SURFACE (A,11,F); array A; real F; integer I1;

for K:= KP1 step 1 until KP2 do

SET YLINE (A,1I,K,F);

sets A = F on the surface $x = x_i$ (i.e. 1 = 1I)

These hierarchic definitions enable one to program as clearly as one can write mathematics.

Similarly with boundary values, if the boundary conditions can be set easily and can be seen to have been set correctly, a program is simpler to handle. The setting of some of the possible boundary conditions at the wall for a plasma experiment are shown in figure 8.

```
WALL;

    GUARDX(PHO,RIGID,ZERO,          ZERO,SINGLE STEPS TO,N1);

    GUARDX(JZ,SYMMETRIC,ZERO,  Y-STAGGERED PT,COUPLE STEPS TO,N1);

    GUARDY(TEMP,RIGID,TC*Z*(1-Z),  ZERO,DOUBLE STEPS TO,N1);
```

Fig.8

The procedure WALL (besides acting as a paragraph heading) sets the current origin on the wall and arranges for it to move along in

184

Symbolic Programming

the x-direction setting suitable values. The procedure GUARDX has mnemonic
arguments to make the boundary conditions clear. The use of mnemonics
is important for although the analytic condition may be simple, the
difference form is often messy. The first set of arguments defines
the physics. For example, we have a rigid boundary on which the
density is set to zero, and the temperature to $T_o Z(1-Z)$. The z
component of the electric current j is set to zero, and so is its gradient.
The second set of arguments pick out the points where values are to be
set. For example, using a leapfrog scheme one may only need values
at alternate points, the mesh in use shifting by one interval between
alternating time steps. The starting point is shifted backwards and
forwards by X-STAGGEREDPT, and values are set at alternate points up to
point $I = HI$.

7. Flexibility

The flexibility of a modular structure, properly constructed,
enables programs to be developed quickly. Each module, besides
being fully tested has a corresponding dummy module. This is
composed of the same procedures as the full bodied module but each
is dummy. Such dummy modules enable parts of the program to be
thoroughly tested without wasting time in execution and compilation
on other pieces of program known to be in working order.

If having developed a program we decide to change the method of
solution of the differential equation, if the program is sufficiently
modular this can be achieved by the simple substitution of one form for
another. This can best be seen in a concrete example.

Thus, let us consider a one-dimensional plasma made up of electron
and ion (singly ionized) fluids whose distribution functions satisfy the
linearized Vlasov equations appropriate for a collisionless plasma

185

$$\frac{\partial f_e}{\partial t} + \frac{\partial}{\partial x} (v_e f_e) + \frac{\partial}{\partial v} (a_e f_e) = 0 \quad \left.\rule{0pt}{14pt}\right\}$$

$$\frac{\partial f_i}{\partial t} + \frac{\partial}{\partial x} (v_i f_i) + \frac{\partial}{\partial v} (a_i f_i) = 0 \quad \left.\rule{0pt}{14pt}\right\} \tag{21}$$

where f_e. and f_i are the electron and ion distribution functions

v_e, and v_i are the velocities of the local elements of the fluids

a_e, and a_i are the accelerations to which they are subjected.

The accelerations a_e, and a_i satisfy

$$m_e a_e = -m_i a_i = -eE \tag{22}$$

where

$$\frac{\partial E}{\partial x} = 4 \pi e \int (f_e - f_i) dV \tag{23}$$

the velocities f_e and v_i satisfy

$$\frac{\partial v_e}{\partial t} = \frac{-eE}{m_e} \quad \left.\rule{0pt}{20pt}\right\}$$

and

$$\frac{\partial v_i}{\partial t} = \frac{eE}{m_i} \quad \left.\rule{0pt}{30pt}\right\} \tag{24}$$

The plasma is assumed collisionless, and the ions and electrons interact only in as much as each species contributes to the electric field which acts on both of them.

To treat these equations by a finite difference method was advocated by Kellogg in 1965[6]. Of course several other methods have been advocated and implemented for this, e.g. the Waterbag Model (for the history of this see Berk and Roberts 1967[7], expansion in terms of Fourier components and orthogonal polynomials[8,9] and the popular sheet/rod model developed by Buneman and Dawson[10,11].

This approach does have its drawbacks[12], but is used here to illustrate the strength of symbolic techniques. Such techniques could be used in the other cases also.

186

Symbolic Programming

The computational steps are clearly

```
solve Poisson's equation;
ion fluid advected;
Electron fluid advected;
```

For a leapfrog scheme, the advection of the equations can be gathered together into a single procedure (Fig.9).

```
      'PROCEDURE'LEAPFROG;        'BEGIN'DT=0.5*DELTAT;
'FOR'I'EQUAL'IP1'STEP'1'UNTIL'IP2'DO'
'FOR'J'EQUAL'JP1'STEP'1'UNTIL'JP2'DO'
'BEGIN'DEFINE O;
NEW FE[O]=FE-DT*(DELX(VE*FE) + DELV(AE*FE));
NEW FI[O]=FI-DT*(DELX(VI*FI) + DELV(AI*FI));
'END'; 'END';
```

Fig.9

IP1, IP2, JP1, JP2 are the bounds for I and J. FE is a procedure which returns the value of the electron phase fluid density appropriate for the current lattice point. It should be added that these difference equations, although apparently a forward difference in time, are actually centred in time and space. The procedure DT is set to 0.5*DELTAT where DELTAT is the time step interval. As quantities are defined on a staggered mesh, they are available at the correct time level when required:

Thus in this case we may write simply

SOLVE POISSONS EQUATION;
LEAPFROG;

in the Symbolic equations module.

For a two-step Lax-Wendroff scheme, provisional values at an intermediate timestep must be calculated. The module could take the form of Fig. 10.

```
'PROCEDURE' AUXILIARY CALCULATION; 'BEGIN'DT = DELTAT;


'REAL''PROCEDURE' ELECTRON PHASE FLUX;
    ELECTRON PHASE FLUX = DELX(VE*FE) + DELV(AE*FE);


'REAL''PROCEDURE' ION PHASE FLUX;
    ION PHASE FLUX = DELX(VI*FI) + DELV(AI*FI);


'REAL''PROCEDURE' FE NEW;
    FE NEW = SAV(FE) - DT*ELECTRON PHASE FLUX;
'REAL''PROCEDURE' FI NEW;
    FI NEW = SAV(FI) - DT*ION PHASE FLUX;


FILL  THE AUXILIARY POINTS'.'
'FOR' I 'EQUAL' IP1 'STEP' 1 'UNTIL' IP2 'DO'
'FOR' J 'EQUAL' JP2 'STEP' 1 'UNTIL' JP2 'DO'
 'BEGIN'  DEFINE 0;

     C = 2; NORTH = 0+DOY;
         NEW FE[NORTH] = EP(FE NEW);
         NEW FI[NORTH] = EP(FI NEW);
            SOUTH = 0-DOY;
         NEW FE[SOUTH] = EM(FE NEW);
         NEW FI[SOUTH] = EM(FI NEW);
    CC = 1; EAST  = 0+DOX:
         NEW FE[EAST] = EP(FE NEW);
         NEW FI[EAST] = EP(FI NEW);
            WEST  = 0-DOX;
         NEW FE[WEST] = EM(FE NEW);
         NEW FI[WEST] = EM(FI NEW);
 'END';
```

Figure 10:   A 'procedure' AUXILIARY CALCULATION, for use in a

              2-step Lax-Wendroff scheme. Procedures FE NEW and

              FI NEW contain a clear statement of how the first

              step of the scheme works.

In this case the Symbolic equations module contains

```
    LAX WENDROFF TWO STEP'.'
        SOLVE POISSONS EQUATION;
        AUXILIARY CALCULATION;
        SOLVE POISSON FOR AUXILIARY VALUES;
        LEAPFROG;
```

Provided the modules have been properly constructed, the change from

one numerical difference scheme to another simply requires the replace-

188

Symbolic Programming

ment of one set by another (e.g. the Lax-Wendroff module is replaced
by the leapfrog one). This makes the comparison of the different
methods over such matters as speed, gross accuracy, and in particular
velocity dispersion, a fairly straightforward matter. With the develop-
ment of advanced methods such as Fromm's[13] hybrid Lax-Wendroff the
close monitoring of methods becomes of greater interest.

Conclusions

Many programs could be written with less wear and tear on the
physicist (and with shorter development times) by adopting methodical
techniques of prefabrication such as those described here.

The use of symbolic methods provides a way of defining a physical
problem clearly in computational terms. Algol and Algol-like lan: ages
are well suited to the symbolic approach especially for the parts of
program dealing with the logic and the physical equations; in Fortran
a control package for time-dependent problems, and the use of pre-
fabrication with acceptance tests has been successfully introduced.

Roberts and Peckover

APPENDIX

A UNIVERSAL CONTROL PACKAGE FOR FORTRAN PROGRAMS

Many time-dependent simulation programs are currently being written,
and most of these are still programmed in Fortran. Whatever the speci-
fied set of differential equations may be, these programs usually have
to carry out the same control processes, and the same general steps in
the calculation, e.g.

DEFINE INITIAL CONDITIONS
START THE RUN
INITIAL OUTPUT

and so on. Often this part takes longest to write, and is hardest for
newcomers to understand.

A Universal Control Package (UCP) is therefore being written at
Culham which will contain a main control subroutine MAIN, together
with utility and diagnostic subroutines, and which will form the
foundation upon which a variety of actual simulation programs can
subsequently be built. The package is being written in ASA Fortran,
so that it can be used on any computer system with only trivial modifica-
tions. Because of this standardization of the structure, it should be
easier for collaborating groups to exchange programs.

So far as possible UCP shares a common structure with DUMMYRUN,
e.g. the Algol Procedure calls of MAIN CONTROL appear as comments in the
UCP routine MAIN. (Fig.11). UCP is however less general, because there
are no analogues for the symbolic modules which deal with vector algebra
and analysis.

Development and Diagnostics

It has been found useful to 'grow' an actual simulation program
from UCP like a tree, checking it out at each stage by means of both
standard and ad hoc diagnostic subroutines. Typical examples of

190

```
C
          SUBROUTINE MAIN
C
C U2    MAIN CONTROL
C
C------------------------------------------------------------------
          COMMON/COMUCP/
     1    NONLIN,   NOUT,     NPRINT,    NREAD,
     2    NSTART,   NSTEP,    NSTOP,
     3    DELTAT,   T
C------------------------------------------------------------------
CL                 1              PROLOGUE
C
C    LABEL THE RUN
          CALL LABRUN
                                        CALL REPORT(1,1)
C    CLEAR VARIABLES AND ARRAYS
          CALL CLEAR
                                        CALL REPORT(1,2)
C    SET DEFAULT VALUES
          CALL PRESET
                                        CALL REPORT(1,3)
C    DEFINE DATA SPECIFIC TO RUN
          CALL DATA
                                        CALL REPORT(1,4)
C    SET AUXILIARY VALUES
          CALL AUXVAL
                                        CALL REPORT(1,5)
C    DEFINE INITIAL CONDITIONS
          CALL INCOND
                                        CALL REPORT(1,6)
C    START THE RUN
          CALL START
                                        CALL REPORT(1,7)
C    INITIAL OUTPUT
          CALL DSPLAY(1)
                                        CALL REPORT(1,8)
C
C------------------------------------------------------------------
CL                 2         MAIN CALCULATION LOOP
C
          DO 20 NSTEP=NSTART,NSTOP
C
          T=T+DELTAT
C    ADVANCE ONE TIMESTEP
          CALL STEPON
C
C    OUTPUT IF REQUIRED
          CALL DSPLAY(2)
C
   20     CONTINUE
                                        CALL REPORT(1,9)
C
C------------------------------------------------------------------
CL                 3         EPILOGUE
C
          NSTEP=NSTOP
C    FINAL OUTPUT
```

Figure 11:   The UCP FORTRAN routine MAIN. The structure is

similar to that for MAIN CONTROL in DUMMYRUN (using ALGOL)

191

standard subroutines are

MESAGE	Print a message of up to 48 characters
IVAR	Print 'NAME = < integer value >'
RVAR	Print 'NAME = < real value >'

while a useful _ad hoc_ subroutine is

CLIST   List names and values of all common non-
subscripted variables in alphanumeric
order, using IVAR and RVAR

These subroutines allow information to be extracted very easily at
critical points of a test run by inserting single cards, without the
need for format statements. Preferably, all the diagnostic tests
are grouped together in a single _ad hoc_ subroutine REPORT, which is
called at suitable intervals by the main part of the program (Fig. 11).
In this way, the program itself remains undisturbed.

For illustration, we consider the development of the FORTRAN
version of TRINITY[1]. This is now being generalized so that it can
deal with a 50x60x60 mesh. The 8Mbytes of data will be stored on
2 IBM 2301 drums on an IBM 360/91 configuration, and transferred in
and out of the core each timestep, using a rotating quadruple buffer,
a generalization of the triple buffer used in GALAXY[4]. Of these,
three sections of the buffer deal with the central plane (O) which is
being calculated, and those on either side (N and S) which are needed
by the difference scheme. The fourth or 'move' section (M) handles
the data transfer. During the first part of the calculation of each
plane, data is transferred out from the far-south plane (FS) on to the
drums on two separate channels. Halfway through, the direction of data
transfer is switched to bring data in for the far-north plane (FN).

The logic of such a scheme is quite complex, since it involves
the alternation implied by the leapfrog difference scheme, as well as
periodicity, guard points on the borders, rotating buffers, switches

192

Symbolic Programming

in the direction of data flow, and keeping count of the location of
360 separate tracks on the drums. The logic can however be checked
out independently of the physics, and, to a large extent, without any
actual transfer of data. To do this, we replace those subroutines
which do the actual work by dummies, which simply print out messages
saying what they are meant to do - a 'rehearsal' for the real calcula-
tion, as it were. A small mesh can also be used for the tests, so
that not too much printout is generated. Fig.12 shows an example,
for which the GO step occupied only 0.28 secs of IBM 360/91 CPU time.
The first two sections print out names and values of the variables in
the Common blocks COMESH, COMUCP by means of statements

        CALL CLISTM
        CALL CLISTU

while section 3 is generated by subroutines called by MAIN. Section 4
monitors the logic of the calculation, using a 4x6x8 mesh. The output
is generated by statements such as

        CALL IVAR('ROW',J)
        CALL IVAR('S-PLANE',MCS)

Using this type of methodical approach, it is being found that programs
can be checked out much more quickly and economically than by the
usual methods.

Acknowledgements

	MESH BLOCK	
DS	=	0.100E 00
I	=	0
J	=	0
K	=	0
L	=	0
N	=	0
NFIPT	=	2
NI	=	2
NIJ	=	0
NJ	=	4
NK	=	6
NW	=	0
PI	=	4
PIJ	=	24
PIMIN1	=	3
PJ	=	6
PJA	=	3
PJB	=	4
PJNIN1	=	5
PK	=	8
PKMIN1	=	7
S	=	0
SE	=	0
SIZE	=	0
U	=	0
W	=	0

CONTROL BLOCK

NONLIN	=	6
NPRINT	=	6
NREAD	=	5
NSTART	=	0
NSTEP	=	0
NSTOP	=	2
DELTAT	=	0.1000E 00
T	=	0.0

ROUTINE	=	I, POINT	=	7
OUTPUT	=	I		
ROUTINE	=	1, POINT	=	8

STEP	=	0
S-PLANE	=	2
O-PLANE	=	3
N-PLANE	=	0
M-PLANE	=	1

STORE C-PLANE ON DRUM

C-PLANE	=	1
D-PLANE	=	5

CALCULATE ROW

ROW	=	2
PLANE	=	2
I-FIRST	=	2

CALCULATE ROW

ROW	=	3
PLANE	=	2
I-FIRST	=	3

FETCH D-PLANE FROM DRUM

C-PLANE	=	1
D-PLANE	=	3

Figure 12   Output from test runs for TRINITY using a small number of mesh points for which the structure is checked out.

Symbolic Programming

References

1. Roberts K.V., and Boris J.P., "Trinity: Programs for 3D Magnetohydrodynamics", IPPS Computational Physics Conference, Culham (1969), paper 44. (Report CLM-CP (1969), H.M.S.O.).

2. Kuo-Petravic, G., Petravic, M., and Roberts K.V., 'The Translation of Symbolic Algol I into Symbolic Algol II by the Stage 2 Macro Processor'. IPPS Computational Physics Conference (1970).

3. Roberts K.V., and Boris J.P., The Solution of PDE Using a Symbolic Style of Algol (to be published).

4. Boris J.P., and Roberts K.V., 'Galaxy', IPPS Comp.Phys.Conference, Culham (1969) paper 4 (Report CLM-CP,H.M.S.O.)

5. Michie D., Ortony A., Burstall R.M., (1968) Computer Programming for Schools (?)

6. Kellogg P.J., (1965) Phys.Fluids $\underline{8}$,102.

7. Berk H.L., and Roberts K.V., (1967) Phys.Fluids $\underline{10}$, 1595.

8. Knorr G., (1963) Z Natur forsch. $\underline{18a}$, 1304.

9. Armstrong T.P., (1967) Phys.Fluids $\underline{10}$, 1269.

10. Buneman O., (1959) Phys.Rev. $\underline{115}$, 503.

11. Dawson J.M., (1962) Phys.Fluids $\underline{5}$, 445.

12. Roberts K.V , and Weiss N.O., (1966) Math.Comp. $\underline{20}$, 272.

13. Fromm J.E., (1968) Journal Comput.Physics $\underline{3}$, 176.

14. Petravic M., Kuo-Petravic G., and Roberts K.V., 'A Program for the Automatic Production of Computer Codes from Difference Equations'. IPPS Computational Physics Conference (1970).

15. A User's Guide to COTAN (1968) Culham Laboratory KDF9 manual, Section $\underline{8}$.

Wave Kinetic Equation Emulation by Numerical Particle-in-Cell Simulation Methods

F. D. Tappert, W. J. Cole, R. H. Hardin, and N. J. Zabusky
Bell Telephone Laboratories, Incorporated
Whippany, New Jersey

The wave kinetic equation has been used in the theory of nonlinear propagation of acoustic waves in solids[1], surface gravity waves in liquids[2], and various types of waves in plasmas[3]. This equation describes waves in terms of a quasiparticle phase space distribution function $f(\underset{\sim}{x},\underset{\sim}{k},t)$ which obeys a Boltzmann-like kinetic equation:

$$\frac{\partial f}{\partial t} + \frac{\partial \omega}{\partial \underset{\sim}{k}} \cdot \frac{\partial f}{\partial \underset{\sim}{x}} - \frac{\partial \omega}{\partial \underset{\sim}{x}} \cdot \frac{\partial f}{\partial \underset{\sim}{k}} = C_E(f,f) + C_I(f), \qquad (1)$$

where $\omega(\underset{\sim}{x},\underset{\sim}{k})$ is the linear dispersion relation, C_E represents the elastic wave-wave collision (scattering) integral, and C_I accounts for inelastic collisions (absorption and emission of waves). In practice, conditions may occur such that the wave collisional mean free paths are very large, but collective effects associated with the nonlinear frequency shifts cannot be neglected. Assuming that the nonlinear dispersion relation

has been determined to be $\omega = \omega(\underline{x},\underline{k},\rho)$, one then obtains
the collisionless, self-consistent wave kinetic equation
(SCWKE):

$$\frac{\partial f}{\partial t} + \frac{\partial \omega}{\partial \underline{k}} \cdot \frac{\partial f}{\partial \underline{x}} - \left(\frac{\partial \omega}{\partial \underline{x}} + \beta \frac{\partial \rho}{\partial \underline{x}}\right) \cdot \frac{\partial f}{\partial \underline{k}} = 0, \qquad (2)$$

where $\rho(\underline{x},t) = \int f(\underline{x},\underline{k},t)d\underline{k}$, and $\beta = \partial\omega/\partial\rho$. A detailed
discussion of the derivation and properties of SCWKE is
given elsewhere[4]. In this paper, we study in depth the
numerical particle-in-cell (PIC)[5,6,7] method as applied
to the solution of Eq. (2).

The basic idea is to represent f in the form of a
Klimontovich[8] distribution:

$$f(\underline{x},\underline{k},t) = \sum_{i=1}^{N} \delta(\underline{x}-\underline{x}_i(t))\delta(\underline{k}-\underline{k}_i(t)). \qquad (3)$$

In a Lagrangian manner, f is convected by numerically
integrating the quasiparticle equations of motion,

$$\frac{d}{dt}\underline{x}_i = \frac{\partial \omega}{\partial \underline{k}_i}, \quad \frac{d}{dt}\underline{k}_i = -\frac{\partial \omega}{\partial \underline{x}_i} - \beta \frac{\partial \rho}{\partial \underline{x}_i}. \qquad (4)$$

Self-consistency is assured by recomputing $\rho(x,t)$ at each
time on a fixed (Eulerian) spatial lattice. Heuristically,
one expects that this method produces an approximation which
converges, in some sense, to the solution of the SCWKE as
$N \to \infty$. The present paper presents a first careful study
that will provide guidance to determine convergence of
PIC methods.

The above described approach has been investigated
by applying it to the propagation in a plasma of transverse,
linearly polarized, plane electromagnetic waves as modeled
by the equation

$$A_{tt} - c^2 A_{xx} + \omega_p^2 (1+e^2 A^2/m^2 c^4)^{-\frac{1}{2}} A = 0, \tag{5}$$

where A is the vector potential, c is the speed of light,
ω_p is the plasma frequency (here taken to be constant),
and e and m are the electron charge and mass. The non-
linear effect in Eq. (5) arises from the relativistic
increase in electron mass. For small-but-finite field
amplitudes, the nonlinear dispersion relation which fol-
lows from Eq. (5) is given by[9,10]

$$\omega = \left[c^2 k^2 + \omega_p^2 \left(1 - \frac{3}{4} \frac{e^2 \langle A^2 \rangle}{m^2 c^4} \right) \right]^{\frac{1}{2}}, \tag{6}$$

where angular brackets denote an average[#] over the high frequency oscillations (the wave envelope is assumed to vary slowly). After normalizing f to

$$\int f(x,k,t)dk = \rho(x,t) = \frac{e^2}{m^2 c^4} \left\langle A^2(x,t) \right\rangle , \qquad (7)$$

the SCWKE becomes

$$\frac{\partial f}{\partial t} + \frac{c^2 k}{\omega} \frac{\partial f}{\partial x} + \frac{3\omega_p^2}{8\omega} \frac{\partial \rho}{\partial x} \frac{\partial f}{\partial k} = 0. \qquad (8)$$

In order to validate this method, the following basic questions should be answered: first, how well do solutions of the SCWKE approximate solutions of Eq. (5)?, and second, how well does the PIC technique approximate solutions of Eq. (8)? We have therefore studied in detail two problems where solutions of the SCWKE can be obtained analytically: 1) linear dispersive spreading of Gaussian wave packets; 2) nonlinear stationary wave packets wherein nonlinear self-trapping balances dispersive spreading.

[#] This is not a statistical average as we are concerned here with coherent waves. A more precise definition can be given in terms of the analytic signal concept.[4]

199

1. After linearizing Eq. (5) at zero amplitude $(eA_0/mc^2 \rightarrow 0)$, one obtains the following asymptotic solution for Gaussian wave packets $(k_0\sigma \gg 1)$:

$$A(x,t) = A_0\left(\frac{\sigma}{\sigma(t)}\right)^{\frac{1}{2}} \exp\left[-\frac{(x-ck_0t/\omega_0)^2}{2\sigma^2(t)}\right]\cos(k_0x-\omega_0t+qt), \quad (9)$$

where $\omega_0 = \left(k_0^2c^2+\omega_p^2\right)^{\frac{1}{2}}$, $\sigma^2(t) = \sigma^2 + c^4\omega_p^4t^2/\omega_0^6\sigma^2$, and q is a complicated function of x and t. The corresponding asymptotic solution of Eq. (8) is

$$f(x,k,t) = \left(\frac{eA_0}{mc^2}\right)^2 \frac{\sigma}{2\pi} \exp\left[-\sigma^2(k-k_0)^2 - \left(x - ck_0t/\omega_0 - \omega_p^2c^2(k-k_0)t/\omega_0^3\right)^2\bigg/\sigma\right]$$

$$(10)$$

and

$$\rho(x,t) = \frac{1}{2}\left(\frac{eA_0}{mc^2}\right)^2 \frac{\sigma}{\sigma(t)} e^{-(x-ck_0t/\omega_0)^2/\sigma^2(t)} \quad (11)$$

We see that $\rho(x,t) = e^2 \langle A^2 \rangle / m^2 c^4$, which demonstrates that
the wave kinetic equation is able to describe correctly
dispersive spreading, a coherent wave process[*]. Fig. 1a
shows the result, at several different times, of a numerical
integration of Eq. (5) using a finite difference technique.
The initial conditions agree with Eq. (9) and $eA_o/mc^2 \to 0$.
At the bottom of each diagram is the numerically computed
contour plot of $f(x,k,\tau)$ as calculated directly from its
analytic definition[4] at each time. Corresponding PIC
calculations are shown in Fig. 1b (random loading) and
Fig. 1c (uniform loading). The rms pulse width as obtained
from the PIC simulation is compared to the above theory in
Fig. 2, which shows the excellent agreement.

2. Asymptotic solutions of Eq. (5) with a stationary
envelope (called "envelope solitons", or for brevity, E-solitons)
can be found following the method of Karpman[11], and Taniuti[12],
et al. to be

$$A(x,t) = A_o \operatorname{sech}\left(\frac{x-c^2 k_o t/\omega_o}{\sigma}\right)\cos\left[k_o x - \omega_c t + \frac{3\omega_p^2}{32\omega_o}\left(\frac{eA_o}{mc^2}\right)^2 t + \alpha\right],$$

$$\tag{12}$$

------

[*] Kadomtsev[3] states a contrary opinion.
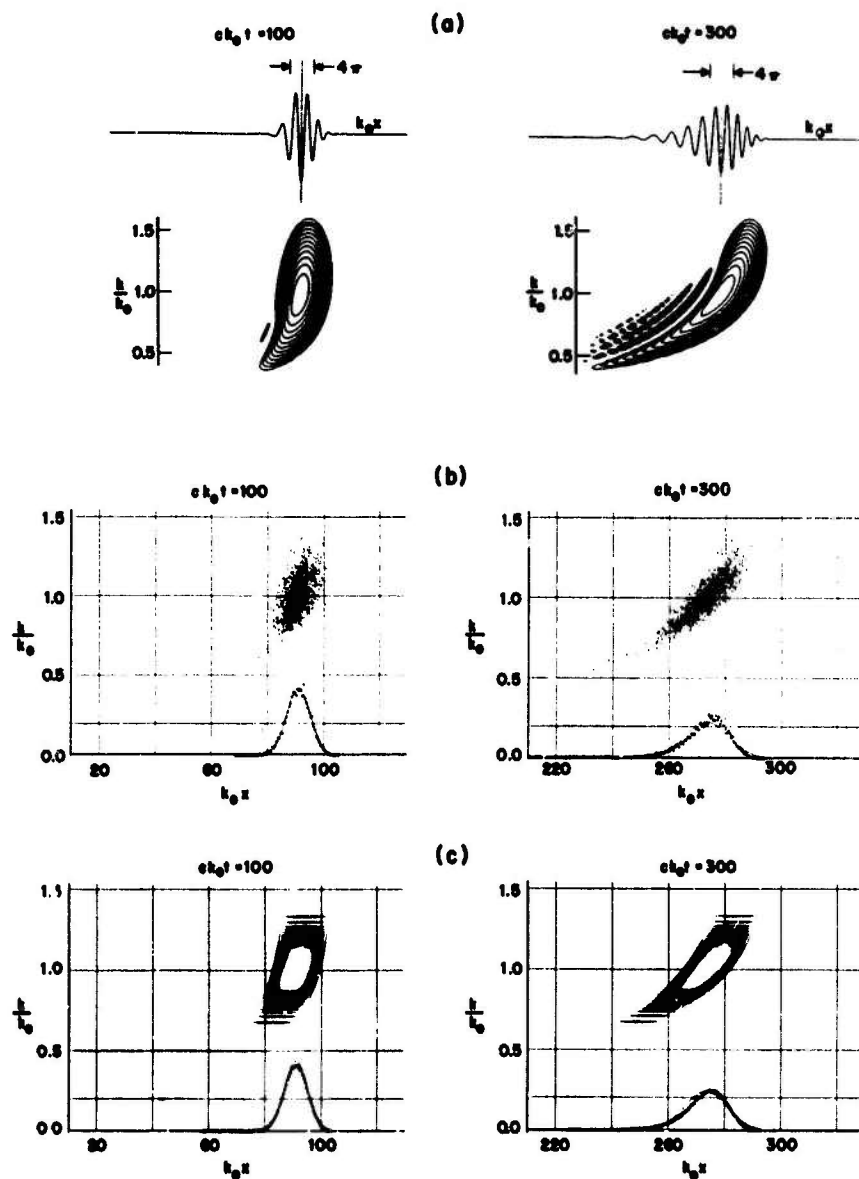
Tappert, Cole, Hardin, and Zabusky

Fig. 1. Dispersive spreading of a linear Gaussian wave packet, $\omega_p^2/c^2k_0^2 = 0.2$, $k_0\sigma = 5$. (a) Numerical solution of Eq. (5), $ck_0\Delta t = k_0\Delta x = 0.1$. Also shown are contours of $f(x,k,t) = $ const. (levels are separated by a factor of two). (b) PIC solution of Eq. (8) with random loading, $ck_0\Delta t = k_0\Delta x = 1.0$, N = 2000. The density is also shown together with a Gaussian fit. (c) PIC solution of Eq. (8) with uniform loading, otherwise same as (b).
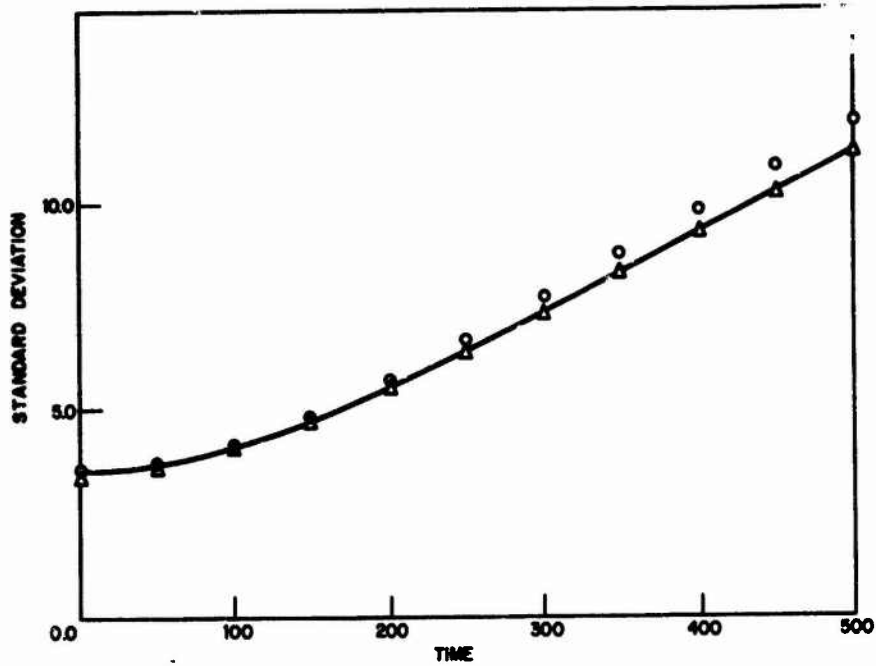
Fig. 2. Dispersive spreading of a linear Gaussian wave packet, $\omega_p^2/c^2 k_0^2 = 0.2$, $k_0\sigma = 5$. Standard deviation (in units of $1/k_0$) vs. time (in units of $1/ck_0$). Conditions same as in Fig. 1. Solid line: theory and numerical solution of Eq. (5), weighted with the energy density. Circles: PIC with random loading. Triangles: PIC with uniform loading.

where $\sigma = 4c/[\sqrt{3} \, \omega_0 (eA_0/mc^2)]$, α is an arbitrary constant, and we have assumed that $k_0\sigma \gg 1$ and eA_0/mc^2 is small but finite. The corresponding solution of the SCWKE can be found following the method of Bohm-Gross[13] and Bernstein-Green-Kruskal[14]. Assuming narrow bandwidth ($\Delta k/k_0 \ll 1$) and no untrapped quasiparticles, stationary solutions of Eq. (8) are given by

$$f(x,k,t) = \left(\frac{eA_0}{mc^2}\right) \frac{\sigma}{\pi} \left[\rho(x - ck_0 t/\omega_0) - \tfrac{1}{4}\left(\frac{eA_0}{mc^2}\right)^2 \sigma^2 (k-k_0)^2\right]^{\frac{1}{2}}, \quad (13)$$

and $f = 0$ where the radicand is negative. Here $\rho = \int f dk$ is an arbitrary function and σ is given by the same formula as above. Choosing $\rho(x) = \tfrac{1}{4}(eA_0/mc^2)^2 \, \text{sech}^2(x/\sigma)$, gives the E-soliton corresponding to Eq. (12). Fig. 3a shows a numerical solution of Eq. (5) having initial conditions in agreement with Eq. (12) and $eA_0/mc^2 = 0.25$. Note, that although wavelets move through the packet, the envelope and phase space distribution are stationary. The corresponding PIC simulation is shown in Fig. 3b. The observed stationarity of the density (the particles of course execute a vortex-like motion in phase space) is remarkable.
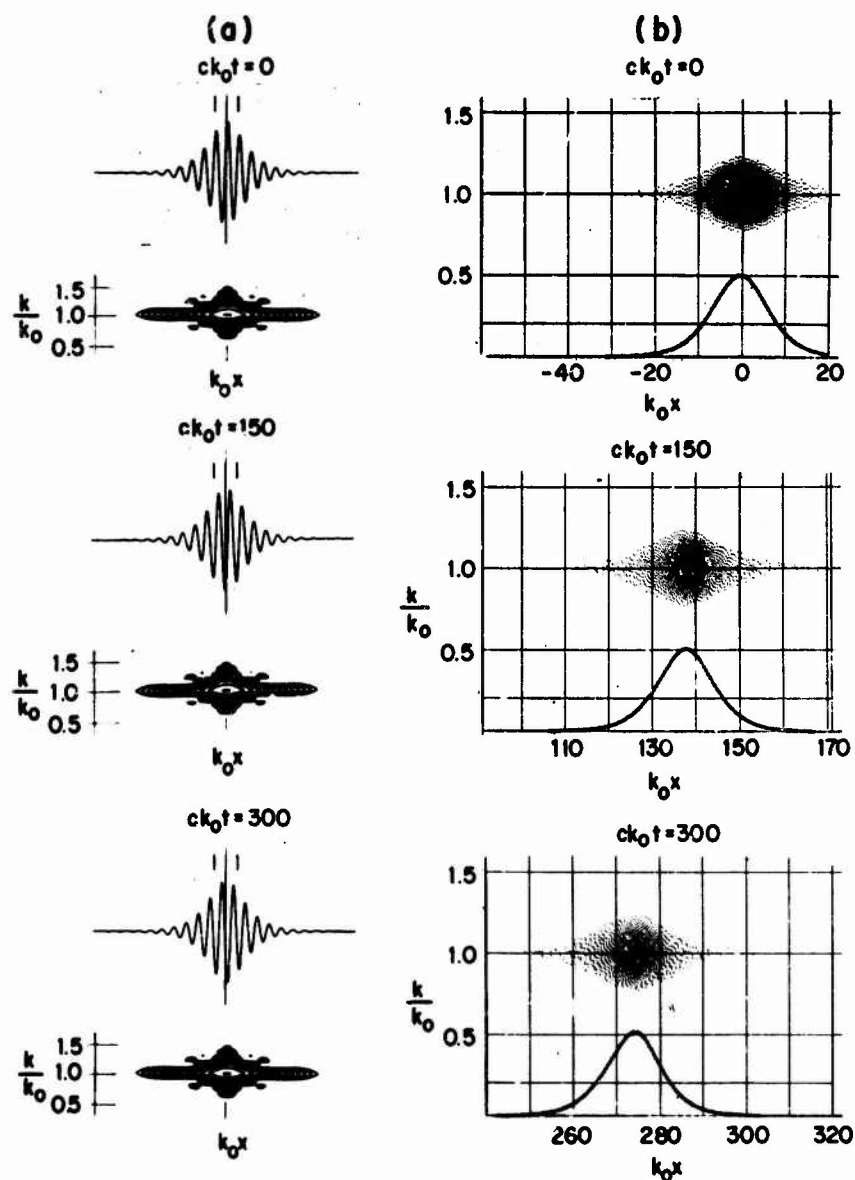
Fig. 3. Stationary E-solution, $\omega_p^2/c^2k_0^2 = 0.2$, $eA_0/mc^2 = 0.25$, $k_0\sigma = 8.5$. (a) Numerical solution of Eq. (5), $ck_0\Delta t = k_0\Delta x = 0.1$. Also shown are contours of $f(x,k,t) = $ const. (levels are separated by a factor of two). (b) PIC solution of Eq. (8) with uniform loading, $ck_0\Delta t = 2k_0\Delta x = 1.0$, $N = 6700$. The density is also shown.

The availability of exact nonlinear solutions of the SCWKE provides an opportunity to study in depth various techniques associated with the PIC method. The following areas have been investigated theoretically and by numerical experimentation:

1. Initial loading: Given $f(x,k,o)$, how does one choose the initial quasiparticle coordinates and momenta, x_i and k_i, $i = 1,2,...,N$? We have used random, semi-random, and several uniform loading methods in order to reduce fluctuation levels.

2. Self-consistent force computation. It is necessary to smooth the interaction in some way to reduce the discrete particle effects. We have used "area weighting", "force interpolation", and Fourier transform smoothing (equivalent to extended particles).

3. Time integration (stability, truncation and roundoff error accumulation). Using a centered, second-order leap-frog scheme, we have observed that when $c\Delta t/\Delta x \gtrsim 4$ a strong numerical instability develops which conserves energy but throws the quasiparticles into a low entropy, highly structured (oscillatory) state.

4. <u>Cell</u> <u>size</u> <u>and</u> <u>number</u> <u>of</u> <u>quasiparticles</u>. Given
   the initial condition, how does one choose the
   optimal Δx and N? We have found that when $N \cdot \Delta x / \sigma$
   is sufficiently small, large fluctuations develop
   which lead to instability.

   In summary, we have demonstrated that the SCWKE
together with PIC numerical techniques provide an efficient,
versatile, and powerful method for solving a variety of problems
concerning nonlinear wave propagation.

   We would like to thank R. J. Mason for helpful
advice about PIC techniques.

REFERENCES

1. R. E. Peierls, Quantum Theory of Solids (Oxford, 1955).

2. K. Hasselmann, J. Fluid Mech. 12, 481 (1962); 15, 273, 385 (1963).

3. B. B. Kadomtsev, Plasma Turbulence (Academic, 1965).

4. F. D. Tappert, to be published.

5. F. H. Harlow, in Methods in Computational Physics, Vol. 3 (Academic, 1964).

6. R. L. Morse and C. W. Nielson, Phys. Rev. Lett. 23, 1087 (1969).

7. R. L. Morse, in Methods in Computational Physics, Vol. 9 (Academic, 1970).

8. Yu. L. Klimontovich, Statistical Theory of Nonequilibrium Processes in Plasma (Pergamon - MIT, 1967).

9. A. I. Akhiezer and R. V. Polovin, Sov. Phys. JETP 3, 696 (1956).

10. P. Kaw and J. Dawson, Phys. Fluids 13, 472 (1970).

11. V. I. Karpman, JETP Lett 6, 277 (1967); V. I. Karpman and E. M. Krushkal, Sov. Phys. JETP 28, 277 (1969).

12. T. Taniuti and N. Yajima, J. Math. Phys. 10, 1369 (1969); N. Asano, T. Taniuti, and N. Yajima, J. Math. Phys. 10, 2020 (1969).

13. D. Bohm and E. P. Gross, Phys. Rev. 75, 1851 (1949).

14. I. B. Bernstein, J. M. Greene, and M. D. Kruskal, Phys. Rev. 108, 546 (1957).

Monday, November 2, 1970
Session II

Chairmar: O. Buneman

Stanford University
Stanford, California

Three-Dimensional Numerical Experiments
on Penetrative Convection in a Rotating Fluid[*]

Steve A. Piacsek
Applied Mathematics Division
Argonne National Laboratory
Argonne, Illinois

.

ABSTRACT

Numerical experiments were performed to simulate convection
currents that arise when fluid in a rectangular geometry is rotated
with constant angular velocity and cooled with uniform heat flux
both from above and below. The time development of the mean-square
vorticity components showed equipartition for circulations in all
planes. The convection rolls with axes parallel to the x- and
y-axes exchanged energy for about 5 cycles, whereas the cyclonic
circulations about the vertical axis maintained the same energy as
the mean of the rolls.

A comparison of the isotherms with circulation lines showed
that the strong divergence of horizontal motion, in regions of
falling blobs of cold fluid from the gravitationally unstable top
layer, is responsible for the generation of vertical vorticity through
the Coriolis term $2\Omega \frac{\partial w}{\partial z}$. An examination of the horizontal planforms
of motion revealed the existence of a weak, four-lobed jet stream
meandering around four centers of strong, closed cyclonic circulations.

211

THREE-DIMENSIONAL NUMERICAL EXPERIMENTS ON PENETRATIVE
CONVECTION IN A ROTATING FLUID

1. Introduction:

Many situations occur in nature in which the convection currents
that arise in gravitationally unstable fluid layers are bounded below
or above by positively or neutrally stable layers. In the former case,
the stable layer is penetrated to a certain extent by the rising or
descending thermal columns but remains stable on the whole. In the
latter case the convection currents will soon involve all of the acces-
sible fluid volume.

Some of the natural phenomena that exhibit such processes are the
atmospheric thermals and cumulus towers impinging on stably stratified
layers above, including inversions and the tropopause; evaporation-
driven ocean currents penetrating into lower regions stably stratified
by solar radiation, or seasonal cooling effects reaching down to the
thermocline; convection in the sun and stars in layers where radiation
causes a super-adiabatic temperature gradient, bounded both below and
above by stable layers. Often the penetration currents are coupled to
larger-scale general circulations, and their mutual interaction is of
great interest to geo- and astrophysicists.

When the scale of the convection currents is sufficiently large
(L >> 10 m in the ocean or L >> 50 m in the atmosphere) the Coriolis
force due to the earth's rotation provides the main balance to the buoy-
ancy forces. On such length scales the nonlinear advective terms and
the friction terms play only a secondary role and the resulting motion
is called "geostrophic."[1]

Penetrative Convection in Rotating Field

Geostrophic motion that is driven by buoyancy forces due to horizontal temperature gradients is also known as the "thermal" wind, and its associated instabilities as "baroclinic instabilities."[2-4] Most commonly known forms of these instabilities occur in cases where the thermal wind is a result of externally applied horizontal temperature contrasts. The atmospheric jet stream may be regarded as an example of such "strong" baroclinic instability, meandering between warm southern and cold northern latitudes in an easterly direction. But horizontal temperature contrasts can also result between up- and down-moving thermals in convection due to vertically imposed heat fluxes or temperature contrasts; the corresponding thermal wind may give rise to a "weak" baroclinic instability. A weak jet connecting or circumventing a group of closed circulation cells or cyclones is an example of such instability.

Geophysical fluid dynamicists have attempted and succeeded to model these instabilities in the laboratory and on the computer by designing experiments in which the relevant non-dimensional parameters have been chosen to approximate the values that are associated with the corresponding natural phenomena.[5-8] These parameters will be defined in the following section where the governing equations are introduced and non-dimensionalized. The advantages of such model experiments are the strict control which can be exercised over the parameters determing the flow, and the possibility of isolating the several concurring processes to study each separately.

The present numerical experiment deals with a situation in which a stably stratified fluid is cooled from above and undergoes rotation at the same time. Heating from below would lead to an identical dynamic situation. Corresponding natural phenomena are:

213

a) the top layer of the ocean (say 200 m), cooled by evaporation and infra-red radiation at the surface and stratified by solar radiation and sensible heat exchange (i.e., molecular warming by the air);

b) the bottom layers of a planetary atmosphere (say 5000 m), heated at the surface by solar radiation and stably stratified by advective and other radiative processes.

The main purpose of the experiment is to exhibit the existence of a "weak" jet stream that connects cyclones of strong circulation about the downward plunging cold thermals from the surface.

The vorticity/vector potential approach has been chosen for formulating the three-dimensional flow problem, since the fluid is assumed to be incompressible and located in a simply-connected, cartesian geometry. This approach has some advantages over the velocity-pressure ("primitive") form of the hydrodynamic equations, where the nonvanishing of the divergence $\vec{\nabla} \cdot \vec{u} = 0$ due to round-off errors can cause conservation problems in the advection terms.[8-10]

II. Governing Equations and Nondimensional Parameters:

The fluid is assumed to be contained in a rectangular volume bounded by planes $x = 0,L$, $y = 0,L$, and $z = 0,D$. The rotation vector $\vec{\Omega}$ points along the positive z-axis and the gravitational acceleration $\vec{g}$ along the negative z-axis. In a cartesian coordinate system rotating with angular velocity $\vec{\Omega}$ the Navier-Stokes equations for viscous flow may be written

$$\rho \left[\frac{\partial \vec{u}}{\partial t} + (\vec{u} \cdot \vec{\nabla})\vec{u} + 2\vec{\Omega} \times \vec{u} \right] = -\vec{\nabla}p + \mu \nabla^2 \vec{u} - \rho g \, \hat{z} \, . \qquad (1)$$

The equations of continuity and thermodynamic state are replaced by the so-called Boussinesq approximation, in which the fluid is assumed to be incompressible in all terms of equation (1) except the buoyancy term, and the density depends linearly on the temperature. Thus

$$\vec{\nabla} \cdot \vec{u} = 0 \qquad (2)$$

$$\rho = \rho_0 [1 - \alpha(T - T_0)] \qquad (3)$$

where ρ_0 and T_0 are the ambient density and temperature of the fluid. In this approximation (1) may be rewritten as

$$\frac{\partial \vec{u}}{\partial t} + (\vec{u} \cdot \vec{\nabla})\vec{u} + 2\vec{\Omega} \times \vec{u} = -\frac{\vec{\nabla}p}{\rho_0} + \nu \nabla^2 \vec{u} + \alpha g (T - T_0)\hat{z} \qquad (4)$$

with $\nu = \mu/\rho_0$ being the coefficient of kinematic viscosity and α the coefficient of thermal expansion. For the same approximation the equation of heat transfer becomes

$$\frac{\partial T}{\partial t} + (\vec{u} \cdot \vec{\nabla})T = \kappa \nabla^2 T \qquad (5)$$

where $\kappa = K/\rho_0 c_p$ is the coefficient of thermometric diffusivity. Both diffusion coefficients are assumed to be independent of temperature as these variations play only a minor role in the flow mechanisms. The following dimensional scaling is introduced now for all the physical variables [u,v,w being components of the velocity vector]

$$(x,y) = L(x',y') \qquad\qquad p = P \cdot p'$$

$$z = D \cdot z' \qquad\qquad t = \tau \cdot t'$$

$$\vec{u}_H = (u,v) = U(u',v') \qquad T - T_o = \Delta T \cdot T' \qquad (6)$$

$$w = W \cdot w'$$

From $\vec{\nabla} \cdot \vec{u} = 0$ it follows that $\dfrac{U}{L} \simeq \dfrac{W}{D}$ and that $(\vec{u} \cdot \vec{\nabla})\vec{u} = \dfrac{W}{D} (\vec{u}' \cdot \vec{\nabla}')\vec{u}$. By introducing the nondimensional operators

$$\vec{\nabla}' = \frac{\partial}{\partial x'}\hat{x} + \frac{\partial}{\partial y'}\hat{y} + \left(\frac{L}{D}\right)^2 \frac{\partial}{\partial z'}\hat{z} \qquad (7(a))$$

$$\nabla'^2 = \left(\frac{D}{L}\right)^2 \left(\frac{\partial^2}{\partial x'^2} + \frac{\partial^2}{\partial y'^2}\right) + \frac{\partial^2}{\partial z'^2} \qquad (7(b))$$

equation (4) may be written (dropping the primes)

$$\frac{\partial \vec{u}}{\partial t} + \frac{W\tau}{D}(\vec{u}\cdot\vec{\nabla})\vec{u} + \tau 2\Omega(\hat{z}\times\vec{u}) = -\frac{P\tau}{\rho_o U L}\vec{\nabla}'p + \frac{\nu\tau}{D^2}\nabla'^2\vec{u}$$

$$+ \frac{\alpha g \Delta T \cdot \tau}{W} \cdot T . \qquad (8)$$

The time scale τ is chosen to be that of momentum diffusion, and the velocity scale W that of advection balancing it, i.e.,

$$\tau = \frac{D^2}{\nu} , \quad W = \frac{\nu}{D} , \quad P = \frac{\rho_o U \nu L}{D^2} . \qquad (9(a,b))$$

Then (8) becomes

$$\frac{\partial \vec{u}}{\partial t} + (\vec{u} \cdot \vec{\nabla})\vec{u} + \frac{2\Omega D^2}{\nu} \, (\hat{z} \times \vec{u}) = -\vec{\nabla}'p + \nabla'^2 \vec{u} + \frac{\alpha g \Delta T \cdot D^3}{\nu^2} \cdot T \qquad (10)$$

and the heat equation

$$\frac{\partial T}{\partial t} + (\vec{u} \cdot \vec{\nabla})T = \frac{\kappa}{\nu} \cdot \nabla'^2 T . \qquad (11)$$

The following definitions are customary:

Grashof number $\qquad Gr = \dfrac{\alpha g \Delta T \cdot D^3}{\nu^2} \qquad\qquad$ (12(a))

Taylor number $\qquad Ta = \dfrac{4\Omega^2 D^4}{\nu^2} \qquad\qquad$ (12(b))

Prandtl number $\qquad Pr = \kappa/\nu . \qquad\qquad$ (12(c))

The final form of the transport equations becomes, therefore

$$\frac{\partial \vec{u}}{\partial t} + (\vec{u} \cdot \vec{\nabla})\vec{u} + \sqrt{Ta} \cdot (\hat{z} \times \vec{u}) = -\vec{\nabla}'p + \nabla'^2 \vec{u} + Gr \cdot T \qquad (13)$$

$$\frac{\partial T}{\partial t} + (\vec{u} \cdot \vec{\nabla})T = \frac{1}{P_r} \cdot \nabla'^2 T . \qquad (14)$$

Operating on (13) with the curl $\vec{\nabla}' \times$ and defining $\vec{\xi} = \vec{\nabla}' \times \vec{u}$ yields

$$\frac{\partial \vec{\xi}}{\partial t} = \vec{\nabla}' \times (\vec{u} \times \vec{\xi}) + \sqrt{Ta} \cdot \frac{\partial \vec{u}}{\partial z} + \nabla'^2 \vec{\xi} + Gr \cdot (\vec{\nabla} \times T \, \hat{z}) \qquad (15)$$

where the relations $(\vec{\nabla}\times\vec{u})\times\vec{u} = (\vec{u}\cdot\vec{\nabla})\vec{u} - \vec{\nabla}\frac{u^2}{2}$ and $\vec{\nabla}\cdot\vec{u} = 0$ are used to obtain the first and second terms on the right-hand-side, respectively.

Stratification is achieved in this experiment by cooling the bottom at the same rate as the top, so that the stabilizing and de-stabilizing forces have the same magnitude and afford an optimum observation of penetrative convection. The surfaces are assumed to be "frictionless lids," i.e., non-deformable, stress-free surfaces where $u_n = 0$, $\frac{\partial u_{||}}{\partial n} = 0$ (n - normal, || - tangential). Under these conditions the tangential components of the vorticity also vanish and the condition on its normal component follows from $\vec{\nabla}\cdot\vec{\xi} \equiv 0$. The kinematic boundary conditions may therefore be summarized as

$$u_n = \frac{\partial u_{||}}{\partial n} = \xi_n = \frac{\partial \xi_{||}}{\partial n} = 0 \qquad \text{on all surfaces.} \qquad (16)$$

The lateral walls are assumed to be thermal insulators and the temperature gradient is fixed at the bottom and top surfaces. The thermal boundary conditions become thus

$$\frac{\partial T}{\partial n} = 0 \qquad \text{on} \qquad x = 0,1; \; y = 0,1$$

$$\frac{\partial T}{\partial z} = \begin{cases} + \beta \\ - \beta \end{cases} \text{on} \quad \begin{rcases} z = 0 \\ 1 \end{rcases} \text{respectively.} \qquad (17)$$

Finally, the introduction of a vector potential $\vec{u} = \vec{\nabla}\times\vec{\psi}$ leads to a simple relation between the velocity and vorticity components.[11] Letting

218

$$\vec{\xi} = \vec{\nabla} \times \vec{u} = \vec{\nabla} \times (\vec{\nabla} \times \vec{\psi}) = \vec{\nabla}(\vec{\nabla} \cdot \vec{\psi}) - \nabla^2 \vec{\psi} \qquad (18)$$

and introducing the gauge $\vec{\nabla} \cdot \vec{\psi} \equiv 0$ (there are no sources of motion other than that associated with vorticity) leads to the simple relations

$$\xi_i = -\nabla^2 \psi_i, \qquad u_i = (\vec{\nabla} \times \vec{\psi})_i, \qquad i = 1,2,3 \qquad (19)$$

which are very suitable for numerical solutions, either by relaxation or fast Fourier-transform methods. The boundary conditions on ψ_i are subtle and must be discussed carefully. Hirasaki and Hellums have shown[12] that if no fluid enters or leaves the volume (i.e., $u_n \equiv 0$ everywhere) the parallel components of $\vec{\psi}$ vanish at each point of the surface and the normal component then is determined from the gauge $\vec{\nabla} \cdot \vec{\psi} \equiv 0$. Thus

$$\psi_{||} = \frac{\partial \psi_n}{\partial n} = 0 \quad \text{on all surfaces} \qquad (20)$$

Finite-difference versions of (14), (15), and (19) have been programmed for a digital computer; the difference schemes employed and their properties are discussed in Appendices A and B.

III. Choice of Parameters and Initial Conditions:

The values of the governing parameters for the experiment were mostly determined by the number of mesh points and corresponding resolution that was available on the computer used, a CDC 6600 with a

64,000 word (60-bit) memory. To represent adequately the flow at large Grashof and Taylor numbers and to ensure numerical stability and accuracy, the mesh size must be chosen small enough to resolve the thinnest boundary layers present in the system. In this case they are associated with heat conduction and the interaction of rotation with viscous diffusion, the so-called Ekman layer.[13] A simple scale analysis of (13) and (14) shows the relevant boundary layer thicknesses to be given by

$$\delta_T \simeq (Gr. \ \beta)^{-\frac{1}{4}} \tag{21(a)}$$

$$\delta_E \simeq Ta^{-\frac{1}{4}} \tag{21(b)}$$

where β is the prescribed surface temperature gradient; β, Ta and Gr are defined in (12).

The maximum mesh size that could be fitted into the computer was 20×20×10, with the horizontal dimensions accentuated to simulate the natural phenomena. Since both the Ekman layers and thermal boundary layers lie along the horizontal surfaces, the mesh spacing Δz in the vertical direction is chosen to be half the horizontal mesh spacing $\Delta x = \Delta y$. To have the non-dimensional height unity a choice of $\Delta z = .1$ must be taken, with $\Delta x = \Delta y = .2$. The total geometric height-to-width ratio therefore becomes $D/L = 1/4$. If the criterion of $\Delta z \simeq \delta_T, \delta_E$ is taken to ensure proper resolution and stability of the system, the corresponding values of Gr. β and Ta should be $\leq 10^4$. Actually, the e-folding distance of boundary layer decay is larger than the expressions given in (21) by factors of π and $\sqrt{2}$, respectively,[14] so that the resolution is much better than the above criterion implies.

220

Initially the fluid is taken to be homogeneous and the cooling is turned on at $t = 0$. No attempt is made in the experiments to determine the minimum time in which the resulting nonlinear temperature profile would yield convective instabilities due to a given finite-amplitude perturbation. Several authors have studied this problem in certain laboratory experiments[15,16] and also theoretically.[17,18] By choosing the amplitude range of the horizontal temperature perturbations from 10^{-4} to 10^{-3} times the temperature difference between the cooled top and the (yet) unaffected interior, finite-amplitude convection results in each case with a rapid, monotonic increase of the kinetic energy. The form of the initial perturbations is that of white noise, i.e.

$$T'(x,y,z) = A \ e^{-(D-z)/H} \cdot \frac{1}{NM} \cdot \left(\sum_{n=1}^{N} \cos (n\pi x) \right) \left(\sum_{m=1}^{M} \cos (m\pi y) \right)$$

(22)

The scale height H is so chosen that most of the perturbation is confined to the top region where the natural noise is likely to originate; this also ensures that in most of the volume $T'(z)$ is small compared to $T(z) - T_o$, T_o being the initial ambient temperature of the homogeneous fluid. The number of Fourier modes N and M is limited by the consideration that at least 2, but preferably 3 or 4, mesh points are needed to numerically resolve the smallest wave lengths.

IV. Results and Discussion

The results of the numerical experiments are presented in two ways: by plotting the isolines of the vorticity components and temperature at successive intervals of time, somewhat in a movie-like fashion, and by plotting the total mean-square vorticities associated with the circulations in each coordinate plane as a function of time.

221

The particular case presented here has the parameter values $\beta = 1$, Pr = 7, Gr = 4000 and Ta = 10000 assigned to it. Based on a comparison with other rotating convection experiments, the effects of rotation were expected to be only moderate and the results are surprising.

An examination of Figure 1 reveals several interesting facts. There is clearly equipartition between the three modes of circulation. The x-rolls and y-rolls (i.e., convection rolls with axes parallel to these directions) exchange energy for about 5 cycles, each of period $t_c \simeq .2$ (in units of L^2/ν, momentum diffusion time) and the z-rolls (actually a group of "cyclones" as seen in Fig. 5-8) grow monotonicly at exactly the same rate as the mean of the x- and y-rolls. At $t' \sim 1.2$ some abrupt changes occur in the system. The x- and y-rolls stop oscillating and start to damp out; the cyclones undergo a sharp drop and rise in intensity and then also settle down to viscous damping; the nature of this strong dip is not understood and can not easily be related to any visible changes in the flow. Lack of computer time prevented the system from being followed to its final steady state, but experience with two-dimensional flows shows that after the oscillations, representing conversion between potential and kinetic energy of the system, damp out the system settles down to a steady state quite readily. In arriving at this steady state the time of thermal diffusion is probably more important since it smoothes out the temperature contrasts that drive the system, between the downward plunging cold blobs and the ambient fluid.

The behavior of the total energy is best understood from an examination of the vertical cross-section of the isotherms as shcwn

in Fig. 2. Initially the stable bottom layer is thin and the downward moving cold thermals can generate a lot of motion. As the bottom layer thickens, the region of instability shrinks; at the same time, viscous damping is beginning to act on the x- and y-cells and thermal diffusion begins to smooth the contrast between the thermals and the ambient fluid. The net result is a sharp decrease in the intensity of the circulation; evidently all three smoothing agents are making their effects felt at the same time.

However, this behavior of the isotherms is not markedly different from the case of no rotation. The particular effects of rotation are most noticeable on the display of the horizontal circulation at various height levels. Figures 3 and 4 display the time development at the top level (top rows) and at the middle level (bottom rows).
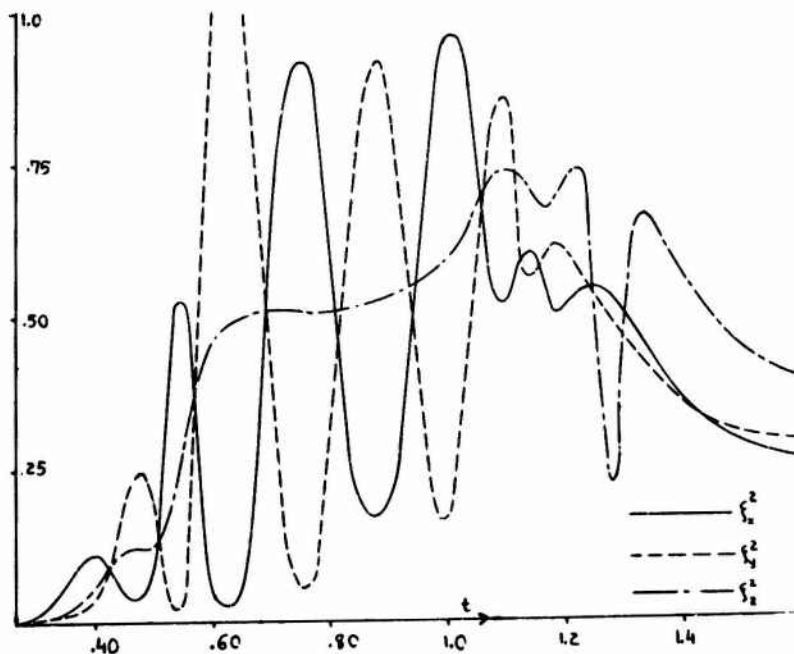
Fig. 1. Total mean-square vorticity components (x, y and z) as a function of time
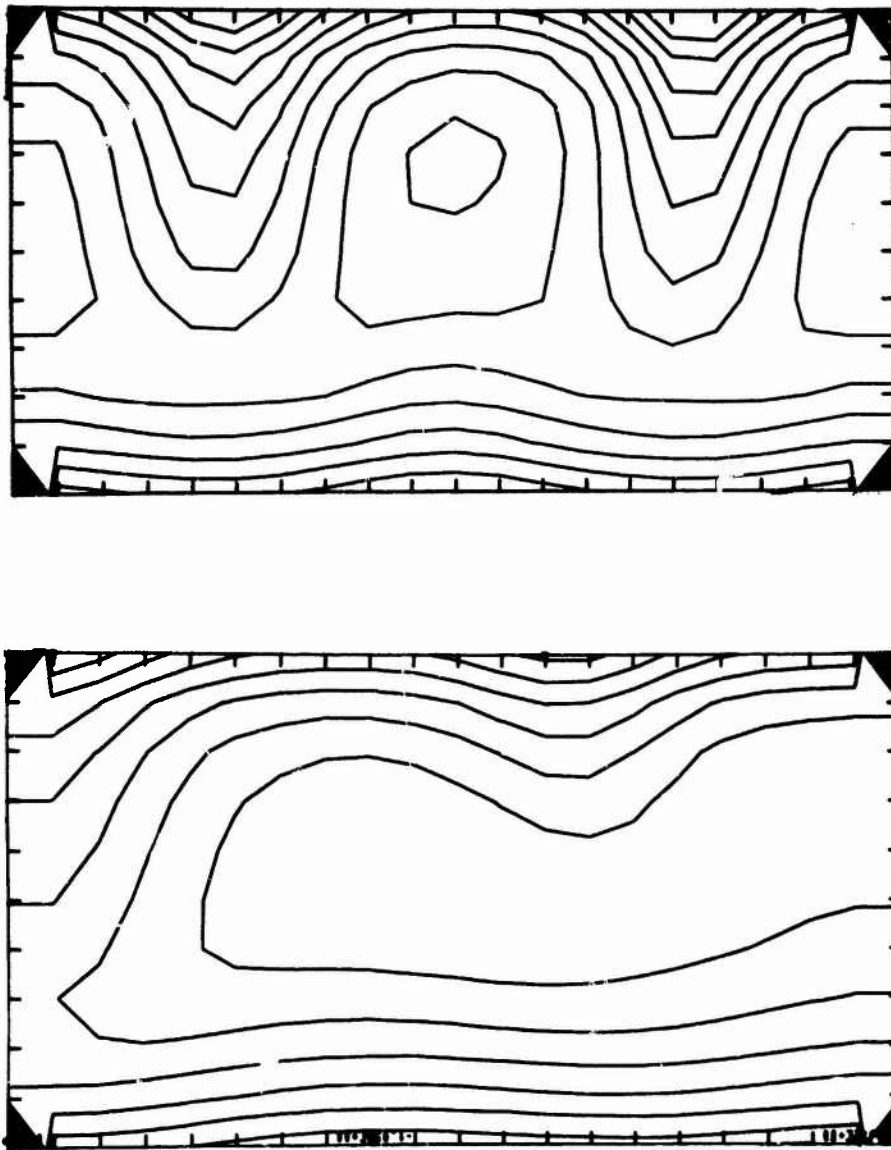
Fig. 2. Vertical (x-z) plots of the isotherms during oscillatory (top)
and near-steady motion (bottom)
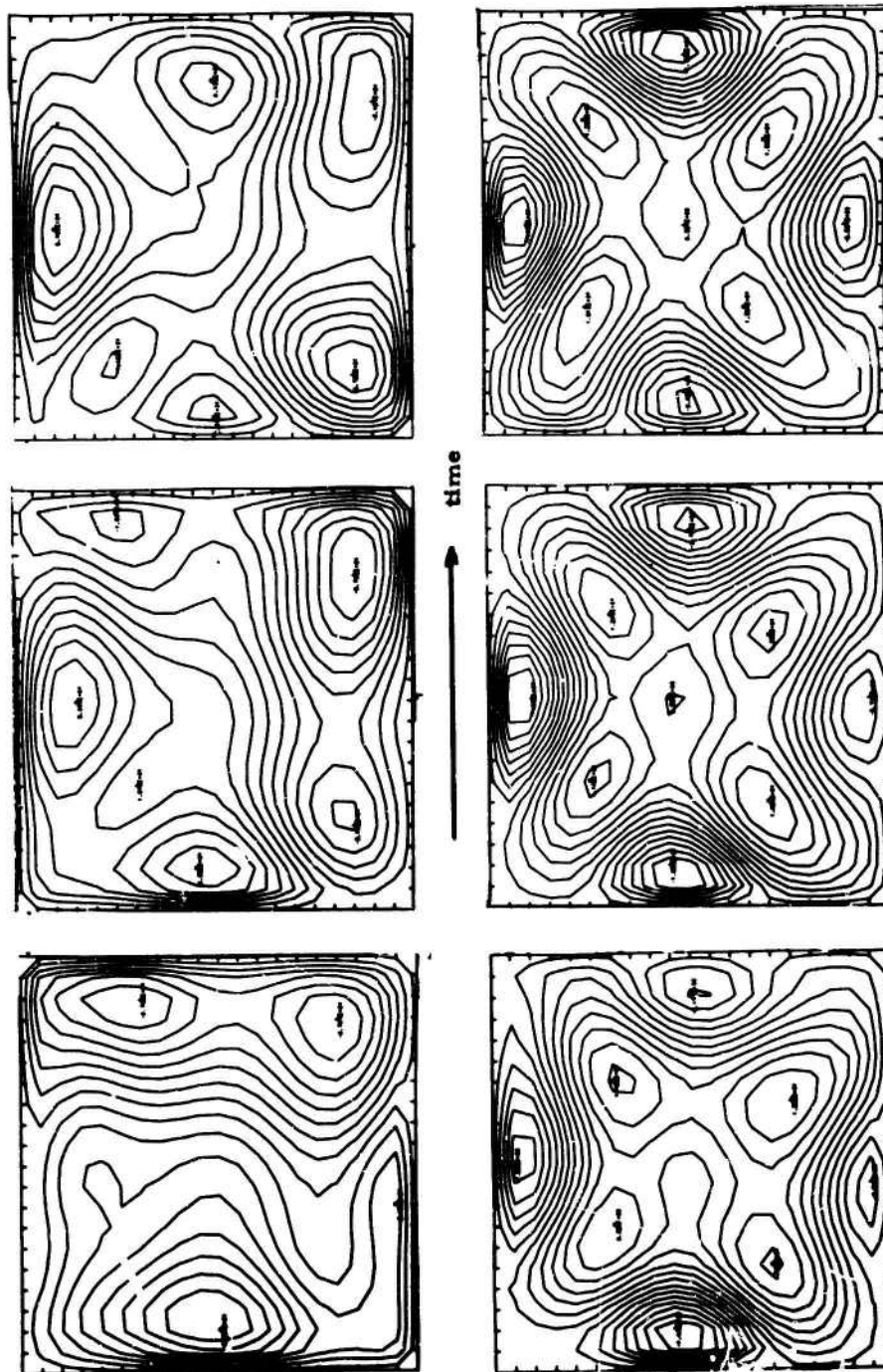
Fig. 3. Horizontal plot of the isolines of the vertical (z) component of vorticity at successive time intervals. Top row represents the surface level (z = 1.0) and bottom row the middle level (z = .50).

225

Fig. 4. Horizontal plot of the isolines of the vertical (z) component of vorticity at successive time intervals. Top row represents the surface level (z = 1.0) and bottom row the middle level (z = .50).

time

Penetrative Convection in Rotating Field

The most noticeable overall features of the circulation are the groups of closed circulation cells, mostly numbering from 3 to 8 and normally referred to as cyclones in meteorology or vortices in hydrodynamics, and a meandering, four-lobed sinusoidal jet str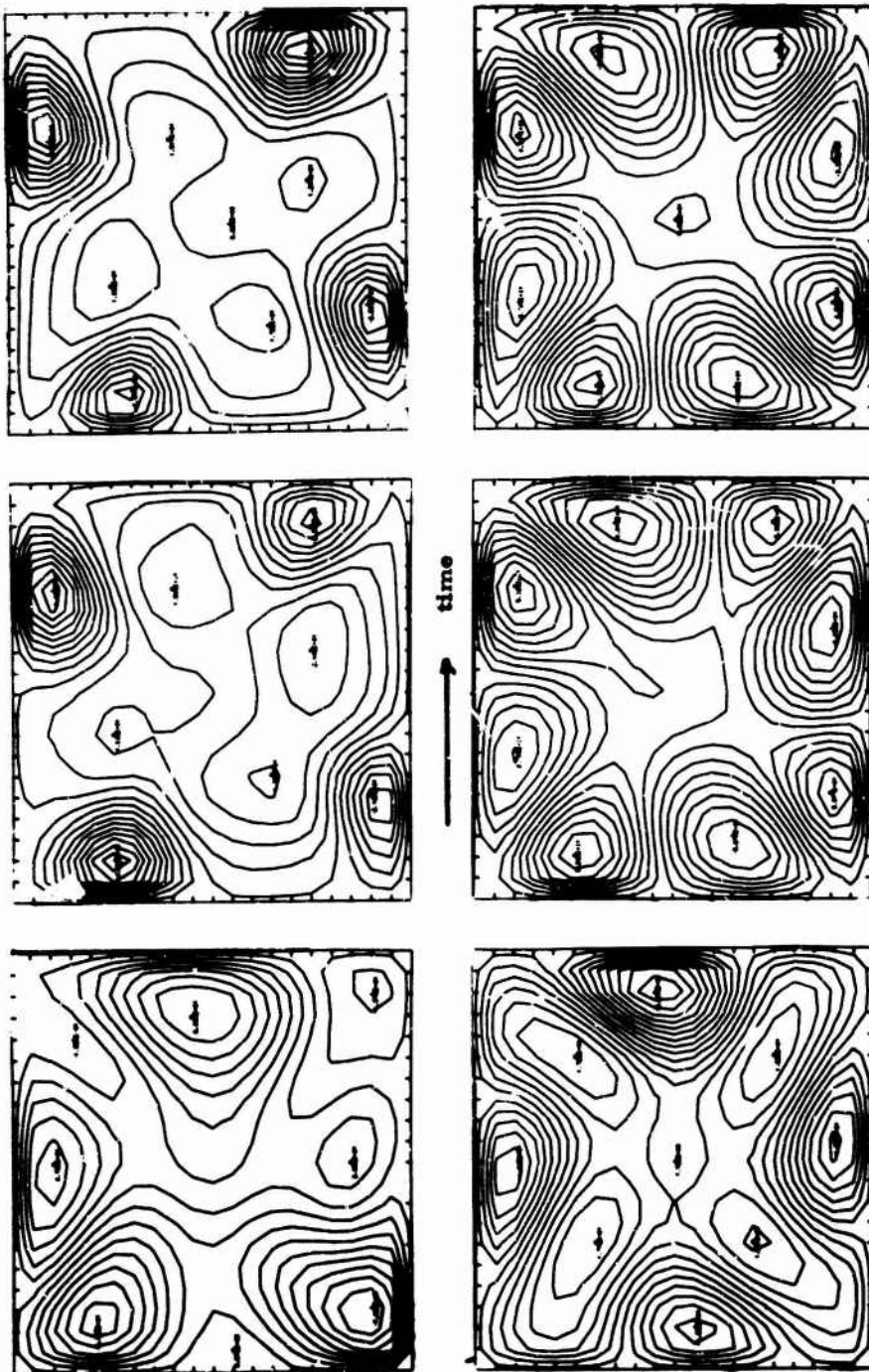eam. In some frames most of the lines belong to the cyclones and in some most to the jet stream, indicating the relative strength of the two phenomena. In the type of baroclinic instability found in rotating annuli as described in references 5-8, most of the streamlines belong to the jet stream, whereas in this experiment there is at most equipartition between the two modes. Mason and Hide[19] have observed such weak jets in a rotating annulus in which one of the cylinders was insulating, one cooled at a fixed temperature and the electrolytic fluid in the gap was heated internally with a current. If one thinks of the jet stream as a conveyor belt rolling on the cyclones, the former case is analoguous to a heavy belt driving some light wheels and the present case to a light belt driven by heavy wheels. Hence the notion of "strong" and "weak" baroclinic instability.

A detailed examination of Figs. 3 and 4 shows that jet stream formation is immediate and strong at the middle level but disappears in the end to yield to a formation of 8 cyclones. At the top, on the other hand, a jet stream is not apparent until the 5th frame and ends in a weak jet between four strong cyclones. The selection of an n=2 mode is obvious when the drastic constraint of a rectangular geometry is considered; in cylindrical annuli modes with 2 to 13 lobes have been observed. The withdrawal of the downward plunging cold thermals toward the surface and their general weakening in time is probably responsible for the vertical variation of these patterns.

An examination of Figs. 5 and 6 reveals the relation between temperature and horizontal circulation, and indirectly sheds some light

Fig. 5. Horizontal plot of the isolines of the z-component of vorticity (left column) and temperature (right column). Top row represents surface level (z = 1.0) and bottom row middle level (z = .50). Illustrates behavior during transient (oscillatory) motion and Fig. 6 near-steady behavior.
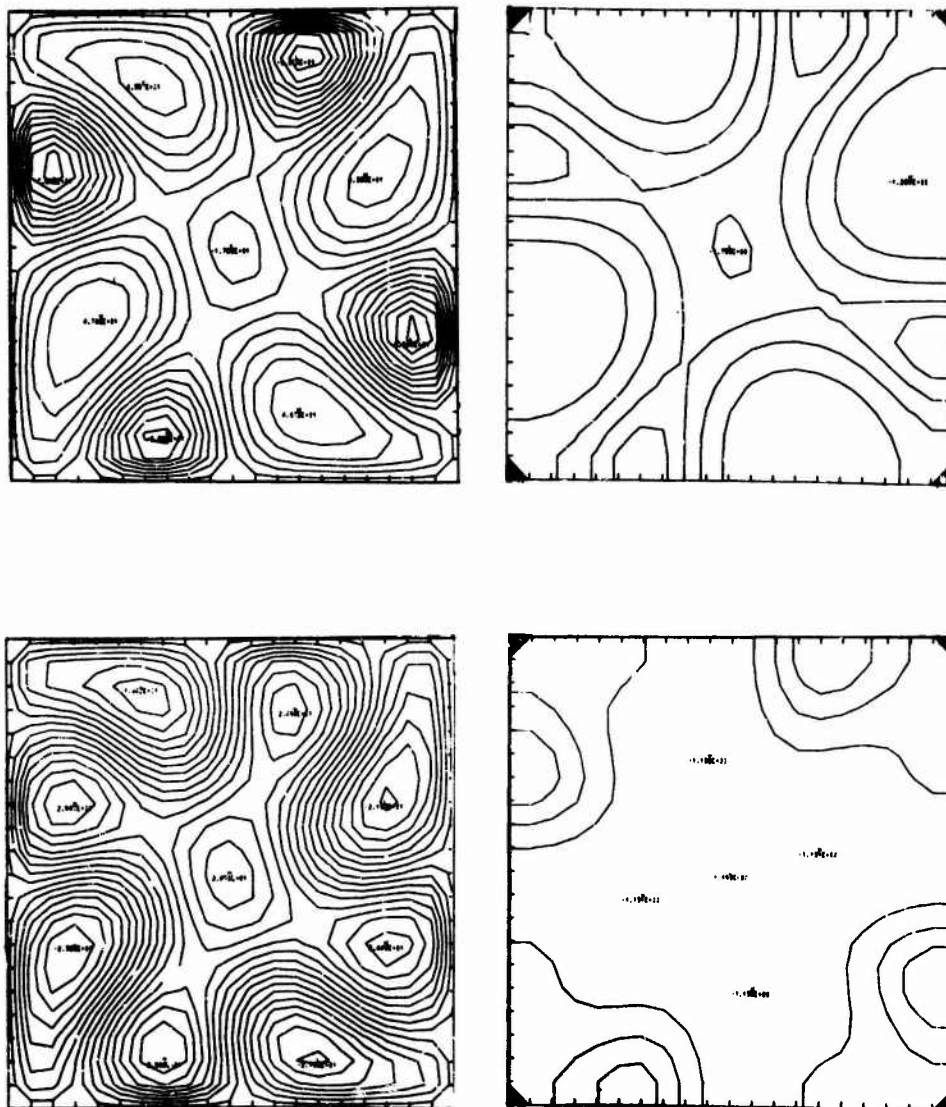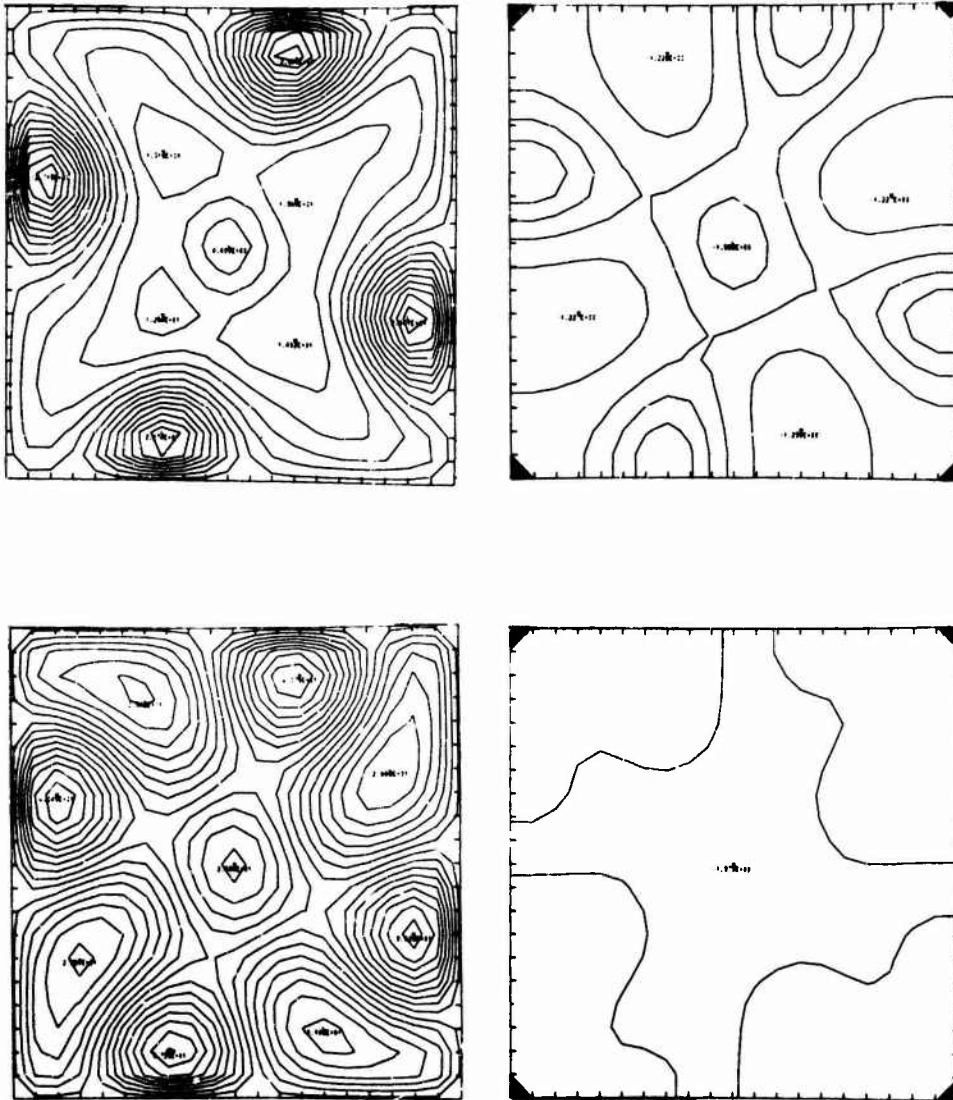
Fig. 6. Horizontal plot of the isolines of the z-component of vorticity (left column) and temperature (right column). Top row represents surface level (z = 1.0) and bottom row middle level (z = .50).

229

on the origin of the strong cyclones. The center of the cyclones
coincides with the center of the semi-circular isothermic regions,
verifying the "thermal wind" relationship, i.e., the horizontal
temperature contrast driving a motion that is constrained to rotate
by the Coriolis force. From (15) we obtain (using $\vec{\nabla}\cdot\vec{\xi} = \vec{\nabla}\cdot\vec{u} \sim 0$)

$$\frac{\partial \zeta}{\partial t} = -(\vec{u}\cdot\vec{\nabla})\zeta + (\vec{\xi}\cdot\vec{\nabla})w + \sqrt{Te} \cdot \frac{\partial w}{\partial z} \tag{23}$$

and from continuity

$$\vec{\nabla}_H \cdot \vec{u}_H = -\frac{\partial w}{\partial z} \tag{24}$$

Since regions of downward plunging cold fluid correspond to strong
regions of convergence, they also correspond to regions of strong
cyclone generation through the last term in (23) which is proportional
to Ω.

Appendix A:

The finite-difference form of equations (14)-(17) will be presented here. For a detailed discussion of iterating in time the initial-value problem the reader is referred to works by Richtmyer[20,21] and Lilly,[22] and for a discussion of differencing the nonlinear advective terms and the property of conservation to works by Arakawa,[23] Roberts and Weiss,[24] and Piacsek and Williams.[9]

The time coordinate is discretised as $t = n\Delta t$ and the space coordinates as $x = i\Delta x$, $y = j\Delta y$, $z = k\Delta z$, with n,i,j,k being integers, and denote the value of a dependent variable, say ϕ, at the discrete mesh points as $\phi(x,y,z;t) = \phi(i\Delta x, j\Delta y, k\Delta z; n\Delta t) = \phi_{ijk}^n$. The following difference operators will simplify the expressions considerably:

$$\delta_t(\phi_{ijk}^n) = (\phi_{ijk}^{n+1} - \phi_{ijk}^n)/\Delta t \tag{A.1}$$

$$\delta_x^-(\phi_{ijk}^n) = (\phi_{i+1,jk}^n - \phi_{i-1,jk}^{n+1})/2\Delta x \tag{A.2(a)}$$

$$\delta_x^+(\phi_{ijk}^n) = (\phi_{i+1,jk}^{n+1} - \phi_{i-1,jk}^n)/2\Delta x \tag{A.2(b)}$$

$$\delta X^-(\phi_{ijk}^n) = (\phi_{i+1,jk}^n + \phi_{i-1,jk}^{n+1} - \phi_{ijk}^n - \phi_{ijk}^{n+1})/\Delta x^2 \tag{A.3(a)}$$

$$\delta X^+(\phi_{ijk}^n) = (\phi_{i+1,jk}^{n+1} + \phi_{i-1,jk}^n - \phi_{ijk}^n - \phi_{ijk}^{n+1})/\Delta x^2 \tag{A.3(b)}$$

$$\delta_x(\phi_{ijk}^n) = (\phi_{i+1,jk}^n - \phi_{i-1,jk}^n)/2\Delta x \tag{A.4}$$

with similar expressions for δ_y^-, Sy^-, δ_y, δ_z^-, etc. Other useful operators will turn out to be

$$\vec{u}\cdot\vec{\delta}^- = u_{ijk}^n \cdot \delta_x^- + v_{ijk}^n \cdot \delta_y^- + w_{ijk}^n \cdot \delta_z^- \tag{A.5}$$

$$SS^- = SX^- + SY^- + SZ^- \tag{A.6}$$

and similar expressions for $\vec{u}\cdot\vec{\delta}^+$ and SS^+.

The differencing of the advective terms follows the so-called "angled-derivative" method, first discussed by Roberts and Weiss[24] and tested extensively by Piacsek and Williams.[9] Applied to a simple system, say $\frac{\partial\phi}{\partial t} = - u \frac{\partial\phi}{\partial x}$, this method takes the following expression

$$\text{Upsweep } (i=1,2,\ldots,I) \quad \delta_t(\phi_i^n) = - u_i^n \cdot \delta_x^-(\phi_i^n) \tag{A.7(a)}$$

$$\text{Downsweep } (i=I,I-1,\ldots,1) \quad \delta_t(\phi_i^{n+1}) = - u_i^n \cdot \delta_x^+(\phi_i^{n+1}) \tag{A.7(b)}$$

The overall truncation error of this scheme over the complete time step is

$$O(\Delta t^2 + \Delta x^2 + (\Delta t/\Delta x)^2) \tag{A.8}$$

and linearized stability analysis (see, e.g., Chapters 4 and 8 of Richtmyer & Morton[20]) shows that its associated eigenvalues have amplitude unity and there is no limitation on the time step Δt. The scheme is therefore neither amplifying nor damping, a very desirable property from the point of view of conservatic . Furthermore, it may be noted that the newly

232

generated values ϕ_i^{n+1} and ϕ_i^{n+2} may be stored in the locations for ϕ_i^n and ϕ_i^{n+1}, respectively, since there is no need for the latter quantities in the sweep once the former values have been computed. The storage of each physical variable at only one time level is needed, therefore, as compared to two for the leap-frog method,[21] and the total mesh size that can be employed with such a scheme is therefore doubled.

The differencing of the diffusion terms follows a related scheme, the so-called "Saul'ev" scheme (p. 191-192, ref. 20). For a simple system such as $\frac{\partial \phi}{\partial t} = \frac{\partial^2 \phi}{\partial x^2}$, this method takes the following form

$$\text{Upsweep } (i=1,2,\ldots,I) \quad \delta_t(\phi_i^n) = SX^-(\phi_i^n) \tag{A.9(a)}$$

$$\text{Downsweep } (i=I,I-1,\ldots,1) \quad \delta_t(\phi_i^n) = SX^+(\phi_i^{n+1}) \tag{A.9(b)}$$

The overall truncation error of this scheme is also that given by (A.8) and there is no limitation on the time step. Admittedly, the error $(\Delta t/\Delta x)^2$ is poor unless $\Delta t \ll \Delta x$, but this is a price one pays for additional storage. The experiments showed that $\Delta t = .1 \Delta z$ yielded quite satisfactory accuracy and the time step was still larger by a factor of 6 than that allowed by the stability conditions associated with three-dimensional explicit schemes ($\Delta z = .1$ in the present problem). Before the complete schemes for (14) and (15) are written down the conditions $\vec{\nabla} \cdot \vec{u} = \vec{\nabla} \cdot \vec{\xi} = 0$ are used to write the right-hand-side of (15) into the "advective" form, i.e.

Placsek

$$\vec{v}' \times (\vec{u} \times \vec{\zeta}) = - (\vec{u} \cdot \vec{v}')\vec{\zeta} + (\vec{\zeta} \cdot \vec{v}')\vec{u}$$

as these are more suitable for the applications of the angled-derivative method. The finite-differenced equations become therefore (ξ, η, ζ being the components of the vorticity vector $\vec{\zeta}$):

$$\delta_t(T_{ijk}^n) = (-\vec{u} \cdot \vec{\delta}^- + ss^-)T_{ijk}^n \tag{A.10(a)}$$

$$\delta_t(T_{ijk}^{n+1}) = (-\vec{u} \cdot \vec{\delta}^+ + ss^+)T_{ijk}^{n+1} \tag{A.10(b)}$$

$$\delta_t(\xi_{ijk}^n) = (-\vec{u} \cdot \vec{\delta}^- + ss^-) \cdot \xi_{ijk}^n + (\vec{\zeta} \cdot \vec{\delta}^-)u_{ijk}^n + \sqrt{Ta} \cdot \delta_z(u_{ijk}^n) + Gr \cdot \delta_y(T_{ijk}^{n+1}) \tag{A.11(a)}$$

$$\delta_t(\eta_{ijk}^n) = (-\vec{u} \cdot \vec{\delta}^- + ss^-) \cdot \eta_{ijk}^n + (\vec{\zeta} \cdot \vec{\delta}^-)v_{ijk}^n + \sqrt{Ta} \cdot \delta_z(v_{ijk}^n) - Gr \cdot \delta_x(T_{ijk}^{n+1}) \tag{A.11(b)}$$

$$\delta_t(\zeta_{ijk}^n) = (-\vec{u} \cdot \vec{\delta}^- + ss^-) \cdot \zeta_{ijk}^n + (\vec{\zeta} \cdot \vec{\delta}^-)w_{ijk}^n + \sqrt{Ta} \cdot \delta_z(w_{ijk}^n) \tag{A.11(c)}$$

$$\delta_t(\xi_{ijk}^{n+1}) = (-\vec{u} \cdot \vec{\delta}^+ + ss^+)\xi_{ijk}^{n+1} + (\vec{\zeta} \cdot \vec{\delta}^+)u_{ijk}^n + \sqrt{Ta} \cdot \delta_z(u_{ijk}^{n+1} + Gr \cdot \delta_y(T_{ijk}^{n+2}) \tag{A.12(a)}$$

$$\delta_t(\eta_{ijk}^{n+1}) = (-\vec{u} \cdot \vec{\delta}^+ + ss^+)\eta_{ijk}^{n+1} + (\vec{\zeta} \cdot \vec{\delta}^+)v_{ijk}^n + \sqrt{Ta} \cdot \delta_z(v_{ijk}^{n+1}) - Gr \cdot \delta_x(T_{ijk}^{n+2}) \tag{A.12(b)}$$

$$\delta_t(\zeta_{ijk}^{n+1}) = (-\vec{u} \cdot \vec{\delta}^+ + ss^+)\zeta_{ijk}^{n+1} + (\vec{\zeta} \cdot \vec{\delta}^+)w_{ijk}^n + \sqrt{Ta} \cdot \delta_z(w_{ijk}^{n+1}) \tag{A.12(c)}$$

234

Penetrative Convection in Rotating Field

In each relation of (A.11) and (A.12) the operators $\vec{u} \cdot \vec{\delta}^-$ and $\vec{u} \cdot \vec{\delta}^+$ have $\vec{u}$ evaluated at time level n. This leads to a cancellation of cross-derivatives of the type $\frac{\partial^2 \phi}{\partial x \partial t}$ in the Taylor expansion of ϕ_{i-1}^{n+1}, etc., and leads to an error of $(\Delta t / \Delta x)^2$ rather than $(\Delta t / \Delta x)$. The operators $\vec{\zeta} \cdot \vec{\delta}^-$ and $\vec{\zeta} \cdot \vec{\delta}^+$ have $\vec{\zeta}$ evaluated at time levels n and n+1, respectively, as these are the only values available in computer storage. The use of the advanced values of T in the buoyancy terms leads to stability regarding the internal gravity waves that arise in the system, and the velocity components are evaluated at level n in the Coriolis terms for lack of a better scheme. Actually, a very weak instability results from this choice of time level but over the length of time iteration performed in these experiments, it did not seem to cause any difficulty. A better scheme would be to take the Coriolis terms as $\frac{1}{2}(\delta_s (u_{ijk}^{n+1} + u_{ijk}^n))$, for example, but the values u_{ijk}^{n+1} are not available in this explicit scheme and several iterative sweeps over the whole system would be required to achieve this condition.

Appendix B:

Here the solutions of equations (19) and (20),

$$\nabla^2 \psi_i = -\xi_i , \qquad i = 1,2,3$$

$$\psi_{||} = -\frac{\partial \psi_n}{\partial n} = 0 \quad \text{on all six surfaces}$$

will be discussed using discrete Fourier series. The expansion functions chosen are pure sine series in those directions which have Dirichlet conditions $\xi_i, \psi_i = 0$ associated with them; the Poisson equations reduces then to a set of ordinary differential equations with Neumann conditions in the remaining coordinate. Thus, e.g., ξ, ψ_x are expanded in discrete Fourier series[25]

$$\xi = \sum_{n=o}^{N} b_n(x,y) \cdot \sin n\pi k\Delta z, \quad \psi_x = \sum_{n=o}^{N} a_n(x,y) \cdot \sin n\pi k\Delta z$$

(B.1)

and again

$$b_n(x,y) = \sum_{m=o}^{M} d_{mn}(x) \cdot \sin m\pi j\Delta y, \quad a_n(x,y) = \sum_{m=o}^{M} c_{mn}(x) \cdot \sin m\pi j\Delta y$$

(B.2)

where $N = I+1$, $M = J+1$ and I, J are the number of mesh intervals in the respective directions. For a detailed discussion of this method see the appendix of Ref. 8. The resulting ordinary differential equations then have the form

$$\frac{d^2c_{mn}}{dx^2} - (m^2 + n^2)\pi^2 c_{mn} = -d_{mn} \qquad \text{(B.3(a))}$$

$$\frac{dc_{mn}}{dx} = 0 \qquad \text{at} \qquad x = 0,1 \qquad \text{(B.3(b))}$$

and may be solved in finite-difference form by the well-known "tridiagonal algorithm" (see p. 200 of Ref. 20).

Footnotes/References

1. For an extensive review of this phenomenon the reader is referred to N. A. Phillips' work in Rev. of Geophysics, 1, 123 (1963).

2. Eady, E. T., Tellus 1, 33 (1949).

3. Charney, J.. Jour. of Meteor. 4, 135 (1947).

4. Pedlosky J., Jour. Atmos. Sci. 21, 201 (1964).

5. Hide, R., Proc. Roy. Soc. A250, 441 (1958).

6. Fultz, D., *Advances in Geophysics 7*, 1 (1961).

7. Pfeffer, R. and Chiang, Y., Mon. Weather Rev. 95, 75 (1967).

8. Williams, G. P., Jour. Fluid Mech. 37, 727 (1969).

9. Piacsek, S. A. and Williams, G. P., Jour. Comp. Phys. 6, (1970) to appear.

10. Hirt, C. W. and Harlow, F. H., Jour. Comp. Phys. 2, 114 (1967).

11. It can be shown that the scalar potential ϕ vanishes for this flow if $u_n \equiv 0$ on all surfaces, for the solution of $\nabla^2 \phi = 0$ with boundary conditions $\partial\phi/\partial n = 0$ (or periodic conditions, for that matter) yields $\phi \equiv 0$.

12. Quarterly of Applied Math. 26, 331 (1968).

13. H. P. Greenspan, *The Theory of Rotating Fluids*, Cambridge University Press (1968).

14. McIntyre, M. E., Jour. Fluid Mech. 32, 625 (1968).

15. Foster, D. T., Phys. of Fluids 8, 1770 (1965).

16. Blair, L. M. and Quinn, J. A., Jour. Fluid Mech. 36, 385 (1969).

17. Foster, D. T., Phys. of Fluids 8, 1249 (1965).

18. Mahler, E. G., Scheehter, R. S. and Wissler, E. H., Phys. of Fluids 11, 1901 (1968).

19. Mason, P. and Hide, R., Proc. Royal Soc. London (1970) to appear.

20. Richtmyer, R. D. and Morton, K. W., *Difference Methods for Initial-Value Problems*, Interscience Publishers, New York, 1967.

21. Richtmyer, R. D., National Center for Atmospheric Research Technical Note 63-2 (1963), Boulder, Col.

22. Lilly, D. K., Monthly Weather Rev. 93, 11 (1964).

23. Arakawa, A., Jour. Comp. Phys. 1, 119 (1966).

24. Roberts, K. V. and Weiss, N. O., Math. of Comp. 20, 272 (1966).

25. Danielsen, G. C. and Lanczos, C., Jour. Franklin Inst. 233, 365 (1943).

Numerical Experiments on Spiral Structure

R. H. Miller
University of Chicago
Chicago, Illinois

In preference to a survey of various computations
in astronomy, I shall concentrate on one calculation
that has led, in the past couple of years, to the
development of computer models of spiral galaxies. Two
groups have been working in this area: that of Roger
Hockney and Frank Hohl at NASA Langley, and the group
at the Institute for Space Studies in New York with
Kevin Prendergast and William Quirk of Columbia Univer-
sity, with whom I have been associated. These calculations
have a lot in common with some work in plasma physics
computations--indeed, Hockney and Hohl became interested
in this problem through a background in plasma physics.

Spiral structure is a puzzle of long standing in
astronomy. Spirals cannot be a transitory evolutionary
phase; the statistics of relative numbers of spirals
among all galaxies (about 2/3 spirals) are not consistent
with such a notion. The basic problem is how to keep the
spirals from wrapping themselves up. They are known to
rotate (from spectroscopic evidence), and do not rotate
rigidly. The typical field of differential rotations
has larger angular velocities (over linear velocities)
in the inner portions than there are farther out. Any
pattern impressed on such a differentially-rotating form

would wrap up and become indistinguishable after a few
rotations. And the rotation times (around 1/4 billion
years for our Galaxy) would wash out any spiral patterns
in times far too short to be consistent with large fraction
of spiral galaxies actually observed.

The way out of this difficulty was given by B. Lindblad,
who started working on this problem around 1925. The
"wrapping-up" occurs if the spiral consists of identifiable
material - what, today, we call a "material arm." Lindblad
pictured the spiral as a pattern--a density wave.
C.C. Lin and his group have built this idea into a pleasing
theory that has caused quite a bit of excitement among
astronomers.

Even with the help of these models, the problem of
spiral structure cannot be regarded as solved --many features
are not yet understood. Neither theory nor observation
can give an unambiguous answer to so simple a question as
whether the spiral patterns lead or trail. The lifetime
and stability of the spiral patterns are open questions.
There are other difficulties as well, but they merely
reinforce the need for alternate approaches to the problem.

One of the nice things about working in astronomy is
that many of the objects are incredibly beautiful. A spiral
galaxy is one of the most pleasing objects. In Figure 1, a
well-known spiral galaxy, M 51, is shown. Ignore the bright
knot at the end of one of the arms. The features that impress
you immediately in this photograph are (1) a general rather
good twofold symmetry that extends over the entire galaxy,

240
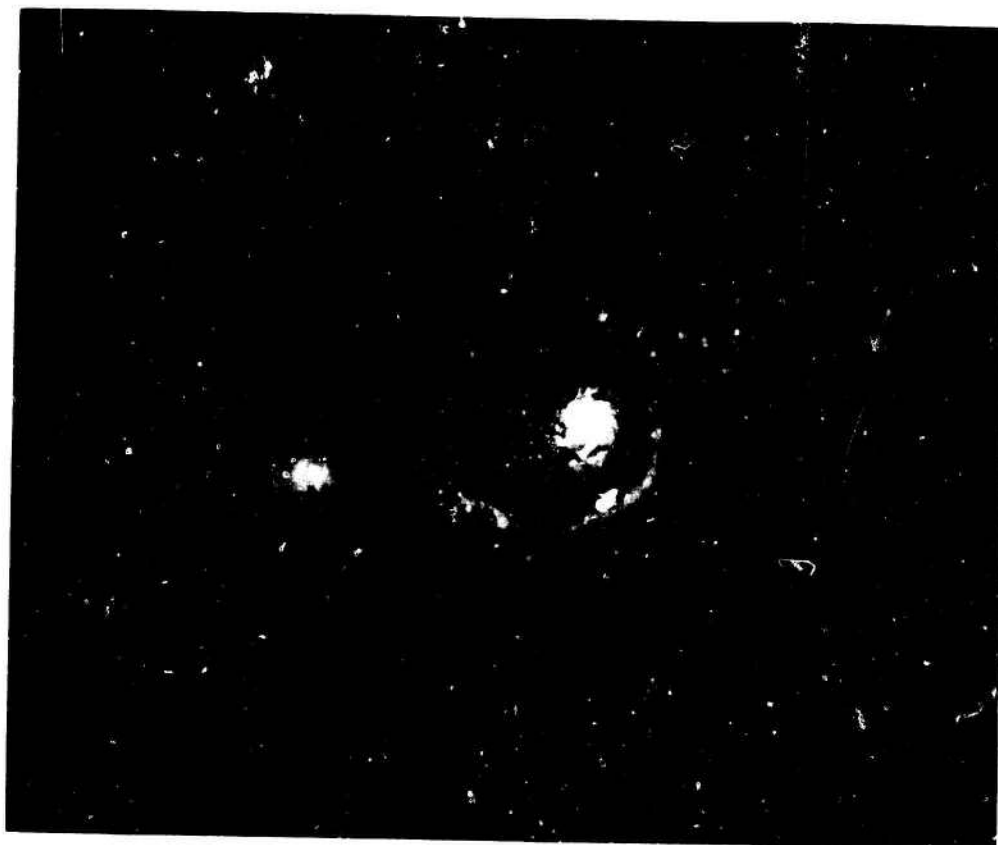
Fig. 1.   A spiral galaxy seen face-on.   This is known to astronomers as M51 or NGC 5194.

in spite of many detailed irregularities, (2) a reasonable amount of contrast, or of brightness difference, between the spiral arms and the inter-arm regions, (3) generally decreasing brightness farther from the center, with a fairly bright center (the photograph does not show this nearly as well as it should--no photograph can), (4) disappearance of the spiral pattern at the center, but the spiral continues outward as far as you can distinguish the galaxy, (5) some dark lanes on the inner edges of the spiral arms (trailing

241

edges, if the arms trail), (6) it looks like a flat
object seen face-on in this photograph--it is a little
difficult to imagine a three-dimensional structure that
would look something like this in any direction, (7) it
is clearly a self-gravitating system, (8) while there
may be neighbors, their influence is small. The ex-
perts will see a lot more in this picture. The bright
spots outside the galaxy image are foreground stars.

Figure 1 was made with an ordinary (i.e., blue-
sensitive) photographic plate. If a red-sensitive plate
is used behind a filter to remove most of the blue light,
the galaxy shows much less structure. If the galaxy is
photographed through a filter that passes H_α or H_β, then
a set of bright "knots" is seen along the spiral arms--
principally near the dark lanes. The interpretation of this
is that most of the light in the spiral arms comes from
very bright, young, blue stars (O and B stars), and from
ionised hydrogen (HII) regions surrounding such stars.
These stars, which may be as much as 1000 to 10000 times
as bright as the sun, but only 10-30 times as massive,
do not live very long--they consume the available fuel
stores much too rapidly. The red background may come from
stars that are less massive, hence longer-lived. Most of
the mass is in the form of stars that produce the red light,

most of the light comes from the blue stars.

Our own Galaxy has all these ingredients as well. We see bright blue stars, many faint red stars, and gas clouds. There are some bright red stars too, but these are much less massive than the bright blue stars, and are at an advanced stage of their aging process. Usually, the bright blue stars are near or inside gas clouds, the gas very near the star often being ionized. The gas density is very irregular. The bright blue stars must have been born recently--presumably out of the concentrations of gas. Moving with typical velocities, they cannot depart from their parental gas cloud very far during their lifetime. Of course, stars of all masses will be formed from these gas clouds--many more low-mass stars than high-mass stars, but almost all the light comes from the bright blue (massive) stars. It is, of course, no accident that we think that extragalactic nebulae are built of the same ingredients that we see in the solar neighborhood of our own Galaxy--it is precisely because we see them here that we think they must be the principal constituents of other galaxies. We also see in our own Galaxy dark regions, or "dust clouds," usually associated with gas clouds and bright blue stars, that we think are similar to the dark lanes in these other galaxies.

Miller

NGC 1300, in Figure 2, shows another common form of spiral galaxy. This is known as a "barred spiral, " and shows the same features as have been pointed out in M51, although perhaps different in detail. The barred spirals usually have the pair of dark lanes symmetrically disposed near the ends of the bar. The bar tends to be redder than the arms. M81, in Figure 3, is a particularly beautiful object, showing again the same kinds of features. Here the spiral pattern is more tightly wound. M81 gives the distinct impression of a flat object seen in some direction other than face-on. Finally, NGC 891, in Figure 4, shows the extreme case of one of these objects seen edge-on. Presumably, if you could see it from another direction, NGC might look like M81 or M51 (without the satellite). Notice the dark lane concentrated rather closely to the median plane. All these pictures are shown in an attempt to convince you that a reasonable model for these objects is a self-gravitating mixture of various constituents, all constrained to move in a plane.

There are other kinds of galaxies--principally the very regular and beautiful ellipticals, which look like (oblate) ellipsoidal mass distributions, and do not show the dark lanes or gaseous regions--and the irregulars, which show a little bit of everything, with much less organization.

Fig. 2. A different kind of spiral galaxy--a barred
spiral. This is NGC 1300, also seen face-on.

Fig. 3.   Another spiral galaxy (M 81 = NGC 3031). This
gives the impression of a flat object seen from some
angle other than face-on.

Fig. 4.   A spiral galaxy seen edge-on (NGC 891). Presumably
M 51 or M 81 would look like this if viewed from the appro-
priate direction, and NGC 891 might look like one of them if
viewed from another direction.

As plasma physicists, you will notice that nothing
has been said about magnetic fields. A few years ago,
most attempts to explain spiral structure centered on
magnetic fields. There is good evidence that magnetic
fields are one of the ingredients of our galaxy. The
main justification for omitting them from the present
discussion is that the influence of the magnetic fields
on the dynamics of the stars is through the gravitational
effect of the ionized gas--which represents a small frac-
tion of the total mass. Failure to construct a convincing
spiral model without magnetic fields would force us to
include them; but it is worth a try without magnetic fields
because a model without them will be much simpler.

The starting point for most current theories of spiral
structure is abstracted from the conditions just described.
Models are to be constructed of self-gravitating systems
restricted to a plane. In that plane, there is a pre-
dominantly axisymmetric mass distribution that generates
axisymmetric potential and force fields. The axisymmetric
part consists of red stars and contains most of the mass.
Superimposed on this background is a gaseous system--also
self-gravitating, but obeying gas-dynamical equations
rather than the particle equations of the stellar dynamical
system. The two subsystems interact to generate a self-
consistent whole. Both subsystems partake of the differential
rotation. The gaseous subsystem contains a spiral pattern
which rotates (almost) rigidly with its own angular velocity.
The material (both stars and gas) flows through the pattern.

There is a slight potential minimum at the pattern (the total potential field is no longer axisymmetric), where the gas tends to concentrate. The gas concentration also induces a slight concentration of stars in the neighborhood of the spiral pattern, but that concentration is much weaker. A shock may form as the gas flow enters the potential minimum at the spiral pattern. New stars are thought to form in regions of high density--thus preferentially near the shock. When old stars die, they return some gas to the medium, to allow this process to continue. However, not all gas is returned, so the process cannot go on forever. The angular velocity of the pattern is lower than the angular velocity of the gas and stars over most of the region in which the pattern can be seen. Lin's models are built by impressing a spiral pattern on this kind of background, then solving the self-consistency problem for the combination of gas and stars in the (linearized) limit of small density variations and of small pitch angles for the spiral patterns.

Computer models, on the other hand, may start from nearly axisymmetric models and allow a process like star formation to go on. The stars move under the usual stellar dynamical equations, with the forces determined by self-gravitation. The "gas" population follows a modified dynamics according to which turbulent energy is artificially removed. So far, the "gas" has not obeyed gas-dynamical equations, but only a crude approximation to them. A shock could not form in these models. We are improving this feature of the calculation. Hohl's models differ in impos-

ing an axisymmetric potential in which the stars move so
only one population is needed. The computer models normally
handle about 10^5 particles---they could be pushed to 10^6 or
10^7 on current machines if there were any clear-cut reason
for doing so. Even so, they fall far short of the 10^{11} in
a real galaxy. Thus the theoretical models (Lin, and others)
and the computer models are complementary approximations to
real stellar systems. The theoretical models ignore the
grainy structure of real stellar systems, while the com-
puter models are far too grainy.

Details of the calculations have been published, and
will not be discussed here. Our calculation has been adver-
tised to be reversible and to have an exact Liouville theorem
in the μ-space, all obtained at the cost of treating the
integrations somewhat crudely. Reversibility is as much a
matter of numerical accuracy and roundoff as it is of the
difference-scheme used. We have taken some pains in these
matters, but cannot give an honest appraisal as to how
important these features are.

The results of a calculation that yielded spiral
patterns are shown in a motion picture. A few frames from
the motion picture are reproduced here as Figures 5 and 6.
The "star" field shown in the upper right-hand corner of
Figure 5 changes very little as the calculation proceeds.
The remainder of Figures 5 and 6 show the "gas," at succes-
sive integration steps at a stage of the calculation in
which the spiral pattern had settled down fairly well. The
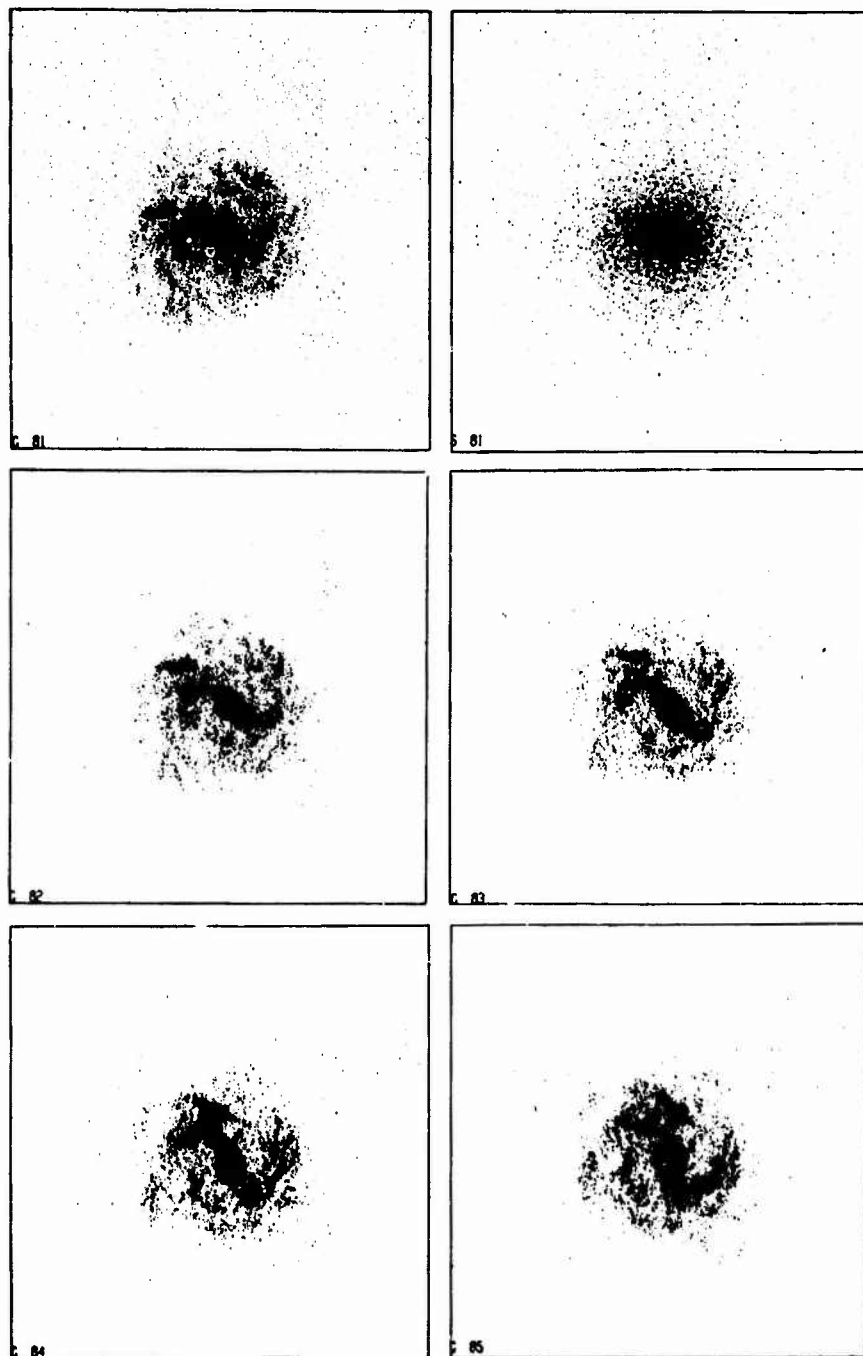pattern rotates in about 30 integration steps, while Fig-
ures 5 and 6 show 11.

Fig. 5. Frames from the motion picture of the computer spirals. The upper-right-hand frame shows the "stars," which change little during the calculation; the rest show the "gas" at various integration steps.
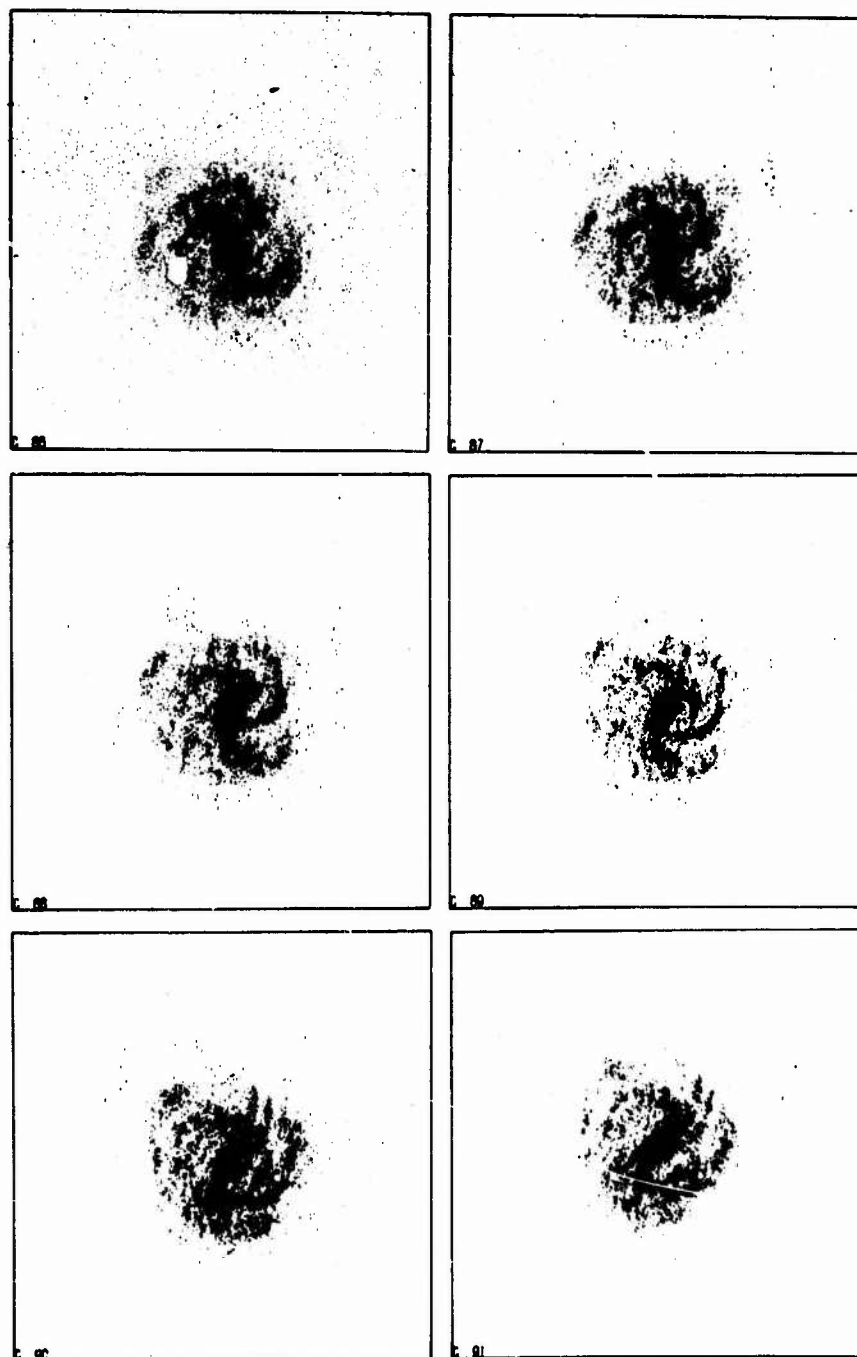
251

Fig. 6.   Continuation of Fig. 5.

Experiments in Spiral Structure

This calculation started from a circular disk that was all "gas," but had a rule for creating "stars" out of the "gas" that is thought to conform to what might go on in a real galaxy. The precise rule must have profound dynamical consequences--certainly altering the rule alters our models - but this particular aspect of the calculation should not be taken too literally. By the time shown in Figures 5 and 6, about 85% of the mass was in the form of "stars," the remaining 15% still being "gas." Star formation had stopped long before the time of these figures. However, once stars were formed, they remained stars for the rest of the calculation--there was none of the recycling of material that is expected in a real stellar system.

The spiral density wave idea is shown in Figures 7 and 8. These figures represent the "gas" portion of the system, with a few "particles" singled out and plotted as large squares. The identity of certain "particles" is retained from frame to frame. In figures 7 and 8, individual "particles" can be seen to approach the spiral feature from behind (the rotation is clockwise), dwell at the feature momentarily, then to pass on through it. We have not been able to show this effect in a sequence of still pictures nearly as dramatically as the motion picture shows it, but the effect is there.

A word of warning. These sequences--and the motion picture--should not be considered as depicting the aging or evolution of a real galaxy. The initial conditions are

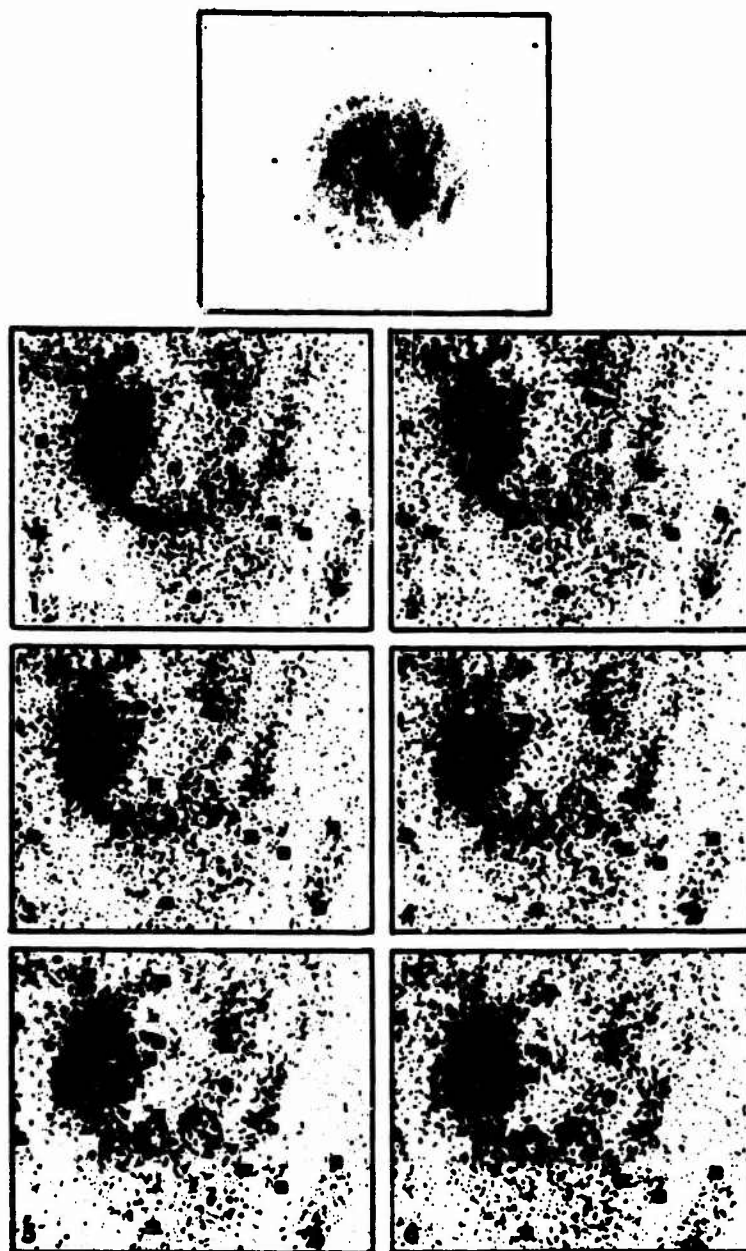Fig. 7. Details of the spiral patterns, showing individual particles moving through the spiral features. The entire system is shown in the top frame, the lower frames are enlargements out of that picture at intervals of 1/5 an integration step. Certain particles are plotted as large squares in each of the frames, to show the motion of those particles relative to the pattern.
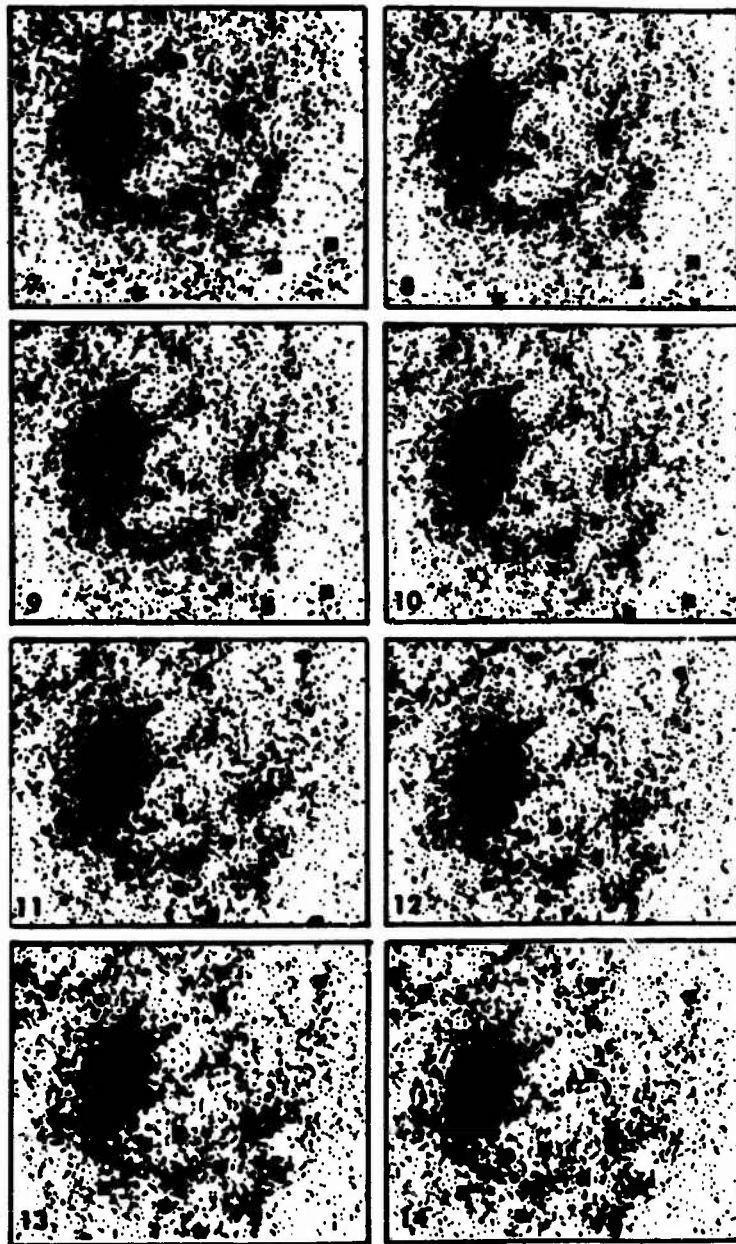
Fig. 8.   Continuation of Fig. 7.

certainly unrealistic, and the real system has a more com-
plex interplay of various properties than we have been able
to include in the computer program. Thus the fact that one
or more of these frames might look like photographs of some
real galaxy does not mean that we have managed to reproduce
the evolutionary history of that particular galaxy, or even
that earlier and later stages of the calculation indicate
what that galaxy would look like at earlier or later stages
of its aging process. The value of the numerical experiments
lies in general indications of how difficult it is to build
spiral patterns that live for a while (these lived for about
3-4 pattern rotations), of the interplay between the
"star" and "gas" populations in the pattern, what
fraction of the mass of the system participates in the
pattern, and so on. It is particularly valuable to be
able to "kick" the computer experiment to see if it
"bounces,"--something that we cannot do with the real
galaxy. The computer experiment is an experimental tool
with which we can try to find out what makes spiral
patterns. While the emphasis in this paper is on spiral
patterns, there are other experiments that both Hohl and
we have done with these systems. These include experi-
ments on gravitational stability and attempts to verify
various stability predictions.

So what have we learned from these computer experi-
ments? We have learned that spiral patterns can be constructed
of self-gravitating systems without need to invoke magnetic
forces. But two populations were needed, or some other
artifice to emphasize the spiral pattern. Real galaxies

have a very effective amplifier of small density variations
to produce large brightness variations. Computer models
need the same thing. On detailed analysis, we find that
there is a spiral density wave in the stars as well as in
the gas-- there is about as much total mass participating
in the spiral phenomenon in the stars as there is in the
gas. But about 1/4 the gas participates and less than 5%
of the stars, so when we plot the star density we do not
see a spiral pattern. So far, there are no spiral patterns
in computer models without two populations (think of Hohl's
background potential as the second population), just as we
know of no spiral systems in the sky that do not have two
populations. But are two populations necessary? We do not
know. Spiral patterns seem to appear when the conditions
re about right, but we find that spiral patterns are diffi-
cult to stir up if the conditions are not just right (this
is the content of Quirk's Ph.D. Thesis).

As with all experiments, the computer experimenter must
be very careful to avoid interpreting situations in which
the experimental results fail to contradict his prior preju-
dices as proof of the correctness of those prejudices. With
these experiments, we have seen some patterns. What we see
fails to contradict our prejudices. We feel that we have a
foot in the door, and a valuable tool for experimenting with
properties of spiral systems. The real test comes now--to see
if we know how to use that tool for some definitive experi-
ments.

For those who may wish to pursue some of these matters further, the following references are starting-points and lead to earlier literature:

(1) Theoretical work on spiral waves, especially the Lin school:

> C. C. Lin, C. Yuan, and F. H. Shu,
> Astrophys. Journ. 155, 721 (1969)

(2) Hohl's computer experiments:

> F. Hohl, "Dynamical Evolution of Disk Galaxies",
> NASA Technical Report NASA TR R-343, July 1970.

> F. Hohl and R. Hockney, Journ. Computational Physics,
> 4, 306 (1969).

(3) Our group:

> R. H. Miller, K. H. Prendergast, and W. J. Quirk,
> Astrophys. Journ. 161, 903 (1970).

(4) General review of astronomical view of spirals (conference proceedings)

> The Spiral Structure of Our Galaxy, IAU Symposium 38
> W. Becker and G. Contopoulos, Editors
> (Dordrecht, Holland: D. Reidel Publishing Co.) 1970.

Chemistry from Computers:
A New Instrument for the Experimentalist

Arnold C. Wahl
Argonne National Laboratories
Argonne, Illinois

INTRODUCTION

Some time ago, being fresh from the enthusiasm of
computing Hartree-Fock (best molecular orbital) wave
functions for non-trivial molecules, I gave a talk[1]
entitled "Hartree-Fock is Here: What Next?" and I received,
from an experimentalist, a reprint request for the article
"Hartree-Fock is Here - Who Cares?" This mis-stating of the
title of my optimistic talk, in addition to being humorous,
contained a very substantial bit of truth; namely, computers
have brought us a great deal - vast numerical tables of
molecular properties, pretty pictures, detailed wave functions
from many small molecules (in many cases, so precise, they
are unusable), and perhaps more "theoretical chemists" than
ever before. But how much chemistry have they really given
to us? This question certainly needs to be answered, and if
we are to make chemists happy we must agree to answer it on
their terms. Thus, we need a precision in potential energy
surfaces of about 1/10 of an eV, we need better than 5%
precision in ionization potentials, binding energies, vibrational

frequencies, term values, and spectroscopic constants. We, further, must go beyond isolated calculations, and into their comprehensive coupling with the traditional tools of the chemist to allow us to obtain macroscopic properties.

In this paper I would like to explore how close we, at Argonne, are to achieving such results from computers. It will become apparent that we must be cautious, but that in certain cases we are able to obtain truly reliable chemical information from our a priori computing systems and that our research is most properly viewed as the development of a new instrument for the chemist by which he can obtain detailed answers often not accessible experimentally. An intriguing and very important aspect of this new apparatus is that it permits us to "look" in unprecedented detail with arbitrary magnification or time scale (when quantum mechanically legal) at a chemical process under study, be it molecular electronic excitation, vibration, collision, or the entire path of a chemical reaction (See note on page 302 and Figures following).

THE MOLECULAR ORBITAL MODEL

As a first step in tracing the development of our new ab initio instrument for exploring molecular structures, let us look at a very popular model of electronic structure; namely, the Hartree-Fock molecular orbital model.[2] This model currently is being applied widely in the name of chemistry to all kinds of systems. However, some typical results obtained by the Hartree-Fock model show that although it is adequate for some molecular properties, the Hartree-Fock model has very well-known and well-substantiated deficiencies

which make it difficult to really do a priori chemistry from Hartree-Fock calculations.

First of all, let us briefly review what the Hartree-Fock model[2-30] is. The Hartree-Fock model is the best orbital model. In the Hartree-Fock model[20] we place electrons in individual three-dimensional functions ϕ_i, include spin functions, and then form a properly antisymmetrized product of these spin orbitals.

$$\Psi = \textcircled{A} \pi_i \phi_i \tag{1}$$

to obtain the total atomic or molecular wave function.

Mathematically, the orbitals i are solutions of integro-differential equations of the form

$$F\phi_i = \epsilon_i \phi_i$$

where F is an operator depending upon all electrons and nuclei of the systems and arising from the variations of its total electronic energy. These equations must be solved iteratively[28] since the orbitals ϕ_i determine the operator F and vice-versa. Convergence on the "best" set of orbitals is achieved when the ϕ_is from two successive iterations agree within some permissible numerical threshold. In Figures 1 through 3 some typical pictures of best molecular orbital and total electron densities for a variety of diatomic molecules are shown. From these pictures it immediately becomes apparent that the Hartree-Fock model forms a very appealing, conceptual and, in fact, symbolically beautiful framework for thinking about molecules.[30,31]

MOLECULAR ORBITAL

	Total	$1\sigma_g$	$1\sigma_u$	$2\sigma_g$
MOLECULE				
$H_2 {}^1\Sigma_g^+$				
$He_2 {}^1\Sigma_g^+$				
$Li_2 {}^1\Sigma_g^+$				
$Be_2 {}^1\Sigma_g^+$				
$B_2 {}^3\Sigma_g^-$				
$C_2 {}^1\Sigma_g^+$				
$N_2 {}^1\Sigma_g^+$				
$O_2 {}^3\Sigma_g^-$				
$F_2 {}^1\Sigma_g^+$				
$Ne_2 {}^1\Sigma_g^+$				

262

$$2\sigma_u \qquad 1\pi_u \qquad 3\sigma_g \qquad 1\pi_g \qquad 3\sigma_u$$
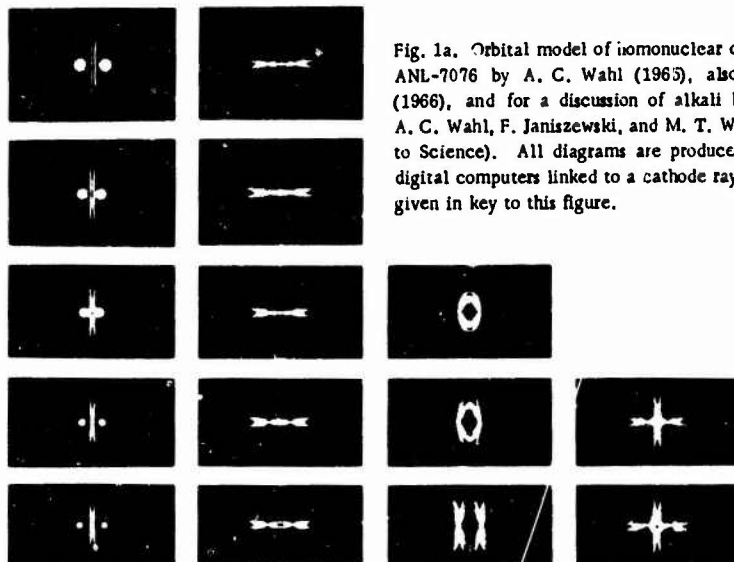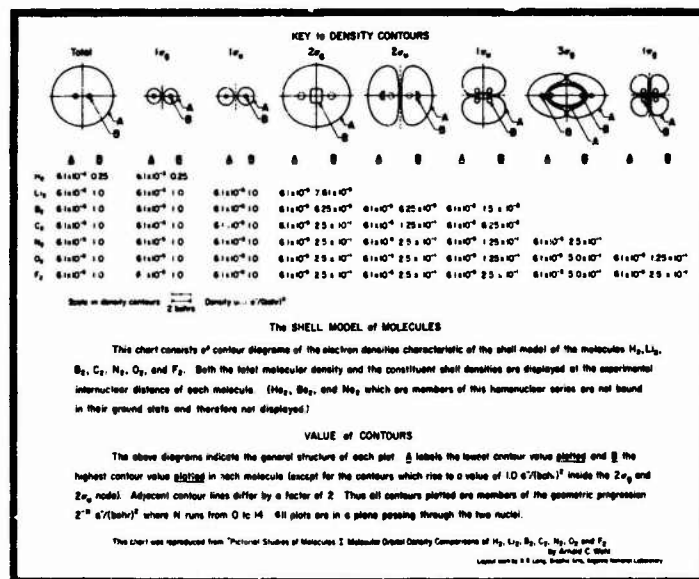
Fig. 1a. Orbital model of homonuclear diatomic molecules, ANL-7076 by A. C. Wahl (1965), also Science 151, 961 (1966), and for a discussion of alkali halide densities see A. C. Wahl, F. Janiszewski, and M. T. Wahl (to be submitted to Science). All diagrams are produced automatically by digital computers linked to a cathode ray tube. Conventions given in key to this figure.
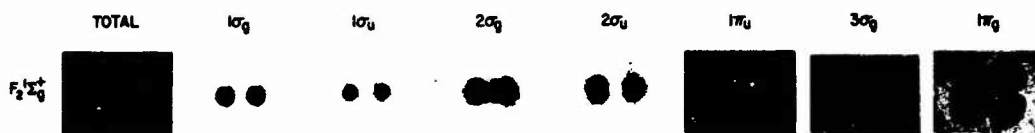
Fig. 1b
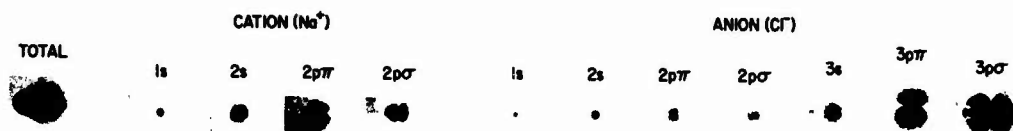
Fig. 2b

Electronic probability "clouds" for F_2 and NaF_2. These also may be mapped as contour diagrams. See Figs. 1a and 2a.
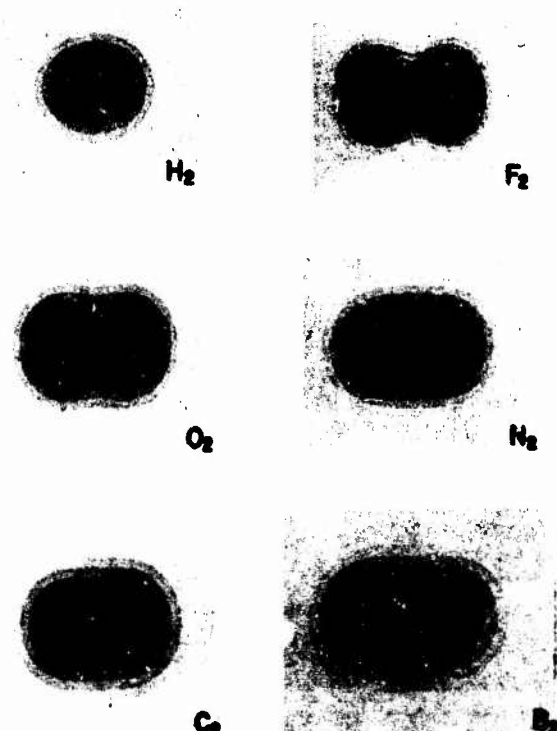
Fig. 1c

Total electron probability clouds for some homonuclear diatomic molecules which can be mapped by contour lines as in Fig. 1a.

Chemistry from Computers

The homopolar cases (Figure 1) have symmetry and covalency; in the ionic systems (Figure 2) the molecular orbitals are really localized on the individual ions and are very much like the isolated ionic orbitals. In looking at "pictures" of molecular processes -- namely, ionization[32,33] and excitation[32,33] (Figure 3) -- it appears that in the orbital framework we get a qualitative feeling for what's happening. An orbital shrinks when we remove an electron, it gets a little smaller, a little tighter, because there is less electron repulsion. Further, the non-active orbitals are relatively insensitive to the ionization process (Figure 3a). In Figure 3b we "see" quite dramatically a σ to π excitation[33] in the hydrogen molecule followed by ionization.

Now let's turn to some typical quantitative results obtained from the model. In Tables 1 and 2 recent results of Hartree-Fock calculations on diatomic systems[34-63] are shown. We are first struck by the rather good geometry predictions -- we can predict internuclear distances, often within less than 1%. Also, a typical one-electron property such as the dipole moment is well predicted. But, looking further at the tables, we find, from a chemist's viewpoint, binding energies are terrible. We can, of course, correct them semi-empirically, but this, after all, cannot be called a priori chemistry from computers. We see that the dissociation energies are often off by 100%; take F_2, as an outstanding example of this deficiency. Also, vibrational frequencies really don't allow us to distinguish between excited states of the same molecule; the precision is not sufficient. We find, for instance, in the excited states of the nitrogen molecule

MOLECULAR ORBITAL DENSITIES*
THE ALKALI HALIDES
CATION PARENTAGE
Total   ls   2s   2pπ   2pσ   3s   3pπ   3pσ
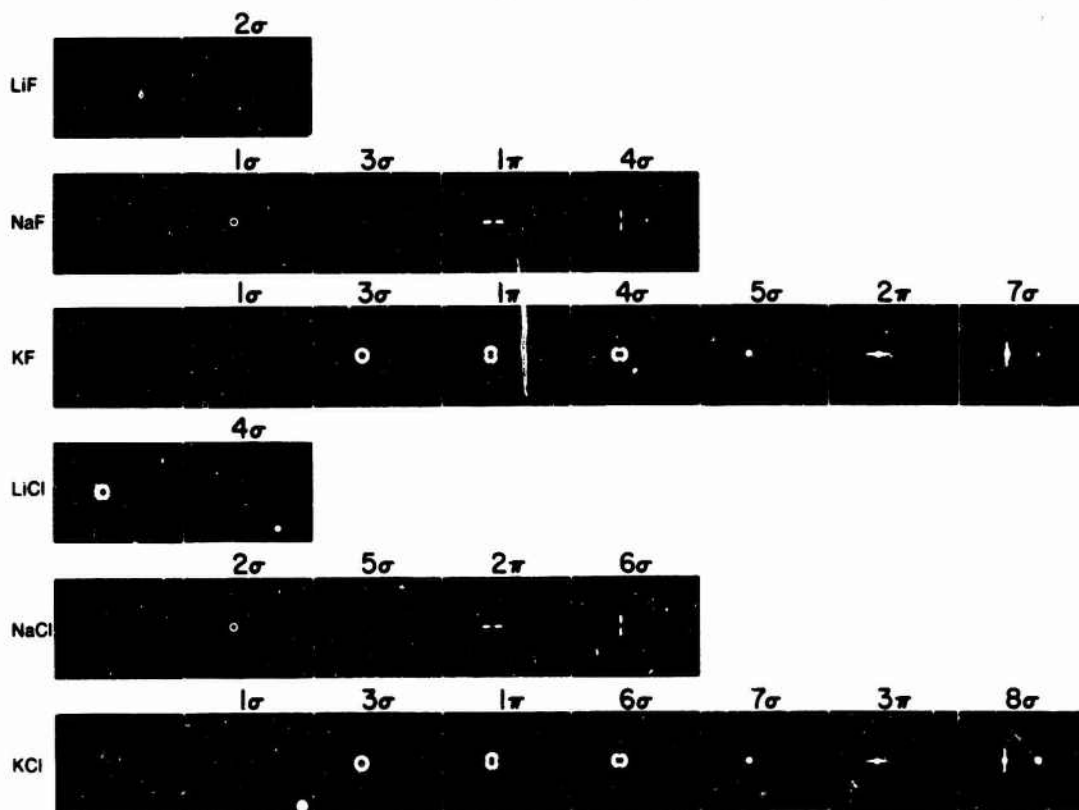
*These molecular orbitals are arranged according to their separated ion parentage
...first the set arising from the cation and then the set from the anion.   The
molecular orbital label is given above each diagram.

ANION PARENTAGE

Is   2s   2pπ 2pσ 3s   3pπ 3pσ
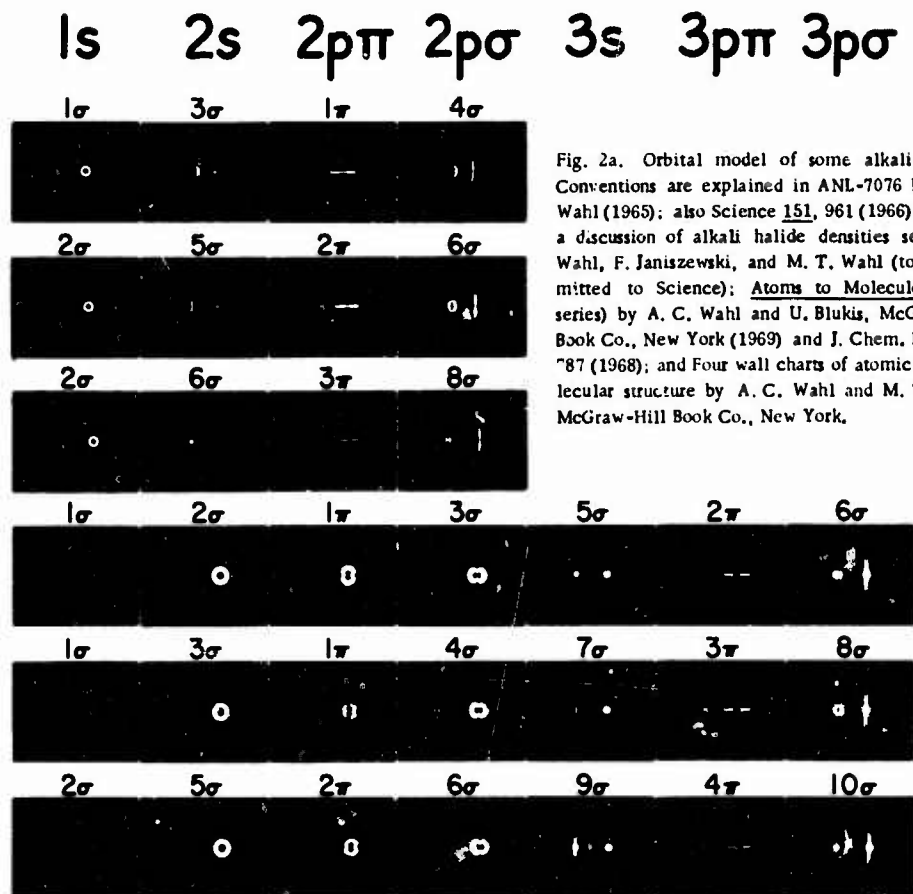
Fig. 2a. Orbital model of some alkali halides. Conventions are explained in ANL-7076 by A. C. Wahl (1965); also Science 151, 961 (1966), and for a discussion of alkali halide densities see A. C. Wahl, F. Janiszewski, and M. T. Wahl (to be submitted to Science); Atoms to Molecules (Film series) by A. C. Wahl and U. Blukis, McGraw-Hill Book Co., New York (1969) and J. Chem. Educ. 45, ¯87 (1968); and Four wall charts of atomic and molecular structure by A. C. Wahl and M. T. Wahl, McGraw-Hill Book Co., New York.

IONIZATION
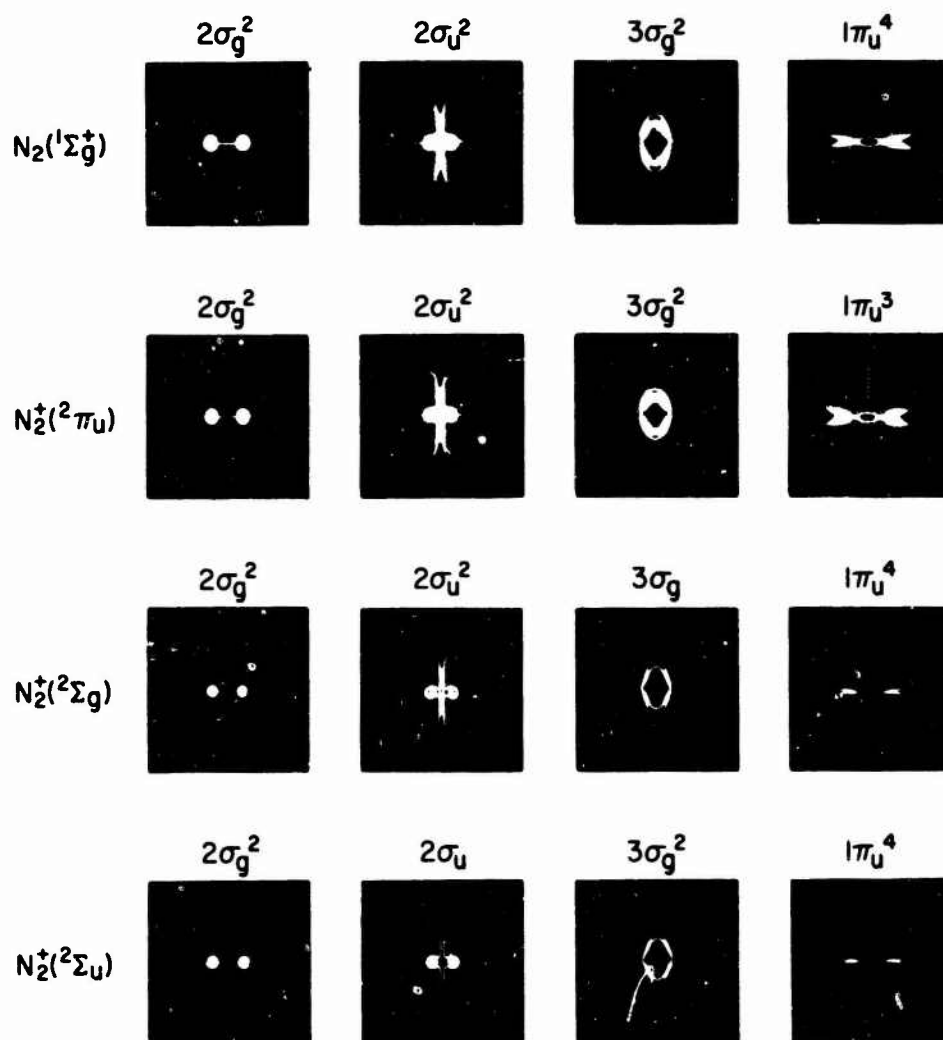
Fig. 3a. In the orbital picture of molecular ionization for the nitrogen molecule only valence orbitals have been plotted. Note that it is primarily the orbital from which an electron has been removed which changes. For conventions see ANL-7076 by A. C. Wahl (1965), also Science 151, 961 (1966), and for a discussion of alkali halide densities see A. C. Wahl, F. Janiszewski, and M. T. Wahl (to be submitted to Science). For wavefunctions see P. E. Cade, K. S. Sales, and A. C. Wahl, J. Chem. Phys. 44, 1973 (1966).
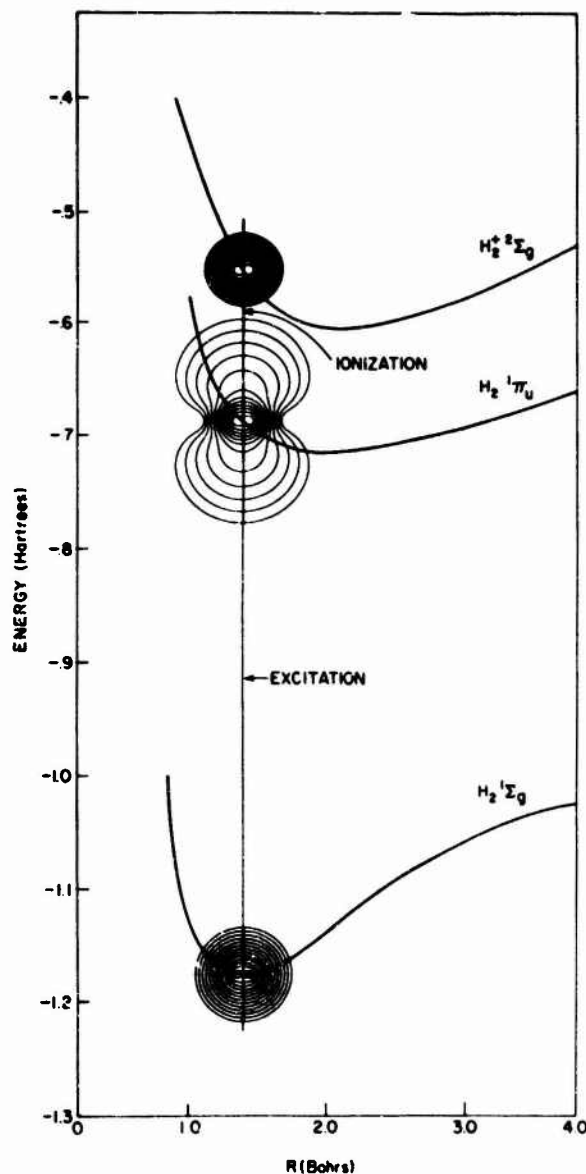
Fig. 3b. The diagrams represent the two fundamental processes in chemistry: excitation and ionization. The diagram representing the excited and ionized states are contour plots of the total electron densities of the three systems; H_2 in its ground state; H_2 in an excited pi state; and H_2^+ in its ground state. In all three diagrams the outermost contour has a value of 6.1 x 10^{-5} electrons/bohr^3 and each successive inner contour increases in value by a factor of 2. Note the disappearance of the inner contour value of .25 in H_2 after it has undergone excitation or ionization. These diagrams were drawn automatically by electronic computers and are based on accurate ab initio calculations of the wavefunctions for the H_2 system. [A Double Config-uration Self-consistent Field Study of the $^1\pi_u$, $^3\pi_u$, $^1\pi_g$, and $^3\pi_g$ States of H_2 by W. Zemke, P. Lykos, and A. C. Wahl (to be submitted to J. Chem. Phys., and Ph.D. Thesis by W. Zemke, I.I.T.); and BISON: A New Instrument for the Experimentalist by A. C. Wahl, P. J. Bertoncini, K. Kaiser, and R. H. Land, Int. J. Quantum Chem., Sanibel Symp. Issue (1969).]

269

TABLE 1. Progress from minimal LCAO–MO–SCF wave functions (1960) to recent extended basis set SCF wave functions (1960–1967) for Li₂, N₂, F₂, CO, BF, LiF, HF, and LiH.

Molecule	Total energy (Hartrees)			Dissociation energy (eV)			Ionization potential (Koopman's) (eV)		
	Minimal[a] STO set	Extended STO set	Experimental	Minimal[a] STO set	Extended STO set	Experimental	Minimal[a] STO set	Extended STO set	Experimental
LiH	−7.9667	−7.9866[a]	−8.0703	1.59	1.44	2.52	8.24	8.54[k]	6.5 ± 0.5
Li₂	−14.84075	−14.8715[c]	−14.9944	0.15	0.17	1.05	4.86	4.93	4.96
N₂	−108.57362	−108.9928[d]	−109.586	1.19	5.31	9.90	14.82	17.36	15.77
F₂	−197.83686	−198.7683[c]	−199.670	−0.30	−1.37	1.68	11.75	18.04	15.7
HF	−99.4785	−100.0571[f]	−100.527	1.21	4.11[l]	6.08	12.63	18.16[l]	15.77
LiF	−106.3652	−106.9885[e]	−107.502	0.37	4.03	5.99	9.26	13.02	14.01
CO	−112.34357	−112.7860[d]	−113.377	5.38	7.84	11.24	13.08	14.978	10.969
BF	−123.61550	−124.1659[i]	−124.777	5.24	6.18	8.58	9.61	10.999	

Dipole moments

	Minimal[a] STO set	Extended STO set	Experimental
CO	0.730 C⁻O⁺	0.274[h] C⁻O⁺	0.118 C⁻O⁺
BF	2.16 B⁻F⁺	0.945[i] B⁻F⁺	—
LiF	2.94 Li⁺F⁻	6.297[i] Li⁺F⁻	6.284 Li⁺F⁻

Dipole moments

	Minimal[a] STO set	Extended STO set	Experimental
HF	0.878 H⁺F⁻	1.827 H⁺F⁻	1.818 H⁺F⁻
LiH	6.41 Li⁺H⁻	5.888[g] Li⁺H⁻	5.882 Li⁺H⁻

a. B J Ransil. Rev. Mod. Phys. 32, 245 (1960).
b. Reference 36. Slightly improved values have been recently obtained (45).
c. The first row homonuclear diatomics. F₂ and N₂ have been published (40, 42) others will appear shortly.
d. Reference 42.
e. References 40 and 103.
f. Reference 35. Slightly improved values have been recently obtained (45).
g. Reference 37.
h. Reference 41.
i. Reference 41.
j. Better values of ionization potentials can sometimes be obtained by direct computation:
$$IP = E_{ion}^{scf} - E_{neutral}^{scf}.$$ (reference 42)
k. Reference 45.
l. Reference 34.

TABLE 2 Some typical calculated (extended basis set; scf–mo and experimental values of R_e, ω_e, and D_e for diatomic molecules.

Molecule	R_e (Bohrs)		ω_e (cm⁻¹)		D_e (eV)		
	Calculated	Experimental	Calculated	Experimental	Calculated	Experimental	δD_e
$H_2(X^1\Sigma_g^+)$[a]	1.385	1.400	4561	4400	3.64	4.75	1.11
$Li_2(X^1\Sigma_g^+)$[b]	5.25	5.051	326	351	0.17	1.05	0.88
$N_2(X^1\Sigma_g^+)$[c]	2.041	2.113	2571	2207	3.24	8.85	5.61
$N_2(X, C_2)$[d]	2.013	2.075	2750	2358	5.27	9.91	4.64
$F_2(X^1\Sigma_g^+)$[e]	2.51	2.725	1257	892	-1.63	1.65	3.28
$LiF(X^1\Sigma^+)$[f]	2.941	2.955	1033	964	4.08	5.95	1.87
$BF(X^1\Sigma^+)$[g]	2.355	2.391	1496	1402	6.18	8.58	2.40
$CO(X^1\Sigma^+)$[y]	2.08	2.132	2431	2170	7.84	11.23	3.39
$Cl_2(X^1\Sigma_g^+)$[g]	3.78	3.76	577	559	0.87	2.51	1.64
$BeO(A^1\pi)$[a]	2.74	2.76	1208	1144	4.93	—	—
$He_2(X^1\Sigma_g^+)$[f]	2.0	—	1790	—	2.7	—	—
$F_2(X^1\Sigma_g^+)$[f]	3.6	—	510	—	1.56	—	—
$Ne_2(X^1\Sigma_g^+)$[f]	3.2	—	660	—	1.55	—	—
$Cl_2(X^1\Sigma_g^+)$[f]	5.0	—	260	—	1.28	—	—
$Ar_2(X^1\Sigma_g^+)$[f]	4.6	—	300	—	1.25	—	—
$NaH(X^1\Sigma^+)$[b]	3.62	3.57	1187	1172	0.932	(2.3)	1.4
$SiH(X^2\Pi_r)$[b]	2.86	2.87	2144	2042	2.23	3.32 ± 0.25	1.1 ± 0.25
$HCl(X^1\Sigma^+)$[g]	2.39	2.41	3181	2989	3.48	4.616	1.14
$NaF(X^1\Sigma^+)$[l]	3.65	3.64	590	536	3.08	4.49	1.41

a. *Reference 103.*
b. *Reference 51.*
c. *Reference 42.*
d. *Reference 40.*
e. *Calculated from results in 50.*
f. *Reference 41.*
g. *Reference 49.*
h. *Reference 44.*
i. *Reference 48.*
j. *Reference 49.*
k. *Reference 46.*
l. *Reference 52.*

271

ion[42] (Figure 7) that there is an inversion of molecular energy
levels, that does not allow us to interpret spectroscopy. Now,
the reasons for these defects are well known. The orbital
picture has an inherent error built into it, the correlation
error. The orbital picture does not allow electrons to get out
of each other's way explicitly and instantaneously. It happens
that this error for the atoms is not the same as the error for
the molecule built from these atoms. Therefore, binding
energies are not good, and further, the error differs for
different states of the same system. Thus, term values are
not accurate.

Secondly, a simple molecular orbital picture, although
relatively good at the equilibrium configuration of most
molecules, deteriorates rapidly as you try to pull the molecule
apart. Thus, the shape of the potential curve is distorted by
the constrained form of the molecular orbital picture. These
two defects of the Hartree-Fock model account for its most
serious shortcomings; namely, improperly shaped energy surfaces.
bad binding energies, and badly computed term values for
transitions between electronic states.

There are notable cases where the Hartree-Fock model does
provide some chemistry, but certainly not a "chemist's"
chemistry. For instance, in Figures 4, 5 and 6 the potential
curves obtained from Hartree-Fock calculations[47] on the rare
gases He, Ne, Ar are plotted. Here, we are obtaining from our
calculations a precision just about as high as currently is
available from experiment. This is due to the fact that the
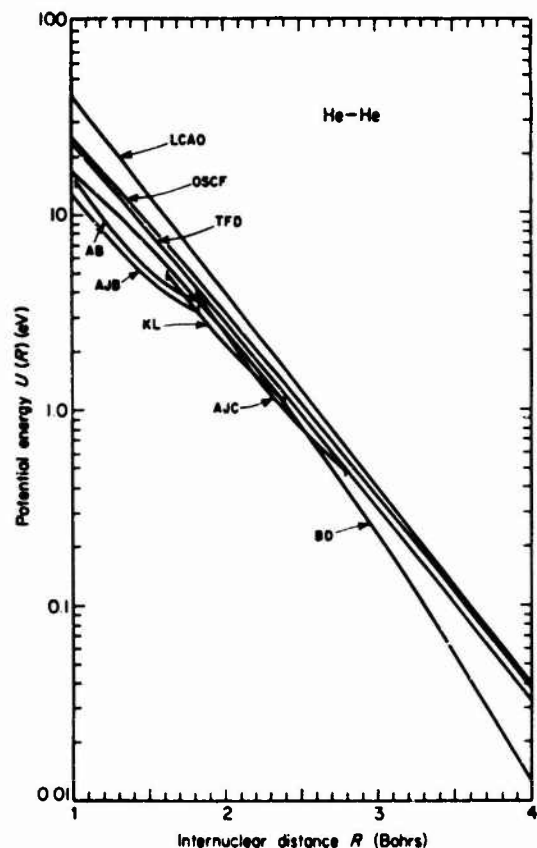
Fig. 4. He-He potential curves. AJC--semiempirical curve from
scattering data; I. Amdur, J. D. Jordan, and S. O. Colgate, J. Chem.
Phys. 34, 1525 (1961). AB--semiempirical curve from scattering data;
I. Amdur and R. P. Bertrand, J. Chem. Phys. 36, 1078 (1962). BD--
semiempirical curve from composite data; R. A. Buckingham and
D. M. Duparc, Progress in International Research on Thermodynamic
and Transport Properties (Symposium on Thermophysical Properties,
Princeton University, 1962; American Society of Mechanical Engi-
neers, Academic Press, New York, 1962), p. 378. TFD--Thomas-
Fermi-Dirac method; A. A. Abrahamson, Phys. Rev. 130, 693 (1963).
AJB--semiempirical curve from scattering data; I. Amdur, J. E. Jordan,
and R. R. Bertrand, Atomic Collision Processes (Ed. M. R. C. McDowell,
Proceedings of the Third International Conference on the Physics of
Electronic and Atomic Collisions, London, 1963; North-Holland,
Amsterdam, 1964), p. 934. KL--semiempirical curve from scattering
data; A. B. Kamnev and V. B. Leonas, Soviet Physics--Doklady 10,
529 (1965). LCAO--linear-combination-of-atomic-orbitals method;
T. L. Gilbert and A. C. Wahl, J. Chem. Phys. 47, 3425 (1967). OSCF--
optimized self-consistent-field (Hartree-Fock) method; loc. cit.

273
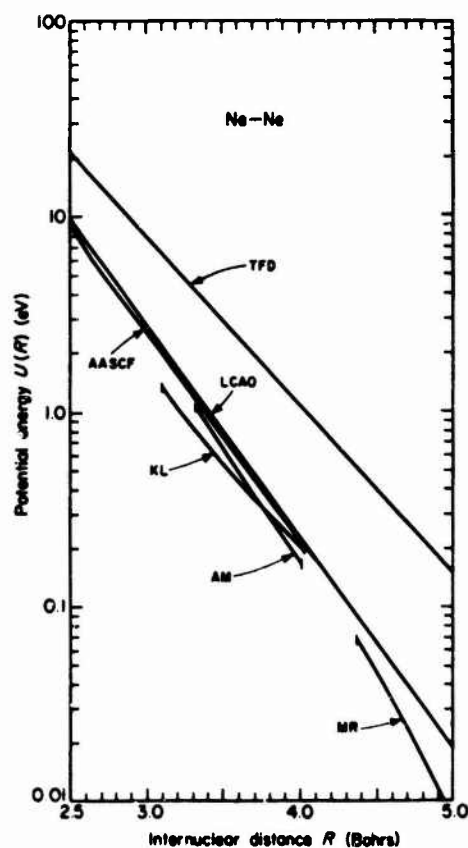
Fig. 5. Ne-Ne Potential curves. MR--semiempirical curve from scattering data; E. A. Mason and W. R. Rice, J. Chem. Phys. 22, 843 (1954). AM--semiempirical curve from scattering data; I. Amdur and E. A. Mason, J. Chem. Phys. 23, 415 (1955). TFD--Thomas-Fermi-Dirac method; A. A. Abrahamson, Phys. Rev. 130, 693 (1963). KL--semiempirical curve from scattering data; A. B. Kamnev and V. B. Leonas, Soviet Phys.--Doklady 10, 529 (1965). LCAO--linear-combination-of-atomic-orbital method; T. L. Gilbert and A. C. Wahl, J. Chem. Phys. 47, 3425 (1967). AASCF--augmented asymptotic self-consistent-field method; loc. cit.
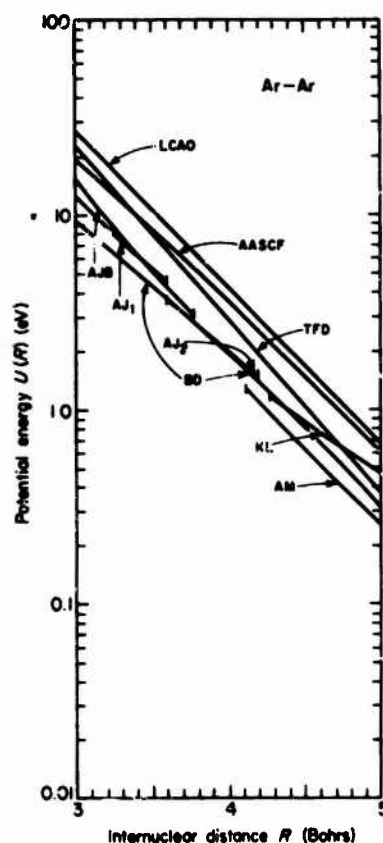
Fig. 6. Ar-Ar potential curves. LCAO--linear-combination-of-atomic-orbitals method; T. L. Gilbert and A. C. Wahl, J. Chem. Phys. 47, 3425 (1967). AASCF--augmented asymptotic self-consistent-field method; loc. cit. TFD--Thomas-Fermi-Dirac method; A. A. Abrahamson, Phys. Rev. 130, 693 (1963). BF--semiempirical curve from composite data; J. A. Barker and A. Pompe, to be published. AJP--semiempirical curve from scattering data; I. Amdur, J. E. Jordan, and R. R. Bertrand, Atomic Collision Processes (Ed. M. R. C. McDowell, Proceedings of the Third International Conference on the Physics of Electronic and Atomic Collisions, London, 1963; North-Holland, Amsterdam, 1964), p. 934. AJ_1 and AJ_2--semiempirical curves from scattering data; I. Amdur and J. E. Jordan, quoted in D. D. Konowalow and S. Carra, "Morse Potential Functions for Nonpolar Gases," Report WIS-TC1-74 from the Theoretical Chemistry Institute of The University of Wisconsin, Dec. 1964. KL--semiempirical curve from scattering data; A. S. Kaminev and V. B. Leonas, Soviet Phys.--Doklady 10, 529 (1965). AM--semiempirical curve from scattering data; I. Amdur and E. A. Mason, J. Chem. Phys. 22, 670 (1954).

correlation error for these closed-shell systems remains relatively constant as the atoms are forced together. There are no new electron pairs formed and, thus, no new strong electron correlations associated with molecular formation.

BEYOND THE MOLECULAR ORBITAL MODEL[65-136]

The Hartree-Fock model is good for predicting geometry and many one-electron properties (this is also true for similar calculations on polyatomic systems). The Hartree-Fock model also yields adequate results for a variety of molecular systems; namely, those arising from closed-shell interactions, for instance the noble gases.[47] Systems in which there is only a one-electron bond are typified by He_2+,[48,49] Li-He, NaHe,[64] NeH+, HeH+[56] (some rather bizarre systems from the chemist's viewpoint), and highly ionic systems for which the shape of the potential curve is rather good are typified by the alkali halides[50,52] which are, in fact, analogous to the rare gas systems held together by a coulomb force.

How can we improve this model without losing its valuable features? I would like to describe what we have been doing to go beyond the Hartree-Fock model with the goal in mind of obtaining results on diatomic and, eventually, larger systems. A condition is that these results be of genuine quantitative use to the experimental chemist and serve to complement his efforts, particularly where the experiment is difficult to perform. Such situations might involve high temperatures, highly corrosive materials or very short-lived transients. The essence of our scheme,[6,103-106] which I am now going to describe, involves
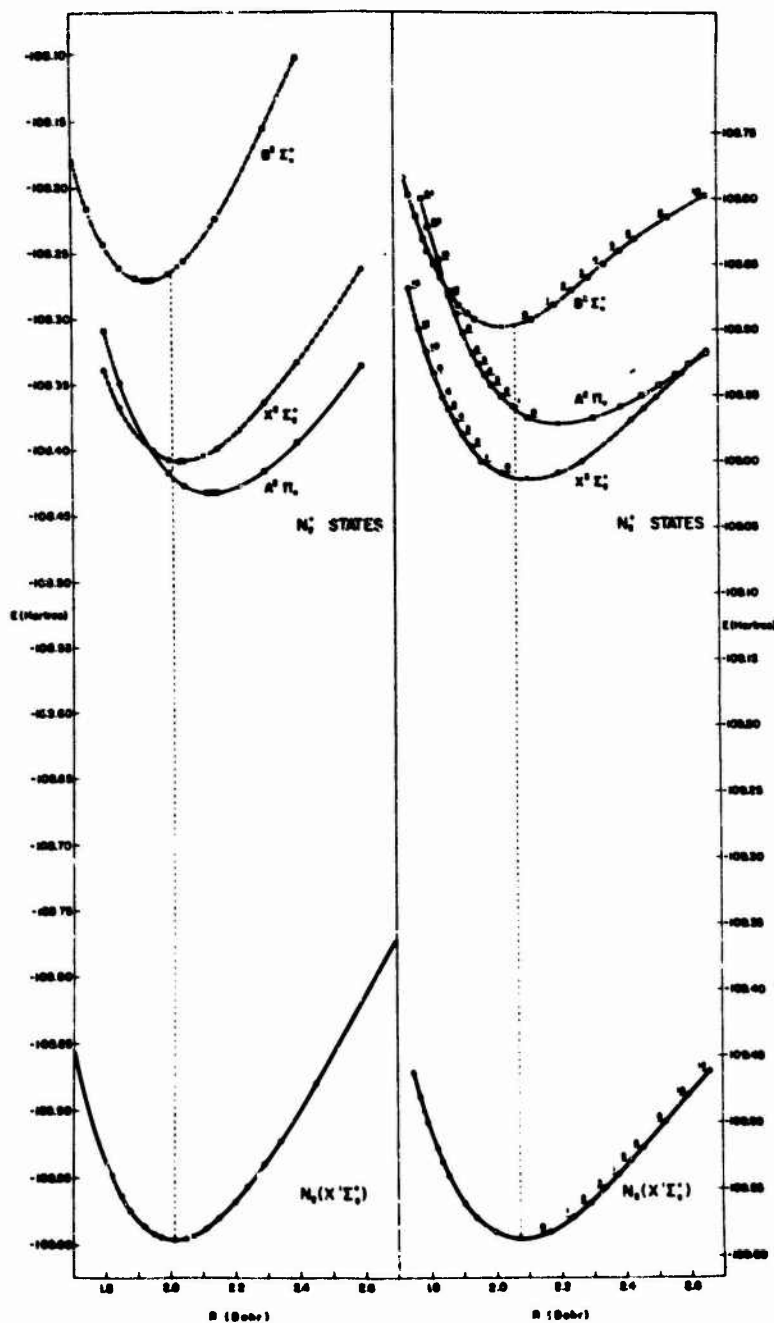
Fig. 7. At the left are shown theoretical potentials for the nitrogen molecule and its ions; at the right, experimental curves. Note the inversion of the $^2\Sigma_g^+$ and $^2\pi_u$ state--a defect of the orbital picture. See P. E. Cade, K. S. Sales, and A. C. Wahl, J. Chem. Phys. <u>44</u>, 1973 (1966). See Fig. 3a for the changes taking place in the orbital picture of these ionizations.

277

a direct pursuit of the two major defects of the Hartree-
Fock model. (1) The molecule is allowed to dissociate
properly (in many cases, this is a trivial extension of the
Hartree-Fock picture), and (2) the correlation error in the
molecule is made the same as the correlation error in the
atoms. The latter is more difficult to achieve - especially
in the general case. However, for systems in which the
chemical bond is isolated by being one quantum number higher
than the rest of the molecular core, the correlation energy
changes associated with molecular formation are isolated by
being placed in this bonding region and we can do a rather good
job of making the correlation error constant, as a function
of inter-nuclear distance.

We see some typical results for the systems H_2, Li_2, and
NaF in Figures 8, 9, and 10. We see in Figures 8b and 9b the
orbitals necessary, in addition to the Hartree-Fock model, for
the bonding electrons to avoid each other as the molecule forms,
and to give us a correct continuous picture of chemical bonding
(Figures 8c and 9c). These correlation terms may be conven-
iently categorized as in-out, left-right, and angular. When
added or subtracted to the ground state molecular orbital they
move the electrons away from each other in an in-out, left-right,
or angular sense. For systems such as H_2 in which there is a
single bond - no other electrons, and Li_2 in which the bond is
quantum level two and the core in quantum level one, the
quantitative results are truly gratifying and, in fact, are of
sufficient quality to be useful to the experimentalist. For
F_2, we have obtained significantly better results than those
obtainable from the Hartree-Fock model, but still have not

CORRELATION

HYDROGEN MOLECULE FORMATION CONTOURS FOR EHF WAVE FUNCTIONS
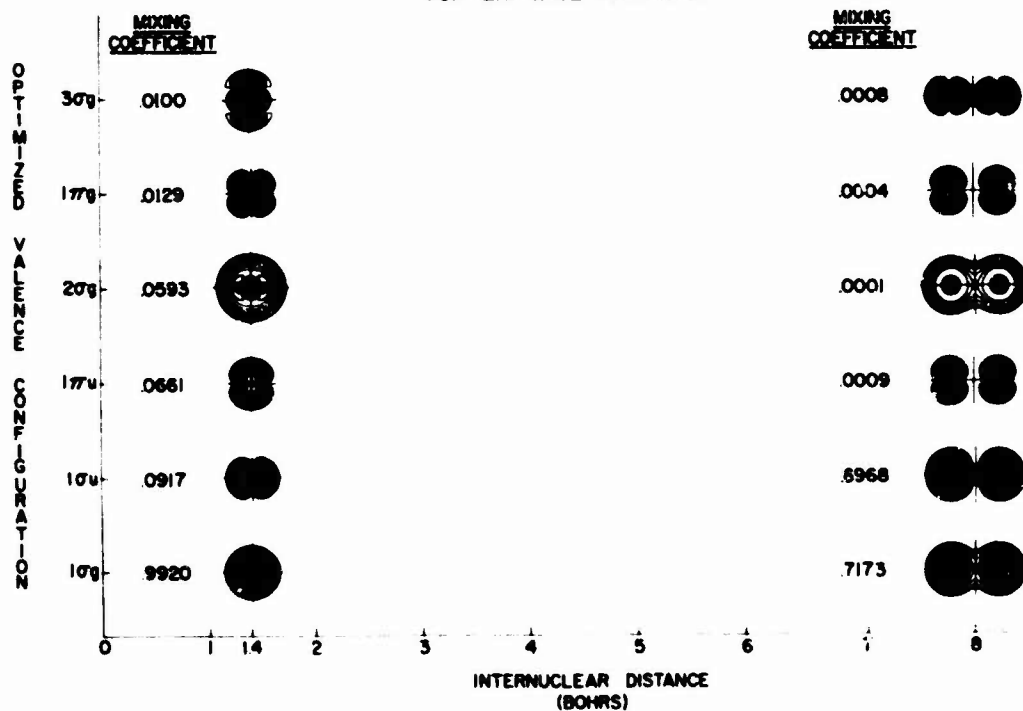
Fig. 8b. The orbitals making up the H_2 OVC wavefunction at R_e and near dissociation.

In Figs. 8b, 8c, 9b, 9c, the outermost contour in all cases corresponds to a density of 6.1×10^{-5} e⁻/bohr³. Each succes-sive inner contour then increases by a factor of 2.

FORMATION

EXTENDED HARTREE-FOCK WAVE FUNCTIONS H$_2$
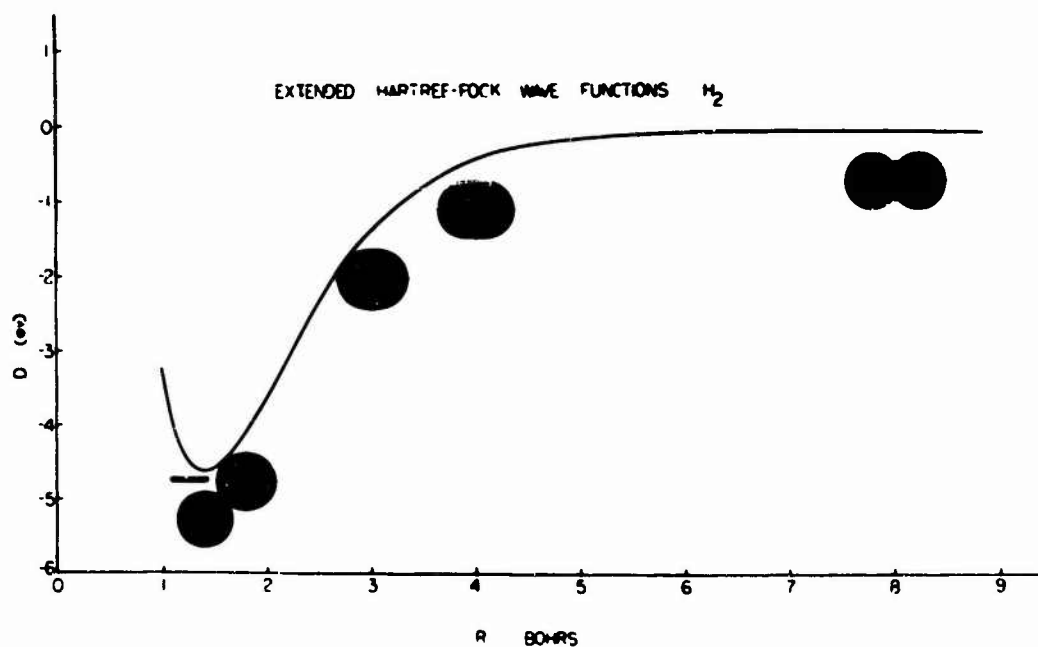
Fig. 8c. Total charge-density contours of the H$_2$ OVC wavefunction as the molecule forms. [G. Das and A. C. Wahl, J. Chem. Phys. 44, 87 (1966) and ibid., 47, 2934 (1967).] The horizontal line is the level of the H$_2$ experimental energy.

COMPARISON OF THEORY WITH EXPERIMENT
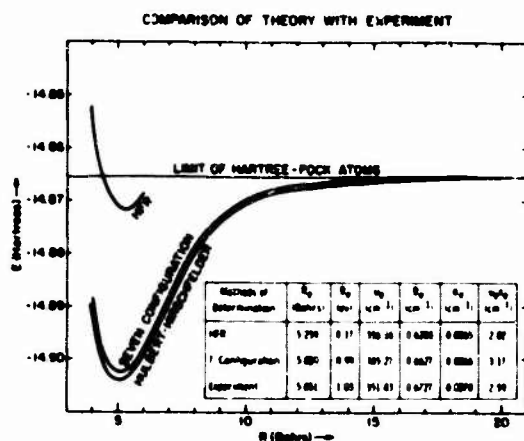
Fig. 9a

Comparison of Hartree-Fock and optimal valence configuration potential curves with experimental one for Li$_2$. [G. Das and A. C. Wahl, J. Chem. Phys. 44, 87 (1966).]

280

LITHIUM MOLECULE FORMATION CONTOURS
FOR EHF WAVE FUNCTIONS

OPTIMIZED VALENCE CONFIGURATION		MIXING COEFFICIENT	MIXING COEFFICIENT
4σg		.0106	.0055
1πg		.0049	.0049
3σg		.1237	.0896
1πu		.2491	.1553
2σu		.1157	.3477
2σg		.9535	.9203
1σu			
1σg			

INTERNUCLEAR DISTANCE
(BOHRS)

4.0   5.0   6.0   7.0   8.0
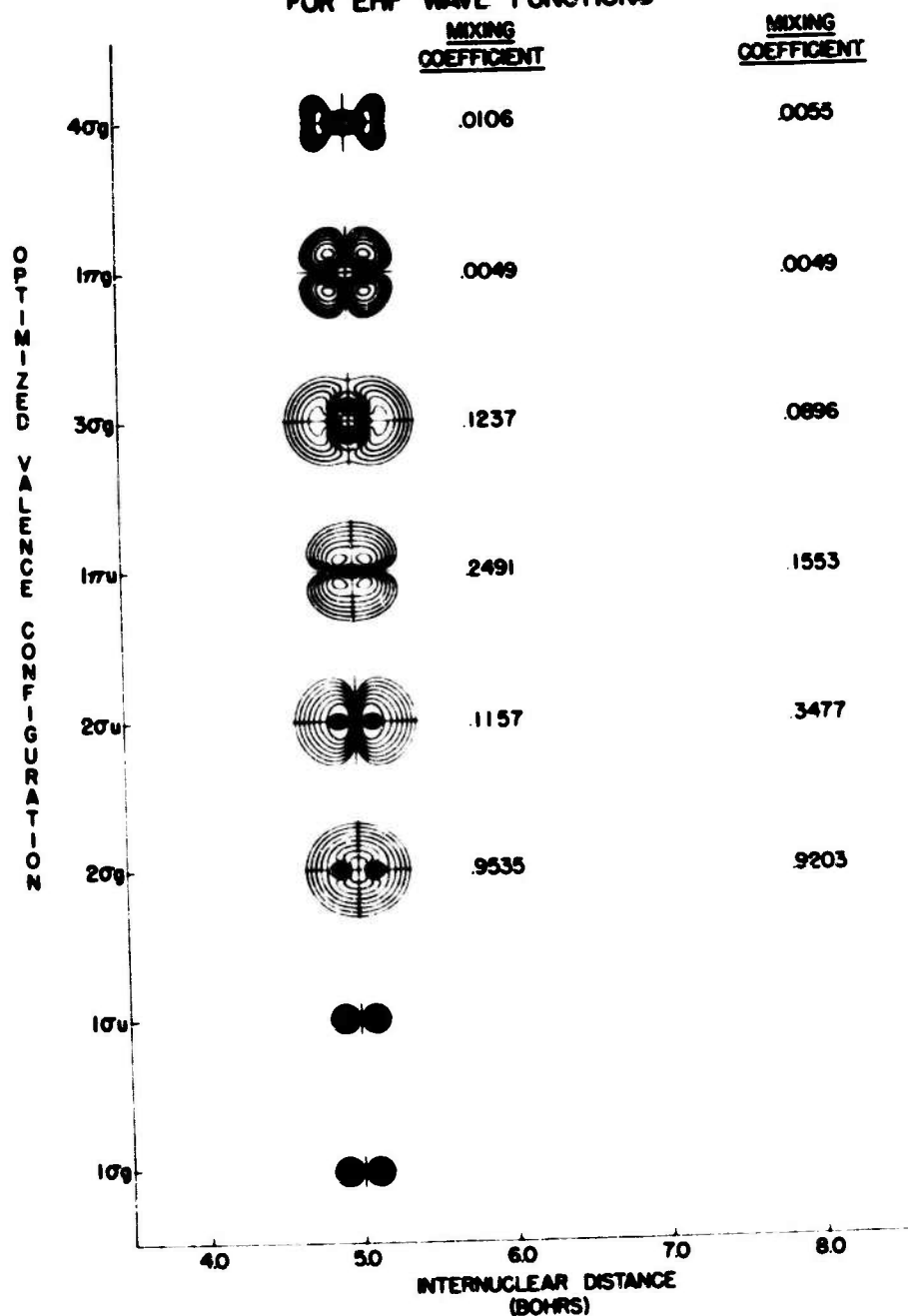
Fig. 9b. The orbitals making up the Li$_2$ OVC wavefunction at R$_e$. [G. Das and A. C. Wahl, J. Chem. Phys. 44, 87 (1966) and ibid., 47, 2934 (1967).]

EXTENDED HARTREE-FOCK WAVE FUNCTIONS L$_2$
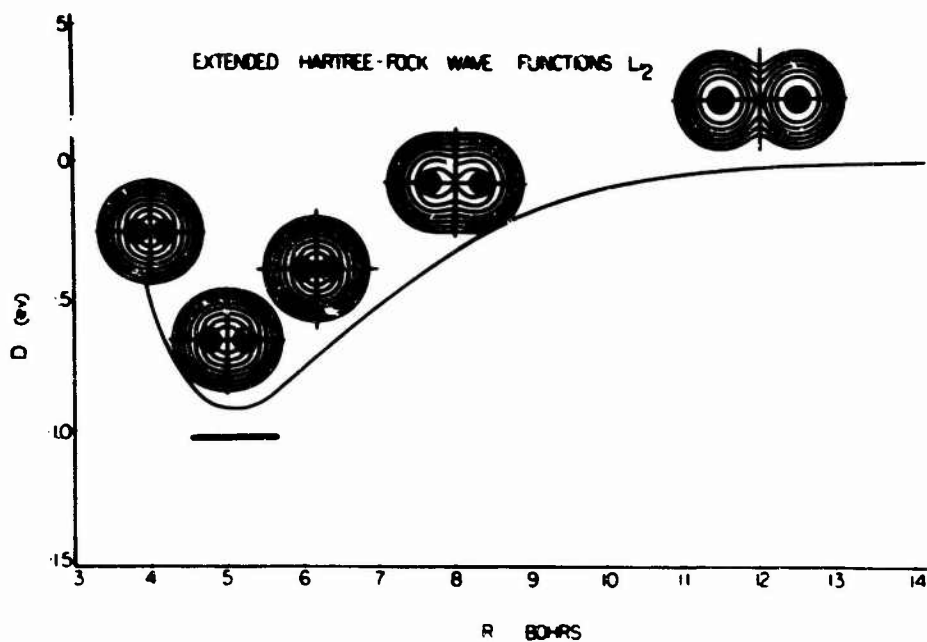
Fig. 9c. Total charge density contours of the Li$_2$ OVC wavefunction as the molecule forms. The horizontal line is the level of the Li$_2$ experimental binding energy. [G. Das and A. C. Wahl, J. Chem. Phys. 44, 87 (1966) and ibid., 47, 2934 (1967).]
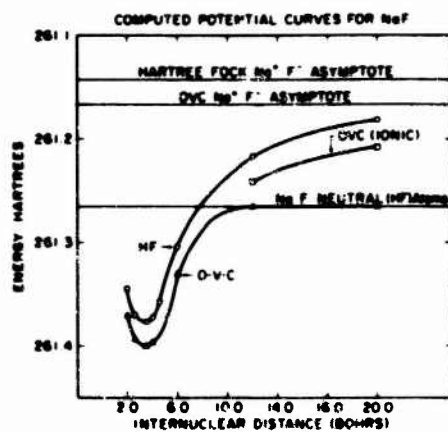
Fig. 10. Comparison of Hartree-Fock and optimized valence configuration potential curves for NaF. [A. C. Wahl, P. J. Bertoncini, G. Das, and T. L. Gilbert, Intern. J. Quantum Chem., Symp. No. 1, 123 (1967).]

done well enough to really aid the experimentalist (Table 3 and Figure 11). The reason for this is that F_2 conventionally is considered to be a single-bonded molecule. However, the two electrons forming the bond are in the same radial quantum shell and, thus, occupy the same physical space as twelve other electrons. Therefore, there are subtle intershell correlation effects, which must be taken into account.

Let me now review the essential ideas of the Optimized Valence Configuration (OVC) method, and then describe its recent application to an experimentally uncharacterized system.

Configurations were added to the Hartree-Fock picture to allow proper dissociation of the molecule. (In H_2 this is merely one extra configuration which subtracts the ionic terms as the atoms separate. Inclusion of such a configuration allows us to "look" continuously at molecular formation. We could not do this with the simple model of the molecular orbitals.) Additional configurations allowed the bonding electrons to avoid each other as the molecule formed; since they were of course, avoiding each other completely when the constituent atoms were at infinite distance. Included were angular and in-out terms in addition to the left-right term which brought about proper dissociation.

The optimized valence configuration wave function thus has the form

$$\psi = A_o \psi_o + \Sigma_k A_k \psi_k$$

where the ψ_k are antisymmetrized products of orbitals ϕ_i similar to equation (1). However, the ϕ_i are now in the general solution

283

Table 3

	ω_e (cm^{-1})	R_e (Bohrs)	D_e (eV)
	H$_2$		
hf[a]	4561	1.99	3.64
odc[b]	4214	1.42	4.13
ovc[c]	4398	1.40	4.63
Experimental	4400	1.40	4.75
	Li$_2$		
hf[d,e]	326	5.26	0.17
odc[b]	344	5.43	0.46
ovc[c]	345	5.09	0.93
ovc[d]	345	5.09	0.99
Experimental	351	5.05	1.05
	NaLi		
hf[d]	264	5.56	0.05
ovc[c]	256	5.48	0.85
Experimental	—	—	—
	F$_2$		
hf[a,f]	1257	2.50	−1.37
odc[b]	678	2.74	0.54
ovc (3σ_g only)[g]	704	2.72	0.81
ovc (All promotions into 3σ_u)[g]	N.C.	2.70	0.95
Experimental	892	2.68	1.68
	NaF		
hf[h]	570	3.65	3.00
ovc[g]	570	3.66	3.70
Experimental[i]	536	3.64	4.94

[a] See [103].
[b] See [104].
[c] See [91].
[d] See [91].
[e] See [138].
[f] See [90].
[g] See [137]. (6)
[h] See [92]. (6)
[i] See [52]. (6)
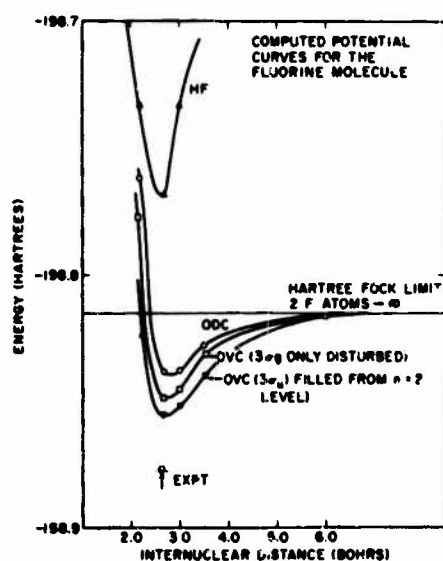
Fig. 11. Comparison of Hartree-Fock ODC and OVC potential curves for F$_2$. [G. Das and A. C. Wahl, J. Chem. Phys. **44**, 87 (1965).]

of individual integro differential equations of the form[103, 104, 105, 106-121]

$$F_1 \phi_1 = \epsilon_1 \phi_1$$

where the F_1 are more complicated operators depending upon all orbitals of the system and all mixing coefficients A_k. Convergence to best orbitals is achieved in this model when the energy of the system is stationary with respect to variation of both the coefficients A_k and the orbitals ϕ_1. We have seen some of these necessary additional orbitals in Figures 8c and 9c. Thus, we evaluate only the increase in correlation energy associated with molecular formation, and we, in addition, allow the core to distort and polarize, but we do not try to correlate the core. We assume that the correlation error in the core is constant. This assumption is supported by calculations on the rare gas systems, (Figures 4-6) and also by our calculations on Li_2 (Table 3). We now feel that we understand this model very well and, as we have stated earlier, for the type of bond which is isolated we can do a very good job in obtaining the proper molecular energy surface. For an ionic bond, the ionic system was handled quite well with the Hartree-Fock approximation and we needed only one additional configuration to allow for proper dissociation. Because of intershell effects, we still are not able to calculate binding energy. However, techniques now being developed are expected to provide the necessary improvement. (See NaF results in Table 3 and Figure 10.)

For F_2, we see that our results are not yet satisfactory; (Table 3, Figure 11) again, because of intershell effects. The correlations between $p\sigma$ and $p\pi$ electrons and between s and p

285

electrons are not taken into account in our method (at this writing).

However, bolstered by our confidence that we can do very well on the alkali-type systems, we decided to try to do a predictive calculation concerning a system of which little is known experimentally. Applying our method, we obtained the results[138] for Na-Li presented in Table 3 and Figures 12 and 13. A binding energy of about .85 eV (quite substantial) and the calculated vibrational frequency, etc. are predicted. We feel we can attach a precision to these results of a few percent and we are hoping that these results will be used by the experimentalist in the near future to guide him in further characterizing this system.

A NEW "INSTRUMENT" FOR CHEMISTS

The next question is, since we now have some ab initio results on the energy surface of the simple but experimentally uncharacterized system, NaLi, what can be done with such results to enhance their chemical utility? As one example of such an application we can turn to thermodynamics. We know that we could describe a vapor mixture of Na and Li thermodynamically if we could obtain its equation of state[139].

We must therefore evaluate the virial coefficients. In the case of NaLi we are fortunate because, as indicated by calculated equilibrium constants for a NaLi mixture (Tables 4 and 5), at the temperatures and pressure of interest, we may assume that the system consists overwhelmingly of isolated atoms. Therefore, we may calculate only the second virial coefficient, assuming the
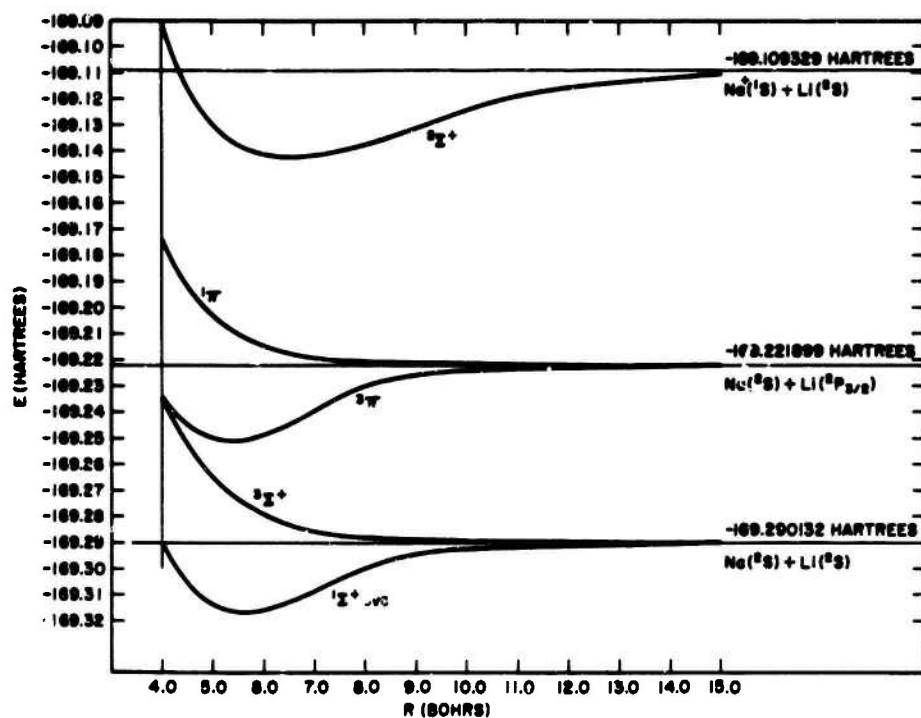
Fig. 12a. Calculated potential curves for NaLi. [A Theoretical Study of the NaI System by P. Bertoncini, G. Das, and A. C. Wahl, ANL-7447 (1969); also submitted to J. Chem. Phys.]

FORMATION
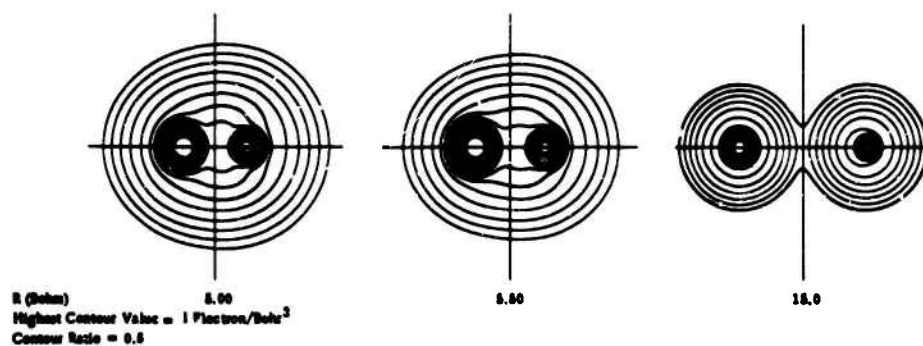
Fig. 12b. OVC $^1\Sigma$ and Hartree-Fock total charge density contours for the $^1\Sigma^+$ state of NaLi at 15 bohr, 5.5 bohr, 5.0 bohr. Picture at 15 bohr is 2/3 the scale of other 2 pictures. (Ibid.)

CHEMICAL BOND

R (Bohrs)   5.00   5.50
Largest Contour Value Plotted = 0.1 Electron/Bohr^3
Contour Ratio = 0.5

R (Bohrs)   5.00   5.50
Largest Contour Value Plotted = 0.1 Electron/Bohr^3
Contour Ratio = 0.5
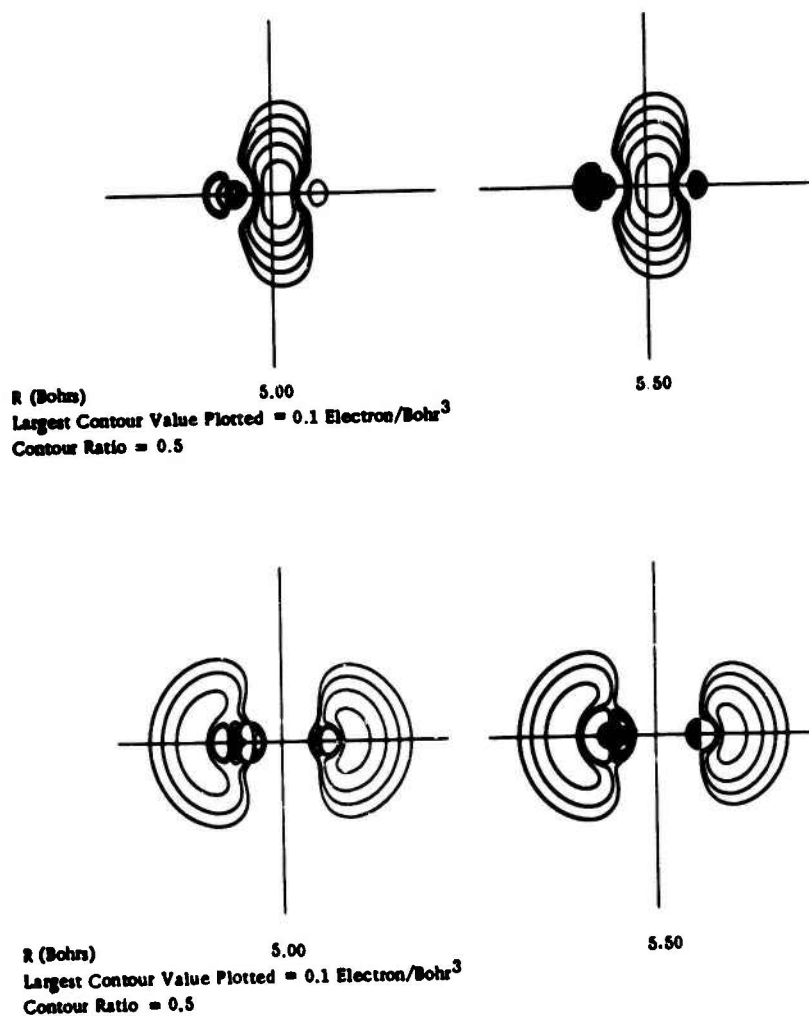
Fig. 13. Contours of charge density difference associated with the formation of the chemical bond in the $^1\Sigma$ state of NaLi. Upper diagram shows the region where charge has increased relative to dissociated atoms. Lower diagram shows where charge density has decreased relative to dissociated atoms. [A Theoretical Study of the NaI System by P. Bertoncini, G. Das, and A. C. Wahl, ANL-7447 (1969); also submitted to J. Chem. Phys.]

Table 4

	Na_2^{23}	Li_2^7	$Na^{23}Li^7$
r_e (Å)	3.078 (In Prog.)	2.673 (2.691)	Not Avail. (2.939)
ω_e (cm^{-1})	159.2 (In Prog.)	351.4 (345.3)	Not Avail. (249.9)
D_e (eV)	0.75 (In Prog.)	1.03 (0.99)	Not Avail. (9.85)

Upper number is experimental one.

Table 5

T (°K)	$K_p^{Na_2}$	K_p^{NaLi}	$K_p^{Li_2}$
1123	5.88016	1.27468	0.3504
1000	2.13976	0.4104	0.0850
973	1.65748	0.3083	0.0565
873	$5.63966 \cdot 10^{-1}$	0.0979	0.0139
773	$1.46223 \cdot 10^{-1}$	8.8202	0.0019
673	$2.56338 \cdot 10^{-1}$	0.0029	0.0002

289

concentrations to be the initial concentrations of the atoms.
The second virial coefficient B(T) in the virial equation of
state may be obtained for a Na-Li mixture from the relation

$$B(T) = B_{Na_2}(T)X_{Na}^2 + B_{Li_2}(T)X_{Li}^2 + B_{NaLi}(T)X_{Li}X_{Na}$$

where X_i represents the mole fraction of component i.

In order to calculate the three $B_{AB}(T)$ we of course
needed the AB interaction potential V_{AB} for both the $^1\Sigma$ ground
state and $^3\Sigma$ excited repulsive state arising from the three
types of collision of atoms in their ground state: NaLi, Li-Li,
Na-Na. It is here that the ab initio calculation plays an
important role. The $^1\Sigma$ potentials are available experimentally
for Li_2 or Na_2 and we used our calculated one for NaLi. A
variety of ways for evaluating $V_{AB}(R)$ for the $^3\Sigma$ state are used
consisting mostly of semiempirical forms or "scaled" or "reduced"
potentials; namely, Rydberg, Morse, Anti-Morse, power series.[140]
We have used our ab initio potentials (in which we have con-
siderable confidence) and compared them with various popular
semiempirical forms.
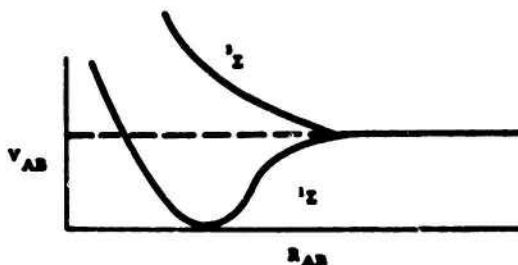
Through the relation:

$$B = \tfrac{1}{4}B^1 + \tfrac{3}{4} B^3$$

and

$$B^3_{AB} = 2\pi Na \int_0^\infty \left\{ 1 - \exp\left[-\frac{V^3(R)}{kt} \right] \right\} R^2 \, dR$$

we can obtain from these potentials the three required virial
coefficients.

Now, what have we done with all of these results? We have
predicted the existence of and computed molecular properties
for NaLi that were not available experimentally; we have gone
further and used our potential curves to calculate the second
virial coefficients and, thus, the degree of ideality of alkali
vapors (alkali systems are difficult systems to look at experi-
mentally and, in fact, Na-Li, as noted previously, has not been
observed), and are now calculating some transport properties for
the vapor mix. [141] We also have been able to criticize the
assumed form of the $^3\Sigma$ potential curves customarily used and are
suggesting a better form based on our calculations.

This study of the alkali vapor presents a good example
of how ab initio results can be dovetailed into traditional
chemistry.

By the further development of the techniques outlined
above to handle cross shell correlations and other types of
molecules, we feel that comparable energy surfaces can be
obtained for other diatomic molecules. In fact, this is currently
our main mission in addition to extending these methods to open-
shell excited state systems so that we may obtain accurate
theoretical term values.

291

It should be emphasized that there is no reason to believe that what we have learned in diatomic systems will be any simpler in polyatomic systems. In fact, it is important to develo diatomic theory and diatomic calculations to a point where they are of use to the experimentalist before jumping into complicated polyatomic systems using old methods with their well-known deficiencies. This is the compelling reason for refining our tools on diatomic molecules which, although perhaps of less immediate interest to the tradiational chemist, provide a much more economical medium for the evolution of new techniques.

We feel that the calculated results on the alkali dimers do represent an example of chemistry from computers. The isolated energy point or wave function did not represent chemistry, but a potential energy surface then used to predict binding energy, and ultimately transport properties must be considered genuine chemistry. More important, we are now thinking more comprehensively in terms of complete chemical processes, potential energy surfaces, ground and excited states, state functions, virial coefficients -- all of which for selected simple systems can now be obtained from computers and from computer calculations. It is more important now, therefore, than previously that theoreticians talk to experimental chemists because I think that many chemists do not know how far the field of computational chemistry has come. Likewise, theoreticians do not know how intimately new experimental techniques are probing molecules and how much interesting chemistry there is in the world of small molecules. It is also important that theoreticians and the experimentalists feed these ab initio numbers into existing semi-empirical theories, and that through this process the semiempirical

rules be upgraded by what might be called semi-ab-initio rules into which new relationships and concepts of molecular inter-actions obtained from accurate calculations are embodied. This is an important added bonus available from the calculations due to the "adiabatic" nature of the computing process. We can "freeze" our numeric model and "look" at any stage of a process. For example, we can now watch a molecule form or atoms collide in terms of their changing electronic charge density continuously being displayed on a cathode ray tube controlled by digital computers (Figure 5) during the chemical process numerically under way.[31] Figures 8, 9, 12-17.

In conclusion, we should say that the chemist is not going to be replaced by the computer -- at least, certainly not by the computer used in a purely theoretical manner. However, I think that times have changed in the sense that the chemist can obtain sophisticated, relevant, and accurate answers from computers, particularly where difficult experimental conditions are required, where the calculation is feasible but the experiment 's not.[142] (Computers don't burn up or melt when the temperature of your theoretical model is increased; computers do nct corrode if you perform a calculation on fluorine; and the time scale of your numeric experiment can be expanded or contracted at will.)

The new capabilities we have with electronic computers should be interwoven into the experimentalist's thinking and he really should consider the alternatives when he seeks a particular physic~. property of a simple system, "Should I measure it or should I compute it?" We shall find that the limits of error in the computation often are comparable to limits of error obtainable experimentally, and sometimes that the derivation is more tractable and economical.

FILM LOOP III
THE COVALENT BOND: FORMATION
OF THE HYDROGEN MOLECULE
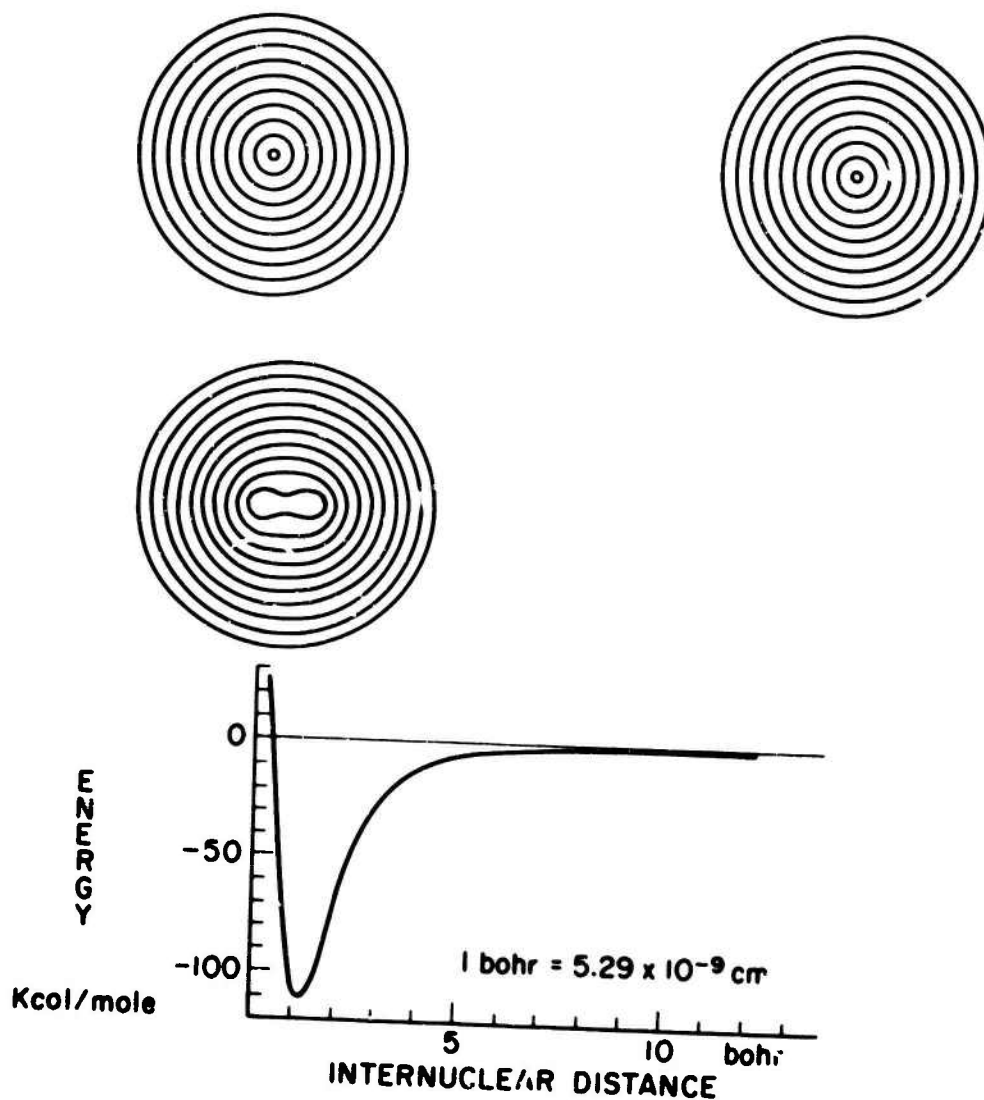
Fig. 14. Displays the beginning and end diagrams in the formation of the H_2 molecule. The innermost contour corresponds to a probable electron density of .25 e⁻/bohr³ and each successive outer contour decreased by a factor of 2 down to 4.9×10^{-4} e⁻/bohr³.

294

FILM LOOP IV
THE IONIC BOND: FORMATION
OF THE LiF MOLECULE
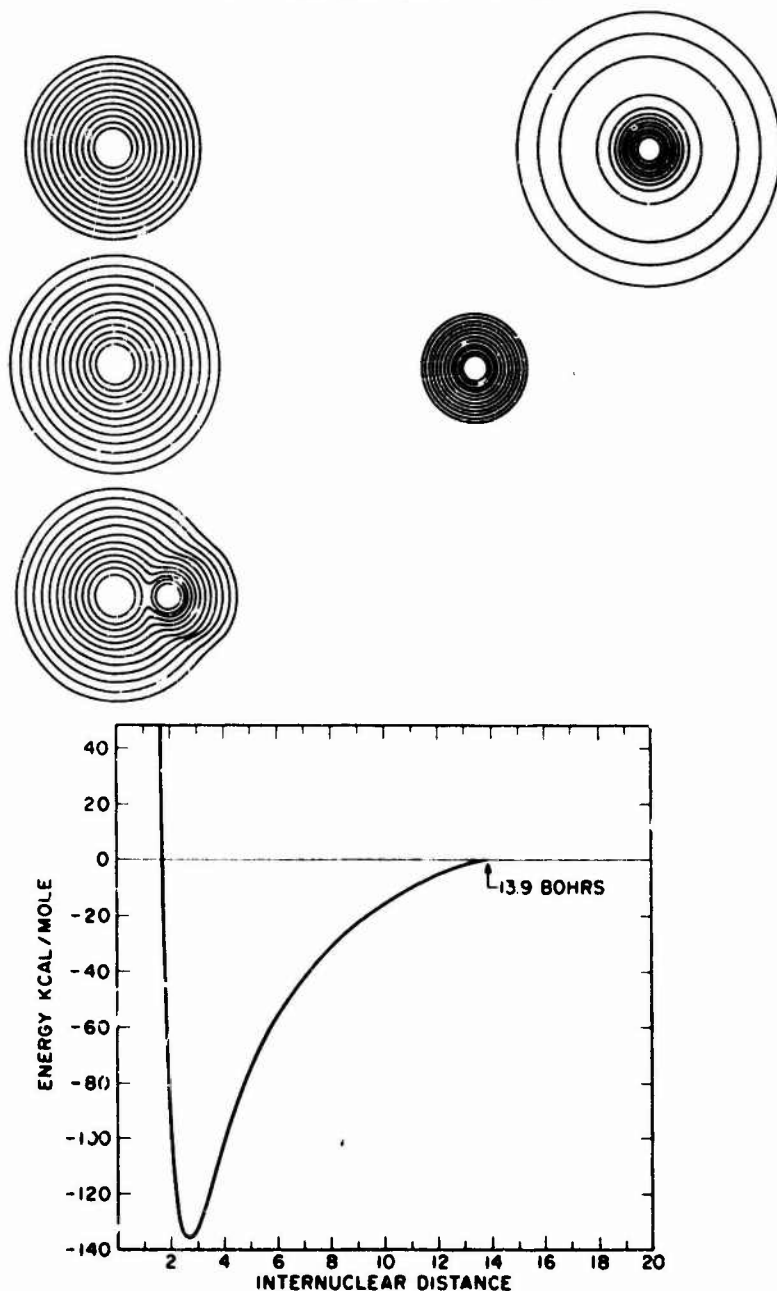
Fig. 15. Displays 3 sequences in the formation of the highly ionic system LiF from the Li and fluorine atoms. Note change from Li and F atoms to Li$^+$ and F$^-$ atoms at a distance of 13.9 bohrs where the ionic configuration becomes more stable. In all diagrams the innermost contour corresponds to a probable electron density of 1.0 e$^-$/bohr^3 and each successive outer contour decreases by a factor of 2 down to 4.9 x 10^{-4} e$^-$/bohr^3.

295

FILM LOOP Ⅴ
THE REPULSION BETWEEN NOBLE GASES:
HE-HE INTERACTION

1 bohr = 5.29 x 10^{-9} cm
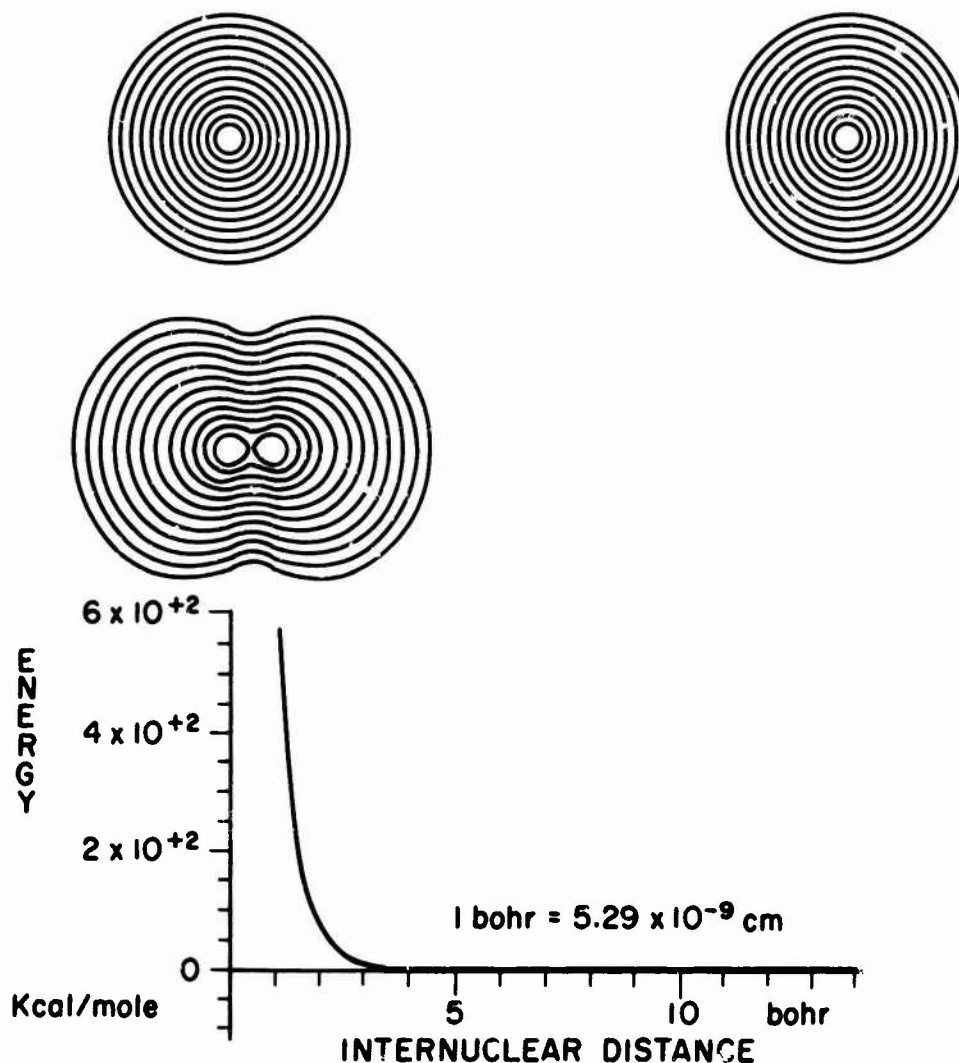
Fig. 16. Displays the beginning and end diagrams in the repulsive interaction of two helium atoms. As atoms move together note how the electron charge is squeezed from between the nuclei to the ends of the molecule. (A consequence of the Pauli Exclusion Principle.) In all diagrams the innermost contour corresponds to a probable electron density of 1.0 e^{-}/bohr^3 and each successive outer contour decreases by a factor of 2 down to 4.9 x 10^{-4} e^{-}/bohr^3.

FILM LOOP VI
The Formation of the Water Molecule from H and OH
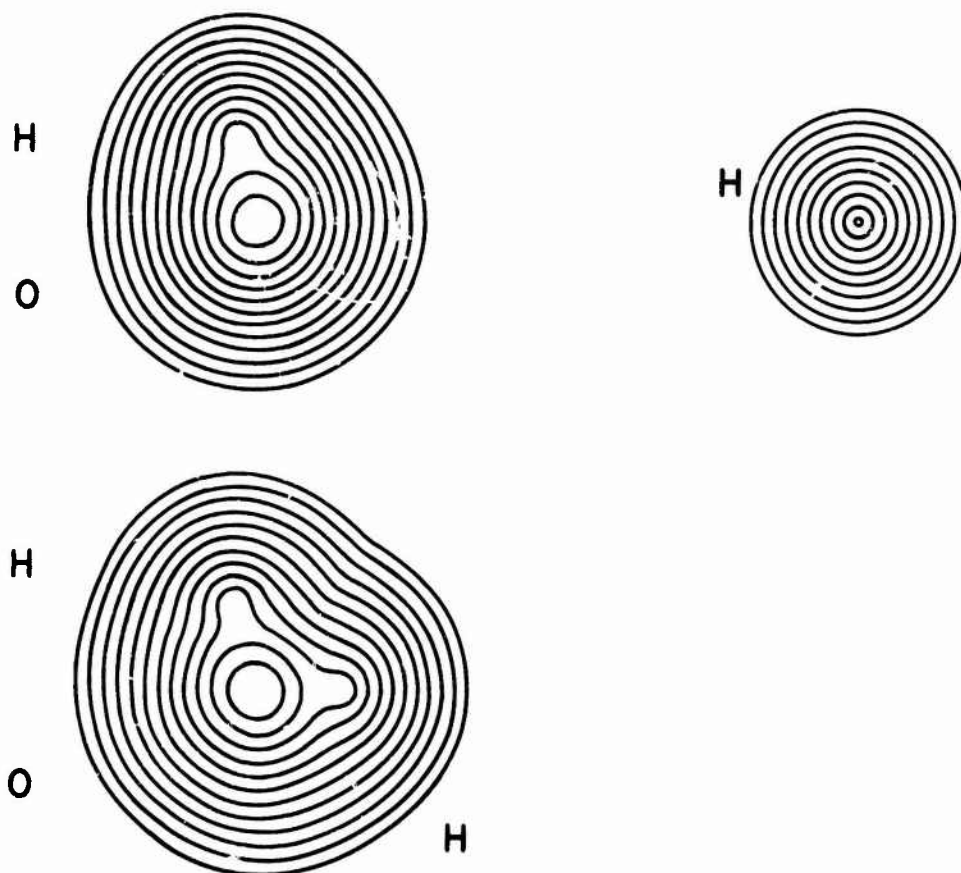
Fig. 17. Displays electron density contour diagrams for the OH molecule and the H atom and the final diagrams for the H_2O molecule in its equilibrium configuration. In the OH and H_2O diagrams the innermost contour corresponds to a probable electron density of 1.0 $e^-/bohr^3$ and each successive outer contour decreases by a factor of 2 down to 4.9×10^{-4} $e^-/bohr^3$. In the H diagram the innermost contour has a value of .25 $e^-/bohr^3$.

297

Towards this view we "computer qu:ntum chemists" are
developing our theory and procedures into self-contained "packages"
or systems which should be treated as a new piece of experimental
apparatus requiring little or no intimate knowledge of its
detailed structure.[143-146] Our ultimate goal is to make these
chemical computing systems so self contained that the experimental
chemist can ask of them truly chemical questions[143] such as "What
is the dipole moment of CaO?" or "What are the vibrational levels
of VCl_2?" or "What are the transport properties of alkali vapors?"
This requires, of course, that our computing systems embody not
only mathematical analysis but our procedures and experience in
utilizing these theoretical techniques and that such systems are
capable of continuous growth, revision and eventually learning
from the system's own accumulating experience. It is further
mandatory, if these systems are to be useful to the non-specialist
that a guarantee of reliability and precision relative to
external reality be made. This has formulated our philosophy
that only methods capable of routinely producing chemically
useful precision be incorporated into the final system concept.
The non-specialist should not be seduced into believing numbers
simply because they are produced in an officious manner. Due
to the meteoric progress being made in computer design and
capacity and the increasing sophistication[143-149] of "computer
chemists", I have confidence that the above and more provocative
chemical questions shall be posed to, answered by, and eventually
even formulated by our new numeric apparatus.

ACKNOWLEDGEMENTS

FOOTNOTES AND REFERENCES

1. Wahl, Arnold C. "Hartree-Fock is Here: What Next?" - a talk delivered at the Alberta Symposium of quantum chemestry, University of Alberta, Edmonton, Canada, 3une, 1965.

2. Recently much has been written elsewhere about the development and present state of the molecular-orbital method, therefore we shall confine ourselves to a brief statement of crucial steps in its history.

The molecular orbital method as introduced by Mulliken (8,9,10) and Hund (11) was used extensively in the semiempirical interpretation of band spectra. However, mathematically and computationally the concept matured rather slowly. Its early development (and the search for the "best" MO's) may be traced from the recognition by Lennard-Jones (12) of its relationship of Hartree's (13) self-consistent field work on atoms followed by the introduction of the determinantal form for the wave function (14,15) with the application of the variational principle (Fock, 16, and Slater, 17,18) to yield the now familiar pseudo-eigenvalue equations of the form

$$F\phi_i = \epsilon_i \phi_i \qquad (2\text{-}1)$$

known as the Hartree-Fock equations, which provide a rigorous mathematical definition of best orbitals. Lennard-Jones (12) presented the equations for an arbitrary system; Coulson foreshadowed their solution by the expansion method; and Roothaan (20,21) developed and perfected the extensively used matrix formulation of the expansion method. Important also are the proofs by Delbrück (22), Löwdin (23), and Roothaan (21) that the Hartree-Fock functions are always self-consistent, symmetry-adapted, and correspond to a specific minimum of the total energy. Extremely relevant to the potency and appeal of Hartree-Fock wave functions was the work of Brillouin (24,25), Moller and Plesset (26) on corrections to the Hartree-Fock approximation. They showed that one-electron properties computed from Hartree-Fock wave functions have first-order corrections in perturbation theory which vanish provided that degeneracy is not present. Koopman (27) developed similar theorems for ionization potentials.

Having clearly defined the Hartree-Fock model of a molecular system, it still remained a formidable practical problem to obtain the MO's ϕ_i. In 1951, Roothaan had cast the Hartree-Fock equations into a solid computational framework remarkably suitable for the then-embryonic digital computers. In what is now referred to as the Roothaan (20,21) method the orbital ϕ_i is expanded in terms of some suitable truncated basis set χ_p

$$\phi_i = \Sigma_p C_{ip} \chi_p. \qquad 2\text{-}2$$

The expansion coefficients C_{ip} are optimized through the iterative self-consistent field process (28). In the full numerology of the process the best truncated set of basis functions is also hunted down, usually by brute force methods. In practice a very close approximation to the Hartree-Fock molecular orbitals can be obtained in this way. Calculations of this type utilizing analysis and computer programs developed recently (29,30) have resulted in the determination of the molecular orbitals for a large number of diatomic molecules in the form of Eq. (2-2). These functions, in which the basis set χ_p, consists of many Slater-type orbitals (STO's), are very close to the Hartree-Fock result.

3. Lowdin, P. -O., Pullman, B. (1964). "Molecular Orbitals in Chemistry, Physics, and Biology," Academic Press, New York.

4. Slater, 3. C. (1965). *J. Chem. Phys.* 43, S11

5. Nesbit, R. K. (1965). *J. Chem. Phys.* 43, 530

6. Wahl, A. C.; Bertoncini, P. 3.; Das, G.; Gilbert, T. L.; I.J.Q.C. IS, 123 (1967).

7. Nesbit, R. K., *Adv. in Qu. Chem.*, ed. P. O. Lowdin, Academic Press, New York, (1967), V. ?

8. Mulliken, R. S. (1928). *Phys. Rev.* 2, 186, 388, 761.

9. Mulliken, R. S. (1929). *Phys. Rev.* 33, 730.

10. Mulliken, R. S. (1932). *Phys. Rev.* 40, 55; 41, 49, 751.

11. Hund, F. (1928). *Z. Physik* 51, 759.

12. Lennard-Jones, 3. E. (1929). *Trans. Faraday Soc.* 25, 668.

13. Hartree, D. R. (1928) *Proc. Cambridge Phil. Soc.* 24, 89.

14. Slater, 3. C. (1930a). *Phys. Rev.* 35, 509.

15. Slater, 3. C. (1932). *Phys. Rev.* 41, 255.

16. Fock, V. (1930). *Z. Physik* 61, 126.

17. Slater, 3. C. (1929). *Phys. Rev.* 34, 1929.

18. Slater, 3. C. (1930b). *Phys. Rev.* 35, 509.

19. Coulson, C. A. (1938). *Proc. Cambridge Phil. Soc.* 34, 204.

20. Roothaan, C. C. J. (1951). *Rev. Mod. Phys.* 23, 69.

21. Roothaan, C. C. 3. (1960). *Rev. Mod. Phys.* 32, 179.

22. Delbruck, M. (1930). *Proc Roy. Soc. (London) Ser.* A 129, 686.

23. Lowdin, P. -O. (1962). *J. Appl. Phys. Suppl.* 33, 270.

24. Brillouin, L. (1933). *Actualities Sci. Ind.* 71.

25. Brillouin, L. (1934). *Actualities Sci. Ind.* 159.

26. Moller, C., and Plesset, M. S. (1934). *Phys. Rev.* 46, 618.

27. Koopman, T. (1933). *Physica* 1, 104.

28. Roothaan, C. C. J., and Bagus, P. (1963). *In "Methods in Computational Physics"* (B. Alder, S. Fernbach, and M. Rotenberg, eds.), Vol. 2, p. 47. Academic Press, New York.

29. Wahl, A. C. (1964). *J. Chem. Phys.* 43, 2600; Wahl, A. C.; Cade, P. E.; Roothaan, C. C. 3. (1964). *J. Chem. Phys.* 41, 2578; Wahl, A. C., Bertoncini, P. 3., Kaiser, K., Land, R. H., *Argonne National Laboratory Report No. 7271* (1968).

30. Wahl, A. C., (1966). *Argonne National Laboratory Report No. 7076*, also *Science*, 151, 961. and for a discussion of alkali halide densities see A. C. Wahl, F. Janiszewski, and M. T. Wahl (to be submitted to *Science*)

31. Wahl, A. C. and Blukis, U., *Atoms to Molecules*, McGraw-Hill, New York (1969). 3. Chem. Ed. 45, 787 (1968). Wahl, A. C., and Wahl, M. T. Four Wall Charts of Atomic and Molecular Structure, McGraw-Hill, New York.

32. Wahl, A. C.; Cade, P. E.; Sales. Unpublished.

33. Zemke, W.; Lykos, P.; and Wahl, A. C.: Ph.D. Thesis, Joint IIT-ANL, and ANL Report.

34. E. Clementi, *J. Chem. Phys.* 36, 33 (1962).

35. R. K. Nesbet, *J. Chem. Phys.* 36, 1518 (1962).

36. S. L. Kahalas and R. K. Nesbet, *J. Chem. Phys.* 39, 259 (1963).

37. A. D. McLean, *J. Chem. Phys.* 39, 2653, (1963).

38. M. Yoshimine, *J. Chem. Phys.* 40, 2970 (1964).

39. R. K. Nesbet, *J. Chem. Phys.* 41, 100 (1964).

40. A. C. Wahl, *J. Chem. Phys.* 41, 2600 (1964).

41. W. Huo, *J. Chem. Phys.* 43, 624 (1965); *J. Chem. Phys.* 45, 1554 (1966).

42. P. E. Cade, K. S. Sales, and A. C. Wahl, *J. Chem. Phys.* 44, 1973 (1966).

43. W. Huo, to appear in *J. Chem. Phys.*

44. W. Huo, to appear in *J. Chem. Phys.*

45. P. E. Cade and W. Huo, *J. Chem. Phys.* 47, 614 (1967).

46. P. E. Cade and W. Huo, *J. Chem. Phys.* 47, 619 (1967).

47. T. L. Gilbert and A. C. Wahl, *J. Chem. Phys.* 47, 3425 (1967).

48. T. L. Gilbert and A. C. Wahl, to be submitted to *J. Chem. Phys.*

49. T. L. Gilbert and A. C. Wahl, in preparation.

50. A. D. McLean and M. Toshimine, *Tables of Linear Molecule Wave Functions* (IBM Research Publication, San Jose, 1967), INT.J.Q.C., IS

51. P. E. Cade, J. B. Greenshields, G. Malli, K.D. Sales, and A. C. Wahl, unpublished work.

52. P. J. Bertoncini, T. L. Gilbert, and A.C. Wahl, unpublished work.

53. P. E. Cade, unpublished work.

54. P. J. Bertoncini and A. C. Wahl, unpublished work.

55. R. L. Matcha and R. K. Nesbet, IBM Research paper RJ 429, to be published.

56. S. Peyerimhoff, *J. Chem. Phys.* 43, 998 (1955).

57. K. D. Carlson and C. M. Moser, *J. Chem. Phys.* 67, 2644 (1963).

58. K. D. Carlson and C. M. Moser, *J. Chem. Phys.* 44, 3295 (1966).

59. W. G. Richards, G. Verhagen, and C. M. Moser, *J. Chem. Phys.* 45, 3226 (1966).

60. G. Verhaegen, W. G. Richards, and C. M. Moser, J. Chem. Phys. 46, 160, (1967).

61. K. D. Carlson, E. Ludena, and C. M. Moser, *J. Chem. Phys.* 43, 2408 (1965).

62. K. D. Carlson, and R. K. Nesbet, J. Chem. Phys. 41, 1051 (1964).

63. K. D. Carlson, C. M. Moser, K. Kaiser and A. C. Wahl (CaO in preparation)

64. Maldonado, P. and Wahl, A. C. "A Priori Calculations on LiHe, LiNe, NaHe, NaNe" (in progress)

65. Substantial progress beyond the Hartree-Fock scheme for molecules has been achieved by a variety of approaches. Direct inclusion of aaplicit correlation terms in the wave function is illustrated by the classic work of Kolos and Roothaan (66) . . . and later Kolos and Wolniewicz (67-69) where the ground and several excited states of H₂ have been computed to an accuracy which challenges experiment. However, it is unlikely that this approach can be aatended to larger molecules. (The recent work of Handy and Boys may modify this view)

Other more practical methods for going beyond the quantitative limits of the Hartree-Fock approximation include a variety of configuration interaction methods, exemplified by the work of Matsen and coworkers, Browne, Boys and coworkers, Nesbet, Moser, Harris, Taylor, Michels, Davidson, McLean, Allen, and others (70-100) . One of the most useful aatensions, which has been developed to the point where reliable predictions (101) can be made on a wide variety of molecules, is the many-electron theory of Sinanoglu (102). We regard these various methods, and the optimized valence configuration method described in this review, as complementary rather than competitive. Further calculations are needed to ascertain whether any one scheme will turn out to be so simple, general, and powerful that it supersedes all others.

There are at least three general approaches to the problem of going beyond the Hartree-Fock approximation: perturbation theory, correlated wave functions, and configuration interaction. If one chooses the third approach, as we have done, then one is immediately faced with the problem of the slow convergence of the multiconfiguration expansion of a many-electron wave function. At this point one must make a choice between trying to cope with very large numbers of configurations and improving the convergence. Although the former choice is now feasible with the large computers available, (and one can always extract simple quantities from a complicated wave function and leave everything else out of sight in the machine), it seemed to us that one would be more likely to be able to comprehend the steps of the calculation and find unexpected relations and regularities by working directly with the most convergent expansion obtainable. If one constructs all configurations from a common set of orthonormal orbitals, then this reasoning leads immediately to variational equations for a finite set of orbitals which must be solved simultaneously with the secular equation for the configuration expansion coefficients. These equations are sometimes referred to as the aatended Hartree-Fock aquations, (103-105, 107-121) although this name is also used for a more restricted set of equations obtained by projecting a wave function from a single determinant before varying the orbitals. (117) In the general case the orbitals which satisfy the extended Hartree-Fock equations are similar to, but not identical with, the natural spin orbitals (117, 122-124, of the system. This is essentially what we would like to evaluate in an a priori way, for the natural-orbital analyses of atoms and molecules have shown their natural orbitals provide a very compact and informative way of characterizing various wave functions. (125-136)

The aatended Hartree-Fock method in its most general form is still rather complicated for the first step beyond the Hartree-Fock approximation, and perhaps more complicated than is needed. Hence, a simpler scheme, the optimized valence configuration (OVC) method, has been proposed by Das and Wahl and used successfully for practical calculations on a number of diatomic molecules. (Excerpt from ref. 6)

66. W. Kolos and C. C. J. Roothaan, *Rev. Mod. Phys.* 32, 205 (1960).

67. W. Kolos and L. Wolniewicz, *Rev. Mod. Phys.* 35, 473 (1963).

68. W. Kolos and L. Wolniewicz, *J. Chem. Phys.* 45, 509 (1966).

69. W. Kolos and L. Wolniewicz, *J. Chem. Phys.* 41, 3663 (1964).

70. S. Rothenberg and E. R. Davidson, *J. Chem. Phys.* 44, 730 (1966).

71. W. M. Wright and E. R. Davidson, J. Chem. Phys. 43, 840 (1965).

72. J. C. Browne, *J. Chem. Phys.* 40, 43 (1964).

73. J. C. Browne, *J. Chem. Phys.* 41, 1583 (1964).

74. E. R. Davidson, *J. Chem. Phys.* 35, 1189 (1961).

75. E. R. Davidson, *J. Chem. Phys.* 33, 1577 (1960).

76. W. Kolos and C. C. J. Roothaan, *Rev. Mod. Phys.* 32, 219 (1960).

77. A. D. McLean, A. Weiss, and M. Yoshimine, *Rev. Mod. Phys.* 32, 211 (1960).

78. J. C. Browne, *J. Chem. Phys.* 42, 1428 (1965).

79. S. Fraga and B. J. Ransil, *J. Chem. Phys.* 37, 1112, (1962).

80. B. G. Anex. *J. Chem. Phys.* 38, 1651 (1963).

81. F. E. Harris, *J. Chem. Phys.* 44, 3636, (1966).

82. P. N. Reagen. J. C. Browne, and F. A. Matsen, *Phys. Rev.* 132, A304 (1963).

83. J. F. Browne, *J. Chem. Phys.* 45, 2709 (1966).

84. H. H. Michels and F. E. Harris, *J. Chem. Phys.* 39, 1464 (1963).

85. C. F. Bender and E. R. Davidson, *J. Phys. Chem.* 70, 2675, (1966).

86. H. S. Taylor and F. E. Harris, *Mol. Phys.* 7, 287 (1964).

87. J. C. Browne, *J. Chem. Phys.* 41, 3495 (1964).

88. R. D. Poshusta and F. A. Matsen, *Phys. Rev.* 132, A307 (1953).

89. P. E. Phillipson, *Phys. Rev.* 125, 1981 (1962).

90. H. S. Taylor and F. E. Harris, *Mol. Phys.* 1. 287 (1964).

91. J. C. Browne, *J. Chem. Phys.* 42, 2826 (1965).

92. D. R. Scott, E. M. Greenwalt, J. C. Browne, and F. A. Matsen, *J. Chem. Phys.* 44, 2381 (1966).

93. J. C. Browne, *Phys. Rev.* 138, A9 (1965).

94. J. C. Browne, F. A. Matsen, *Phys. Rev.* 135, A1227 (1964).

95. D. D. Ebbing, *J. Chem. Phys.* 36, 1361 (1962).

96. J. C. Browne, J. Chem. Phys. 36, 1814 (1962).

97. F. E. Harris and H. S. Taylor, *Physica* 30, 105 (1964).

98. P. L. Moore, J. C. Browne, and F. A. Matsen, *J. Chem. Phys.* 43, 903 (1965).

99. R. F. Fourgere and R. K. Nesbet, *J. Chem. Phys.* 44, 285, (1966).

100. L. C. Allen, *Quantum Theory of Atoms, Molecules and the Solid State* (Academic Press, New York, 1966).

101. C. Hollister and O. Sinanoglu, *J. Am. Chem. Soc.* 88, 13 (1966).

102. O. Sinanoglu, *Advan. Chem. Phys.* 2 (1964).

103. G. Das and Arnold C. Wahl, *J. Chem. Phys.* 44, 87 (1966).

104. G. Das, *J. Chem. Phys.* 46, 1568 (1967).

105. G. Das, and Arnold C. Wahl, *J. Chem. Phys.* 47, 2934 (1967).

106. References 107-117 present the historical development of the formation of best orbitals for a multiconfigurational wave function.

107. J. Frenkel, "Wave Mechanics," Advanced General Theory (Clarendon Press, Oxford, 1934. Reprinted by Dover Publications, Inc., New York, 1950), pp. 460-462.

108. J. C. Slater, *Phys. Rev.* 91, 528 (1953).

109. P. O. Lowdin, *Phys. Rev.* 97, 1497 (1955), Sec. 5.

110. (a)R. McWeeny, *Proc. Roy. Soc.* (London), Ser. A. 232, 114 (1955); (b)R. McWeeny and R. Steiner, *Advan. Quantum Chem.* 2, 93 (1965).

111. D. R. Hartree, W. Hartree, and B. Swirles, Phil. Trans. Roy. Soc. (London), Ser. A, 238, 292 (1939).

112. A. P. Yutsis, Zh. Eksperim. i Tenet. Fix. 23, 129 (1952).

113. A. P. Yutsis, V. V. Kibartas, and I. I. Glembotskiy, Zh. Eksperim, i Theo. Fiz. 24, 425 (1954).

114. V. V. Kibartas, V. I. Kavetskis, and A. P. Yutsis, *Soviet Phys. – J. E. T. P.* 2g, G23 (1955).

115. R. E. Watson, *Ann. Phys.* 13, 250 (1961).

116. T. L. Gilbert, *J. Chem. Phys.* 43, S248 (1965).

117. P. O. Lowdin, *Phys. Rev.* 97, 1509 (1955).

118. A. Veillard, *Theoret. Chim. Acta* 4, 22 (1966).

119. E. Clementi and A. Veillard, *J. Chem. Phys.* 44, 3050 (1966); *Theoret. Chim. Acta* 7, 133 (1967).

120. E. Clementi, *J. Chem. Phys.* 46, 3842 (1967).

121. Jurgen Hinze and Clemens C. J. Roothaan, to be published.

122. W. Kutzelnigg, *J. Chem. Phys.* **40**, 3640 (1964).

123. . . . O. Lowdin, *Advan. Chem. Phys.* **2** (1959).

124. H. Shull and P. O. Lowdin, *J. Chem. Phys.* **30**, 617 (1959).

125. S. Rothenberg and E. R. Davidson, *J. Chem. Phys.* **45**, 2560 (1966).

126. C. F. Bender and E. R. Davidson, *J. Chem. Phys.* **70**, 2675 (1966)

127. E. R. Davidson and L. L. Jones, *J. Chem. Phys.* **37**, 1918 (1962).

128. E. R. Davidson and L. L. Jones, *J. Chem. Phys.* **37**, 2966 (1962).

129. M. A. Eliason and J. O. Hirschfelder, *J. Chem. Phys.* **30**, 1397 (1959).

130. H. Shull, *J. Chem. Phys.* **30**, 1405 (1959).

131. S. Hagstrom and H. Shull, *Rev. Mod. Phys.* **35**, 624 (1963).

132. H. Shull and F. Prosser, *J. Chem. Phys.* **40**, 233 (1964).

133. C. Edmiston and M. Krauss, *J. Chem. Phys.* **45**, 1833 (1956).

134. C. F. Bender and E. R. Davidson, *J. Chem. Phys.* **70**, 2675 (1966).

135. D. D. Ebbing and R. C. Henderson, J. Chem. Phys. **42**, 2225 (1965).

136. W. Lyon and J. O. Hirschfelder, J. Chem. Phys. **46**, 1788 (1967).

137. G. Das and A. C. Wahl, *Optimized Valence Configuration Wave functions for NaF and F$_2$*, in preparation.

138. P. Bertoncini, G. Das, and A. C. Wahl, *A Theoretical Study of the NaLi System* (ANL Report 7447) 1969. (Submitted to J.C.P.)

139. See, for example, Hirschfelder, Curtiss and Bird, *Molecular Theory of Gases and Liquids*, John Wiley and Sons, Inc., New York (1954).

140. O. Sinanoglu and K. S. Pitzer, *J. Chem. Phys.* **31**, 960 (1959), R. H. Davis, E. A. Mason, and R. J. Munn, *Phys. of Fluids* **8**, 444 (1965), F. Jenc, *J. Mol. Spec.* **24**, 284 (1967). D. Miller, *Argonne National Laboratory Report No. 7210*, 280 (1966).

141. D. Miller, P. J. Bertoncini and A. C. Wahl, *Comparison of ab initio and Semiempirical Interatomic Potentials in the Calculation of the Transport Properties of Alkali Vapors* (in preparation).

142. R. S. Mulliken, *Science*, **157**, 13 (1967). (Nobel Prize Lecture) and *Physics Today*, **21**, 52, (1968).

143. A. C. Wahl, P. J. Bertoncini, K. Kaiser and R. H. Land, "BISON: A New Instrument For the Experimentalist I.J.Q.C. Sanibel Symposium Issue (1969).

144. A.C. Wahl, P.J. Bertoncini, K. Kaiser and R.H. Land, "BISON: A Fortran Computing System for the Calculation of Wavefunctions, Properties and Charge Densities for Diatomic Molecules," *Argonne National Laboratory Report No. 7271* (1968).

145. S. Rottenberg, *MOLE: A System for Quantum Chemistry* (Available from the author.)

146. L.M. Sachs and M. Geller, "MOSES" A Fortran IV System for Polyatomic Molecules," I.J.Q.C., *IS*, 445 (1967).

147. *IBMOL: Computation of Wave-function for Molecules of General Geometry*, IBM Research Laboratories, San Jose, California

148. Bowman, T.; Chung, A.; Goodman, G. L.; *Automation of Molecular Point Theory, Sigma Molecular Orbital Theory*, W. Benjamin, New York (1969). See also: T. Bouman, *Instant Group Theory* and A. Chung.

149. We chemists are also becoming aware of parallel developments in other disciplines. An outstanding example of this is the work of Stanley Cohen, of the Argonne Physics Division on Interactive Graphics and its application to Nuclear Structure problems.

NOTE: An interesting aspect of the pictorial material dealing with electronic charge density and its change during molecular formation, excitation and ionization presented in this paper is that all diagrams are produced and drawn *automatically* by digital computers linked to plotting devices (CRT and paper). This pictorial project is currently being made interactive through the use of the Laboratory's new graphical equipment. The author and his associates are developing what they call an *Interactive Quantum Mechanics Laboratory* through which a researcher or student can sit at a CRT graphic console and by request "watch" a series of fundamental chemical processes which he personally may control and modify. Material similar to these diagrams has been organized into a book and series of charts "Atomic and Molecular Structure: A Pictorial Approach," A.C. Wahl and M.T. Wahl, McGraw-Hill (1969), and a set of motion pictures "Atoms to Molecules," A.C. Wahl and U. Blukis, McGraw-Hill (1969).

Numerical Solutions of the Vlasov Equation

J. Denavit
Plasma Physics Division
Naval Research Laboratory
Washington, D.C.

ABSTRACT

This paper present a review of numerical solutions of the Vlasov equation
by the Fourier-Fourier transform method and by the direct method of integra-
tion in which the distribution function is pushed in the phase plane. Computer
codes were written to implement both methods and numerical solutions of two-
stream instability problems by both methods are compared. The Fourier-Fourier
transform code uses fast Fourier transforms to compute the convolution term
which appears in the transformed Vlasov equation. This technique allows solu-
tions with a large number of modes. In the direct integration code, the dis-
tribution function is not generally reconstructed at every time step. The
examples presented in the paper suggest that, by properly choosing the
frequency of reconstruction of the distribution function, it may be possible
to minimize both the noise due to discrete particle interactions and the dif-
fusion which occurs every time the distribution function is reconstructed.

I. INTRODUCTION

Collective phenomena in collisionless plasmas have been studied analyti-
cally in terms of the Vlasov equation, which describes the dynamics of a systems
of many charged particles, and Maxwell's equations to describe the electromag-
netic field. Analytical solutions have often been based on a decomposition of
the spatial dependence of the distribution function into linearly independent
modes, followed by studies of nonlinear coupling between modes. In numerical
simulation of plasmas, a more direct method has been widely used. Here the
positions and velocities of a large number of particles moving in their self-
consistent field are computed as a function of time.[1-5] Thus the complete
dynamical state of the system is known at every time step, and average quanti-
ties of interest, such as number densities or temperatures, are computed when-
ever desired. Although the number of particles which may be followed on a
computer is much smaller than the number of particles found in actual plasmas,
particule simulations are conceptually similar to actual experiments and have
been successful to provide an understanding of a variety of plasma phenomena.

An alternate approach to the computational study of collisionless plasmas
is provided by numerical solutions of the Vlasov equation.[6-11] Since it is
based directly on the same equation, this approach lies close to analytical
methods. It yields itself easily to the study of linearized solutions and
mode coupling effects. However, it is also applicable to strongly nonlinear
problems and can therefore provide a useful link between particle simulations
and theoretical results. Since it differs fundamentally in its approach from
the particle simulation method, comparison of the two methods gives an insight
into the validity and limitations of both methods.

The present paper will be limited to one-dimensional problems involving
only electrons moving over a uniform positively charged background, and periodic
boundary conditions in space will be assumed. Let L denote the periodicity

Solutions of Vlasov Equation

length of the plasma and ω_p the plasma frequency. Distances will be measured in units of L and times will be measured in units of ω_p^{-1}. It follows that the electric field is measured in units of $mL\omega_p^2/e$ where e and m are the electron charge and mass. The one-dimensional Vlasov equation then takes the form

$$\frac{\partial f}{\partial t} + v \frac{\partial f}{\partial x} - E \frac{\partial f}{\partial v} = 0 , \qquad (1)$$

where $f(x,v,t)$ denotes the electron distribution function and $E(x,t)$ is the electric field. Let $E(x,t) = E^{ext}(x,t) + E^{int}(x,t)$, where E^{ext} is an external electric field and E^{int} is the internal field due to electrons and the positively charged background. The internal field is determined by Poisson's equation,

$$\frac{\partial E^{int}}{\partial x} = 1 - \int_{-\infty}^{+\infty} f \, dv . \qquad (2)$$

The solutions of the Vlasov equation obey the principle of conservation of density in phase. The density in phase is the distribution function itself in the present case. Let (x_o, v_o) denote the coordinates of a particle in the phase plane at time t_o. At time t, the particle has moved to the phase point (x,v). Conservation of density in phase requires $f(x,v,t) = f(x_o,v_o,t_o)$. We will see in Section III that this property is used for the direct integration of the Vlasov equation in phase plane.

An important property of the solutions of the Vlasov equation is their tendency to acquire increasingly fine structures in phase plane as time increases. This phenomenon may be illustrated in terms of the oscillations of an electron gas trapped in the potential trough of an external electric field of the form $E = E_o \sin 2\pi x/L$. Neglecting the internal field which would not change the results qualitatively, the electron trajectories are given by Jacobi elliptic functions,

$$\sin \frac{\pi x}{L} = \mathcal{K} \, sn(u,\mathcal{K}) \quad ,$$

$$\frac{v}{v_{TR}} = \mathcal{K} \, cn(u,\mathcal{K}) \quad ,$$

with $u = 2\pi t/\tau_{TR} + u_o$. Here τ_{TR} denotes the trapping period and v_{TR} the trapping velocity. The modulus $\mathcal{K}$ and the constant u_o depend on the initial electron corrdinates in the phase plane. The limit cycle defining the boundary between trapped and untrapped electrons in the phase plane is shown in Fig. 1. If the electrons are initially distributed uniformly over the shaded area shown in Fig. 1(a), their phase density at $t = 2\tau_{TR}$ will be uniformly distributed over the shaded area shown in Fig. 1(b). In the present case, the development of the fine spiral structure near the limit cycle is cause? by the sharp amplitude dependence of the period of oscillations of trapped electrons in this region. As time increases, the description of the distribution function requires an ever finer resolution which ultimately exceeds the finite capacity of computer storage.

This phenomenon has been discussed by Lynden Bell[12] in relation to the approach to equilibrium of solutions of the Vlasov equation. When the structure becomes so fine that its scale is much smaller than the characteristic lengths and velocities of the plasma phenomena of interest, its description may be abandoned and a coarse-grained distribution function $\tilde{f}(x,v,t)$ defined by averaging $f(x,v,t)$,

$$\tilde{f}(x,v,t) = \int_0^1 \int_{-\infty}^{+\infty} w_x(x')w_v(v')f(x + x',v + v',t)dx'dv'. \quad (3)$$

The weight functions $w_x(x)$ and $w_v(v)$ define the resolution and the exact form of the averaging operation. The choice of these functions is an important consideration in numerical solutions of the Vlasov equation.
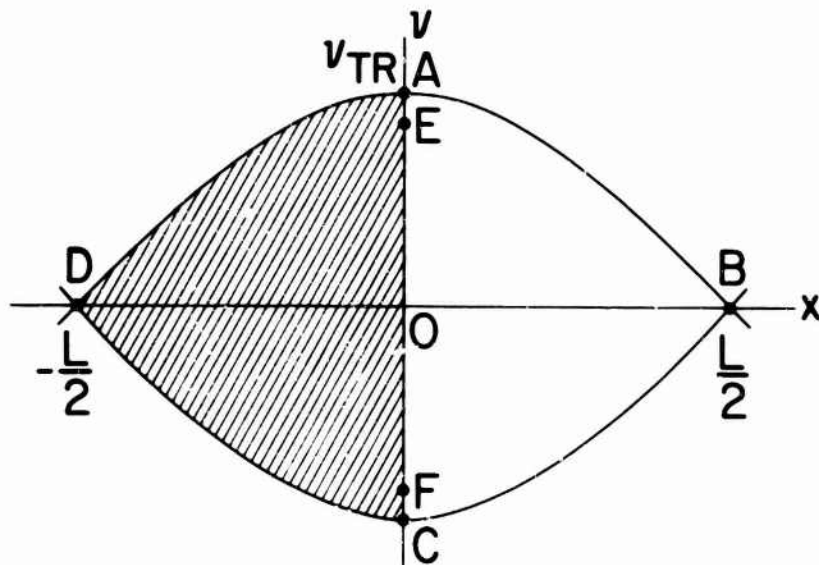
(a) $t = 0$
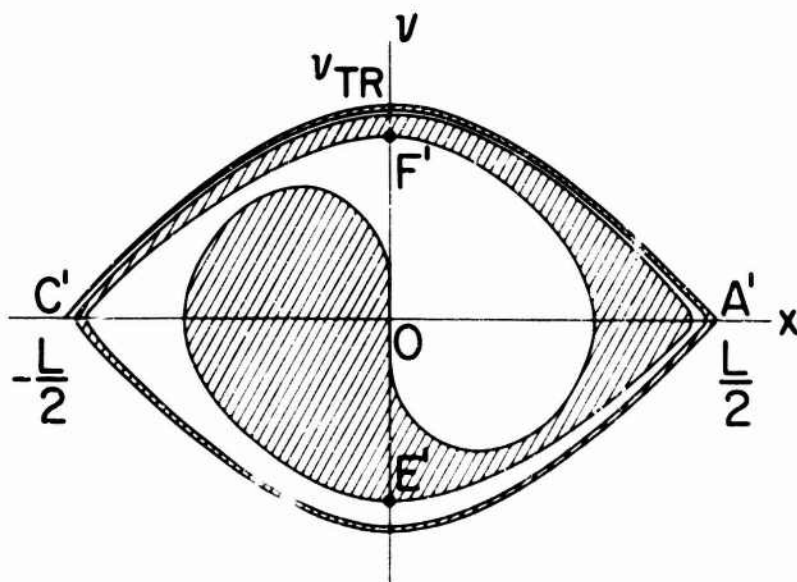
(b) $t = 2\tau_{TR}$

Figure 1   Example of the development of fine structures in the solutions of the Vlasov equation.

309

By reversing the sign of t in Eq. (1) it may be observed that solutions of
the Vlasov equation are reversible. However, the averaging operation defined
by (3) amounts to neglecting some of the information contain ' in the fine
structure of $f(x,v,t)$. Thus numerical solutions of the Vlasov equation using
this averaging operation are not exactly reversible. Since the computation
of the coarse-grained distribution function also involves the averaging of
different neighboring values of the original distribution function, the princi-
ple of conservation of density in phase no longer applies exactly to the coarse-
grained distribution function.

Numerical methods for the solution of the Vlasov equation may be classified
as (A) direct methods, in which the distribution function is represented
directly in the (x,v) plane, and (B) transform methods, in which the distribu-
tion function is first transformed (Fourier transformed for example) and the
transformed Vlasov equation is then integrated numerically. Two types of direct
methods have been used: (a) the distribution function may be pushed in the
(x,v) plane along its characteristics,[6-8] or (b) the phase plane may be ini-
tially divided into a number of uniform-density regions representing the ini-
tial distribution function, and then only boundary points need to be followed
in time.[9] Transform methods can also be subdivided into several types depend-
ing on the type of transform used. (a) The distribution function may be
Fourier transformed with respect to both position and velocity,[10] this is called
the Fourier-Fourier transform method, or (b) the distribution function may be
Fourier transformed with respect to position only and the velocity dependence
of each mode represented by an expansion in Hermite polynomials.[11] The
latter method is called the Fourier-Hermite method.

This paper presents a review of the Fourier-Fourier transform method and
of the direct method of integration in which the distribution function is

pushed in the (x,v) plane. Computer codes were written to implement both methods and numerical solutions of two-stream instability problems by both methods are compared.

The Fourier-Fourier transform method, originated by Knorr,[10] is considered in Section II. Previous solutions using this method had been limited to a few modes. The present code uses fast Fourier transforms to compute the convolution term which appears in the transformed Vlasov equation. This technique yields a considerable saving in computing time and solutions with up to 85 modes, capable of representing strong nonlinear effects have been obtained.

The code written to implement the direct method of integration is capable to generate "hybrid" solutions in which particles of different masses are advanced as in a particle code, but the distribution function is reconstructed periodically as in a Vlasov code by an averaging operation similar to Eq. (3). The examples presented in Section III suggest that, by properly choosing the frequency of reconstruction of the distribution function, it may be possible to minimize both the noise (or spurious oscillations) due to discrete particle interactions and the diffusion which occurs every time the distribution function is reconstructed.

II. THE FOURIER-FOURIER TRANSFORM METHOD

1. Fourier Transforms

The spatial dependence of the distribution function $f(x,v,t)$ and of the electric field $E(x,t)$ is represented in Fourier series as

$$f(x,v,t) = \sum_{n=-\infty}^{+\infty} g_n(v,t) e^{2\pi i n x} ,$$

and

$$E(x,t) = \sum_{n=-\infty}^{+\infty} E_n(t) e^{2\pi i n x} ,$$

311

with

$$g_n(v,t) = \int_0^1 f(x,v,t)e^{-2\pi inx}dx \quad ,$$

and

$$\overline{E}_n(t) = \int_0^1 E(x,t)e^{-2\pi inx}dx \quad .$$

The distribution functions $g_n(v,t)$ for each mode n are now Fourier transformed with respect to velocity,

$$H_n(q,t) = \int_{-\infty}^{+\infty} g_n(v,t)e^{iqv}dv \quad ,$$

with

$$g_n(v,t) = \frac{1}{2\pi} \int_{-\infty}^{+\infty} H_n(q,t)e^{-iqv}dg \quad .$$

Since $f(x,v,t)$ and $E(x,t)$ are real, we must have

$$g_{-n}(v,t) = g^*_n(v,t), \quad \overline{E}_{-n}(t) = \overline{E}^*_n(t) \qquad (4,5)$$

and

$$H_{-n}(q,t) = H^*_n(-q,t) \quad . \qquad (6)$$

The functions $H_n(q,t)$ with n = 0, ±1, ... are the characteristic functions[13] of the velocity distributions corresponding to the spatial modes. These functions have an **interesting property** relating them to the moments of the corresponding distributions. Let $\langle v^\nu \rangle_n$ denote the moment of order ν of $g_n(v)$, we have

$$\left(\frac{\partial^\nu H_n}{\partial q^\nu} \right)_{q=0} = i^\nu \langle v^\nu \rangle_n \quad . \qquad (7)$$

This property is used in Section II-5 to evaluate the plasma density, momentum and kinetic energy. We observe in addition that fine structures of the distribution function in the (x,v) plane, correspond to values of $H_n(q)$ for large n and q. Thus truncating the set of functions $H_n(q)$ at some finite values

312

m_{max} and q_{max} provides a simple way to neglect the fine structure of the distribution function without affecting any of its moments for $|n| \leqslant m_{max}$. A further discussion of the significance of this truncation will be given in Section II-4.

After transformation and truncation at $\pm m_{max}$, the Vlasov equation (1) yields

$$\frac{\delta H_n}{\delta t} + 2\pi n \frac{\delta H_n}{\delta q} = \frac{q}{2\pi} C_n(q,t) \quad , \quad (8)$$

where

$$C_n(q,t) = \sum_{m = -m_{max}}^{m_{max}} (-2\pi i \overline{E}_m) H_{n-m}(q,t) \quad . \quad (9)$$

Poisson's equation (2) gives

$$-2\pi i \overline{E}_n^{int} = \frac{1}{n} H_n(q=0,t) \quad (10)$$

for $n \neq 0$ and $\overline{E}_o^{int} = 0$.

The term C_n is a convolution which comes from the nonlinear term of the Vlasov equation. Solutions of the linearized Vlasov equation may be obtained by simply setting

$$C_n(q,t) = -2\pi i E_n H_o(q) \quad , \quad (11)$$

where $H_o(q)$ is the characteristic function of the assumed spatially homogeneous velocity distribution. In the linear case Eqs. (8) decouple and their solutions may be carried out independently for each mode $n \neq 0$. The equation for $n = 0$ becomes trivial. In the analysis of some problems, such as in the quasi-linear theory, the Vlasov equation is solved including wave-particle interactions but neglecting mode-coupling terms. Such solutions may be obtained by using the convolution term (11) for $n \neq 0$ and setting

$$C_o(q,t) = \sum_{-m_{max}}^{m_{max}} (-2\pi i \overline{E}_m) H_{-m}(q,t) \quad . \qquad (12)$$

In this case Eq. (8) for $n = 0$ is of course not trivial and $H_o(q)$ in the term (11) is time dependent. An example of such a solution will be given in Section II-6.

2. Algorithm

The characteristics of Eqs. (8) are straight lines of slope $2\pi n$ in the (t,q) plane as shown in Fig. 2. Because of the reality condition (6) it is only necessary to solve these equations for $n \geqslant 0$ so that all characteristics have positive slopes. At each time step, the value of $H_n(q,t)$ is obtained from the iterative formula

$$H_n^{(1+1)}(q,t) = H_n(q-2\pi n \Delta t, t-\Delta t) + \frac{1}{4\pi}(q-2\pi n \Delta t)\Delta t C_n(q-2\pi n \Delta t, t-\Delta t)$$

$$+ \frac{1}{4\pi} q \Delta t C_n^{(1)}(q,t) \quad , \qquad (13)$$

in which the superscript denotes the number of iterations carried out. The results presented later in Section II-6 were obtained using a sinlge iteration.

The (t,q) plane is covered with a grid with mesh sizes Δt and Δq. Values of q in Eq. (13) are chosen to fall at grid points as shown in Fig. 2. The values of $q-2\pi n \Delta t$ then do not fall at grid points and the first two terms in Eq. (13) must be interpolated. A nine-point Lagrangian interpolation was used in the computations presented. With the mesh size Δq, we expect the distribution function $f(x,v,t)$ to be adequately defined over the interval $-v_{max} < v < v_{max}$, in which $v_{max} \sim 1/\Delta q$. At the lower boundary $q = -q_{max}$, the values of $H_n(q-2\pi n \Delta t, t-\Delta t)$ needed in Eq. (13) are unknown. These values are set equal to zero thus truncating the characteristic function at $q = \pm q_{max}$.

The convolution terms (9) are evaluated using discrete Fourier transforms. Consider two arrays of N elements X_m and Y_m, where the subscript m is defined modulo N, and take the discrete Fourier transforms of both arrays,

314
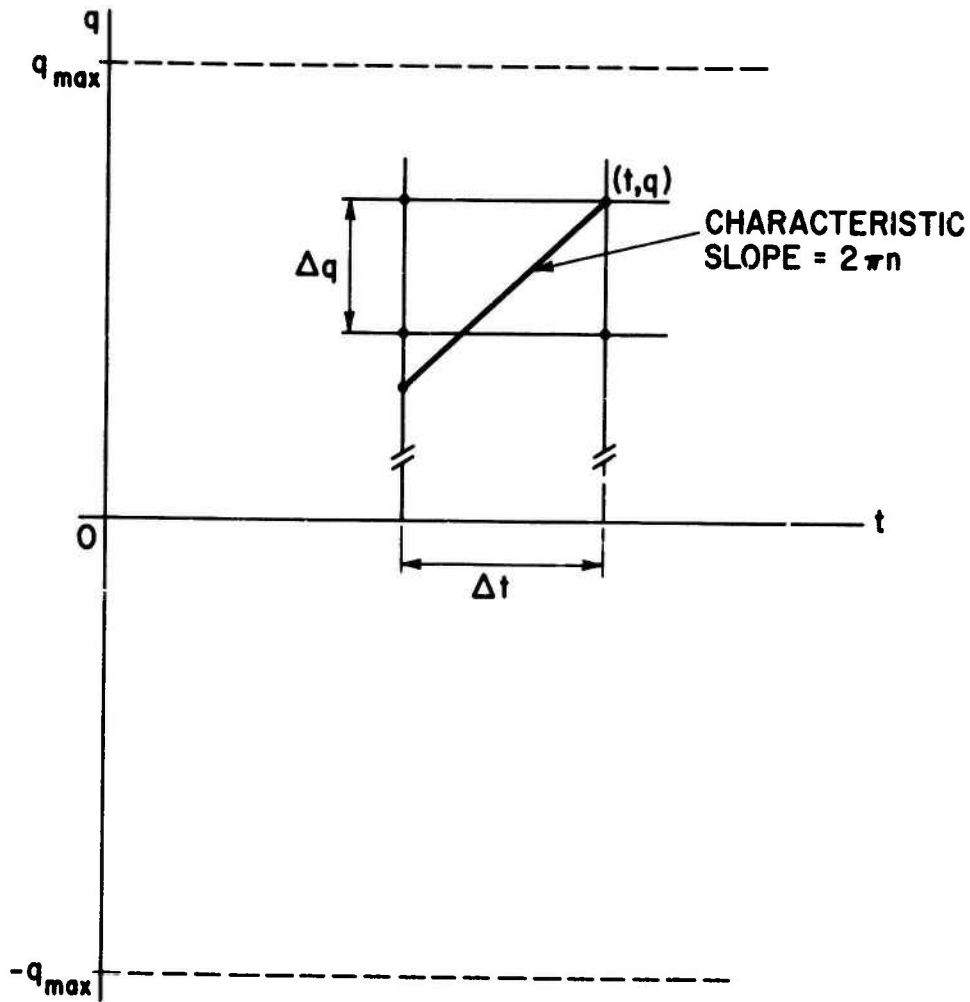
Figure 2   Characteristics of Eq. (8) in the (t,q) plane.

$$\overline{X}_j = \sum_{m=0}^{N-1} X_m e^{\frac{2\pi i}{N} mj} \qquad ,$$

$$\overline{Y}_j = \sum_{m=0}^{N-1} Y_m e^{\frac{2\pi i}{N} mj} \qquad ,$$

where j is also defined modulo N. The discrete Fourier transform of the product $\overline{X}_j \overline{Y}_j$ yields

$$Z_n = \sum_{j=0}^{N-1} \overline{X}_j \overline{Y}_j \, e^{\frac{2\pi i}{N} nj} = N \sum_{m=0}^{N-1} X_m Y_{-n-m} \quad . \qquad (14)$$

Thus the convolution may be computed in terms of discrete Fourier transforms. However, the modes $\overline{E}_m$ and H_m in the definition of C_n are not cyclic in the subscript but are zero for $|m| > m_{max}$. To achieve the same result with periodic arrays it is necessary to increase the size of the arrays by appending zeros. Let N be chosen such that $3m_{max} + 1 \leqslant N = 2^G$, where G is an integer, and set

$$X_m = -2\pi i E_{m-\frac{N}{2}} \quad \text{and} \quad Y_m = H_{m-\frac{N}{2}}$$

for $N/2-m_{max} \leqslant m \leqslant N/2+m_{max}$ and $X_m = Y_m = 0$ for all other values of m in the internal $0 < m < N-1$. Then comparing (9) and (14) yields

$$C_n = \sum_{m=0}^{N-1} X_m Y_{n-m} = \frac{Z_{-n}}{N} \quad . \qquad (15)$$

Using a fast Fourier transform algorithm[14,15] the computing time becomes proportional to $m_{max} \log_2 m_{max}$. This compares with a computing time proportional to m^2_{max} when the convolution C_n is evaluated by direct summation. Letting $j_{max} = 2q_{max}/\Delta q$ denote the number of grid points in the velocity transform direction and neglecting the logarithmic dependence, the computing time per time step is given by $\alpha j_{max} m_{max}$. The constant α for a non-optimized code on the IBM 360/91 was found to be 0.24 ms.

3. Convergence

At each time step the first two terms in the right member of Eq. (13) are known quantities evaluated at the previous time step while the convolution terms $C_n^{(i)}(q,t)$ are linear combinations of the preceeding approximation $H_n^{(i)}(q,t)$. The matrix of the coefficients of these linear combinations is

$$
\underset{\sim}{\Lambda} = -\frac{iq\Delta t}{2}
\begin{bmatrix}
0 & \overline{E}_{-1} & \overline{E}_1 & \overline{E}_{-2} & \cdots \\
\overline{E}_1 & 0 & \overline{E}_2 & \overline{E}_{-1} & \cdots \\
\overline{E}_{-1} & \overline{E}_{-2} & 0 & \overline{E}_{-3} & \cdots \\
\overline{E}_2 & \overline{E}_1 & \overline{E}_3 & 0 & \cdots
\end{bmatrix}
$$

$$
\cdots\cdots
$$

The iterative process defined by Eq. (13) converges only if all the eigenvalues λ_j, for $j = -m_{max}, \ldots, +m_{max}$, of this matrix are smaller than unity. Let $\underset{\sim}{\Lambda}^T$ denote the transposed matrix of $\underset{\sim}{\Lambda}$. We have

$$
|\lambda_j|^2 \leqslant \text{Trace}(\underset{\sim}{\Lambda\Lambda}^T) = q^2 \Delta t^2 m_{max} \sum_{m=1}^{m_{max}} |\overline{E}_m|^2 \quad ,
$$

or

$$
|\lambda_j| \leqslant q\Delta t \sqrt{m_{max} U} \quad ,
$$

where $U = \sum_{m=1}^{m_{max}} |\overline{E}_m|^2$ is the electrostatic energy of the system. The iterative process is therefore convergent if

$$
q_{max} \Delta t \sqrt{m_{max} U} < 1 \quad . \tag{16}
$$

This condition is satisfied by adjusting the time step Δt according to the magnetude of the electrostatic energy. In the examples presented in Section II-6, values of Δt larger than 0.05 were found to satisfy the convergence condition.

4. Truncation

We have observed earlier that the truncation of the functions $H_n(q,t)$ at $n = \pm m_{max}$ and $q = \pm q_{max}$ results in the elimination of the fine structure of the distribution which is represented in the high-order modes (in position and velocity) of $H_n(q,t)$. The truncations at $\pm m_{max}$ and $\pm q_{max}$ are equivalent to an averaging operation of the form defined by Eq. (3) with weight functions

$$w_x(x) = 1 + 2 \sum_{n=1}^{m_{max}} \cos 2\pi n x \quad ,$$

and

$$w_v(v) = \frac{\sin q_{max} v}{\pi v} \quad .$$

The function $w_x(x)$ has a half-width $\Delta x \simeq 1/2 m_{max}$ and the function $w_v(v)$ has a half-width $\Delta v \simeq \pi/q_{max}$. The choice of the cutoff values m_{max} and q_{max} must be made such that the half-widths Δx and Δv are small compared to the characteristic lengths and velocities of the system. For example, if the phenomenon being studied involves trapping oscillations with a trapping length L_{TR}, it is generally found that a half-width $\Delta x \simeq L_{TR}/16$ is required. Thus the study of a two-stream instability in which the mode $n = 5$ is dominant requires a solution including approximately 40 modes. Both weight functions have negative side lobes which introduce ripples in the distribution function. For sufficiently small half-widths, however, these ripples remain on a small scale and have no effect on the large-scale features of the solutions. As noted earlier, the present averaging operation does not affect the moments of the distribution to any order.

5. Conservation Laws

Setting $n = 0$ and $q = 0$ in Eq. (8) yields

$$\frac{\partial}{\partial t} H_0(0,t) = 0 \quad . \tag{17}$$

318

Solutions of Vlasov Equation

Let $H_n^R(q,t)$ and $H_n^I(q,t)$ denote the real and imaginary parts of $H_n(q,t)$. The reality condition (6) requires $H_0^I(0,t) = 0$ and $H_0^R(0,t)$ denotes the (normalized) number of particles in the system. Thus, Eq. (17) is an expression of the conservation of particles in the system. From Eq. (13) we observe that $H_0(0,t)$ must remain constant, and particle conservation is therefore satisfied exactly in the numerical solution.

Taking the derivative of Eq. (8) with respect to q and setting $q = 0$ and $n = 0$, in the case where no external fields are applied, yields

$$\frac{\partial}{\partial t} \left(\frac{\partial H_0}{\partial q} \right)_{q=0} = 0 \quad .$$

The reality condition (6) requires $H_0^R(q)$ to be an even function and $H_0^I(q)$ to be an odd function. Thus, the above equation reduces to

$$\frac{\partial}{\partial t} \left(\frac{\partial H_0^I}{\partial q} \right)_{q=0} = 0 \quad , \tag{18}$$

which is an expression of momentum conservation in the system.

Taking the second derivative of Eq. (8), truncated at $\pm m_{max}$, and setting $q = 0$ and $n = 0$ yields

$$\frac{\partial}{\partial t} \left\{ -\frac{1}{2} \left(\frac{\partial^2 H_0^R}{\partial q^2} \right)_{q=0} + \sum_{m=1}^{m_{max}} \frac{1}{(2\pi m)^2} \left| H_m(q=0) \right|^2 \right\} = 0 \tag{19}$$

In deriving the above equation, it has been assumed that no external fields are applied, and use has been made of the reality condition (6) which implies $\left(\partial^2 H_0^I / \partial q^2 \right)_{q=0} = 0$. The first term in the bracket represents the kinetic energy of the system,

$$T = -\frac{1}{2} \left(\frac{\partial^2 H_0^R}{\partial q^2} \right)_{q=0} ,$$

and the second term represents electrostatic energy,

Denavit

$$U = \sum_{m=1}^{m_{max}} \frac{\left| H_m(q=0) \right|^2}{(2 \pi m)^2} \quad .$$

Thus, Eq. (19) is an expression of the conservation of energy in the system, $T + U = $ constant. Since Eq. (19) was derived from Eqs. (8) truncated at $\mp m_{max}$, a check of the energy cannot reflect errors due to truncation but only errors due to other causes.

Momentum and energy checks are carried out in the numerical solution by differentiations of the central difference interpolation formula[16] for the functions $H_o^R(q)$ and $H_o^I(q)$ at $q = 0$. Five points on either side of $q = 0$ are used.

6. Examples

Case 1: Two-Stream Instability with Equal Beams

Consider a two-stream instability resulting from the initial conditions defined by the distribution function

$$f(x,v, t=0) = f_o(v) \left[1 + 2 \epsilon \cos 2\pi x \right] \quad ,$$

with

$$f_o(v) = \frac{1}{v_{th}^3 \sqrt{2 \pi}} \quad v^2 e^{-v^2/2 v_{th}^2} \quad ,$$

and $v_{th} = 0.3/\pi$, $\epsilon = 2.5 \ 10^{-2}$. These initial conditions correspond to a system length $L = 10.5 \lambda_D$ where $\lambda_D = v_{th}/\omega_p$ is the Debye Length. The initially excited mode has a wavelength equal to the length of the system, i. e., corresponds to the first mode $n = 1$. The linear growth rates for this problem have been computed by Grant and Feix[17]. The first mode is the only unstable mode and has a growth rate $\gamma = 0.24$.

The solid curve in Fig. 3 corresponds to the electrostatic energy with $m_{max} = 21$, $q_{max} = 256$ and $\Delta q = 4$. This energy grows at approximately the linear growth rate from $t = 10$ to $t = 20$ and saturates at 2.2% of the total energy. The frequency of trapped electron oscillations at saturation is
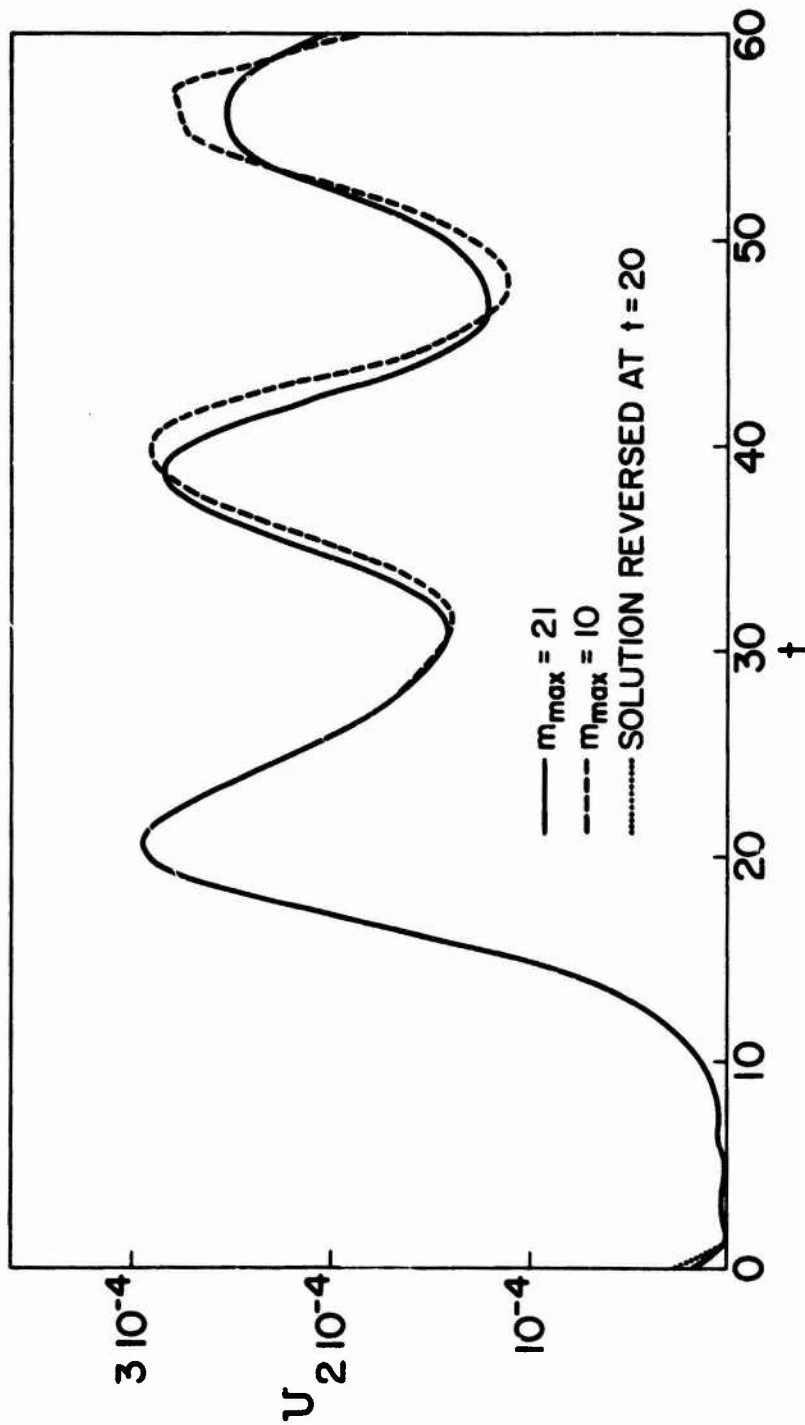
Figure 3   Electrostatic energy for two-stream instability with equal beams,

Case 1, by the Fourier-Fourier transform method.

$\omega_B = 0.33$, which corresponds to a trapping period $\tau_{TR} = 19.2$. After saturation the electrostatic energy oscillates with a period of approximately 20. The amplitude of the first mode (n = 1) is approximately on order of magnitude larger than the amplitudes of the other modes (n $\geqslant$ 2). The higher-order modes, however, have a significant effect on the solution as shown by the broken line in Fig. 2 which corresponds to a truncation at $m_{max} = 10$. The solution was checked by reversing it at t = 20 and the small broken line near t = 0 in Fig. 3 shows the deviation of the reversed solution from the forward solution. The relative energy error is $2 \cdot 10^{-4}$.

Vlasov solutions for this example have been carried out by Armstrong Nielson[11] using the Fourier-Hermite method. These solutions, however, were limited to five and six spatial modes and deviate from the present results for t $\geqslant$ 25. Particle simulations have also been carried out by Armstrong and Nielson[11] and by Denavit and Kruer[18]. The results of these simulations are in close agreement with the results of the present Vlasov solution.

Case 2: Two-Stream Instability with Unequal Beams

Consider now an instability resulting from the interaction of a small beam with a Maxwellian plasma. The initial conditions are

$$f(x,v,t=0) = f_o(v) \left[1 + 2\epsilon \sum_{n=1}^{21} n \cos (2\pi n x + \phi_n) \right] ,$$

with

$$f_o(v) = \frac{1}{\sqrt{\pi} v_p} \left[n_p e^{-v^2/v_p^2} + n_b e^{-(v-v_d)^2/v_b^2} \right] ,$$

and $v_p = \sqrt{2} \cdot 10^{-2}$, $v_d = 2.6 \, v_p$, $v_b = 0.25 \, v_p$, $n_p = 0.95$, $n_b = 0.05$, $\epsilon = 2.5 \cdot 10^{-4}$ and initial phases ϕ_n chosen at random. Thus the small beam contains 5% of the plasma and its mean velocity is 3.66 thermal velocities. These initial conditions correspond to a system length of 100 λ_D.

Solutions of Vlasov Equation

The dispersion relation for this case is

$$Z'\left(\frac{\zeta}{v_p}\right) + \frac{n_b}{n_p}\left(\frac{v_p}{v_b}\right)^2 Z'\left(\frac{\zeta - v_d}{v_b}\right) = \frac{2m}{n_p} \tag{20}$$

in which $\zeta = \omega/k$ and Z' is the derivative of the plasma dispersion function[23].
Solving this equation for the growth rate $\gamma = \mathrm{Im}\,\omega$ gives the curve shown in
Fig. 4. We note that modes $n = 1$ through 9 are unstable.

Linear numerical solutions, based on the convolution term (11), were
carried out and the corresponding growth rates are shown by the circles in
Fig. 4. The values of γ given in Fig. 4 correspond to the growing modes of
the plasma. For each value of n, however, the plasma also has damped modes
which correspond to other zeros of the dispersion relation (20). An initial
perturbation in density generally excites several damped modes in addition to
the growing mode corresponding to a given value of n. Linear solutions thus
generally display an initial transcient which must damp away before the growth
rates corresponding to Fig. 4 can be observed. In the case of the weakly grow-
ing modes such as $n = 1$, the transcient behavior was found to be dominant for
long times ($t \approx 100$). Thus it is unlikely that such weakly growing modes
can be observed in a nonlinear problem.

A "quasi-linear" numerical solution, in which mode-coupling terms were
neglected, was carried out using the convolution terms (11) and (12). The
electrostatic energy for this solution is shown in Fig. 5. The most unstable
mode, $n = 5$, is dominant in this solution. The electrostatic energy saturates
at approximately 2.1% of the total energy. The frequency of oscillations of
electrons trapped in the potential trough of the dominant mode is $\omega_B = \left(2m\,\overline{E}_n\right)^{\frac{1}{2}}$
$= 0.148$, for $n = 5$. We observe that this value is close to the growth rate of
mode 5. After saturation, the electrostatic energy drops sharply and oscillates
at a lower level.
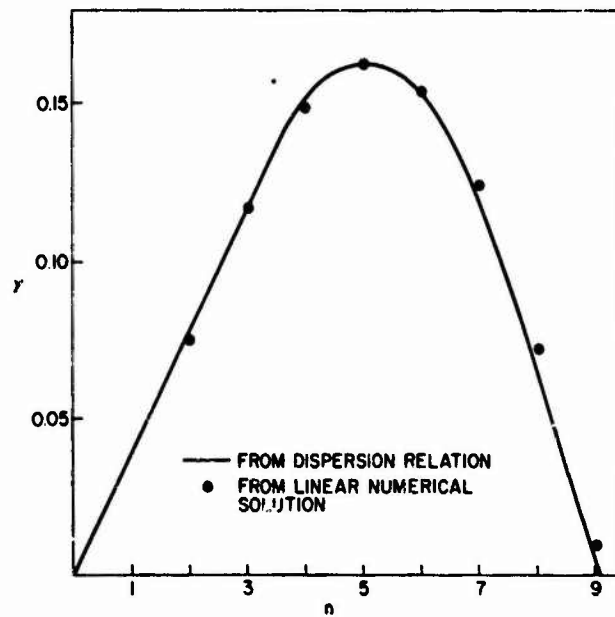
Figure 4   Linear growth rates for two-stream instability with unequal beams, Case 2.
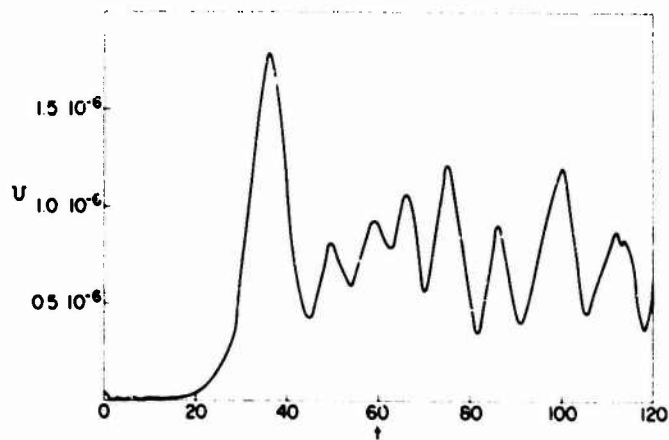
Figure 5   Electrostatic energy for "quasi-linear" solution of two-stream instability ith unequal beams, Case 2. (mode coupling is neglected).

324

Solutions of Vlasov Equation

The electrostatic energy for the nonlinear solution, including mode coupling, is shown in Fig. 6. This solution was carried out with $m_{max} = 42$, $q_{max} = 25/v_p$ and $\Delta q = q_{max}/128$. The electrostatic energy saturates at approximately 1.6% of the total energy then falls and shows several oscillations at a lower level. We observe that the "quasi-linear" solution shown in Fig. 5 is qualitatively correct. The effect of mode coupling is to decrease the growth rate and lower the saturation value.

The density in phase near saturation is shown in Fig. 7. Numbers from 1 to 9 indicate relative densities. Blanks correspond to densities which are less than one-tenth of the maximum density. Negative signs correspond to negative values of the density larger in magnitude than one-tenth of the maximum density.

Particle simulations have been carried out for this example by Morse and Nielson[3] and Denavit and Kruer[18]. The results of Morse and Nielson agree only qualitatively with the present Vlasov solution. The differences, however, may be attributed to the longer periodicity length considered by these authors and the random nature of their initial conditions. The results obtained using Kruer's finite-size particle code with a quiet start[18] agree quantitatively with the present solution out to $t \simeq 70$, after which the two solutions remain in qualitative agreement.

Case 3: Echo

The echo problem considered here corresponds to an example given by O'Neil and Gould[19]. A uniform plasma with a Maxwellian velocity distribution is initially excited by an external electric field pulse with wave number k_1. Mode k_1 then decays exponentially at the Landau damping rate and the perturbation part of the distribution function takes the form $f_1(v) \exp(-i k_1 x + i k_1 v t)$. For large t the integral over v of this distribution function phase mixes and
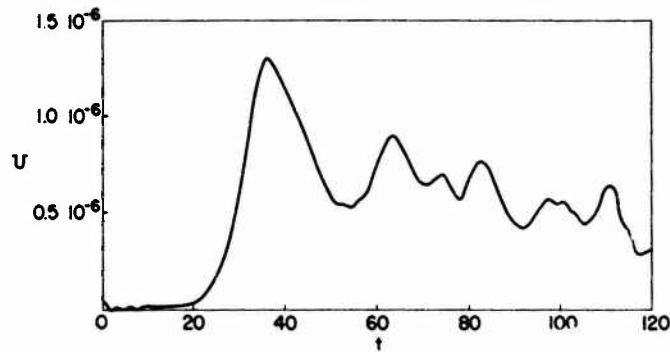
Figure 6   Electrostatic energy for nonlinear solution of two-stream
            instability with unequal beams, Case 2, by Fourier-Fourier
            transform method.

t = 36.38
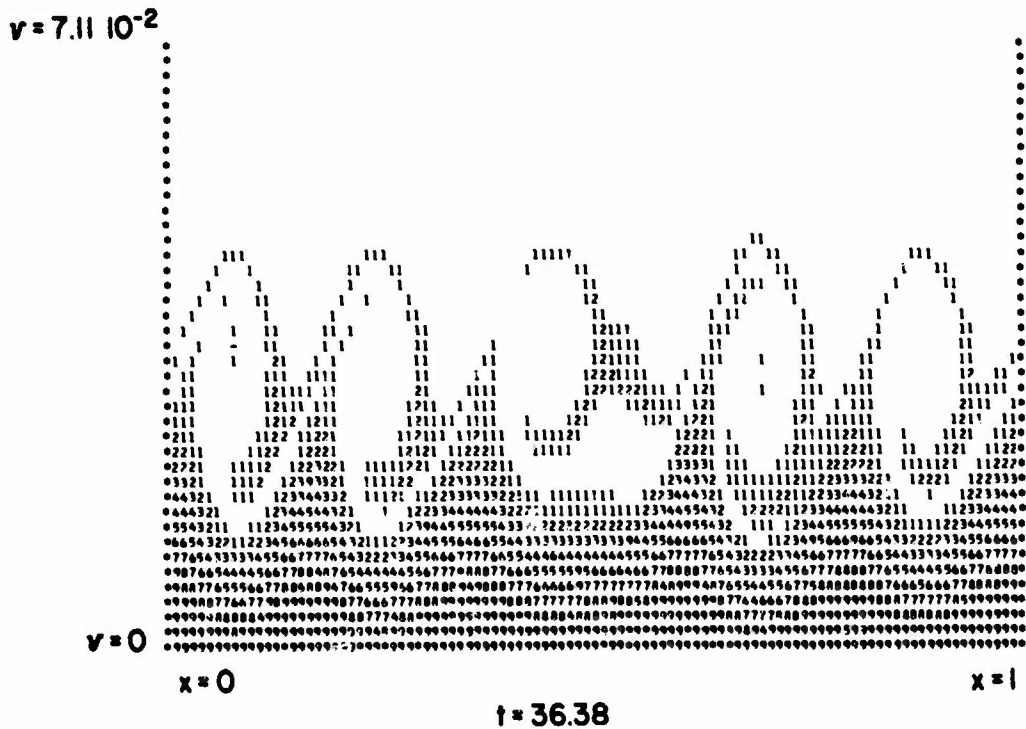
Figure 7   Density in phase near saturation for two-stream instability with
            unequal beams, Case 2, by Fourier-Fourier transform method.

326

Solutions of Vlasov Equation

does not result in any density perturbation. A second wave of wave number k_2 is then excited by an external pulse at time τ. This wave also damps out but it modulates the distribution function of the first wave to give a second order distribution function of the form $f_1(v)f_2(v)\exp\{i(k_2-k_1)x-i(k_2-k_1)v[t-k_2\tau/(k_2-k_1)]\}$. At time $\tau' = k_2\tau/(k_2-k_1)$ the coefficient of v in this exponential vanishes and the integral over v no longer vanishes. A new wave, called echo, then appears in the plasma with wave number $k_3 = k_2-k_1$.

In the example considered here, $k_1\lambda_D = 1\sqrt{2}$ and $k_2\lambda_D = \sqrt{2}$. Thus $k_3\lambda_D = 1/\sqrt{2}$ and the echo appears in the initially excited mode at time $\tau' = 2\tau$. The thermal velocity is chosen as $v_{th} = 1/2\pi\sqrt{2} = 0.113$ so that k_1 and k_2 both correspond to mode $n = 1$, while k_2 corresponds to mode $n = 2$. Mode $n = 1$ is excited initially by applying an external electric field $E_o^{ext}(x) = E_{DR}\sin 2\pi x$ with $E_{DR} = 0.444v_{th}$ from $t = 0$ to $t = 0.2$, and mode $n = 2$ is excited by applying the external field $E_\tau^{ext}(x) = E_{DR}\sin 4\pi x$ from $t = 10$ to $t = 10.2$. Only five spatial modes are retained in the present computation. Since the echo depends on the fine structure of the distribution function it is important in the present case to retain this structure and q_{max} is chosen so that modes $n = 1$ to $n = 4$ are not turncated out to $t_{max} = 30$, thus $q_{max} = 8\pi t_{max} = 755$. With $\Delta q = q_{max}/256$ the distribution function is adequately represented out to $v_{max} \simeq 1/\Delta q = 3v_{th}$.

The density perturbation for mode $n = 1$ is shown on a logarithmic scale at (a) in Fig. 8. It rises rapidly during the short driving period, then decays exponentially at the Landau damping rate ($\gamma \simeq -0.40$). The echo appears between $t = 10$ and $t = 30$ with a maximum at $t = \pi' = 20$. The echo is shown on a linear scale at (b) in Fig. 8. The results shown on this figure agree with the results shown in Fig. 1(A) of O'Neil and Gould.

III. DIRECT INTEGRATION PHASE PLANE

1. Algorithm

According to the principle of conservation of density in phase, the solution of the Vlasov equation may be written formally as

(a)

H₁(q=0,t): DENSITY PURTURBATION FOR MODE m = 1

Figure 8. Particle density perturbation for echo problem, Case 3.

(b)

H₁(q=0,t): DENSITY PERTURBATION FOR MODE m = 1
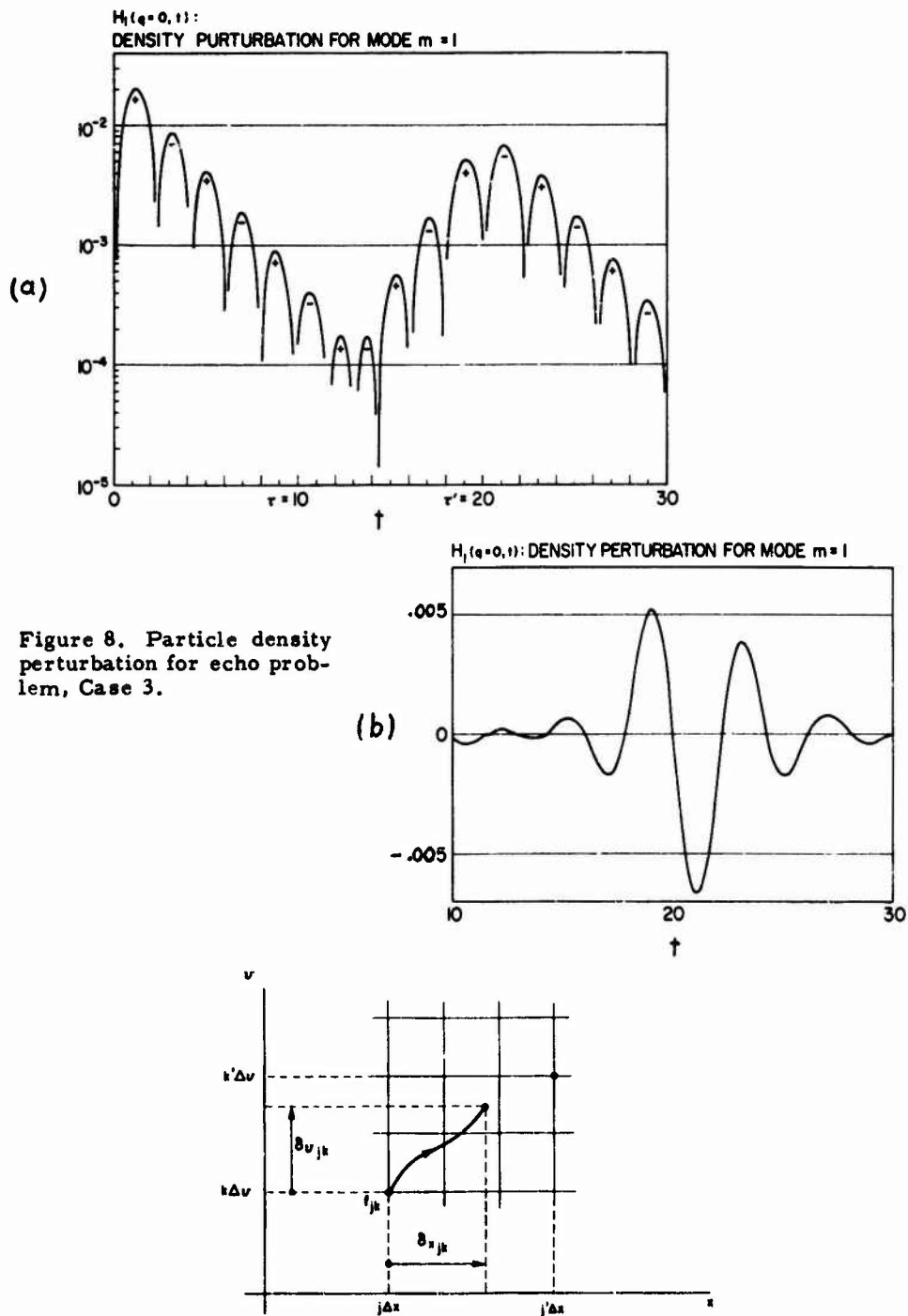
Figure 9   Characteristics of Vlasov equation in phase plane.

328

Solutions of Vlasov Equation

$$f(x + \delta x, v + \delta v, t + \Delta t) = f(x,v,t) \tag{21}$$

in which δx and δv are the position and velocity increments during the time interval Δt of a particle located at (x,v) at time t. The phase plane is covered with a rectangular grid with mesh sizes Δx and Δv as shown in Fig. 9. The grid extends from $-v_{max}$ to $+v_{max}$ and the value of v_{max} is chosen large enough so that the grid covers all significant portions of the phase plane.

The position and velocity increments are computed by considering sample particles of masses $f(x_j, v_k, t)$ located at the grid points (x_j, v_k), and computing their position and velocity increments δx_{jk} and δv_{jk} during the time interval Δt. The sample particle locations in the phase plane at $t + \Delta t$ no longer correspond to grid points and the distribution function must be reconstructed at that time by distributing the mass of each sample particle among the neighboring grid points,

$$\widetilde{f}(x_j{}', v_k{}', t+\Delta t) = \sum_{j,k} f(x_j + \delta x_{jk}, v_k + \delta v_{jk}, t+\Delta t) \, w_x(x_j{}'-x_j-\delta x_{jk}) w_v(v_k{}'-v_k-\delta v_{jk}) \tag{22}$$

Applying this operation to the solution of Vlasov's equation (21) yields

$$f(x_j{}', v_k{}', t+\Delta t) = \sum_{j,k} f(x_j, v_k, t) w_x(x_j{}'-x_j-\delta x_{jk}) w_v(v_k{}'-v_k-\delta v_{jk}) \tag{23}$$

The weight functions w_x and w_v determine what fraction of the mass of a sample particle is assigned at each neighboring grid point. The discrete sum in Eq. (22) defines an averaging operation similar to Eq. (3). In the present method the averaging operation must be carried out by a discrete sum instead of an integral since the phase plane itself has been discretized by the introduction of a grid. Weight functions for which the averaging operation conserves any finite number of moments are derived in Sec. III-2. It is not possible, however, to derive functions w_x and w_v for which all moments of the distribution function are conserved, as was done in the Fourier-Fourier transform method. This results in some diffusion of the distribution function in the phase plane.

329

The evaluation of the position and velocity increments δx_{jk} and δv_{jk} of the sample particles is presented in Sec. III-3. The method uses an area weighting scheme and is based on a Lagrangian formulation of particle dynamics in which energy is conserved[20].

In a number of problems of physical interest, the initial distribution function consists of several relatively cold beams and only a fraction of the phase plane is occupied by particles. As the solution proceeds in time, the principle of conservation of density in phase (which is still approximately satisfied by the numerical solution) requires that this fraction must remain constant. Where no particles are present, the distribution function is zero and does not need to be advanced. This is achieved in the code by setting a threshold value (for example 10^{-5} times the maximum value of the distribution function) below which no sample particle is considered. The electric potential is computed by Fourier transforms so that the electron density is automatically renormalized at each time step. Thus, the slight loss of particles resulting from a finite threshold does not result in the build up of a net charge in the plasma. This feature of the direct method of integration, which has no counterpart in transform methods, may yield a considerable saving of computing time when multidimensional problems are considered.

It is not necessary to reconstruct the distribution function by the averaging operation (23) for every time step at which the electric field is computed. If Δt is the time step used to advance the sample particles, the electric field needs to be computed after each Δt increment, but the distribution function can be reconstructed only every $N\Delta t$, where N is a properly chosen integer. In addition to saving computing time, this procedure reduces the diffusion in phase plane caused by application of the averaging operation.

The Vlasov solution described above in which the distribution function is reconstructed only every Nth time step begins to resemble particle solutions.

330

Solutions of Vlasov Equation

Particle solutions in which particle of different masses are loaded on an (x,v) grid to represent the initial distribution function have been used by Byers[5]. In such solutions the plasma consists of a number of discrete small beams, which are subject to instabilities having growth rates $\gamma \simeq k \Delta v$ where $k = 2\pi n$ is the wave number and Δv is the velocity interval between beams (equal to the mesh size). In particle solutions, the distribution function is never reconstructed ($N = \infty$), and beaming instabilities occur at time $t_{max} = 2\pi/k \Delta v$ (see Appendix). By reconstructing the distribution function at time intervals which are small compared to $(k \Delta v)^{-1}$, the plasma is forced to behave as a continuum and no beaming instabilities can develop.

2. Weight Functions

To derive weight functions $w_x(x)$ and $w_v(v)$ for which the averaging operation defined by Eq. (22) conserves a finite number of moments it is sufficient to consider the one-dimensional operation

$$f(v_{j'}) = \sum_j f(v_j + \delta v_j)w(v_{j'} - v_j - \delta v_j). \tag{24}$$

The weight functions thus found will be applicable to either coordinate or velocity. Such weight functions, conserving zeroth, first and second order moments have been derived by K-W Li[7].

a. Moment Conservation Conditions

The moment of order n before averaging is

$$\langle v^n \rangle = \sum_j (v_j + \delta v_j)^n f(v_j + \delta v_j). \tag{25}$$

After averaging the same moment becomes

$$\langle \tilde{v^n} \rangle = \sum_{j'} v_{j'}^n \, \tilde{f}(v_{j'}). \tag{26}$$

Substituting (24) into (26) and reversing the order of the sums over j and j' yields

$$\langle \widetilde{v^n} \rangle = \sum_j f(v_j + \delta v_j) \sum_{j'} v_{j'}^n \, w(v_j - v_j - \delta v_j) .$$

The moments (25) and (26) are therefore equal if the equality

$$\sum_{j'} v_{j'}^n \, w(v_j - v_j - \delta v_j) = (v_j + \delta v_j)^n \qquad (27)$$

holds for all values of $v_j + \delta v_j$.

b. Derivation of Weight Functions

Let $k = j' - j$, since the variable v is represented on a grid with mesh size Δv we have $v_{j'} = (j + k)\Delta v$, $v_j - v_j = k\Delta v$ and $v_j = j\Delta v$. The moment condition (27) becomes

$$\sum_k (j+k)^n \, w[(k-p)\Delta v] = (j+p)^n \qquad (28)$$

where $p = \delta v_j / \Delta v$. We may assume without loss of generality that δv_j is positive and smaller than the mesh size Δv so that $0 \le p < 1$. The function $w(v)$ is now assumed to be even and to extend over Q meshes Δv on either side of the origin. The condition (28) is satisfied if

$$\sum_{k=1-Q}^{Q} k^m w[(k-p)\Delta v] = p^m \qquad (29)$$

for $m = 0, 1, \ldots, n$. All moments up to order n will then be conserved.

We first assume that n is odd and set $Q = (n+1)/2$. Consider the Lagrangian interpolation with $n + 1$ points of the function p^m. Since $m \le n$, the interpolation is exact and we have[21]

$$\sum_{k=1-Q}^{Q} k^m A_k^{(n+1)}(p) = p^m \qquad (30)$$

in which the functions $A_k^{(n+1)}(p)$ for $1-Q \le k \le Q$ and $0 \le p \le 1$ are the Lagrangian coefficients with $n + 1$ points. Comparing (29) and (30) yields the desired

332

Solutions of Vlasov Equation

weight function,

$$w[(k-p)\Delta v] = A_k^{(n+1)}(p),$$

or

$$w(v) = A_k^{(n+1)}(k - \frac{v}{\Delta v}), \qquad \text{for} \qquad (k-1)\Delta v \le v \le k\Delta v \quad (31)$$

with $k = (1-n)/2, \ldots, (1+n)/2$. For n even, we set $Q = 1 + n/2$. The Lagrangian coefficients in this case do not yield even weight function. Even weight functions may, however, be obtained by symmetrization as follows,

$$w(v) = \begin{cases} \frac{1}{2} A_{-\frac{n}{2}}^{(n+1)}(1 + \frac{n}{2} + \frac{v}{\Delta v}) & -(\frac{n}{2}+1)\Delta v \le v \le -\frac{n}{2}\Delta v \\ \frac{1}{2}\left[A_k^{(n+1)}(k - \frac{v}{\Delta v}) + A_{1-k}^{(n+1)}(1-k + \frac{v}{\Delta v})\right] & (k-1)\Delta v \le v \le k\Delta v \qquad (32) \\ \frac{1}{2} A_{-\frac{n}{2}}^{(n+1)}(1 + \frac{n}{2} - \frac{v}{\Delta v}) & \frac{n}{2}\Delta v \le v \le (\frac{n}{2}+1)\Delta v \end{cases}$$

with $k = 1-n/2, \ldots, n/2$.

c. Examples

For $n = 1$ the averaging operation (24) conserves particles and momentum. Since n is odd, Eq. (31) is applicable and we have

$$w^{(1)}(v) = A_1^{(1)}(1 - \frac{v}{\Delta v}) = 1 - \frac{v}{\Delta v}$$

for $0 \le v \le \Delta v$. In the interval $-\Delta v \le v \le 0$, the function $w^{(1)}(v)$ is defined by symmetry and it is zero for $|v| > \Delta v$. This function is illustrated at (a) in Fig. 10. For $n = 2$ the averaging operation conserves particles, momentum and energy. Since n is even we apply Eqs. (32),

Solutions of Vlasov Equation

weight function,

$$w[(k-p)\Delta v] = A_k^{(n+1)}(p),$$

or

$$w(v) = A_k^{(n+1)}\left(k - \frac{v}{\Delta v}\right), \qquad \text{for} \qquad (k-1)\Delta v \le v \le k\Delta v \quad (31)$$

with $k = (1-n)/2, \ldots, (1+n)/2$. For n even, we set $Q = 1 + n/2$. The Lagrangian coefficients in this case do not yield even weight function. Even weight functions may, however, be obtained by symmetrization as follows,

$$w(v) = \begin{cases} \frac{1}{2} A_{-\frac{n}{2}}^{(n+1)}\left(1 + \frac{n}{2} + \frac{v}{\Delta v}\right) & -(\frac{n}{2}+1)\Delta v \le v \le -\frac{n}{2}\Delta v \\[2mm] \frac{1}{2}\left[A_k^{(n+1)}\left(k - \frac{v}{\Delta v}\right) + A_{1-k}^{(n+1)}\left(1-k + \frac{v}{\Delta v}\right)\right] & (k-1)\Delta v \le v \le k\Delta v \qquad (32) \\[2mm] \frac{1}{2} A_{-\frac{n}{2}}^{(n+1)}\left(1 + \frac{n}{2} - \frac{v}{\Delta v}\right) & \frac{n}{2}\Delta v \le v \le (\frac{n}{2}+1)\Delta v \end{cases}$$

with $k = 1-n/2, \ldots, n/2$.

c. Examples

For $n = 1$ the averaging operation (24) conserves particles and momentum. Since n is odd, Eq. (31) is applicable and we have

$$w^{(1)}(v) = A_1^{(1)}\left(1 - \frac{v}{\Delta v}\right) = 1 - \frac{v}{\Delta v}$$

for $0 \le v \le \Delta v$. In the interval $-\Delta v \le v \le 0$, the function $w^{(1)}(v)$ is defined by symmetry and it is zero for $|v| > \Delta v$. This function is illustrated at (a) in Fig. 10. For $n = 2$ the averaging operation conserves particles, momentum and energy. Since n is even we apply Eqs. (32),

$$
w^{(2)}(v) = \begin{cases} \tfrac{1}{2}\left[A_1^{(3)}(1-\tfrac{v}{\Delta v}) + A_0^{(3)}(\tfrac{v}{\Delta v})\right] = 1-\tfrac{v}{\Delta v} + \tfrac{1}{4}\tfrac{v}{\Delta v}(1-\tfrac{v}{\Delta v}) \\ \qquad\qquad\qquad\qquad\qquad\qquad \text{for } 0 \le v \le \Delta v \\[2mm] \tfrac{1}{2}A_{-1}^{(3)}(2-\tfrac{v}{\Delta v}) = \tfrac{1}{4}(2-\tfrac{v}{\Delta v})(1-\tfrac{v}{\Delta v}) \\ \qquad\qquad\qquad\qquad\qquad\qquad \text{for } \Delta v \le v \le 2\Delta v \end{cases}
$$

This function is illustrated at (b) in Fig. 10, it extends over four meshes and has negative side lobes. The fifth degree weight function $w^{(5)}(v)$ is illustrated at (c) in Fig. 10. This function extends over six meshes and has negative and positive side lobes reminiscent of the weight function $\sin(\pi v/\Delta v)/(\pi v/\Delta v)$ used in the Fourier-Fourier transform method.

Most of the computations presented in Sec. III-4 are based on the quadratic weight function $w^{(2)}(v)$ for $w_x(x)$ and $w_v(v)$. However, some computations using linear and fifth-degree weight functions are also presented.

3. Position and Velocity Increments

Let $f_{jk} = f(x_j, v_k, t_0)$ denote the value of the distribution function at the grid point (x_j, v_k) at time t_0 and let $\delta x_{jk}(t)$ denote the displacement of the sample particle of mass f_{jk} located at (x_j, v_k) at time t_0. The position and velocity increments δx_{jk} and $\delta v_{jk} = \dot{\delta x}_{jk}$ will be computed as functions of time using a Lagrangian formulation derived by R. Lewis[20]. This formulation yields an algorithm for advancing sample particles which conserves energy independently of the mesh size Δx.

a. Lagrangian Formulation

The electrostatic potential $\Psi(x,t)$ is defined in terms of a base function $\Phi(x)$ and a set of time dependent coefficients $\alpha_j(t)$ by the linear combination

$$
\Psi(x,t) = \sum_{j=0}^{J-1} \alpha_j(t)\Phi(x-x_j). \tag{33}
$$

334
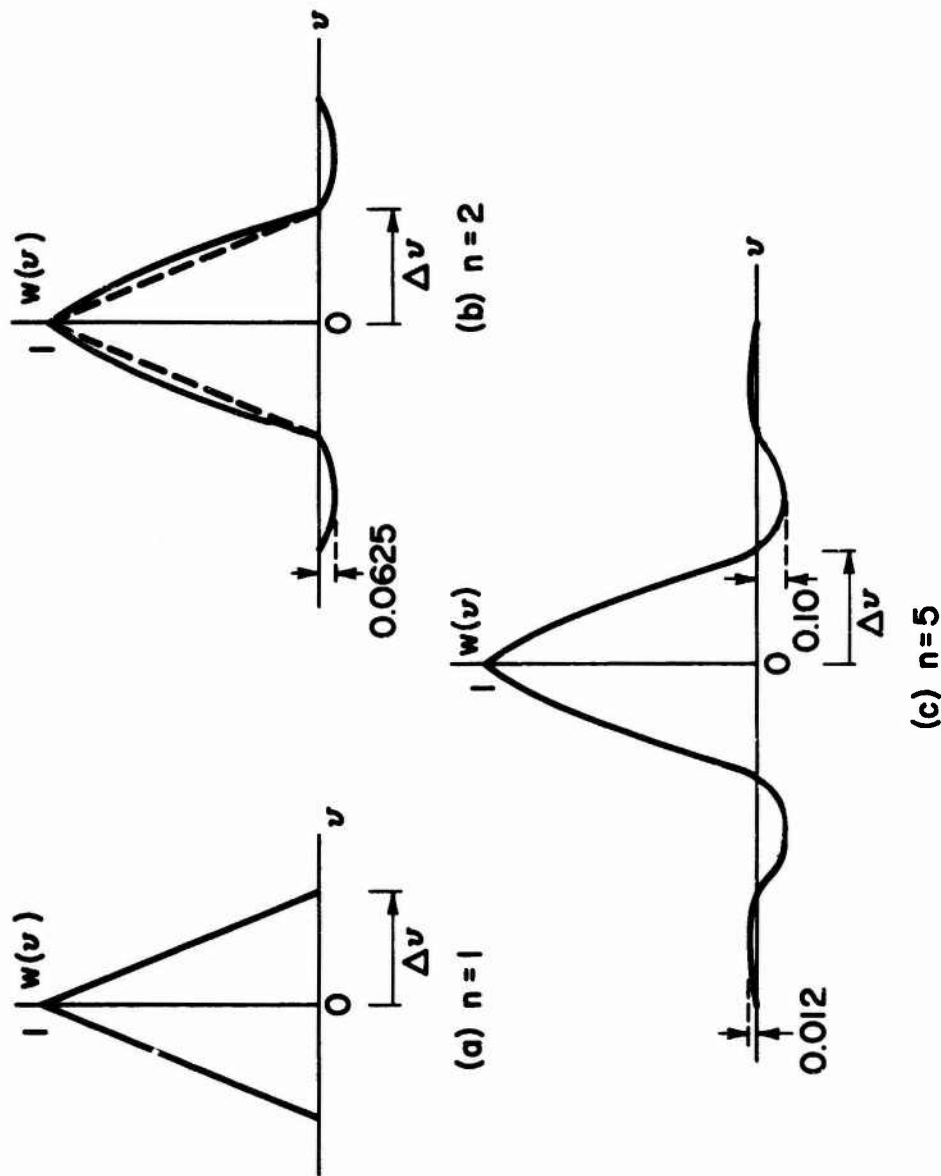
Figure 10   Examples of weight functions for averaging of the distribution
in phase plane.

Here $x_j = j\Delta x$, for $j = 0, \ldots, J-1$, denote the grid point locations and J is the number of grid points in the x direction. The Lagrangian for a system of charged particles is

$$L = \sum_{j=0}^{J-1} \sum_{k=1}^{K} \tfrac{1}{2} f_{jk} \dot{\delta x}_{jk}^2 + \sum_{j=0}^{J-1} \sum_{k=1}^{K} f_{jk} \sum_{i=0}^{J-1} \alpha_i \phi(x_j + \delta x_{jk} - x_i)$$

$$+ \int_0^1 \left\{ \tfrac{1}{2} \left[\sum_{j=0}^{J-1} \alpha_j \phi'(x-x_j) \right]^2 - \sum_{j=0}^{J-1} \alpha_j \phi(x-x_j) \right\} \, dx \tag{34}$$

where K is the number of grid points in velocity and $\phi'(x) = d\phi/dx$. The first term in Eq. (34) is the kinetic energy, the second term is the negative of the interaction energy and the third term is the electrostatic energy of the system.

The equations of motion are obtained by taking variations with respect to the particle displacements δx_{jk},

$$\ddot{\delta x}_{jk} = \sum_{i=0}^{J-1} \alpha_i(t) \phi'(x_j + \delta x_{jk} - x_i) \tag{35}$$

and Poisson's equation is obtained by taking variations with respect to the potential coefficients α_i,

$$\sum_{i=0}^{J-1} \alpha_i \int_0^1 \phi'(x-x_i) \phi'(x-x_j) dx = \int_0^1 \phi(x-x_j) dx - \sum_{i=0}^{J-1} \sum_{k=1}^{K} f_{ik} \phi(x_i + \delta x_{ik} - x_j) \tag{36}$$

b. Base Function

The specific algorithm to be used now depends on the form of the base function $\phi(x)$, which determines the charge sharing scheme to be used in advancing particles. In the present algorithm, particles having a triangular charge distribution with half-width Δx are used. The corresponding base function is

$$\phi(x) = \begin{cases} \frac{1}{2}\left(\frac{3}{2} + \frac{x}{\Delta x}\right)^2 & \text{for } -\frac{3\Delta x}{2} \leq x \leq -\frac{\Delta x}{2} \\[2mm] \frac{3}{4} - \left(\frac{x}{\Delta x}\right)^2 & \text{for } -\frac{\Delta x}{2} \leq x \leq +\frac{\Delta x}{2} \\[2mm] \frac{1}{2}\left(\frac{3}{2} - \frac{x}{\Delta x}\right)^2 & \text{for } \frac{\Delta x}{2} \leq x \leq \frac{3\Delta x}{2} \end{cases}$$

Let x_j, denote the grid point location closest to the sample particle (jk) and set $p = (x_j + \delta x_{jk} - x_j)/\Delta x$, then $|p| \leq \frac{1}{2}$. When the above base function is substituted into the right member of Eq. (35) the sum reduces to three terms and we have

$$\delta x_{jk} = \frac{1}{\Delta x}\left[-\alpha_{j-1}\left(\frac{1}{2}-p\right) - 2\alpha_j p + \alpha_{j+1}\left(\frac{1}{2}+p\right)\right] \tag{37}$$

Substituting the base function into Eq. (36) yields

$$\frac{1}{6\Delta x}\left[-\alpha_{j-2} - 2\alpha_{j-1} + 6\alpha_j - 2\alpha_{j+1} - \alpha_{j+2}\right] = \Delta x \cdot \beta_j, \tag{38}$$

where

$$\beta_j = \sum_{i=0}^{J}\sum_{k=1}^{K} f_{ik}\phi(x_i + \delta x_{ik} - x_j) \tag{39}$$

is the charge assigned to grid point j. Note that the left member of Eq. (38) is a finite-difference representation of the second derivative of the potential.

Since periodic boundary conditions are assumed it is convenient to solve Poisson's equation by discrete Fourier-transforms. Let

$$\bar{\alpha}_n = \sum_{j=0}^{J-1} \alpha_j e^{\frac{2\pi i}{J}nj}$$

and

$$\bar{\beta}_n = \sum_{j=0}^{J-1} \beta_j e^{\frac{2\pi i}{J}nj}$$

denote the transforms of the arrays α_j and β_j. Multiplying Eq. (38) by $\exp(2\pi inj/J)$, summing over j and solving for $\bar{\alpha}_n$ yields

337

$$\overline{\alpha}_n = \frac{-\overline{\beta}_n}{4J\sin^2 \frac{\pi n}{J} \left(1-\frac{2}{3} \sin^2\frac{\pi n}{J}\right)} \quad .$$ (40)

The array α_j is then obtained by taking the inverse transform of $\overline{\alpha}_n$.

The time integration for the quantities δx_{jk} and α_j is carried out by a conventional leap-frog scheme. Since the distribution function requires simultaneous knowledge of the particle positions and velocities, a half-time step is taken just before and after each reconstruction of the distribution function.

The computing time to advance the sample particle was found to be approximately 0.5 ms per particle, per time step, on the CDC 3800. The computing time to reconstruct the distribution function with quatratic weight functions was approximately 0.7 ms per particle.

c. Energy Conservation

As a consequence of the Lagrangian formulation, the present algorithm for advancing the sample particle conserves momentum and energy independently of the mesh size Δx. The expression for the total energy is provided by the Hamiltonian

$$H = \frac{1}{2} \sum_{j=0}^{J-1} \sum_{k=1}^{K} f_{jk} \, \delta \dot{x}^2_{jk} + \frac{1}{2} \sum_{i,j=0}^{J-1} \alpha_i \alpha_j \int_0^1 \phi'(x-x_k)dx$$ (41)

The first term in the right member of Eq. (41) represents the kinetic energy of the system and the second term represents the electrostatic energy U. The latter term may be conveniently evaluated using the Fourier transformed array $\overline{\alpha}_n$,

$$U(\cdot) = 2\sum_{n=0}^{J-1} \overline{\alpha}_n \overline{\alpha}_{-n} \sin^2 \frac{\pi n}{J} \left(1-\frac{2}{3} \sin^2 \frac{\pi n}{J}\right).$$ (42)

4. Examples

The problems of two-stream instability solved in Sec. II-6 by the Fourier-Fourier transform method are reconsidered in the present section using the direct method of integration.

338

Solutions of Vlasov Equation

Case 1: Two-Stream Instability with Equal Beams

The electrostatic energy for three solutions of this problem is shown in Fig. 11. All three curves correspond to the same maximum velocity, $v_{max} = 4.2 \, v_{th}$, the same mesh sizes, $\Delta x = 1/32$ and $\Delta v = 2v_{max}/120$ and the same time step $\Delta t = 0.2$. The threshold, i.e., the minimum value of the distribution function for which a sample particle is considered was set to zero.

The solid curve corresponds to a reconstruction of the distribution function every ten time steps, using quadratic weight functions. This curve shows good agreement with the 21-mode Fourier-Fourier solution given in Fig. 3. The broken line corresponds to a reconstruction of the distribution function at every time step, also using quadratic weight functions. We observe a decrease in the amplitude of trapping oscillations. This is attributed to a diffusion of the distribution function in phase plane due to repeated applications of the averaging operation defined by Eq. (22). Note that although energy is conserved in the averaging operation, higher moments are not conserved. This tends to flatten the distribution function resulting in the escape of trapped particles. The curve drawn with dashes and dots in Fig. 11 corresponds again to a reconstruction of the distribution function at every time step. This time, however, linear weight functions were used. The distribution function flattens rapidly in this case, filling the hole located at the center of the trapping region.

Because of the rather long tails in the distribution function in the present problem, particles are lost over the boundaries at $v = \pm \, v_{max}$. For both solutions with quadratic weight functions, the relative particle loss is $4 \, 10^{-4}$. After corrections for particles lost over the boundary, the relative energy error is $5.5 \, 10^{-5}$. For the solution with linear weight functions, the relative particle loss is $2.7 \, 10^{-3}$ and the relative energy error after correction for lost particles is $6.2 \, 10^{-2}$.
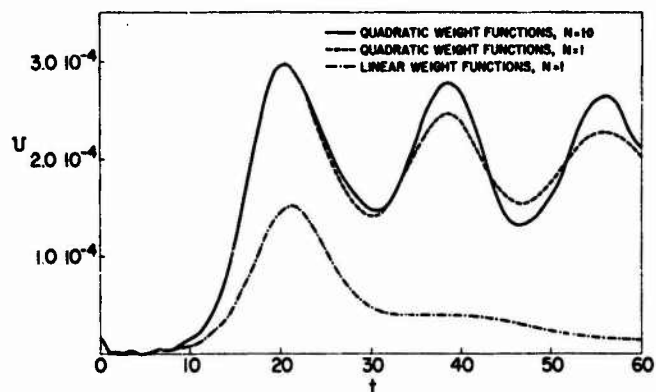
339

Figure 11   Electrostatic energy for two-stream instability with equal

beams, Case 1, by direct integration method.
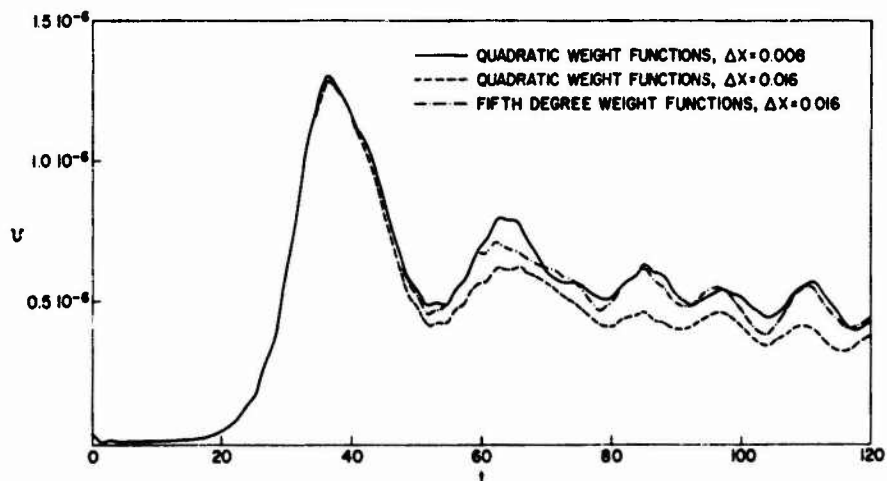
Figure 12   Electrostatic energy for two-stream instability with unequal

beams, Case 2, by direct integration method.

An additional computation was carried out in which the distribution function was never reconstructed. The code then operated as a particle code with particles of different masses initially arranged in a regular array in the phase plane. Phase plots for this run showed beaming instabilities starting to appear at $t = 10$. The total electrostatic energy showed only minor deviation from the solid curve in Fig. 11 out to $t \simeq 22$, after which it broke into spurious oscillations.

Case 2: Two-Stream Instability with Unequal Beams

The total electrostatic energy for three solutions of this problem is shown in Fig. 12. All three curves correspond to the same maximum velocity $v_{max} = 4v_p$, velocity interval $\Delta v = 2v_{max}/120$ and time step $\Delta t = 0.2$ with the distribution function reconstructed every 10 time steps. A threshold equal to 10^{-5} times the maximum value of the distribution function was set. Below this threshold no sample particles were considered.

Note that the present case involves five trapping regions (mode $n = 5$ is the most unstable mode) so that smaller values of Δx should be considered than in the previous case. The solid line in Fig. 11 corresponds to $\Delta x = 1/128$ with quadratic weight functions. This curve shows good agreement with the Fourier-Fourier solution shown in Fig. 6 out to $t \simeq 60$, after which the two solutions remain qualitatively similar. The broken line corresponds to $\Delta x = 1/64$, again using quadratic weight functions. The amplitude of trapping oscillations is reduced in this case. The curve drawn with dashes and dots in Fig. 12 corresponds to $\Delta x = 1/64$ using fifth-degree weight functions. We observe that the use of higher-order weight functions tends to reduce somewhat the diffusion of the distribution function in phase space.

The density in phase near saturation with $\Delta x = 1/64$ and fifth-degree weight functions is shown in Fig. 13. This phase plot may be compared with Fig. 7 which shows the density in phase from the Fourier-Fourier code at approximately the same time.

341
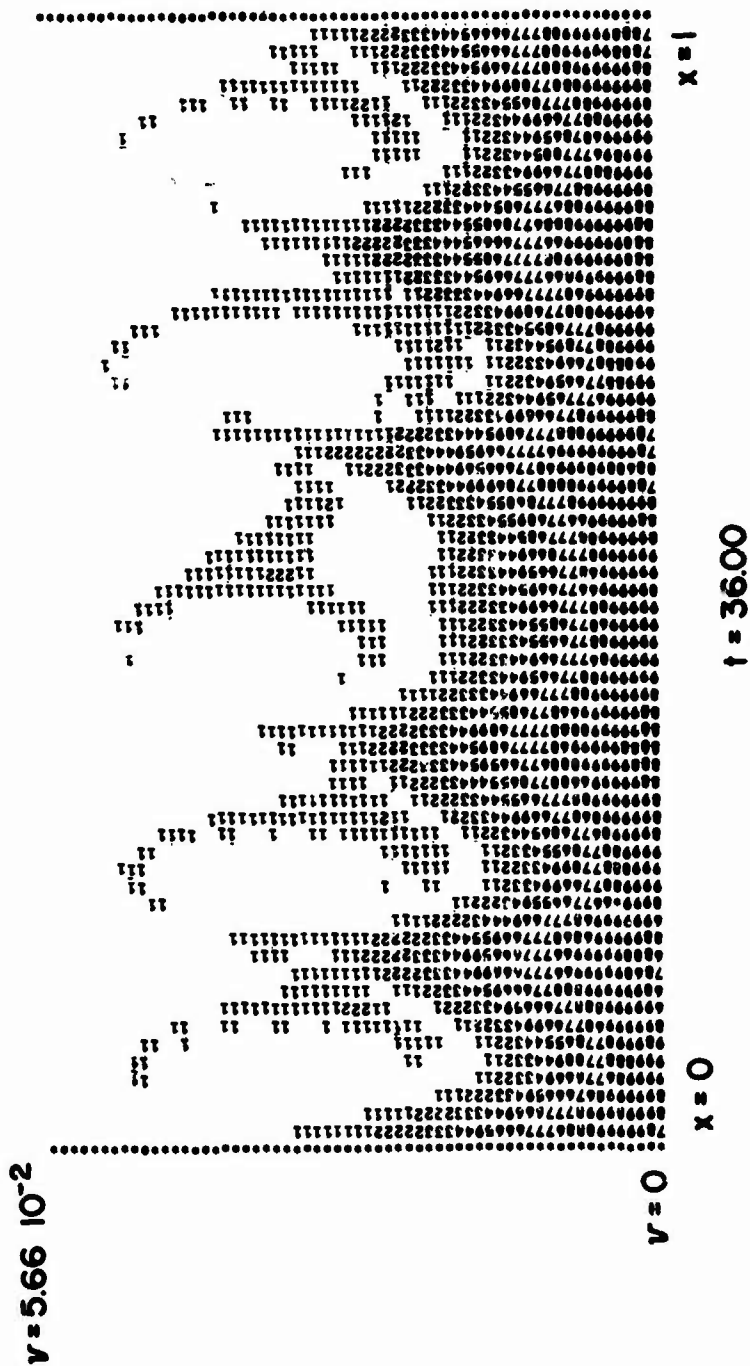
Figure 13   Density in phase near saturation for two-stream instability
with unequal beams, Case 2, by direct integration method.

The relative particle loss with $\Delta x = 1/128$ and quadratic weight functions is $4 \ 10^{-6}$ and the relative energy error is $3.5 \ 10^{-4}$. Comparable values of the particle loss and energy error are found in the other two computations.

ACKNOWLEDGMENTS

Denavit

APPENDIX

Beaming Instability

The time interval between reconstructions of the distribution function in the method of Sec. III may be estimated in terms of Dawson's theory of plasma oscillations of electron beams[22]. Consider a one-dimensional system of electron beams with velocities $V_\sigma = \sigma \Delta v$ and densities $N_\sigma = N(V_\sigma) \Delta v$, with $\sigma = 0, \pm 1, \pm 2, \ldots$, moving over a neutralizing positively charged background. Let $n_\sigma(x,t)$ and $v_\sigma(y,t)$ denote perturbations in density and velocity for each beam. The linearized equations of motion and continuity for each beam and Poisson's equation yield

$$\frac{\partial v_\sigma}{\partial t} + V_\sigma \frac{\partial v_\sigma}{\partial x} = \frac{-eE}{m} ,$$

$$\frac{\partial n_\sigma}{\partial t} + N_\sigma \frac{\partial v_\sigma}{\partial x} + V_\sigma \frac{\partial n_\sigma}{\partial x} = 0,$$

$$\frac{\partial E}{\partial x} = -4\pi e \sum_\sigma n_\sigma .$$

Assuming solutions of the form $A(x,t) = A(\omega,k)e^{-i(\omega t - kx)}$ for the perturbation quantities yields

$$n_\sigma(\omega, k) = \frac{4\pi e^2}{m} \frac{N_\sigma}{(\omega - kV_\sigma)^2} \tag{43}$$

$$v_\sigma(\omega, k) = \frac{4\pi e^2}{m} \frac{1}{k(\omega - kV_\sigma)} \tag{44}$$

$$E(\omega,k) = -\frac{4\pi e i}{k} \tag{45}$$

with the dispersion relation

$$\frac{4\pi e^2}{m} \sum_\sigma \frac{N_\sigma}{(\omega - kV_\sigma)^2} = 1 . \tag{46}$$

Dawson has shown that for $\Delta v \to 0$, the left member of Eq. (46) may be written as the sum of an integral and a singular term. For a Maxwellian beam densi

distribution $N(V_\sigma) = (n_0/\sqrt{2\pi}\, v_{th})\exp(V_\sigma^2/2v_{th}^2)$ the dispersion relation becomes

$$\frac{4\pi^2}{\sqrt{2\pi}}\frac{v_{th}}{\Delta v}\; e^{-\zeta^2}\, e^{\pm 2\pi i\omega/k\Delta v} = 1 + k^2\lambda_D^2 + \zeta Z(\zeta) \qquad (47)$$

where $Z(\zeta)$ is the plasma dispersion function with $\zeta = \omega/\sqrt{2}\, kv_{th}$. The positive sign is to be used in Eq. (47) for $\text{Im}\,\omega > 0$ and the negative sign for $\text{Im}\,\omega < 0$. For each k, Eq. (47) has two complex conjugate roots corresponding to each beam. Letting $\omega_\sigma = \alpha_\sigma + i\beta_\sigma$ and $\zeta_\sigma = \sigma \Delta v/\sqrt{2}\, v_{th}$ yields

$$\alpha_\sigma = \frac{k\Delta v}{2\pi}\tan^{-1}\left(\frac{\zeta_\sigma \text{Im}\,Z(\zeta_\sigma)}{1 + k^2\lambda_D^2 + \text{Re}\,Z(\zeta_\sigma)}\right) + k\sigma\Delta v, \qquad (48)$$

and

$$\beta_\sigma = \pm\frac{k\Delta v}{2\pi}\left\{\ln\frac{4\pi^2 v_{th}}{\sqrt{2\pi}\Delta v} - \zeta_\sigma^2 \right.$$
$$\left. - \tfrac{1}{2}\ln\left[(1 + k^2\lambda_D^2 + \zeta_\sigma \text{Re}\,Z(\zeta_\sigma))^2 + (\zeta_\sigma \text{Im}\,Z(\zeta_\sigma))^2\right]\right\} \qquad (49)$$

Eqs. (43) and (44) are normal modes for a given k and satisfy the normalization relation

$$\sum_\sigma \frac{1}{2N_\sigma}(\omega + \omega' - 2kV_\sigma)n_\sigma(\omega,k)n_\sigma(\omega',k) = \begin{cases} 0 \text{ for } \omega \neq \omega' \\ H(\omega,k) \text{ for } \omega = \omega' \end{cases} \qquad (50)$$

For $\Delta v \to 0$ and a Maxwellian beam distribution the function $H(\omega,k)$ reduces to

$$H(\omega_\sigma,k) = \mp\frac{2\pi i}{k\Delta v}\left\{1 + \frac{1}{k^2\lambda_D^2}\left[1 + \zeta_\sigma Z(\zeta_\sigma)\right]\right\} \qquad (51)$$

To verify that the instability occurring in the code described in Sec. III, when the distribution function is not reconstructed, is indeed a beaming instability, a computation was carried out for a Maxwellian beam distribution with $v_{th}/\Delta v = 5$. An initial density perturbation was applied to the central beam,

$$n_\sigma(x, t = 0) \quad = \quad \begin{cases} \epsilon N_{\sigma \, = \, 0} \cos kx & \text{for } \sigma = 0 \\ \\ 0 & \text{for } \sigma \neq 0 \end{cases} \tag{52}$$

with $\epsilon = 0.0025$ and $k\lambda_D = \pi/5$. No initial velocity perturbation was applied. The central beam velocity at $x = \pi/2k$ from the code of Sec. III is given by the solid curve in Fig. 14. There is a gentle growth out to $t = 46$, followed by a sign reversal at $t = 48$ and a very steep growth for $t > 48$. The electric field for this computation first drops rapidly to very low values, then suddenly reappears to reach a maximum 23 times its initial value at $t = 2\pi/k\Delta v = 50$.

Expanding the velocity perturbation of the central beam into normal modes and using the normalization relations (50), the initial conditions (52) yield

$$\frac{v_{\sigma = 0}}{\Delta v} = \frac{\omega_p^2 \, \epsilon}{(2\pi)^{3/2}} \frac{\Delta v}{v_{th}} k^2 \lambda_D^2 \sin kx \sum_\sigma \frac{\pm e^{-i\omega_\sigma t}}{\omega_\sigma^2 [1 + k^2 \lambda_D^2 + \zeta_\sigma Z(\zeta_\sigma)]} \; . \tag{53}$$

The terms of the sum in Eq. (53) oscillate with the frequencies α_σ given by Eq. (48), approximately equal to the Doppler frequencies $k\sigma\Delta v$ of the beams and grow exponentially with growth rates β_σ given by Eq. (49). The damped terms corresponding to the negative sign in Eq. (49) are ignored. The expression in brackets in the denominator of Eq. (53) is the Landau denominator which in the present case has a minimum near $\zeta_\sigma = 1.8$. Thus, the dominant terms of the sum in Eq. (53) occur for $\sigma \simeq 0$, which corresponds to the minimum of ω_σ^2 and $\sigma \simeq \pm (1.8) \sqrt{2} v_{th}/\Delta v \simeq 13$ which corresponds to the minimum of the Landau denominator.

For $t < 2\pi/k\Delta v = 50$, the terms corresponding to $\sigma \simeq \pm 13$ phase mix and the behavior of the velocity perturbation $v_{\sigma = 0}$ is given by the terms near $\sigma = 0$. The growth rates for these terms is $\beta_{\sigma = 0} = 0.08$. The circles in Fig. 14 give values computed by taking $\sigma = 0, \pm 1, \pm 2$. These values are in good agreement with the computer results obtained by the method of Sec. III.

346

The growth rate for the terms corresponding to $\sigma \simeq \pm 13$ is $\beta_{\pm 13} = 0.06$. For $t \simeq 2\pi/k\Delta v = 50$ these terms no longer phase mix. By this time they have grown by a factor of approximately 20 and therefore give rise to a strong echo. This is evident in the solid line in Fig. 14 for $t > 48$, and also agrees with the electric field results which show a sudden regrowth with a maximum at $t = 50$ which is 23 times the initial electric field.
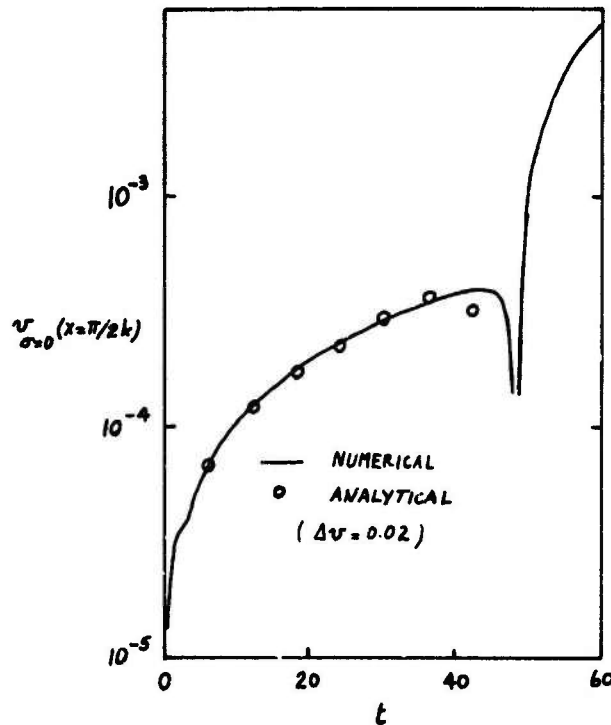
Figure 14   Velocity perturbation of central beam for beaming instability test.

REFERENCES

1. J.M. Dawson and R. Shanny, Phys. Fluids $\underline{11}$, 1506 (1968).

2. C.K. Birdsall and D. Fuss, J. Comput. Phys. $\underline{3}$, 494 (1969).

3. R.L. Morse and C.W. Nielson, Phys. Fluids $\underline{12}$, 2418 (1969).

4. J.P. Boris and K.V. Roberts, J. Comput. Phys. $\underline{4}$, 552 (1969).

5. J.A. Byers and M. Grewal, Phys. Fluids $\underline{13}$, 1819 (1970).

6. G. Knorr, Z. Naturforsch $\underline{16a}$, 1320 (1961).

7. K-W Li, Plasma Physics Group University of Wisconsin Report PLP 360,

8. P. H. Sakanaha, C. K. Chu and T. C. Marshall (to be published, Physics of Fluids)

9. H.L. Berk and K.V. Roberts, Phys. Fluids $\underline{10}$, 1595 (1967).

10. G. Knorr, Z. Naturforsch $\underline{18a}$, 1304 (1963).

11. T.P. Armstrong, Phys. Fluids $\underline{10}$, 1269 (1967); see also

    T.P. Armstrong and C.W. Nielson, Phys. Fluids $\underline{13}$, 1880 (1970).

12. D. Lynden-Bell, Mon.Not.R.Astr.Soc. $\underline{136}$, 101 (1967).

13. H. Cramér, Mathematical Methods of Statistics (Princeton University
    Press, Princeton, N.J., 1946) pp. 89-103.

14. J.W. Cooley and J.W. Turkey, Mathematics of Computation $\underline{19}$, 297 (1965).

15. Computer programs implementing the fast Fourier transform algorithm
    were contributed by Jay Boris.

16. Z. Kopal, Numerical Analysis (Chapman and Hall, London 1955) p. 99.

17. F.C. Grant and M.R. Feix, Phys. Fluids $\underline{10}$, 696 (1967).

18. J. Denavit and W.L. Kruer (to be published).

19. T.M. O'Neil and R.W. Gould, Phys. Fluids $\underline{11}$, 134 (1968).

20. H.R. Lewis, Los Alamos Scientific Laboratory Report IA-DC-10775.

21. M. Abramowitz and I.A. Stegun, Handbook of Mathematical Functions
    (Dover Publications, Inc., New York, 1965), pp. 878, 879.

22. J.M. Dawson, Phys. Rev. $\underline{118}$, 381 (1960).

Choice of Grids in Low-β Fluid Computations

N. K. Winsor and E. C. Bowers
Princeton University
Princeton, New Jersey

ABSTRACT

When the magnetic stress is large compared to the plasma pressure, the magnetic field geometry controls the plasma behavior. For finite difference calculations of this behavior, the grid should be chosen to fit the geometry. Three coordinate systems are presented, and their relative merits are compared. Some general techniques for a low-β simulation -- in particular, the conservation-law form of the equations and the "symbolic" style of programming -- are discussed and recommended. A proposed simulation of the adiabatic toroidal compression experiment is used as an illustration of the advantages of writing a fluid code in curvilinear coordinates.

I INTRODUCTION

Numerical calculations in plasma physics are routinely more complicated than hydrodynamic or gas-dynamic calculations with similar initial and boundary conditions. First this is because we are dealing with a minimum of two species. Fields are usually important as well: an electrostatic field in the B=0 case, or the combined electric and magnetic fields in the general case.

We consider here the low-β regime of plasma physics in which the magnetic field is so strong that the effect of the plasma on it can be ignored. Then the physics of the problem looks even' less like the field-free one; the magnetic field plays a dominant role in the determination of the fluid motion. Velocity and current components are very different in magnitude parallel and perpendicular to the magnetic field.

The low-β case can be studied numerically by particle simulation, and this treatment is essential when details of the velocity distribution function are important, as in collisionless regimes, or when loss cones are present. However, when the plasma is collisional and velocity-space instabilities are not important in transport processes, a fluid model can usually obtain the results of physical interest with less computation. For the low-β case, this means going from an essentially Lagrangian coordinate system associated with the particles to an Eulerian coordinate system associated with the magnetic field.

There is a class of "local" and "slab" problems of interest in this case, but for comparison with experiment, a fluid model must deal with the global properties of a plasma and must take note of the magnetic-field geometry of interest: cylindrical, toroidal, dipole, etc. We will discuss some of the important considerations in tailoring a coordinate system to the geometry, and reducing the system of differential equations for the fluid variables to difference equations on a mesh.

Low-β Fluid Computations

In the finite and high-β regimes it is frequently convenient (Boris, 1969) to use a Cartesian coordinate system, with β one of the variables to be determined; then quantities such as current and mass flux are not readily related to magnetic surfaces. Thus Cartesian coordinates have the drawback that some physically interesting parameters are inconvenient to calculate. On the other hand, they have the advantage that derivatives of the basis vectors vanish. This greatly simplifies the difference form of the equations of motion. As an example, consider the convective derivative $d\underline{v}/dt$:

$$\frac{d\underline{v}}{dt} = \frac{\partial \underline{v}}{\partial t} + \underline{v} \cdot \underline{\nabla}\underline{v} .$$

In Cartesian (x, y) coordinates, it can be approximated by the centered differences

$$\underline{e}_x \cdot \frac{d\underline{v}}{dt}\Bigg|_{Cart} = v_x \left[v_x(x+\delta x/2, y) - v_x(x-\delta x/2, y) \right]/\delta x + O(\delta x^2)$$

$$+ v_y \left[v_x(x, y+\delta y/2) - v_x(x, y-\delta y/2) \right]/\delta y + O(\delta y^2) .$$

In curvilinear coordinates, additional terms are present:

$$\underline{e}_x \cdot \frac{d\underline{v}}{dt}\Bigg|_{Curv} = \underline{e}_x \cdot \left[\frac{d\underline{v}}{dt}\Bigg|_{Cart} + \underline{\Omega}(\underline{r}, \underline{v}) \times \underline{v} + \underline{\omega}(\underline{r}, t) \times \underline{v} + \underline{a}(\underline{r}, t) \right] .$$

These arise from the acceleration experienced by a fluid element following a coordinate line. Here the $\underline{e}$'s are unit vectors in the indicated directions. The effect of coordinate curvature is given by the $\underline{\Omega} \times \underline{v}$ term; the last two terms are present only when the coordinates are explicitly time-dependent. Terms such as these will appear wherever the equations of motion apply a differential operator to a vector quantity. Thus curvilinear coordinates have the drawback that differential operators take a more complicated form.

351

Curvilinear coordinates have the advantage of freedom of choice: once a curvilinear coordinate system is admitted, it can be chosen to fit the boundaries and to minimize the effect of special cases, such as curvature of the boundary or the origin of a cylindrical coordinate system. One can also put more mesh points where they are needed: where the physical behavior shows more detail, or where velocities are larger.

In low-β problems, the geometry of a curvilinear coordinate system is usually dictated by the magnetic field. When containment of plasma is desired, it is helpful to have a magnetic field geometry with magnetic surfaces, surfaces everywhere tangent to the magnetic field. Plasma confinement times can be expressed most readily in terms of mass flux through a magnetic surface, divided by the total mass contained by it.

In general, magnetic surfaces need not exist, but they are present when the hydromagnetic fluid equations,

$$\underline{J} \times \underline{B} = \underline{\nabla} p ,$$
$$\underline{J} = \underline{\nabla} \times \underline{B} ,$$
$$\underline{\nabla} \cdot \underline{B} = 0 .$$

are satisfied (Kruskal, Kulsrud, 1958). For problems with cylindrical or toroidal symmetry, the magnetic surfaces can be coordinate surfaces. The interesting geometries for containment are those in which the magnetic surfaces are nested; for closed magnetic surfaces, these must be toroids. For open geometries, fluid calculations often neglect end effects and apply periodic boundary conditions so that the model resembles one with closed surfaces.

II COORDINATES

We are now going to introduce three coordinate systems for geometries possesing magnetic surfaces, starting with the most popular (and restricted) and ending with the most general. Each is a candidate for a numerical differencing grid.

The first has been called the "toroidal slab model." It appears to be the simplest magnetic field model which permits realistic computation of plasma behavior in an axisymmetric torus. It is shown in Figure 1. (The usual cylindrical coordinate system is a special case, with R infinite.) The magnetic surfaces are circular, and the rotational transform (the pitch angle around the magnetic axis for a field line going around the major axis once) is an arbitrary function of radius. This magnetic field has the advantage of simplicity, as we shall see in detail later, but it has the drawback that $\nabla \times B$ is not zero. That is, the current producing the transform is

$$J_{ext} \equiv \nabla \times B = e_z \frac{B_o}{r} \frac{\partial}{\partial r} \frac{rRf}{R - r\cos\theta} \, ,$$

and in a low-β model this current must be carried by imaginary "wires" immersed in the plasma. When electrostatic, axisymmetric systems are considered this current is ignorable, since $E \cdot J_{ext} = 0$, and it does not affect the dynamics. The metric of this coordinate system is

$$d\ell^2 = dr^2 + r^2 d\theta^2 + (1 - \frac{r}{R} \cos\theta)^2 dz^2 \, ,$$

and the surface and volume elements can readily be obtained from this.

$$\underline{B} = B_0 \, [\, \underline{e}_\theta \, f(r) + \underline{e}_z \,]/[\, 1 - (r/R) \cos \theta \,]$$
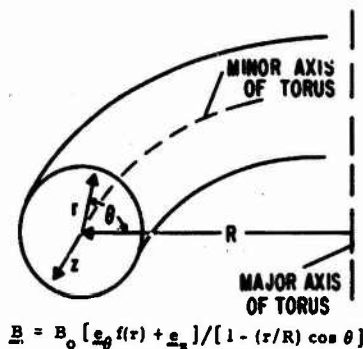
Figure 1. The geometry cf Pfirsch coordinates, and the magnetic field expressed in these coordinates.

This is the geometry Pfirsch and Schlüter (1962) introduced to study diffusion in a torus. Bineau (1967) believed the lack of self-consistency cast doubt on their result, but Johnson and von Goeler (1969) demonstrated that the essential results of Pfirsch and Schluter were valid for a general vacuum field. This geometry therefore seems adequate for equilibrium or diffusion calculations with toroidal symmetry.

The second coordinate system describes an axisymmetric vacuum field and is closely related to the magnetic flux. In the toroidal case, the field is separated into toroidal and poloidal components $\underline{B} = \underline{B}_T + \underline{B}_P$. The toroidal part B_t has the usual $1/R$ dependence relative to the major axis, and the poloidal field can be described by a potential Φ, or by the magnetic flux the short way χ, and the angle Θ the long way. Thus,

$$\underline{B} = R \, B_T \, \underline{\nabla} \Theta + \underline{\nabla} \Phi$$

$$= R \, B_T \, \underline{\nabla} \Theta + \underline{\nabla} \Theta \times \underline{\nabla} \chi$$
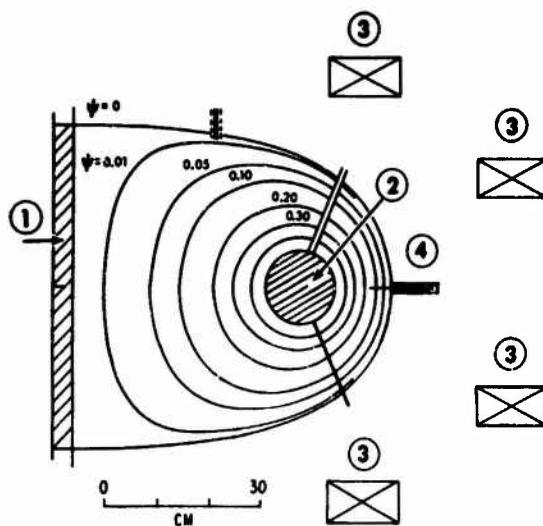
1 Toroidal field coil (TP)
2 Poloidal field coil (PF)
3 External field coils (EF)
4 Horizontal probe

Local shear length

$$\frac{1}{L_S} = \frac{2 B_P B_T}{B^2} \nabla \psi \frac{d}{d\psi} \ell n \, B_P R$$

(a)

Figure 2. The machine diagram of a spherator, showing the cross-sectional shape of magnetic surfaces.

Here RB_T is a constant, and R is the distance from the major axis to the field point (χ, Φ, Θ). For purposes of computation, $R(\chi, \Phi, \Theta)$ is a coordinate function needed for the metric,

$$d\ell^2 = \frac{d\chi^2}{R^2 B_p^2} + \frac{d\Phi^2}{B_p^2} + R^2 d\Theta^2 .$$

The computationally useful quantities R and B_p determine the scale factors in it.

These coordinates have proved useful in calculations of the magnetic field in a spherator (Figure 2 is a typical

355

example). They can describe a true vacuum field, as well as fields in the presence of currents, but axisymmetry is built in. The coordinate gradients are orthogonal, but the metric shows that they are not unitary.

The third curvilinear coordinate system was introduced by Hamada (1959). Its utility in analytic work has been demonstrated, for example, by Greene and Johnson (1962), and by Frieman (1970). It begins by parameterizing a (closed) magnetic surface by the volume, V, contained within it. Then, writing the fluxes the long way ψ and the short way X as functions of V, one chooses the scalars ξ and ζ such that

$$\underline{B} = \underline{\nabla} V \times \underline{\nabla} [\psi'\xi + X'\zeta] ,$$

where the primes indicate derivatives with respect to V. If we also require $\underline{\nabla} V \cdot \underline{\nabla} \xi \times \underline{\nabla} \zeta = 1$, the lines of constant ξ will close on themselves the long way, and ξ will be periodic, with period 1, the short way. Similarly, lines of constant ζ will close on themselves the short way, and ζ increases by 1, once around the long way. Observe that the basis vectors are not in general orthogonal. The metric is

$$d\ell^2 = \sum_{i,j} g^{ij} d\xi_i d\xi_j ,$$

where $\xi_1 = V$, $\xi_2 = \xi$, and $\xi_3 = \zeta$. Six scalars are needed to relate $d\ell$ to coordinate displacements, since g^{ij} is a symmetric tensor. These scalars are the dot products of $\underline{\nabla} \xi \times \underline{\nabla} \zeta$, $\underline{\nabla} \zeta \times \underline{\nabla} V$ and $\underline{\nabla} V \times \underline{\nabla} \xi$, taken in pairs. For numerical computations in these coordinates, it would be necessary to tabulate these quantities at each mesh point.
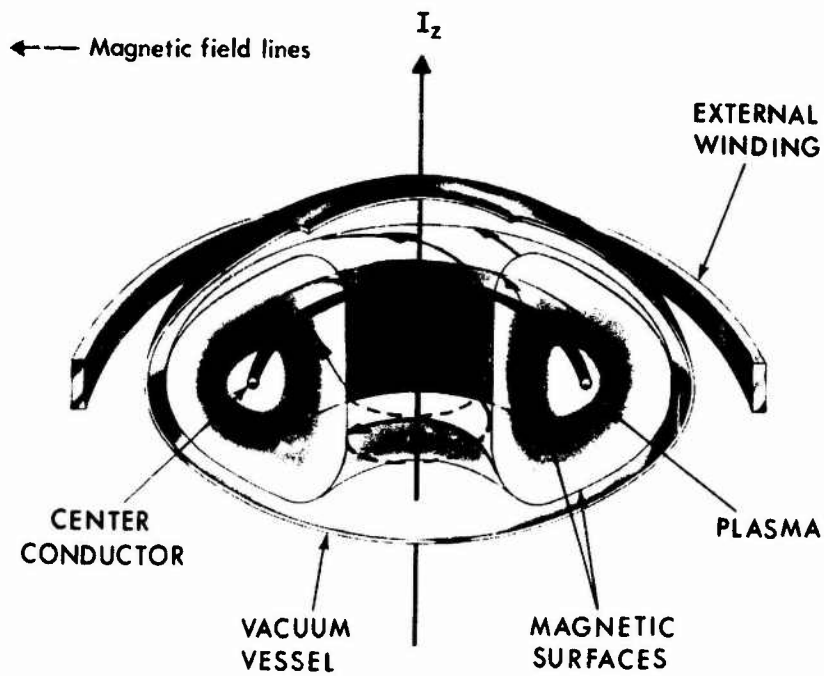
Figure 3. Perspective view of a spherator, showing the variation in pitch of representative magnetic field lines.

In return for the complexity of the metric, one obtains a coordinate representation in which integrals and derivatives are easily computed. Furthermore, the magnetic field lines, and the lines of the generating current, are straight. This greatly simplifies calculations such as magnetic line integrals. Figure 3 shows why straightening the magnetic field lines can be a big help; it shows several field lines in a spherator geometry.

These are the three coordinate systems. They are convenient, respectively, for simple calculations, for problems with axisymmetry, and for computations in a general magnetic field. They have been presented in their toroidal form for convenience. Each can obviously be specialized to cylindrical geometry ($R=\infty$). Spherator and Hamada coordinates can be applied to multipoles, with the separatrix as a special case. Hamada coordinates can be applied to open-ended or mirror geometries, with V replaced by a suitable surface label.

III ALGEBRA

We will now show how fluid calculations are performed in these coordinates, and how to decide which is best suited to a particular problem. We will illustrate these points through calculation of geometric factors in line, surface and volume integrals, the acceleration terms in the momentum equations, and the form of the conservation laws.

First let us see what is involved in the computation of integrals. Physically, the quantities which are likely to be needed in the formulation of the equations or in the diagnostics are magnetic line integrals, magnetic surface integrals, and integrals of a volume bounded by magnetic surfaces. Magnetic line integrals occur in the evaluation of equations like Ohm's law,

$$\underline{E} + \frac{1}{c}\underline{v}\times\underline{B} = \eta\,\underline{J} \ .$$

the parallel component of which yields

$$\underline{B}\cdot\underline{\nabla}\phi = -\eta\,\underline{B}\cdot\underline{J}$$

in the electrostatic limit $\underline{E}=-\underline{\nabla}\phi$. They are also obtained by application of Stokes' theorem to Maxwell's equations. Magnetic surface integrals come from the divergence theorem, and from formulations of conservation laws; e.g.,

conservation of charge,

$$\oint \underline{J} \cdot \underline{dS} = 0 .$$

In toroidal geometry such magnetic surface integrals are important in calculating the time evolution of the system (Winsor, 1970; Bowers, this conference). Volume integrals appear in averages, diagnostics, etc.

The cylindrical limit of Pfirsch coordinates is a convenient and familiar starting point for comparison of these expressions. The line, magnetic surface and volume elements are written

$$\underline{d\ell} = \underline{e}_r \, dr + \underline{e}_\theta \, r \, d\theta + \underline{e} \, d$$

$$\underline{dS} = \underline{e}_r \, r \, d\theta \, dz ,$$

and

$$d\tau = dr \, r \, d\theta \, dz .$$

The effects of curvature are introduced through a single parameter $N = 1 - r \cos\theta/R$, the ratio of axial lengths $d\ell = N dz$ at the field point (r, θ, z) to the length at the magnetic axis $d\ell = dz$. Thus,

$$\underline{d\ell} = \underline{e}_r \, dr + \underline{e}_\theta \, r \, d\theta + \underline{e}_z \, N \, dz ,$$

$$\underline{dS} = \underline{e}_r \, r \, d\theta \, N \, dz ,$$

$$d\tau = dr \, r \, d\theta \, N \, dz .$$

in Pfirsch coordinates. In spherator coordinates, the

magnetic line and volume integrals require the two additional functions described before:

$$d\boldsymbol{\ell} = \underline{e}_\chi \, (d\chi/RB_p) + \underline{e}_\Phi \, (d\Phi/B_p) + \underline{e}_\Theta Rd\Theta \, ,$$

$$dS = \underline{e}_\chi \, (R/B_p) d\Phi \, d\Theta \, ,$$

$$d_\tau = (1/B_p^2) d\chi \, d\Phi \, d\Theta \, .$$

The components in the line element are orthogonal. In Hamada coordinates, the line element can be written

$$d\boldsymbol{\ell} = dV \, \underline{\nabla}\xi \times \underline{\nabla}\zeta + d\xi \, \underline{\nabla}\zeta \times \underline{\nabla}V + d\zeta \, \underline{\nabla}V \times \underline{\nabla}\xi \, .$$

The particular choice of metric elements simplifies the surface and volume elements:

$$\underline{dS} = \underline{\nabla}V \, d\xi \, d\zeta \, ,$$

$$d\tau = dV \, d\xi \, d\zeta \, .$$

Note that $B_\xi/B_\zeta = \chi'/\psi'$ is constant in these coordinates.

The simplest means of numerically performing an integral is to set up a grid along coordinate lines, evaluate the line, surface or volume elements for the cells of the grid, and perform the appropriate sum, using the trapezoidal rule for points on the mesh and the midpoint rule for points displaced from it. In a coordinate system suited to the problem at hand, this is likely to be quite adequate. Thus, only the metric coefficients indicated above, and no additional weighting factors, are required.

Any textbook on differential equations presents the gradient, divergence and curl operators in coordinates other than Cartesian. A quick glance at these expressions shows that metric elements appear inside the derivatives in div and curl, but not inside grad. This is because div and curl operate on vectors, and grad operates on scalars. The dyad $\nabla \underline{v}$ is quite complicated in curvilinear coordinates, and will be discussed below in connection with the acceleration terms.

The difference approximation to differential operators must be selected with numerical stability in mind, but generally speaking, the simpler the better. The second programming example below illustrates a "centered" difference in spherical coordinates; the coordinate is highly nonlinear, but the stability of the difference formulation is unaffected by this.

If both integrals and derivatives appear in the expression of the problem, it is very important that the operators be compatible, i.e.,

$$\int_{\phi_1}^{\phi_2} \underline{d\ell} \cdot \underline{\nabla}\phi = \phi_2 - \phi_1$$

and

$$\oint_{\partial D} \underline{dS} \cdot \underline{A} = \int_D \underline{\nabla} \cdot \underline{A} \, d\tau$$

should be identically satisfied in difference form.

Integrals such as these are frequently derived from conservation laws, and it is good practice to insure that these laws are obeyed by the difference formulation of the problem. We shall say more about these considerations shortly.

The programming of differential equations in one of these coordinate systems involves replacement of the differential operators by suitable difference operators. How great a task that will be depends both on the form of the operators and on the choice of the difference approximations. The operators are presented in the next paragraph, to indicate the amount of work that is required to code them.

The form of the differential operators in Pfirsch and spherator coordinate systems is readily calculated. In Pfirsch coordinates,

$$\nabla\phi = \underline{e}_r \frac{\partial\phi}{\partial r} + \underline{e}_\theta \frac{\partial\phi}{r\partial\theta} + \underline{e}_z \frac{\partial\phi}{N\partial z} \; ,$$

$$\underline{\nabla}\cdot\underline{A} = \frac{\partial rNA_r}{rN\partial r} + \frac{\partial NA_\theta}{rN\partial\theta} + \frac{\partial A_z}{N\partial z} \; ,$$

$$\underline{\nabla}\times\underline{A} = \frac{\underline{e}_r}{N}\left[\frac{\partial NA_z}{r\partial\theta} - \frac{\partial A_\theta}{\partial z}\right] + \frac{\underline{e}_\theta}{N}\left[\frac{\partial A_r}{\partial z} - \frac{\partial NA_z}{\partial r}\right] + \frac{\underline{e}_z}{r}\left[\frac{\partial NA_\theta}{\partial r} - \frac{\partial A_r}{\partial\theta}\right].$$

In spherator coordinates,

$$\underline{\nabla}\phi = \underline{e}_\chi RB_p \frac{\partial\phi}{\partial\chi} + \underline{e}_\Phi B_p \frac{\partial\phi}{\partial\Phi} + \underline{e}_\Theta \frac{\partial\phi}{\partial\Theta}$$

$$\underline{\nabla}\cdot\underline{A} = B_p^2 \frac{\partial RA_\chi/B_p}{\partial\chi} + B_p^2 \frac{\partial A_\Phi/B_p}{\partial\Phi} + \frac{\partial A_\theta}{R\partial\Theta} \; ,$$

$$\underline{\nabla}\times\underline{A} = \underline{e}_\chi\left[B_p\frac{\partial RA_\theta}{R\partial\Phi} - \frac{\partial A_\Phi}{R\partial\Theta}\right] + \underline{e}_\Phi\left[\frac{\partial A_\chi}{R\partial\Theta} - B_p\frac{\partial RA_\Theta}{\partial\chi}\right] + \underline{e}_\Theta RB_p^2\left[\frac{\partial A_\Phi/B_p}{\partial\chi} - \frac{\partial A_\chi/RB_p}{\partial\Phi}\right].$$

In Hamada coordinates, we are again in need of tensor notation:

$$(\nabla \phi)^i = \frac{\partial \phi}{\partial \xi} \ , \qquad \qquad \nabla \cdot A = \sum_i \frac{\partial A_i}{\partial \xi_i} \ .$$

$$(\nabla \times A)_i = \sum_{jk\ell} \epsilon_{ijk} \frac{\partial}{\partial \xi_j} \ g^{k\ell} A_\ell \ ,$$

where derivatives of covariant quantities are indicated. Here ϵ_{ijk} is the usual antisymmetric tensor. The operators involve derivatives of the $g^{k\ell}$, but the difference version still requires only these six parameters tabulated on the mesh.

The dyad $\underline{\nabla v}$ usually appears only in the combination $\underline{v} \cdot \underline{\nabla v}$, and for time-independent coordinates we can write this as

$$\underline{v} \cdot \underline{\nabla v} = \sum_i \ \underline{e}_i \underline{v} \cdot \underline{\nabla} + \underline{\Omega} \times \underline{v} \ .$$

The problem of calculating the acceleration is then reduced to the differencing of the scalar components (discussed in the section on convection) and the calculation of $\underline{\Omega}$. In Pfirsch coordinates,

$$\underline{\Omega} = \frac{v_\theta}{r} \underline{e}_z + \frac{v_z}{RN} \ (\underline{e}_r \cos\theta + \underline{e}_\theta \sin\theta) \times \underline{e}_z \ ,$$

and in spherator coordinates,

$$\underline{\Omega} = \frac{v_\theta}{R} B_p \frac{\partial R}{\partial \phi} \underline{e}_\chi - v_\Theta B_p \frac{\partial R}{\partial \chi} \underline{e}_\phi + \left(\frac{v_\chi}{R} \frac{\partial R B_p}{\partial \phi} - v_\phi R \frac{\partial B_p}{\partial \chi} \right) \underline{e}_\Theta \ .$$

The expression in Hamada coordinates involves the curvature tensor, and is best tabulated in approximate form. The generalization of $\underline{\Omega}$ for this case is the Christoffel symbol, with 18 independent components.

The grid formulation of integrals and derivatives will require the functionals in the equations of this section. This determines how many arrays of parameters are needed on the mesh. For a simple steady-state or eigenvalue problem in two or three variables, the Pfirsch geometry with its two parameters $f(r)$ and $H(r,\theta)$ is appropriate, unless the problem is sensitive to the details of the magnetic field structure. For a simulation of transport processes with 10 or 15 variables, the additional functions required to describe the coordinate system will not add much to storage requirements, but the additional calculation required in derivatives and integrals may add substantially to computation time. The availability of computer time may decide the choice between spherator and Hamada coordinates. Of course, the additional complexity and computation should provide a closer approximation to the actual physics of the problem.

IV CONSERVATION LAWS

One of the most important reasons for using magnetic coordinates is the necessity to evaluate conservation laws, either in the calculation of the fluid dynamics or in diagnostics. For example, conservation of mass,

$$\frac{\partial \rho}{\partial t} = - \nabla \cdot \rho \underline{v} ,$$

can be integrated over any volume,

$$\frac{\partial}{\partial t} \int_D \rho \, d\tau = - \oint_{\partial D} \rho \underline{v} \cdot \underline{dS} ,$$

but we only obtain useful information about diffusion when the surface D is a magnetic surface. Velocities along the lines are typically an order of magnitude larger than perpendicular (guiding center) velocities, so a small parallel component passing through the surface of integration can completely mask the diffusive contribution to the flux.

There is a relatively simple prescription for preserving such essential aspects of the physics:

(1) use a coordinate system appropriate to the geometry of the problem, and

(2) write the important parts of the equations in conservation-law form.

Basically, (1) means that if the velocity is large in one direction and small in another, it is necessary to orient the coordinates so that these components are computed independently and the larger one does not "wash out" the smaller. Next, one selects a finite difference mesh in these coordinates. Then (2) suggests that the divergence theorem should be applied, where possible, to the elementary cells of the mesh, so that the quantity of interest is conserved as it moves among the cells.

Conservation of mass (or charge, or energy) may appear as a continuity equation,

$$\frac{\partial\rho}{\partial t} + \nabla\cdot\rho\underset{\sim}{v} = 0,$$

or a source term may be present on the right, accounting for ionization, charge exchange, etc. The difference formulation of this equation usually is used to evaluate the time rate of change of ρ at the center of a grid cell, given the flux $\rho\underset{\sim}{v}$ at its faces.

In a large fraction of the codes solving this equation, the computation sometimes encounters regions in which the mass tries to become negative. A "floor" is frequently provided by the programmer, limiting the density to zero or to some small positive value. Such a heuristic rule must be applied with caution, however, if conservation is to be maintained. The "lost" density must be compensated in the

367

adjacent cells. For further observations on misuse of the conservation-law techniques, see Moretti (1969b).

The remarks about mass conservation apply also to momentum conservation, but it presents additional difficulties in a curvilinear coordinate system, because of its vector nature. Specifically, when the equation is written out, the acceleration terms cannot in general be absorbed into perfect derivatives. The nonconservative contributions can often be included implicitly in the difference equations, but terms which involve spatial averages of quantities cannot be conveniently treated.

The momentum equations perpendicular to the magnetic field will involve the components of the $\underline{J} x \underline{B}$ force. In low-β systems there is no relation between the current and the magnetic field since the latter is assumed curl-free. Thus the $\underline{J} x \underline{B}$ force cannot appear in conservative form and must be treated with care. In some applications (Winsor, 1970; Bowers, this conference) the perpendicular momentum equation is used to solve for the current. Then the perpendicular momentum must be obtained from Ohm's law, or some other equation.

V BOUNDARIES

The simulation problems which relate to laboratory experiments, and many that are of astrophysical interest, require the treatment of boundaries. If walls are present in the specification of a hyperbolic problem, characteristics can be found which intersect the wall. The model must therefore determine what happens when plasma flows toward, along, or away from the wall. The correct treatment of boundaries can be extremely important, as in the gas-dynamic case of flow past an obstacle (Moretti, 1970). Computations of drag and torque, for example, are critically dependent upon the treatment of boundary conditions.

In the plasma case, the actual boundary layer (electrostatic sheath) is much too thin (a few Debye lengths) to be modeled on the grid, so its effects must be included analytically in the computation of the grid cells adjacent to the boundary, treating the sheath as one face of the cell.

In an open-ended geometry one must either treat the ends explicitly or ignore them by applying periodicity. In

369

closed geometry, the boundaries can sometimes be avoided by solving a particular initial-value problem, either free expansion or expansion into a low-density plasma layer separating the bulk of the plasma from the wall. Experience has shown that the interior may then be very insensitive to the boundary conditions.

Computations including the Hall terms in Ohm's law indicate that this buffer layer does not last as long as in the zero Larmor radius limit. Nevertheless, the inclusion of a low-density region near the wall has proved helpful in reducing the sensitivity of plasma calculations to initial and boundary conditions.

Our experience with containment calculations has been that the boundary effects can be both important and difficult to treat; however, the main body of the plasma may be insensitive to them. One can study the bulk effects first, and bring in boundary effects later.

VI CONVECTION

Convection is important along the magnetic field lines, since parallel velocities frequently are comparable to the sound speed. In addition, E/B drifts lead to convection across lines. (For a perfect conductor, $\underline{B}$ may be considered to convect with the fluid.) If the ion Larmor radius is comparable with $|\underline{\nabla}\ln(n)|^{-1}$, the diamagnetic drift terms can also produce important convection. We have found that for cases of physical interest, the E/B and diamagnetic drift velocities can enhance one another, leading to very sizable convection across $\underline{B}$.

The calculation of vector components need not be along the basis vectors. For velocity calculations in which the component parallel to $\underline{B}$ is much larger than the perpendicular components, it is convenient to compute perpendicular and parallel components directly. For example the velocity can be decomposed into orthogonal components

$$\underline{v} = v_r \underline{e}_r + v_s \underline{e}_b \times \underline{e}_r + v_b \underline{e}_b ,$$

and the $\underline{v}\cdot\underline{\nabla}\underline{v}$ operator described above can be applied to these components. The problem of convection then becomes the problem of differencing the components of $\underline{v}$ along some convenient set of coordinates, in a manner which is

371

numerically stable.

This has a special importance in Hamada coordinates. If the covariant components of vectors are stored on the mesh, computation of a contravariant quantity such as $(\nabla\phi)^i$ normally requires computation of g and a sum to obtain the covariant components. However, if the equations of motion have been written so that only $\underline{B}\cdot\nabla\phi$ and $\underline{B}x\nabla\phi$ appear, they can be computed as $\sum_i B_i (\nabla\phi)^i$ and $\sum_{ijk} B_i (\nabla\phi)^i g^{ik} \epsilon_{gk\ell}$, and the covariant form of the metric tensor is not needed.

One possible treatment of convection, characteristic integration, is provided by the Courant, Isaacson, Rees (1952) technique. Adapting it to curvilinear coordinates is accomplished by writing the difference equations in the given coordinates (i.e., assuming that the fluid elements tend to follow coordinate lines), and then adding an appropriate acceleration term, as indicated above. We have found that this method is satisfactory for a fine mesh and for velocities small compared with the characteristic speeds. For computations in which convection plays a dominant role, the numerical viscosity introduced by it can mask the long-term behavior of the fluid. However for a discussion of its advantages in the treatment of shocks, see Moretti (1969a).

If viscosity is present in the equations, the $\underline{v}\cdot\nabla \underline{v}$ term

can be replaced by a centered difference (plus the usual acceleration term) provided the treatment of the viscous term -- for example DuFort and Frankel (1953) -- is such as to give stability to the complete system. For specialized problems in which a single sweep through the mesh is performed, the angled-derivative method (Roberts, 1963) can give comparable accuracy without the stability problems of centered differences.

The Lax-Wendroff (1960) method, as generalized in Richtmyer and Morton (1967), can be applied even when viscosity is not important. It possesses second-order accuracy and good stability properties. On the other hand, it requires computation of intermediate quantities, which can nearly double the computation time, and it involves space averages which may affect local phenomena.

An illustration of the importance of a proper treatment of convection is provided by the calculations reported elsewhere in this conference (Bowers). The calculations reported there, demonstrating shock structure in a toroidal plasma, were performed with a modified Lax-Wendroff technique. Previous calculations with less careful treatment of convection suffered from numerical damping of rotational modes. In any calculation in which steady flow is present, proper treatment of convection is essential.

VII SYMBOLIC PROGRAMMING

We have spent a lot of time discussing coordinate systems, and have not worried much about the actual difference formulation of the equations. The treatment of difference equations, and the analysis of their stability is certainly well-known, at least in Cartesian coordinate systems. We now wish to show how conventional difference schemes can be adapted to a general coordinate system.

The proposed technique is a style of writing programs, called symbolic programming (Boris and Roberts, this conference). We will use it now to illustrate the ease with which a difference scheme can be written in coordinate-independent form, and then used in different coordinate systems. The resulting programs are clear and easy to read, and the treatment of a complex geometry is reduced to looking up the differential operators in a mathematics textbook.

The method is exactly that of analysis; one writes the equations in terms of differential operators, and then changes the definition of the operators to go from one coordinate system to another. Consider the scaled linear wave equations

$$\frac{\partial v}{\partial t} + \nabla p = 0 , \qquad \frac{\partial p}{\partial t} + \nabla \cdot v = 0 .$$

374

The simplest difference formulation of this problem in one dimension (Courant, Friedrichs, Levy, 1928) involves displacing the v lattice one half-step from the density lattice and using centered differences in space and time:

$$v_{x+1/2}^{t+1/2} = v_{x+1/2}^{t-1/2} - \delta t \times (p_{x+1}^{t} - p_{x}^{t})/\delta x ,$$

$$p_{x}^{t+1} = p_{x}^{t} - \delta t \times (v_{x+1/2}^{t+1/2} - v_{x-1/2}^{t+1/2})/\delta x .$$

This is the conservation-law formulation of the problem.

The key to using this effectively is to separate the physics from the mathematics: write the assignment statements

```
V(X) := V(X) - DT * GRAD(P(X));
P(X) := P(X) - DT * DIVE(V(X));
```

and write the GRADient and DIVErgence functions to reproduce the preceding difference equations. Here P(X) and V(X) are subscripted arrays, and these two statements must be executed at integral and half-integral times respectively.

Figure 4 presents a program which implements these concepts. It is written in Stanford University's Algol W (Wirth, 1966). This program is complete with graphical output; only the sin function for initialization and the I/O routines are not shown.

The box near the top contains the mathematics: the derivative operators. The pressure and velocity mesh points

375

are indicated to the right. The subscripts for V are 1/2 less than the value of the spatial grid position. DDX is the difference operator. GRAD, which will be applied to P, is simply DCX. DIVE must be shifted back one step to difference the correct elements in V. For those who are not familiar with Algol-like languages: a replacement is made of the formal parameter (Y) in each procedure body by the corresponding actual parameter [e.g., P(X)], so that changing X changes the value of Y.

The box near the bottom contains the physics: the differential equations. The code sweeps through the mesh once for V and once for P at each time step. The pressure is graphed once every NP steps. This description of the problem is coordinate-independent; the geometry of the coordinate system is in the difference operators above.

Figure 5 is the output of this program. The space coordinate is plotted vertically and time advances to the right. The initial conditions are p=1+sin(x) and v=0, and the boundary conditions are p=const. at the edges, so the plot can be visualized as the amplitude of a vibrating string. The time step is $\delta t=\delta x$, equal to the stability limit. The individual printed lines represent the pressure every second time step. Treating the boundaries as x=0 and x=N, the exact solution is

$$p = 1 + 1/2 \left\{ \sin\left[2\pi(x+t)/N\right] + \sin\left[2\pi(x-t)/N\right] \right\} .$$

and the recurrence time is t=2N. The time axis ranges from t=0 to t=2N.

This is a simple example in which the physics is transparent, and the mathematical treatment is the standard example of textbooks. The physical equations can be readily checked and debugged in this form. The next step in this approach is to select a coordinate system appropriate to the problem of interest. Here we shall select spherical coordinates as an example. The problem of interest can then be treated by changing the form of the operators.

Figure 6 presents a program which solves the same wave equation, with the same initial and boundary conditions, but in spherical coordinates. Here X represents the radial coordinate, and ranges from x=N0 to x=N0+N. The only changes are in the upper box; the divergence operator has been replaced by

$$\text{div} = \frac{1}{x^2} \frac{\partial}{\partial x} x^2$$

$$\text{div } v = \left[(x + \frac{\delta x}{2})^2 v(x + \frac{\delta x}{2}) - (x - \frac{\delta x}{2}) v(x - \frac{\delta x}{2}) \right] / x^2 \delta x + O(\delta x^2).$$

These changes are exclusively in the mathematics of the differential operators, where they belong. Note that the details associated with the half-step displacement of the velocity mesh are also located here. The remainder of the program is identical with the previous example.

The output of this program is shown in Figure 7. In

377

```
%ALGOL

0001        BEGIN INTEGER N, NO, NP, TMAX;  REAL DX, DT;
0002          READ (N, TMAX, DX, DT, NO, NP);  WRITE (N, TMAX, DX, DT, NO, NP);
0003          BEGIN
0004
0005            REAL PROCEDURE DDX   (REAL Y);
0006            BEGIN                     REAL Z;
0007              X := X+1;               Z := Y;
0008              X := X-1;               (Z-Y)/DX
0009            END DDX;
0010
0011            REAL PROCEDURE GRAD (REAL Y);
0012                                 DDX (Y);
0013
0014            REAL PROCEDURE DIVE (REAL Y);
0015            BEGIN                     REAL D;
0016              X := X-1;               D := DDX (X);
0017              X := X+1;               D
0018            END DIVE;
0019
0020            INTEGER X;
0021            REAL ARRAY P, V (NO::NO+N);
0022
0023            PROCEDURE GRAPH (REAL ARRAY Y(*));
0024            BEGIN FOR X := 0 UNTIL N DO
0025                    LINE(X|1) := AMPLITUDE (ROUND(ABS( Y(X+NO) )) | 1);
0026              WRITE (LINE);
0027            END GRAPH;
0028            STRING (130) AMPLITUDE, LINE;
0029            AMPLITUDE := "0 1 2 3 4 5 6 7 8 9 A B C D E F G H I J ????????";
0030
0031
0032            FOR X := NO UNTIL NO+N DO
0033            BEGIN P(X) := 10 * (1+SIN(2*PI*(X-NO)/N));  V(X) := 0 END;
0034
0035            FOR T := 1 UNTIL TMAX DO
0036            BEGIN
0037
0038              FOR I := 0 UNTIL N-1 DO
0039                    BEGIN X := NO+I;  │V(X) := V(X) - DT * GRAD(P(X));│  END;
0040
0041              FOR I := 1 UNTIL N-1 DO
0042                    BEGIN X := NO+I;  │P(X) := P(X) - DT * DIVE(V(X));│  END;
0043
0044              IF T REM NP = 0 THEN GRAPH (P);
0045
0046            END;
0047          END;
0048          WRITE ("END OF EXECUTION.");
0049        END.
```

Figure 4. A program which solves the linear wave equation in Cartesian coordinates. The boxes contain the differential operators and the physical equations.
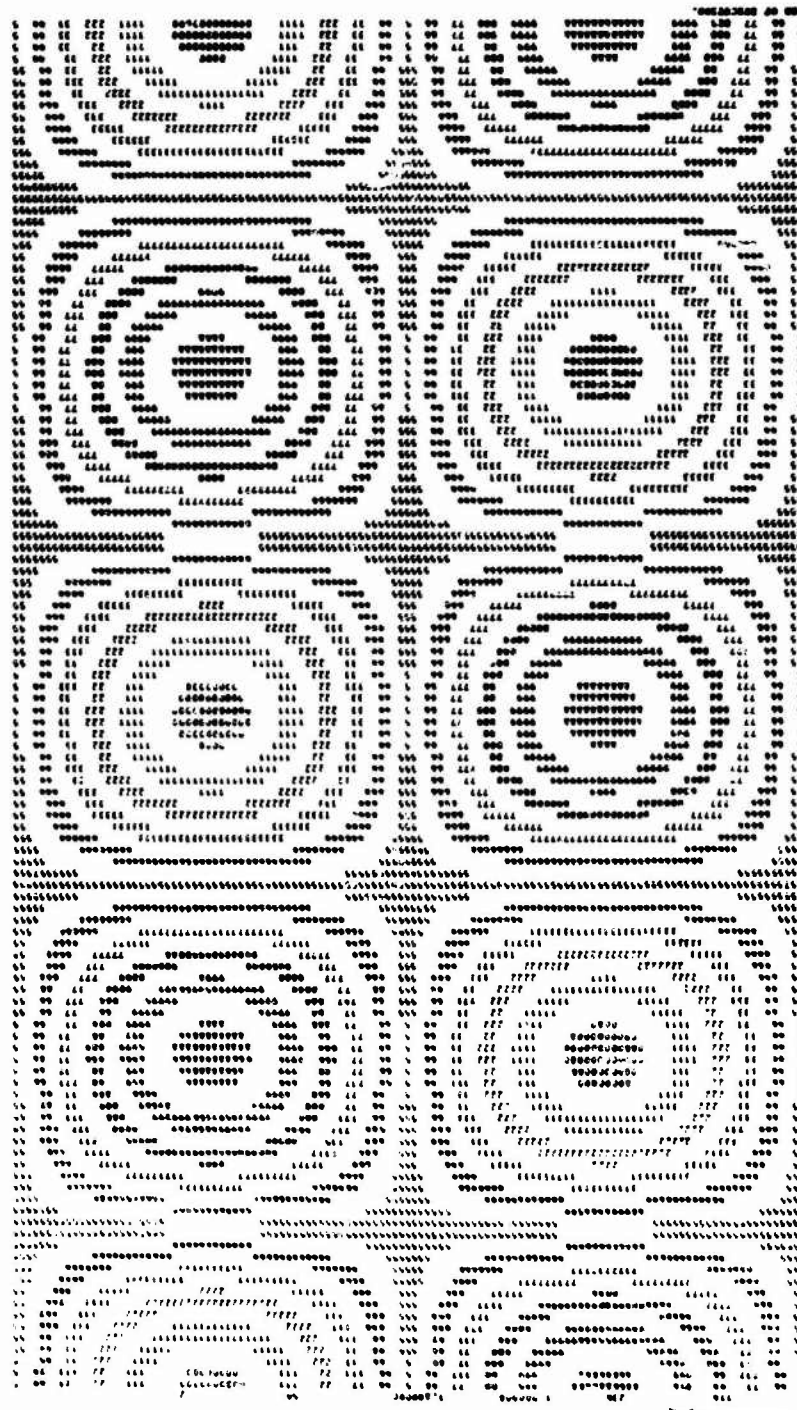
378

Figure 5. Output of the preceding program. The top and bottom are rigid boundaries, and time advances to the right.

Winsor and Bowers

```
XALGOL

0001      BEGIN INTEGER N, NO, NP, TMAX;  REAL DX, DT;
0002        READ (N, TMAX, DX, DT, NO, NP);  WRITE (N, TMAX, DX, DT, NO, NP);
0003        BEGIN
0004
0005          REAL PROCEDURE DDX   (REAL Y);
0006          BEGIN                 REAL Z;
0007            X := X+1;           Z := Y;
0008            X := X-1;           (Z-Y)/DX
0009          END DDX;
0010
0011          REAL PROCEDURE GRAD  (REAL Y);
0012                               DDX (Y);
0013
0014          REAL PROCEDURE DIVE  (REAL Y);
0015          BEGIN                 REAL D;
0016            X := X-1;           D := DDX (SHORT( Y * (X+1/2) **2 ));
0017            X := X+1;           D / X**2
0018          END DIVE;
0019
0020          INTEGER X;
0021          REAL ARRAY P, V (NO::NO+N);
0022
0023          PROCEDURE GRAPH (REAL ARRAY Y(*));
0024          BEGIN FOR X := 0 UNTIL N DO
0025                  LINE(X)1) := AMPLITUDE (ROUND(ABS( Y(X+NO ) )) ) 1);
0026            WRITE (LINE);
0027          END GRAPH;
0028          STRING (130) AMPLITUDE, LINE;
0029          AMPLITUDE := "0 1 2 3 4 5 6 7 8 9 A B C D E F G H I J ?????????";
0030
0031
0032          FOR X := NO UNTIL NO+N DO
0033          BEGIN P(X) := 10 * (1+SIN(2*PI*(X-NO)/4)); V(X) := 0 END;
0034
0035          FOR T := 1 UNTIL TMAX DO
0036          BEGIN
0037
0038            FOR I := 0 UNTIL N-1 DO
0039                  BEGIN X := NO+I;  V(X) := V(X) - DT * GRAD(P(X));  END;
0040
0041            FOR I := 1 UNTIL N-1 DO
0042                  BEGIN X := NO+I;  P(X) := P(X) - DT * DIVE(V(X));  END;
0043
0044            IF T REM NP = 0 THEN GRAPH (P);
0045
0046          END;
0047        END;
0048        WRITE ("END OF EXECUTION.");
0049      END.
```

Figure 6. A program which solves the linear wave equation
    in spherical coordinates. The boxes contain the
    differential operators and the physical equations.
    Note the form of the divergence operator DIVE; it is
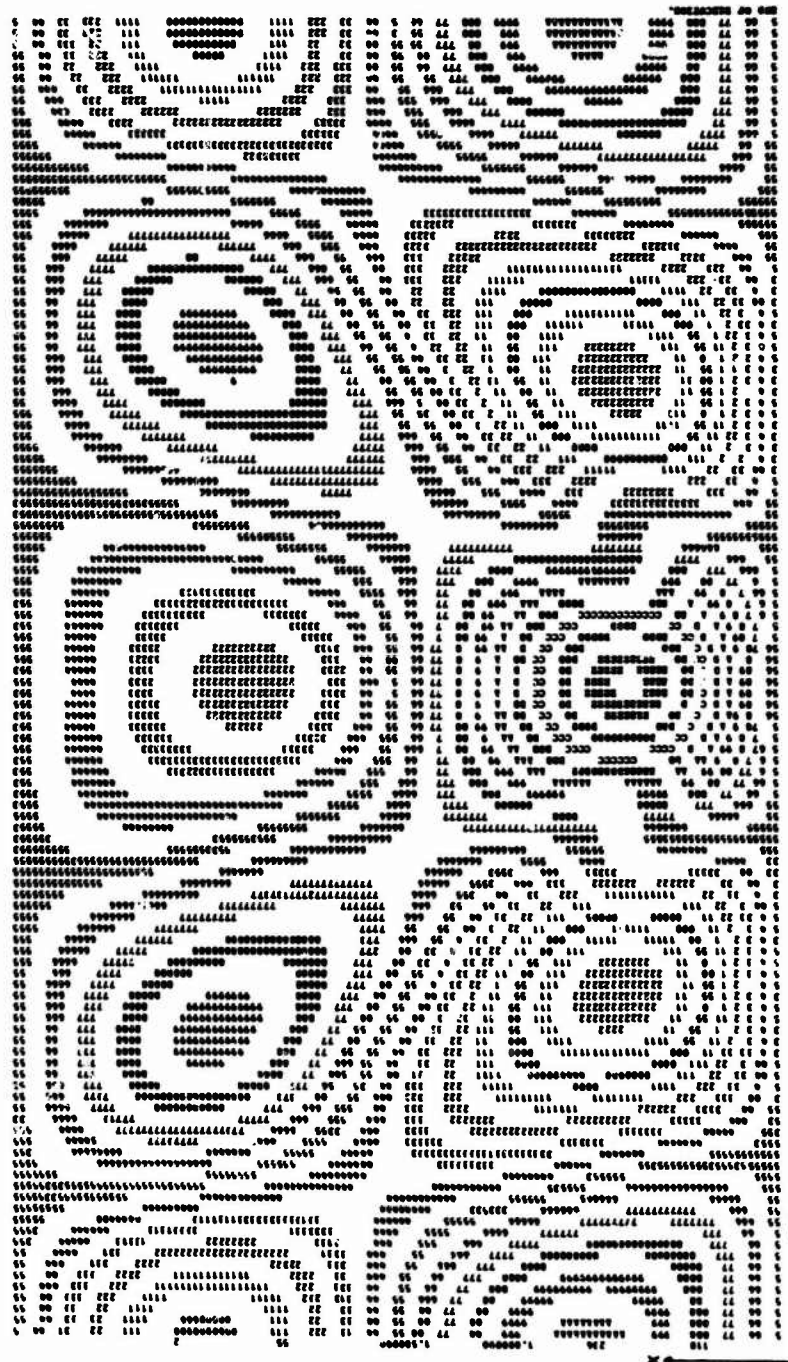   the only change from Figure 4.

380

Figure 7. Output of the preceding program. The top and bottom are rigid boundaries, representing X=16.8 and X=50 respectively.

this case the exact solution is

$$p = 1 + \left\{ (x+t)\sin\left[2\pi(x+t)/N\right] + (x-t)\sin\left[2\pi(x-t)/N\right] \right\} \times \frac{N}{2x} \ .$$

The output is again plotted for one recurrence time. The more complicated structure of the solutions is due to the fact that the sin(x) initial pressure distribution is not a solution of $\nabla^2 p = -p$ in these coordinates, so the time dependence is not separable. The symmetry of the graph is due to the special choice of boundary conditions and the constant characteristics of the differential equations.

The point of these demonstrations is that symbolic programming techniques allow the separation of simulation problems in hairy geometries into

(1) an invariant expression of the differential (and/or integral) equations representing the physics, and

(2) a mathematical expression of the operators, including all the details of the coordinate system.

The first part can essentially be copied from a physics textbook, while the second can be obtained from Chapter 5 of Horse and Feshback (1953) or some other appropriate source of mathematical detail.

VIII TIME-DEPENDENT COORDINATES

We have not yet made any reference to the problem of a time-dependent magnetic field. Actually that problem is n as difficult as it might seem. In magnetic coordinates, the plasma is stuck to the coordinate lines, to lowest order, and the most important feature of the calculation is the explicit time dependence of the metrics.

Looking again at the acceleration, we examine the additional terms due to the acceleration of the coordinate system. Using unitary basis vectors,

$$\frac{\partial v}{\partial t} + \underset{\sim}{v} \cdot \nabla \underset{\sim}{v} = \sum_i \underset{\sim i}{e} \underset{\sim}{v} \cdot \nabla v_i + \underset{\sim}{\Omega} \times \underset{\sim}{v} \quad + \quad \underset{\sim}{\omega} \times \underset{\sim}{v} + \underset{\sim}{a}$$

These additional terms can be made small by keeping the time variation slow. Computationally, the metric elements are made to change slowly in time, so that their explicit time derivatives are negligibly small compared to other terms in the equations of motion.

This is how the proposed adiabatic toroidal compressor experiment at Princeton can be simulated. Figure 8 shows how the magnetic field is expected to change over a period of milliseconds (Johnson, Greene, Weimer, 1970). The heating and inductive effects can then be studied. The effect of the plasma on the field can be examined to lowest
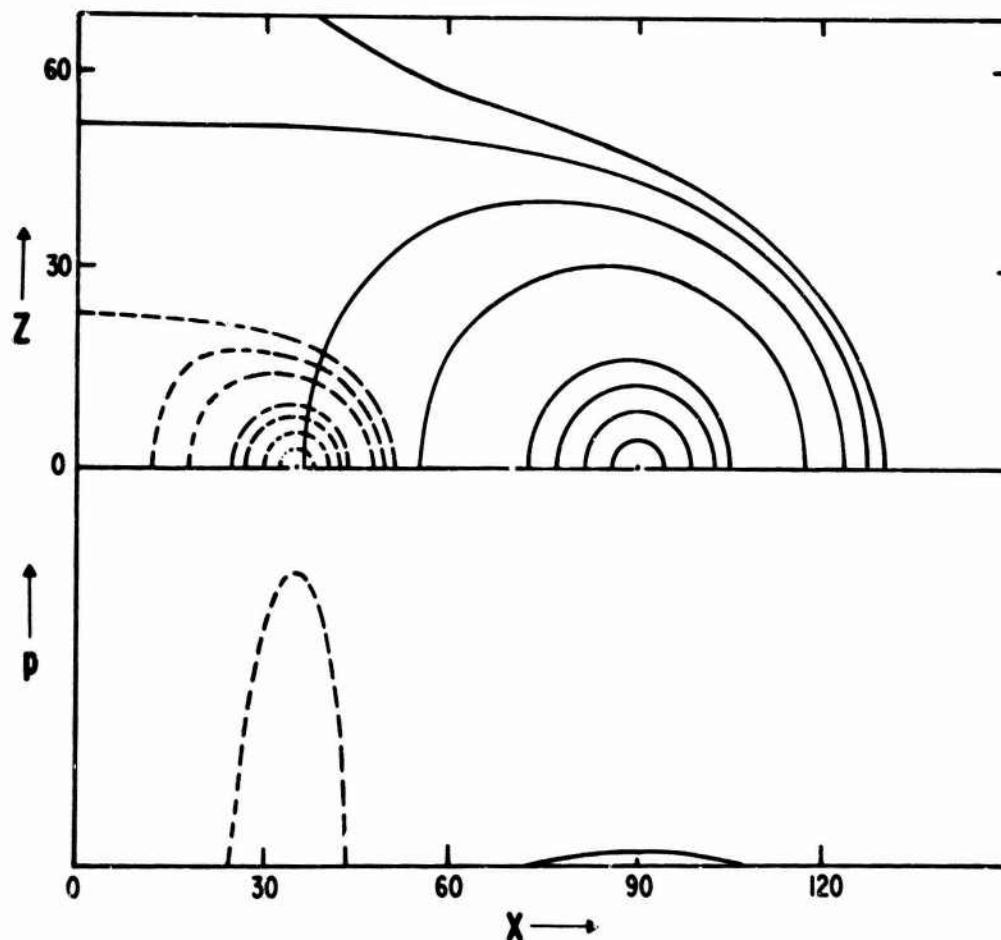
Figure 8. Magnetic surfaces and pressure distribution in a tokomak compression experiment. Compression of the magnetic field from the solid configuration to the broken one causes a corresponding increase in plasma pressure.

order by allowing the computed plasma current to slowly modify the field. In magnetic coordinates, flux conservation is built into the calculation. Equations written in conservation form in terms of the (time-dependent) geometrical factors will remain invariant. Where accelerations of coordinate vectors are involved, the net effect of the motion must be examined. For example the compression of a plasma ring with stored angular momentum should not change its total angular momentum. Thus, even if the $\underline{\omega} x \underline{v}$ term is negligible compared with other terms in the difference equations, the net effect must be included (for example by the addition of an average $\delta \underline{v}$ to each element of the velocity) to conserve angular momentum.

Similar techniques can be applied to low-frequency studies of a self-consistent magnetic field problem. The field can be changed slowly to reflect changes in the plasma current. We emphasize slowly, to avoid propagation of waves at the Alfvén speed. Physically, unmodified Alfvén modes involve too short a time scale to make simulation of laboratory plasmas practical. On the other hand, the longer-term effects of a self-consistent magnetic field seem readily accessible to this technique.

VIII SUMMARY

In the low-β problems of plasma physics, the magnetic field geometry usually controls the plasma dynamics. The components of current and velocity, parallel and perpendicular to the magnetic field, may be very different in magnitude. Thus it is important to choose a coordinate system which takes note of these differences, and allows the equations of motion to be expressed naturally.

The available coordinates range in complexity from a simple Cartesian system to general curvilinear ones. The best coordinate system for a given problem represents a compromise between physics and geometry. Difference algorithms are more easily expressed, and integrals and derivatives take simpler forms, in Cartesian coordinates. On the other hand, the physical equations, and important diagnostics such as the flux thorugh a magnetic surface, are more conveniently written in magnetic coordinates.

Three coordinate systems have been introduced: Pfirsch, spherator and Hamada. These systems demonstrate the trade-off between generality and complexity. The treatment of integrals, derivatives, and acceleration has been discussed for these coordinates.

The importance of the correct choice of coordinate system was further illustrated by evaluation of conservation laws in them. The "conservation-law form" of the equations

386

of motion was recommended. Some remarks of a practical nature regarding boundaries followed, and several methods for treating convection were discussed.

The "symbolic programming" style was introduced as a systematic means of reducing a general low-β problem to a numerical code. It was applied to the familiar linear wave equation, to demonstrate the ease of changing coordinate systems in the "symbolic" form. Solutions in linear and spherical geometry were exhibited.

As an example of the utility of general coordinates, the case of time-dependent coordinates was considered. A proposed simulation of the Princeton "tokopressor" was described to demonstrate these advantages.

BIBLIOGRAPHY

Bineau, B. (1967), Phys. Fluids 10, 1540.

Boris, J. P. (1969), Private communication (TRINITY and OCTOPLAS programs).

Courant, R., K. O. Friedrichs and H. Levy (1928), Math. Ann. 100, 32.

Courant, R., E. Isaacson and H. Rees (1952), Comm. Pure and Appl. Math. 5, 243.

DuFort, E. C., and S. P. Frankel (1953), Math Tables and Other Aids to Computation 7, 135.

Frieman, E. A. (1970), Phys. Fluids 13, 490.

Greene, J. M., and J. L. Johnson (1962), Phys. Fluids 5, 510.

Greene, J. M., J. L. Johnson and K. E. Weimer (1970), Princeton Plasma Physics Laboratory Report MATT-792.

Hamada, S. (1959), Prog. Theor. Phys. (Kyoto) 22, 145.

Hamada, S. (1962), Nuclear Fusion 2, 23.

Johnson, J. L. and S. von Goeler (1969), Phys. Fluids 12, 255.

Kruskal, M. D., and R. M. Kulsrud (1958), Phys. Fluids 1,

265.

Lax, P. D., and B. Wendroff (1960), Comm. Pure and Appl. Math. 13, 217.

Moretti, G. (1969a), "A Critical Analysis of Numerical Techniques: Piston-Driven Inviscid Flow," Polytechnic Institute of Brooklyn Report PIBAL No. 69-25.

Moretti, G. (1969b), "The Choice of a Time-Dependent Technique in Gas Dynamics," Polytechnic Institute of Brooklyn Report PIBAL No. 69-26.

Moretti, G. (1970), "Transient and Asymptotically Steady Flow of an Inviscid, Compressible Gas Past a Circular Cylinder," Polytechnic Institute of Brooklyn Report PIBAL No. 70-20.

Morse, P. M. and H. Feshbach (1952), Methods of Theoretical Physics, Vol. I, (McGraw-Hill, New York).

Pfirsch, D. and A. Schlüter (1962), Max Planck Institut Report MPI/PA/7/62 (unpublished).

Richtmyer, R. D., and K. W. Morton (1967), Difference Methods for Initial-Value Problems (Interscience, N. Y.).

Roberts, K. V., F. Hertweck and S. J. Roberts (1963), Culham Laboratory Report CLM-R 29.

Winsor, N. K., J. L. Johnson and J. M. Dawson (1970), J. Comp. Phys. 6, 000.

Wirth, N. and C. A. R. Hoare (1966), Comm. ACM 9, 413.

A Modified Particle-in-Cell Method
for Collisional Plasmas

C. K. Chu and W. P. Gula
Columbia University
New York, N.Y.

and

R. J. Mason
Bell Telephone Laboratories
Whippany, New Jersey

Abstract

A modification of the standard simulation codes is proposed, in which each simulation particle is interpreted as an element of phase space, with the value of the distribution function attached. For a collisionless plasma, this value is constant for each particle; when collisions are present, this value is modified according to the collision operator. In this paper, one-dimensional problems are considered, and the Krook model operator is used for the collisions. Results are obtained for shock wave formation in a rarefied neutral gas, and for collisional damping of the two-stream instability in a plasma.

Introduction

This paper describes an extension of the well-known particle-in-cell or cloud-in-cell collisionless codes (see e.g. Refs. 1, 2, 3) in one dimension to collisional plasmas. The procedure differs from the collisional code of Oliphant and Nielsen[4] in that we do not use a Monte-Carlo simulation of the collision

process, but operate directly on the distribution function as given by kinetic theory (Boltzmann operator, Fokker-Planck operator, Krook model, etc.). This method has previously been used for rarefied neutral gases with success[5], and the present paper is an extension of that work to include self-consistent electric fields in plasmas.

The essence of our method is the following: Each simulation particle is to be interpreted not as a physical particle, or a fixed number of physical particles, but as a portion of the x-v phase space, and each will be assigned a weight representing the distribution function[6]. Collisions are handled by changing the values of this weight function, in accordance with the collision operator. In this manner, the value of the distribution function attached to each simulation particle (or the number of physical particles represented by it) is changed continuously, and the high statistical fluctuation introduced by Monte-Carlo methods is avoided. Thus, we expect relatively smooth and accurate solutions with a relatively small number of simulation particles. This scheme also has an advantage in purely collisionless problems, in that a given velocity distribution can be represented by fewer or better distributed, simulation particles.

In the next section, we describe the procedure in detail for one-dimensional plasma problems, in which the collision operator is the Krook model operator. This is followed by some representative results from rarefied neutral gas problems, in particular, the formation of shock waves in the piston problem and in the Riemann problem (initial pressure discontinuity or shock tube problem). In the last section, typical results

are presented for the damping of a two-stream instability in plasmas by collisions.

General Procedure.

For definiteness, we restrict our attention to problems in one space dimension, in which the plasma is represented by a single charged species, say electrons, and a neutralizing background of constant density n_0. The collisions are given by a Krook collision operator[7], i.e., the number of particles scattered out of an element of the phase space is given by the product of a collision frequency and the difference between the distribution function and the local Maxwellian distribution. The distribution function is a function of 5 arguments, $f = f(x, t, v_x, v_y, v_z)$, and the equation governing it is

$$\frac{\partial f}{\partial t} + v_x \frac{\partial f}{\partial x} + \frac{eE_x}{m} \frac{\partial f}{\partial v_x} = \nu (F - f) \tag{1}$$

$$\frac{dE_x}{dx} = 4 \pi e (n - n_0) \tag{2}$$

There are no other terms on the left side of (1), because in one-dimensional problems, there are neither y- and z-derivatives nor E_y and E_z components. The local Maxwellian distribution F is defined in terms of the three moments of f: the density n, the macroscopic velocity u_x ($u_y = u_z = 0$ if they were so initially), and the temperature T. The collision frequency ν can be taken as constant, or as given function of n and T; in more sophisticated Krook models, it can also be taken as a function of the molecular velocities, but we shall not do that here.

392

As is well known[8], the absence of y-, z-, v_y-, and v_z-derivatives on the left side of (1) allows us to introduce two reduced distributions

$$g = g(x,t,v_x) = \iint_{-\infty}^{\infty} f \, dv_y dv_z$$

$$h = h(x,t,v_x) = \iint_{-\infty}^{\infty} (v_y^2 + v_z^2) f \, dv_y dv_z \, . \tag{3}$$

Each of these two functions satisfies a kinetic equation of exactly the same form as (1), with the corresponding reduced Maxwellian distributions G and H on the right side. The coupling occurs through the three moments thus:

$$n(x,t) = \int_{-\infty}^{\infty} g \, dv_x$$

$$n \, u_x(x,t) = \int_{-\infty}^{\infty} g v_x \, dv_x \tag{4}$$

$$(3/2) \, nkT \, (x,t) = \int_{-\infty}^{\infty} (1/2) \, m v_x^2 \, g \, dv_x + \int_{-\infty}^{\infty} (1/2) mh \, dv_x$$

In ref. 8, equation (1) for a neutral gas (no E_x, no eq. (2)) was solved by a finite difference procedure, and in ref. 5, it was solved by the present procedure. We now describe the modified particle-in-cell (or cloud-in-cell) procedure for a plasma.

The left side of (1), together with (2), is the usual Vlasov-Poisson system. We treat it by the standard particle-in-cell (or cloud-in-cell) method[1,2,3], complete with charge sharing, except that each simulation particle now represents a portion of the x-v_x phase space, and it is assigned a function value of g and a function value of h initially. If the plasma is collisionless, then (1) insures that the values of g and h

393

would be preserved, and each particle would keep its initial values of g and h for all time. With collisions, these values are changed at each time step by amounts proportional to the difference between the value and the corresponding Maxwellian value. The local Maxwellian value is completely determined by the moments of g and h in accordance with (4).

Two finer points should be raised. The first is that the moments n, u_x, T are calculated by integration at grid boundaries, and not at the instantaneous particle locations. This is exactly analogous to calculating the charge density at grid boundaries in standard collisionless codes, using area weighing or inverse linear interpolation. In order to get the values of the Maxwellian distributions G and H at each particle location, we must first interpolate for the values of n, u_x, and T at that particular location. This is analogous to the treatment of the electric field in standard collisionless codes.

The second point refers to the interpretation of the distribution function $g(v)$ or $h(v)$ from the calculated results. In standard collisionless codes, each simulation particle represents an equal number of actual particles, and the velocity distribution is represented by the varying number of simulation particles in various regions of the velocity space. In contrast, we use initially equally spaced velocity intervals, so that each simulation particle represents an equal volume of phase space, and the number of particles it represents is proportional to the distribution function. For neutral gas problems, these velocity intervals never change, and at any time, the distribution at any position x can be read off directly from the values of g. In the charged particle case, however, the elec-

394

tric field alters these velocity intervals significantly from the equal initial spacings, so that the distribution function $g(v)$ (and $h(v)$) cannot be read off directly; not only does it depend on the value attached to each particle, but it also depends on how closely the simulation particles are spaced. Thus, whenever the actual distribution function $g(x,v)$ is needed explicitly, we must assign the weights attached to each particle to the appropriate grid points in phase space, using again area weighing or inverse linear interpolation. This is not needed in the calculations, but only in presenting the results at specified time steps or at the end of the calculation.

Examples from Neutral Gas Calculations.

In this section, we give two examples of calculations made with this modified particle-in-cell procedure, showing the formation of shock waves in a rarefied neutral gas. These examples are taken from ref. 5. The code is identical to that described in the previous section, except that the Poisson equation and the electric field are absent.

In the first example (fig. 1(a) and (b)), the shock is formed by a uniformly moving piston into a gas. The excess density (i.e., the difference between the density and the initial density) is plotted against distance at various time. Time is nondimensionalized to the initial collision time (v_{II}^{-1}), length to the initial mean free path. In fig. 1(a), the piston speed
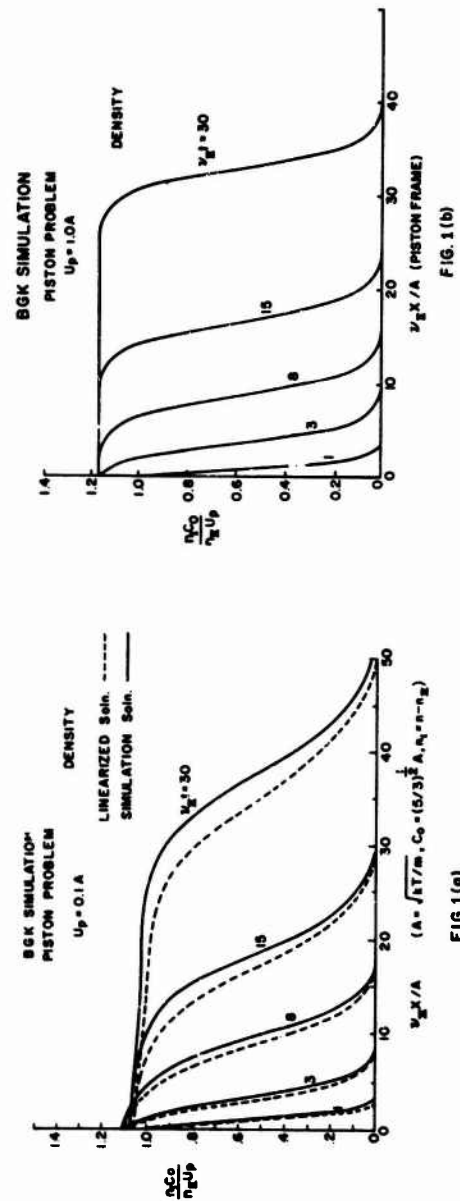
Fig. 1. Density vs. position at various instants for the piston problem. (a) Low speed piston, (b) high speed piston.
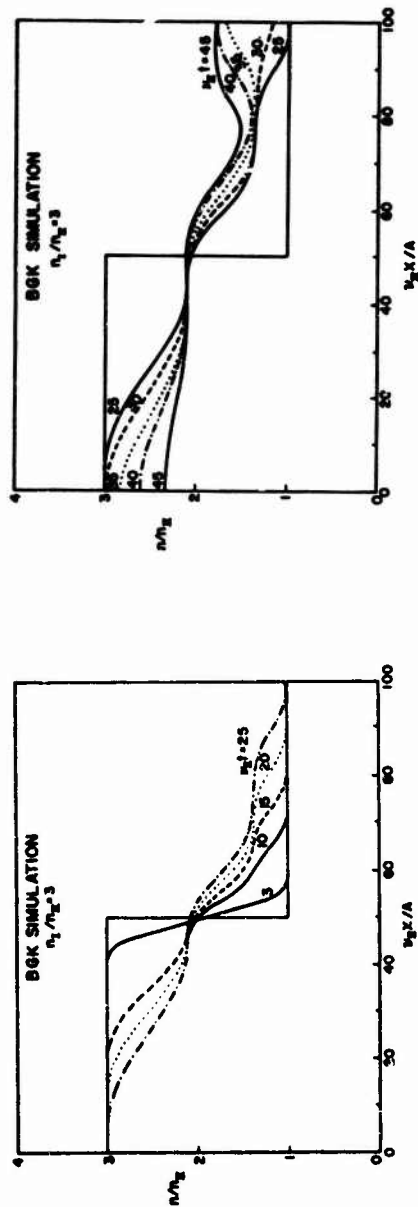
Fig. 2. Density vs. position at various instants for the shock tube problem. (a) Early time, (b) after reflection from right wall.

is small (10% of sound speed), and we would expect good agreement with linearized theory, here shown in dotted lines [9]. In Fig. 1(b), the same is shown for a higher speed piston.

Fig. 2 shows a shock wave produced in a conventional shock tube, in which a diaphragm is ruptured at t = 0 (the classical Riemann problem). Again, density is plotted against position at various instants of time. The initial motion of the gas is free flow, and between 10-15 collision times, a well-formed shock appears. The various uniform regions are separated by a constant width shock at the extreme right, a contact surface diffusing as the square root of time, and an expansion wave spreading linearly in time. These results agree with classical fluid dynamics, and also with the computed results of ref. 8.

Collisional Damping of the Two-Stream Instability

To test our method, we study the effect of collisions on the electron two-stream instability, by now a standard test for all simulation codes. It is recognized (cf. Morse and Nielsen[10]) that a one-dimensional two-stream calculation does not adequately portray real physics, as a two- or three-dimensional calculation gives qualitatively different results. Nevertheless, we feel it is instructive to test our method on this problem in one dimension, as it is much simpler, and there are numerous collisionless calculations to compare our results with.

Modified Method for Collisional Plasmas

We use 20,000 simulation particles for the electrons, corresponding to 200 x-points and 100 v-points. Δx is chosen $= 0.5 \lambda_D$, and $\Delta v = 0.141 v_{th}$. The drift velocity of the two streams are $+2 v_{th}$ and $- 2v_{th}$, and each stream has an initial Gaussian velocity spread. The total length of the configuration is 100 Debye lengths, and the problem is periodic in x, as usual. The time step is $0.04 \omega_p$, and we generally run 600 steps or 24 plasma periods. Round-off errors provide the initial perturbations.

Our parameters are essentially the same as used by Morse and Nielsen[10], and we also have n=3 as the most unstable mode. The first saturation in field energy corresponds to the formation of three vortices in phase space. Fig. 3 shows the evolution of the total field energy as a function of time, for collision frequencies $\nu = 0$, $.01 \omega_p$, and $.03 \omega_p$ respectively. The total duration of the runs were 600 steps in the first two cases, and 500 steps for the last case, corresponding to 24 and 20 plasma periods respectively, and also to 0.24 and 0.60 of a collision time in the latter two cases.

The subsequent peaks in field energy correspond to the coalescing and oscillation of the vortices, as described in detail by Berk and Roberts[11], who chose a smaller length and started off with two vortices as against our three. Our phase plane plots of the distribution function, and the energy corresponding to various spatial Fourier modes, all agree with their description; we shall not repeat these arguments here.
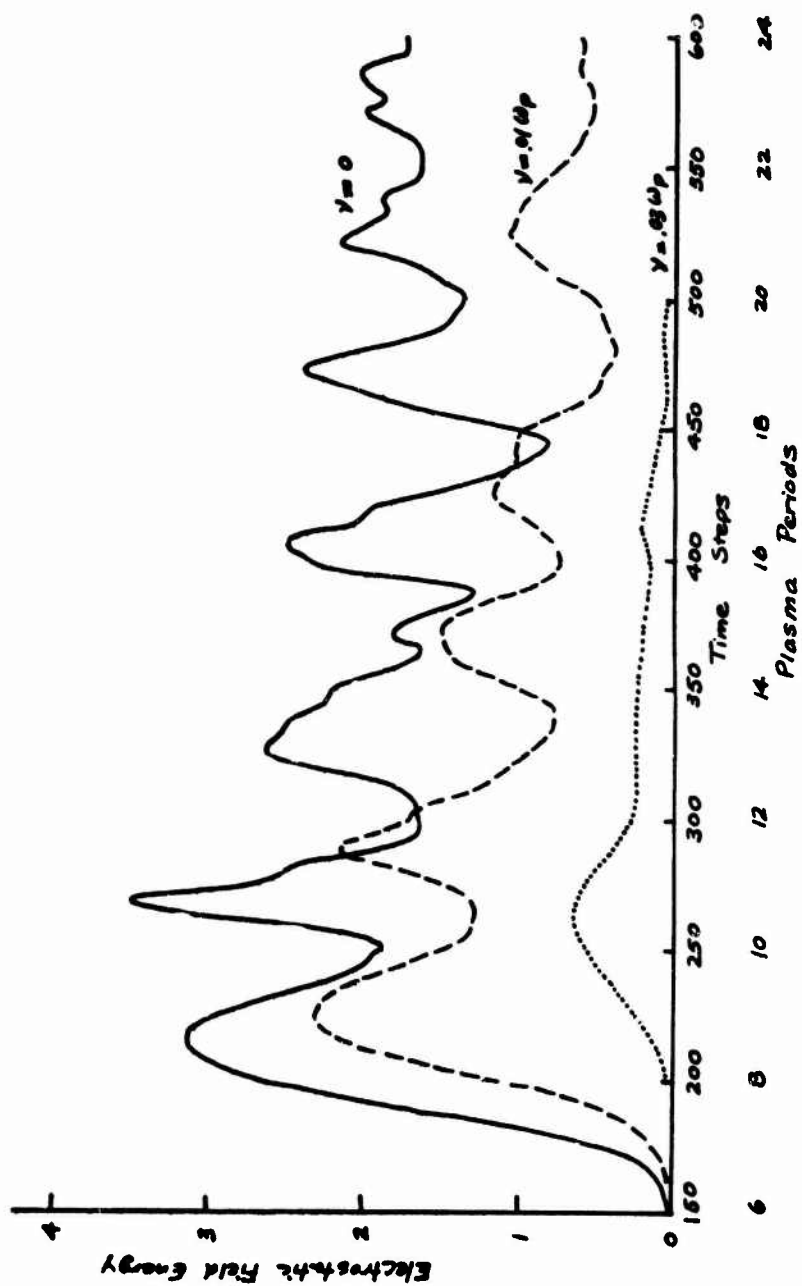
Fig. 3. Time evolution of electrostatic field energy (in nor-
malized units) for two-stream instability and differ-
ent collision frequencies

400

Fig. 4. Cumulative velocity distributions for collisionless and collisional two-stream instabilities at two different instants.

The effect of the collisions on the evolution of the field energy is quite obvious. First, it decreases the growth rate of the instability, and generally slows down the entire process. Second, it reduces the amplitudes of the various peaks of the electrostatic energy. What may not be expected, however, is seen in fig. 4, in which the cumulative velocity distribution over all space ($\bar{g}$ (v) $= \int_{-\infty}^{\infty} g\,dx$, which is identical to F (v) in ref. 10) is shown at two different instants for $\upsilon = 0$ and .03. The collisionless case is seen to fill the center hole of the cumulative velocity distribution faster than in the slightly collisional case! The explanation for that is that the filling process is mainly phase mixing, which depends on the electric field, and for small collisions, the dominant effect of the collisions is the reduction of this electric field. Of course, at high collision frequencies, the filling will be increased over the collisionless case.

On the other hand, if we examine the local velocity distribution rather than the cumulative distributions as expected. Fig. 5 shows the distribution functions plotted in x-v space for $\upsilon = 0$ and .03 ω_p, at their respective first saturation. It is evident that the slight collisions have greatly smoothened the distribution at each x-position, which is precisely the cause of the decrease in the amplitudes of the electrostatic energy oscillations. Fig. 6 shows the same distribution at the respective second saturation peaks, and fig. 7 shows them at long times ($t = 24\ \omega_p^{-1}$ for the
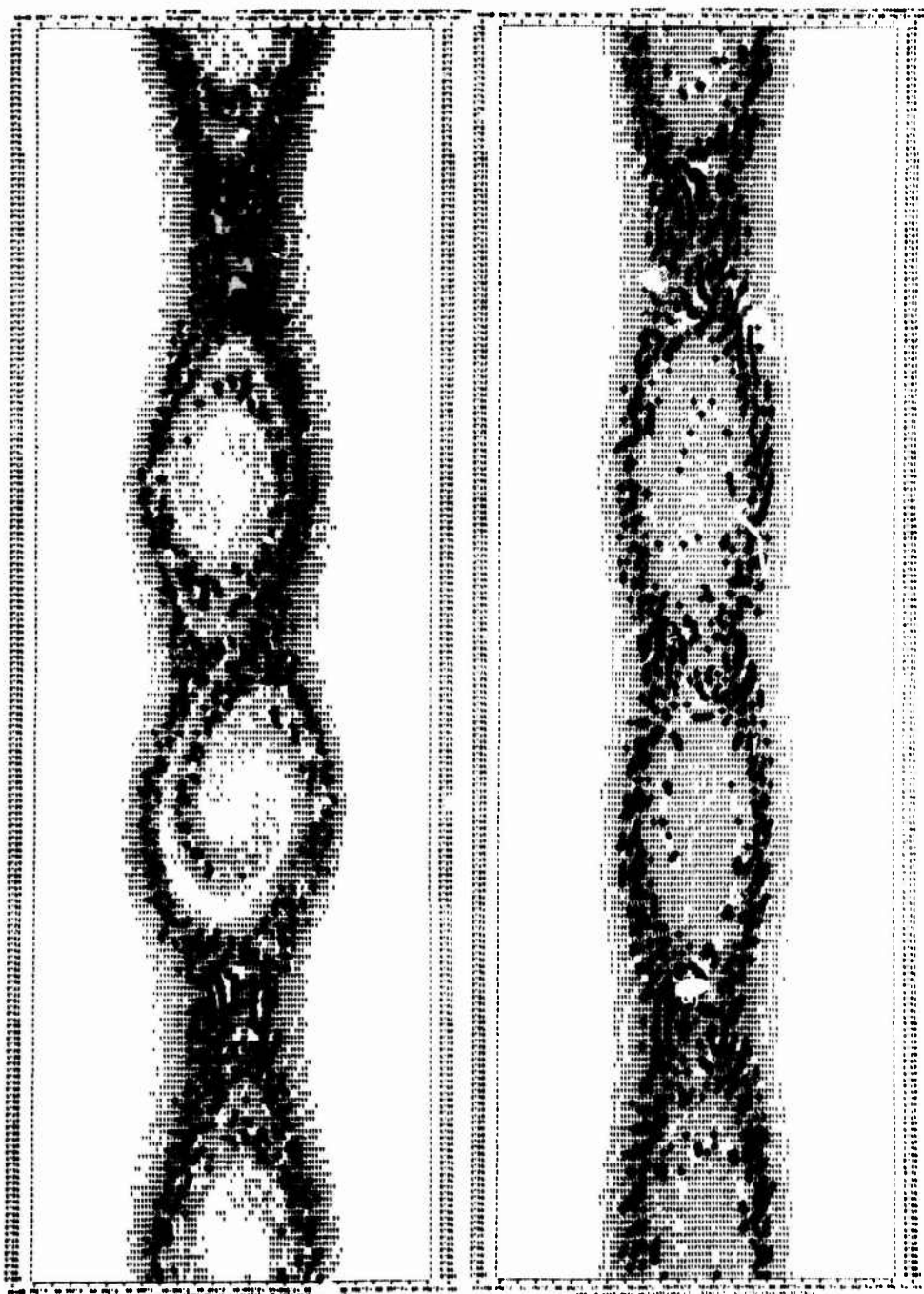
Fig. 5. Velocity distribution $g(x,v)$ at first saturation peak for collisionless plasma (top) and $\nu = 0.03 \ \omega_p$

Fig. 6. Velocity distribution g(x,v) at second saturation peak for collisionless plasma (top) and $\nu \approx 0.03$ ω_p.
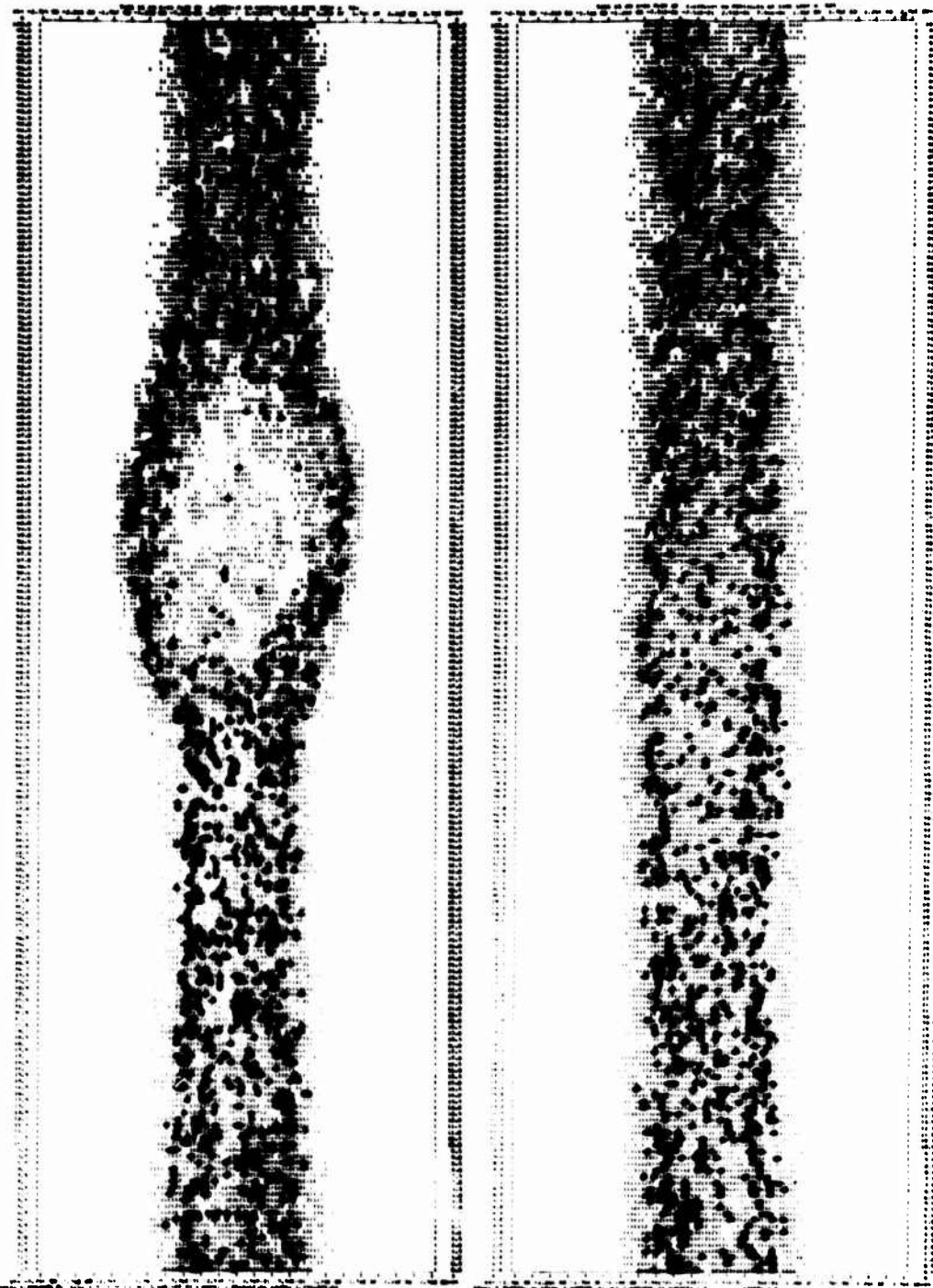
Fig. 7. Velocity distribution g(x,v) at long times (t = 24 ω_p^{-1} for the collisionless case, 20 ω_p^{-1} for the collisional case).

collisionless case, 20 ω_p^{-1} for the collisional case). At this stage, the collisional case is essentially uniform in x already, although it is not yet Maxwellianized.

Acknowledgments

Bibliography and Footnotes

1. R.W. Hockney, Phys. Fluids 9, 1826 (1966).

2. C. K. Birdsall and D. Fuss, J. Comp. Phys. 3, 494 (1969).

3. R. L. Morse and C. W. Nielsen, Phys. Fluids 12, 2418 (1969).

4. T. A. Oliphant and C. W. Nielsen, Phys. Fluids 13, 2103 (1970).

5. R. J. Mason and C. K. Chu, in Proc. 7th Intern. Symp. Rarefied Gas Dynamics, Pisa, Italy, 1970; Academic Press, to appear.

6. This is in spirit similar to F. H. Harlow's original particle-in-cell method for continuum fluids, in which the particles carry with them density and internal energy. See, for example, F. H. Harlow in "Methods of Computational Physics", Vol.3, ed. B. Alder et al, Academic Press, 1964.

7. P. L. Bhatnagar, E. P. Gross and M. Krook, Phys. Rev. 94, 511 (1954).

8. C. K. Chu, Phys. Fluids 8, 12 (1965) and Phys. Fluids 8, 1450 (1965).

9. R. J. Mason, Phys. Fluids 11, 2524 (1968) and Phys. Fluids 13, 1467 (1970).

10. R. L. Morse and C. W. Nielsen, Phys. Rev. Lett. 23, 1087 (1969).

11. K. V. Roberts and H. L. Berk, Phys. Rev. Lett. 19, 297 (1967) and NASA Rept. SP-153, 1967.

The Alternating-Direction Implicit (ADI) Numerical Solution of Time-Dependent Two-Dimensional Two-Fluid Magnetohydrodynamic (MHD) Equations

Irvin Lindemuth[*]
Department of Applied Science
University of California at Davis
Livermore, California

John Killeen[**]
Department of Applied Science
and
Lawrence Radiation Laboratory
University of California
Livermore, California

INTRODUCTION

A very general method for solving numerically two-dimensional, two-fluid magnetohydrodynamic equations is being developed. The method uses second order accurate, alternating direction implicit finite difference equations. The accuracy and implicitness of the codes which have been developed using the method are features not available in previously reported codes.[1] The equations which are solved by the codes are written in vector form as

$$\frac{\partial \rho}{\partial t} + \bar{v} \cdot \nabla \rho + \rho \nabla \cdot \bar{v} = 0 \tag{1}$$

$$\frac{\partial \bar{v}}{\partial t} + \bar{v} \cdot \nabla \bar{v} + \frac{1}{\rho} \nabla [\rho(\theta_i + \theta_e)] + \frac{\bar{B}}{\rho \mu_0} \times (\nabla \times \bar{B}) = 0 \tag{2}$$

$$\frac{\partial \theta_i}{\partial t} + \bar{v} \cdot \nabla \theta_i + (\gamma - 1)\theta_i \nabla \cdot \bar{v} - \frac{1}{\rho} \nabla \cdot (K_i \nabla \theta_i) + \frac{(\theta_i - \theta_e)}{\tau_{EQ}} = 0 \tag{3}$$

$$\frac{\partial \theta_e}{\partial t} + \bar{v} \cdot \nabla \theta_e + (\gamma - 1) \theta_e \nabla \cdot \bar{v} - \frac{1}{\rho} \nabla \cdot (K_e \nabla \theta_e) + \frac{(\theta_i - \theta_e)}{\tau_{EQ}}$$

$$- \frac{(\gamma - 1)}{\rho \mu_0^2} \eta (\nabla \times \bar{B})^2 = 0 \qquad (4)$$

$$\frac{\partial \bar{B}}{\partial t} + \bar{v} \cdot \nabla \bar{B} + \bar{B}(\nabla \cdot \bar{v}) - \bar{B} \cdot \nabla \bar{v} + \frac{1}{\mu_0} \nabla \times (\eta \nabla \times \bar{B}) = 0 \quad (5)$$

where K_i and K_e are the ion and electron thermal conductivities, η the resistivity, τ_{EQ} the equipartition time, ρ is the density, $\bar{v}$ the fluid, or average, velocity, θ_i and θ_e the ion and electron temperatures, and $\bar{B}$ the magnetic field. The equations are solved in cylindrical coordinates with axial symmetry, so that no variation in the azimuthal direction occurs.

Denoting $\bar{U}$ as a nine-component vector whose components are dependent variables and $\bar{K}$ as a four-component vector whose components are the transport coefficients, each a function of $\bar{U}$, so that

$$\bar{U} = (\rho, v_r, v_\phi, v_z, \theta_i, \theta_e, B_r, B_\phi, B_z) \qquad (6)$$

and

$$\bar{K} = \bar{K}(\bar{U}) = (K_i, K_e, 1/\tau_{EQ}, \eta) \qquad (7)$$

the equations (1) through (5) can be written in cylindrical coordinates with axial symmetry as

$$\frac{\partial \bar{U}}{\partial t} + \bar{T} \left(\bar{U}, \frac{\partial \bar{U}}{\partial r}, \frac{\partial \bar{U}}{\partial z}, \frac{\partial^2 \bar{U}}{\partial r^2}, \frac{\partial^2 \bar{U}}{\partial z^2}, \bar{K}, \frac{\partial \bar{K}}{\partial r}, \frac{\partial \bar{K}}{\partial z} \right) = 0 \qquad (8)$$

where $\bar{T}$ is a nine-component nonlinear, coupled vector function of the arguments indicated. The alternating direction implicit finite difference approximations to equation (6) have on one time step the form

408

$$(\bar{\bar{A}})^n_{i,j} \cdot \bar{U}^{n+1}_{i,j} + (\bar{\bar{B}})^n_{i,j} \cdot \bar{U}^{n+1}_{i+1,j} - (\bar{\bar{C}})^n_{i,j} \cdot \bar{U}^{n+1}_{i-1,j} = \bar{V}^n_{i,j} \qquad (9)$$

and on the following time step

$$(\bar{\bar{A}}')^{n+1}_{i,j} \cdot \bar{U}^{n+2}_{i,j} + (\bar{\bar{B}}')^{n+1}_{i,j} \cdot \bar{U}^{n+2}_{i,j+1} - (\bar{\bar{C}}')^{n+1}_{i,j} \cdot \bar{U}^{n+2}_{i,j-1} = \bar{V}'^{n+1}_{i,j} \quad (10)$$

In equations (9) and (10) $\bar{\bar{A}}$, $\bar{\bar{A}}'$, $\bar{\bar{B}}$, $\bar{\bar{B}}'$, $\bar{\bar{C}}$, and $\bar{\bar{C}}'$ are 9×9 matrices, $\bar{V}$ and $\bar{V}'$ are nine-component vectors, and the superscript n and subscripts i and j refer to the space-time point (t^n, r_i, z_j). The difference equations (9) and (10) are "tridiagonal" in the implicit quantities and are solved by a generalization to vector equations of the method given by Richtmyer[2] and Morton for scalar equations.

Tokamak and Levitron geometries involve all three components of the fluid velocity and magnetic field. The computer codes written to calculate all nine dependent variables given in (6) are also set up to calculate several subsets of the nine. The subsets are

$$\bar{U} = (\rho,\ v_r,\ \theta_i,\ \theta_e,\ B_z) \qquad (11)$$

applicable to one-dimensional theta pinches,

$$\bar{U} = (\rho,\ v_r,\ \theta_i,\ \theta_e,\ B_\phi,\ B_z) \qquad (12)$$

applicable to one-dimensional stabilized z pinches, and

$$\bar{U} = (\rho,\ v_r,\ v_z,\ \theta_i,\ \theta_e,\ B_r,\ B_z) \qquad (13)$$

appropriate for two-dimensional theta-pinch geometries and laser produced plasma expansion studies. For one-dimensional calculations, of course, $\bar{\bar{B}}'$ and $\bar{\bar{C}}'$ of equation (10) are zero and the calculations are performed for only one value of j.

For a uniform space mesh with equal increments Δr in the radial direction and equal increments Δz in the axial direction, the truncation error e (as defined by Richtmyer[2]) of each of the difference equations (9) and (10) is rigorously

$$e = o[\Delta t] + o[(\Delta r)^2] + o[(\Delta z)^2] \tag{14}$$

and, when (9) and (10) are combined, the over-all two-step truncation error is

$$e = o[(\Delta t)^2] + o[(\Delta r)^2] + o[(\Delta z)^2] \tag{15}$$

so that the finite difference equations are second order in the same spirit as the Peaceman-Rachford[3] equations for a simple diffusion equation. The second order accuracy (15) means essentially that a degree of implicitness is given to the transport coefficients and the coefficients of all spatial derivatives in equation (8).

FINITE DIFFERENCE METHOD -- FIRST TIME STEP

The finite difference equations (9) and (10) are derived by dividing the components of the vector $\overline{T}$ into two separate parts, one involving all radial derivatives and one involving all axial derivatives. Thus the β component of $\overline{T}$ is written as

$$T_\beta = \overline{f}^\beta(\overline{U}, \frac{\partial \overline{U}}{\partial r}, \frac{\partial^2 \overline{U}}{\partial r^2}, \overline{K}, \frac{\partial \overline{K}}{\partial r}) \cdot \overline{g}^\beta(\overline{U}, \frac{\partial \overline{U}}{\partial z}, \frac{\partial^2 \overline{U}}{\partial z^2}, \overline{K}, \frac{\partial \overline{K}}{\partial z}) \tag{16}$$

where $\overline{f}^\beta$ and $\overline{g}^\beta$ are nonlinear vector functions of the arguments indicated; in general, the number of components of $\overline{f}^\beta$ and $\overline{g}^\beta$ will depend on β.

On the first time step (corresponding to (9)) $\overline{f}^\beta$ is treated implicitly and $\overline{g}^\beta$ explicitly. Because $\overline{f}^\beta$ is a nonlinear function, it is linearized in the implicit quantities. After the linearization $\overline{T}$ has the form

$$(\overline{T})^{n+1}_{i,j} = (\overline{\overline{a}})^n_{i,j} \cdot \overline{U}^{n+1}_{i,j} + (\overline{b})^n_{i,j} \cdot (\frac{\partial \overline{U}}{\partial r})^{n+1}_{i,j}$$

$$+ (\overline{\overline{c}})^n_{i,j} \cdot (\frac{\partial^2 \overline{U}}{\partial r^2})^{n+1}_{i,j} - (\overline{v})^n_{i,j} \qquad (17)$$

where $\overline{\overline{a}}$, $\overline{b}$, and $\overline{\overline{c}}$ are 9 x 9 matrices with elements

$$a_{\beta\alpha} = g^\beta_\epsilon \left[\frac{\partial f^\beta_\epsilon}{\partial U_\alpha} + \frac{\partial f^\beta_\epsilon}{\partial K_\gamma} \frac{\partial K_\gamma}{\partial U_\alpha} + \frac{\partial f^\beta_\epsilon}{\partial K_\gamma} \frac{\partial^2 K_\gamma}{\partial U_\alpha \partial r} \right] \qquad (18)$$

$$b_{\beta\alpha} = g^\beta_\epsilon \left[\frac{\partial f^\beta_\epsilon}{\partial (\frac{\partial U_\alpha}{\partial r})} + \frac{\partial f^\beta_\epsilon}{\partial (\frac{\partial K_\gamma}{\partial r})} \frac{K_\gamma}{\partial U_\alpha} \right] \qquad (19)$$

$$c_{\beta\alpha} = g^\beta_\epsilon \frac{\partial f^\beta_\epsilon}{\partial (\frac{\partial^2 U_\alpha}{\partial r^2})} \qquad (20)$$

and $\overline{v}$ is a vector with nine components

$$v_\beta = - g^\beta_\epsilon f^\beta_\epsilon + a_{\beta\alpha} U_\alpha + b_{\beta\alpha} \frac{\partial U_\alpha}{\partial r} + c_{\beta\alpha} \frac{\partial^2 U_\alpha}{\partial r^2} . \qquad (21)$$

In equations (18) through (21) the superscript n and subscripts i and j are expressly implied for all quantities, and the

411

repeated subscripts γ and ϵ indicate a summation over all components of the subscripted vectors, but no summation is indicated by the repeated superscript β. The final difference equation (9) results from using the standard one-sided finite difference approximation to the time derivative in (8) and the standard space-centered finite difference approximation to all spatial derivatives in (17) through (21). The matrices $\bar{\bar{A}}$, $\bar{\bar{B}}$, and $\bar{\bar{C}}$ of (9) are then given by

$$A_{\beta\alpha} = a_{\beta\alpha} + \frac{\delta_{\beta\alpha}}{\Delta t} + \frac{(\Delta r_+ - \Delta r_-)}{\Delta r_+ \Delta r_-} b_{\beta\alpha} - \frac{2}{\Delta r_+ \Delta r_-} c_{\beta\alpha} \qquad (22)$$

$$B_{\beta\alpha} = \frac{\Delta r_-}{\Delta r_+ (\Delta r_- + \Delta r_+)} b_{\beta\alpha} + \frac{2}{\Delta r_+ (\Delta r_- + \Delta r_+)} c_{\beta\alpha} \qquad (23)$$

$$C_{\beta\alpha} = \frac{\Delta r_+}{\Delta r_- (\Delta r_- + \Delta r_+)} b_{\beta\alpha} - \frac{2}{\Delta r_- (\Delta r_- + \Delta r_+)} c_{\beta\alpha} \qquad (24)$$

and the vector $\bar{v}$ is given by

$$V_{\beta} = \frac{\delta_{\beta\alpha} U_{\alpha}}{\Delta t} + v_{\beta} . \qquad (25)$$

In equations (22) through (25) the superscript n and subscripts i and j are expressly implied. The "Kronecker delta" $\delta_{\beta\alpha}$ appears in (22) and (25).

FINITE DIFFERENCE METHOD -- SECOND TIME STEP

On the second time step (corresponding to (10)), $\bar{g}^{\beta}$ of (16) is treated implicitly and $\bar{f}^{\beta}$ is treated explicitly. The procedure for deriving the final difference equation (10) is analogous to that for deriving (9). Thus, the matrices $\bar{\bar{A}}'$, $\bar{\bar{B}}'$, and $\bar{\bar{C}}'$ of (10) are given by

$$A'_{\beta\alpha} = a'_{\beta\alpha} + \frac{\delta_{\beta\alpha}}{\Delta t} + \frac{(\Delta z_+ - \Delta z_-)}{\Delta z_+ \Delta z_-} b'_{\beta\alpha} - \frac{2}{\Delta z_+ \Delta z_-} c'_{\beta\alpha} \qquad (26)$$

$$B'_{\beta\alpha} = \frac{\Delta z_-}{\Delta z_+ (\Delta z_- + \Delta z_+)} b'_{\beta\alpha} + \frac{2}{\Delta z_+ (\Delta z_- + \Delta z_+)} c'_{\beta\alpha} \qquad (27)$$

$$C'_{\beta\alpha} = \frac{\Delta z_+}{\Delta z_- (\Delta z_- + \Delta z_+)} b'_{\beta\alpha} - \frac{2}{\Delta z_- (\Delta z_- + \Delta z_+)} c'_{\beta\alpha} \qquad (28)$$

and the vector $\bar{v}'$ is given by

$$V'_{\beta} = \frac{\delta_{\beta\alpha} U_{\alpha}}{\Delta t} + v'_{\beta} . \qquad (29)$$

Analogous to (18) through (21), the matrices $\bar{\bar{a}}'$, $\bar{\bar{b}}'$, and $\bar{\bar{c}}'$ and the vector $\bar{v}'$ appearing in (26) through (29) are given by

$$a'_{\beta\alpha} = f^{\beta}_{\epsilon} \left[\frac{\partial g^{\beta}_{\epsilon}}{\partial U_{\alpha}} + \frac{\partial g^{\beta}_{\epsilon}}{\partial K_{\gamma}} \frac{\partial K_{\gamma}}{\partial U_{\alpha}} + \frac{\partial g^{\beta}_{\epsilon}}{\partial \left(\frac{K_{\gamma}}{\partial z}\right)} \frac{\partial^2 K_{\gamma}}{\partial U_{\alpha} \partial z} \right] \qquad (30)$$

$$b'_{\beta\alpha} = f^{\beta}_{\epsilon} \left[\frac{\partial g^{\beta}_{\epsilon}}{\partial \left(\frac{U_{\alpha}}{\partial z}\right)} + \frac{\partial g^{\beta}_{\epsilon}}{\partial K_{\gamma}} \frac{\partial K_{\gamma}}{\partial U_{\alpha}} \right] \qquad (31)$$

$$c'_{\beta\alpha} = f^{\beta}_{\epsilon} \frac{\partial g^{\beta}_{\epsilon}}{\partial \left(\frac{\partial^2 U_{\alpha}}{\partial z^2}\right)} \qquad (32)$$

$$v'_{\beta} = - g^{\beta}_{\epsilon} f^{\beta}_{\epsilon} + a'_{\beta\alpha} U_{\alpha} + b'_{\beta\alpha} \frac{\partial U_{\alpha}}{\partial z} + c' \frac{\partial^2 U_{\alpha}}{\partial z^2} . \qquad (33)$$

In equations (26) through (33) the superscript n + 1 and the subscripts i and j are expressly implied for all quantities, and the repeated subscripts α, γ, and ϵ indicate a summation.

TRUNCATION ERROR

The first order truncation error indicated in (14) is a result of using one-sided time differences for the time derivative in (8) and from treating $\bar{g}^{\beta}$ explicitly on the first

413

time step and implicitly on the second time step, i.e., $\overline{g}^{\beta}$ is evaluated at t^n and t^{n+2}, rather than twice successively at t^{n+1}. However, when (9) and (10) are used alternately the $o[\Delta t]$ truncation errors cancel. For a nonuniform mesh, the spatial truncation error for terms involving second spatial derivatives is actually $o[\Delta r] + o[\Delta z]$ because of the use of the standard three point finite difference approximation, but, for a uniform mesh, the truncation error has the form given in (14) and (15).

AN ELEMENTARY EXAMPLE

For a simple two-dimensional diffusion equation

$$\frac{\partial U}{\partial t} - K \left(\frac{\partial^2 U}{\partial r^2} + \frac{\partial^2 U}{\partial z^2} \right) - \frac{\partial K}{\partial r} \frac{\partial U}{\partial r} - \frac{\partial K}{\partial z} \frac{\partial U}{\partial z} = 0 \tag{34}$$

the vectors $\overline{f}$ and $\overline{g}$ corresponding to equation (16) are

$$\overline{f} = \left(\frac{\partial^2 U}{\partial r^2}, \ K, \ \frac{\partial K}{\partial r} \frac{\partial U}{\partial r}, \ 1 \right) \tag{36}$$

and

$$\overline{g} = \left(-K, \ -\frac{\partial^2 U}{\partial z^2}, \ -\downarrow, \ -\frac{\partial K}{\partial z} \frac{\partial U}{\partial z} \right) \tag{36}$$

The calculation of the matrices and vectors corresponding to equations (18) through (21) and equations (30) through (33) and the calculation of the final difference equations corresponding to (9) and (10) is straightforward. For the very simple case when K is independent of U, r, and z, and for a uniform mesh, the complete difference equations are

414

$$\left[\frac{1}{\Delta t} + \frac{2K}{(\Delta r)^2} \right] U_{i,j}^{n+1} - \frac{K}{(\Delta r)^2} U_{i+1,j}^{n+1} - \frac{K}{(\Delta r)^2} U_{i-1,j}^{n+1}$$

$$= \frac{U_{i,j}^{n}}{\Delta t} + \frac{K}{(\Delta z)^2} (U_{i,j+1}^{n} - 2U_{i,j}^{n} + U_{i,j-1}^{n})$$

and

$$\left[\frac{1}{\Delta t} + \frac{2K}{(\Delta z)^2} \right] U_{i,j}^{n+2} - \frac{K}{(\Delta z)^2} U_{i,j+1}^{n+2} - \frac{K}{(\Delta z)^2} U_{i,j-1}^{n+2}$$

$$= \frac{U_{i,j}^{n+1}}{\Delta t} + \frac{K}{(\Delta r)^2} (U_{i+1,j}^{n+1} - 2U_{i,j}^{n+1} + U_{i-1,j}^{n+1})$$

which are merely the Peaceman and Rachford[3] equations.

CONCLUSION

The alternating direction implicit method presented above is novel in that all factors in all terms, not just the spatial derivatives, are treated implicitly at one time step or the other. It must be mentioned, however, that there is a degree of arbitrariness in the determination of the vectors $\overline{f}^{\beta}$ and $\overline{g}^{\beta}$ of (16), and experience has shown that how the vectors are selected can affect the performance of the codes. The method described in this paper requires that all r and z derivatives be written out completely so that the different'al equations do indeed have the functional form given in (8). Experience has shown that there are some computational advantages if the differential equations are written as "conservatively" as possible and differenced in the conservative form. The codes

developed to date solve the equations both in the form (8) and
a conservative form. The conservative equations are somewhat
more difficult to handle, but the method used, to be reported
at a later date, is a generalization of that presented above
and the final difference equations are identical in form to
equations (9) and (10). The method for deriving the finite
difference equations (9) and (10) has also been used to solve
the equations corresponding to (6) and (13) with the radial
and axial magnetic field components B_r and B_z replaced by a
stream function Ψ, which is the azimuthal component of the
vector potential multiplied by the radius r. The differential
equations solved have the same form as equation (8). The
method is quite general and may actually be applicable to more
sets of differential equations than the MHD equations for which
it has actually been implemented.

It is difficult to assess at this time the extent of the
advantages of the alternating direction implicit MHD calcula-
tions over the several explicit schemes reported[1] with respect
to enhanced numerical stability. Our calculations performed
to date indicate numerical stability for time steps several
times larger than would be allowed with an explicit method,
but the maximum allowable time step has not yet been fully
determined. It is expected that the implicitness and second
order accuracy of the method presented above will allow calcu-
lations covering a longer real time than is presently feasible

with explicit methods. With the advent of the new generation of computers it is certain that alternating direction implicit calculations in magnetohydrodynamics and other areas of computational physics will be performed more and more frequently.

REFERENCES

1. Roberts, K. V., and Potter, D. E., Methods in Computational Physics, Vol. 9, edited by Alder, B., Fernbach, S., and Rotenbert, M., Academic Press (1970)

2. Richtmyer, R. D., and Morton, K. W., Difference Methods for Initial Value Problems, Interscience (1967)

3. Peaceman, D. W., and Rachford, H. H., Jr., J. Soc. Ind. App. Math. 3, 28 (1955)

Computing the Nonlocal Conductivity

William M. Leavens
Military Airplane Systems Division
The Boeing Company
Seattle, Washington

Carl H. Love
Environmental Science Services Administration
Boulder, Colorado

and

Ronal W. Larson
Georgia Institute of Technology
Atlanta, Georgia

ABSTRACT

The nonlocal conductivity provides a useful representation of the a-c properties of nonuniform plasmas. A computer program is described which computes the conductivity for high frequency longitudinal perturbations. The routine is efficient and accurate. Its logical structure and the more novel algorithms are described. Overall numerical accuracy is described in terms of the convergence of the positions of the ω-plane poles of the conductivity. The great care required to obtain this convergence probably is illustrative of what is needed in many calculations.

I. INTRODUCTION

The behavior of weak disturbances in a plasma can be characterized by a nonlocal conductivity tensor.[1] This "conductivity kernel" is specified by the steady state (assumed to be known) of the plasma. Because the unknown velocity dependence in the kinetic equation does not appear explicitly in the conductivity kernel, and because the same kernel determines the response to a variety of external forces, numerical computation of the conductivity kernel is sometimes more attractive than a direct numerical attack on the kinetic equation. Several authors have used the conductivity kernel to study one-dimensional electron-plasma oscillations in inhomogeneous plasmas.[2-5]

The purpose of this paper is to describe a method of computing the conductivity kernel which is efficient and converges well. The procedure is applicable to arbitrary monotonic density variations, and could be extended to two-dimensional problems or to include model collisions in a natural way.

In Section II, the conductivity kernel is given for one-dimensional electrostatic oscillations in a Maxwellian plasma. Algorithms, the dominant logical considerations, and details of the numerical techniques are given in Section III. Evaluating convergence is facilitated by a normal mode interpretation of the results.[6] A set of detailed results is included in an earlier report.[7] Flow charts are given in the Appendix.

II. THE NONLOCAL CONDUCTIVITY

The general form of the nonlocal conductivity tensor has been derived[1,3] from the Vlasov equation. Only the conductivity for high

frequency, one-dimensional electrostatic oscillations will be considered explicitly, although much of the work can be carried over to other situations.

A. Description of the Steady State

For frequencies near the electron plasma frequency, $\omega_p(x) = [4\pi N_0(x)e^2/m]^{1/2}$, where $N_0(x)$ is the unperturbed electron density, the massive ions cannot respond significantly to electric fields, and only the electrons contribute to the conductivity. The unperturbed plasma is then specified by an electron distribution function, $F_0(x,v) = N_0(x)f_0(x,v)$, and an electrostatic potential, $\phi_0(x)$.

The unperturbed collisionless electron paths in phase space are determined by the initial conditions,

$$\left. \begin{array}{l} x' = x \\ \\ v' = v \end{array} \right\} \quad \text{at } t' = t,$$

and by the equations of motion,

$$\frac{dx'}{dt'} = v' \quad ,$$

$$\frac{dv'}{dt'} = -\frac{e}{m} E_0(x') \quad ,$$

(1)

where $E_0(x') = -\partial\phi_0(x')/\partial x'$. The distribution function must be consistent with ϕ_0,

$$F_0(x',v') = F_0(x,v) \quad . \tag{2}$$

Whenever an electron strikes a wall it sticks long enough to recombine, and we should set

$$F_o(x',v') = 0 \qquad\qquad (2')$$

for all later times. So few electrons reach floating walls, however, that the error in assuming reflection at the wall is negligible.

In most experimental situations, the potential, $\phi_o(x)$, will be such as to trap the negatively charged electrons, with the minimum potential, $-\phi_F$, the "floating potential," at the boundaries.

An orbit may connect two points, x and x', either directly, or by going through a turning point one or more times. Going backward along the orbit from (x,v), let p be the number of times that the orbit has gone through turning points to reach x'. Then, for a particular potential function, the segment of the orbit connecting x and x' is specified by x, v, x', and p. The velocity at x' is written as $v'(x,v'x',p)$, and the time to go from x' to x is denoted by $\tau(x,v;x',p)$.

The characteristics of the steady state which will determine the nonlocal conductivity are the orbit times, $\tau(x,v;x',p)$, and the number of electrons on an infinitesimal set of orbits, $F_o(x,v)dxdv$. The actual choice of the model plasma is a matter of computational convenience and the availability of experimental data or a detailed theory. The rigid ion density can always be chosen to satisfy Poisson's equation.

B. The Nonlocal Conductivity

Formal solution of the linearized Vlasov equation by the method of characteristics[1-3] leads directly to the nonlocal Ohm's law,

Leavens, Love, and Larson

$$J_1(x) = \int_0^L \sigma(x;x')E_1(x')dx' \qquad , \qquad (3)$$

where $0 \leq x \leq L$. The nonlocal conductivity is

$$\sigma(x;x') = -\frac{e^2}{m} \sum_{p=0}^{\infty} \int_{-\infty}^{\infty} \frac{vu(x,v;x',p)}{|v'(x,v;x',p)|} \frac{\partial F_o(x',v')}{\partial v'} e^{i\omega\tau(x,v;x',p)}dv, \quad (4)$$

where

$$u(x,v;x',p) = \begin{array}{l} 1, \text{ on allowed orbit segments,} \\ 0, \text{ on forbidden orbit segments.} \end{array}$$

The orbit segment $(x,v;x',p)$ is "forbidden" if an electron from x' cannot reach (x,v) after p turning points. The other factors are defined above.

The perturbing field, E_1, is the sum of any externally applied driving field, E_d, and the field set up by charges in the plasma, E_p, that is

$$E_1(x) = E_p(x) + E_d(x) \qquad , \qquad (5)$$

where, for electrostatic oscillations,

$$i\omega E_p(x) = 4\pi J_1(x) \qquad , \qquad (6)$$

and

$$E_p(x) = \int_0^L K(x;x')E_1(x')dx' \qquad , \qquad (7)$$

where

$$K(x;x') = \frac{4\pi}{i\omega} \sigma(x;x') \qquad . \qquad (8)$$

We shall usually refer to K, rather than σ, as the conductivity kernel.

Derivations[1,3] of the conductivity kernel make it clear that Eq. (7) corresponds to Landau's form of the initial value problem, and that we must follow the Landau convention with respect to any poles in the integrand of Eq. (4). The only poles in the lower half of the ω-plane arise from the sum of successive passages (p) for orbits which are periodic with period equal to an integer multiple of the oscillation period. These poles are easily destroyed by weak collisions,[3] and probably can be safely dropped in most unmagnetized plasmas. We shall use a model in which there are no periodic orbits (u ≈ 0 for p > 1), and only the principle value of the integral over velocity contributes to the conductivity. This model corresponds exactly to a one-sided nonuniform plasma.

II. COMPUTING THE NONLOCAL CONDUCTIVITY

A. Simplification by Choice of Model

We have just made one important simplification by choosing a one-sided model, keeping only p = 0 and p = 1. Choosing F_0 to be Maxwellian makes a very important difference, specifically it allows us to eliminate v' from K by substituting

$$\frac{\partial F_0(x',v')}{\partial v'} = -\frac{mv'}{kT} F_0(x',v') = -\frac{mv'}{kT} F_0(x,v),$$

and

$$\frac{v'(x,v;x',p)}{|v'(x,v;x',p)|} = (-1)^P ,$$

(9)

into Eqs. (4) and (8), obtaining

$$K(x;x') = \frac{\omega_p^2(x)}{i\omega} \frac{m}{kT} \sum_{p=0}^{1} (-1)^P \int_{-\infty}^{\infty} f_0(v) u(x,v;x',p) e^{i\omega\tau(x,v;x',p)} v \, dv,$$

(10)

423

where

$$f_o(v) = \left(\frac{m}{2\pi kT}\right)^{3/2} e^{-mv^2/2kT} \quad .$$

Provided that all orbits have a turning point, i.e. for every electron at (x,v) there is one at $(x,-v)$, it is readily shown that

$$K(x;x') = K(x';x) \qquad . \qquad (11)$$

Since the number of electrons reaching a typical floating wall is $O(m/M_+)^{1/2}$, we may safely ignore the asymmetry resulting from wall recombination. This not only saves half the computing, but also simplifies the logic, since choosing $x \geq x'$ $(-e\phi_o(x) \geq -e\phi_o(x'))$ guarantees that any electron having sufficient energy to reach x will also reach x'. Wall effects can be easily included if necessary.

B. Numerical Representations

Algorithms must be chosen for three integrations:

1. The orbit time,

$$\tau(x,v;x',p) = \int\limits_{(x,v)}^{(x',p)} \frac{dx''}{v(x'')} \qquad . \qquad (12)$$

Let $\phi_o(x) = 0$ at $x = 0$, and let $1/2\ mv^2 - e\phi_o(x) = \mathcal{E}$, then

$$\tau(x,v;x',0) = \tau(x,\mathcal{E}) - \tau(x',\mathcal{E}), \quad x > x'$$

and $\qquad\qquad\qquad\qquad\qquad\qquad\qquad\qquad\qquad\qquad (13)$

$$\tau(x,v;x'1) = 2\tau(x_{tp},\mathcal{E}) - \tau(x,\mathcal{E}) - \tau(x',\mathcal{E}) \ ,$$

where $-e\phi_o(x_{tp}) = \mathcal{E}$, and

$$\tau(x,\mathcal{E}) = \int_0^x \frac{dx'}{\sqrt{\mathcal{E}+e\phi_o(x')}} \; , \; 0 \le x \le x_{tp} \qquad . \tag{14}$$

Only $\tau(x,\mathcal{E})$ needs to be computed and stored. This is the familiar numerical problem of computing orbits in a static potential. We use Gaussian quadrature over each space step,

$$\tau(x_{n+1},\mathcal{E}) - \tau(x_n,\mathcal{E}) = \sum_{i=1}^{N} a_i \, g(y_i) \qquad , \tag{15}$$

where the a_i, y_i are the Gaussian weights and points in the interval. Usually (far from turning points), we choose

$$y = x, \; g(y) = 1/\sqrt{\mathcal{E}+e\phi_o(x)} = v(x) \qquad . \tag{16}$$

Very close to turning points any polynomial quadrature of Eq. (16) breaks down, so we use the standard transformation,

$$y = \sqrt{x-x_{tp}}, \; g(y) = \sqrt{x-x_{tp}}/v(x) \qquad . \tag{17}$$

Because the potentials are sometimes fairly rapidly varying it is necessary to have an intermediate approximation, which is obtained by defining a virtual turning point, x_{tp}^{*}, to be used in the transformation of Eq. (17), where

$$x_{tp}^{*} = x_{n+1} + \frac{\mathcal{E}+e\phi_o(x_{n+1})}{e[-\phi_o(x_{n+1})+\phi_o(x_n)]} \; (x_{n+1}-x_n) \tag{18}$$

Leavens, Love, and Larson

2. The velocity integrals,

$$I(x;x',p) \equiv (-1)^p \int_{-\infty}^{\infty} f_0(v)u(x,v;x',p)e^{i\omega\tau}v\,dv \quad ,$$

can be rewritten, for $x > x'$, as

$$I(x;x',o) = \int_0^{\infty} f_0(v)e^{i\omega\tau(x,v;v',o)}v\,dv \quad , \qquad (19)$$

and

$$I(x;x',1) = -\int_{-\infty}^0 f_0(v)e^{i\omega\tau(x,v;x',1)}v\,dv \quad ,$$

or

$$I(x;x',1) = \int_0^{\infty} f_0(v)e^{i\omega\tau(x,-v;x',1)}v\,dv \quad . \qquad (20)$$

The integration is done by separate Gaussian quadratures over five ranges,

$$I(x;x',1) = \sum_{N=1}^{5} I_N \quad ,$$

where

$$I_n = \sum_{i=1}^{i_N} a_i^{i_N} h(v_{i,i_N})w_i \qquad (21)$$

where $h = f_0 e^{i\omega\tau}v$, and $a_i^{i_N}, v_{i,i_N}$ are the weights and points for i_Nth order Gaussian quadrature in the range

$$v_{i-1} \le v \le v_i, \; w_i = v_i - v_{i-1}, \; v_o = 0 .$$

Integration in energy space, incidentally, is less accurate, the rapid phase variations being even more compressed into the bottom of the range.

Various choices of the ranges and orders of integration have been tried. So long as the five velocity ranges cover the kinetic energy range from zero to about 15 kT, and are compressed at the low end, the lowest extending from zero to approximately kT/25, the overall accuracy, using i_N = 10 in each range, is better than four significant figures even for fairly large x-x'. In sheaths, where the d-c field is strong, even the longest orbit times are fairly short, and the low velocity ranges can extend to about kT/3.

An alternative procedure, used in an earlier version of this program,[3] is to choose a single set of orbits, uniformly spaced in energy. Then any one orbit can be used for many pairs of points (x,x') rather than a single row. Although, at first hand, this seems more efficient than a technique requiring completely different sets of orbits for each row, it is, in fact, an inferior procedure. The difficulty is simply that numerical accuracy requires a very fine mesh for the lower velocities (at any given x), while the same orbits will be on a wastefully fine mesh for points, x, far from their turning points. One winds up calculating a very large set of orbits, and picking out an appropriate subset for each row. The gain due to overlap of the subsets does not compensate for losing the advantages of Gaussian integration.

3. The space integration,

$$E_p(x) = \int_0^L K(x;x')E_1(x')dx' \quad ,$$

is the most difficult. Let $K = K_o + K_1$, where, in Eq. (10), K_o is the p = 0 contribution, and K_1 is the contribution of reflected particles.

427

On the diagonal we have $\tau(x,v;x,o) = 0$, and

$$\lim_{\epsilon \to o} \text{Im} K_o(x;x-\epsilon) = \frac{\omega_p^2(x)}{\omega} \frac{m}{kT} \int_0^\infty F_o(v)v\,dv \quad ,$$

and obtain the same limit approaching x from above. Consequently, $\text{Im}K_o$ is a smooth function with a maximum at the diagonal. The same applies to both the real and imaginary parts of K_1, and conventional quadrature techniques are suitable for these three parts of K.

However, $\text{Re}K_o$ requires a special algorithm. From Eq. (10) we see that $\text{Re}K_o(x;x) = 0$, again approaching from either side, but that

$$\lim_{\epsilon \to o} \frac{d}{dx'} \text{Re}K_o(x,x\pm\epsilon) = \omega_p^2(x) \frac{m}{kT} \int_{-\infty}^\infty f_o(v)u(x,v;x,o) \frac{v\,dv}{(\pm v)} = \pm \frac{\omega_p^2(x)u}{2kT} \quad , \tag{22}$$

is nonzero and changes sign at the diagonal. Thus, $\text{Re}K_o$ has a cusp on the diagonal.

There are several possible techniques for handling the cusp. Most require a finer mesh that we can afford (see the next section). By far the best procedure is to generate smooth continuations of $\text{Re}K_o$ across the diagonal in both directions. Clearly the smooth continuations cannot be generated by extrapolation. That would be equivalent to using the end point formulas with their large errors.

Define the extended functions $\text{Re}K_o^\pm(x;x')$, by

$$\text{Re}K_o^-(x;x'\leq x) = \text{Re}K_o(x;x') \quad ,$$

$$\text{Re}K_o^-(x;x'\geq x) = -\frac{\omega_p^2(x')}{\omega_p^2(x)} \text{Re}K_o(x;x') \quad , \tag{23}$$

$$\mathrm{ReK_0}^+(x;x' \leq x) = -\frac{\omega_p^2(x)}{\omega_p^2(x')} \, \mathrm{ReK_0}(x;x') \qquad ,$$

$$\mathrm{ReK_0}^+(x;x' \geq x) = \mathrm{ReK_0}(x;x') \qquad .$$

To the extent that $\phi_0(x)$ is smooth, there are no discontinuities in $\mathrm{ReK_0}^{\pm}$ and their derivatives. Now we may write

$$\int_0^L \mathrm{ReK_0}(x;x')E_1(x')dx' = \int_0^x \mathrm{ReK_0}^-(x;x')(E_1(x')dx' + \int_x^L \mathrm{ReK_0}^+(x;x')E(x')dx' \quad ,$$

and use midrange integration formulas right up to the diagonal.

Difficulties at the boundaries have been avoided by doing problems where either the fields or the kernel are small there, so that the errors in the end point integration formulas will not matter. Except at the boundaries, the six-point midrange integration formulas were used. Higher order quadratures did not help because the relatively large mesh spacing puts mesh points, other than the nearest six, sufficiently far away that the behavior of the kernel is distinctly non-polynomial.

Convergence of the results is best determined by examining the convergence of the eigenfrequencies of the system. These have been found[6] by a fairly elaborate numerical analysis of the results of this calculation. For a fairly realistic model of a nonuniform plasma with a sheath, we obtained clear-cut convergence using the algorithms described above and 73 space points. Under these conditions the collisionless damping is determined to within no better than a few percent, even though the calculation is generally two orders of magnitude better.

C. Logical Structure

Efficient execution depends primarily on the logical structure of the programs. The present routines are designed to work on a 32-64K memory sequential processor (CDC 3600). Fast masking operations are essential, as is at least a 48 bit word. Larger memory, mass memory, and/or a parallel processor could be used to great advantage. The logical structure is largely determined by the following considerations:

1. K must fit entirely in core. A 73×73 complex matrix can be inverted by the Gauss-Jordan method in about one minute of CPU time. The inversion time goes like N_x^3, but blows up much more rapidly when input-output operations are required. It does not seem likely, for this reason, that problems with two unknown space dependences will ever be done this way. Separable cylinder and sphere problems can be done.

2. The kernel program consists of loops nested three deep (x, v, x'). Cylinder and sphere problems would have a second velocity dimension. It is, therefore, important to minimize:

   (a) The number of space points (see (1) above), and the number of velocity points. This requires careful choice of the algorithms, as considered in III.B.

   (b) The execution time for the innermost loop. Standard trigonometric and modulus functions must not be used. The number of multiplications must be as small as possible, there should be no dividions, and integer arithmetic should be used.

3. A separate program to compute the orbits, $\tau(x, \ell)$, will be executed only once for any given model. In this program we can afford extra

time to store the orbits in the form most useful to the kernel program. The orbit calculations can be more accurate, removing them as a source of final errors.

Summary of the Orbits Program - ORBGAUSS

The routine chooses a set of energies suitable for the multiple range Gaussian quadrature of the velocity integration. These same energies are used for all columns, j, in the ith row, where x_i is uphill from x_j (this fills half the matrix, the other half is obtained by symmetry). Within this set, the orbit times, $\tau(\mathcal{E}, x_i \leq x_j)$, are computed and stored on tape, along with identifying information. Each such block of information is referred to as a "cluster"; there is one cluster per row, stored as a single logical record of binary information containing both integer and floating point information.

Summary of the Kernel Program - GAUSSKSIX

A key preliminary calculation is a sine table, scaled to integers $(1 \rightarrow 10^6)$, with arguments θ_n, where

$$\theta_n = \frac{(n-.5)}{4096} \times 2\pi, \quad 1 \leq n \leq 5120 \quad . \tag{24}$$

Cosine is the first four-fifths of the table, sine the last four-fifths. Phases will be scaled such that $2\pi = 4096 = 2^{12}$, and truncated to integers. Modulo 2π can be taken in approximately one cycle time with a masking operation. The error in any one use of this table is

$$\delta \approx 2\pi \times 10^{-4} \qquad ,$$

which is relatively large. These errors, however, seem to cancel out very well.

By using the table we save, every time the one-dimensional kernel program runs, approximately 10^6 calls of the trigonometric and modulus functions. Instead, the operations which are executed 10^6 times are of the forms

$$M = IM - IOT(I) \tag{25}$$

$$M = M.AND.NOY \quad , \tag{26}$$

and

$$KR(I) = KR(I) + IEXWO*ISITBL(M) \quad , \tag{27}$$

where (26) is the modulus 2π operation, NOY = 4096-1, and (27) increments a piece of the kernel.

IV. CONCLUSIONS

The present routine takes about two CPU minutes per run, balancing the time needed to compute the nonlocal conductivity with time to invert the dielectric matrix, and nearly balancing computing and input-output operations during the calculation of the kernel. About 10^2 frequencies, i.e. several hours of CPU time, are needed to give a detailed and accurate picture of the high frequency properties of an inhomogeneous plasma.

In order of importance, this performance depends on:

(1) Keeping the kernel in core during the inversion;

(2) Streamlining the innermost loop; and

(3) Careful choice of integration algorithms.

Our experiences obtaining satisfactory accuracy from these programs encourage a skeptical attitude about numerical calculations. In particular,

when checking convergence, it is important to work at frequencies in the neighborhood of the eigenfrequencies of a system. Far from the eigenfrequencies the response depends on just a few parameters, and it seems to be easier to get a few parameters to converge than many parameters.

V. ACKNOWLEDGMENTS

APPENDIX

Flowcharts

Detailed flow charts are too long to give here. The charts show only large-scale structure. They, taken with the discussions of the algorithms and logical structure in the main text, are an adequate introduction to the programs. The programs themselves are too long to list here, but we can furnish listings on request. The programs have been left entirely in FORTRAN, since the 3600 compiler assembled a very efficient innermost loop. The notes below refer to points in the flow charts.

Note 1: Aside from being monotonic, the potential is arbitrary. Subroutine POT defines the potential and its first four derivatives at the mesh points. POT may also specify the sheath edge, if present, to help ORBGAUSS choose the velocity integration ranges.

Note 2: To avoid excessive starts and stops of the magnetic tape units, both integer and floating point data are stored in the same array, under dummy names when there is a type conflict.

Note 3: Between mesh points, ϕ_0 is taken to be defined exactly by a truncated Taylor series using the derivative supplied by POT.

Note 4: We do not, of course, ever carry out the space integration. The algorithm merely converts the integral equation to a matrix equation.

ORBGAUSS

START

INITIALIZATION
Allocate memory, read Gaussian
tables, and mesh sizes, store
d-c potential (note 1), and cal-
culate cluster lengths. Put ini-
tial data in array NLL (note 2),
and store NIL on tape. Print
initial data.

1

Choose a row, x, the number of
ranges in the velocity integra-
tion, and the limits of those
ranges. Save these in the array,
CLUSTER (note 2).

2

Choose a velocity for Gaussian
integration. Compute energy, .
Find NJ, the last mesh point for
which $> -e\phi_o (NJ)$ (note 3). Save
in CLUSTER.

ORBIT REACHES WALL? —— NO

YES

Set turning point at wall.

3

435

3

Calculate turning point, x_{tp}, by repeated interpolartion. Calculate time to go from x_{tp} to x(NJ). Choose appropriate algorithim and compute, and save, time for each step from NJ down to 1(x'=0). Store total time from x_{tp} to x in array CLUSTER. Store time steps from x to zero in CLUSTER

Is this the final point on the velocity mesh? — NO → **2**

YES

Buffer out CLUSTER

All rows done? — YES → Print potential and other data.

NO

1

End

GAUSSKSIX

START

INITIALIZATION
Define six point integration con-
stants, read scaling constants,
calculate sine and cosine table.

Buffer in the preliminary
data record, NLL

Buffer in CLUSTER
for first row

Print preliminary
Information

4

Choose row, start buffering
next row

Choose point on velocity mesh,
and calculate contribution to
kernel at each $x' \leq x$.

Completed
velocity
mesh?

NO

YES

5

437

REFERENCES

1. J. E. Drummond, R. A. Gerwin, and B. G. Springer, J. Nucl. Energy Part C: Plasma Physics 2, 98 (1961).

2. J. Pavkovich, Am. Phys. Soc. Plasma Physics Division, San Diego, 1963.

3. W. M. Leavens, J. Res. NBS 69D (Radio Science) 1321 (1965).

4. R. Buckely, Proc. Roy. Soc. (London) A290, 186 (1966).

5. C. W. Horton, Dissertation, University of California at San Diego, 1967.

6. W. M. Leavens and C. H. Love, Phys. Fluids 12, 330 (1969).

7. W. M. Leavens and C. H. Love, Environmental Science Services Administration Technical Memorandum ERLTM-AL-1 (1968).

Vortices, the "Particles" of Fluid and Gasdynamics

O. Buneman
Electrical Engineering Department
Stanford University
Stanford, California

ABSTRACT

An inviscid but vortical gas can be simulated as a
quasi-continuous distribution of vortices. The triple
infinity of mass elements should be enumerated in such a
way that two of the three indices identify the vortex
filament to which the element belongs. If these indices
are chosen as discretized Clebsch variables, the velocity
field is obtained from them by gradient formation. Four
dependent variables (arrays), namely x, y, z and a velocity
potential for the irrotational part of the motion, then
suffice to describe the gas in three dimensions. A space-
and time-symmetric leap frog scheme allows the variables
to be advanced in time, with readily controllable numerical
stability.

INTRODUCTORY REMARK

In this article is described an ambitious scheme for
the numerical simulation of turbulence in an ordinary non-
ionized gas. While the central idea can be generalized to
charge-and current-carrying compressible fluids, the scheme
is not primarily offered as a means for solving plasma

440

problems. The link with numerical plasma simulation is not
of a physical nature; it lies in the common feature of
describing a continuum by discrete interacting elements.
At the time of writing the scheme is only a blueprint.
Programming has not advanced beyond the stage of sketching a
flow sheet (see Section IV).

I. OUTLINE OF PROJECT

The calculation of small-scale "turbulent" gas or fluid
movements has two distinct applications:

1. Actual prediction of local atmospheric conditions
   in meteorology and air pollution control (or the
   corresponding application for the liquid phase).

2. Extraction (from a range of numerical experiments)
   of "effective" viscosity and heat conduction
   coefficients to be used for the simulation of
   turbulence in large-scale calculations, together
   with the verification of statistical turbulence
   theories.

It is proposed to perform the small scale calculations
by means of large digital computers. Such calculations
have, hitherto, presented a severe challenge in numerical
gas and fluid simulation; difficulties arise in conventional
schemes from having to go to large Reynolds numbers. (The
proposed new scheme will start at the limit $R = \infty$.)

It is intended to use techniques which originated, and
succeeded, in plasma physics and related areas involving
many body problems. The link is the particle concept, namely
to identify vortices as the "particles" of aerodynamics.

Vortices were recognized to be "locked" into a fluid or
gas by Helmholtz and Kelvin*, over a century ago. There have

---

*Kelvin even proposed a vortex theory of fundamental particles.

441

already been several suggestions, and even successful attempts
to calculate continuous two-dimensional vorticity by tracing
large numbers of straight parallel vortex filaments through
their mutual interactions, exactly as one traces "rod
particles" in two-dimensional numerical plasma experiments.

However, it is well known that the third dimension is
extremely important in vortex and turbulence theory (how else
would a wing fly?), and while global weather prediction can
be performed, with fair success, as a two-dimensional exercise,
local prediction will always require the terrain and obstacles
to be taken into account.

The new element by which the third dimension is to be
introduced into large-scale numerical tracing of vortices
is an old idea due to Clebsch.[1]

Three variables were introduced by Clebsch from which
the velocity field of a vortical medium is derived in three
dimensions. (This operation requires only a couple of
gradient formations and a multiplication.) Two of the
Clebsch variables are the labels of the vortex filaments,
the third is the velocity potential cf the irrotational part
of the motion.

Since the vortex filaments are locked into the medium,
we can use their labels to identify mass elements of the
medium. A third label (not the third Clebsch variables) will
be used to identify a mass element as to position along its
vortex line. From the first two labels, and Clebsch's
velocity potential, we derive the velocity of the mass
element. This, together with a Bernoulli equation for the

442

potential, is equivalent to solving the Navier-Stokes equations for infinite Reynolds number.

Computationally, this procedure has the following attractions:

(1) The fluid element positions are recorded as a three-dimensional array, with the <u>addresses</u> containing two-thirds of the information on the velocities. Only four data (three position co-ordinates and a potential value) need to be stored under each address. In conventional three-dimensional particle tracing one has six data per particle, but the addresses remain without physical significance.

(2) The information can be so arranged that "leap-frogging" becomes possible in forming gradients and advancing the particles in time. In other words, one gets the benefit of central difference precision and strict reversibility. (We shall take up the topic of dissipation through molecular viscosity seperately.)

(3) All operations are algebraic, with only one division per particle per step.

(4) The scheme is completely Lagrangian; there is no "mesh" as in Eulerian schemes and, one would hope, no worry about numerical stability.

In essence, then, the Clebsch variables offer a high-economy computational scheme for tracing three-dimensional microturbulence, and one ought, at least, to try this out. First studies are to be confined to simple problems, such as turbulence in consequence of instability of laminar shear flow, or behind a finite wing of simple shape.

II. BACKGROUND

In this section, the area of numerical turbulence studies will be surveyed very broadly, and the proposed attack will be linked to past efforts.

For an introduction to vortical flow theory, Lamb's classical Hydrodynamics[1] is still an excellent start. Early theorists were preoccupied with ideal flow problems and tended to shy away from viscous fluids except where elegant closed mathematical solutions to the Navier-Stokes equations could be given.

There followed a period when lack of detailed mathematical analysis was overcome by means of statistics, and great strides were made in the macroscopic description of turbulence (see, for instance, G.K. Batchelor[2]). This description will, for quite some time, remain the best way of introducing turbulence effects into large scale numerical weather prediction[3-9] where turbulence is simulated* by a pseudo viscosity, thus allowing the use of the Navier-Stokes equations on false pretenses. For it has been recognized that genuine molecular viscosity plays a significant part only on the smallest scale, in particular in the boundary layer, and that the evolution of eddy patterns is essentially governed by Euler's equations. Turbulent phenomena and their statistics are often surprisingly insensitive to the value of the molecular viscosity (see, for instance, Townsend[10]).

Computers have been used with spectacular success to solve the Navier-Stokes equations, both on the large scale with a pseudo viscosity and on a small scale with molecular viscosity. The latter application has advanced our understanding of boundary layers. A sequence of conference proceedings[11,12] supplies a useful bibliography for this

*The term "simulation" has, in this context, not the same connotation as in "numerical plasma simulation" where it means making a computer model of the plasma.

fast developing subject. For low and moderate Reynolds
numbers the numerical schemes are quite successful.

With high Reynolds numbers, there has been less success[13].
A number of papers in the proceedings deal with this subject[14].
It is recognized that the high-Reynolds number problem is the
missing link between the small and large scale Navier-Stokes
computations, but the drastic step of going right back to the
Euler equations for computational work has not been taken by
many[15,16].

Much of the numerical work is, of course, restricted to
two dimensions, and the idea of solving Euler's equations
numerically by tracing vortices was first proposed, and
implemented, without the third dimension[17]. It is interesting,
to note that this method of attack was developed further by
researchers[18-20] with a plasma background.

The extension to three dimensions seems to be novel and
untried. It is made attractive by the use of Clebsch
variables in place of the vorticity and stream function,
introduced for two-dimensional computations by Fromm and
Harlow[21]. The author has not found any reference to
Clebsch variables in an attempt to re-formulate classical
electrodynamics. Directly from the interpretation[23] of
Dirac's variables one can deduce that the ideas presented
here can be extended to charge- and current-carrying
relativistic compressible fluids.

III. DISSIPATION

The conservation of vortices, and the validity of the
Clebsch representation of the velocity field, are subject to

the absence of viscosity. It may be that a simple modification of the Clebsch representation could be made to account for the viscous term in the Navier-Stokes equation (this will be looked into). Alternatively, one could design a scheme for writing off occasional vortices--perhaps with random selection--provided this does not cause excessive numerical noise.

However, one of the objectives of the proposed studies is to account for the anomalous viscosity, or "eddy viscosity" which has to be introduced into large-scale aerodynamical calculations to fit the observations. From this point of view, it is almost desirable to start with the unrealistic "ideal" fluid or gas model, and to ignore molecular viscosity altogether. Indeed, our objective is to explain apparently irreversible phenomena in terms of strictly reversible fundamental laws. Here we have another point of contact with plasma physics where one looks for causes of "anomalous" resistance and diffusion under conditions where the strictly reversible "collisionless" Boltzmann equation should apply.

There is, of course, some numerical noise present in all computations--mainly due to replacing continua by finite elements. Rounding-off errors tend to lie well below this noise level which often makes it reasonable to use the shortest possible word that one's computer will allow. (It is intended to keep to 16 bit words on the local IBM 360.) However, by careful choice of one's finite-difference scheme one can maintain reversibility down to machine accuracy. This we do by using central differences in time (Sec. IV). With it would go a gamma of five-thirds in the gas law for relating the pressure

446

in Bernoulli's equation to the "particle" density. The
remaining numerical noise may possibly have the diffusion
character of the typical viscosity term, or perhaps enhance the
realism of the simulation in other ways.

IV. THE PROGRAM

The work proposed here is almost entirely "from scratch",
and it is therefore necessary to give more than a verbal
description of how it is to be done. The basic equations,
(i) Navier-Stokes equations for $Re \rightarrow \infty$, i.e., Euler's
equations, (ii) continuity equation, (iii) equation of state,
need not be recorded here, but everything beyond these is
novel or unconventional.

Clebsch's variables -- ξ, η and ϕ, as we shall call them --
are relatively unknown; Clebsch showed that in the absence of
viscosity, one can write the velocity field in the form

$$\frac{d\vec{r}}{dt} = -\text{grad } \phi + \xi \text{ grad } \eta \tag{1}$$

and ξ, η are quantities carried by the medium

$$\frac{d\xi}{dt} = 0 \tag{2}$$

$$\frac{d\eta}{dt} = 0 \tag{3}$$

while ϕ evolves according to the generalized Bernoulli
equation:

$$\frac{\partial \phi}{\partial t} = \xi \frac{\partial \eta}{\partial t} + \frac{1}{2} \left(\frac{d\vec{r}}{dt}\right)^2 + \int \frac{dp}{\rho} \tag{4}$$

447

or (after adding $d\vec{r}/dt$ times equation (1) and using equation (3))

$$\frac{d\phi}{dt} = \int\frac{dp}{\rho} - \frac{1}{2}(\frac{d\vec{r}}{dt})^2 \qquad (5)$$

The vorticity is obtained from ξ and η by:

$$\text{curl}\left(\frac{d\vec{r}}{dt}\right) = \text{grad }\xi \times \text{grad }\eta \qquad (6)$$

The obvious physical irrelevance of potential zeros, in our case the zero levels of ϕ and η, makes one wonder whether introduction of Clebsch's variables does not violate the rule that numerical simulations are usually most efficient when one adheres most closely to physical reality. (There is an even more severe arbitrariness in the choice of ξ, η and ϕ: note that the "gauge" transformation

$$\phi^1 = \phi - \xi\eta$$

$$\eta^1 = -\xi$$

$$\xi^1 = \eta$$

leads to the same representation of $d\vec{r}/dt$ as in equation 1.) However, the accompanying picture of a family of vortex filaments, each representing some small unit of circulation, shows that ξ and η provide a count for these filaments and the arbitrariness in their choice is nothing other than the arbitrariness of where to begin this two-variable count. The concept of finite size (rather than infinitesimal) elementary vortices, and the discretization of the variables ξ, η which the computer demands, provide the link with reality. (What is even more encouraging is that in superfluidity one really does encounter quantized vortices!)

Vortices

The evolution of the density ρ in accordance with the conservation of mass elements of gas, will be provided for in the computations by giving each element a third label, ζ, in addition to ξ and η. All three labels are discrete variables. They become integers in the program (after suitable scaling) and they become the triple indices of four arrays, $\phi(\zeta, \eta, \xi)$, $x(\xi, \eta\ \zeta)$, $y(\xi, \eta, \zeta)$, $z(\xi, \eta, \zeta)$. Equations (1) and (5) sav how each member of these arrays is to be updated in time. We must also derive the density ρ at each step and we take $p \propto \rho^{5/3}$. (The fractional power will be pre-tabulated in core rather than evaluated by subroutine.)

The density will <u>not</u> be evaluated by a count per mesh-cube in this program. Likewise the gradients will <u>not</u> be formed by working over an Eulerian mesh. Instead, we look only at the spacing of the "particles" or mass-elements: there will be no need to introduce any mesh other than the ξ, η, ζ mesh resulting from making ξ, η, r into integer indices. Figure 2 shows the mesh of mass-elements as it appears in x, y, z-space. The volume of the element labeled ξ, η, ζ is that of a parallelo-piped. We calculate this volume from its six face-centers. These face-centers can be identified as "particles" with labels $(\xi \pm \delta\xi/2, \eta, \zeta)$, $(\xi, \eta \pm \delta\eta/2, \zeta)$ and $(\xi, \eta, \zeta \pm \delta\zeta/2)$. The volume and hence the density. then follow from:

$$\text{density}^{-1} \propto \text{volume } V = \vec{a} \cdot \vec{b} \times \vec{c} \qquad (7)$$

where $\vec{a}$, $\vec{b}$, $\vec{c}$ are given by the representative definition

$$\vec{a} = \vec{r}_{\xi + \delta\xi/2,\ \eta, \zeta} - \vec{r}_{\xi - \delta\xi/2,\ \eta,\ \zeta} \qquad (8)$$

449

Note the spatial symmetry of this difference formula - it means that we have central difference precision. Evidently, we need records of $\vec{r}$ at face-centers of the ξ, η, ζ mesh, rather than at the cell centers. From V, or V^{-1} (here is _the_ division in our program), and $\vec{a}$, $\vec{b}$, $\vec{c}$ one also obtains the gradients of ξ, η, ζ:

$$\text{grad } \xi \approx V^{-1} \vec{b} \times \vec{c} \qquad (9)$$

etc., as readily deduced from the fact that the direction of grad ξ is along $\vec{b} \times \vec{c}$.

Moreover, grad ϕ follows from:

$$\text{grad } \phi = \frac{\partial \phi}{\partial \xi} \text{ grad } \xi + \frac{\partial \phi}{\partial \eta} \text{ grad } \eta + \frac{\partial \phi}{\partial \zeta} \text{ grad } \zeta \qquad (10)$$

where, representatively,

$$\frac{\partial \phi}{\partial \xi} \approx \frac{1}{\delta \xi} \left(\phi_{\xi + \delta \xi/2, \eta, \zeta} - \phi_{\xi - \delta \xi/2, \eta, \zeta} \right) \qquad (11)$$

(the division by $\partial \xi$ will be eliminated by scaling.) The record of ϕ should, likewise, be available at the face-centers.
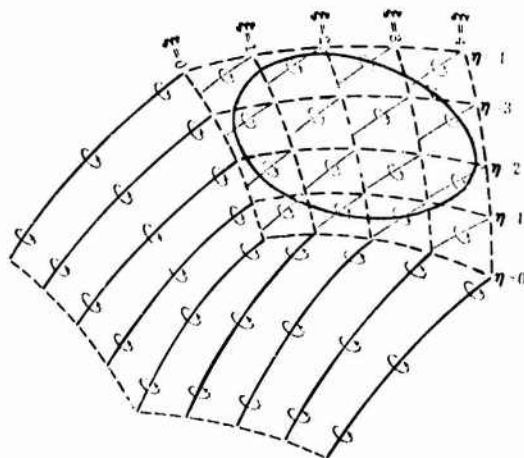

Figure 1. Showing family of vortex filaments (ringed) and surfaces on which ξ and η are constant. Circulation around closed curve = 9 units, approx.
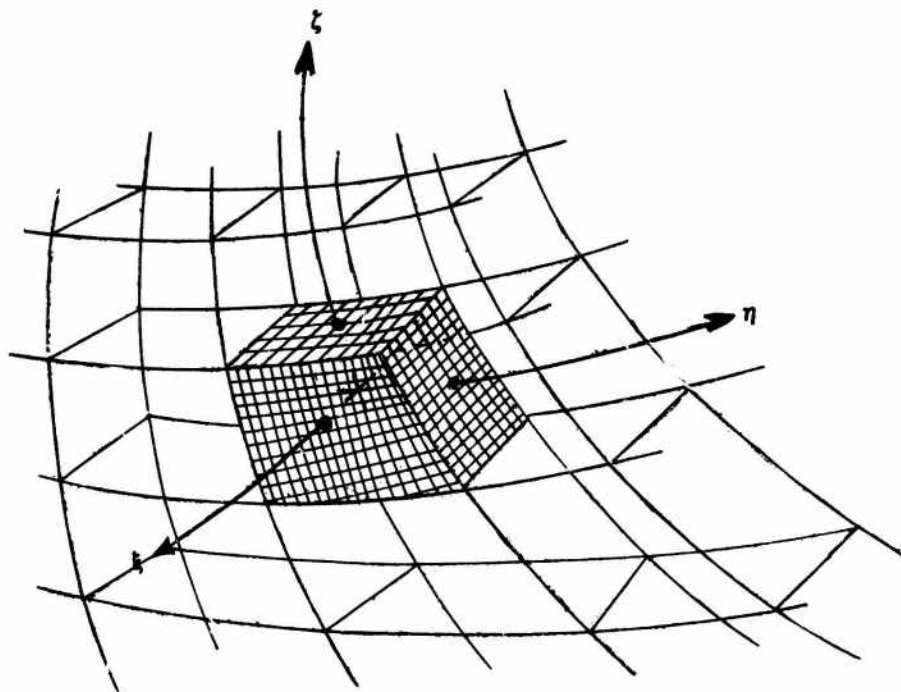
Figure 2. Lagrangian mesh: mass element labelled (ξ, η, ζ) – according to its center at $\vec{r}(\xi, \eta, \zeta)$ – is a parallelopiped with face centers at $\vec{r}(\xi \pm \delta\xi/2, \eta, \zeta)$, $\vec{r}(\xi, \eta \pm \delta\eta/2, \zeta)$, $\vec{r}(\xi, \eta, \zeta \pm \delta\zeta/2)$.

Indeed, ϕ is rather like a fourth co-ordinate. The density and the gradients given here are for the cell centers and can therefore be used to update four co-ordinates there:

$$\vec{r}_{new} = \vec{r}_{old} + \delta t \left(\frac{d\vec{r}}{dt}\right)_{present} \qquad (12)$$

$$\phi_{new} = \phi_{old} + \delta t \left(\frac{d\phi}{dt}\right)_{present} \qquad (13)$$

For central difference precision in time, and for numerical reversibility, we must interpret "old", "present" and "new" as three successive time steps, separated by intervals $\delta t/2$. At successive time steps, we therefore need coordinate records alternately at the cell centers and the face centers. Now the cell centers are the face centers of a lattice centered on the original face center and all we need to do is to switch from one lot to the other.

When indexing the two alternate lattices one can use the rule that for even time-steps a cell center has one index even and the remaining two indices either both even or both odd while at odd time-steps one has either all indices odd or only one index odd for a cell center. In other words, the sum of the cell center indices and the time step index is always even, while the corresponding sum for face centers is always odd.

We are now in a position to outline the main loop of the program which advances a vortex distribution in time:

1. Leap-frog through the vortex array, in accordance with the odd-even index rules just described, and:

2. Calculate the three displacement vectors $\vec{a}$, $\vec{b}$, $\vec{c}$ from equation (8)

3. Calculate the volume and its inverse from equation (7).

4. Calculate the gradients of ξ, η, ζ from equation (9).

5. Calculate $\partial\phi/\partial\xi$, $\partial\phi/\partial\eta$, $\partial\phi/\partial\zeta$ from equation (11).

6. Calculate grad ϕ from equation (10).

7. Calculate the velocity components from equation (1).

8. Advance the position from equation (12).

9. Look up the value of $\int dp/\rho \propto V^{-2/3}$ in a table.

10. Calculate $d\phi/dt$ from equation (5).

11. Advance ϕ from equation (13).

12. Increase time step and go back to instruction 1.

V. STABILITY

The development of turbulence (meaning the grouping of vortices into intricate patterns of various scales) from sheared flow (a simple, ordered initial state of continuous vorticity) is the result of repeated Kelvin-Helmholtz instabilities. In computer simulations we must make sure that any observed instability is not of numerical origin. The analytical tests for physical and numerical instabilities are quite similar; one follows the evolution of small perturbations about a given state. An analytical study of shear flow stability in a compressible gas has already been made, using the co-ordinates ξ, η, ζ, t of the present scheme: the results seem to be related, non-trivially, to those

453

obtained by the Eulerian scheme (stability depending on shear
profile).

No rigorous test for the <u>numerical</u> stability of our scheme
has, as yet, been applied to the same state. It is a matter of
relatively minor modifications to the test for physical
instability - essentially replacing differentials by finite
differences - and this would be a preliminary task to the
execution of our program. One can already predict the
familiar numerical instability due to taking $\Delta t > \Delta x/c_s$ since
ordinary sound waves are included in our analysis. We shall,
of course, avoid this instability by making Δt smaller than
the critical limit. In view of the simplicity of the
algebraic operations in each step, we hope, nevertheless,
to realize good speeds in following the time evolution of
the system.

There may be other sources of numerical instability, but
it should be kept in mind that many of the conventional fluid
dynamics schemes are fraught with numerical instabilities
because of violations of causality. (The classical instability
cited in the preceding paragraph is really an example of the
simulation becoming non-causal when one steps ahead too fast.)
We are avoiding, here, a typical non-causal step used in many
conventional simulations, that of determining the velocity
field from the vorticity* rather than from the momentum equation.
This inversion of causality is associated with the incompres-
sibility assumption which leads one to eliminate the pressure

---

*This involves solving the elliptic (non-causal) Poisson
equation, a time consuming operation for which fluid dynamicists
have, in the past, employed what to plasma simulators seem
clumsy and outdated methods.

from the three momentum equations and to calculate the pressure distribution aposteriori, if at all. Causally, it is the pressure distribution which determines the evolution of all three momentum and velocity components, while constant volume is maintained by the extreme pressures which result from contraction or expansion of fluid elements. Inasmuch as our scheme is Lagrangian, we may derive confidence from the fact that no numerical instabilities (other than that arising from the limitation of Δt by propagation speeds) have been reported by plasma particle simulators.

VI. MESH STRETCHING AND DISORDERING

In our Lagrangian representation the simple state of uniform unit shear (y-velocity increasing with x) in a gas of constant density can be given in the form:

$$x = \xi, \; y = \eta + \xi t, \; z = \zeta, \; \phi = -\xi^2 t/2.$$

While at $t = 0$ the Lagrangian (ξ, η, ζ) mesh and the Eulerian (x, y, z) mesh coincide, as time progresses the Lagrangian mesh will manifest itself in physical space as an array of more and more skewed parallelopipeds. In principle, there arises no inconsistency in the basic differential equations (1)-(5) from this skewing of the coordinate system. However, in practice, when the differentials are replaced by finite differences, as in equations (7)-(13), "neighboring" mesh points get pulled further and further apart, so that differences give poorer and poorer approximations to differentials.

It will therefore be necessary, from time to time, to give up the original labelling of the gas elements and to start with

a new labelling, as if beginning a new run, using the finish of the old run as initial input. The new labeling must be of the "Clebsch" type, i.e., ξ^1 = const and η^1 = const must describe the same vortex lines as ξ = const and η = const, and the density of these lines must be the same everywhere: $d\xi^1 \cdot d\eta^1$ = $d\xi \cdot d\eta$. The new labeling, however, should reflect physical proximity better than the old. While it is easy enough to devise a relabeling scheme for the uniform shear state given above, one will have to look very closely at the more disordered vortex patterns which result from the development of Kelvin-Helmholtz instabilities to large amplitudes before one re-orders the vortices into new groups exhibiting less stretching.

The order-disorder transition was manifested quite dramatically in some early one-dimensional simulations of a cold, unstable plasma. We expect similarly disordered, patterns to develop here - meaning patterns too intricate for the human mind to comprehend and utilize. In the relabeling, it is likely that rejection of information will be necessary. There will be too much detail for even the computer to handle economically. It is interesting to reflect that in writing off information, <u>we</u>, and neither the physical system nor the computer, raise the entropy of the system. We shall be taking the first step towards the macroscopic, phenomonological description of turbulence.

Exactly how to re-order* an excessively turbulent gas configuration cannot be determined until we have seen the first 'turbulent' configurations emerge from our simulation.

---

*One is tempted to try a three-dimensional version of the Livermore FLAG code (2nd conf. Num Fluid Dyn. contribution by W.P. Crowley), but it should be realized that the proposed scheme is based on quadrilateral, not triangular cells.

Obviously, a good computer - human interface is required here, and in addition to standard "Input/Output" devices, including maps printed out at frequent steps, we require some funds for filming our output. In plasma simulations, filming is now quite an accepted routine.

The problem of re-ordering may be complicated by the possible development of large domains with low vorticity so that very few tracer particles are kept in auch almost irrotational domains. One may have to resort to the ugly scheme of using different scales in the different places.

VII. BOUNDARY CONDITIONS

In an ideal fluid satisfying the Euler equations one can only impose one condition on the three velocity components at a boundary, namely that the fluid ahould flow along the boundsry. A two-dimensional subgroup of the three-dimenaional srray of elements will have to stay at the boundary, meaning its (x,y,z) valuea have to conform with the equation of the boundary surface. Our method cannot simulate the boundary layer itself - this would require a finite Reynolda number.

However, we may wiah to release occaaional vortices from the boundary (which, in fact, ia itself a vortex sheet producing the transition from zero to non-zero to apatial velocity). In so doing, we must make aure thst no maaa ia injected along with the vorticea. The third label in our acheme (measuring mass density along a vortex filsment) gives us the necessary control. Injection of vortices is physically justified where the fluid becomes highly atressed, i.e., where our Lagrangian grid becomes highly distorted. In the first runs,

we would find such places by inspection and release vortices accordingly. Later, a subroutine might be developed to achieve this automatically.

REFERENCES:

1. H. Lamb, "Hydrodynamics", ch. 7, art. 167 (C.U.P. 1932)

2. G. K. Batchelor, "The Theory of Homogeneous Turbulence" (C.U.P. 1953)

3. L. F. Richardson, "Weather Prediction by Numerical Processes" (C.U.P. 1922)

4. J. Smagorinsky, S. Manabe and J. L. Holloway, Jr., "Numerical Results from a Nine-Level Circulation Model of the Atmosphere", Monthly Weather Rev. 93, 727 (1965)

5. C. E. Leith, "Numerical Simulation of the Earth's Atmosphere", Methods in Computational Physics, Vol. 4, Academic Press, New York, (1965), 1-27

6. Y. Mintz, "Very Long Term Global Integration of the Primitive Equations of Atmospheric Motion", W.M.O. Technical Note No. 66, W.M.O.-I.U.G.G. Symposium on Research and Development Aspects of Long Range Forecasting (1965), 141-167

7. D. K. Lilly, Phys. of Fluids 12, Suppl. II, 240 (1969)

8. S. A. Orszag, Phys. of Fluids 12, Suppl. II, 250 (1969)

9. C. E. Leith "Two Dimensional Turbulence and Atmospheric Predictability", 2nd International Conference on Numerical Methods in Fluid Dynamics, University of California, Berkeley, September 1970

10. A. A. Townsend, "The Structure of Turbulent Shear Flow", ch. 5.4 (C.U.P. 1956)

11. Proceedings of the International Symposium of High-Speed Computing in Fluid Dynamics, Phys. Fl. 12, Suppl. II, December 1969

12. Abstracts of papers presented at the Second International Conference on Numerical Methods in Fluid Dynamics, University of California, Berkeley, September 1970

13. J. W. Deardorff, "A Three-Dimensional Numerical Study of Turbulent Channel Flow at Large Reynolds Numbers" NCAR Manuscript 69-19, Boulder, Colorado, January 1969

Vortices

14. e.g. C. W. Hirt, Phys. Fl, 12, Suppl. II, 219 (1969)

15. K. Roesner, "Numerical Integration of the Euler Equations for Three-Dimensional Unsteady Flow", 2nd International Conference on Numerical Methods in Fluid Dynamics, University of California, Berkeley, September 1970

16. P. Kutler and H. Lomax, "The Computation of Supersonic Flow Fields About Wing-Body Combinations by 'Shock Capturing' Finite Difference Techniques", 2nd International Conference on Numerical Methods in Fluid Dynamics, University of California, Berkeley, September 1970

17. F. H. Abernathy and R. E. Kronauer, J. Fluid Mech. 13, 1 (1962)

18. J. P. Christiansen and K. V. Roberts, papers 40 and 52, Proc. of Computational Physics Conference, Culham Laboratory (1969)

19. J. P. Christiansen, "Vortex, a Two-Dimensional Hydrodynamics Simulation Code", UKAEA Report CLM-R 106 (Culham Laboratory 1970)

20. T. Koga, "A Kinetic Theory of Turbulence in Incompressible Fluids" PIBAL Report No. 68-5 (Polytechnic Institute of Brooklyn, 1968)

21. J. E. Fromm and F. H. Harlow, Phys. Fl. 6, 975 (1963)

22. P. A. M. Dirac, Proc. Roy. Soc. A., 212, 330 (1952)

23. O. Buneman, Proc. Roy. Soc. A., 215, 346 (1952)

Three Schemes for Drift Motion

D. C. Stevens
Courant Institute of Mathematical Sciences
New York University
New York, N.Y.

Courant Institute of Mathematical Sciences, New York University

Three numerical schemes for solving for the time evolution of a plasma are discussed and the results of numerical experiments compared.

We are interested in the time evolution of physical systems obeying equations (1) - (4).

$$\frac{\partial f}{\partial t} - \mu \frac{\partial (B,f)}{\partial (x,y)} = 0 \tag{1}$$

$$p = \int \mu \, f \, d\mu \tag{2}$$

$$\frac{1}{2} B^2 + p = 1 \tag{3}$$

$$\vec{v} = \mu \, \vec{k} \times \nabla B \tag{4}$$

Here $f = f(x,y,\mu,t)$ is the density of guiding centers of particles in a plasma. The time scale is slow and electric field effects are neglected. $\vec{k}$ is a unit vector perpendicular to the x,y plane. The magnetic field is perpendicular to the x,y plane and has magnitude B. μ is the component of the particle's energy perpendicular to the magnetic field. There is assumed to be no variation in

the perpendicular direction.

Remark 1. A consequence of (1) - (3) is that $\partial/\partial t \int f \, d\mu = 0$. Using (1) and (2) we get $\int \partial f/\partial t \, d\mu - \int \mu \, \partial(B,f)/\partial(x,y) \, d\mu = 0$ and then $\partial/\partial t \int f \, d\mu - \partial(B, \int \mu \, f \, d\mu)/\partial(x,y) = 0$. The second term of the last equation is zero because of (2) and (3), proving the remark.

Remark 2. A consequence of (1) and (4) is that the particles in the plasma, moving with velocity $\vec{v}$, always see the same constant value of f at each successive position. This follows directly from (1) and (4).

The initial state from which solutions will be followed has only 2 μ values occurring (i.e. $f(x,y,\mu,t)$ = $f_1(x,y,t)\delta(\mu-\mu_1) + f_2(x,y,t)\delta(\mu-\mu_2)$). We take $\mu_1 = 1$ and $\mu_2 = 2$. The function $f_1(x,y,0)$ which was chosen has circular symmetry about the point (.35, .5) and has

radial distributi$\cdots$ $f(r) = \begin{cases} .5(1 - (r/.3)^2)^2, & r < .3 \\ 0, & r > .3 \end{cases}$.

The function $f_2(x,y,0)$ has circular symmetry about the point (.65, .5) and has radial distribution

$f(r) = \begin{cases} .125(1 - (r/.3)^2)^2, & r < .3 \\ 0 & r > .3 \end{cases}$. The time evolution

for a system having only one of f_1 or f_2 present would be such that f would remain constant and all particle motions would be circular. The time evolution of the combination of f_1 and f_2 will be a swirling intermixing motion. A consequence of Remark 1 is that the aggregate plasma should not wander from its initial position.

In each of the three schemes studied, the stepping forward of the pertinent quantities (e.g. particle position

461

or f value) is done by a Runge-Kutta differential equation solving subroutine. In each case run, the dt increment was reduced so much that the final halving of dt produced only minor variation in the evolution.

A basic 20 by 20 grid is used for comparing the solutions of the three schemes at various times. Grid point i,j has coordinates (i-1)/19, (j-1)/19. The distance between two distributions is defined to be the maximum difference of the f_2 densities taken over all basic grid points i,j.

Scheme G.

Simple differencing techniques are used to step forward the plasma, using equations (1) - (3). The grid schemes have size (19n + 1) by (19n + 1) so as to facilitate comparison on the 20 by 20 comparison grid. The largest grid used was 115 by 115, which filled the 6600. (Several arrays this size are needed by the Runge-Kutta subroutine.)

Scheme P.

The particle scheme used particle in cell (pic) methods, i.e., bilinear interpolation of densities and gradients. Equations (2) - (4) were used. The background grid was 20 by 20 or 39 by 39. Quiet starts were used. Only about 14000 particles would fit in the 6600. This seemed to be insufficient with the 39 by 39 grid because of observed noise effects, but was sufficient in the 20 by 20 grid.

462

Scheme C.

Characteristic curves of the differential equation (1) were numerically determined. Particles move on characteristic curves. To obtain greater accuracy, no background grid is used. Several hundred "representative" particles are selected (uniform spacing for convenience) at the start and tagged with an f value. By Remark 2 this f value will not change during the time evolution of the system. To find either density (f_1 or f_2) and its gradient at any point, the nine nearest representative particles are found and a least squares second degree fit is made to their f values, which yields f and $\partial f/\partial x$ and $\partial f/\partial y$ at the given point. (The choice of nine as opposed to 8, or 10, etc., is somewhat arbitrary.) The representative points are stepped forward in this manner using equations (2) - (4). This method works well initially, but as the gradients become steeper the time step dt must be reduced drastically, and as the two species swirl, more representative points are needed. This method is limited more by computing time limitations than by computer size. An accurate run to t = .05 required 3 hours, while this required only seven minutes with scheme G.

Comparisons of the Schemes.

Table I gives distances between several schemes at t = .05. The subscripts on G tell the size of the grid schemes, while the subscript on C tells the number of particles. The subscript on P tells the background grid size. All of the P schemes used 13960 particles.

463

D. C. Stevens

It appears that the G and C methods can give accurate solutions on the 6600, while the particle method would need additional storage for such accuracy. Table II gives distances at $t = .2$.

Acknowledgment.

Table I

$t = .05$

	G_{20}	G_{39}	G_{96}	G_{115}	P_{20}	P_{39}	C_{496}	C_{1984}
G_{20}	0	.016	.020	.021	.021	.071	.027	.021
G_{39}	.016	0	.010	.012	.024	.074	.026	.015
G_{96}	.020	.010	0	.001	.024	.075	.021	.012
G_{115}	.021	.012	.001	0	.024	.075	.021	.012
P_{20}	.021	.024	.024	.024	0	.066	.030	.035
P_{39}	.071	.074	.075	.075	.066	0	.066	.075
C_{496}	.027	.026	.021	.021	.030	.066	0	.024
C_{1984}	.021	.015	.012	.012	.035	.075	.024	0

Table II

$t = .2$

	G_{20}	G_{39}	G_{96}	G_{115}	P_{20}	P_{39}
G_{20}	0	.080	.084	.084	.180	.804
G_{39}	.080	0	.067	.053	.110	.804
G_{96}	.084	.067	0	.063	.108	.804
G_{115}	.084	.053	.063	0	.108	.804
P_{20}	.180	.110	.108	.108	0	.804
P_{39}	.804	.804	.804	.804	.804	0

Tuesday, November 3, 1970

Session IV

Chairman: John M. Dawson

Princeton University
Princeton, New Jersey

465

Nonphysical Modifications to Oscillations, Fluctuations and Collisions Due to Space-Time Differencing

A. Bruce Langdon
Lawrence Radiation Laboratory
University of California
Livermore, California

ABSTRACT

In recent years computer simulation has become a powerful tool for the study of plasmas. Much effort and computer time is being expended in applications to new and more difficult problems. In support of this work we have performed an extensive theoretical analysis of a common class of many-particle simulation methods. As one does to learn basic properties of real plasmas, we examine oscillations, fluctuations and collisions in the idealized case of uniform and infinite or periodic plasma. Even in this simple situation there are several instances in which the models fail (mildly to grossly) to reproduce plasma behavior. This paper outlines the theory and discusses such non-physical behavior caused by the finite-difference methods. The plasma interacts coherently with the periodicity of the spatial grid on which the electromagnetic fields are defined and with the periodicity of the finite-difference time integration. Various parametric instabilities are sometimes induced, which may be either weak or strong and may be difficult to distinguish from real instabilities. There is also high-frequency noise associated with the rate at which particles cross the spatial grid cells. If the time

467

step is large enough that the frequency of this noise exceeds the time
sampling frequency then this noise degrades normal fluctuations and
collisions and can become excessive. The theory has helped others
examine experimentally the nature of such nonphysical effects. Some
suggestions are made as to how researchers using these models might
respond to these results.

I.   INTRODUCTION

The plasma models I am going to discuss originated at Stanford
in 1963. In order to make simulation in two dimensions economically
practical, Buneman and Hockney developed a model which uses a spatial
grid on which the charge density is found from the particle positions,
Poisson's equation is solved in finite difference form, and then the particle
forces are interpolated from the grid.[1,2,3] This is much more efficient
than summing N^2 Coulomb interactions among N particles.

They also realized that computational and physical problems
associated with the divergent character of the Coulomb field are
eliminated; the interactions at small separations are smoothed reducing
the large-angle binary collisions which are of little interest in hot
plasmas and which had been exaggerated in simulation because of the
small number of particles used.[3]

Although simulation in one dimension was possible by other
means, the new model offered simplicity and speed there too.[4]

Part of the gain was in the method of integrating the system
forward in time. The algorithms were fast and preserved certain
physical properties.[5]

Oscillations, Fluctuations, Collisions

The advantages of the Stanford approach were not immediately recognized elsewhere, and much simulation was done for which the gridded model would have been more efficient.

Other people developed versions of the model with more accurate interpolation and different methods of solving Poisson's equation, etc.[6-9]

In 1968 wide interest was aroused in the plasma community by large scale simulations done at Los Alamos of several problems in the controlled thermonuclear fusion research program. Since then simulation by these methods has been widely accepted as a plasma research tool.

The models obviously do not accurately reproduce the microscopic dynamics of a plasma. One must consider if and how such errors will modify the macroscopic behavior. There are usually far too few particles. This causes discrete-particle effects such as fluctuations and collisions to be exaggerated. There may also be too few particles for adequate representation in phase space of plasma phenomena such as the Landau damping wave-particle resonance. There can be serious problems with initial and boundary conditions. Roundoff errors can usually be made negligible compared to other errors. The principle concern of this paper is errors caused by the finite-difference representation in space and time of the field equations and particle dynamics.

Such sources of error are difficult to assess in practice. Some study of their nonphysical effects was needed. Much of this has been done through experiments with the models.[10-14]

In addition to empirical results, some theoretical analysis is desirable. This is true for the usual reasons that adding a good theory

implies a better understanding than a stack of oscillograms or computer output alone. One also hopes the theory will predict unexpected interesting results that can be verified experimentally, and I will describe some results which I think are in this category.

There has been some approximate discussion of the models. Smoothing and noise aspects of the spatial grid were recognized early[3,6] and approximate theoretical descriptions made of each.[10,15,16] The time integration was considered heuristically.[5]

However regarding the space-time grid simply as a source of smoothing and of noise fails to uncover some very important effects involving coherent interaction between the plasma and the sampling in space and time. Some theory has appeared which includes exactly the effects of the finite-differencing and is applied to linear wave dispersion and stability and to energy conservation.[17,18] We have also looked at fluctuations and collisions. The theory is quite complete now, and in about as tidy a form as is possible for such a system.[19] Different parts of the simulation algorithms are easily identified and changes made. We keep the results in a form permitting easy comparison with real plasma theory, where possible. Mathematical details will not be emphasized here.

Although our techniques can be used for more general cases, we have confined our examples to models having only Coulomb interactions; in one instance an external magnetic field is imposed. This is because such models have so far been prevalent, and because it is the longitudinal field in general models which is expected to cause the greatest difficulties in simulation.

We are not so interested in the accuracy of individual particle orbits as in the accuracy of collective plasma phenomena. Therefore, our analytical approach, terminology and criteria are more that of the plasma physicist than of the numerical analyist studying, say, an initial value problem for a small system of differential equations with no application in mind. In several places the collective properties of warm plasmas play a crucial role.

II.   THE SIMULATION MODEL ALGORITHMS

We now give the calculations made to advance one time step in a proto-typical model of the class considered. For simplicity this example is one-dimensional. This paper will not consider boundary conditions; the models are assumed to have periodic boundary conditions.

The position of particle i at time $t_s = s\Delta t$ is $x_{i,s}$ and its velocity at time $t_{s-1/2}$ is $v_{i,s-1/2}$. The first step is to calculate a charge density, defined on a fixed spatial grid whose j'th mesh point is located at $X_j = j\Delta x$, by means of the charge sharing

$$\rho_{j,s} = \sum_i q_i S(X_j - x_{i,s}) \ .$$

This can be interpreted as the charge density for finite size particles, sampled on the grid.[18] Opinions vary on the choice between zero order (nearest-grid-point or NGP, Fig. 1a) and first order (or linear, as in CIC or PIC, Fig. 1b) interpolation; other methods are rarely used.
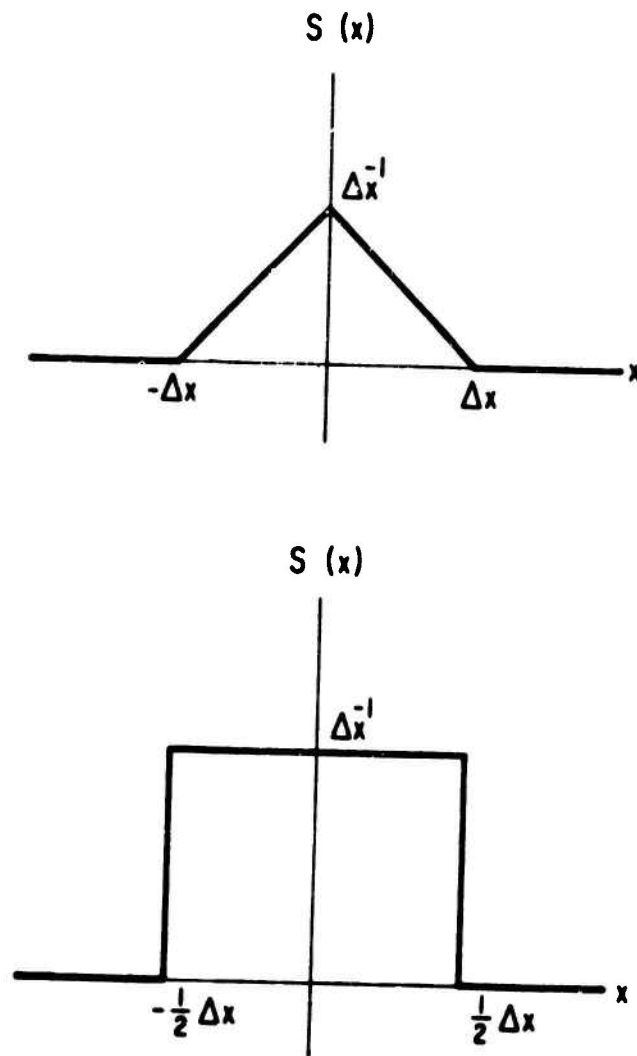
Fig. 1. Interpolating function, or cloud shape, for (a) zero order (NGP) and (b) first order (linear) interpolation.

.

From ρ an electric field is found, usually on the same grid, by a grid approximation to Gauss' law. For example, one solves

$$- 4\pi\rho_{j,s} = \frac{\phi_{j+1,s} - 2\phi_{j,s} + \phi_{j-1,s}}{\Delta x^2} \ ,$$

$$E_{j,s} = \frac{\phi_{j+1,s} - \phi_{j-1,s}}{2\Delta x} \ .$$

This is the 1-D version of the original 2-D scheme and is mathematically equivalent to simpler 1-D-only methods.[4,17]

There is nothing in our analysis that requires the use of these field equations. Other field equations are often used to emphasize the Fourier modes differently in order to reduce short-wavelength noise, include only selected modes, improve long-wavelength accuracy, etc. Only when numerical examples are given do we particularize to these equations.

The particle force is interpolated from the electric field

$$F_{i,s} = q_i \sum_j E_{j,s} S(X_j - x_{i,s})$$

using the same weighting function as earlier.

Now we come to the integration of the particle equations of motion. In the "exact" sheet and rod models special handling was commonly given to binary collisions. Corrections were made when sheets crossed, or the model could even be made exact (to within roundoff error). In 2-D time steps could be made smaller to handle near encounters. These measures become too expensive if very large numbers of particles are used.

473

With the grid it was now less clear how to go about handling crossings and near encounters. At the same time, it was realized that such special handling was no longer needed because the short range interactions were made very inaccurate in a useful manner, i.e., they were smoother. Buneman, et al., ignore the encounters and choose the following algorithm by other criteria:[4,5]

$$\frac{1}{m_i} F_{i,s} = \frac{v_{i,s+1/2} - v_{i,s-1/2}}{\Delta t} , \quad v_{i,s+1/2} = \frac{x_{i,s+1} - x_{i,s}}{\Delta t}$$

This scheme is simple and fast, and is now the most popular. Two other schemes that have been used are certainly no simpler and in fact they turn out to be slightly unstable. I shall stick to this scheme.

The model dynamics are now specified. The model conserves particles and momentum (despite the spatial nonuniformity), but not energy. It is not Hamiltonian. It is reversible in time and space.

III. ANALYSIS OF THE MODEL

The analysis makes use of Fourier transforms in space and time, as is usual for uniform collisionless plasmas. This also makes possible exact description of the finite difference methods. It seems more informative to work with the deflections from zero-order orbits caused by the fields rather than to seek a finite-difference analogue to the Vlasov equation; the relevant features are seen directly.

We first find the dispersion function which describes the linear response of the plasma to perturbing fields and whose zeroes give the dispersion and stability of free oscillations.

Oscillations, Fluctuations, Collisions

Finite Δt makes the simplest change possible; the resonant denominator becomes[19]

$$\frac{1}{\omega-\underset{\sim}{k}\cdot\underset{\sim}{v}} \rightarrow \frac{\Delta t}{2} \cot(\omega-\underset{\sim}{k}\cdot\underset{\sim}{v}) \frac{\Delta t}{2} = \sum_q \frac{1}{\omega-\underset{\sim}{k}\cdot\underset{\sim}{v}-q\omega_g} , \quad \omega_g = 2\pi/\Delta t.$$

The principal difference in the roots $\omega(\underset{\sim}{k})$ is a relative upward shift of $\frac{1}{24}(\omega_p\Delta t)^2$.

The periodicity in ω reflects the fact that frequencies differing by harmonics of $\omega_g=2\pi/\Delta t$ represent the same change in phase during a time step ($\exp[-i(\omega-q\omega_g)\Delta t] = \exp[-i\omega\Delta t]$) and are therefore equivalent as seen by the difference equations. This is a sort of stroboscopic effect that fools not only the observer but also the system dynamics. The frequencies $\{\omega-q\omega_g\}$ are called "aliases" because they are different designations for the same thing.

For simple harmonic oscillations, as in the small $k\lambda_D$ limit, it is well known that this scheme becomes unstable when $\omega_p\Delta t \geq 2$. Collective effects change this to $\omega_p\Delta t \geq 1.62$ for a Maxwellian[19]. This is because Bohm-Gross dispersion increases ω above ω_p, not because particles traverse a large part of a wavelength in one time step. So one can't use large $\omega_{pe}\Delta t$ just because one is only interested in ion frequencies, say.

The spatial grid introduces much greater complication. Analogous aliasing for spatial grid fields makes k space periodic; the periods are called Brillouin zones. For the particles, however, the aliases $\{k_p=k-pk_g\}$, $k_g=2\pi/\Delta x$, are not equivalent. Consider a field $E_j=E \exp(ik_0 x_j)$. The interpolated force is not sinusoidal, its spectrum has components

at the wavenumbers $\{k_p\}$ with relative amplitudes given by $S(k_p)$. There results a nonsinusoidal density perturbation at these wavenumbers, which are indistinguishable when sampled for ρ . Thus the interpolation errors are fed back, coupling the particle perturbations at the wavenumbers k_p.

The dispersion function therefore contains a sum over aliases:[17-19]

$$\epsilon(\underset{\sim}{k},\omega) = 1 + \frac{\omega_p^2}{K^2(\underset{\sim}{k})} \sum_p S^2(\underset{\sim}{k}_p) \left| d\underset{\sim}{v} \; \underset{\sim}{\kappa} \cdot \frac{\partial f}{\partial \underset{\sim}{v}} \frac{\Delta t}{2} \cot(\omega + i0 - \underset{\sim}{k}_p \cdot \underset{\sim}{v}) \frac{\Delta t}{2} \right.$$

where

$$k_p = k - pk_g = k - 2\pi p/\Delta x \text{ in 1-D,}$$

for Im $\omega \geq 0$. The functions $\underset{\sim}{\kappa}$ and K play the same role for the difference equations as does $\underset{\sim}{k}$ in $\underset{\sim}{E} = - i\underset{\sim}{k}\phi$ and $4\pi\rho = - k^2\phi$ respectively; in our 1-D case $\kappa = \Delta x^{-1} \sin k\Delta x$, $K^2 = [(2/\Delta x) \sin \frac{1}{2} k\Delta x]^2$. For NGP $S(k) = \sin(\frac{1}{2} k\Delta x)/(\frac{1}{2}k\Delta x)$; for linear interpolation $S = [\sin(\frac{1}{2} k\Delta x)/(\frac{1}{2} k\Delta x)]^2$

IV.   NONPHYSICAL INSTABILITIES

We now discuss the ability of coherent interaction with the space-time grid to destabilize plasma oscillations. The first examples are in an unmagnetized plasma and are due to the spatial grid. A variation of the model, proposed by Lewis, should improve the stability. Then we give an example of instability due to the time sampling in a magnetized plasma.

1. Spatial Grid Instability

Since the time integration is not a part of the instability mechanism let us assume continuous time. Also for simplicity we consider a one-dimensional system.

Oscillations, Fluctuations, Collisions

The feature of the oscillations which is central is that plasma perturbations of different wavelengths are coupled together.[17,18] This can be thought of as a parametric interaction in which the spatial grid plays the role of the pump. The pump wavenumbers are k_g and its harmonics pk_g; the frequency is zero. As a result plasma perturbations characterized by $(\omega, k_p = k - pk_g)$, p integral, are coupled and in the dispersion relation we had a sum over all these sub-modes. The coupling strength is given by $S^2(k_p)$; and is weaker for linear interpolation than the less accurate nearest-grid-point.

There are now many wave phase velocities ω/k_p with which particles may resonantly interact. Unless the coupling is very strong there is no qualitative change in $\mathrm{Re}\,\varepsilon$ for real ω; in particular the sign of its derivative is unchanged. This need not be true for the imaginary part

$$\mathrm{Im}\ \varepsilon = -\pi\,\frac{\omega_p^2}{k^2}\,\kappa\sum_p S^2(k_p)\,\frac{1}{|k_p|}\,f_0'\,(\frac{\omega}{k_p})$$

so that the plasma stability may be changed.[17,13] Reference 17 gave values for $\omega\Delta x/v_t$ and $k\Delta x$ for which $\mathrm{Im}\ \varepsilon$ had the wrong sign for a Maxwellian, showing that a clearly nonphysical instability could occur, but incorrectly stated that this was not possible for wavelengths enough larger than Δx. Reference 18 gives ω-k plots for two Maxwellian cases, one stable except for very weak growth at small $k\Delta x$, the other strongly unstable at $k\Delta x \simeq \pi/2$. We now explain these results and come to additional conclusions.[¶] The dispersion relation is periodic in k; we will keep $k < k_g/2$ (i.e., in the first Brillouin zone), which is the k one would think of physically. Then the physical phase velocity ω/k is larger than the alias velocities

Langdon

ω/k_p, $p \neq 0$. Thus ω/k may be much larger than v_t, leading to negligible Landau damping, at the same time that the slow waves are interacting strongly with the thermal particles, as shown in Fig. 2, if $k_g v_t \gtrsim \omega_p$. The contributions from waves with equal $|p|$ nearly cancel; the net effect turns out to be destabilizing. Although it is small for small $k\Delta x$ (being $\propto (k\Delta x)^2$ for NGP and $(k\Delta x)^4$ for CIC-PIC), the Landau damping of the principal wave goes to zero even faster as $k \to 0$. Thus the grid can destabilize oscillations even with wavelengths $\gg \Delta x$.

For $\lambda_D \gtrsim \Delta x/2$ the alias wave velocities fall on the flat part of the particle velocity distribution, and Landau damping occurs unless $k\Delta x \lesssim 2k\lambda_D$ is small. Therefore, the instability is confined to long wavelengths and is very weak.

When $\lambda_D \sim .1\Delta x$ the lowest and strongest aliases interact with the steep sides of f_0 and there is little Landau damping even for $k\Delta x \sim 2$ where the coupling is strong. The result is a strong instability; Im ω is as large as 0.1 ω_p for NGP and 0.014 ω_p for CIC-PIC.

If $\lambda_D/\Delta x$ is decreased further only the weaker, large p aliases contribute and the instability goes away; as it should since, of course, a cold stationary plasma is inactive.

If the plasma is drifting through the grid at about the thermal velocity the lowest aliases can lie on one side of f_0 so their contributions will all have the same sign, eliminating the near-cancellation at small $k\Delta x$. Thus the instability should be significant for larger values of $\lambda_D/\Delta x$ than for the stationary plasma.[9] Recently, I became interested in electron beams, so I looked at the simplest case, that of an electron beam in a fixed ion background, moving relative to the grid. This should

478

be stable. The dispersion relation is now

$$0 = \varepsilon(k,\omega) = 1 - \frac{\omega_p^2}{k^2} \sum_p S^2(k_p) \frac{k k_p}{(\omega - k_p v_0)^2}$$

For any fixed k the dispersion relation has a structure similar to that for many beams. One difference is that the effective plasma frequency for half of the "beams" is negative. The particles all react strongly when the Doppler-shifted frequency $\omega - k v_0$ is near a harmonic of the grid crossing frequency $k_g v_0$.

One can show that there are two roots corresponding to each alias term in the sum above. The roots are either real or occur in conjugate pairs.

In Fig. 3 we roughly plot ε for small $k\Delta x$. One sees easily the pairs of real roots associated with p=0,1 and p≤-2. For each of the other resonances there is a pair of complex roots, one unstable. For larger $|p|$ the modes are highly resonant and therefore hard to excite and also easily destroyed by any dissipation or spread in resonance, e.g. if $|\omega - k_p v_0| < |k_p v_t|$.

The growth rates from the p=-1 and 2 modes, and from p=1 at larger $k\Delta x$, are very substantial. In numerical solutions for $v_0 = 0.12 \, \Delta x \, \omega_p$ we found a growth rate of .017 ω_p at $k\Delta x = 1$ for p=1, and a maximum growth rate greater than .22 ω_p at $k\Delta x = 2.2$.

The only way to eliminate the aliasing in a simulation model using a spatial grid is to use band-limited interpolation, but even linear interpolation is often inconveniently expensive. Another possibility
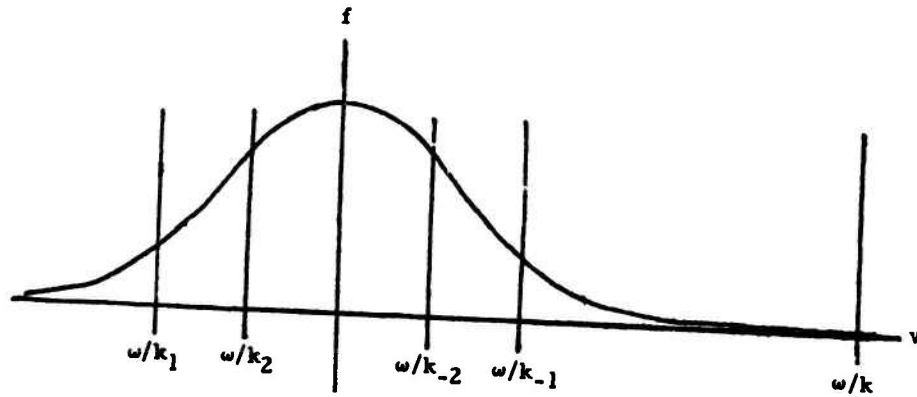
479

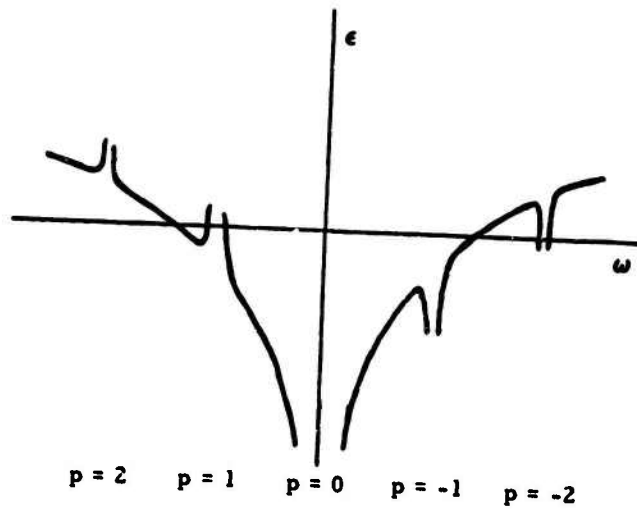Fig. 2. Alias wave phase velocities ω/k_p and $f(v)$ for $k_g v_t \sim \omega_p$.

p = 2   p = 1   p = 0   p = -1   p = -2

Fig. 3. Sketch of $\varepsilon(k, \omega)$ vs. ω for a cold beam.

is to change the sign of the coupling so that the instability goes away.
A model which does this in some cases has already been proposed by Lewis,
though not with this in mind.[9,20] He shows that a simple modification
makes the model Hamiltonian; one calculates the particle force as

$$\underline{F}(\underline{x}) = - \frac{\partial}{\partial \underline{x}} \sum_j q \phi_j S(\underline{X}_j - \underline{x}) .$$

This can be computed quickly (the gradient of S is done analytically).

The dispersion relation for the Maxwellian is now[18]

$$\varepsilon = 1 - \frac{\omega_p^2}{2K^2 v_t^2} \sum_p S^2 Z'(\frac{\omega}{\sqrt{2} \, k_p v_t})$$

Examination of Im ε shows that now each alias contributes to damping.
Thus the nonphysical instability is now nonphysical decay; this will
usually be preferable.

If the Maxwellian is drifting an instability is again possible,
but the aliases partially cancel instead of adding as they did earlier.
Thus an instability is expected to be weaker.

For the cold drifting beam we now have

$$\varepsilon = 1 - \frac{\omega_p^2}{K^2} \sum S^2 \frac{k_p^2}{(\omega - k_p v_0)^2}$$

In a plot similar to Fig 3, $\varepsilon \to -\infty$ at the alias resonances. One
expects no instability for small $k\Delta x$ when $k_g v_0 > \omega_p$. Faster drift may
be needed to avoid instability for larger $k\Delta x$.

To the extent that Lewis' models still conserve energy when Δt is
finite, the growth of an oscillation is limited by the available

481

kinetic energy. This is not true in the normal model, in which total energy increased by a large factor in Okuda's observations of a strong grid instability.[13]

2. An instability in the time integration.

The difference equations in time are equivalent to differential equations with appropriate time-dependent dynamics. The "pump" now has infinite wavelength and frequency $\omega_g = 2\pi/\Delta t$. The interacting waves have the same wave vector and frequencies which differ by harmonics of ω_g.

We have so far found no interesting instability in the unmagnetized time integration, so we turn to the magnetized case.

For propagation across the magnetic field at wavelengths ~ Larmor radius there are waves at harmonics of the cyclotron frequency. Both $\omega_p \Delta t$ and $\omega_c \Delta t$ may be small but the cyclotron harmonic frequency may be comparable to $\pi/\Delta t$. This can lead to the simplest example of a non-physical cyclotron harmonic instability, involving interaction between $n\omega_c$, $-n\omega_c$ and ω_g when $\omega_c \simeq \omega_g/2n$. We examine this further.

An external magnetic field can be incorporated into the particle equations in such a way that the zero-order orbits in constant fields are the exact helices plus E x B drift with the correct gyrofrequency ω_c. We shall use Hockney's algorithm with B parallel to the z axis.[3] The equations are

$$\frac{\underset{\sim}{v}_{\perp,s+\frac{1}{2}} - \underset{\sim}{v}_{\perp,s-\frac{1}{2}}}{\Delta t} = \left(\frac{\tan\frac{\omega_c \Delta t}{2}}{\frac{\omega_c \Delta t}{2}}\right)\left\{\frac{1}{m}\underset{\sim}{F}_\perp + \frac{\underset{\sim}{v}_{\perp,s+\frac{1}{2}} + \underset{\sim}{v}_{\perp,s-\frac{1}{2}}}{2} \times \omega_c \hat{z}\right\},$$

$$\frac{v_{z,s+\frac{1}{2}} - v_{z,s-\frac{1}{2}}}{\Delta t} = \frac{1}{m}F_z, \quad \frac{\underset{\sim}{x}_{s+1} - \underset{\sim}{x}_s}{\Delta t} = \underset{\sim}{v}_{s+\frac{1}{2}}$$

482

The longitudinal response is accurate to perpendicular forces which vary slowly or near the resonance frequencies $\pm \omega_c$. As a result the dispersion function

$$\epsilon (\underline{k},\omega) = 1 + \frac{\omega_p^2}{k^2} \int d\underline{v} \sum_n J_n^2(\frac{k_\perp v_\perp}{\omega_c}) \frac{\Delta t}{2} \cot(\omega - k_z v_z - n\omega_c)\frac{\Delta t}{2}$$

$$\cdot (\frac{n\omega_c}{v_\perp} \frac{\partial f}{\partial v_\perp} + k_z \frac{\partial f}{\partial v_z}) \ ,$$

where $v_\perp \equiv \omega_c \times$ actual Larmor radius, is the Harris function with the cotangent replacement.[19] We have ignored the spatial grid for simplicity since it plays no role in the following.

If $\Delta\omega = \ell\omega_c + m\omega_c + n\omega_g$ is small enough for some integers 1, m and n, then the l'th and m'th harmonics have artificially been brought close together, opening the possibility of unstable interaction. For an example we choose $\omega_c\Delta t = 6\pi/25$ (about 8 steps per period), $\omega_p^2/\omega_c^2 = 2$ with $k_\parallel = 0$ and a monoenergetic velocity distribution. (This is done to get a more viable harmonic wave, not to create a "negative energy" wave. Instability can exist regardless of what signs the wave energies would have physically; only the required sign of $\Delta\omega$ is affected. Even a Maxwellian can be unstable.) This case should be stable, but the 4th and -4th harmonics represent nearly the same phase change (π) per time step and there results an odd-even instability with rapid growth, e.g., Im $\omega/\omega_c = .15$ at $k v_\perp/\omega_c = 3.6$. There is also a weaker instability from interaction of the 3rd and -5th harmonics.

The instability mechanism is little affected by the choice of difference equations, but $\omega_c \Delta t$ must be the gyro-rotation actually produced by the <u>difference</u> equations.

Jack Byers has tried the above example and found good agreement with the theory. The wave grew to amplitudes comparable to those for real cyclotron instabilities. A change of $\omega_c \Delta t$ to $6\pi/24$ (exactly 8 steps per period) eliminated the instability, also as predicted by the theory.

For high harmonics the "tuning" is delicate and growth rates are small. Thus the instability is not a problem for small enough Δt.

Even if the electron cyclotron harmonic waves are not the object of study, if they exist physically then they should be taken into account in choosing Δt. As we have seen, it may not be enough that $\omega_{pe}\Delta t$ and $\omega_{ce}\Delta t$ be small.

3. Remarks

One may wonder why these instabilities, which are so easy to find theoretically, have never been reported by people doing computer experiments. Perhaps there is something wrong with the theory. It is worthwhile to do some experiments to see if the instabilities really are there, and if so what their eventual evolution is. The few cases done by Okuda and Byers gave good quantitative agreement, so far, on all three instabilities. Okuda is reporting these experiments at this conference, but I would like to emphasize here also some important features. The instabilities were found both in obvious forms and disguised as real physics. They do not quench themselves at negligible amplitudes but can grow to amplitudes as large or larger than those for real instabilities under similar circumstances (i.e., of beam and of cyclotron harmonic

modes in the examples given). Last, but not least, they are harder to ignore than the rather clumsy theoretical results.

Possible nonphysical instabilities may be unimportant if there is real instability with a sufficiently strong growth. This is hard to judge quantitatively, and besides the nonphysical growth rate can be large too.

Although the examples have been dealt with in one dimension the instabilities will certainly be present in 2 or 3 dimensions because if k is directed along an axis of the grid the dispersion relation reduces to the 1-D case.

Some people have smoothed grid quantities, either directly or by suppressing higher modes if fast Fourier transformation is used in solving Poisson's equation. The aim is to reduce the effect of the spatial grid by suppressing wavelengths $\sim\Delta x$. We point out that this eliminates only the most violent instabilities, leaving intact the milder but still dangerous long-wavelength cases. This is because the aliasing arises in the interpolation between particle and grid quantities and therefore is unaffected.

Since the instability is caused by coherent interaction between plasma and grid, one might try displacing the grid randomly between time steps. This is fairly easy to do in any direction in which the plasma is periodic.

Another possibility is to use different grid spacing for ϕ and E than for ρ. This is not hard if fast Fourier transforms handling prime factors 3 or 5 as well as 2 are used to solve Poisson's equation. The intent is to break up the feedback of aliases.

One could try varying the grid spacing between time steps.

We recommend that some experimental checks for instabilities be
made on Lewis' models.

IV.   KINETIC THEORY

Last year we reported some results for fluctuations and collisions
in which the spatial grid was taken into account exactly but the effects
of finite time step were ignored. Those results were extended to include
finite time step, for an unmagnetized plasma.[19]

For simplicity our expressions are for only one (mobile) species.
This can be remedied by adding summation over species where needed.

1. Fluctuations and Noise.

We now consider a stable ensemble of systems such that its averages
are independent of where and when they are taken, i.e., a uniform and
stationary (constant) ensemble. This will mean that the ensemble average
of the field, say, at some x and t will be zero. However, due to the
finite particle density, a given realization from the ensemble will
certainly not be uniform or field free. Thus, averages of products
can be nonzero.   We find for the charge density fluctuation spectrum

$$(\rho^2)_{\underline{k},\omega} = \frac{2\pi n_0 e^2}{|\epsilon(\underline{k},\omega)|^2} \sum_p S^2(\underline{k}_p) \int d\underline{v}\, f(\underline{v}) \sum_q \delta(\omega - \underline{k}_p \cdot \underline{v} - q\omega_g).$$

The fluctuations of other grid quantities are related in a simple
way. For instance

$$(\underline{EE})_{\underline{k},\omega} = \left(\frac{4\pi}{K}\right)^2 \underline{KK}\, (\rho^2)_{\underline{k},\omega}$$

486

All averages approach their real plasma analogues smoothly when Δx, Δt are taken to zero in any manner, holding other parameters constant

2. Velocity Diffusion and Drag.

We first calculate the effect of a fluctuating field on the velocity distribution of the particles moving through it.

We find a diffusion in velocity given by the tensor

$$\underset{\sim}{D}(\underset{\sim}{v}) = \frac{e^2}{2m^2} \int \frac{d\underset{\sim}{k}}{(2\pi)^3} S^2(\underset{\sim}{k}) (\underset{\sim}{EE})_{\underset{\sim}{k}, \underset{\sim}{k} \cdot \underset{\sim}{v}}$$

Here and in the following the k integrals imply an infinite system. For a finite periodic system they are replaced by sums over all modes[18] except the $\underset{\sim}{k} = \underset{\sim}{0}$ mode. In addition, the fluctuations produce a net average force (drag) which pulls the particle velocities towards the phase velocities of the strongest waves. This turns out to be

$$\underset{\sim}{a}_{fluct} = \frac{\partial}{\partial \underset{\sim}{v}} \cdot \underset{\sim}{D}(\underset{\sim}{v})$$

The remaining source of drag is due to the distortion of the surrounding plasma by the test particle. We obtain

$$\underset{\sim}{F}(\underset{\sim}{v}) = \int \frac{d\underset{\sim}{k}}{(2\pi)^3} \frac{4\pi e^2 \underset{\sim}{k}}{k^2} S^2(\underset{\sim}{k}) \; Im \; \frac{1}{\epsilon(\underset{\sim}{k}, \underset{\sim}{k} \cdot \underset{\sim}{v})}$$

3. The Kinetic Equation and Collisions.

If we combine these results into a Fokker-Planck equation for $f(v)$ we obtain the computer simulation plasma kinetic equation:

$$\frac{\partial f}{\partial t} = \frac{\partial}{\partial \underline{v}} \cdot \frac{\omega_p^4}{\pi n_0} \int_g \frac{d\underline{k}}{(2\pi)^3} \sum_{pp'} \frac{S^2(\underline{k}_p)S^2(\underline{k}_{p'})}{|\varepsilon(\underline{k},\underline{k}_p \cdot \underline{v})|^2} \frac{\underline{k}\underline{k}}{k^4}$$

$$\cdot \int d\underline{v}' \sum_q \delta(\underline{k}_p \cdot \underline{v} - \underline{k}_{p'} \cdot \underline{v}' - q\omega_g)(\frac{\partial}{\partial \underline{v}} - \frac{\partial}{\partial \underline{v}'})f(\underline{v})f(\underline{v}')$$

This formidable result reduces to the Balescu-Lenard equation[21] (itself very complex) in the limit of small Δx and Δt. Intermingled here are normal collisions modified by the force smoothing[15,16] plus all the other grid effects such as stochastic heating from the grid noise.[10] There do not seem to be any nice approximations to make in the interesting cases, but there are several physical features which can be seen analytically.

4. Exact Properties of the Kinetic Equation.

After deriving his kinetic equation, Lenard[21] considers several conservation principles and inequalities which are true microscopically, and the H theorem. His kinetic equation is found satisfactory in all these respects. We begin by making the same checks on our kinetic equation. It can be shown that phase space density f remains positive, and average particle density and momentum are conserved—as they should be since the models conserve them exactly.

However, we know that energy is not conserved exactly, and indeed we find we can make no general statement about energy here. (To the order considered the rate of change of total energy is just the rate for kinetic energy.) We leave the question open for the moment.

For the H theorem we find

$$\dot{H} < 0$$

with equality not possible. Thus, there is no stationary f, not even the Maxwellian! This remains true in one dimension or when either Δx or Δt is separately set to zero. We can say the space-time grid creates entropy even for a plasma which should have the greatest possible entropy for the given density, momentum and energy. Since H is then an extremum the only way it can be changing is if a constraint is changing. In this case it must be that the energy is increasing. Indeed for the Maxwellian case one can show the energy is increasing by the right amount to account for the change in entropy.

The H theorem result provides a likely expression to study further as something which is due solely to the non-physical heating of the model, and which is easily measured in a computer experiment. In fact, the total energy is commonly monitored in simulation codes.

We have tried unsuccessfully to see if a distribution which is Maxwellian will remain so, though with increasing spread.

We have also derived the kinetic equation for Lewis' models.[19] The derivations follow those for the normal models very closely with the replacements of $\underset{\sim}{\kappa}$ by $\underset{\sim}{k}$ or aliases thereof. It is

$$\frac{\partial f}{\partial t} = \frac{\partial}{\partial \underset{\sim}{v}} \cdot \pi \frac{\omega_p^4}{n_0} \int dv' \int_{\underset{\sim}{g}} \frac{d\underset{\sim}{k}}{(2\pi)^3} \sum_{pp'} \frac{S^2(\underset{\sim}{k}_p) S^2(\underset{\sim}{k}_{p'})}{|\varepsilon(\underset{\sim}{k},\underset{\sim}{k}_p \cdot \underset{\sim}{v})|^2} - \sum_q \delta(\underset{\sim}{k}_p \cdot \underset{\sim}{v} - \underset{\sim}{k}_{p'} \cdot \underset{\sim}{v}' - q\omega_g)$$

$$\cdot \frac{\underset{\sim}{k}_p}{k^4} (\underset{\sim}{k}_p \frac{\partial}{\partial \underset{\sim}{v}} - \underset{\sim}{k}_{p'} \frac{\partial}{\partial \underset{\sim}{v}'}) f(\underset{\sim}{v}) f(\underset{\sim}{v}')$$

489

where

$$\epsilon(\underset{\sim}{k},\omega) = 1 + \frac{\omega_p^2}{k^2} \sum_p S^2(\underset{\sim}{k}_p)\int d\underset{\sim}{v}\ \underset{\sim}{k}_p \cdot \frac{\partial f}{\partial \underset{\sim}{v}} \frac{\Delta t}{2} \cot(\omega + i0 - \underset{\sim}{k}_p \cdot \underset{\sim}{v}) \frac{\Delta t}{2}$$

Again following Lenard we can show that f remains positive and particles are conserved. Since momentum and energy are not conserved microscopically it is to be expected that they are not conserved by the kinetic equation (except for the energy when $\Delta t = 0$).

A Maxwellian distribution which is not drifting is constant in the $\Delta t = 0$ limit. Otherwise the H theorem shows that f changes in a fashion which increases entropy.

If f is instantaneously Maxwellian we can say more about the rates of change of momentum, energy and H. We find that the changes in energy and momentum have no obvious sign separately, but the combination

$$\frac{d}{dt} \frac{1}{2} \overline{(\underset{\sim}{v} - \overline{\underset{\sim}{v}})^2} > 0$$

shows that the spread in the drifting frame is increasing and this is how entropy is increased.

When $\Delta t = 0$ we can see that $\overline{v}$ decreases. Thus, one can say that "collisions with the grid" slow the drift, and the velocity spread increases so as to maintain $\overline{v^2}$ constant.

With finite but small time step we still expect the drift to slow, or rather to move toward the nearest $\underset{\sim}{j} \cdot \Delta x / \Delta t$ since for such a velocity the grid looks stationary to the plasma.

5. Remarks

Our kinetic equations fail to retain a physical property in just those case where the model itself does not. Thus, the defects are not

in the kinetic equation but in the models, and these microscopic errors do not "average out" to zero as one might hope. Furthermore, these non-physical properties are in qualitative agreement with what the normal models are observed to do in practice (there is at present no experience with Lewis' model). All this lends credibility to the analysis.

Of course, the results suffer from the same difficulties as for real plasmas with regard to the adiabatic hypothesis at small k, and are similarly limited to stable systems. However, the large k divergences of real plasma theory are absent.

The results apply equally well to one, two and three dimensions with the appropriate adjustment to the k integral. Note in particular that the 1-D collision integral does not vanish identically as it does for a sheet plasma. Therefore, when grid effects become important 1-D collision times will be proportional to $N_D = n\lambda_D$ rather than to N_D^2. Here may be the explanation for the decrease rather than increase in collision time observed by Montgomery and Nielson[12] when Δx was increased above λ_D . Unfortunately, they give so little information that one would have to repeat the experiment in order to resolve this point.

Hockney has made the interesting experimental observation that, as $v_t \Delta t / \Delta x$ is increased from below to above unity, the ratio of heating time to velocity scattering time decreases rapidly from well above to below unity.[14] We now venture an explanation. The steps in the reasoning are easily identified with steps in the development of our theory, and can be verified or disproved by numerical study of the appropriate expressions.

Consider first the case with very small time step. In the fluctuation spectrum there is first of all the usual plasma fluctuations given by the $p = 0$ term. This extends up to frequencies of kv_t or ω_p, depending on $k\lambda_D$, then drops off quickly. There is also a grid noise component, given by the $p \neq 0$ terms, with a characteristic frequency $2\pi v_t/\Delta x$ and falling off slowly above that. This grid noise dominates the high frequencies and is little modified by collective effects as it is above the plasma frequency (assuming $2\pi\lambda_D > \Delta x$, which is also desirable to avoid the grid instability). However, the grid noise contributes relatively little to "collisions", which are due to phase velocities $\lesssim v_t$. Thus, velocity space evolution is fairly normal, with diffusion, etc and little heating.

When $v_t\Delta t > \Delta x$ the grid noise extends up past the sampling frequency $2\pi/\Delta t$, and therefore is the same to the difference equations as a low frequency and contributes to velocity scattering. There is no obvious reason why the drag should increase much; if not then diffusion dominates and the heating and scattering times will be comparable, as Hockney observed.

However, we feel there is no justification at present for Hockney's complete rejection of this regime $v_t\Delta t > \Delta x$ if the heating time is still large enough, which will depend on the object of study (e.g. plasma echoes are very sensitive to velocity diffusion). Recall also that other plasma phenomena may not be adversely modified at all; e.g. plasma oscillations seem little affected. On the other hand if one is studying kinetic theory then probably $v_t\Delta t > \Delta x$ should be avoided.

VI. CONCLUDING REMARKS

In addition to improving our understanding of the internal
workings of simulation plasmas, we believe this analysis can aid resolu-
tion of several open questions, such as: How does one choose the opti-
mum grid-particle interpolation to use when the spatial grid is coarse?
What algorithm changes ameliorate the nonphysical behavior? In what
sense is a low amplitude oscillation, using the "ordered start" with a
finite number of particles, the same as such an oscillation in a Vlasov
gas? How do we choose Poisson algorithms to make the long wavelength
fields very accurate while suppressing unwanted short-wavelength phenomena?

Of course, the situations discussed in detail in this work are
too idealized to directly support or discredit most actual computer
experiments. For instance they are of small relevance to strongly non-
linear phenomena. One can hardly do the simulation theory when the
corresponding "real" plasma theory is intractable. But I do hope to
have convinced you that computer experiments can turn out very badly,
sometimes in a deceptive manner, and I hope to have sensitized you
to some of the circumstances which can cause this to happen.

Furthermore, I believe these circumstances will be much harder
to avoid in the future, e.g., in three dimensions where the spatial grid
will be coarse, and when disparate time scales make the time step large
for some phenomena.

These models, even more than computing hardware and software
in general, are highly fallible. No one will anticipate all dangers and
compile a catalogue from which one can obtain unambiguous guidance for
experiments. But one can apply at least as thorough checks as either

the laboratory experimentalist or the theoretician. The common check
of repeating key experiments with different Δx and Δt, etc. helps some.
It also helps to have an independent check, a closely related situation
with behavior understood by some other means, e.g., the linear theory
for the low amplitude behavior of the situation is often very useful,
if available. Other simulation methods, such as integrating the Vlasov
equation itself, will be useful.[9]

Under the present circumstances, it would seem that anyone
reporting computer experiment results should include information on the
spatial grid, time step, initial conditions, etc., and their effects on
the results. The onus is on the author to show that he is presenting
physics and not numerical artifacts.

REFERENCES

1.   R. W. Hockney, J. Assoc. Comput. Mach. 12, 95 (1965).

2.   S. P. Yu, G. P. Kooyers and O. Buneman, J. Appl. Phys. 36,
       2550 (1965).

3.   R. W. Hockney, Phys. Fluids 9, 1826 (1966).

4.   P. Burger, D. A. Dunn and A. S. Halstead, Phys. Fluids
       8, 2263 (1965).

5.   O. Buneman, J. Comp. Phys. 1, 517 (1967).

6.   C. K. Birdsall and D. Fuss, J. Comp. Phys. 3, 494 (1969).

7.   R. L. Morse and C. W. Nielson, Phys. Fluids 12, 2418 (1969).

8.   J. P. Boris and K. V. Roberts, J. Comp. Phys. 4, 552
       (1969).

9.   Good coverage of various methods of plasma simulation from
       several points of view may be found in Methods in Compu-
       tational Physics, Vol. 9, Academic Press (1970), and
       references therein.

10.   R. W. Hockney, Phys. Fluids 11, 1381 (1968).

Oscillations, Fluctuations, Collisions

11.   R. W. Hockney, Proceedings of the Conference on Computational Physics, UKAEA Culham Laboratory, England, July 1969, Vol. 1, Her Majesty's Stationery Office, London.

12.   D. Montgomery and C. W. Nielson, Phys. Fluids $\underline{13}$, 1405 (1970).

13.   H. Okuda, this conference and to be published.

14.   R. W. Hockney, to be published.

15.   A. B. Langdon and C. K. Birdsall, Phys. Fluids $\underline{13}$, 2115 (1970).

16.   H. Okuda and C. K. Birdsall Phys., Fluids $\underline{13}$, 2123 (1970).

17.   E. L. Lindman, J. Comp. Phys. $\underline{5}$, 13 (1970).

18.   A. B. Langdon, J. Comp. Phys. $\underline{6}$, 247 (1970).

19.   A. B. Langdon, several papers in preparation. Preliminary discussions of the material may be found in the Quarterly Reports on Progress in Research in Plasma Physics. Electronics Research Laboratory, University of California, Berkeley.

20.   H. R. Lewis, J. Comp. Phys. $\underline{6}$, 136 (1970).

21.   A. Lenard, Ann. Phys. $\underline{10}$, 390 (1960).

Noise Suppression Techniques in Macroparticle Models of Collisionless Plasmas *

J. A. Byers
Lawrence Radiation Laboratory
University of California
Livermore, California

ABSTRACT

Noise reduction techniques are examined as
applied to macro particle computer models of col-
lisionless plasmas. The quiet start technique,
particle weighting, and the usefulness of forcing
the system to a linear one are discussed.

496

Macroparticle Model

I. **INTRODUCTION**

We emphasize, in this paper, noise elimination or reduction techniques as applied to macroparticle models of collisionless plasmas. We take the view that we are really interested in an absolutely collisionless system and that we desire a solution of the Vlasov equation, discretized though it may be. Choosing the macroparticle concept as a basic starting point, we first of all would like to stop thinking of our limited number of particles as an extremely poor plasma (very low number of particles per Debye length) with all the attendant enhanced kinetic properties such as fluctuations and collisions. Rather we take the view that the particles are discretized elements of a continuous Vlasov phase fluid. The goal is to obtain, with a manageable number of particles, a model which approaches as closely as possible a Vlasov plasma, i.e., a true continuous system. Results presented last year[1] employed for the first time a technique of noise suppression in macroparticle models that has acquired the name "quiet start". The technique allows one to suppress to a near zero level the natural fluctuations expected from a finite set of particles near an equilibrium state. Thus for a finite amount of time the quiet start technique has repressed all observable kinetic effects. Of course, our system is still a discretized one and will eventually run into coarse graining problems and the only recourse is to obtain finer resolution, i.e., increase the number of particles. But the coarse graining problem is common to all discretized

models. It is our main point that the quiet start procedure has
allowed our (admittedly grainy) collection of particles to behave
for a finite amount of time precisely as a true continuous system.
That is, there are no observables that might be ascribed to fluctu-
ational or collisional phenomena. Once the system has started to
become too coarse grained, it is still perhaps a moot point whether
one should describe the coarse graining effects in terms of enhanced
collisions or enhanced fluctuations. The system has arrived at
this state precisely as a true continuous system, and, while the
further development will undoubtedly be affected by the coarse
graining, one can still claim a better representation of the con-
tinuous solution than a code that allowed the collisional·fluctua-
tional phenomena to be present from the beginning. It is clear
that these remarks are particularly relevant for problems where
only a small part of the phase fluid becomes heavily disto. .en.
The undistorted parts of the phase fluid will continue to act in
an ordered manner as a continuous system and will contribute
nothing to fluctuational or collisional phenomena. In this paper
we examine the quiet start techniques and other methods of noise
suppression.

II.   QUIET START

The essence of the quiet start technique is to load the
initial values of the particles' phase space positions uniformly
along the equilibrium orbits and, in addition, to smooth out all
wavelengths equal to and smaller than the repetition length,

defined as the distance over which the velocity distribution re-
peats. One obtains an ordered regular pattern in phase space. For
example, in the simplest one-dimensional homogeneous system where
the equilibrium trajectories are simple straight line orbits, the
quiet start loading produces a number of beams. That is, one
starts with a given total number of particles, NP, which are to
represent some $f(v)$ over the system length L. One first chooses
some small fractional part of L over which it is determined physically
sensible to smooth the charge density. Call this length H-- this is
the repetition length over which we will repeat our representation
of $f(v)$. Then, instead of using NP different velocity values to
represent $f(v)$, which would result in the usual fluctuation level,
we use only $NP/(L/H) = NV$. In each distance H we represent $f(v)$
with only NV different values of velocity and in each succeeding
length H we again represent $f(v)$ with the same NV values of velocity.
For each value of velocity used we have L/H number of particles
and, since we smooth the charge density over distances $\leq$ H, each
such set of particles will appear as a continuous beam. Now, for
computational efficiency, the smoothing is applied to the charge
density, i.e., to the collection of all of the particles with dif-
ferent velocity values. But, since each velocity value is represented
by a uniform-in-space set of particles, the smoothing applied to
the collection of all the particles also will smooth each set of
particles with a particular value of velocity into the appearance
of a continuous beam. It is clear that the unperturbed motion of

499

a continuous beam will result in no fluctuation. In practice the
codes give proof of the success of this idea by producing fluctua-
tion levels of an undisturbed system corresponding to machine round-
off levels. Also the real frequencies and growth rates predicted
by linear Vlasov theory are reproduced within the precision of
measurement. For spatially homogeneous problems, the technique
works equally well for any type of equilibrium orbit, and the ex-
tension to 2 and 3 dimensions is also quite straightforward.

The quiet start occasionally produces problems of its
own that threaten to ultimately produce a noise level comparable to
that produced by a random start. For the simplest one dimensional
problems with straight line orbits one has a multibeam representation
of $f(v)$, and as is well known such a distribution is subject to
multibeam instabilities. They appear not to be troublesome in cases
where $f(v)$ itself is subject to a sufficiently strong instability
of its own, but in more subtle cases one can expect multibeam phenom-
ena to become apparent in times on the order of $1/(k\Delta v)$, where Δv
is a typical beam separation. Denavit and Kruer have recently
(unpublished work) clearly identified a multibeam instability in a
quiet start and were able to cure the problem by randomizing only a
few of the beams; the majority of the beams were left in an undis-
turbed state, and the noise level induced by the randomizing of a
few beams was much reduced over that of a fully random start. This
technique, as successful as it was in this particular case, clearly
requires knowledge of which beams to randomize, something that is not

likely to be known in more complicated cases. What is clearly
needed is a smoothing technique that is applied to all of the parti-
cles and is capable of smoothing out the fine grained multibeam
phenomena while leaving the coarse grained phenomena relatively un-
disturbed. In fact, Denavit (unpublished work) has recently been
working on a technique whereby periodically (not every time step)
a new smoothed $f(v)$ is established and a new set of particle posi-
tions and velocities chosen to represent the smoothed $f(v)$. Initial
results were very promising and the usefulness of the techn.que now
seems to hang on 1) its computing economy and 2) long term effects
of the smoothing on the desired coarse-grained phenomena.

III.   PARTICLE WEIGHTING

It also proves extremely beneficial from a noise reduction
point of view to use particles of different charge (and mass) values
so that the resolution can be focussed on that part of $f(v)$ that is
the most active. This is not a new suggestion and probably is now
widely used, but, in our opinion, the use of particle weighting has
overwhelming advantages in certain problems, and we want to emphasize
its usefulness as a noise reduction technique. An obvious algorithm
for any given $f(v)$ is to load the particles in velocity space uni-
formly and then apply a wieghting factor $\sim f(v)$ to the charge and
mass of each particle, thus producing equal resolution over all
velocity space. The modifications required to concentrate the
resolution in special velocity regions are straightforward.

We now discuss several examples of computer simulations

for one-dimensional homogeneous problems using the quiet start com-
bined with various weighting procedures. For a test of Landau
damping the particles were loaded uniformly in veloci$y$ and a weight-
ing factor $\exp(-v^2)$ produces the desired $f(v)$. We oltain a clean,
accurate Landau damped signal for several cycles until reaching a
noise level that is a function of the number of particles used.
See Fig. 1.

A second example is the simulation of an instability caused
by a very low density $(n_b/n_c \ll 1)$ cold beam at some $v \gg v_{th}$ super-
imposed on a Maxwellian plasma. The important weighting procedure
in this case concerns the beam particles; an equal number of particles
are used to represent the beam and the main plasma, so we have a
good resolution of the beam which is the active region of velocity
space, despite the very low relative density of the beam. Similar
resolution without the weighting procedure would require n_o/n_b
more particles, in some cases an extremely large factor.

A third example is the simulation of an unstable bump-on-
tail distribution, $f(v) = \exp(-v^2) + .05 \exp(-(v-3)^2)$. The
system is ten times as long as the wavelength of the fastest
growing mode, and we have three or four modes with phase velocity
in the positive slope region. Here again we load the particles
uniformly and weight the particles in order to achieve the desired
$f(v)$. Without weighti$n$ the particles, equivalent resolution of
the beam region requires approximately 20 times as many particles
$(2 \times 10^5$ compared to our $10^{-})$. The absence of quiet starting causes
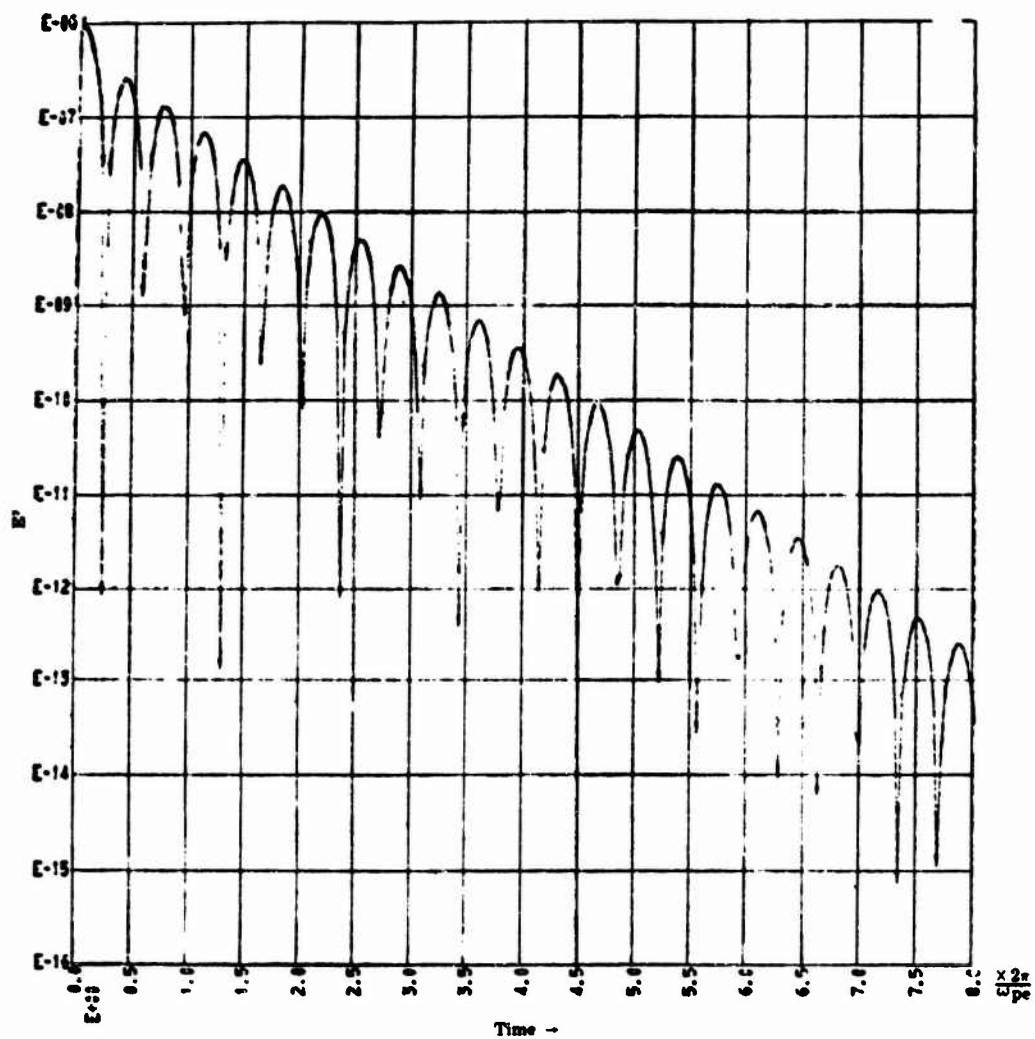
Figure 1.   Landau Damping Test. E^2 vs. time.

high initial amplitudes in all the modes of the system, including
those with phase velocities outside the positive slope region.
In contrast, the quiet start run had precise control over the
initial amplitudes and phases of all modes and for this case the
system was perturbed at very low energy so that at saturation time
the only large amplitude modes present are those with large linear
growth rates. It should be clear that particle weighting is parti-
cularly useful in any problem where a low density region of velocity
space is crucially important.

IV.   EXTENSIONS TO INHOMOGENEOUS PROBLEMS

For homogeneous problems with other than straight line
orbits, it is not quite fair to state that the essence of the quiet
start is the uniform loading of the equilibrium orbits. Rather it
is the uniform loading, for each particular value of velocity, in
configuration space coupled with the smoothing that achieves the
desired result. For inhomogeneous problems one naturally cannot
load uniformly in the inhomogeneous direction(s), and one must rely
entirely on uniform loading of the equilibrium orbits. The degree
of success for inhomogeneous problems seems to depend on the details
of the particular problem, such as the degree of complication of
the equilibrium orbit. See the work of Birdsall[2] and Harding and
Berk[3] for the two recent applications of the quiet start to inhomo-
geneous problems.

We are presently examining some further extensions of the
quiet start concept to inhomogeneous problems. First, one would

again load the particles uniformly on the equilibrium orbits and
then attempt to smooth the data with reference to these orbits,
in the spirit of the concept as applied in homogeneous problems.
The data would first be charge shared between neighboring equilibrium
orbit "grids". The smoothing would then be done on each of these
grids with the aid of the fast Fourier transform and the smoothed
transformed data would then be transformed back to configuration
space. The concept appears straightforward but may well require
an uneconomical amount of computing effort, since the above
smoothing steps must be carried out for each equilibrium orbit
"grid". The concept has not been tested.

Harding and Berk[4] have suggested the use of moving back-
ground particles to ensure the cancellation of equilibrium fluctua-
tions. The concept has not yet been fully tested.

V.   LINEAR THEORY via MACROPARTICLE SIMULATION

A technique similar to the latter suggestion, which we
have tested in homogeneous problems, is to force the system to a
fully linear one, i.e., integrate along the equilibrium orbits and
accumulate only the perturbation charge density[5]. This naturally
ensures absolutely no noise fluctuations due to equilibrium orbits,
regardless of finite difference errors, but of course one is limited
to the linear regime. Besides the noise reduction, however, there
is an additional major advantage of this technique first pointed
out by J. Freidburg[5]. One can bring in the effects of any homogeneous
direction simply by assuming an exp(iky) dependence where y is the

homogeneous direction. One need resolve the $f(v)$ only at one representative y plane, with all particles contributing to the charge density as $\exp(iky)$. One has the requirements of following one equilibrium orbit and two linearized orbits (to get amplitude and phase information) for each value of velocity used, but this is a minor price to pay for the reduction of the dimensionality of the problem.

Despite prior publication of the concept[5], we believe some more detail of the technique deserves exposition. We first linearize the equations of motion for each particle

$$\ddot{X} = \ddot{X}_o + \ddot{X}_1$$

$\ddot{X}_o$ represents the equilibrium orbit and can be as simple as pure one dimensional streaming motion, $\ddot{X}_o = 0$, or as complicated as one desires. X_1 represents the deviation from the equilibrium orbit. The first crucial point is that $\ddot{X}_o$ does not change as X_1 grows, in fact the magnitudes of X_o and X_1 are completely independant as they should be in a linear system. The second crucial point is that X_1 is calculated at the current position of X_o. That is

$$\ddot{X}_1 = \frac{e}{m} E_1 (X_o)$$

The charge density is then obtained only from the X_1

$$n_1 = - \frac{\partial}{\partial x} \left(n_o \Sigma \, x_1\right)$$

The above changes to a particle code actually make it computationally more involved. One has to follow the equilibrium orbit as well as the deviation. Also one has lost the possibility of exploring nonlinear behavior; the system is fully linearized and,

506

Macroparticle Model

for example, an instability will not saturate but will keep on growing. The perturbed quantities amplitudes have no relation to the magnitudes of equilibrium quantities. The gain has been an apriori rejection of the ordinary type of noise due to fluctuations of the equilibrium orbits.

A second major gain is available if the problem is spatially homogeneous. As stated above one then can transform all perturbed quantities as $\exp(ikx)$; the problem will then be solved for only one value of k. One treats all perturbed quantities as sinusoidally distributed in x. This requires two quantities for each perturbation particle, an amplitude and a phase. In practice we represent this complex particle as two real particles, X_1 and X_2, located 90° apart in X_0. The real and imaginary parts of the displacement then are

$$RX = X_1 \cos(kX_0) + X_2 \cos(kX_0 + \frac{\pi}{2})$$

$$IX = -X_1 \sin(kX_0) - X_2 \sin(kX_0 + \frac{\pi}{2})$$

The contributions to RX and IX are summed up from all of the particles and the perturbed electric field is trivially obtained from the resulting dipole density. As an example of the technique we present results from a simple problem of some current interest. The problem is a spatially homogeneous two species plasma being driven by a spatially homogeneous external electric field, $E_0 \cos(\omega_0 t)$, where $\omega_0 \sim \omega_{pe}$. The transformation technique reduces this spatially one dimensional problem to a problem of resolving only velocity space. Only 200 particles were used in obtaining the results of Fig. 2.

507
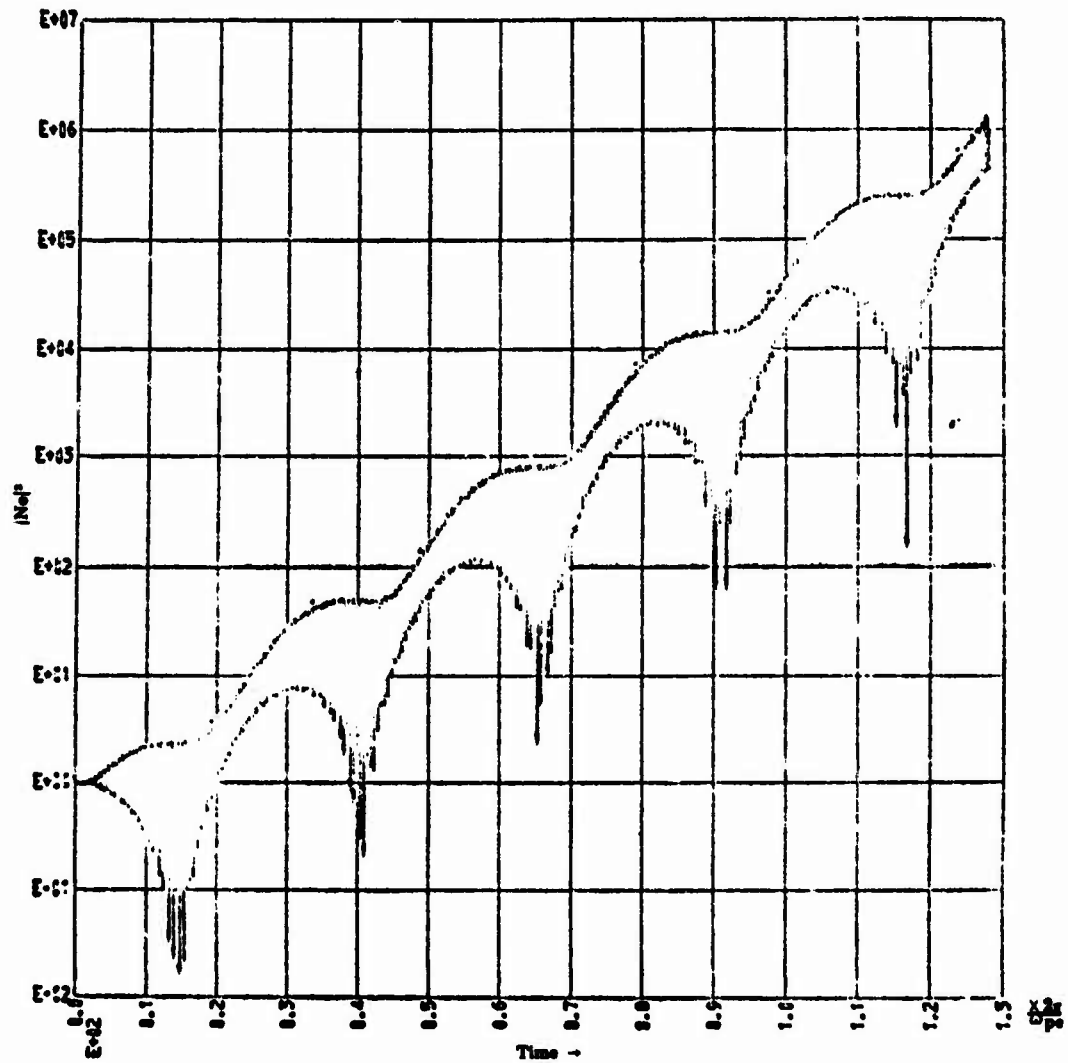
Figure 2a. $\left|n_e\right|^2$ vs. time. Total timespan $= 128 \times 2\pi/\omega_{pe}$

$E_{ext} = E_0 \cos(1.06\,\omega_{pe})$, $k\lambda_{De} = .14$

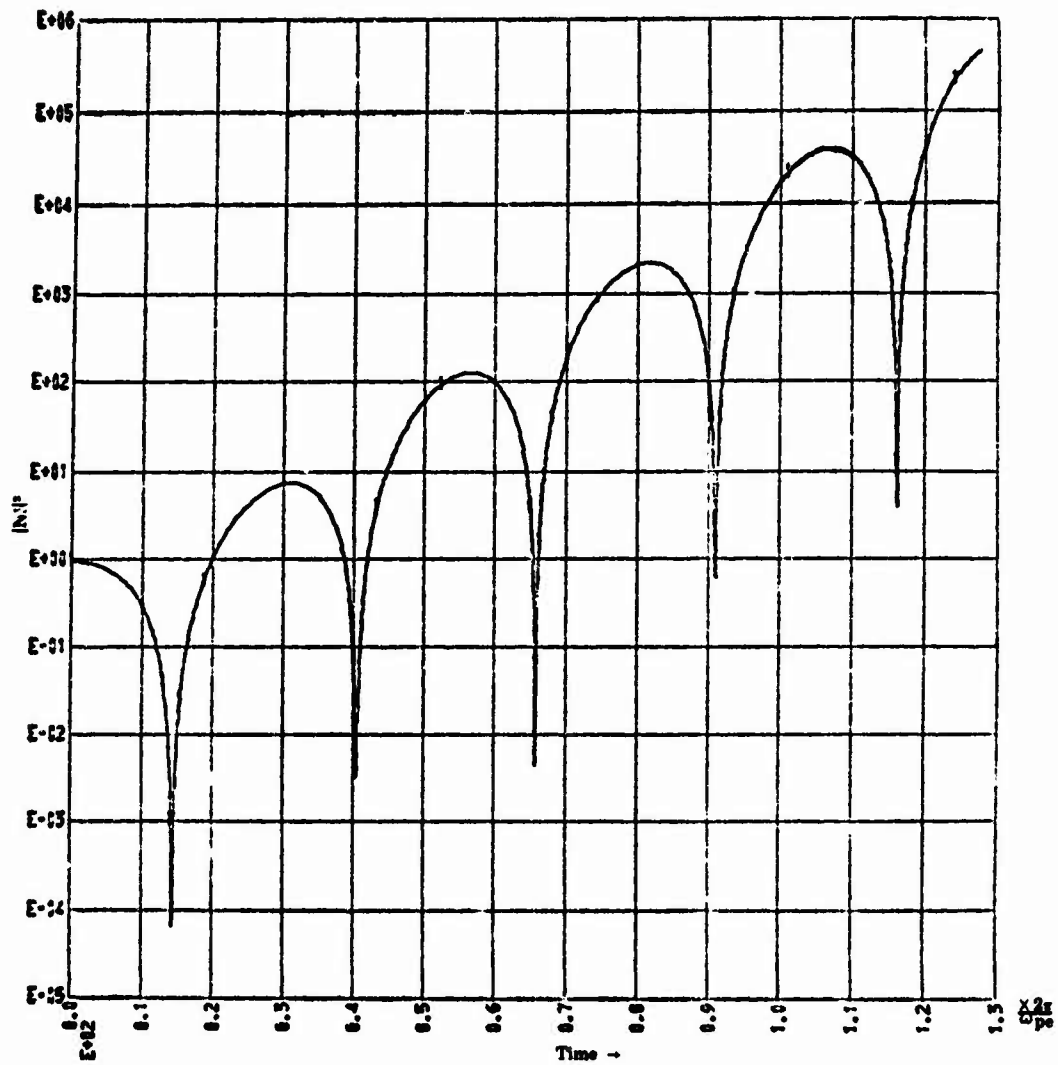Figure 2b. $\left|n_1\right|^2$ vs. time. Total timespan = 128 x $2\pi/\omega_{pe}$

E_{ext} = $E_0 \cos(\omega_{pe}$ x 1.06), k λ_{De} = .14

REFERENCES

1.   J. A. Byers and M. S. Grewal, Physics of Fluids, $\underline{13}$, 1819 (1970).

2.   C. K. Birdsall, D. Fuss, A. B. Langdon, "Drift Loss Cone Simulation Experiments and Theory for Large Orbits, $a_1 R_p$.",   p. D2, Sherwood Theoretical Meeting, April, 1970, Princeton, New Jersey.

3.   R. C. Harding and H. L. Berk, "Electron Bounce Motion in Mirror Machines", p. 28 in Proc. 3rd Annual Numerical Plasma Simulation Conference, Stanford 1969.

4.   Private Communication.

5.   J. P. Freidburg, R. L. Morse and C. W. Nielson, Numerical Method for Studying Linear Stability of Highly Inhomogeneous Plasmas, in Proc. 3rd Annual Numerical Plasma Simulation Conference, Stanford 1969, p. 15, (1969).

For presentation at the 4th Conference on Numerical Simulation of Plasmas, Naval Research Laboratory, Nov. 2-3, 1970, Washington, D.C.

Nonphysical Instabilities in Plasma Simulation
due to Small $\lambda_D/\Delta x$

Hideo Okuda*

*Department of Electrical Engineering and Computer Sciences
and the Electronics Research Laboratory
University of California
Berkeley, California*

Abstract

Plasma computer experiments have been performed with a one-dimensional particle model in order to understand a nonphysical instability due to the use of a spatial grid. A violent instability was observed with the theoretically predicted growth rate of $\omega_i/\omega_{pe} \approx 0.1$ for $\lambda_D/\Delta x = 0.1$ with the Nearest Grid Point (NGP) model, where λ_D is the Debye length and Δx is the grid size; in addition, when the field energy reached several percent of the kinetic energy, the total energy began to grow rapidly, violating conservation. The growth rate was reduced either by using linear interpolation of charge and force (CIC,PIC) or by increasing the Debye length with the NGP model. The experimental results are in good agreement with Langdon's theory.

---

*Present address: Princeton University, Plasma Physics Laboratory, P.O.Box 451, Princeton, New Jersey 08540.

I. Introduction

This paper presents several experiments which verify a nonphysical instability in a simulation plasma due to the use of a spatial grid as predicted by Lindman[1] and Langdon[2]. Langdon predicts that when the Debye length is small compared with the grid size, the coupling among perturbations with different wavelengths, called aliases, can destabilize plasma oscillations, even in a thermal plasma (uniform in space and Maxwellian in velocity, hence physically stable). The predicted growth rate of the instability has a maximum of $\omega_i/\omega_{pe} \approx 0.1$ at $k \Delta x \approx \pi/2$ for $\lambda_D/\Delta x = 0.1$ with the NGP model.[3]

The use of a spatial grid in plasma simulation with particles is now widespread, and there is a general inclination to economize, using coarse time and space grids and zero[th] order (NGP) or first order (linear) inter-polations (CIC[4];PIC[5]) for charge and force assignments. It is important to understand the effects of such time and space grids and interpolations, especially in the enhancement of nonphysical noise or instabilities in order to distinguish physical information from nonphysical information. Theoretical investigations have been carried out extensively toward this direction by Langdon.[6]

II. Experimental results

The particle model used is a one-dimensional electrostatic system with periodic boundary conditions described elsewhere in detail.[7] The electrons move and are loaded initially uniformly in space; the ions are assumed to be immobile with uniform density. The parameters are listed in Table I. The initial velocities were chosen to produce the Maxwellian distribution function, $f(v) = \exp(-v^2/2v_t^2)/\sqrt{2\pi}\, v_t$. In experiments 1,3, and 4

512

Nonphysical Instabilities

Table I

Parameters of the Experiments

experiment	Debye length λ_D	interpolation scheme	length of one period L	thermal velocity v_t	total no. of particles N	predicted linear growth rate, ω_i/ω_{pe} (most unstable mode)
1	0.1	NGP	8	0.1	3168	0.1
2	0.1	NGP	20	0.1	4000	0.1
3	0.1	CIC,PIC	8	0.1	2376	0.013
4	0.2	NGP	8	0.2	3168	0.03

time step of integration $\omega_{pe}\Delta t = 0.2$

length of run (all exp.) $\omega_{pa}t = 40$

$\Delta x = 1$

$\omega_{pa} = 1$

the velocities were chosen from a uniform distribution of $F(v) = \int_o^v f(v)\, dv$, with the same velocities used in each spatial cell in order to produce a noiseless (or quiet) start[8]; in experiment 2, $F(v)$ was uniform but for all of the particles used with x,v uncorrelated (randomly related), so as to have all modes initially excited. The Debye length is defined as $\lambda_D = v_t/\omega_{pe}$. Except for the third experiment where the CIC,PIC model was used, the NGP model was used throughtout the experiments.

Experiment 1

3168 particles (sheets) were arranged into 32 groups each with 99 particles. All groups have the same Maxwell velocity distribution. A small modulation in velocity space was added to the Maxwell distribution

to excite the second mode ($\lambda = L/2$) which is the most unstable mode in the present model; with the uniform initial loading being essentially noiseless, the initial modulation was found necessary.

Fig. 1 shows the evolution of the instability in phase space at different time steps. The field, kinetic and total energies with the development of the instability are given in Fig. 2. A small modulation emerges at the early time steps, which is due to the initial modulation. The growth rate ($\omega_i/\omega_{pe} \approx 0.1$) and the oscillation frequency ($\omega_r/\omega_{pe} \approx 0.78$) of the second mode are in good agreement with the linear theory. The modulation continues to grow and becomes appreciable at $\omega_{pe}t \approx 20$ which is about three plasma periods. At this stage, the field energy reached several percent of the kinetic energy and the total energy itself begins to increase appreciably as shown in Fig. 2. After this stage, the energy continues to grow without appreciable saturation or limiting. Near the end of the calculation ($\omega_{pe}t \approx 40$), the kinetic energy reaches several times its initial value, resulting in the increase of the Debye length by factor two and reduction of the growth rate. However, the catastrophe has already taken place. Higher spatial harmonics are generated with the development of the instability as seen in Fig. 1.

Experiment 2

In order to see the effects of the change of the initial conditions, especially, using a random loading in phase space and also to see the effects of many Fourier modes, we tried the second experiment as shown in the table. Particles are distributed uniformly in x and randomly in v according to the Maxwell distribution. As will be expected, all possible Fourier modes were excited initially and the development of each mode was observed.

Nonphysical Instabilities
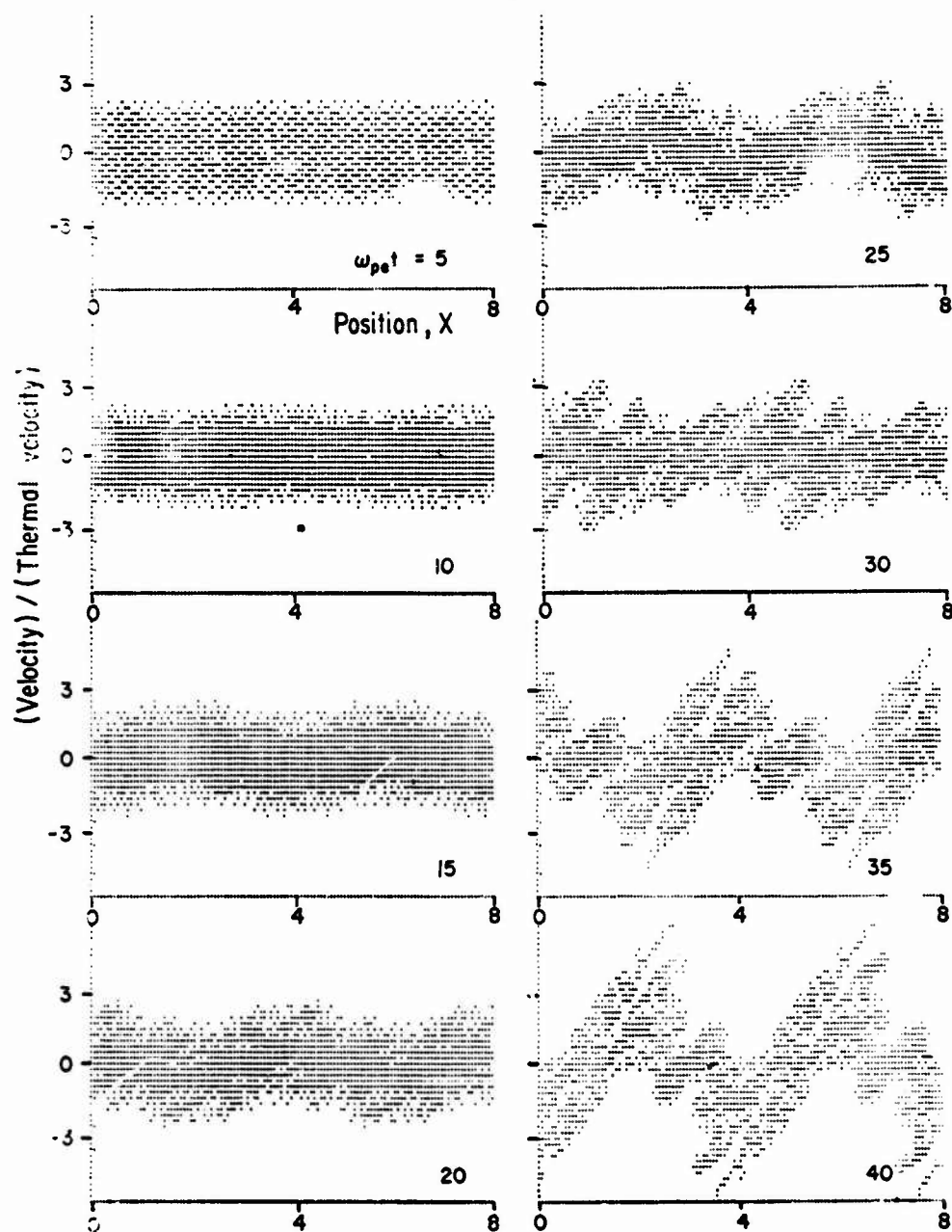
Phase-space distribution

Fig. 1 - Evolution of a grid instability in phase space for a Maxwellian plasma. A quiet start with a small perturbation to the second mode was employed as the initial condition. $\lambda_D/\Delta x = 0.1$, $N_D = 40$, and $L/\Delta x = 8$. Experiment 1. NGP.
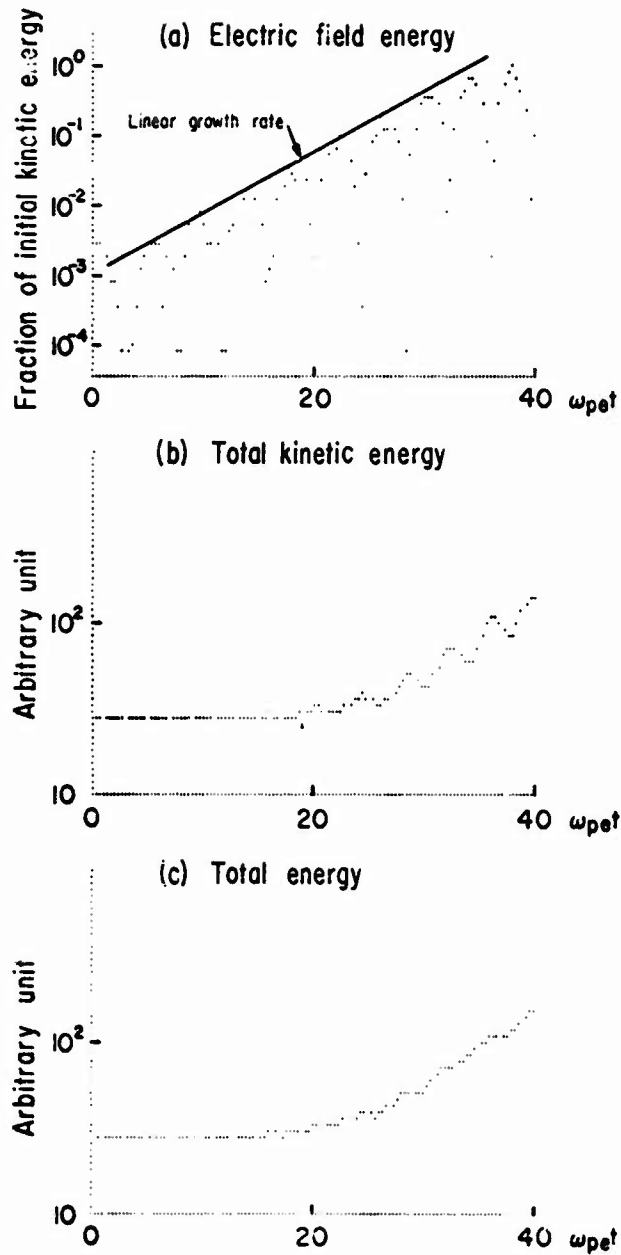
Fig. 2 - Growth of the total field (a), kinetic (b) and the total (c) energies with time. Field energy normalized by the initial kinetic energy increases exponentially with the expected growth rate and the oscillation frequency. The total energy also increases, showing the nonconservative nature of the instability. Experiment 1. NGP.

Nonphysical Instabilities

Figs. 3 and 4 show the phase space plot of the instability and the development of the field, kinetic and total energies respectively. Unlike Exp. 1, there is no initial modulation for any mode. Until $\omega_{pe} t \approx 20$, it is not clear from Fig. 3 whether the instability is developing or not except for a gradual increase of the number of particles with large velocities. The field energy increases nearly exponentially with the overall growth rate of $\omega_i / \omega_{pe} \approx 0.07$. After $\omega_{pe} t \approx 20$, bunching of particle density can be seen clearly with the corresponding wavelength roughly equal to the 5th or 6th modes of the model, the most unstable modes. After the total field energy reaches several percent of the kinetic energy, the instability develops just like Exp. 1, again violating the conservation of total energy. After $\omega_{pe} t \approx 30$, bunching of the particles goes on rapidly, leading to the development of large amplitude waves.

Fig. 5 shows the development of energies of the Fourier modes (mode 3, 4, 5, and 6). The solid straight lines are the growth rate, predicted for each mode from liner analysis. The observed growth rates are close to the predictions.

It may be expected that the error arising from the finite difference scheme of the integration of the equation of motion will have some effect on the development of the instability, especially for very fast particles. This was checked by running the same experiment with the time step of $\omega_{pe} \Delta t = 0.1$ instead of 0.2 which was used thoughout the experiments. No appreciable differences, such as the behavior of the field energy and the beginning of the increase of the total energy at $\omega_{pe} t \approx 20$, have been observed up to the limit of calculation ($\omega_{pe} t = 40$).

So far, we have examined the most unstable situation with small Debye length with the NGP model. We next show how the instability is reduced or stabilized by smoothing the interaction between particles and grid using smoother interpolation or by increasing the Debye length.
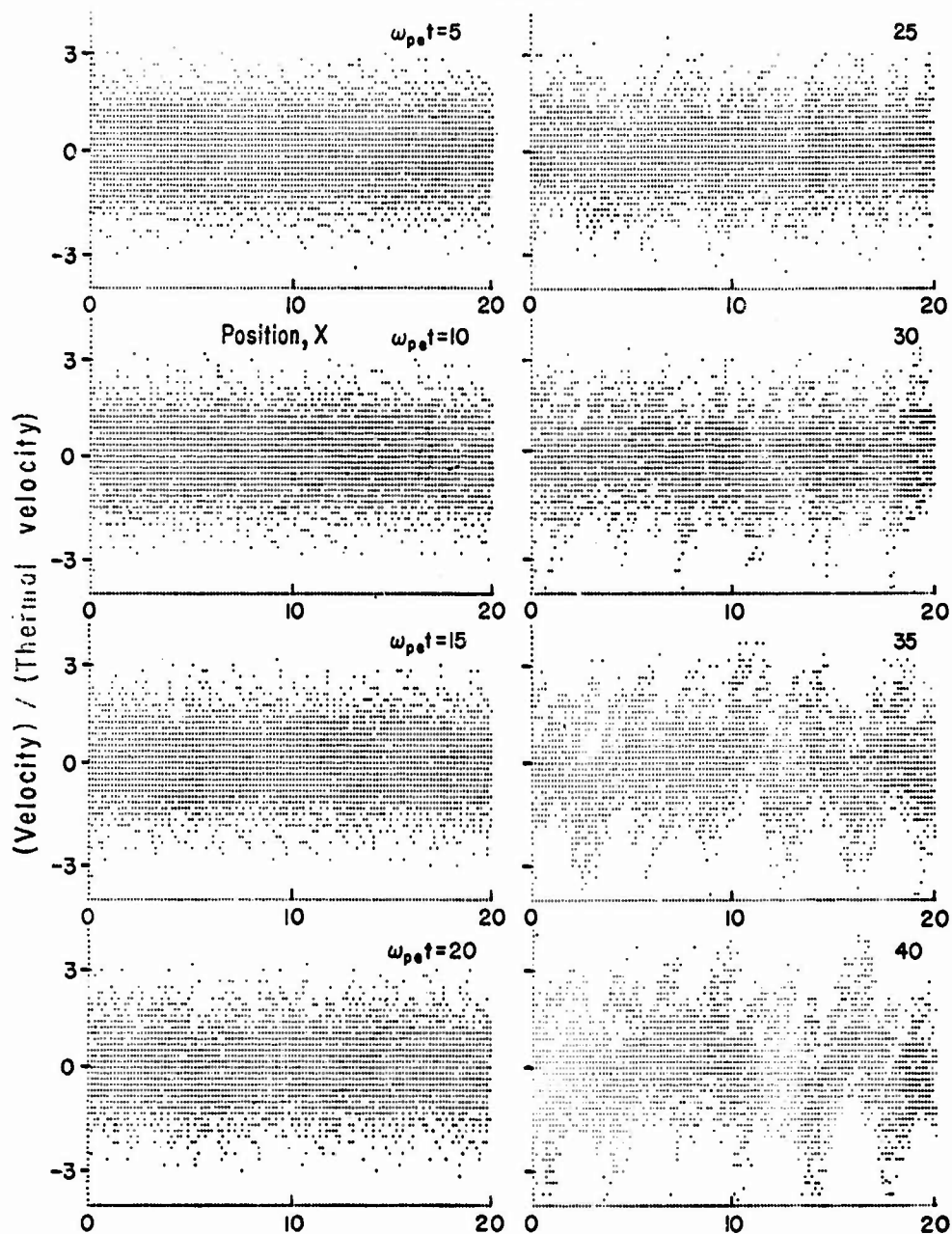
Phase-space distribution

Fig. 3 - Phase-space plot with random initial loading. Many modes are excited simultaneously at the initial stage of the calculation due to the initial condition. The dominant modes are those which are linearly most unstable. $\lambda_D/\Delta x = 0.1$, $N_D = 20$, and $L/\Delta x = 20$. Experiment 2. NGP.
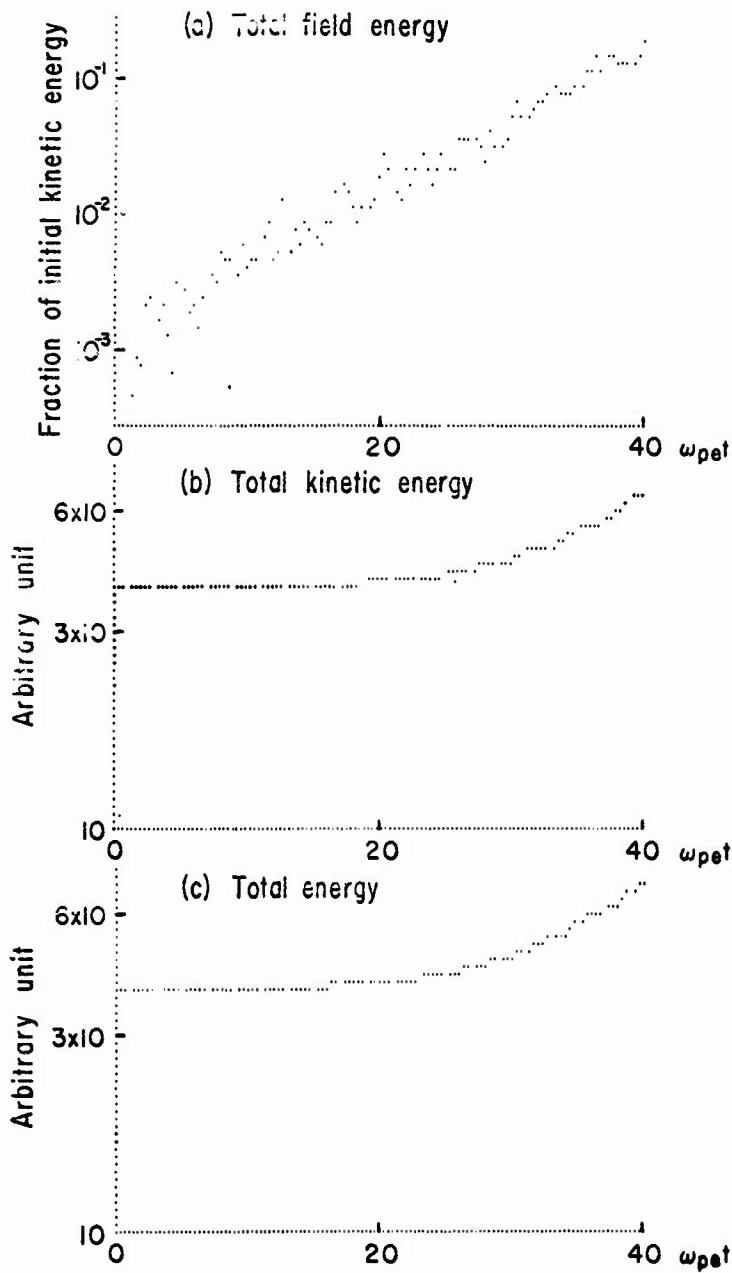
518

Fig. 4 - Total field energy normalized by the initial kinetic energy (a), kinetic (b) and the total energy (c) in the experiment 2. The overall behavior of the instability is quite similar to that of exp. 1. Experiment 2. NGP.

Energy of Fourier modes
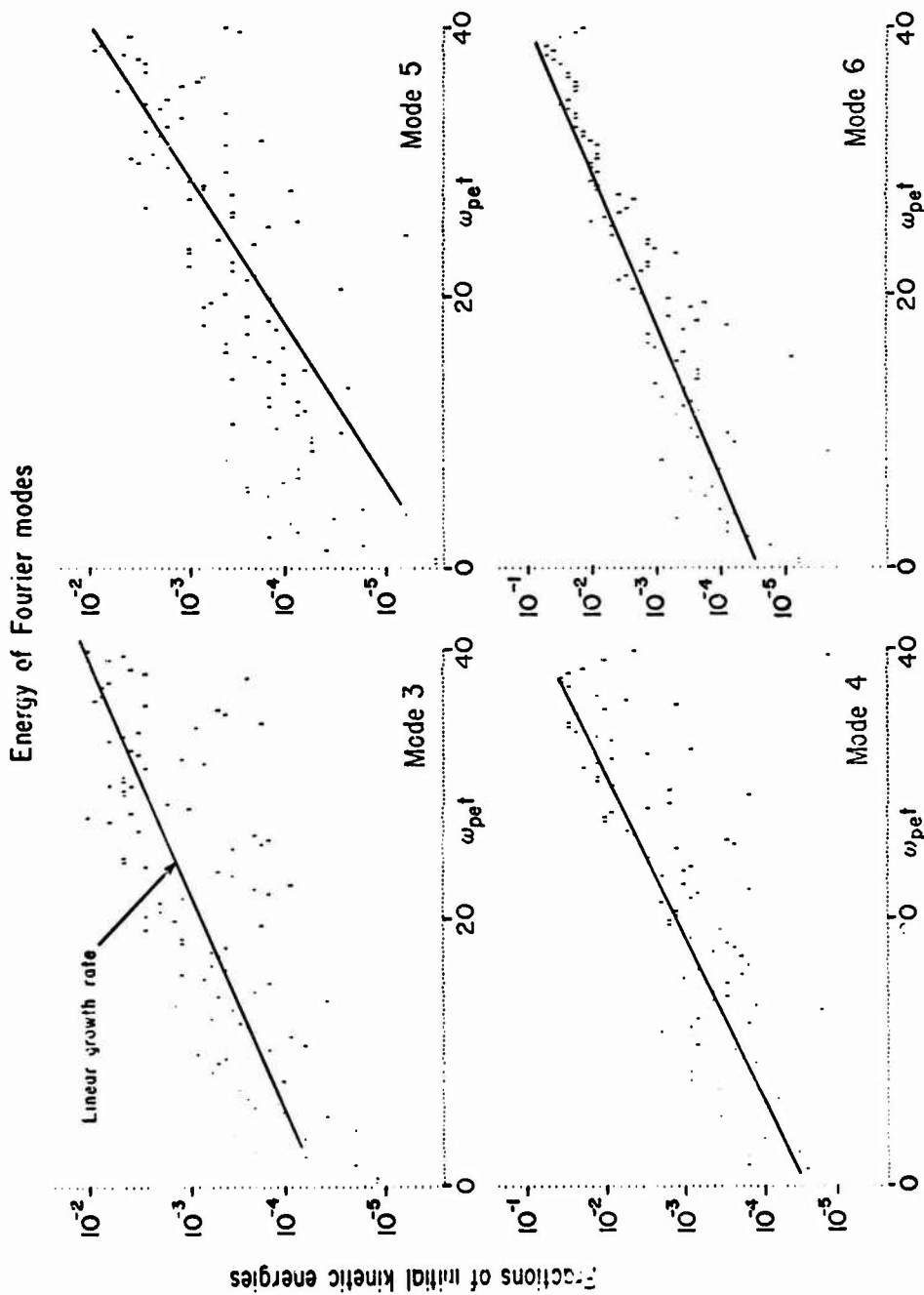
Fig. 5 - Growth of the energy of the Fourier modes of the electric field normalized by the initial kinetic energy. All modes were excited initially and grew with roughly the expected rate, although the fluctuations are very large. Experiment 2. NGP.

Experiment 3

Here we consider the case in which linear interpolation is used for
charge and force assignment (CIC,PIC). The parameters of the experiment
are the same as in Exp. 1 except for the total number of particles is now
reduced to 2376. Linear analysis shows that the maximum growth rate is
$\omega_i/\omega_{pe} \cong 1.3 \times 10^{-2}$, which is one order of magnitude smaller than the NGP
model due to the smoothing of the interaction.

Fig. 6 shows the development of the field energy of Fourier modes in
the model. It is predicted that the first mode ($k\Delta x = \pi/4$) is very
weakly unstable ($\omega_i/\omega_{pe} \cong 10^{-3}$) and the second mode ($k\Delta x = \pi/2$) is at
the maximum growth rate ($\omega_i/\omega_{pe} \cong 1.3 \times 10^{-2}$) and the third mode will
Landau-damp. The first and the second modes grow with nearly the expected
growth rate and the oscillation frequency. ($\omega_r/\omega_{pe} \cong 0.94$ and 0.77 for
the first and the second mode respectively). The total energy (not shown)
was conserved within 0.5 percent up to the end of calculation. Hence the
growth rate of the instability is quite small for the present calculation,
the maximum total field energy was 0.25 percent of the kinetic energy and
this value is not large enough to lead the plasma to blow up. Fourier modes
are still in the linear stage during the calculation. Although the in-
stability is quite weak it is expected that the effects of the instability
will not be negligible for a much longer run.

Experiment 4

We come back to the NGP model again and try to see the effects of
larger Debye length. We consider the case with $\lambda_D/\Delta x = 0.2$ where the
Debye length is just twice as large as that of Exp. 1. The linear theory
predicts that the maximum growth rate is reduced to $\omega_i/\omega_{pe} \cong 3 \times 10^{-2}$.
Fig. 7 shows the development of the total field energy which increases
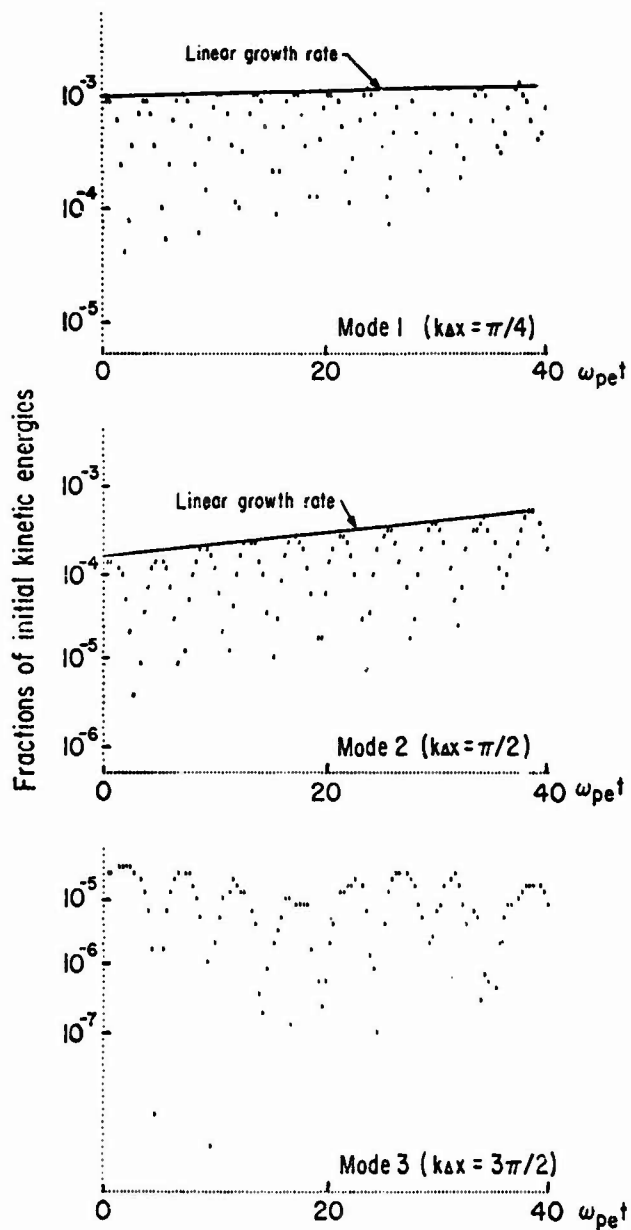
Energy of Fourier modes

Fig. 6 - The energies of the Fourier modes normalized by kinetic energy in the exp. 3 where linear interpolation of charge and force is used. The plasma is much less noisy than the NGP model and the growth rate and the oscillation frequency of the 1st and the 2nd mode are quite close to the prediction. $\lambda_D / \Delta x = 0.1$, $N_D = 30$, and $L / \Delta x = 8$. Experiment 3. CIC, PIC.
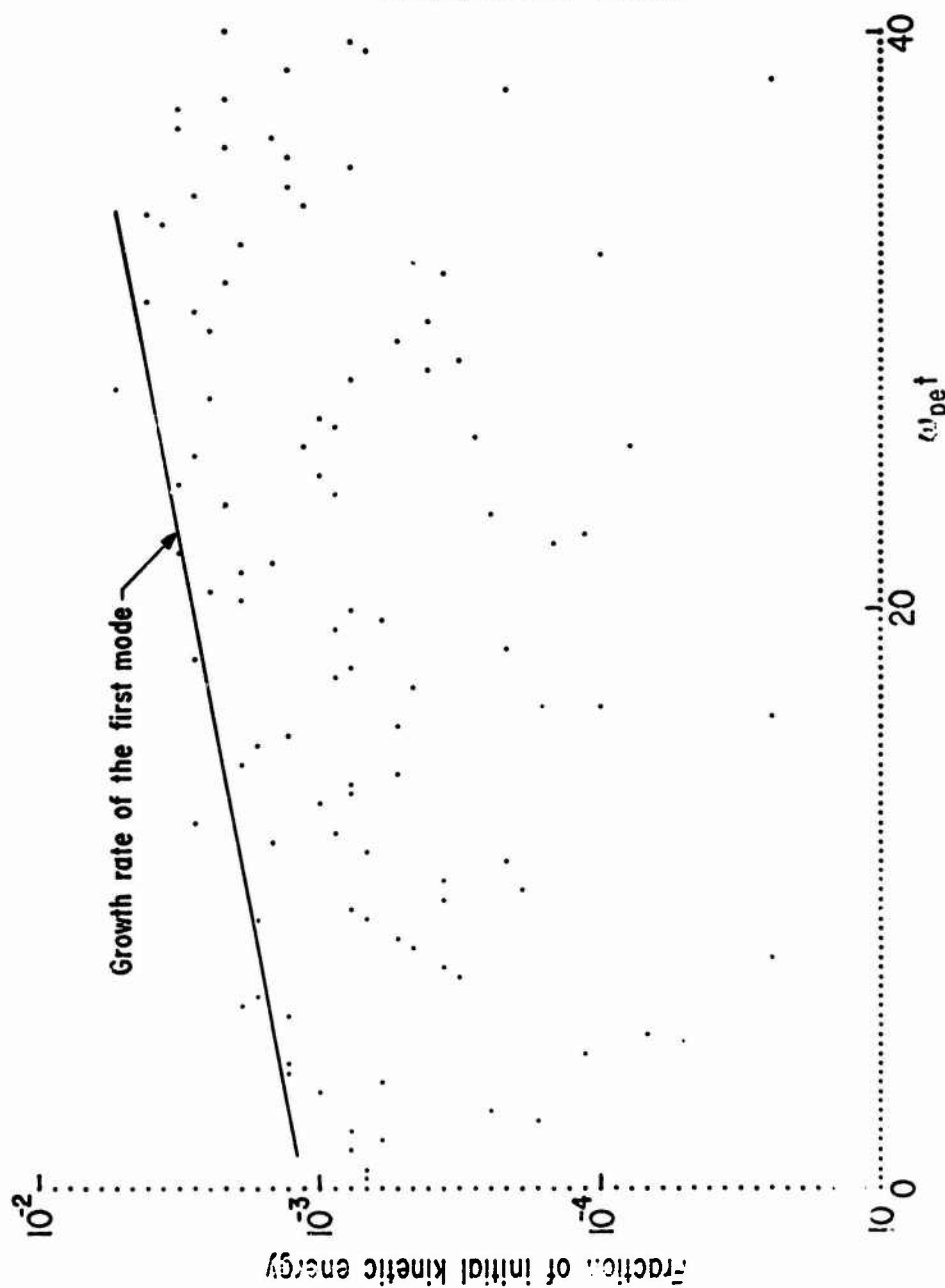
Fig. 7 - Total field energy of the experiment 4 normalized by the kinetic energy. It fluctuates very much compared to the CIC, PIC model, however, the overall growth is close to the prediction. Total energy was conserved within one percent in this experiment. $\lambda_D/\Delta x = 0.2$, $N_D = 80$ and $L/\Delta x = 8$. Experiment 4. NGP.

523

roughly with the expected rate, although the NGP model is much noisier than the CIC model as was emphasized by Hockney[9]. The ratio of the field to the kinetic energy at the end of the calculation was an order of 5×10^{-3} which is not large enough to lead the plasma to a catastrophe. The total energy was conserved within one percent in this experiment. However, it must be cautioned that if the initial noise level of the unstable modes were high enough, then the conservation of the total energy might be violated early in time, within several plasma periods due to the development of large amplitude waves as was seen in Exp. 1.

We have also checked the case with $\lambda_D/\Delta x = 0.3$ and confirmed that the growth rate was further reduced to $\omega_1/\omega_{pe} \cong 5 \times 10^{-3}$ as was predicted.

III. Discussion

We have confirmed that a nonphysical instability can develop due to the use of a spatial grid in simulation even in thermal plasma. The instability can grow to large amplitudes, causing the total energy to increase. The experiments show good agreement with Langdon's theory. It is important to realize that NGP requires larger $\lambda_D/\Delta x$ so that NGP can deal only with small diameter plasma, while CIC,PIC can go further, crucial in two and three dimensional simulation.

Acknowledgment

Nonphysical Instabilities

References

1. E. L. Lindman, J. Comp. Phys. $\underline{5}$, 13 (1970)

2. A. B. Langdon, To be published in J. Comp. Phys.

3. P. Burger, D. A. Dunn, and A. S. Halsted, Phys. Fluids $\underline{8}$, 2263 (1965),
   R. W. Hockney, Phys. Fluids $\underline{9}$ 1826(1966).

4. C. K. Birdsall and D. Fuss, J. Comp. Phys. $\underline{3}$, 494 (1969).

5. R. L. Morse and C. W. Nielson, Phys. Fluids $\underline{12}$, 2418 (1969).

6. A. B. Langdon, To be published.

7. H. Okuda, to be published.

8. J. A. Byers and M. Grewal, Phys. Fluids $\underline{13}$, 1819 (1970).

9. R. W. Hockney, "Particle Models in Plasma Physics" in Proceedings
   IPPS Conference on Computational Physics, Culham, England, 1969.

Optimization Techniques for Particle Codes

J. H. Orens, J. P. Boris, and I. Haber
Naval Research Laboratory
Washington, D.C.

I.   INTRODUCTION

Optimization of computer simulation codes requires a balance between flexibility, development time, core requirements, and computational speed.[1] Codes should be flexible enough that minor conceptual modifications do not require significant revisions. Similarly, specific machine language programming should be used only when absolutely necessary in order to allow for machine independence and greater readability. Well known optimization techniques can often be applied without severely constraining the simulation. For example, requiring the number of grid points to be a power of two allows application of readily available Fast-Fourier-Transform techniques. Also, if constant factors can be scaled by powers of two, shifting operations can often be used instead of multiplications and divisions. Such techniques yield significant savings in computation time. Optimization also includes a consideration of data accuracy and external-device timings. It is rarely necessary to calculate a quantity more accurately than the value that it is going to update. Similarly if it is necessary to store intermediate quantities on an external device, there is little

526

advantage in optimizing internal calculations to so great a degree that the computation time is bounded by the external data transfer rate. Following these general considerations an electrostatic plasma simulation code, P POWER, was developed for solving one- and two-dimensional problems on a rectangular, doubly periodic region. A discussion of this code follows and some typical applications are presented.

II. THE P POWER SIMULATION CODE

Figure 1 is a flow chart for the code. Each block represents a modularized segment which is designed to be re-placed easily. This allows for independence of each major section and flexibility in modifications. The code is divided into seven major segments: the initialization section, where all paramete s are read in, the particle tables initialized, and important constant calculated; the Poisson solver, where Poisson's Equation $\nabla^2\phi = -4\pi\rho$ is solved by Fast-Fourier-Transform Techniques; the electric field solver, where the equation $\underset{\sim}{E} = -\nabla\phi$ is solved by a difference scheme; the field diagnostic routines, where modes of the electric field are available and where the electric field energy is calculated both in k-space and x-space; the particle diagnostic routines, where the momenta, energies, and temperatures of each individual type of particle are calculated; the particle pusher, where the particle veloci-ties and positions are updated according to a desired scheme (e.g., classically or relativistically, nearest-grid-point, dis-critized interpolation in cell, etc.); and the charge counter routine, where the charge density matrix, $\rho(X)$, is calculated by a scheme corresponding to the type of particle pusher used.
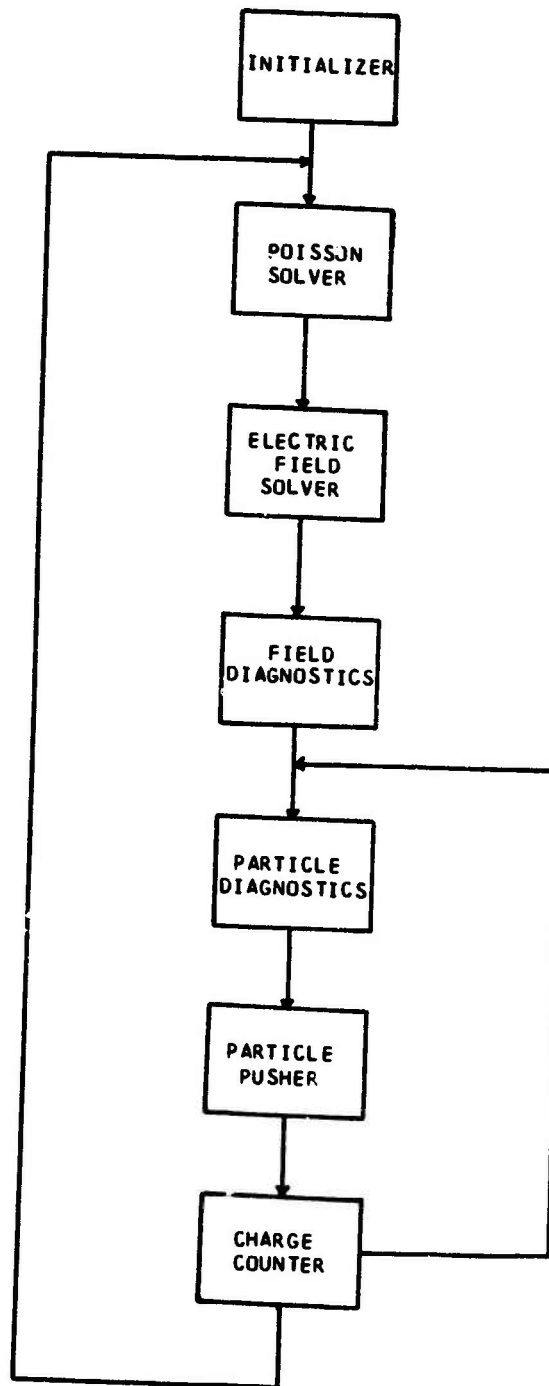
527

Figure 1.   Flow Chart of the PPOWER Particle Simulation
            Code.

Particle Codes

The code is designed so that the main loop for diagnosing, updating, and counting the particles requires only one pass per time step through the particle tables. This is extremely important when the particle tables are stored on an external device and each pass involves the (usually expensive) external device timings. When the particles are stored in core, an option in the P POWER code, no particular saving accrues from the single-pass aspect of the algorithm. However, to ensure flexibility, the most restrictive constraints, in this case those imposed by external-device buffering, must be satisfied.

The initialization segment is designed to prepare the data (e.g., particle velocities and positions) in a format that will facilitate the operation of the simulation code. The particles are divided into classes in which all the particles have the same charge, mass, drift velocity, thermal velocity, and spatial distribution. Each particle is represented by one or two position coordinates and one, two, or three velocity components depending on the physical problem being simulated. Both the positions and velocities are represented in an integer format[2] and only integer-register operations are used to update these particle quantities. The positions are stored in a vector form (Figure 2a) in which 32 bits (one word) are used for both coordinates, therefore allowing both the Y and the X position to be updated with a single integer-add operation. Each coordinate is represented by 16 bits without a sign (positions are always positive) and the binary point is positioned such that a lost
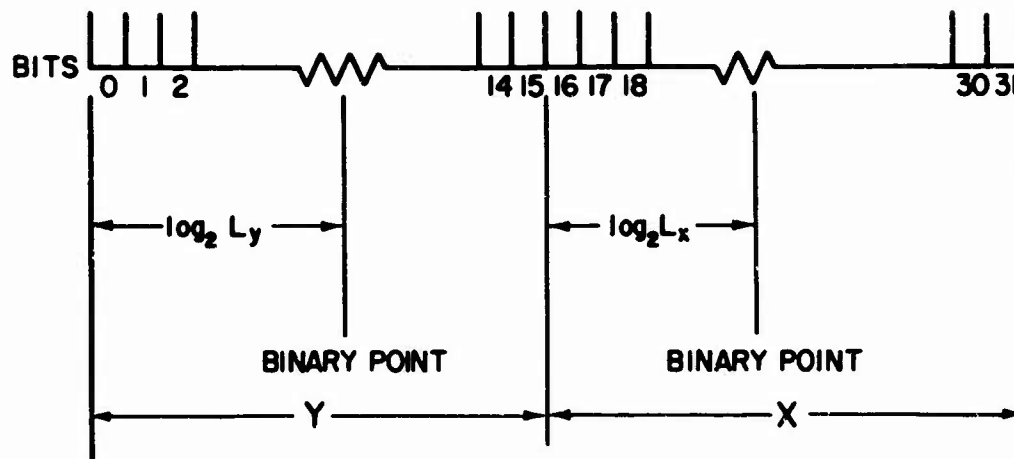
POSITION

Figure 2a. Data Structure for Particle Positions (Y and X
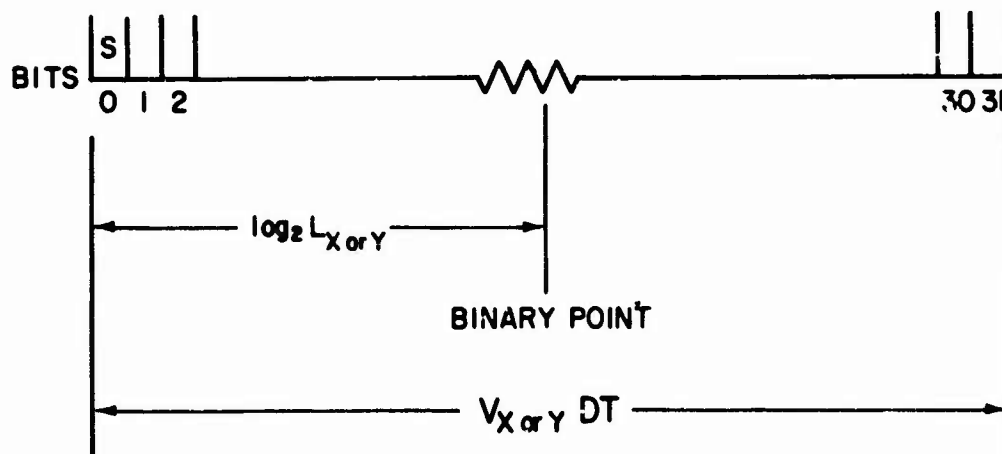Coordinates).

VELOCITY TIMES DT (X OR Y)

Figure 2b. Data Structure for Particle Velocities (X, Y,
or Z Components).

"carry" from the highest order bit causes the system to be cyclic. A "carry" from the highest order X bit does affect the lowest order Y bit, but generally is negligible. To facilitate the updating of the positions, the velocities are stored as the velocity times DT (the time step). This quantity is represented by 32 bits (Figure 2b) of which the highest order bit is a sign. The binary point is such that the velocity of a particle that travels more than half the system length in a time step cannot be represented properly. Due to the details of the integer-register operation, however, it happens that the positions of such a particle will always be given correctly. If a particle is accelerated by more than half a system length per time step, the excess is treated as a negative velocity in a way which always takes the particle to the correct position even though by travelling through the periodicity in the wrong direction. Thus the energy of the particle will be improper but the effect of this particle on the system evolution will be correct.

Depending on the dimensionality of the problem and the properties of the simulations, therefore, a particle can be represented by a minimum of two words (one position coordinate and one velocity component) and a maximum of four words (two position coordinates and three velocity components). Particles of the same class are grouped into records each with a header containing all pertinent information about the particles in that record (number of particles in the record, charge, mass, class, and system size). Thus all records are independent and need be stored in no particular order. The independent nature of the records is a great advantage when the particles are stored on an external device.

531

The initialization segment also sets up all pertinent constants. These include constants necessary to scale quantities to the size of the system and constants to reflect the fact that the electric field times q/m times DT squared is the accelerating field for the integer velocities. Here constants for external electric and magnetic fields are prepared.

Each time step begins with a solution of Poisson's Equation, $\nabla^2\phi=-4\pi\rho$, to determine the electrostatic potential from the position of the charged particles. Fast-Fourier-Transform Techniques[2,3,4,5] are utilized to solve this equation and are highly optimized for a sine and cosine transform, since the charge density and potential are real quantities. Due to the necessity of repeated applications of the innermost segments of the transform routine, they have been written in machine language. Besides periodic boundary conditions, [$\rho(N+X)=\rho(X)$ where N is the length of the system], there are also similar optimized Fourier techniques known[3,5] for reflecting [$\rho(2N-X-1) = \rho(X)$], and inverting [$\rho(2N-X-1) = -\rho(X)$] boundary conditions.

In numerical simulations, as discussed by several authors,[6-13] the binary collision phenomena are greatly enhanced relative to collective plasma phenomena because the simulation plasmas have many fewer particles per Debye sphere than the corresponding physical plasmas. When slow phenomena are being studied which would be collisionless in the actual problem under study, very great care must be taken to ensure that the simulation is also collisionless. Once $\phi(k)$ has been determined by Fourier transforms, therefore, two techniques are applied to reduce the particle collision frequency. A Gaussian

532

$e^{-k^2a^2}$ form factor[9,11,12] is applied to the potential coefficients and the high-k, short wavelength, potential coefficients are truncated[2,11,12] (set to zero). This latter correction has the added advantage that fewer Fourier transforms need to be performed and therefore it also helps in reducing the execution time of the code.

Multiplying by the Gaussian form factor in k-space creates the same effective potential as would gaussian particles with a spread in x-space. Spreading the particles smooths the force law thereby reducing the fluctuations (collisions) due to close interactions. Cutting off the large k-value modes removes the short wavelength modes where the enhanced fluctuations are most serious, and thus has the same effect as the Gaussian form factor. Figure 3 depicts the effect of these two techniques on the particle shape. Initially the particle has the form of a delta function. After applying the $e^{-k^2a^2}$ factor the particle would have a Gaussian form and cutting off the large value k-modes gives the particle shape the ringing characteristic of $\frac{\sin x}{x}$. The effective particle shape is further modified, of course, by the use of a spatial grid and an interpolating algorithm but these modifications, while included in the code, are treated in detail elsewhere.[11,13]

In order to determine the effect of these techniques on the collision rate, "thermal tests" were conducted where electrons and ions $\left(M_i/M_e = 64, \ T_i = T_e \right)$ were drifting at a relative velocity much smaller than the acoustic velocity.
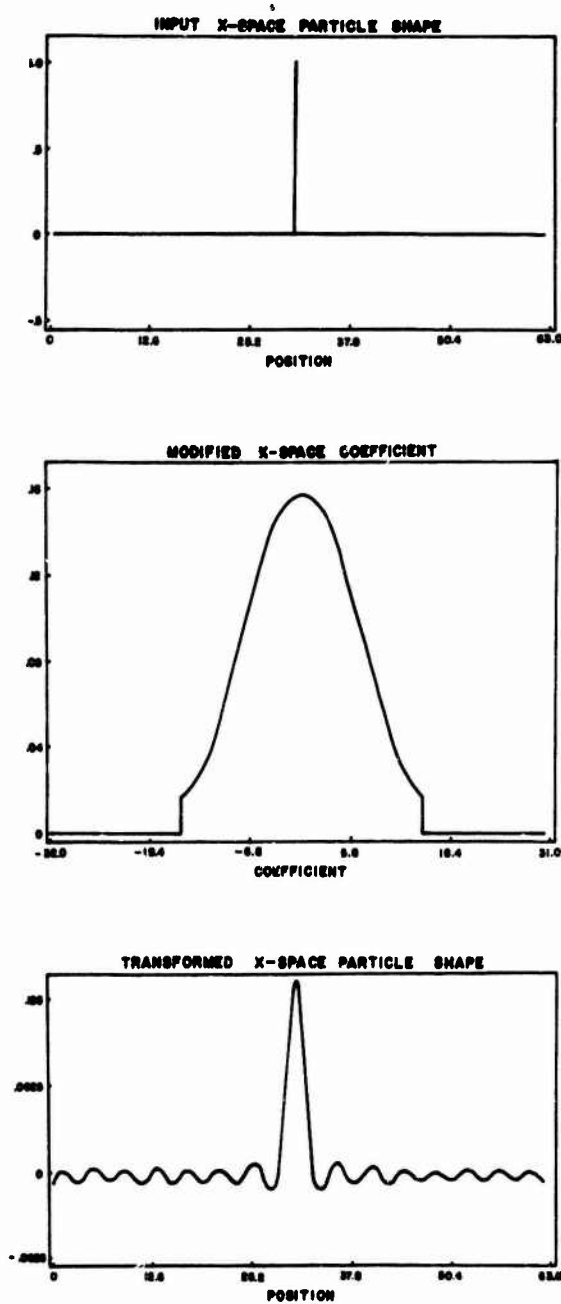
Figure 3. Shape of a Simulation Particle After Application of a $e^{-k^2a^2}$ Form Factor and Cutoff of Short Wavelength Modes.

This physical situation is stable and the collisions were measured by considering the slow-down rate of the relative velocity and the stocastic heating rate of the system energy. These tests are similar to those performed by Hockney[8] for a different simulation model. Figure 4 is a plot of these quantities for a typical "thermal test". For this case the particle spread was one grid cell and one quarter of the k-modes were retained. Here the e-folding time for the slowing down of the drift is about 1800 ω_{pe}^{-1} and the e-folding time for the stocastic heating of the energy is approximately 20,000 ω_{pe}^{-1}. Figure 5 is a table comparing the results of the series of "thermal tests". It is generally evident that increasing the particle size while holding the number of modes fixed or decreasing the number of modes retained while keeping the particle size constant, decreases both the collision rate (the rate of relative velocity slow down) and the rate of stocastic heating. This table also notes the case where the correction factor for the electric field differencing scheme has not been applied. This correction factor allows for a more accurate calculation of the electric field, but, due to its roughening effect upon the force law, tends to slightly increase the stocastic heating of the system energy. It is evident that very long simulation calculations may be made before the collisions begin to dominate, provided that sufficient care is exercised in choosing the particle size, the mode cutoff, and $n\lambda_D^2$.

There are several possible techniques for calculating the electric field $\underset{\sim}{E}(\underset{\sim}{X})$ from the potential. In k-space $\underset{\sim}{E}(\underset{\sim}{k}) = -i\underset{\sim}{k}\phi(\underset{\sim}{k})$ and this quantity may be inverse Fourier Trans-
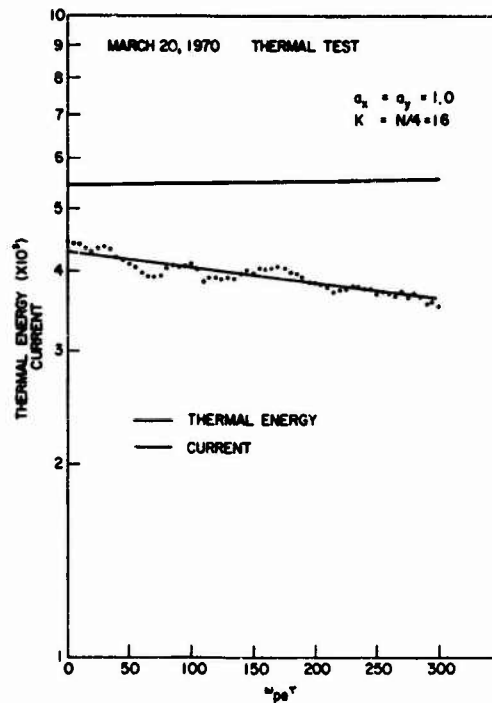
Figure 4. Plot of a Typical Thermal Test Showing Collisional Slow Down of the Relative Drift Velocity and Stochastic Heating of the System Energy.
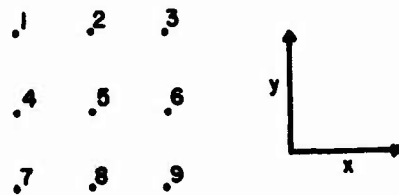
THERMAL TESTS
64 X 64
$n\lambda_D^2 = 16$

a	k	E-field Corr	$T_c \omega_p (x10^3)$	$T_h \omega_p (x10^3)$
0	16	N	1.0	12.2
0	16	Y	1.11	3.9
0	10	Y	1.2	15.1
0	8	Y	2.03	15.2
1	16	Y	1.77	20.0
1	10	Y	2.02	>30.0
2	16	Y	6.9	>30.0

Figure 5. Comparison of Thermal Test Results for Varying Particle Spread and Varying Number of Modes Retained.

536

$$\underline{E} = -\nabla \phi$$

A SIX POINT DIFFERENCE SCHEME

.1   .2   .3

.4   .5   .6   y

.7   .8   .9   └── x

$$E_x(5) = \frac{1}{12}(\phi_3 - \phi_1) + \frac{1}{3}(\phi_6 - \phi_4) + \frac{1}{12}(\phi_9 - \phi_7)$$

$$E_y(5) = \frac{1}{12}(\phi_1 - \phi_7) + \frac{1}{3}(\phi_2 - \phi_8) + \frac{1}{12}(\phi_3 - \phi_9)$$

Figure 6. The Six Point Difference Scheme Used to Calculate The X and Y Electric Field, $\underline{E}(\underline{X})$, From the Potential $\phi(\underline{X})$.

formed to obtain $\underline{E}(\underline{X})$. In general this would require three applications of the Fast Fourier Transform routine — one to obtain $\phi(\underline{k})$ from $\rho(\underline{X})$ and two to obtain $\underline{E}(\underline{X})$ from $\phi(\underline{k})$.[14] Also $\underline{E}(\underline{X})$ may be calculated by a differencing scheme from $\phi(\underline{X})$.[2,11,12] This method requires only two applications of the Fast Fourier Transform Routine -- one to calculate $\phi(\underline{k})$ from $\rho(\underline{X})$ and one to calculate $\phi(\underline{X})$ from $\phi(\underline{k})$. Numerous numerical differentiation techniques are available for differencing $\phi(\underline{X})$ to obtain $\underline{E}(\underline{X})$ and generally are faster than the extra Fast Fourier Transform necessitated by the first method. In the P POWER simulation code, the second method was utilized and a six point difference scheme was chosen to solve for the electric field. This scheme is shown in Figure 6 and is designed such that one correction factor per mode[11,12] can be applied to the potential in order to concur-

rently improve the accuracy of both the X and the Y electric fields.

If one evaluates the behavior of the usual two-point difference formula for E_x and E_y on the exponential eigenmodes of the two-dimensional rectangular Poisson Equation, he finds that the numerically computed field differs from the correct analytical field, found by differentiating the functional form of the potential, in both magnitude and direction. The errors become quite severe at short wavelength. The six-point formula used for differencing corrects the direction of $\underset{\sim}{E}$, as calculated numerically from ϕ, up through second order. The magnitude can be corrected by application of a single multiplicative factor to each of the Fourier coefficients of the potential.

The application of the six-point formula is very much shorter than performing the third Fourier transform and, in fact, competes with the two-point formula because the factor between the central difference and the two side differences is four and can be evaluated by a shift in fast arithmetic registers.

As noted earlier this improvement in electric field accuracy creates a small increase in the stocastic heating because the inaccuracies of the usual difference formula for $\underset{\sim}{E}$ tend to be smoothing.[11]

Optimization of the data structure tends to decrease the efficiency in the diagnostic routines since all quantities must be converted to an unoptimized form to make them meaningful. This is not a great limitation as the simulation is diag-

nosed at intervals of many time steps. Diagnostics should be
extremely flexible and highly modularized in order that many
qualities of interest can be readily available. The most
important consideration has been that all desired diagnostics
can be done with only one pass through the particle tables.
This is highly desirable when the tables are stored on an ex-
ternal device. Typical diagnostics available in the P POWER
program include kinetic energies, currents, and drift veloci-
ties for each individual class. Also k-modes of the electric
field and total electric field energies in both k-space and
x-space are available. Velocity space (V_x vs V_y) and phase
space (any coordinate vs. any velocity component) are displayed
for each class in a contour format where each point represents
the number of particles at that point in the space. Also
graphical display packages can be easily inserted into the
diagnostic routines. Sometimes certain simulation parameters
must be varied depending on the outcome of the diagnostics.
For instance, to simulate "pump out" it is possible to decrease
the charge of a class as a function of the electric field
energy while keeping the charge-to-mass ratio constant. Simi-
larly a time variation of the external electric field is often
of interest. One significant example is called "charging the
boundaries", where a $\underset{\sim}{k} = 0$ mode, which cannot be self consis-
tently supported in a periodic system, is externally applied.
Here the current flux throughout the system is converted to an
amount of charge building upon the walls of a nonconducting box
surrounding the computational region. This yields a laminar

539

electric field which opposes the current flow and gives rise
to plasma-frequency oscillations. This may be called a total-
current-constant (zero) boundary condition because the plasma
plus displacement current adds to zero. There are two techni-
ques for calculating this electric field. One is to use
Poisson's Equation $\nabla \cdot \underset{\sim}{E} = 4\pi\rho$, where ρ is the density of charge
that crosses the boundary during a sampling time. Solving this
equation by means of a Gaussian "Pill Box" would then yield the
electric field. This method is unsatisfactory as it gives rise
to a violent numerical instability. A superior technique is to
find the electric field from the dynamic Maxwell equation
$4\pi\underset{\sim}{j} + \dfrac{\partial \underset{\sim}{E}}{\partial t} = 0$. This equation is then integrated over the sampling
time to give the desired electric field.[15,16] This method yields
quite satisfactory results and Appendix B describes a typical
"charging the boundaries" experiment.

Several different specialized particle pushers have
been developed. Each utilizes the terms of the Lorentz Equation
appropriate for the specific simulation and updates the veloci-
ties and positions by a reversible, time-centered algorithm.
Here the velocities are defined at half a time step from the
positions and electric fields (see Figure 7). There are avail-
able two basic integration schemes -- nearest-grid-point
(N.G.P.)[7,8,12] and discretized interpolation in cell (D.I.C.).[12]
The N.G.P. technique attributes all charge of a particle to
the nearest grid point and considers the resultant electric
field as constant throughout the cell. The D.I.C. technique,
as shown in Figure 8, divides each cell into a specified num-
ber of subcells (16 x 16 in the P POWER code) and uses a pre-

$$\frac{d\underline{p}}{dt} = e\left(\underline{\underline{E}} + \frac{\underline{v} \times \underline{B}}{c}\right)$$
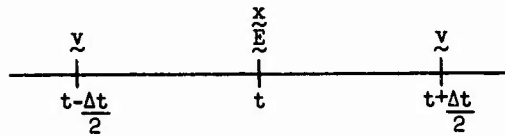
LEAP FROG SCHEME

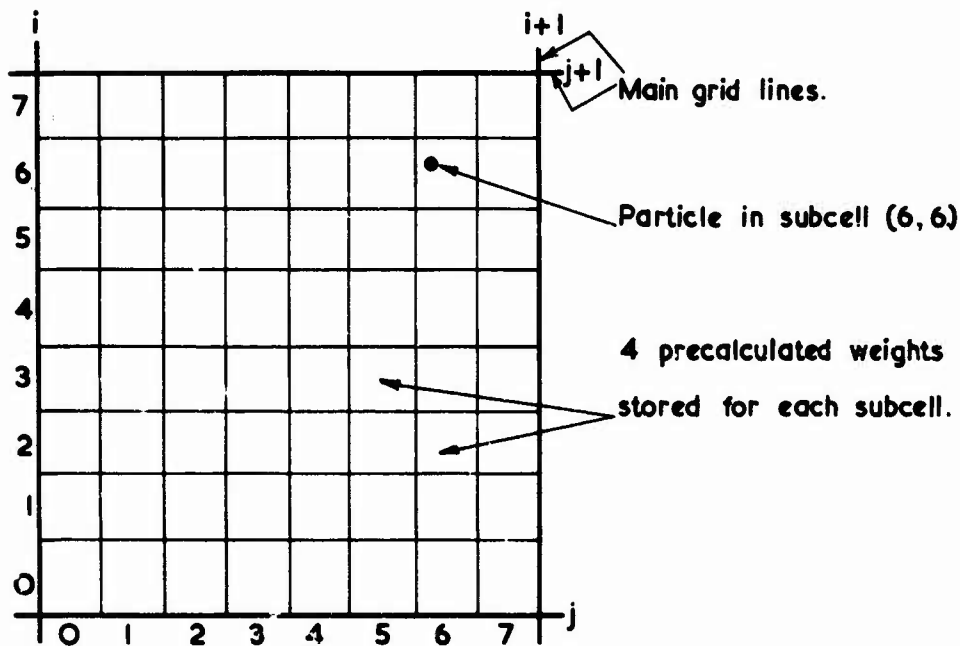Figure 7. The Lorentz Equation of Motion and the Leap Frog Scheme Used to Update the Velocities and Positions.

Figure 8. The Discretized Interpolation in Cell Sub-Grid Scheme (D.I.C.) for Calculating the Charge Density $\phi(X)$ and Distributing the Electric Field $\underline{E}(X)$.

541

calculated set of weights to apportion the charge of a particle to the nearest four grid points. The resultant electric field is then apportioned in an analogous manner. Due to the heavy use of the particle pusher, it is usually advantageous to write it in machine language. Both two-dimensional classical and one-dimensional relativistic particle pushers are available. The relativistic pusher updates momenta rather than velocities. The classical pushers include an electrostatic N.G.P. and D.I.C., and a constant $\underline{B}$ D.I.C. Also a specialized N.G.P. pusher has been developed to approximate the effects of a longitudinal magnetic field by suppressing transverse motions of the particles. This particular particle pusher was used to simulate anomalous resistivity in the stellarator.[17] The one-dimensional relativistic code has been used to simulate relativistic electron-electron and electron-ion two beam instabilities,[24] and Appendix A contains a discussion of these problems.

The charge counter prepares the charge density matrix $\rho(\underline{X})$ for the following step by one of the methods determined by the type of particle pusher used. The charge counter uses the NGP approximation when the accelerating fields are being calculated Nearest Grid Point and uses the DIC apportionment algorithm when the accelerating fields are being interpolated by DIC. In this way the total linear momentum of the system is rigorously conserved. In practice, of course, the charge counting and particle pushing are done simultaneously while the particle positions and velocities are being held in the registers. This saves unnecessary fetch and store times.

III.   <u>CONCLUSIONS</u>

The P POWER electrostatic, plasma-simulation code
has been described in some detail. The methods used are
largely well known but we feel that the juxtaposition of all
these techniques into an extremely efficient, flexible, read-
able code is unique. Since such an important role has been
assigned to optimization it is fitting to close this paper
with a few timing considerations. The program has been written
and optimized for the IBM 360/91, a computer which has roughly
350 K words of 32 bits each in fast core and a transfer rate
of 12 μsec/word to or from disk. These transfers can be over-
lapped with each other and with CPU operations. The 91 has 16
integer-index registers (32 bit) and 4 floating-point registers
(64 bit also used for 32 bit). As a rule of thumb, all register
operations take .1 μsec to complete, including divisions, and
all stores or fetches from core take .7 μsec. Thus most pro-
grams are limited by store-fetch time.

The Poisson solver solves a 128 x 128 system in .51
seconds including application of all the form factors, etc. A
256 x 256 system takes 2.0 seconds to solve. The six-point
electric field formula generates both E_x and E_y matrices for a
128 x 128 system in 0.06 sec and takes about 0.24 seconds for a
256 x 256 system. The two-dimensional N.G.P. pusher requires
5.2 μsec per particle while the D.I.C. interpolating pusher
requires ~15.0 μsec. These two times also include charge
apportionment for the electrostatic case without magnetic field.

A typical 128 x 128 simulation with 64K particles
takes about 1.2 seconds per cycle, about 1.0 second for phy-

sics and 0.2 seconds for overhead and diagnostics. At $\omega_{pe}\delta t = 0.2$, we get 600 ω_{pe}^{-1} per hour of CPU time. The program runs correspondingly faster on one-dimensional problems and the cost of a typical run using external storage for the particle tables is usually less than the corresponding run using core because the I/O transfers can be overlapped with other jobs in the system and because the job charge is reduced for the core released by storing particles on disk.

The largest runs to date were performed on a 256 x 256 system with 200 K particles. With diagnostics and overhead the CPU time charged is slightly under 4 seconds per cycle. Thus 3 ω_{pe}^{-1} per minute or 180 ω_{pe}^{-1} per hour can be integrated.

Appendix A - Simulation of Relativistic Electron-Electron and Electron-Ion Two-Stream Instabilities

Development of a one-dimensional electrostatic relativistic code has enabled us to investigate cold electron-electron and electron-ion two-stream instabilities for beams with drift velocities near the speed of light.[24] In this one-dimensional limit the electric field and particles decouple. The fields are unaffected by retardation while the particle velocities are constrained by c. We have examined growth rates and maximum electric field levels for the range of cases where the drift velocities vary from much smaller than the speed of light to about .95 c. We have also considered the case where both beams have been given an additional equal relativistic velocity in the perpendicular direction. Similar experiments have been conducted by another author[18], and the results, in the limit of no perpendicular velocity which he considers, agree quite closely.

Figure 9 is an analysis of the linear dispersion for both the electron-electron (e-e) and the electron-ion (e-i) cases. It is evident that the dispersion relation is identical to the classical version for cold beams with a redefinition of the plasma frequency. This dispersion relation has the desired property that it is Lorentz invariant along the direction of propagation and therefore the choice of a coordinate

545

DISPERSION   RELATION

$$1 = \sum_i \frac{\Pi_i^2}{(\omega - ku_{n_i})^2}\left(1 - \frac{u_{n_i}^2}{c^2}\right)\left(1 - \frac{u_i^2}{c^2}\right)^{\frac{1}{2}}$$

where $\qquad \Pi_i^2 = \frac{4\pi n_i q_i^2}{m_i}$

defining $\qquad Q_i^2 = \Pi_i^2\left(1 - \frac{u_{n_i}^2}{c^2}\right)\left(1 - \frac{u_i^2}{c^2}\right)^{\frac{1}{2}}$

$$1 = \sum_i \frac{Q_i^2}{(\omega - ku_{n_i})^2}$$

For two beams (e-e) where $\quad Q_1 = Q_2 = Q \quad$ and $\quad u_{n_1} = -u_{n_2} = u_n$

unstoble for	most unstoble mode

$$\frac{k^2 u_n^2}{Q^2} < 2 \qquad\qquad \frac{k^2 u_n^2}{Q^2} = \frac{3}{4} \qquad \gamma_{max} = \frac{Q}{2}$$

For two beams (e-i) where $\quad Q_i^2 \ll Q_e^2, \quad u_{n_i} = u_n \quad$ and $\quad u_{n_e} = 0$

most unstoble mode

$$\frac{k^2 u_n^2}{Q_e^2} \lesssim 1 \qquad\qquad \gamma_{max} \approx \frac{\sqrt{3}}{2}\left(\frac{Q_i^2}{2Q_e^2}\right)^{\frac{1}{3}} Q_e$$

Figure 9.   Analysis of the Linear Dispersion Relations for a Relativistic Electron-Electron (e-e) and a Relativistic Electron-Ion (e-i) Two Beam Instability.

546

system is not critical. Calculation of the band of unstable
modes and the most unstable mode follows analogously to the
classical solutions.

Three electron-electron simulations were considered.
For each case c and $u_\perp$ were changed with the constraint that
Q and $u_{||}$ be the same for all experiments. By keeping Q and
$u_{||}$ constant, the band of unstable modes, the most unstable
mode, and its growth rate should be the same for all three
cases. Figure 10 shows the graphs of energy vs. time for the
most unstable mode in all three simulations. The first plot
is for a classical case, the second is for a relativistic
case with only a parallel velocity, and the third is for a
relalivistic case with both a parallel and perpendicular
velocity. All three simulations have the same most unstable
mode and similar growth rates as expected. The experimental
sults and theoretical predictions agree quite closely. The
maximum electric field for e-e interactions is predicted to
be:

$$E_m \sim \frac{mu_{||}}{e\sqrt{1-u^2/c^2}} \, Q \, .$$

This equation may be viewed physically as a saturation
occurring when a relativistic trapping time for the most
unstable mode is on the order of the growth time for that
mode. This field level can stop the relative motion of
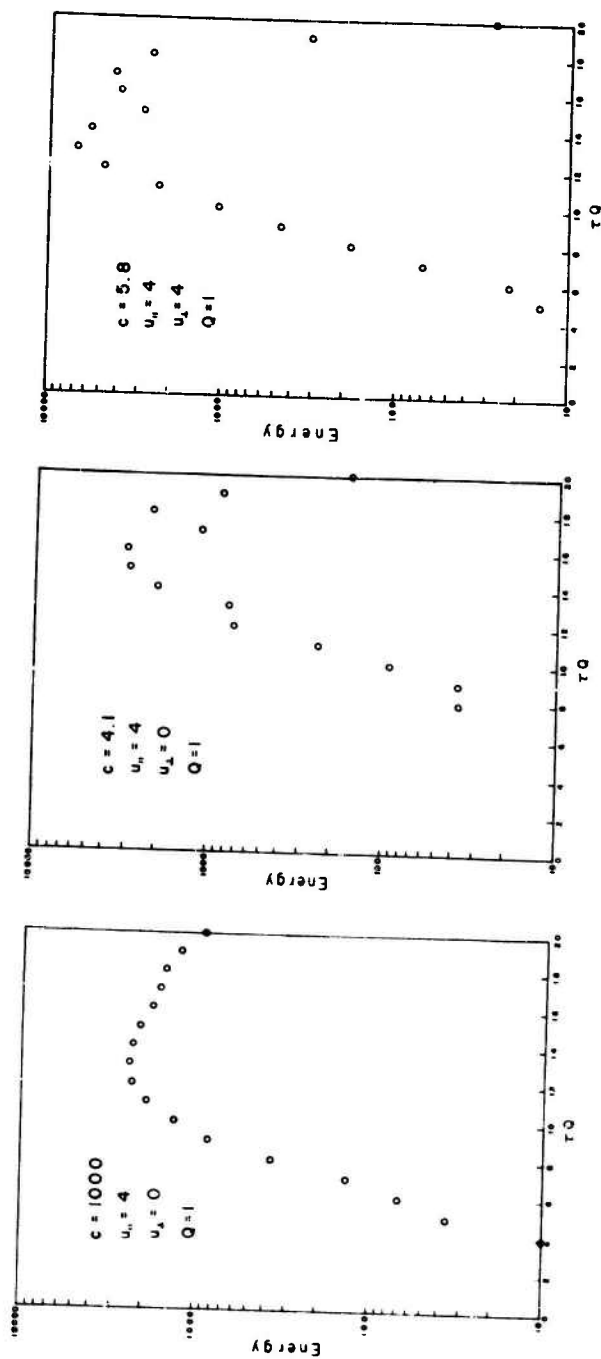the beams in approximately a growth time for the most

547

Figure 10. Plots of Energy vs. Time for the Most Unstable
Mode in Analogous Classical and Relativistic e-e Two
Beam Instabilities.

unstable mode.[18] Our simulations qualitatively follow the prediction of this equation but the quantitative results, as yet, are only approximate.

Electron-ion simulations have been considered but the results are still preliminary. These experiments require more careful analysis than the electron-electron cases since solving the dispersion relation in a particular limit may destroy the Lorentz invariant nature of this equation.

These relativistic two-stream instability simulations were undertaken mainly to test the relativistic particle pusher for the P POWER program and to demonstrate its capabilities. More interesting problems like relativistic weak beam interactions are currently being considered.[25]

Appendix B - Counterstreaming Plasmas with Self Consistent Polarization Fields

In application of the charging-the-boundaries algorithm, we discuss the electrostatic interaction of unequal density counterstreaming plasmas[19]. The problem is treated as spatially homogeneous, but the motivation for the study is a basically inhomogeneous problem, the so-called electro-static shock problem. When a dense plasma collides with a more rarified background plasma, several instabilities can occur—electron-electron, electron-ion, ion-ion, etc. depend-ing on the temperatures and drift velocities of the electrons and ions in the beam and in the background. A condition of prime interest is when the electron bath, which forms very rapidly from the two separate classes of electrons, becomes sufficiently hot for the ion-ion instability between the beam and background ions to occur. In this case the beam and background will interact strongly and an electrostatic shock may form even in the absence of a magnetic field.

In previous calculations[20,21,22] electron heating to permit the ion-ion instability has been of primary interest. The electron-electron and electron-ion instabilities do not provide sufficient heating. The problem of major interest is essentially inhomogeneous; therefore, momentum conservation implies that a net longitudinal current will flow when the electron-ion instability occurs (but not when the electron-electron two-stream occurs). This current in the inhomo-geneous configuration leads to a polarization charge and

hence the development of a laminar longitudinal electric field opposing the current. This situation may be thought of as a constant current situation; the total current, plasma plus displacement, is zero. The laminar electric field which develops induces a net current in the opposite direction and thus an oscillation is set up at the plasma frequency.

This problem, in a homogeneous analog, is exactly the situation that our "charging the boundaries" algorithm was designed to handle. The problem is similar to work performed by Kruer[23] et al in that a high frequency k=0 electric field is present but in the present problem this laminar electric field develops simultaneous with, and is driven by, a strong electron-ion instability in the plasma itself. Figures 11, 12 and 13 show sample results from a two dimensional 128x128 cell run where the relative beam to background density is taken as 10:1. This was accomplished by running twice as many beam particles as in the background, but with each particle having five times the mass and five times the charge of the background particles. The ion to electron mass ratio was taken as 64 for both the beam plasma and the background plasma. The situation shown was run for $700 \ \omega_{pe}^{-1}$ with 32K beam particles and 16K background particles (K=1024).

Compare Figures 11 and 12. Figure 11 shows the development of the laminar electric field and Figure 12 shows the time evolution of the thermal velocities of the four classes of particles present in the simulation. The very rapid rise
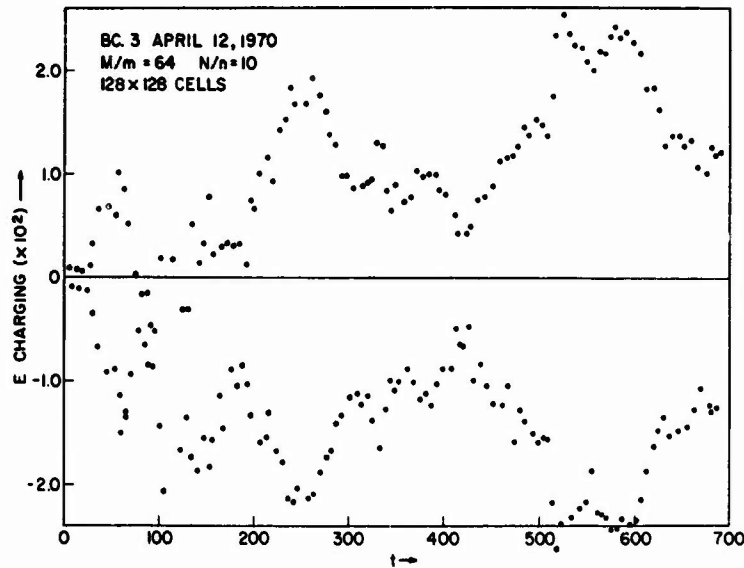
Figure 11. Self-Content k=0 Component of the Electrostatic
Field. The Plasma-Frequency Oscillation at Roughly
the Data Point Separation Gives the Double Envelope
in $E_0(t)$ vs. t. The Charging Field is not Negative
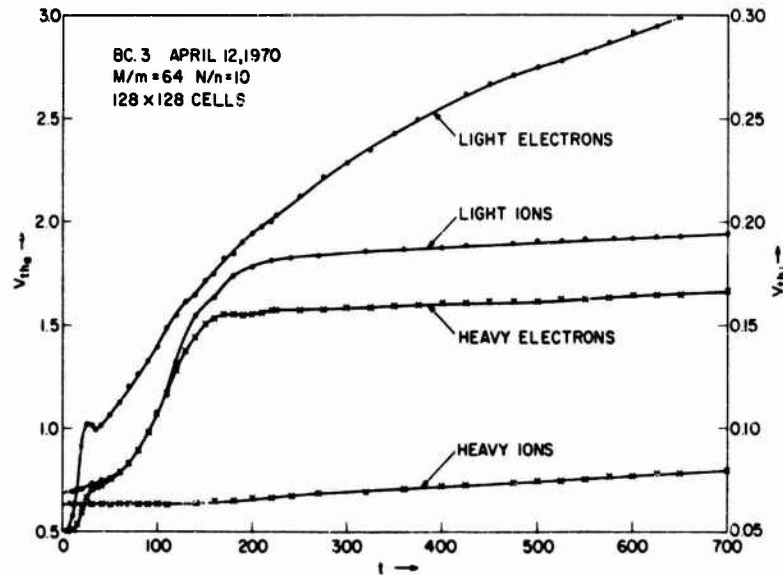while the Electron-Ion Two Stream is Occurring.

Figure 12. Thermal Velocities of the Four Particle Classes
as a Function of Time. With the Electric Field From
the Constant-Total-Current Boundary Condition, Strong
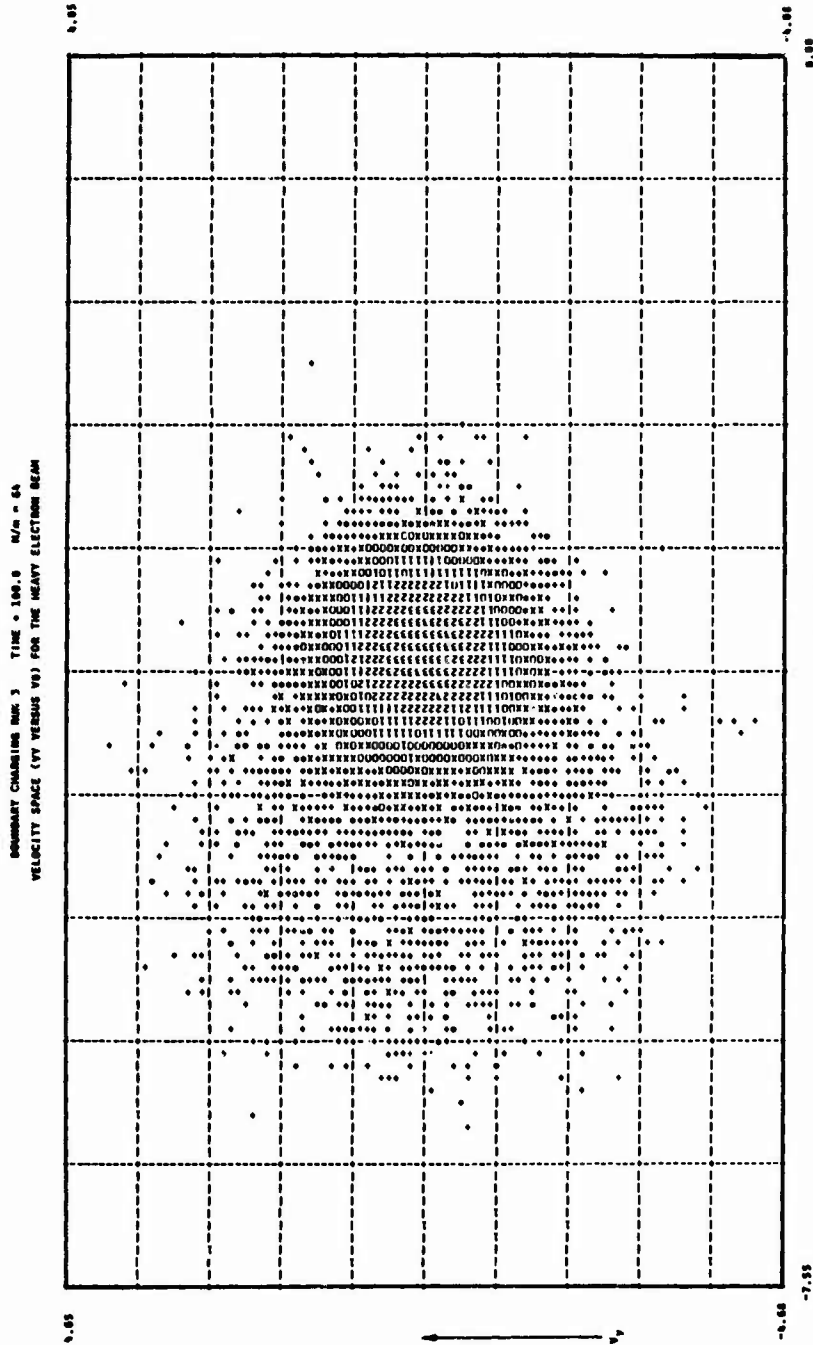Heating of the Heavy Ion Beam is Observed.

552

Figure 13. Space Averaged Velocity Distribution of the Heavy Electron Beam. The Electron-Electron and Ion-Electron Instabilities have Heated the Heavy Beam Appreciably. Increasing Particle Densities are Indicated by Different Characters Plotted. The Ratio is a Factor of in Each Case. Thus + = 1, * = 2, X = 3 or 4, 0 = 5-8, etc.

of the electron thermal velocities prior to t=20 is indicative of the two-stream (electron-electron) instability. The two electron beams merge but the heating stops as shown, when $V_d \tilde{} V_{th_e}$. This temperature is very small compared to the value needed for the ion-ion instability. Since the two classes of electrons conserve momentum and current simultaneously during their interaction the laminar field shown in Figure 11 is nearly zero for t<20.

From t≈20 ω_{pe}^{-1} to t≈150 ω_{pe}^{-1}, the electron-ion instability grows and saturates. Both electron classes now interact with the weaker background ions. The electrons are further heated until the electron-ion instability is stabilized but the heavy ion beam is not affected since the center of velocity of the electron distribution (Figure 13) is not strongly displaced from the high density beam ions. In fact, except in the vicinity of the background ions at V_x=-3,0, the more dense "heavy" electrons of the beam are hardly disturbed in passing through the relatively low density background.

During the electron-ion instability, momentum and current cannot be conserved simultaneously, as true for electrons, because the mass ratio is not unity. Since momentum must be conserved, a net average current is driven in the positive X direction as the lighter electrons move toward the background ion beam with a negative V_x. This effect is shown in Figure 11 between times t~20 and t~200. A positive current leads to a negative electric field because the total current, plasma plus displacement, must remain zero through

the "charging the boundaries" algorithm. In Figure 11 the
apparently wild fluctuations arise because the sampling rate
for plotting the data points was chosen to be roughly π.
A strong plasma frequency oscillation is superimposed on
the systematic laminar fields so only the positive and nega-
tive maxima of the charging fields are plotted in the figure.

The laminar field loses its systematic bias at about
$t=200 \ \omega_{pe}^{-1}$ when the electron-ion instability turns off, as
can be seen by the knee in the thermal velocity curve of
the light (background) ions. The light (background) electrons
continue to heat however and a substantial amount of heating
is observed in the beam ions. This heating occurs because
a substantial number of ions are being accelerated in the
positive X direction.

When the boundary charging is not performed but the
run is otherwise identical, the thermal velocities develop
as in Figure 12 up to $t \sim 200 \ \omega_{pe}^{-1}$ but after this time the
"heavy" beam ions don't heat and the background electrons
heat at a much slower rate. To explain the anomalous
heating when the constant-total-current boundary condition
is applied, one has to invoke a mechanism which depends on
the laminar displacement field either directly or indirectly.
The pulsations of the charging-field envelope with a time-
scale of several ion plasma periods further suggests that
some sort of interaction, perhaps parametric[23], is causing
the strong heating at late times.

This problem was studied in different sized systems,
with different mass ratios, different beam ratios and in

one dimension and the same qualitative behavior was observed.
By looking at phase space plots of the various particle
classes and by correlating the behavior, one sees that the
ions are being drawn off the high density beam in a vortex-
like structure with the same wavelength as the vortex struc-
ture left over from the electron-ion instability. However, the
electron-ion vortices give fluctuating fields at entirely
the wrong frequency to account for the beam ion heating.
In fact, one would expect interaction with the beam ions
on the negative V_x side of the ion beam which is closer
to the background ions. This is not the case—the posi-
tive V_x ions are affected.

We conjecture that the frequency difference between
the electron-ion waves, excited to large amplitude by the
fully saturated instability, and the oscillating laminar
field from the displacement current is small, of order the
ion plasma period as would be required for strong inter-
action with the beam ions. Further, the wavelength of the
mode-mode interaction would be the same as the ion-electron
vortices since the wave number of the laminar electric field
is zero. Thus mode coupling is plausible, but by no means
conclusively proven. A major point to be established is
whether or not the amplitude of the laminar field envelope
continues to grow. If this field becomes larger, by about
another factor of two, the criteria for the high frequency
parametric instabilities will be satisfied.

REFERENCES

1. J.P. Boris and J.H. Orens, "Topics in Optimization for Computational Plasma Physics," to be published.

2. J.P. Boris and K.V. Roberts, "Optimization of Particle Calculations in 2 and 3 Dimensions," Journal of Computational Physics 4(4), Dec. 1969.

3. B. Rice, J.H. Orens, and J.P. Boris, "Fast Fourier Transforms for Symmetric and Anti-Symmetric Systems," to be published in J.A.C.M.

4. J.P. Boris and J.H. Orens, "Solving Poisson's Equation by Fast Fourier Transform Techniques," to be published.

5. J.W. Cooley, P.A.W. Lewis, and P.D. Welsh, "The Fast Fourier Transform Algorithm: Programming Considerations in the Calculation of Sine, Cosine and Laplace Transforms," Journal of Sound and Vibration 12(3), 315-337 (1970).

6. C.K. Birdsall, D. Fuss and A.B. Langdon (private communications, Plasma Simulation Users Conference, Livermore, California (1968).

7. R.W. Hockney, Physics of Fluids 9, 1826 (1966).

8. R.W. Hockney, "Measurements of Collision and Heating Times in a Two-Dimensional Thermal Computer Plasma," IBM Research #RC 2933, Yorktown Heights, New York, June 1970 (to be published).

9. J.M. Dawson; C.K. Birdsall, A.B. Langdon and H. Okuda; R.L. Morse, Chapters in Methods of Computational Physics, Vol. 9, ed B. Alder, S. Fernbach, and Manuel Rotenberg (Academic Press, New York, 1970).

10. J. Byers, also J. Denavit, contributions to Fourth Conference on the Numerical Simulation of Plasmas, proceedings, Naval Research Laboratory, Washington, D.C., 2-3 November 1970.

11. J.P. Boris and A.B. Langdon, "The Acceleration Calculation in Numerical Simulation," to be published.

12. J.P. Boris, "The Acceleration Calculation from a Scalar Potential," Princeton Plasma Physics Laboratory Report MATT-769, (March 1970).

13. A.B. Langdon and C.K. Birdsall, "Theory of Plasma Simulation Using Finite-Size Particles," Physics of Fluids 13 (8), p.2115-2123, August 1970.

14. B. Rosen and W. Kruer, "Suds - A Faster Version of the Dipole Expansion," Fourth Conference on the Numerical Simulation of Plasmas, proceedings, Naval Research Laboratory, Washington, D.C., 2-3 November 1970. See also references to the original dipole method (finite-sized particles), G. Hsi, J.M. Dawson, J.P. Boris and W.L. Kruer, Bulletin of the American Physical Society, 13, 1555 (1968).

15. O. Buneman, "Fast Numerical Procedures for Computer Experiments on Relativistic Plasmas," in Relativistic Plasmas - The Coral Gables Conference, University of Miami, 1968, eds. O. Buneman and W. Pardo, (W.A. Benjamin, N.Y., 1968).

16. J.P. Boris, "Relativistic Plasma Simulation - Optimization of a Hybrid Code," Fourth Conference on the Numerical Simulation of Plasmas, proceedings, Naval Research Laboratory, Washington, D.C., 2-3 November 1970.

17. J.H. Orens, J.P. Boris, J.M. Dawson, "Turbulent Resistance in the Stellarator," Annual Sherwood Theory Meeting, Princeton University, 23-24 April 1970.

18. C.F. McKee, "Simulation of Relativistic Streaming Instabilities," to be published.

19. J. Boris, J. Orens, K. Papadopoulos and R. Shanny, "The Electrostatic Interaction and Heating of Counter-streaming Two-Dimensional Plasmas," Bulletin of the American Physical Society, paper BJ15, April 1970.

20. R. Shanny, R.C. Davidson, N.A. Krall and K. Papadopoulos, "Behavior of Counterstreaming Ion Beams I, II," Bulletin of the American Physical Society, papers 7E9, 7E10, November 1969.

21. D.W. Forslund and C.R. Shonk, Phys. Rev. Letters 25(5), p. 281 (1970).

22. R.C. Davidson, N.A. Krall, K. Papadopoulos and R. Shanny, Phys. Rev. Letters 24, 579 (1970).

23. W.L. Kruer, P.K. Kaw, J.M. Dawson and C. Oberman, "Anomalous High Frequency Resistivity and Heating of a Plasma," Phys. Rev. Letters 24(18), 987 (1970).

24. J.H. Orens and J.P. Boris, "Computer Simulation of Relativistic Two Stream Instabilities," Bulletin of the American Physical Society, paper 6B1, 15(11), 1455 (1970).

25. S. Kainer, J. Dawson, R. Shanny, and T. Coffey, "Interaction of a Highly Energetic Electron Beam with a Plasma," to be published.

Alternate Papers for
Oral Presentation

A New Version of the Dipole Expansion Scheme

B. Rosen
Stevens Institute of Technology
Hoboken, New Jersey

and

W. L. Kruer and J. W. Dawson
Plasma Physics Laboratory
Princeton University
Princeton, New Jersey

ABSTRACT

Here we present a modified version of the dipole expansion technique for particle simulation of plasmas. In this version the field calculations do not take significantly longer than in nearest-grid-point calculations. This is particularly important in two- and three-dimensional simulations. We also discuss an optimization of the coding, particularly for the operations that must be done for each particle (computing its contribution to the charge density and updating its position and velocity). For example, this optimization has given a one-dimensional, nearest-grid-point code (lowest order in the multipole expansion scheme) that takes ~ 1.8 μsec/particle on the IBM 360/91. Finally, we assess the value of the dipole correction by comparing dipole and nearest-grid-point simulations.

561

INTRODUCTION

Recently a dipole expansion technique has been developed and used for particle simulation of plasmas.[1,2] This scheme employs a multipole expansion of finite-size particles about their nearest-grid-point (NGP) locations. This approach is quite physical and indeed helps one to relate numerical approximations to the physics. In addition, the scheme represents a systematic expansion and may be carried to higher order. In practice, the technique has proven very satisfactory and has given detailed agreement with a Vlasov code.[3] Computationally, the scheme favors more operations on each grid point over fewer operations on each particle. Since there are many more particles than grid points, this can be a useful trade-off.

Here we describe a modified version of the dipole expansion scheme in which the field calculations do not take significantly longer than in nearest-grid-point calculations. We further discuss an optimization of the coding — in particular, the coding for those operations that must be done for each particle (computing its contribution to the charge density and updating its position and velocity). Finally, we assess the value of the dipole correction by comparing dipole and nearest-grid-point simulations.

DIFFERENCED-DIPOLE TECHNIQUE

The modification we present relates to the grid calculation and reduces the number of Fourier transforms to a minimum. The basic new feature is that we approximate derivatives appearing in higher-order

562

expansion terms by differences over the cells. The error incurred represents a correction to a correction, and hence is higher order in the expansion parameter. Let us illustrate the procedure in one dimension, since its extension to more dimensions is obvious. Consider a collection of finite-size particles. The charge density is

$$\rho(x) = \sum_i F(x - x_i) \ ,$$

where F is the form factor giving the shape of the particle, and x_i is the location of the ith particle. We now perform a multipole expansion of the particles' charge density about their NGP locations:

$$\rho(x) = \sum_g \sum_{i \in g} \left\{ F(x - x_g) + \Delta x_i F'(x - x_g) + O\left[\frac{1}{10}\left(\frac{\delta}{a}\right)^2 \right] \right\}.$$

Here, x_g is the nearest grid point location and Δx_i is the displacement of the ith particle from that location. Truncating the expansion at the dipole term incurs an error of order $\frac{1}{10}\delta^2/a^2$, where δ is the cell size and a the effective size of the particle. Performing the second summation yields

$$\rho(x) = \sum_g \rho_{NGP}(g) F(x - x_g) + d(g) F'(x - x_g) + \dots \ ,$$

where

$$\rho_{NGP}(g) = \sum_{i \in g} 1$$

$$d(g) = \sum_{i \in g} \Delta x_i \ .$$

563

ρ_{NGP} and d are, respectively, the monopole and dipole charges associated with the grid location g.

The charge density can now be Fourier-transformed, but this means that the correction term involves computation of additional transforms (one in one-dimensional and two in two-dimensional simulations). Let us then approximate the derivative of the form factor by using a centered difference over the adjacent cells:

$$F'(x-x_g) = \frac{F(x-x_{g+1}) - F(x-x_{g-1})}{2\delta} + O\left(\frac{\delta^2}{a^2}\right)$$

Then,

$$\rho(x) = \sum_g F(x-x_g)\left[\rho(g) - \left(\frac{d(g+1)-d(g-1)}{2\delta}\right)\right].$$

Now the charge density can be Fourier-transformed simply by making one transform of the modified array shown in brackets. In this way we save one, two, or three transforms, depending on the dimensionality of the problem.

Figure 1 shows the two functions

$$f'(x) \quad \text{and} \quad \frac{[f(x+1)-f(x-1)]}{2}$$

where $f(x) = \exp-(x^2/2)$ and indicates the nature of the approximation for what would be the worst case in practice; namely, the particle width equal to a cell size. In physical terms we are replacing the dipole $d \cdot f'(x)$ by a dipole which consists of two extended charges $f(x)$, of equal but opposite charge $(d/2\delta)$, a distance of 2δ apart. The dipole moments of these two charge distributions agree, but the higher moments differ.
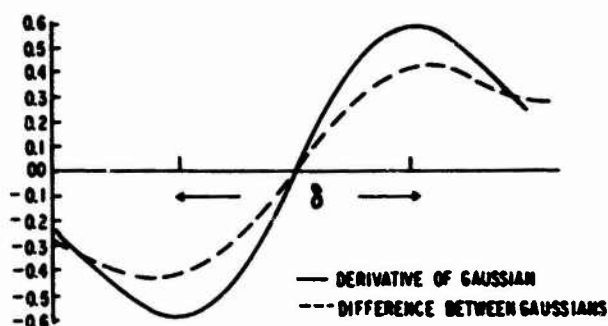
564

New Dipole Expansion Scheme

Fig.1. A comparison of the derivative of a Gaussian with the difference of two Gaussians. The Gaussian half-width is equal to a cell size.

The same technique is used when we expand the electric field to determine the force on the particle. The net force on the particle is given by the monopole moment times the electric field plus the dot product of the dipole moment and the gradient of the electric field. By approximating the derivatives of the field using central differences, we again avoid performing Fourier transforms to compute those derivatives. This saves two additional transforms in two-dimensional, and five in three-dimensional simulations. Of course, we must perform some additional operations to difference the various quantities, but the number of Fourier transforms now required is the same as in nearest-grid-point calculations.

The multipole expansion scheme, when truncated at the dipole order, is similar to the usual charge-sharing schemes.[5,6] Indeed, these latter schemes in effect apportion the charge on the grid in such a way as to conserve both the monopole and dipole moments of the original charge. The way to do this is not uniquely defined, and corresponds to our freedom to difference the derivative terms in various ways. For

565

example, in one-dimensional simulations charge sharing apportions the
charge over the two nearest grid points, while the differenced dipole
scheme presented here apportions the charge over the three nearest
grid points (a centered difference about the nearest grid point location).
The particle force calculation in the dipole scheme also differs from that
in a charge-sharing scheme. For example, in the dipole scheme the force
on each particle is simply the electric field at its NGP location plus the
dot product of its dipole moment and the derivative of the electric field
there. By comparison, charge-sharing schemes obtain the force by
using weighted averages for each particle of the electric fields at the
neighboring grid points. Lastly, finite-size particles are introduced in
a very natural and systematic way via the dipole scheme.

IMPLEMENTATION AND OPTIMIZATION

The modified version of the dipole scheme has been implemented
and has given close agreement with the usual dipole technique. As a simple
example, we consider a two-dimensional simulation of a thermal equilibrium
plasma. The system consists of 5000 particles in a doubly periodic system
($8\lambda_D$ by $8\lambda_D$). Figure 2 shows a comparison of energy conservation for
all three techniques – NGP, dipole, and modified dipole. Energy
conservation is quite good for both dipole techniques, and is an order of
magnitude better than that for NGP.

The grid calculation is observed to be nearly twice as fast in the
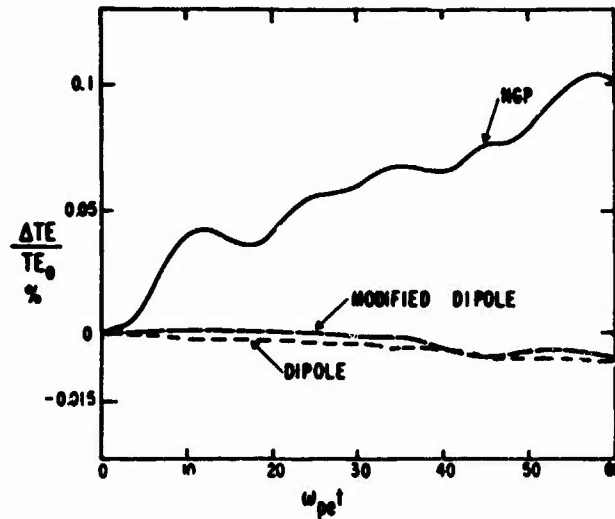modified dipole version for this two-dimensional simulation. Furthermore,

Fig. 2. A comparison of energy conservation in NGP, dipole, and modified dipole solutions (thermal equilibrium plasma).

the grid calculation has been speeded up by an addional factor of ~ 4 through the use of an optimized Fourier transform package. For example, in ~ 0.15 sec on the IBM 360/91 we can now Fourier-transform the charge density on a 64 by 64 grid, convert to the Fourier components of E_x and E_y, and invert the transform to find the fields. The basic transform package is a general-purpose one, and may be of value to other people in computational physics.

We have concentrated on discussing the field calculations, since the technique for doing these has been modified. For completeness, let us now briefly discuss the time required for the operations that must be performed for each particle (computing its contribution to the charge density and updating its position and velocity). At Princeton a two-dimensional NGP code (lowest order in the multipole expansion) has been de-

567

veloped which requires ~4 μsec/particle on the IBM 360/91.[7] In this code the two particle coordinates are packed into one double word, and similarly for the two components of the velocity.[8] In a similar code, one of the authors (B. R.) has developed a one-dimensional NGP code that takes ~1.8 μsec/particle. In this latter code each particle's velocity and position are packed into one double word. Both of these codes take advantage of the architecture of the IBM 360/91. In particular, such features as the double-word fetch and the parallel execution of fixed and floating point instructions are exploited. A dipole version of this opti- mized one-dimensional code requires ~4 μsec/particle, and we estimate that an optimized dipole version of the two-dimensional code will take ~8 μsec/particle.

COMPARISON OF DIPOLE AND NGP SIMULATIONS

Finally, let us indicate the value of the dipole correction (or any charge-sharing type of correction) by comparison with simulations using the nearest-grid-point approximation. It is particularly convenient to do this in the dipole expansion scheme, since NGP is simply zero order in this expansion. In the following examples we use the modified dipole technique.

First we consider a strong two-beam instability – two Maxwellian beams separated by $4\sqrt{2}$ thermal velocities.[6] We use 5000 particles in a doubly periodic system ($32\lambda_D$ by $32\lambda_D$). This is a convenient problem for numerical tests, but of course we would use both a larger grid and

more particles to investigate the physics with confidence. Figure 3 shows
the total electrostatic wave energy for both the dipole and NGP simulations.
This energy exponentiates to ~ 2.6% of the total energy. The NGP results
agree reasonably well with the dipole results. In the course of the simu-
lation, the energy for the NGP solution varies from the initial total
energy of the system by ~ 0.2%, but this is adequate to quantitatively
follow the gross behavior of this rapidly growing instability.

However, let us now investigate a weaker instability. We consider
a small beam moving at 6.4 thermal velocities in a Maxwellian plasma.
The ratio of the beam density to the background plasma density is ~ 0.25%.
The main plasma contains 19,000 simulation particles and the beam con-
tains 1000 particles, each with 0.05 of the charge and mass of a plasma
particle. The system is one-dimensional with a periodicity length of
256 λ_D.

Figure 4 shows both the electrostatic wave energy and the change
in the total energy versus time for both of the techniques. The wave energy
at $\omega_{pe} t = 120$ has grown to ~ 1.2% of the initial total energy of the
system. The NGP result agrees qualitatively with the dipole result, but
it does not agree quantitatively. Indeed, by $\omega_{pe} t \sim 100$ the total wave
energies in the two solutions differ by ~ 25%. This quantitative disagree-
ment is not surprising when we note that the energy conservation for NGP
is rather poor in this case. The total energy varies by ~ 0.8% of the
initial total energy, while the wave energy becomes ~ 1.2%.

Figure 5 shows a comparison of phase space at $\omega_{pe} t = 118$ for
both of the techniques. We see quite noticeable differences, showing that
significant errors have accumulated in the particle orbits in the NGP
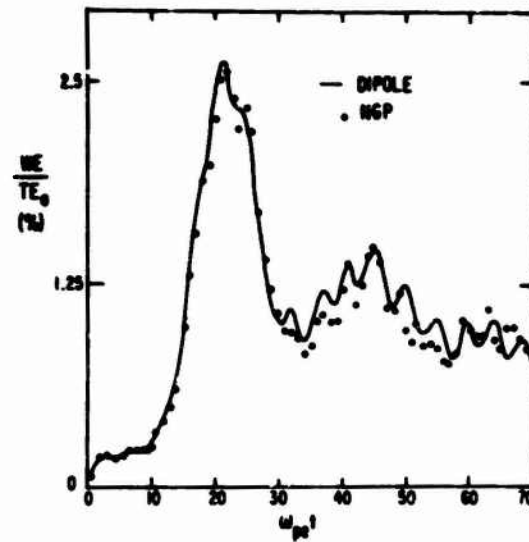
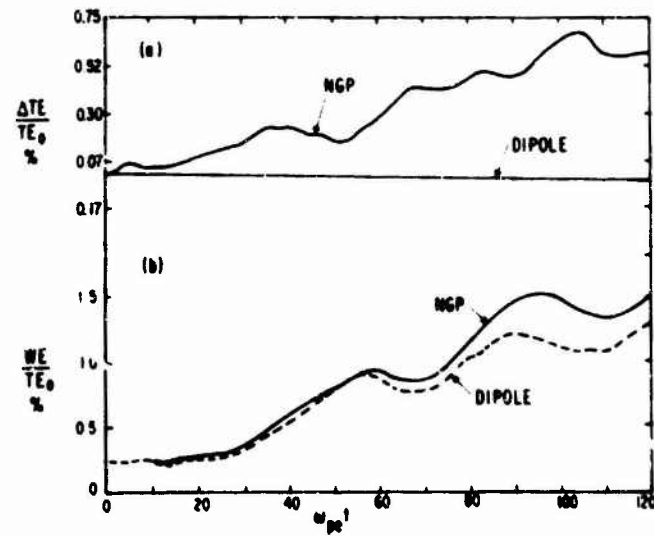Fig. 3. Dipole and NGP solutions for the electrostatic wave energy vs time for a strong two-beam instability.

Fig. 4. Dipole and NGP solutions for (a)the total energy vs time and (b) the electrostatic wave energy vs time for a weak two beam instability.
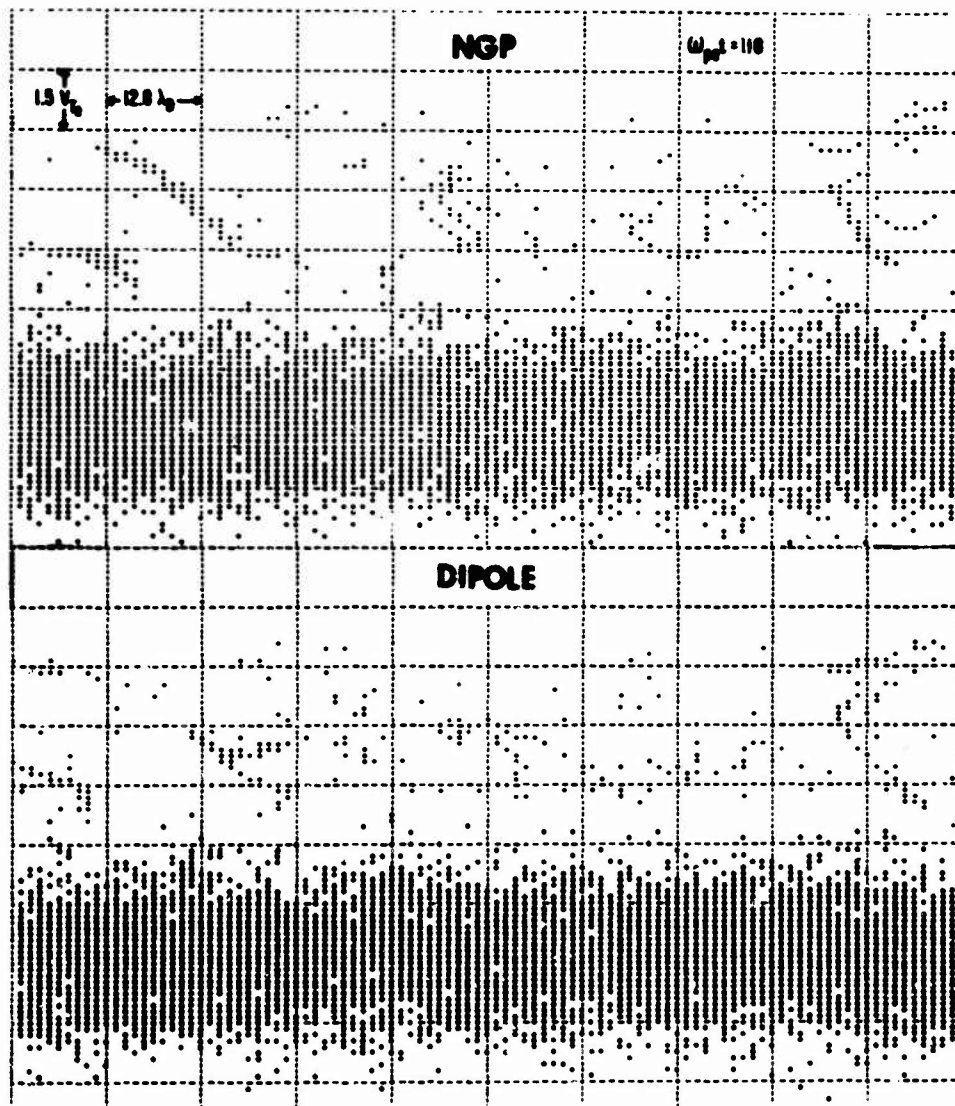
570

Fig. 5. A comparison of phase space at $\omega_{pe} t = 118$ for NGP and dipole solutions (weak two-beam instability).

solution. (The phase space plots in the dipole and the modified dipole solutions agree closely.)

In conclusion, we have presented a modified version of the dipole expansion technique in which the field calculations do not take significantly longer than in NGP calculations. In addition, we have discussed an optimization of the coding – particularly for the operations that must be performed for each particle. Lastly, we have compared the dipole and NGP techniques for several simple problems. The results show that NGP does reasonably well in describing gross behavior – for example, in determining growth rates of strong instabilities. However, features which are more sensitive to higher moments of the distribution function can be poorly given, since significant errors can accumulate in the particle orbits. As in all simulations, the choice of technique is connected with the subtlety of the phenomena under investigation.

ACKNOWLEDGMENTS

New Dipole Expansion Scheme

REFERENCES

[1] J. M. Dawson, C. Hsi, and R. Shanny, Princeton University Plasma Physics Laboratory MATT-719 (1969).

[2] W. L. Kruer and J. M. Dawson, Bull. Am. Phys. Soc. 14, 1025 (1969); also paper No. A 1 presented at the Third Conference on Numerical Simulation of Plasmas, Stanford, California (1969).

[3] J. Denavit and W. L. Kruer, "Comparison of Numerical Solutions of the Vlasov Equations with Particle Simulations of Collisionless Plasmas," submitted to Phys. Fluids (1970).

[4] R. W. Hockney, Phys. Fluids 9, 1826 (1966).

[5] C. K. Birdsall and Dieter Fuss, J. Comp. Phys. 3, 494 (1969).

[6] R. L. Morse and C. W. Nielson, Phys. Rev. Letters 23, 1087 (1969).

[7] H. Fallon, N. Winsor, and W. L. Kruer, Bull. Am. Phys. Soc. 14, 1025 (1969).

[8] J. P. Boris and K. V. Roberts, J. Comp. Phys. 4, 4 (1969).

Numerical Simulation of Relativistic Electrons Confined in an Axisymmetric Mirror Field

M. Brettschneider, John Killeen, and A. A. Mirin
Lawrence Radiation Laboratory
University of California
Livermore, California

I. INTRODUCTION

In the controlled-fusion experiment Astron a beam of relativistic electrons is injected into an evacuated cylindrical region in which an externally applied magnetic field has been established. The cylindrical region is bounded by two concentric aluminum shells. The outer shell is 12 cm thick and its inner radius is 74 cm. The thin inner shell has a radius of 20 cm. The velocity of the injected electrons makes an angle of 85 deg with the axis of the region. In order to facilitate trapping, a cylinder of resistor wires, azimuthally oriented, has been installed at a radius of 52 cm. The electrons that are trapped form a cylindrical layer (shell) known as the E-layer. The mean radius of the E-layer is 40 cm; its length varies from 1 to 4 meters, depending on the initial conditions. The aim is to confine a sufficient number of electrons in the E-layer so that the self field of the E-layer exceeds the applied field. The resulting field configuration contains a region that is minimum $|B|$ and has no loss cones.

The E-layer consists of about 10^{15} electrons. It is, of course impractical to follow each electron individually. Furthermore, we are not interested in the position and velocity of each electron; we are only interested in the electron density. Since the electron density in the E-layer is about 10^{8}/cc it is logical to treat the E-layer as

574

an electron fluid. The electron density can then be obtained from the solution of the Vlasov equation. The approach was successfully used by Killeen[1] in the LAYER CODE. An alternate approach, the one we use here, is to approximate the E-layer by a large number of particles and follow each particle individually. The electron density is, then, obtained from the particle density. The force on a particle is obtained from the full electromagnetic field and its trajectory is determined from the solution of the relativistic equations of motion. The number of particles used must be sufficiently large to give an accurate statistical representation of the E-layer and yet small enough to be practical. In practice we use between 10^4 and 3×10^4 particles. The principal advantage of this method over the fluid method is that it requires considerably less computation time to solve a given problem, and is more accurate for injection problems.

The computation proceeds as follows: First the charge and current densities are determined from the known positions and velocities of the particles. These charge and current densities are then used to determine the vector and scalar potentials by solving the respective wave equations. The new values of the vector and scalar potentials are used to calculate the force on each particle. These forces are used to move each particle in accordance with the relativistic equations of motion. The above process is then repeated.

The Astron geometry is axisymmetric. Furthermore, it is experimentally observed that the E-layer, during most of its life is essentially axially symmetric. We therefore feel that the assumption of axial symmetry, dictated by economic factors, is a reasonable one to make.

575

This paper is divided into three chapters. In Chapter II we discuss the mathematical model. Additions to the model, relating to the Astron experiment, are introduced in Chapter III. In Chapter IV the difference approximations that we use and the energy checks are described.

II. MATHEMATICAL MODEL

A. Basic Equations

If we employ the relations

$$\underline{B} = \nabla \times \underline{A}, \qquad \underline{E} = -\nabla\phi - \frac{1}{c}\frac{\partial \underline{A}}{\partial t}, \qquad \nabla \cdot \underline{A} + \frac{1}{c}\frac{\partial \phi}{\partial t} = 0 \qquad (1)$$

with Maxwell's equations, we obtain the following wave equations

$$\nabla^2 \underline{A} - \frac{1}{c^2}\frac{\partial^2 \underline{A}}{\partial t^2} = -\frac{4\pi}{c}\left(\underline{j} + \underline{j}_{res}\right) \qquad (2)$$

$$\nabla^2 \phi - \frac{1}{c^2}\frac{\partial^2 \phi}{\partial t^2} = -4\pi\rho \qquad (3)$$

where $\underline{A}$ and ϕ are the vector and scalar potentials respectively, $\underline{j}$, $\underline{j}_{res}$, and ρ are the E-layer current density, resistor current density, and the charge density, respectively.

Assuming axial symmetry, Eqs. (2) and (3) become, in cylindrical coordinates

$$\frac{\partial}{\partial r}\left[\frac{1}{r}\frac{\partial}{\partial r}(rA_r)\right] + \frac{\partial^2 A_r}{\partial z^2} - \frac{1}{c^2}\frac{\partial^2 A_r}{\partial t^2} = -\frac{4\pi j_r}{c} \qquad (4)$$

$$\frac{\partial}{\partial r}\left[\frac{1}{r}\frac{\partial}{\partial r}(rA_\theta)\right] + \frac{\partial^2 A_\theta}{\partial z^2} - \frac{1}{c^2}\frac{\partial^2 A_\theta}{\partial t^2} = -\frac{4\pi}{c}(J_\theta + J_{\theta\ res}) \tag{5}$$

$$\frac{1}{r}\frac{\partial}{\partial r}\left(r\frac{\partial A_z}{\partial r}\right) + \frac{\partial^2 A_z}{\partial z^2} - \frac{1}{c^2}\frac{\partial^2 A_z}{\partial t^2} = -\frac{4\pi}{c}(J_z + J_{z\ res}) \tag{6}$$

$$\frac{1}{r}\frac{\partial}{\partial r}\left(r\frac{\partial\phi}{\partial r}\right) + \frac{\partial^2\phi}{\partial z^2} - \frac{1}{c^2}\frac{\partial^2\phi}{\partial t^2} = -4\pi\rho \tag{7}$$

The equations of motion for a relativistic electron can be derived from Lagrange's equations

$$\frac{d}{dt}\left(\frac{\partial L}{\partial \dot{q}_j}\right) - \frac{\partial L}{\partial q_j} = 0 \tag{8}$$

where $q_j = (r,\theta,z)$ and L is the Lagrangian given by

$$L = -m_0 c^2\sqrt{1 - \beta^2} - e\phi + \frac{e}{c}\underline{A}\cdot\underline{v}$$

where m_0 and e are respectively the rest mass and charge of the electron and $\beta = v/c$.

Assuming axial symmetry, we get the following equations of motion

$$m_0(\gamma\ddot{r} + \dot{\gamma}\dot{r} - \gamma r\dot{\theta}^2) = -e\frac{\partial\phi}{\partial r} - \frac{e}{c}\frac{\partial A_r}{\partial t}$$

$$+ \frac{e}{c}\left[r\dot{\theta}\frac{1}{r}\frac{\partial}{\partial r}(rA_\theta) - \dot{z}\left(\frac{\partial A_r}{\partial z} - \frac{\partial A_z}{\partial r}\right)\right] \tag{10}$$

$$m_0\gamma r^2\dot{\theta} + \frac{e}{c}rA_\theta = \text{const.} = P_\theta \tag{11}$$

$$m_0(\gamma \ddot{z} + \dot{\gamma} \dot{z}) = -e \frac{\partial \phi}{\partial z} - \frac{e}{c} \frac{\partial A_z}{\partial t} + \frac{e}{c} \left[\dot{r} \left(\frac{\partial A_r}{\partial z} - \frac{\partial A_z}{\partial r} \right) + r\dot{\theta} \frac{\partial A_\theta}{\partial z} \right] \quad (12)$$

where P_θ is the canonical angular momentum and $\gamma = 1/\sqrt{1 - \beta^2}$.

B. Boundary Conditions

The domain of the model consists of two concentric grounded cylinders as shown in Fig. 1. The walls of the cylinders are assumed to be perfect conductors. This assumption is legitimate because of the short time scales. The boundary conditions at a perfect conductor are

$$B_\perp = 0, \qquad E_\parallel = 0. \quad (13)$$

These conditions require that

$$A_{\theta \text{ int}}(r,z) = 0 \qquad \text{at all boundaries} \quad (14)$$

$$\phi(r,z) \qquad = 0 \qquad \text{at all boundaries} \quad (15)$$

$$A_z(r,z) \qquad = 0 \qquad \text{at } r = r_1, r_2 \text{ for all } z \quad (16)$$

$$A_r(r,z) \qquad = 0 \qquad \text{at } z = z_1, z_2 \text{ for all } r, \quad (17)$$

where $A_{\theta \text{ int}}$ is that part of A_θ which is generated by internal sources, i.e. currents in the E-layer and in the resistors. The rest of A_θ, henceforth designated $A_{\theta \text{ coil}}$, is generated by current in the external coils. These currents are dc. Hence, the $A_{\theta \text{coil}}$ has ample time to soak through the walls. The remaining boundary conditions are obtained from the gauge condition

$$\nabla \cdot \underline{A} + \frac{1}{c} \frac{\partial \phi}{\partial t} = 0 \quad (18)$$

They are

$$\frac{\partial}{\partial r}\left[rA_r(r,z)\right]\Big|_{r=r_1,r_2} = 0 \qquad \text{for all } z \qquad (19)$$

and

$$\frac{\partial}{\partial z}\left[A_z(r,z)\right]\Big|_{z=z_1,z_2} = 0 \qquad \text{for all } r. \qquad (20)$$

C. Superparticle Model

The superparticles in this model are composed of a large number of electrons uniformly distributed throughout their volume. The shape of each superparticle is that of a ring of rectangular cross section.

The velocity of a superparticle has three components v_r, v_θ and v_z. Since the superparticle is ring shaped, v_r refers to the speed with which it is expanding (contracting) and v_θ to the speed with which it rotates about the axis. v_z is the usual axial component of velocity.

The charge density ρ of a superparticle is given by

$$\rho = n_e \frac{e}{2\pi r \, \Delta r \, \Delta z} \qquad (21)$$

where n_e is the number of electrons per superparticle, e the electronic charge, r the radius of the superparticle, Δr its radial thickness, and Δz its axial thickness.

The three components of the current density of a superparticle are given by

$$J_r = n_e \frac{ev_r}{2\pi r \, \Delta r \, \Delta z} \qquad (22)$$

$$J_\theta = n_e \frac{ev_\rho}{2\pi r \, \Delta r \, \Delta z} \qquad (23)$$
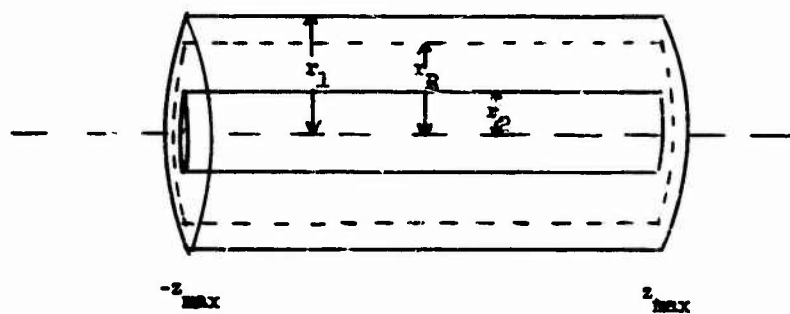
Fig. 1. Domain of the model r_1 is the radius of the cantilever, r_R is the radius of the resistors, and r_2 is the inner radius of the outer wall.
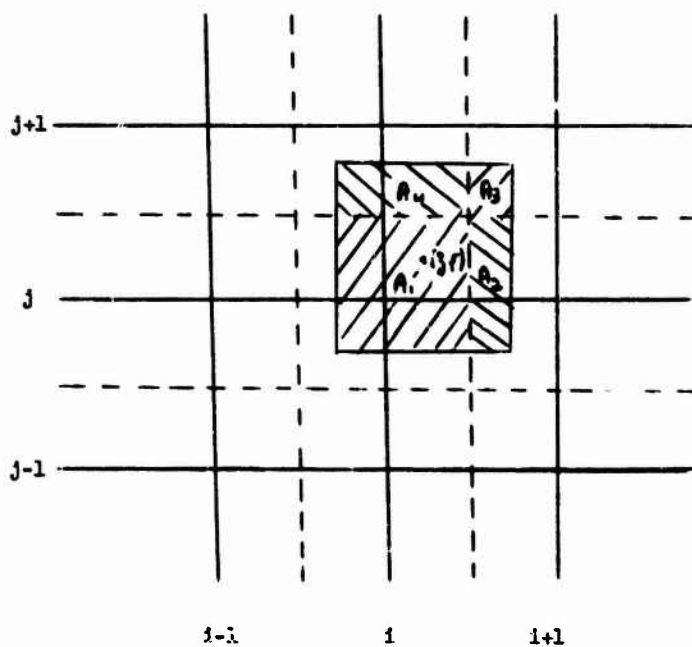

Fig. 2. Area weighting scheme for a superparticle.

$$J_z = n_e \frac{ev_z}{2\pi r \, \Delta r \, \Delta z} . \tag{24}$$

The field equations are solved in a domain that is subdivided by a finite difference mesh. The extent of this domain is given by

$$0 \leq r_j \leq r_{max}, \quad -z_{max} \leq z_i \leq z_{max}, \quad j = 1 \cdots J, \quad -I_2 \leq i \leq I_1,$$

where $r_j = j\Delta r$, $z_i = i\Delta t$, $r_{max} = J\Delta r$, $z_{max} = I_1\Delta z$, and $-z_{max} = -I_2\Delta z$.

The charge and current densities must be known on the mesh points. The equations of motion yield the positions of the centers of the superparticles. These positions, usually, do not coincide with any mesh point. Therefore some method must be devised whereby we can obtain the charge and current densities at the mesh points from the known positions and velocities of the superparticles. In the method that we use the charge and current of a superparticle is shared among each of the four neighboring grid points in accordance with the standard area weighting procedure. A simple way of visualizing this procedure is shown in Fig. 2 (we assume the charge to be uniformly distributed over the shaded region). Let the center of the particle be located in the zone (i,j) and let its coordinates be (z,r). The regions of the particle that are assigned to the neighboring grid points are denoted by A_1, A_2. A_3, and A_4. A_1 is allocated to (i,j), A_2 to $(i + 1,j)$, A_3 to $(i,j + 1)$ and A_4 to $(i + 1,j + 1)$. The values of the A's are given by

$$A_1 = \left[(i + 1)\Delta z - z \right]\left[(j + 1)\Delta r - r \right]$$
$$A_2 = \left[(i + 1)\Delta z - z \right](r - j\Delta r)$$

581

$$A_3 = (z - i\Delta z)\left[(j + 1)\Delta r - r\right]$$

$$A_4 = (z - i\Delta z)(r - j\Delta r).$$

To obtain the current and charge densities at a mesh point, the contributions from all the superparticles to that mesh point are summed.

D. Dimensionless Formulation

We assume that the canonical angular momentum is a constant of the motion

$$m_0\gamma r^2\dot\theta + \frac{e}{c} rA_\theta = P_\theta = \text{const.} \tag{11}$$

It is convenient to introduce the function

$$\psi = \frac{\gamma}{c} r^2\dot\theta \tag{25}$$

so that

$$\psi = \frac{P_\theta}{m_0 c} - \frac{e}{m_0 c^2} rA_\theta \tag{26}$$

and since we are assuming that all the particles have the same P_θ we can use ψ in place of A_θ. The rationale for introducing ψ is that it obviates the necessity of calculating v_θ, as will be apparent shortly.

We now introduce the dimensionless velocity $\underline{u}$ defined by

$$\underline{u} = \frac{\gamma}{c}\underline{v} \tag{27}$$

where

$$\gamma = \frac{1}{\sqrt{1 - \underline{v}^2/c^2}}$$

Substituting Eq. (27) into the expression for γ we get

$$\gamma = (1 + u_r^2 + u_\theta^2 + u_z^2)^{1/2}. \tag{28}$$

From Eq. (26) we have $\psi = ru_\theta$, hence

582

$$\gamma = \left(1 + u_r^2 + u_z^2 + \frac{\psi^2}{r^2}\right)^{1/2} \tag{29}$$

If we differentiate Eq. (27) with respect to time and rearrange the terms, we get

$$\ddot{r} = \frac{c}{\gamma} \dot{u}_r - \frac{c}{\gamma^2} \dot{\gamma} u_r$$

$$\ddot{z} = \frac{c}{\gamma} \dot{u}_z - \frac{c}{\gamma^2} \dot{\gamma} u_z . \tag{30}$$

Substitution of Eqs. (27) and (30) into Eqs. (10) and (12) yields for the radial equation of motion

$$\frac{du_r}{dt} = -\frac{c}{\gamma} \frac{\partial}{\partial r}\left(\frac{\psi^2}{2r^2}\right) - \frac{e}{m_0 c} \frac{\partial \phi}{\partial r} - \frac{e}{m_0 c^2}\left[\frac{\partial A_r}{\partial t} - \frac{c}{\gamma} u_z\left(\frac{\partial A_r}{\partial z} - \frac{\partial A_z}{\partial r}\right)\right]. \tag{31}$$

Similarly the axial equation of motion becomes

$$\frac{du_z}{dt} = -\frac{c}{\gamma} \frac{\partial}{\partial z}\left(\frac{\psi^2}{2r^2}\right) - \frac{e}{m_0 c} \frac{\partial \phi}{\partial z} - \frac{e}{m_0 c^2}\left[\frac{\partial A_z}{\partial t} + \frac{c}{\gamma} u_r\left(\frac{\partial A_r}{\partial z} - \frac{\partial A_z}{\partial r}\right)\right]. \tag{32}$$

We now introduce the dimensionless function $\bar{\mu}$ defined by

$$\bar{\mu} = \frac{\psi}{(P_\theta/m_0 c)} \tag{33}$$

In order to evaluate the denominator we consider an equilibrium orbit in a uniform vacuum field. For such a field it is true that

$$A_\theta(r,z) = \frac{1}{2} B_0 r \tag{34}$$

where B_0 is that axial component of the field. From the radial

583

equation of motion we have

$$m_0 r_0 \dot{\theta}^2 = -\frac{e}{c} r_0 \dot{\theta} B_0 \tag{35}$$

where r_0 is the radius of the orbit. Hence

$$P_\theta = -\frac{e}{c} B_0 r_0^2 + \frac{1}{2} \frac{e}{c} B_0 r_0^2 = -\frac{1}{2} \frac{e}{c} B_0 r_0^2. \tag{36}$$

Hence

$$\bar{\mu} = -\frac{2m_0 c^2}{e B_0 r_0^2} \psi. \tag{37}$$

We now introduce the rest of our dimensionless variables

$$R = \frac{r}{r_0}, \qquad Z = \frac{z}{r_0}, \qquad \tau = \frac{ct}{r_0} \tag{38}$$

$$\bar{a}_\theta = \frac{A_\theta}{B_0 r_0}, \qquad \omega = \frac{2rA_r}{B_0 r_0^2}, \qquad \kappa = \frac{2A_z}{B_0 r_0}, \qquad X = \frac{e}{m_0 c^2} \phi \tag{39}$$

$$\bar{b}_r = \frac{B_r}{B_0}, \qquad \bar{b}_z = \frac{B_z}{B_0}, \qquad b_\theta = \frac{B_\theta}{B_0}$$

and $\tag{40}$

$$e_r = \frac{E_r}{B_0}, \qquad e_z = \frac{E_z}{B_0}, \qquad e_\theta = \frac{E_\theta}{B_0}$$

From these definitions and Eqs. (1), (26), and (37)

$$\bar{\mu} = 1 + 2R\bar{a}_\theta \tag{41}$$

$$\bar{b}_r = -\frac{1}{2R} \frac{\partial \bar{\mu}}{\partial Z}, \qquad b_\theta = \frac{1}{2R} \frac{\partial \omega}{\partial Z} - \frac{1}{2} \frac{\partial \kappa}{\partial R}, \qquad \bar{b}_z = \frac{1}{2R} \frac{\partial \bar{\mu}}{\partial R} \tag{42}$$

$$e_r = -\frac{e}{B_0 r_0 r_e} \frac{\partial X}{\partial R} - \frac{1}{2R} \frac{\partial \omega}{\partial \tau}, \qquad e_\theta = -\frac{1}{2R} \frac{\partial \bar{\mu}}{\partial \tau},$$

$$e_z = -\frac{e}{B_0 r_0 r_e} \frac{\partial X}{\partial Z} - \frac{1}{2} \frac{\partial \kappa}{\partial \tau} \tag{43}$$

where e_r, e_θ, and e_z are the dimensionless components of the electric field and $r_e = e^2/m_0 c^2$ is the classical radius of the electron.

It is convenient to let

$$\bar{\mu} = \mu_c + \mu \qquad (44)$$

where μ_c represents the vacuum field and μ represents the field of the E-layer. The function μ_c satisfies the equation

$$\frac{\partial^2 \mu_c}{\partial \tau^2} - \frac{\partial^2 \mu_c}{\partial Z^2} - R \frac{\partial}{\partial R}\left(\frac{1}{R} \frac{\partial \mu_c}{\partial R} \right) = 0 . \qquad (45)$$

We introduce the parameter

$$C = -\frac{eB_0 r_0}{2m_0 c^2} = -(2.93 \times 10^{-4}) B_0 r_0 \qquad (46)$$

and define the function $P(R,Z,\tau)$ by

$$P = \frac{1}{2} C^2 (\bar{\mu}^2/R^2). \qquad (47)$$

Using Eqs. (37) through (39) and (46) we can write the equations of motion (31) and (32) in dimensionless form as follows

$$\frac{du_r}{d\tau} = -\frac{1}{\gamma}\frac{\partial P}{\partial R} - \frac{\partial K}{\partial R} + \frac{C}{R}\frac{\partial \omega}{\partial \tau} - \frac{C}{\gamma} u_z \left(\frac{1}{R}\frac{\partial \omega}{\partial Z} - \frac{\partial K}{\partial R} \right) = \frac{-F_r}{\gamma} \qquad (48)$$

$$\frac{du_z}{d\tau} = -\frac{1}{\gamma}\frac{\partial P}{\partial Z} - \frac{\partial K}{\partial Z} + C\frac{\partial K}{\partial \tau} + \frac{C}{\gamma} u_r \left(\frac{1}{R}\frac{\partial \omega}{\partial Z} - \frac{\partial K}{\partial R} \right) = \frac{-F_z}{\gamma} . \qquad (49)$$

We now introduce the dimensionless quantities I_θ, I_{χ}, I_z, and I_ρ corresponding to the dimensionless current and charge densities

$$I_\theta = \frac{8\pi r_0 R}{cB_0} \sum J_\theta = - \frac{2n_e r_e}{\Delta R \Delta Z r_0} \sum \frac{\bar{u}}{R\gamma} \qquad (50)$$

$$I_r = \frac{8\pi r_0 R}{cB_0} \sum J_r = \frac{4n_e e}{B_0 \Delta R \Delta Z r_0^2} \sum \frac{\mu_r}{\gamma} \qquad (51)$$

$$I_Z = \frac{8\pi r_0}{cB_0} \sum J_Z = \frac{4n_e e}{B_0 \Delta R \Delta Z r_0^2} \sum \frac{\mu_z}{R\gamma} \qquad (52)$$

$$I_\rho = \frac{4\pi e r_0^2}{m_0 c^2} \sum \rho = \frac{2n_e r_e}{\Delta R \Delta Z r_0} \sum \frac{1}{R} \qquad (53)$$

where we used Eqs. (25), (27), (37), and (38) to write the right-hand sides of Eqs. (21) through (24) in terms of dimensionless quantities. The symbol $\sum$ in the above equations represents a sum over the contributions of all the particles in that region of space, as explained in IB.

Finally, using Eqs. (38) and (39), we can write the wave equations (4) through (7) in dimensionless form

$$R \frac{\partial}{\partial R}\left(\frac{1}{R}\frac{\partial \omega}{\partial R}\right) + \frac{\partial^2 \omega}{\partial Z^2} - \frac{\partial^2 \omega}{\partial \tau^2} = - I_r \qquad (54)$$

$$R \frac{\partial}{\partial R}\left(\frac{1}{R}\frac{\partial \mu}{\partial R}\right) + \frac{\partial^2 \mu}{\partial Z^2} - \frac{\partial^2 \mu}{\partial \tau^2} = - (I_\theta + I_{\theta res}) \qquad (55)$$

$$\frac{1}{R}\frac{\partial}{\partial R}\left(R\frac{\partial \kappa}{\partial R}\right) + \frac{\partial^2 \kappa}{\partial Z^2} - \frac{\partial^2 \kappa}{\partial \tau^2} = - (I_Z + I_{Zres}) \qquad (56)$$

$$\frac{1}{R}\frac{\partial}{\partial R}\left(R\frac{\partial \chi}{\partial R}\right) + \frac{\partial^2 \chi}{\partial Z^2} - \frac{\partial^2 \chi}{\partial \tau^2} = - I_\rho \qquad (57)$$

The boundary conditions in dimensionless form are

$$\mu(R,Z) = 0 \qquad \text{at all boundaries} \qquad (58)$$

$$\chi(R,Z) = 0 \qquad \text{at all boundaries} \qquad (59)$$

$$\kappa(R,Z) = 0 \qquad \text{at } R = R_1, R_2 \qquad \text{for all } Z \qquad (60)$$

$$\omega(R,Z) = 0 \qquad \text{at } Z = Z_1, Z_2 \qquad \text{for all } R \qquad (61)$$

$$\frac{\partial \omega}{\partial R}(R,Z) = 0 \qquad \text{at } R = R_1, R_2 \qquad \text{for all } Z \qquad (62)$$

$$\frac{\partial}{\partial Z}\kappa(R,Z) = 0 \qquad \text{at } Z = Z_1, Z_2 \qquad \text{for all } R \qquad (63)$$

III. SPECIAL FEATURES OF THE ASTRON MODEL

A. Current in the Resistors

The function of the resistors is to extract energy from the E-layer electrons. The resistors consist of a large number of very fine (1.5 mil) wires. They are wound on a cylindrical frame of fixed radius such that the current in them flows in the θ direction only. It is convenient to replace the individual resistor wires with a resistor sheet.

The current density in the resistors is given by

$$J_{\theta res} = \sigma_\theta E_\theta \qquad (64)$$

where σ_θ is the conductivity of the resistor sheet and E_θ the θ component of the electric field at the resistors. E_θ is calculated from

587

$$E_\theta = - \frac{1}{c} \frac{\partial A_\theta}{\partial t} \tag{65}$$

where A_θ is the θ component of the vector potential. The current density j_θ, given above, cannot be used in the field calculation since no allowance has been made for the fact that the radial thickness of a zone Δr is much greater than the radial thickness of the resistor sheet. The proper current density is given by

$$j_{\theta res} = - \frac{\sigma_\theta \delta_\theta}{\Delta r} \frac{1}{c} \frac{\partial A_\theta}{\partial t} \qquad \text{at } r = r_{res} \tag{66}$$

$$j_{\theta res} = 0 \qquad \text{at } r \neq r_{res}$$

where δ_θ is the radial thickness of the resistor sheet, and r_{res} is the radius of the resistor layer.

In the present Astron experiment, the current in the resistors is allowed to flow in the θ-direction only. In order to study the effect of allowing the current in the resistors to flow in the z-direction also, we have included this option in our model.

The current density in the z-resistors is given by

$$j_{zres} = \sigma_z E_z \tag{67}$$

where σ_z is the conductivity of the z-resistor sheet, and E_z is the z-component of the electron field at the resistors. E_z is given by

$$E_z = - \frac{\partial \phi}{\partial z} - \frac{1}{c} \frac{\partial A_z}{\partial t} \tag{68}$$

where A_z is the z-component of the vector potential. Again we have

to make allowance for the difference in the radial thickness of the resistors δ_z and Δr. The resulting current density is

$$J_{zres} = - \frac{\sigma_z \delta_z}{\Delta r} \left(\frac{\partial \phi}{\partial z} + \frac{1}{c} \frac{\partial A_z}{\partial t} \right) \qquad \text{at } r = r_{res} \tag{69}$$

$$J_{zres} = 0 \qquad \text{at } r \neq r_{res}$$

B. Injection Scheme

1. Injection Radius

The radial equation of motion of a particle is

$$m_0 (\gamma \ddot{r} + \dot{\gamma}\dot{r} - \gamma r \dot{\theta}^2) = e E_r + \frac{e}{c} (r \dot{\theta} B_z - \dot{z} B_\theta). \tag{70}$$

We wish to inject the particle into a region where the radial force on it is small, in order to minimize fluctuations. In Astron, the injection conditions on the electrons are normally

$$\ddot{r} = \dot{r} = \dot{\gamma} = E_r = B_\theta = 0. \tag{71}$$

Using these conditions, Eq. (70) reduces to

$$\gamma r \dot{\theta}^2 = - \frac{e}{c} r \dot{\theta} B_z . \tag{72}$$

Writing $v_\theta = r \dot{\theta}$ and solving for v_θ, we get

$$v_\theta = - \frac{e r B_z}{c \gamma m_0} . \tag{73}$$

Substituting Eq. (73) into (25) we get

$$\psi = - \frac{e r^2 B_z}{m_0 c^2} . \tag{74}$$

589

Substituting Eq. (74) into (37) and using Eq. (34) we get

$$\bar{\mu} = 2R^2 \bar{b}_z .$$

(75)

Solving for R, we get

$$R = \sqrt{\bar{\mu}/2\bar{b}_z} .$$

(76)

The procedure then is to pick a value of z at which we wish to inject and then find the point at which Eq. (76) is satisfied.

2. Injection Rate

The number of superparticles injected per time step is given by $N_T \Delta \tau / \tau_{PL}$, where N_T is the total number of particles that will be used per pulse, $\Delta \tau$ is the time step, and τ_{PL} is the pulse length.

A superparticle is a ring of circulating charge. The current of this ring is given by $n_e e / \tau_B$, where e is the electronic charge, n_e is the number of electrons per superparticle, and τ_B is the cyclotron period. Hence the current injected per time step is given by

$$I_{\Delta t} = \frac{n_e e}{\tau_B} \cdot \frac{N_T \Delta \tau}{\tau_{PL}} .$$

(78)

If a current I is injected into Astron we have, at the end of one cyclotron period, a current I circulating in the machine. Therefore the current that has to be injected per time step is

$$I_{\Delta t} = \frac{\Delta \tau}{\tau_B} .$$

(79)

Equating the right hand side of Eqs. (78) and (79) we obtain

$$n_e = \frac{I\tau_{PL}}{eN_T} \, .$$

<div align="right">(80)</div>

C. Neutralization Scheme

In order to see how we can incorporate the neutralization pheno-
menon into the model we must look at the process in detail. We will
do so by looking at one region in space and see how neutralization
proceeds with time. Consider a small region of neutral gas
into which a bunch of electrons has entered. The electrons remain in
this region for a time δt. By the time they leave they will have under-
gone n_i ionizing collisions. Since the incident electron bunch has a
high electric field associated with it, the cold electrons that are
freed by the ionizing collisions are accelerated out of the region.
When the electron bunch leaves, the region contains n_i positive ions.
Now let another bunch of electrons with the same density and pulse
length enter this region. It too undergoes ionizing collisions and
the electrons liberated by these collisions are again accelerated out
of the region, only not as fast as the first ones since the electric
field of the second bunch is slightly masked by the field of the
residual n_i positive ions. If we now imagine similar bunches entering
the region in succession, the number of positive ions in the region
will build up until the number of ions equals the number of electrons
in the incident beam.

Each region in space must be given a certain amount of positive
charge. This amount depends on how much cumulative time electrons
have spent in that region. Therefore the net amount of charge in a

given region at a given time is the number of electrons in the region minus the number of positive ions in the region.

As explained earlier, the r,z configuration space in the model is divided into a finite-difference grid. The smallest region in the model is that of a zone. Each zone is, therefore, assigned a number of positive ions comensurate with the amount of neutralization that occurred in that zone.

Let us consider a beam of M electrons circulating in one zone. The number of ionizing collisions made by this beam of electrons in a distance $c\delta t$ is given by

$$n_i = NQMc\delta t \tag{81}$$

where N is the number of gas atoms per cm^3, Q is the ionization cross section and M is the number of beam electrons, and c the velocity of light. Note that the ratio $n_i/M = NQc\delta t$ is independent of electron density. This ratio can also be interpreted as the fraction of the beam neutralized in time δt. Replacing electrons with superparticles, we can say that $NQc\delta t$ is the fraction of the superparticle charge that is neutralized in time δt. If we give the pressure in microns and use $Q \approx 2.5 \times 10^{-19} \ cm^2$, we have $NQc\delta t = 2.7 \times 10^{-4} p\delta t$.

We now summarize the process. Let M superparticles enter a zone. After one time step, $\Delta \tau$, they contribute $n_i = 2.7 \times 10^{-4} Mp\Delta\tau$ positive ions to that space.

D. Current in the Cantilever

The current in the cantilever J_c is an externally applied axial current. It can be applied after the E-layer has reached steady state. J_c is time dependent and we represent it by

$$\vec{J}_c(t) = J_c \delta(r - r_c)\delta(t - \tau_s)F(t) \tag{82}$$

where J_c is the magnitude of the current density, r_c is the radius of the cantilever, τ_s is the initiation time, and $F(t)$ is the response function of the circuit.

If the current in the cantilever is established initially and is not changed in the course of the run, then it is more accurate to represent the resulting field analytically. It is convenient to specify the B_θ desired at a given radius. Let $B_{\theta s}$ be the desired field at r_s, then

$$B_{\theta c} = \frac{r_s B_{\theta s}}{r} \tag{83}$$

where $B_{\theta c}$ is the field due to the current in the cantilever. We now write Eq. (83) in terms of our dimensionless variables

$$b_{\theta c} = \frac{R_s B_{\theta s}}{R B_0} . \tag{84}$$

E. Plasma Equilibria

We wish to find the E-layer distribution and the magnetic field when the E-layer is in equilibrium with plasma. We will confine ourselves to those cases where the E-layer is sufficiently strong to

reverse the field. Furthermore, we will assume an MHD model for the plasma with the additional restriction that the pressure be isotropic. The MHD equations which describe the plasma reduce to the magneto-hydrostatic equations

$$\frac{1}{c} \underline{j}_p \times \underline{B} = \nabla p \tag{85}$$

$$\nabla \times \underline{B} = \frac{4\pi}{c} \underline{j}_p \tag{86}$$

$$\nabla \cdot B = 0 \tag{87}$$

where p is the plasma pressure and $\underline{j}_p$ the plasma current (excluding the E-layer current).

From Eq. (85) we see that

$$\underline{j}_p \cdot \nabla p = 0 \tag{88}$$

and
$$\underline{B} \cdot \nabla p = 0. \tag{89}$$

The p = const. surfaces are both magnetic level surfaces and plasma current level surfaces.

We further assume that the plasma current has no axial or radial components. With this assumption Eq. (85) yields the following equations

$$\frac{\partial p}{\partial r} = \frac{1}{c} J_p B_z \ , \qquad \frac{\partial p}{\partial z} = -\frac{1}{c} J_p B_r . \tag{90}$$

Now B_r and B_z are given by

$$B_r = -\frac{B_0 r_0^2}{2r} \frac{\partial \bar{\mu}}{\partial z} \ , \qquad B_z = \frac{B_0 r_0^2}{2r} \frac{\partial \bar{\mu}}{\partial r} \tag{91}$$

hence
$$\dot{\imath}_{\mu\theta} = \frac{2cr}{B_0 r_0^2} \frac{\partial p}{\partial \bar{\mu}} \quad . \tag{92}$$

The pressure profile $p = P(\bar{\mu})$ cannot be derived without solving the buildup problem so we pick a reasonable $P(\bar{\mu})$. We wish $P(\bar{\mu})$ to be positive and finite on closed flux surfaces, and we expect the pressure to be greatest on the innermost flux surfaces. With these considerations we choose as our pressure profile

$$P(\bar{\mu}) = k_4(\bar{\mu}_0 - \bar{\mu})^m \theta(\bar{\mu}_0 - \bar{\mu}) \frac{B_0^2}{8\pi} \quad . \tag{93}$$

Requiring that $k_4 > 0$ insures that the plasma pressure and density are positive definite.

From Eq. (92) we get the plasma current

$$\dot{\jmath}_{p\theta} = - \frac{cB_0}{4\pi r_0} Rk_4 m(\bar{\mu}_0 - \bar{\mu})^{m-1} \theta(\bar{\mu}_0 - \bar{\mu}) \tag{94}$$

where we used the relation $r = r_0 R$. In analogy with the previously defined quantities I_θ, I_r, I_z, etc., we now introduce the dimensionless quantity I_p

$$I_p = \frac{8\pi}{c} \frac{r_0 R}{B_0} \dot{\jmath}_{p\theta} \tag{95}$$

$$= - 2R^2 k_4 m(\bar{\mu}_0 - \bar{\mu})^{m-1} \theta(\bar{\mu}_0 - \bar{\mu}). \tag{96}$$

IV. DIFFERENCE EQUATIONS

The field equations are solved on a finite difference mesh. The mesh spacing is given by $\Delta R = h$, $\Delta Z = mh$, where m is an integer. The position on the mesh is given by $R_j = jh$, $Z_i = imh$, where $-I_2 \leq i \leq I_1$ and $0 \leq j \leq J$. A given time is denoted by an integral numer of time

steps, i.e. $\tau_n = n\Delta\tau$, where $n = 0, 1, 2, \cdots$. We now introduce the notation $\mu_{1j}^n = \mu(R_j, Z_i, \tau_n)$, etc.

The difference approximation that we use in solving the field equations is called the Alternating Direction Implicit method. The difference approximation is written as two equations. As a convenience we use half time steps. In the first half time step the equation is implicit in the R direction and explicit in the Z direction, and in the second half time step the equation is explicit in R and implicit in Z.

The difference equations for the first half time step are

$$\frac{\omega_{1j}^{n+1/2} - 2\omega_{1j}^n + \omega_{1j}^{n-1/2}}{(\Delta t/2)^2} = \frac{2j}{h^2}\left[\frac{\omega_{1,j+1}^{n+1/2} - \omega_{1j}^{n+1/2}}{2j+1} - \frac{\omega_{1j}^{n+1/2} - \omega_{1,j-1}^{n+1/2}}{2j-1}\right]$$

$$+ \frac{\omega_{i+1,j}^n - 2\omega_{1j}^n + \omega_{i-1,j}^n}{m^2 h^2} + I_{R1j}^n$$

$$\frac{\mu_{1j}^{n+1/2} - 2\mu_{1j}^n + \mu_{1j}^{n-1/2}}{(\Delta t/2)^2} = \frac{2j}{h^2}\left[\frac{\mu_{1,j+1}^{n+1/2} - \mu_{1j}^{n+1/2}}{2j+1} - \frac{\mu_{1j}^{n+1/2} - \mu_{1,j-1}^{n+1/2}}{2j-1}\right]$$

$$+ \frac{\mu_{i+1,j}^n - 2\mu_{1j}^n + \mu_{i-1,j}^n}{m^2 h^2} + c_1 \frac{\mu_{1j}^{n+1/2} - \mu_{1j}^{n-1/2}}{\Delta t}$$

$$+ I_{\theta 1j}^n$$

$$\frac{\kappa_{1j}^{n+1/2} - 2\kappa_{1j}^n + \kappa_{1j}^{n-1/2}}{(\Delta t/2)^2} = \frac{1}{2jh^2}\left[(2j+1)(\kappa_{1,j+1}^{n+1/2} - \kappa_{1j}^{n+1/2})\right.$$

$$\left. - (2j-1)(\kappa_{1j}^{n+1/2} - \kappa_{1,j-1}^{n+1/2})\right]$$

$$+ \frac{\kappa_{i+1,j}^n - 2\kappa_{1j}^n + \kappa_{i-1,j}^n}{m^2 h^2} + I_{Z1j}^n$$

$$+ c_2 \frac{\chi_{i+1,j}^n - \chi_{i-1,j}^n}{2mh} + c_3 \frac{\kappa_{1j}^{n+1/2} - \kappa_{1j}^{n-1/2}}{\Delta t}$$

$$\frac{x_{ij}^{n+1/2} - 2x_{ij}^n + x_{ij}^{n-1/2}}{(\Delta t/2)^2} = \frac{1}{2jh^2}\left[(2j+1)(x_{i,j+1}^{n+1/2} - x_{ij}^{n+1/2})\right.$$

$$\left. - (2j-1)(x_{ij}^{n+1/2} - x_{i,j-1}^{n+1/2})\right]$$

$$+ \frac{x_{i+1,j}^n - 2x_{ij}^n + x_{i-1,j}^n}{m^2 h^2} + I_{\sigma ij}^h .$$

The difference equations for the second half time step are

$$\frac{\omega_{ij}^{n+1} - 2\omega_{ij}^{n+1/2} + \omega_{ij}^n}{(\Delta t/2)^2} = \frac{\omega_{i+1,j}^{n+1} - 2\omega_{ij}^{n+1} + \omega_{i-1,j}^{n+1}}{m^2 h^2}$$

$$+ \frac{2j}{h^2}\left[\frac{\omega_{i,j+1}^{n+1/2} - \omega_{ij}^{n+1/2}}{2j+1} - \frac{\omega_{ij}^{n+1/2} - \omega_{i,j-1}^{n+1/2}}{2j-1}\right] + I_{Rij}^{n+1/2}$$

$$\frac{\mu_{ij}^{n+1} - 2\mu_{ij}^{n+1/2} + \mu_{ij}^n}{(\Delta t/2)^2} = \frac{\mu_{i+1,j}^{n+1} - 2\mu_{ij}^{n+1} + \mu_{i-1,j}^{n+1}}{m^2 h^2}$$

$$+ \frac{2j}{h^2}\left[\frac{\mu_{i,j+1}^{n+1/2} - \mu_{ij}^{n+1/2}}{2j+1} - \frac{\mu_{ij}^{n+1/2} - \mu_{i,j-1}^{n+1/2}}{2j-1}\right] +$$

$$+ c_1 \frac{\mu_{ij}^{n+1} - \mu_{ij}^n}{\Delta t}$$

$$\frac{\kappa_{ij}^{n+1} - 2\kappa_{ij}^{n+1/2} + \kappa_{ij}^n}{(\Delta t/2)^2} = \frac{\kappa_{i+1,j}^{n+1} - 2\kappa_{ij}^{n+1} + \kappa_{i-1,j}^{n+1}}{m^2 h^2}$$

$$+ \frac{1}{2jh^2}\left[(2j+1)(\kappa_{i,j+1}^{n+1/2} - \kappa_{ij}^{n+1/2})\right.$$

$$\left. - (2j-1)(\kappa_{ij}^{n+1/2} - \kappa_{i,j-1}^{n+1/2})\right] + c_3 \frac{\kappa_{ij}^{n+1} - \kappa_{ij}^n}{\Delta t}$$

$$+ c_2 \frac{x_{i+1,j}^{n+1/2} - x_{i-1,j}^{n+1/2}}{2mh} + I_{Zij}^{n+1/2}$$

$$\frac{x_{ij}^{n+1} - 2x_{ij}^{n+1/2} + x_{ij}^{n}}{(\Delta t/2)^2} = \frac{x_{i+1,j}^{n+1} - 2x_{ij}^{n+1} + x_{i-1,j}^{n+1}}{m^2 h^2}$$

$$+ \frac{1}{2jh^2}\left[(2j + 1)x_{i,j+1}^{n+1/2} - x_{ij}^{n+1/2}) \right.$$

$$\left. - (2j - 1)(x_{ij}^{n+1/2} - x_{i,j-1}^{n+1/2}) \right] + I_{\sigma ij}^{n+1/2}$$

where $c_1 = -\frac{4\pi}{ch}\sigma_\theta\delta_\theta$, $c_3 = -\frac{4\pi}{ch}\sigma_z\delta_z$, and $c_2 = -\frac{8\pi}{ch}\sigma_z\delta_z\frac{e}{B_0 r_0 r_e}$ when $R = R_{res}$ and $c_1 = c_2 = c_3 = 0$ when $R \neq R_{res}$.

We solve the above difference equations by the method described in Ref. 1. The boundary conditions are

$$\mu(-I_2, j) = \mu(I_1, j) = \mu(i, J_{min}) = \mu(i, J) = 0$$

$$x(-I_2, j) = x(I_1, j) = x(i, J_{min}) = x(i, J)$$

$$\kappa(i, J_{min}) = \kappa(i, J) = 0$$

$$\kappa(-I_2, j) = \kappa(-I_2 + 1, j), \qquad \kappa(I - 1, j) = \kappa(I, j)$$

$$\omega(-I_2 j) = \omega(I_1, j) = 0$$

$$\omega(i, J_{min}) = \omega(i, J_{min}+1), \qquad \omega(i, J-1) = \omega(i, J)$$

where J_{min} is the radius of the cantilever.

We use a leapfrog scheme to difference the equations of motion (43) and (49). For the axial motion we have

$$\frac{u_z^{n+1/2} - u_z^{n-1/2}}{\Delta\tau} = -\frac{F_z^{n}}{\gamma^n}, \qquad \frac{Z^{n+1} - Z^n}{\Delta\tau} = \frac{u_z^{n+1/2}}{\gamma^n}.$$

Similarly for the radial motion

$$\frac{u_r^{n+1/2} - u_r^{n-1/2}}{\Delta\tau} = -\frac{F_r^{n}}{\gamma^n}, \qquad \frac{R^{n+1} - R^n}{\Delta\tau} = \frac{u_r^{n+1/2}}{\gamma^n}.$$

All the above quantities u_z, u_r, γ, Z, R, F_z, F_r are evaluated at the particle centers. Since F_z and F_r are calculated from the fields

which are given at the mesh points only, we use linear interpolation to get their values at the particle centers.

A. Energy Conservation Check

The total energy present in the system at a give time is the sum of the energy in the electromagnetic field $\mathcal{E}_{EM}$ and the kinetic energy of the particles T. The energy in the electromagnetic field is given by

$$\mathcal{E}_{EM} = \frac{1}{8\pi} \int_0^{2\pi} d\theta \int_{-L_2}^{L_1} dz \int_0^{r_{max}} r dr (B^2 + E^2) \tag{97}$$

where $B^2 = B_r^2 + B_\theta^2 + B_z^2$ and $E^2 = E_r^2 + E_\theta^2 + E_z^2$. Using the definitions (38) and (40) Eq. (97) becomes

$$_{EM} = \int_{-L_2}^{L_1} dZ \int_0^{R_{max}} R dR (\bar{b}_r^2 + b_\theta^2 + \bar{b}_z^2 + e_r^2 + e_\theta^2 + e_z^2) \tag{98}$$

where we have integrated over θ and divided by $B_0^2 r_0^3/4$.

The kinetic energy of a superparticle is given by the expression

$$T_\nu = n_e \gamma_\nu m_0 c^2. \tag{99}$$

Therefore the kinetic energy of all the particles is given by

$$T = \frac{4 n_e m_0 c^2}{B_0^2 r_0^3} \sum_{\nu=1}^{N} \gamma_\nu \tag{100}$$

where we have divided T by $B_0^2 r_0^3/4$.

Energy leaves the system by two principal ways; through dissipation in the resistors and through particles striking the boundaries. The rate of energy dissipation in the resistors is

$$\frac{d\mathcal{E}}{dt} = \sum_i I_{\theta i}^2 R_\theta + \sum_i I_{zi}^2 R_z \tag{101}$$

where $I_{\theta i}$ and I_{zi} are, respectively, the total azimuthal and axial current in the ith resistor zone, $\sum_i$ is a summation over the axial zones, R_θ and R_z are, respectively, the azimuthal and axial resistance per resistor zone. R_z and R_θ are the same for all the resistor zones, although they need not be.

The amount of energy dissipated in one time step is

$$
\begin{aligned}
\mathcal{E}_{\Delta t} &= \Delta t \left[\sum_i (I_{\theta i}^2 R_\theta + I_{zi}^2 R_z) \right] \\
&= \Delta t \left[\frac{1}{\sigma_\theta \delta_\theta} \left(\frac{2\pi r}{\Delta z} \right) (\Delta z \Delta r)^2 \sum J_{\theta res}^2 + \frac{1}{\sigma_z \delta_z} \left(\frac{\Delta z}{2\pi r} \right) (2\pi r \Delta r)^2 \sum J_{zres}^2 \right]
\end{aligned}
$$

$$(102)$$

We now introduce the dimensionless quantities $\bar{J}_\theta$ and $\bar{J}_z$

$$
\begin{aligned}
\bar{J}_\theta &= \frac{8\pi}{c} \frac{r_0 R}{B_0} J_\theta \\
&= - \left(\frac{8\pi}{cR} \right) (\sigma_\theta \delta_\theta) \frac{1}{2} \frac{\partial \mu}{\partial \tau}
\end{aligned}
$$

$$(103)$$

$$
\begin{aligned}
\bar{J}_z &= \frac{8\pi}{c} \frac{r_0}{B_0} J_z \\
&= - \left(\frac{8\pi}{cR} \right) (\sigma_z \delta_z) \frac{e}{B_0 r_e r_f} \frac{\partial X}{\partial z} + \frac{1}{2} \frac{\partial \kappa}{\partial \tau} .
\end{aligned}
$$

$$(104)$$

Substituting these quantities into the equation for $\mathcal{E}_{\Delta t}$ and dividing the whole expression by $B_0^2 r_0^3 / 4$, we get the following expression for the dimensionless energy lost to the resistors in one time step

$$
\mathcal{E}_{\Delta \tau} = \Delta \tau \frac{c}{8\pi} \Delta Z (\Delta R)^2 \left[\frac{R}{\sigma_z \delta_z} \sum_i \bar{J}_{zi}^2 + \frac{1}{\sigma_\theta \delta_\theta} \frac{1}{R} \sum_i \bar{J}_{\theta i}^2 \right] .
$$

$$(105)$$

When a particle hits the wall the only energy lost from the problem is its kinetic energy. This is because the image charge and image current

cancel the field of the particle as it nears the wall. We denote this energy by

$$T_{loss} = \frac{4 n_e m_0 c^2}{B_0^2 r_0^3} \sum_{\nu=1}^{N_{loss}} \gamma_\nu \tag{106}$$

where N_{loss} is the number of particles lost. Therefore the quantity

$$\mathcal{E}_{EM} + T + \mathcal{E}_{\Delta t}^n + T_{loss} \tag{107}$$

must be constant throughout the calculation. $\mathcal{E}_{\Delta t}^n$ is the energy dissipated in the resistors up to time n.

V. APPLICATION

Our aim in constructing this model was to make it into a flexible experimental tool. We have made provision for varying a large number of parameters. A large number of graphs are also provided. At present, we can vary the injection current, the pulse length, the number of pulses, and the number of particles used. The resistance and the position of the resistors are variable; a minor modification will enable us to vary their configuration as well. The applied magnetic field can be evaluated in two distinct ways, through the use of one of two analytical models or from a computer program called COILS, which calculates the field at any desired point in space due to a set of coils whose centers are on the axis. In addition, we can include an arbitrary toroidal field, as shown in section II D. The neutralization rate and the plasma pressure profile are also quite arbitrary, as seen from sections III C and III E. All the above variables can, with a minor modification, be made time dependent.

The graphs fall into two distinct groups. One group describes the state of the system at a given time. This group includes two-

phase space plots R vs u_r and Z vs u_z, a graph showing the positions of all the particles, at a given time, in real space, and the current in the resistors at a given time. Three magnetic field plots are given. The first is a plot of B_z vs Z at two radial positions, the second is a plot B_z vs R at three axial positions, and the third is a contour plot of $\underline{B}$. We also include a plot of the axial distribution of the particles. The other group describes the time evolution of a number of system parameters. This group includes a plot of the kinetic energy vs time, a plot of the electromagnetic energy vs time, and a plot of the energy lost to the resistors vs time.

ACKNOWLEDGMENTS

---

[1]J. Killeen and S. L. Rompel, J. Comp. Phys. $\underline{1}$ 29 (1966).

Other Contributions

Computation of Plasma Equilibria
in Three Dimensions*

David V. Anderson† and John Killeen
Lawrence Radiation Laboratory
University of California
Livermore, California

ABSTRACT

Plasma equilibria corresponding to cases of finite β have been computed for various containment schemes which share the common feature of effective two-dimensional symmetry. We present a code which will solve the general nonsymmetric three-dimensional equations for equilibria. We restrict our model by assuming open field lines but note that the case for closed field lines could be solved by a similar numerical method differing only in details. The hydromagnetic equilibrium equation for tensor pressure is reduced to one scalar elliptic equation. An implicit iterative algorithm is used to solve the finite difference form of the equation. The number of grid points is minimized by exploiting the many-fold symmetries found in most stabilized mirror confinement schemes. Results for an $\ell = 2$ stabilized mirror device are presented. Application is intended to be extended to the ALICE and 2-X devices.

I. INTRODUCTION

Two-dimensional models for plasma equilibria have been used to
compute the equilibrium fields for various containment schemes includ-
ing Astron,[1] Levitron,[2] Tokomak,[3] and the stuffed cusp.[4] Several con-
tainment schemes, including the stabilized mirror devices, do not
possess an ignorable coordinate, allowing a reduction of the equilibrium
equations to two dimensions. A code has been developed to handle the
general case for open containment where confinement is achieved by the
mirror effect. We note that the equilibrium equations for closed con-
finement is a vector equation but we comment that the same algorithm
described here could be directly generalized to that case.

II. THE EQUILIBRIUM EQUATIONS

For open containment, equilibrium requires a tensor pressure of
the form

$$\underline{P} = P_\perp(B)\underline{I} + \frac{P_\parallel(B) - P_\perp(B)}{B^2} \underline{B}\underline{B} . \tag{1}$$

The object of the computational program is to use pressure profiles
$P_\parallel(B)$ and $P_\perp(B)$ which obey the stability conditions of Taylor and
Hastie[5]

$$B - \frac{dP_\parallel}{dB} > 0; \qquad B + \frac{dP_\perp}{dB} > 0 \tag{2}$$

and construct equilibria from these. If we take the equations of
hydromagnetic equilibrium

$$\mathbf{j} \times \underline{B} = \nabla \cdot \underline{\underline{P}} \tag{3}$$

$$\nabla \times \underline{B} = \mathbf{j} \tag{4}$$

$$\nabla \cdot \underline{B} = 0 \tag{5}$$

and assume the functional dependence for the pressure components

$$P_\perp = P_\perp(B), \qquad\qquad P_\parallel = P_\parallel(B). \tag{6}$$

Then the equilibrium equations reduce to[4]

$$\underline{B} \times \nabla \times (\nu \underline{B}) = 0 \tag{7}$$

or $\qquad \nabla \times \nu \underline{B} = k\underline{B} \qquad$ for some scalar k

where $\qquad \nu = \dfrac{P_\parallel - P_\perp}{B^2} - 1. \tag{8}$

From Eq. (7) we obtain the current

$$\mathbf{j} = \left(\frac{k}{\nu}\right) \underline{\Gamma} - \frac{1}{\nu} \underline{\nabla \nu} \times \underline{B} \tag{9}$$

and $\qquad \nabla \cdot (\nabla \times \underline{\nu B}) = \nabla \cdot k\underline{B} = \underline{B} \cdot \nabla k = 0.$

Since each field line leaves the plasma boundary, the current along that line must vanish at the boundary. That is, k = 0 at the boundary. The condition $\underline{B} \cdot \nabla k = 0$ insures that $k \equiv 0$ inside the plasma also. From Eq. (7) we obtain the equation

$$(\nabla \times \nu \underline{B}) = 0. \tag{10}$$

We define a potential by

$$\nu \underline{B} = \nabla \varphi, \tag{11}$$

607

so then $(\nabla \cdot \nu \underline{B}) = \nabla^2 \varphi = \underline{B} \cdot \nabla \nu$. The scalar equation

$$\nabla^2 \nu = \frac{1}{\nu} \nabla \varphi \cdot \nabla \nu \qquad (12)$$

then represents the equilibrium.

The decomposition $\varphi = \varphi_c + \varphi_p$ is made in which φ_c denotes the contribution of the vacuum field which is given and where φ_p is the unknown potential function giving the plasma fields. Then for a vacuum

$$\nabla^2 \varphi_c = 0; \qquad \underline{B}_c = -\nabla \varphi_c; \qquad \nu_c = -1. \qquad (13)$$

So the equation to be solved is

$$\nabla^2 \varphi_p = \frac{1}{\nu} \left[\nabla \nu \cdot (\nabla \varphi_p - \underline{B}_c) \right] \qquad (14)$$

which is readily seen to be an elliptic partial differential equation. Dirichlet-type boundary conditions are specified with $\varphi_p = 0$ on a surface far from the plasma region, that is, at some finite but large distance from the plasma center we neglect the fields produced by the plasma.

When Eq. (14) is solved in two dimensions an algorithm known as the alternating direction implicit (ADI)[6] method is used to obtain the solution. For three dimensions the ADI scheme can produce numerical instabilities and a generalization of it is used which is better behaved. Instead we use an algorithm developed by Douglas and Gunn[7] (DG) to solve Eq. (14).

Before the DG algorithm can be used we convert Eq. (14) to a parabolic equation in which the time variable plays the role of iteration parameter. So instead of solving (14) we solve the equation

608

$$\nabla^2 \varphi_p - \frac{1}{\nu} \left[\nabla \cdot (\nabla \varphi_p - \underline{B}_c) \right] = \rho \frac{\partial \varphi_p}{\partial t} \tag{15}$$

and look for the steady state solutions which then satisfy Eq. (14) also.

Although t is really an iteration parameter, it is sometimes useful to identify it as the time and consider $\rho(\partial \varphi_p / \partial t)$ as some sort of dissipative term which allows the initial non-equilibrium plasma to relax into an equilibrium state. The solution of Eq. (15) is initiated by choosing a trial set of iterates φ^1_{ijk} and applying the algorithm to generate a second set φ^2_{ijk}. We continue iterating forward until the difference $\rho(\varphi^n - \varphi^{n-1})$ is acceptably small, thus assuring us of a steady-state solution which also solves (14).

III. DIFFERENCE EQUATIONS AND THEIR SOLUTION

For any orthogonal geometry the finite difference form of the equilibrium equations can be reduced to one scalar equation of the form

$$A\varphi_{i-1} + B\varphi_{i+1} + C\varphi_{j-1} + D\varphi_{j+1} + E\varphi_{k-1} + F\varphi_{k+1} + G\varphi = g. \tag{16}$$

Here we have suppressed all the non-varied subscripts, i.e., $A = A_{ijk}$, $\varphi_{i-1} = \varphi_{i-1,j,k}$ etc. The i, j, and k indices give the spatial location in terms of the orthogonal coordinates x_1, x_2, and x_3 so $\varphi_{ijk} = \varphi\left[(x_1)_i, (x_2)_j, (x_3)_k\right]$. A restriction on Eq. (16) is that it represents an elliptic partial differential equation. The coefficient G can be decomposed into the form

$$G = G_1 + G_2 + G_3 \tag{17}$$

where each successive term involves the i, j, ' operators respectively.

609

We then define the generalized difference operators Δ_{x_1}, Δ_{x_2}, and Δ_{x_3} by

$$\Delta_{x_1} \varphi = A\varphi_{i-1} + B\varphi_{i+1} + G_1\varphi$$

$$\Delta_{x_2} \varphi = C\varphi_{j-1} + D\varphi_{j+1} + G_2\varphi \qquad (18)$$

$$\Delta_{x_3} \varphi = E\varphi_{k-1} + F\varphi_{k+1} + G_3\varphi.$$

The difference equation corresponding to Eq. (14) is

$$(\Delta_{x_1} + \Delta_{x_2} + \Delta_{x_3})\varphi = g. \qquad (19)$$

Taking the finite difference form of Eq. (15) we get the parabolic difference equations

$$(\Delta_{x_1} + \Delta_{x_2} + \Delta_{x_3})\varphi = g + \rho(\varphi^{n+1} - \varphi^n) \qquad (20)$$

which we solve by the DG method. The superscript n or n+1 is intentionally deleted from the LHS and it is the DG algorithm which specifies the exact mixture of φ^{n+1} and φ^n to be used. Three equations result in the DG method. The first equation treats the Δ_{x_1} operator implicitly and the other two equations treat Δ_{x_2} and Δ_{x_3} implicitly. The equations are

$$\frac{1}{2}\Delta_{x_1} (\varphi^{n+1} + \varphi^n) + \Delta_{x_2}\varphi^n + \Delta_{x_3} \varphi^n = g + \rho(\varphi^{n+1} - \varphi^n) \qquad (21a)$$

$$\frac{1}{2}\Delta_{x_1} (\varphi^{n+1} + \varphi^n) + \frac{1}{2}\Delta_{x_2} (\varphi^{n+2} + \varphi^n) + \Delta_{x_3}\varphi^n = g + \rho(\varphi^{n+2} - \varphi^n) \qquad (21b)$$

$$\frac{1}{2} \Delta_{x_1}(\varphi^{n+1} + \varphi^n) + \frac{1}{2}\Delta_{x_2} (\varphi^{n+2} + \varphi^n) + \frac{1}{2}\Delta_{x_3} (\varphi^{n+3} + \varphi^n)$$

$$= g + \rho(\varphi^{n+3} - \varphi^n) \qquad (21c)$$

A more useful set is obtained by subtracting Eq. (21b) from Eq. (21a) and Eq. (21c) from Eq. (21b), so the set is

$$\frac{1}{2}\Delta_{x_1}(\varphi^{n+1} + \varphi^n) + \Delta_{x_2}\varphi^n + \Delta_{x_3}\varphi^n = g + \rho(\varphi^{n+1} - \varphi^n) \qquad (22a)$$

$$\frac{1}{2}\Delta_{x_2}(\varphi^{n+2} - \varphi^n) = \rho(\varphi^{n+2} - \varphi^{n+1}) \qquad (22b)$$

$$\frac{1}{2}\Delta_{x_3}(\varphi^{n+3} - \varphi^n) = \rho(\varphi^{n+3} - \varphi^n). \qquad (22c)$$

Given φ^n we solve Eq. (22a) for φ^{n+1} and use it sequentially to obtain φ^{n+2} and φ^{n+3} from Eqs. (22b) and (22c). We then set $\varphi^{n+3} \to \varphi^n$ and repeat until the iterative process converges. We check convergence by computing the residual error $|\varphi^{n+3} - \varphi^n|$ summed over the grid space.

Each of the equations (22a), (22b), and (22c) are now one-dimensional two-point boundary value problems respectively in the x_1, x_2 and x_3 coordinates and each is solved by the double sweep algorithm. For example, we give the algorithm for Eq. (22a). Since φ^{n+1} is the unknown in this equation we write it as

$$\Delta_{x_1}\varphi^{n+1} - 2\rho\varphi^{n+1} = 2g - \Delta_{x_1}\varphi^n - 2(\Delta_{x_2} + \Delta_{x_3})\varphi^n - \rho\varphi^n$$
$$= S\varphi^n \qquad (23)$$

where $S\varphi^n$ is shorthand for the right side which is a known function. We now expand the Δ_{x_1} to obtain

$$A\varphi_{i-1}^{n+1} + B\varphi_{i+1}^{n+1} + G_1\varphi_i^{n+1} - 2\rho\varphi_i^{n+1} = S\varphi^n. \qquad (24)$$

Let $$\varphi_{i-1}^{n+1} = e_{i-1}\varphi_i^{n+1} + f_{i-1} \qquad (25)$$

and substitute this into Eq. (24). One obtains

$$(Ae_{i-1} + G_i - 2\rho)\varphi_i^{n+1} + B\varphi_{i+1}^{n+1} + A f_{i-1} = S\varphi^n \qquad (26)$$

or

$$\varphi_i^{n+1} = \frac{-B}{(Ae_{i-1} + G_i - 2\rho)} \varphi_{i+1}^{n+1} + \frac{S\varphi^n - A_{i-1}}{(A f_{i-1} + G_i - 2\rho)} \quad , \qquad (27)$$

which is of the same form as Eq. (25), so we get

$$e_i = \frac{-B}{(A e_{i-1} + G_i - 2\rho)} \qquad (28)$$

$$f_i = \frac{S\varphi^n - A f_{i-1}}{(Ae_{i-1} + G_i - 2\rho)} \; . \qquad (29)$$

Equations (25), (28), and (29) give us the machinery to solve Eq. (23). The boundary condition at $i = 1$ is used to give e_1 and f_1. By sweeping to the right using Eqs. (28) and (29) we generate the entire sequence of e's and f's. The upper boundary condition is used to determine $\varphi_{I_{max}}$. Then Eq. (25) is used in a sweep to the left to obtain the solution φ^{n+1} at each grid point. Hence the name double sweep is used to describe the process. This equation is solved for each i line specified by a j, k pair of indices except for those j, k pairs lying on the boundary surface. Equations (22b) and (22c) are solved in a similar manner. After each full iteration cycle (generating a φ^{n+3} from a φ^n) we must also change the coefficients A, B, C, D, E, and F which are, in general, functions of φ. The function g must also be recomputed. These dependences on φ make the equations nonlinear.

If the equations were linear then the DG algorithm is unconditionally stable in the numerical sense. Introduction of the nonlinearities may lead to cases in which stable convergence requires the convergence constant ρ to exceed some critical value. In practice, where the non-
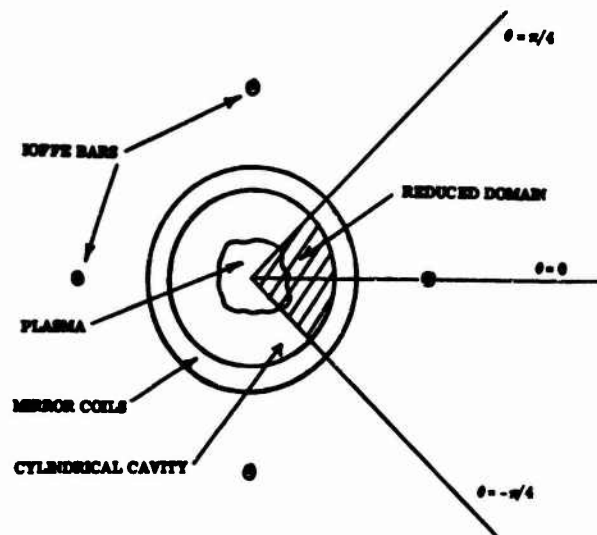
612

Fig. 1. Configuration of simple stabilized mirror device

linearities are not too pathological, one usually obtains stable con-
vergence to a solution.

The uniqueness property of solutions is often lost in the nonlinear
case. Equations frequently have no solution or multiple solutions, and
the algorithms are often incapable of finding all the solutions when
more than one exists.

IV. SIMPLE STABILIZED MIRROR MACHINE EQUILIBRIA

To a simple mirror field $\underline{B}_m$ we have added the field $\underline{B}_I$ produced by
four Ioffe bars. Figure 1 shows the configuration. For $\underline{B}_m$ we use the
analytical form appropriate to cylindrical coordinates

$$B_{m_r} = \lambda A_2 I_1(\lambda R) \sin \lambda z$$

$$B_{m_z} = 2A_1 + \lambda A_2 I_0(\lambda R) \cos \lambda z \qquad (30)$$

$$B_{m_\theta} = 0.$$

Similarly we compute the components B_{I_r}, B_{I_θ} from the currents in
the Ioffe bars. The total vacuum field is then

$$\underline{B}_c = \underline{B}_m + \underline{B}_I . \tag{31}$$

The parameters are adjusted so $\underline{B}_c$ is a minimum B field. In cylindrical coordinates Eq. (14) is

$$\frac{1}{r} \frac{\partial}{\partial r} \left(r \frac{\partial \phi}{\partial r} \right) + \frac{1}{r^2} \frac{\partial^2 \phi}{\partial \theta^2} + \frac{\partial^2 \phi}{\partial z^2} = \frac{1}{\nu} \left[\frac{\partial \nu}{\partial r} \left(\frac{\partial \phi}{\partial r} - B_{r_c} \right) + \right.$$

$$\left. \frac{1}{r} \frac{\partial \nu}{\partial z} \left(\frac{\partial \phi}{r \partial \phi} - B_{\theta_c} \right) + \frac{\partial \nu}{\partial z} \left(\frac{\partial \phi}{\partial z} - B_{z_c} \right) \right] \tag{32}$$

We let the indices i, j, and k now stand for the variables r, θ, and z respectively. If we now write all the derivatives of ϕ in their second order difference form we obtain Eq. (16) with the following definitions for the coefficients

$$A_{ijk} = \frac{(r_{i-1} + r_i)}{(r_{i+1} - r_{i-1})(r_i - r_{i-1}) r_i} + \left(\frac{1}{\nu} \frac{\partial \nu}{\partial r} \right)_{ijk} \frac{1}{(r_{i+1} - r_{i-1})} \tag{a}$$

$$B_{ijk} = \frac{(r_i + r_{i+1})}{(r_{i+1} - r_{i-1})(r_{i+1} - r_i) r_i} - \left(\frac{1}{\nu} \frac{\partial \nu}{\partial r} \right)_{ijk} \frac{1}{(r_{i+1} - r_{i-1})} \tag{b}$$

$$C_{ijk} = \frac{2}{r_i^2} \frac{1}{(\theta_{j+1} - \theta_{j-1})(\theta_j - \theta_{j-1})} + \left(\frac{1}{\nu r^2} \cdot \frac{\partial \nu}{\partial \theta} \right)_{ijk} \cdot$$

$$\frac{1}{(\theta_{j+1} - \theta_{j-1})} \tag{c}$$

$$(33)$$

$$D_{ijk} = \frac{2}{r_i^2} \frac{1}{(\theta_{j+1} - \theta_{j-1})(\theta_{j+1} - \theta_j)} - \left(\frac{1}{\nu r^2} \frac{\partial \nu}{\partial \theta} \right)_{ijk} \cdot$$

$$\frac{1}{(\theta_{j+1} - \theta_{j-1})} \tag{d}$$

$$E_{ijk} = \frac{2}{(z_{k+1} - z_{k-1})(z_k - z_{k-1})} + \left(\frac{1}{\nu} \frac{\partial \nu}{\partial z} \right)_{ijk} \frac{1}{(z_{k+1} - z_{k-1})} \tag{e}$$

$$F_{ijk} = \frac{2}{(z_{k+1} - z_{k-1})(z_{k+1} - z_k)} - \left(\frac{1}{\nu} \frac{\partial \nu}{\partial z} \right)_{ijk} \frac{1}{(z_{k+1} - z_{k-1})} \tag{f}$$

$$G_{1_{ijk}} = \frac{-(r_i + r_{i+1})}{r_i(r_{i+1} - r_{i-1})(r_{i+1} - r_i)} - \frac{(r_{i-1} + r_i)}{r_i(r_{i+1} - r_{i-1})(r_i - r_{i-1})} \quad (g)$$

$$G_{2_{ijk}} = \frac{-2}{r_i^2} \left[\frac{1}{(\theta_{j+1} - \theta_{j-1})(\theta_{j+1} - \theta_j)} + \frac{1}{(\theta_{j+1} - \theta_{j-1})(\theta_j - \theta_{j-1})} \right] \quad (h)$$

$$G_{3_{ijk}} = -2 \left[\frac{1}{(z_{k+1} - z_{k-1})(z_{k+1} - z_k)} + \frac{1}{(z_{k+1} - z_{k-1})(z_k - z_{k-1})} \right] \quad (i)$$

$$g_{ijk} = -\left\{ \frac{1}{\nu} \left[\frac{\partial \nu}{\partial r} B_{r_c} + \frac{1}{r} \frac{\partial \nu}{\partial \theta} B_{\theta_c} + \frac{\partial \nu}{\partial z} B_{z_c} \right] \right\}_{ijk}$$

These coefficients have been defined for a mesh with variable spacing. If we are to have a fine mesh in the plasma region it is useful to use the variable mesh which allows us to have a sparse array of grid points in the exterior region.

The various components of the equilibria fields are assumed to have the same symmetries as the vacuum fields produced by the coils. If the Ioffe bars are located at $\theta = 0$, $\pi/2$, π, $3\pi/2$ respectively then the symmetries involved give

$$B_r(r = \quad = 0 \qquad (a)$$

$$(34)$$

$$B_\theta(\theta = -\pi/4) = 0; \quad B_\theta(\theta = \pi/4) = 0 \qquad (b)$$

These suggest that one may study a reduced domain bounded in the following manner

$$0 < r < r_{max} \qquad (a)$$

$$-z_{max} < z < z_{max} \qquad (b) \qquad (35)$$

$$-\pi/4 < \theta < \pi/4 \qquad (c)$$

It is evident that Eq. (35c) gives a four-fold reduction

of the volume to be studied. To have a well-posed problem we need two more conditions. We assume that the distortion of the original vacuum field by the plasma is negligible at the outer boundaries. These conditions with those given in Eq. (34) give us the following boundary conditions on the potential function ϕ (see Eq. (11)).

$$\phi(r=r_{max}) = 0 = \frac{\partial\phi}{\partial r}\ (r=0)$$

$$\frac{\partial\phi}{\partial\theta}\ (\theta=\pi/4) = 0 = \frac{\partial\phi}{\partial\theta}\ (\theta=-\pi/4 \tag{36}$$

$$\phi(z=z_{max}) = 0 = \phi(z=-z_{max})$$

Eqn. (14) with Eq. (36) comprises a well posed partial differential system which we solve by the DG algorithm.

The physical model used for the pressure profile is needed to compute $\nu(B)$ at each step in the iteration. This is obtained from Eq. (8) once we know $P_{\perp}(B)$ and $P_{11}(B)$. We use the pressure tensor of Taylor[8] given by

$$\begin{aligned} P_{11} &= CB(B_0-B)^m \\ P_{\perp} &= CmB^2(B_0-B)^{m-1} \end{aligned} \quad \text{If } B < B_0 \text{ and in the interior region} \tag{37}$$

$$P_{11} = P_{\perp} = 0 \text{ otherwise.}$$

In this case the stability conditions Eq. (2) reduce to

$$B - C[(1+m)B - B_0](B_0-B)^{m-1} > 0$$

and $\tag{38}$

$$1 + mc\ [2B_0 - C(1+m)B](B_0-B)^{m-2} > 0$$

To demonstrate that the above methods work we have made a preliminary set of runs and computed the equilibria of an
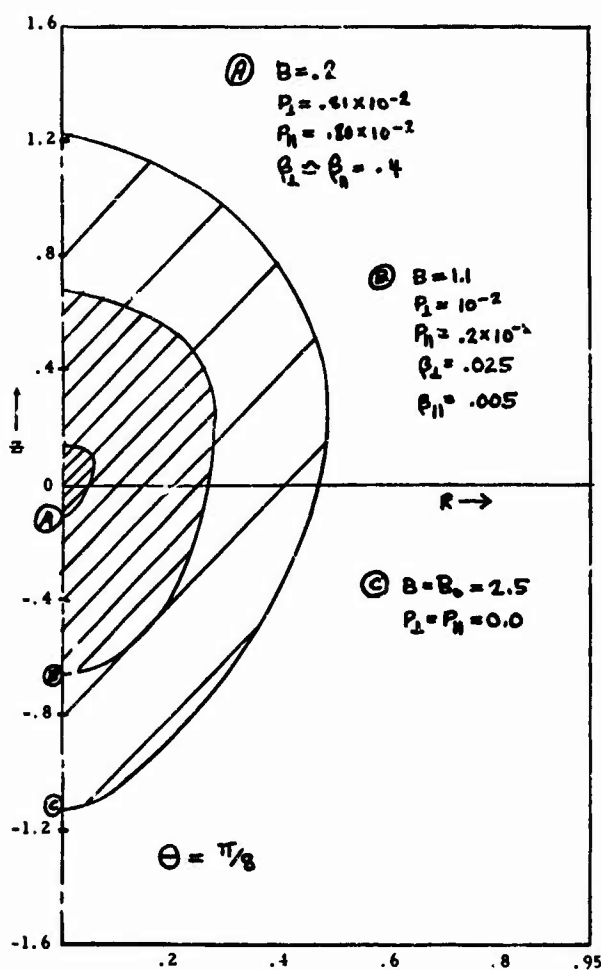
Fig. 2. |B| contours with $P_\perp$, P_{11}, $\beta_\perp$, and β_{11} specified. In the 1st and 3rd quadrants the pear shaped profile is "top-heavy" as here. In the 2nd and 4th quadrants the profiles are inverted. At $\theta = 0$, $\pi/2$, π, $3\pi/2$ the profiles are symn.etric. They are also invariant with respect to a rotation of $\Delta\theta = \pi$.

$m \neq 4$ type plasma for various values of C. In every case the Hastie-Taylor Stability criteria, Eq. (38), are satisfied.

The results are weakly dependent on θ so we present them for a typical angle $\theta = \pi/8$ and show the variations due to r and z in the contour plots below. Fig. 2 shows the contours for B and hence for $P_\perp$ and P_{11}.

The intended goal is to study the equilibria of the ALICE and 2-X devices utilizing a similar program. In the preliminary runs a very coarse grid was employed (11 x 11 x 11) in (r, θ, z). A much more refined grid will be used for the ALICE and 2-X studies.

ACKNOWLEDGEMENTS

REFERENCES

1. D. V. Anderson, J. Killeen, and M. E. Rensink, UCRL-72730 (1970).

2. S. Fischer and J. Killeen, to be published in Phys. Fluids, (1970).

3. S. Fischer and B. Marder, Bull. APS, Series 11, 14, 1016 (1969).
   R. A. Dory, Bull. APS, Series 11, 14, 1016 (1969).

4. J. Killeen and K. J. Whiteman, Phys. Fluids 9, 1846 (1966).

5. J. B. Taylor and R. J. Hastie, Phys. Fluids 8, 323 (1965).

6. D. W. Peaceman and H. H. Rachford, Jr., J. Soc. Industrial Appl. Math. 3, 28 (1955).

7. J. Douglas and J. Gunn, Numer, Math. 6, 428 (1964).

8. J. B. Taylor, Phys. Fluids 6, 1529 (1963).

Tensor-Pressure Fluid Simulation of an MHD Plasma

E. Bowers and N. Winsor
Plasma Physics Laboratory
Princeton University
Princeton, New Jersey

ABSTRACT

A one-fluid model of a low-pressure plasma in a toroidal geometry is presented. For laboratory parameters, it demonstrates the existence of shock structure in the presence of resistivity and viscosity leading to containment times of the order of milliseconds. The model computes the time evolution on a two-dimensional mesh of the plasma density, potential, and three velocity and current components. The momentum equation includes the effects of bulk viscosity and gyroviscous stress. The generalized Ohm's law contains the resistive, Hall, and electron pressure terms. The time step can be taken large enough (of order 1 μsec for the stellarator case) for simulations comparable to a complete laboratory experiment to be performed in a reasonable amount of computer time (about 20 minutes of 360/91 time). Mathematically, the equations are in integro-differential form. We present a linear stability criterion for our sum-difference formulations of these equations. Acoustic, geodesic acoustic, drift, and convective modes severely constrain the choice of

difference formulations. We have used both the Courant-Isaacson-Rees and the Lax-Wendroff schemes for the convective term in the momentum equation. We found that the Courant-Isaacson-Rees scheme introduced a numerical viscosity which was unacceptably large in the presence of the resistive rotational instability. On the other hand, the Lax-Wendroff scheme may couple surfaces more strongly when large-amplitude modes or dissimilar shock structures are present on adjacent surfaces.

I. INTRODUCTION

Encouraging experimental results have recently been obtained from the study of tokamak devices. Since the plasma loss from these toroidal machines is on a classical time scale, rather than the shorter Bohm time scale, it becomes necessary in computer simulation to run for times comparable with classical diffusion. Clearly this puts emphasis on a fluid description of plasma which has averaged out velocity space instabilities, enabling time steps to be taken orders of magnitude larger than the plasma period. The program reported here is an extension of a previous code.[1] There the behavior of a resistive toroidal plasma in a static magnetic field was considered. The effects of rotational transform, plasma inertia and pressure gradients along the lines of force were included. We now take into account the effects of the Hall terms in Ohm's law, together with finite ion Larmor radius (FLR) and viscous terms in the pressure tensor.

A critical feature of the code is the differencing of the momentum equation parallel to the magnetic field. Initially, the method of Courant,

Fluid Simulation of MHD Plasma

Isaacson, and Rees[2] was used. With the drift terms, numerical viscosity introduced by this scheme became unacceptably large in the presence of rotation, causing the plasma to settle down to a numerical steady state rather than a physical equilibrium. In its place the Lax-Wendroff two-step calculation[3] was employed. This two-step procedure has been used to great advantage elsewhere in plasma physics, in particular by Potter[4] in simulation of the dense Plasma Focus experiment. Since the errors in treating the convective terms are now of higher order, they no longer mask the diffusion processes and the rotation velocity increases until, for certain parameters, a shock forms.

The main computational results of this code can be summarized as follows:

In the absence of rotation, the plasma is in an unstable equilibrium. At this stage the flux out of the system has the classical Pfirsch-Schlüter value.[5] In a short time a positive potential builds up on the inside of the plasma, leading to rotation about the minor axis. For small values of the rotational transform, the effect of viscosity is decreased and the rotation reaches a critical speed, first pointed out by Stringer,[6] leading to the formation of a shock. At this stage the flux out of the system is an order of magnitude larger than the Pfirsch-Schlüter value. For larger rotational transform, the effective viscosity coefficient is increased and the rotation reaches an equilibrium without shock formation. The classical flux value is then enhanced by a factor of order 3.

In the next section the fluid equations are presented. Section II shows the differencing of the equations. The final section presents the computa-

tional results, while the Appendix deals with the numerical stability of the model.

II. FLUID EQUATIONS

We use an isothermal one-fluid plasma model with an externally imposed static magnetic field. In Gaussian units, the fluid equations are:

$$mn\left(\frac{\partial \underline{v}}{\partial t} + \underline{v} \cdot \nabla \underline{v}\right) + \nabla \cdot \underline{\underline{P}} - \frac{\underline{j} \times \underline{B}}{c} = 0 \quad , \tag{1}$$

$$\underline{E} + \frac{\underline{v} \times \underline{B}}{c} = \eta \underline{j} + \frac{1}{en}\left(\frac{\underline{j} \times \underline{B}}{c} - KT^e \nabla n\right) \quad , \tag{2}$$

$$\frac{\partial n}{\partial t} + \nabla \cdot (n \underline{v}) = 0 \quad . \tag{3}$$

Maxwell's equations take the simple form:

$$\nabla \times \underline{E} = 0 \quad , \tag{4}$$

$$\nabla \cdot \underline{j} = 0 \quad , \tag{5}$$

$$\nabla \cdot \underline{B} = 0 \quad . \tag{6}$$

The coordinate system used is depicted in Fig. 1 with the magnetic field satisfying Eq. (6) identically. Equation (5) has already restricted consideration to low frequency with the assumption of charge neutrality. Equation (4) embodies the static magnetic field assumption, and is satisfied identically by

$$\underline{E} = -\nabla \Phi \quad . \tag{7}$$

Following Simon and Thompson,[7] the pressure tensor with FLR corrections can be expressed in the form:
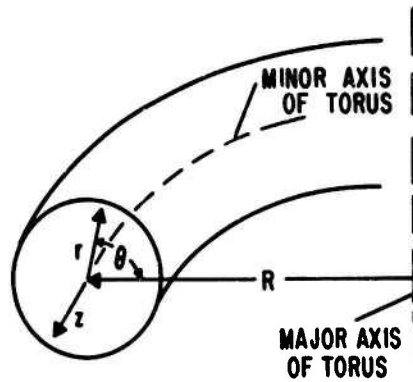
$$\underline{B} = B_o [\underline{e}_\theta f(r) + \underline{e}_z]/[1 - (r/R) \cos \theta]$$

Fig. 1. The toroidal coordinate system.

$$P_{rr} = \sum P - \frac{P}{2\Omega} (\underline{e}_s \underline{e}_r + \underline{e}_r \underline{e}_s):\nabla \underline{v} \quad ,$$

$$P_{ss} = \sum P + \frac{P}{2\Omega} (\underline{e}_s \underline{e}_r + \underline{e}_r \underline{e}_s):\nabla \underline{v} \quad ,$$

$$P_{rs} = P_{sr} = \frac{P}{2\Omega} (\underline{e}_r \underline{e}_r - \underline{e}_s \underline{e}_s):\nabla \underline{v} \quad ,$$

$$P_{rb} = P_{br} = - \frac{P}{\Omega} (\underline{e}_s \underline{e}_b + \underline{e}_b \underline{e}_s):\nabla \underline{v} \quad ,$$

$$P_{bs} = P_{sb} = \frac{P}{\Omega} (\underline{e}_r \underline{e}_b + \underline{e}_b \underline{e}_r):\nabla \underline{v} \quad .$$

Here, $\underline{e}_r$, $\underline{e}_s$, $\underline{e}_b$ describe a right-handed orthogonal coordinate system, with $\underline{e}_r$ and $\underline{e}_s$ defining the radial and poloidal directions lying in the plane perpendicular to the direction, $\underline{e}_b$, of the magnetic field. Only the ion Larmor radius is assumed finite, so that the hydrostatic pressure refers to the ions unless a summation sign appears. These corrections also assume that parallel and perpendicular pressures are equal, which is reasonable for the collisional plasmas under consideration. The main effect

623

of the FLR corrections occurs in the parallel momentum equation, where the inertial term $\underset{\sim}{v} \nabla v_{\parallel}$ is replaced by $(\underset{\sim}{v} - \underset{\sim}{V}_d) \cdot \nabla v_{\parallel}$, $\underset{\sim}{V}_d$ being the ion diamagnetic velocity $(\underset{\sim}{e}_b \times \underset{\sim}{\nabla} p)/\rho\Omega$.

For the parameters of interest the coefficient of parallel viscosity far exceeds that of perpendicular viscosity, and from Braginskii[8] the most important effect is the addition of $\mu_{\parallel} (f^2/r^2)(\partial^2 v_{\parallel}/\partial\theta^2)$, where $f = \iota r/2\pi R$, to the right-hand side of the parallel component of Eq. (1). Examination of this term shows that small values of rotational transform, ι, greatly reduce the effect of parallel viscosity. For experimental parameters, however, it is still the dominant viscous term. The differential equation used to advance the parallel momentum is given at the end of the Appendix. The Lax-Wendroff procedure requires equations in conservation form. Thus, where possible, the FLR and inertia terms have been cast in derivative form. The remaining nonconservative terms are small for the physical parameters of interest.

The parallel component of Ohm's law, Eq. (2), can be expressed in the form

$$- \nabla_{\parallel} \phi = \eta j_{\parallel} \quad , \tag{8}$$

where

$$\phi = \Phi - \frac{KT^e}{e} \ln n \quad .$$

Taking the cross product with $\underset{\sim}{e}_b$, the same equation yields the perpendicular velocity

$$\underset{\sim}{v}_{\perp} = \frac{c}{B} \underset{\sim}{e}_b \times \left[\eta \phi + \eta \underset{\sim}{j} + \frac{m}{e} \left(\frac{\partial \underset{\sim}{v}}{\partial t} + \underset{\sim}{v} \cdot \nabla \underset{\sim}{v} \right) \right.$$
$$\left. + \frac{1}{en} \nabla \cdot \underset{=}{T} + \frac{\Sigma KT}{en} \nabla n \right] \quad . \tag{9}$$

624

Here, Eq. (1) has been utilized to substitute for the perpendicular current, and the pressure tensor has been expressed as

$$\underset{=}{P} = \sum n\,KT\,\underset{=}{I} + \underset{=}{\tau} \quad ,$$

In similar fashion, the vector product of Eq. (1) yields the perpendicular current

$$\underset{\sim}{j}_{\perp} = \frac{c}{B}\,\underset{\sim}{e}_{b} \times \left\{ \sum KT\,\nabla n + \nabla \cdot \underset{=}{\tau} + mn\left[\frac{\partial \underset{\sim}{v}}{\partial t} + (\underset{\sim}{v}\cdot\nabla)\underset{\sim}{v}\right]\right\} \quad . \tag{10}$$

The parallel component of Eq. (1) (with the rearrangement given in the Appendix) and Eq. (3) serves to advance parallel momentum and density in time. Both of these equations use the Lax-Wendroff two-step procedure. Equation (10) gives the perpendicular current, which leads through Eq. (5) to the parallel current. Integration of Eq. (8) determines the potential up to an arbitrary constant. This constant is obtained from the condition that no charge accumulate on a magnetic surface,

$$\int \underset{\sim}{j}\cdot\nabla r\;dS/|\nabla r| = 0 \quad ,$$

as explained in Ref. 1. Armed with the potential, Eq. (9) yields the perpendicular velocity.

III. DIFFERENCE EQUATIONS

An r^2, θ mesh[1] is used, dividing up a cross section of the torus into equal area cells. Velocity and density are evaluated at the same space-time points, but since most of the current arises through the gradient of density, it is displaced a half step in θ from the density.
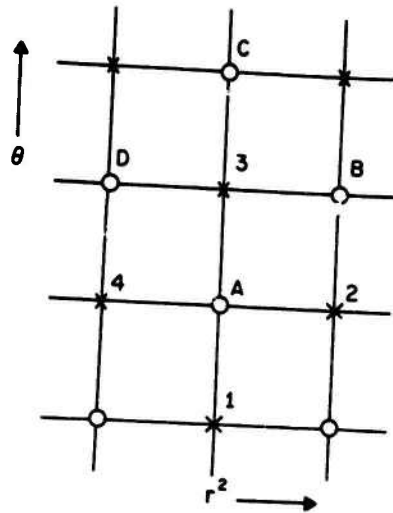
Fig. 2. The Lax-Wendroff mesh.

To illustrate the Lax-Wendroff procedure, we consider the differencing of the density conservation equation. Figure 2 shows the Lax-Wendroff lattice with auxiliary and main values on alternate mesh points marked by crosses and circles, respectively. In order to compute density at the center circle A at time $t + 1$, fluxes are required at the four auxiliary points 1, 2, 3, 4 at time $t + 1/2$. The calculation of the auxiliary density at 3 takes the form

$$
n^{t+1/2}(3) = [n^t(A) + n^t(B) + n^t(C) + n^t(D)]/4
$$

$$
- \frac{\Delta t}{2N} \left[\frac{(rNnv_r)^t (B) - (rNnv_r)^t (D)}{\Delta r^2} \right.
$$

$$
\left. + \frac{[Nn(v_s + f v_b)]^t (C) - [Nn(v_s + f v_b)]^t (A)}{r h \Delta \theta} \right] .
$$

626

Fluid Simulation of MHD Plasma

The main density is then obtained by

$$n^{t+1}(A) = n^t(A) - \frac{\Delta t}{N} \left[\frac{(rNnv_r)^{t+1/2}(2) - (rNnv_r)^{t+1/2}(4)}{\Delta r^2} \right.$$

$$\left. + \frac{[Nn(v_s + fv_b)]^{t+1/2}(3) - [Nn(v_s + fv_b)]^{t+1/2}(1)}{r h \Delta \theta} \right] \quad .$$

Here, $N = 1 - r/R \cos\theta$ and $h^2 = 1 + f^2$, where R is the major radius. The merits of this procedure have been thoroughly discussed e.g., Richtmyer and Morton.[9] One point of interest, however, arises in the behavior of the electron drift wave. The equation for this wave is

$$\frac{\partial n}{\partial t} + \frac{v_d^e}{r} \frac{\partial n}{\partial \theta} = 0 \quad ,$$

where

$$v_d^e = - \frac{cKT^e}{|e|nB} \frac{\partial n}{\partial r} \quad .$$

Its difference formulation is [taking the limit $R \to \infty$ of Eq. (A4) of the Appendix]

$$\frac{\partial n}{\partial t} + \frac{v_d^e}{4r} \left[\left(\frac{\partial n}{\partial \theta}\right)_{r_{i+1}} + 2\left(\frac{\partial n}{\partial \theta}\right)_{r_i} + \left(\frac{\partial n}{\partial \theta}\right)_{r_{i-1}} \right] = 0 \quad .$$

Thus, perturbations with different phases or frequencies on neighboring surfaces can be expected to interact. Since the electron drift wave depends on the local density gradient, the frequency changes with radius, and in numerical studies of this mode the amplitude on one surface was found to grow at the expense of the amplitude on the neighboring surfaces. This did not occur with acoustic modes, where the frequency is almost independent of radius. Clearly this exchange of energy will decrease with the radial mesh size, and in practice the number of radial points used was sufficient
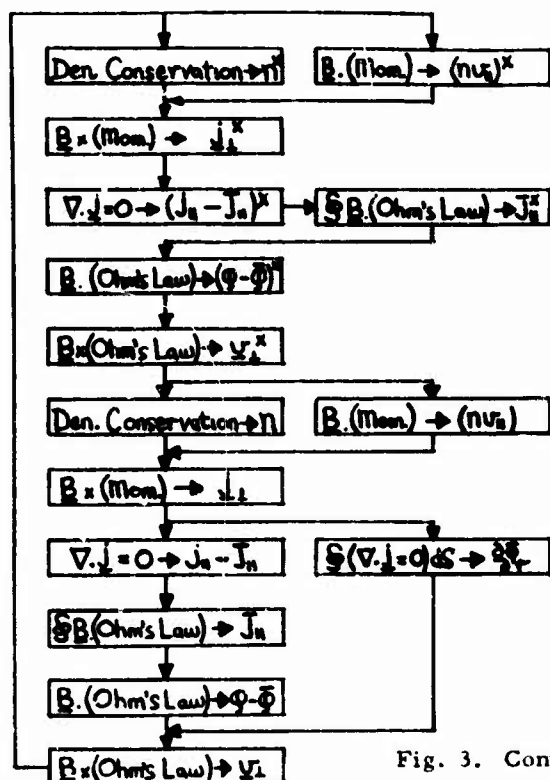
627

Fig. 3. Computational procedure.

Flowchart boxes (top to bottom):

- Den. Conservation $\to \tilde{n}^x$
- $\underline{B} \cdot (\text{Mom}) \to (n v_{\parallel})^x$
- $\underline{B} \times (\text{Mom}) \to \underline{J}_\perp^x$
- $\nabla \cdot \underline{J} = 0 \to (J_\parallel - \bar{J}_n)^x$
- $\oint \underline{B} \cdot (\text{Ohm's Law}) \to \bar{J}_n^x$
- $\underline{B} \cdot (\text{Ohm's Law}) \to (\varphi - \bar{\varphi})^x$
- $\underline{B} \times (\text{Ohm's Law}) \to \underline{v}_\perp^x$
- Den. Conservation $\to n$
- $\underline{B} \cdot (\text{Mom}) \to (n v_{\parallel})$
- $\underline{B} \times (\text{Mom}) \to \underline{J}_\perp$
- $\nabla \cdot \underline{J} = 0 \to J_\parallel - \bar{J}_n$
- $\oint (\nabla \cdot \underline{J} = 0) dS \to \bar{\varphi}$
- $\oint \underline{B} \cdot (\text{Ohm's Law}) \to \bar{J}_n$
- $\underline{B} \cdot (\text{Ohm's Law}) \to \varphi - \bar{\varphi}$
- $\underline{B} \times (\text{Ohm's Law}) \to \underline{v}_\perp$

to keep the effect small.

Figure 3 shows a flow chart for the program, with crosses marking
auxiliary quantities. The first calculations in the time loop are the evalua-
tion of auxiliary density and parallel momentum, both of these equations
being the first step in the Lax-Wendroff scheme. Next comes the evaluation
of the perpendicular current, using Eq. (10). Here the density gradient
contribution is properly centered in space and time; however, the inertial
and FLR terms must use the perpendicular velocity at a previous time. In
doing this it is assumed that these terms are small. In practice this sets
an upper limit on the radial density gradient that can be considered, since
for very large density gradients the diamagnetic contribution to $\underline{v}_\perp$ becomes

sizable, with a resulting large inertia. A discussion of the density profile used is given in the next section. Integration of the charge-conservation equation determines parallel current to within a surface constant, while integration of Eq. (8) over the surface eliminates ϕ and yields that constant. Integration of Eq. (8) also serves to determine the potential up to a surface constant. The last three operations are detailed in Ref. 1. The constant part of the potential has already been determined in the previous time step, as will be explained. We are now able to gain the perpendicular velocity using Eq. (9). Again we note that the inertial terms appearing on the right-hand side of this equation are the only ones not centered in time, having to use $\underset{\sim}{v}_\perp$ from a previous time. However, for large magnetic fields the coefficient of this term is greatly reduced.

The next part of the code determines the calculation of the main density, currents, and velocities. The parallel viscosity term was included implicitly in the momentum equation in the following way:

$$
\begin{aligned}
nv_\parallel^{t+1}(r_i \theta_j) = {} & nv_\parallel^{t}(r_i \theta_j) + \frac{f^2 \mu_\parallel \Delta t}{r^2 (\Delta \theta)^2} \, [v_\parallel^{t}(r_i \theta_{j+1}) \\
& - 2 v_\parallel^{t+1}(r_i \theta_j) + v_\parallel^{t}(r_i \theta_{j-1})] + \dots \quad .
\end{aligned}
$$

The second term in the bracket can then be taken over to the left-hand side. This method of treating viscosity was found to enhance the numerical stability of the system, allowing one to take larger time steps. When the effective viscous coefficient is small, shock structure develops, resulting in steep azimuthal density gradients. In order to eliminate the spurious short-wavelength oscillations that occurred in the presence of these gradients, a

smoothing viscosity of the form suggested by Lapidus[10] was applied. For example, in one dimension a new quantity would be replaced by a corrected value

$$
n^{*t+1}(\theta_j) - n^{t+1}(\theta_j) + \epsilon \, \delta \, [\, | \, \delta v_\theta(\theta_{j+1}) \, | \, \frac{\Delta t}{r \, \Delta \theta} \, \delta n^{t+1}(\theta_{j+1})] \qquad ,
$$

where $\delta F(\theta_j) = F(\theta_j) - F(\theta_{j-1})$ and ϵ is a small number. This is equivalent to adding a diffusion term with a coefficient that becomes effective only when a wavelength becomes of order or less than the mesh size. Following on from the main density and parallel momentum, the currents and perpendicular velocities are calculated in a way similar to the calculations of the auxiliary quantities, with the addition of a loop to calculate the average potential on a magnetic surface. The procedure for obtaining $\bar{\phi}$ is the same as that considered in Ref. 1. The method used enables determination of $\partial^2 \phi / \partial t \, \partial r$ on the main mesh, and hence $\bar{\phi}$ half a time step ahead on the auxiliary mesh. This value of $\bar{\phi}$ is correctly centered for the calculation of the auxiliary velocity in the next time step. In order to gain $\bar{\phi}$ on the main mesh, the quantity $\partial^2 \bar{\phi} / \partial t \, \partial r$ is averaged with its value at the previous time.

The boundary conditions assume that plasma is scraped off at the wall. As a result, the velocity there is put to zero and the density is assumed small and independent of azimuth. The dominant modes occurring in this low-β plasma are of the drift-acoustic type and are highly localized (i.e., the radial wavelength is extremely short compared with the scale length of density variations), so boundary conditions cannot be expected to influence the interior of the plasma to any great extent.

IV. COMPUTATIONAL RESULTS

Analytically, we can show[11] that an equilibrium exists when there is no average radial electric field on a magnetic surface. Using an expansion in the ratio r_o/R, values of density and velocity were calculated from the equations of Sec. III, with partial time derivatives set to zero. These values were used as initial conditions. Attempts to start the program away from this equilibrium resulted in large-scale oscillations which masked the long-term behavior.

The initial density distribution was chosen to be nearly a "similarity solution" for the irrotational equilibrium, with a region of constant density between its outer boundary and the wall. The "similarity solution" would resistively decay without changing its shape, if its outer boundary were held fixed. The constant-density region insulates the diffusing portion of the plasma from the wall, making detailed treatment of the boundary unnecessary. Thus, our calculations describe an expanding plasma, diffusing into a low-density exterior region, and we would not, for example, expect to accurately describe effects that depend on the characteristics of the wall or the limiter.

We found that numerical calculations of similarity profiles actually suggested a tendency toward such a low-density "tail" on the density profile for lower magnetic fields; e.g., 5×10^3 gauss and the parameters quoted in the next paragraph. In this irrotational equilibrium the flux out of the system scaled classically, even with the drift terms present.

631

The density profile, averaged over a magnetic surface, changes much less rapidly than the azimuthal variation. Thus, the profile can be considered a persistent feature of the calculation. Such a similarity profile is shown in Fig. 4 for the parameters $n_o = 10^{13}$ cm^{-3} of hydrogen at equal ion and electron temperatures of 25 eV, a magnetic field of 10^4 gauss, a 100-cm major radius, a 5-cm minor radius, Spitzer resistivity, and a uniform rotational transform $\iota = 120°$.

The equilibrium investigated above is unstable to a rotational mode,[1] so the more interesting case, physically, is the one in which rotation is allowed to develop. Figure 5 illustrates two cases of the buildup of average $\underline{E} \times \underline{B}$ rotation on a surface over a period of 250 μsec. The velocity is scaled to the drift velocity $c\Sigma KT/2eB_o r_o$. Curve (a) shows the average poloidal velocity on a magnetic surface at r = 4 cm for the parameters listed in the previous paragraph. By the end of the run the rotation has reached its maximum and the time derivative of the average potential has fallen to a small value. An important feature of the rotation is a shift of plasma density towards the outside of the torus, resulting in an enhancement of order 3 over the Pfirsch-Schlüter flux. For t > 250 μsec the rotation speed decreases very slowly as the density is lost from the surface, indicating the dependence of the rotational equilibrium on the density gradient.

Curve (b) shows the development of rotation for the same density and magnetic field, but the ion and electron temperatures are 15 eV, the uniform rotational transform is 90°, and the magnetic surface is at r = 3.6 cm.
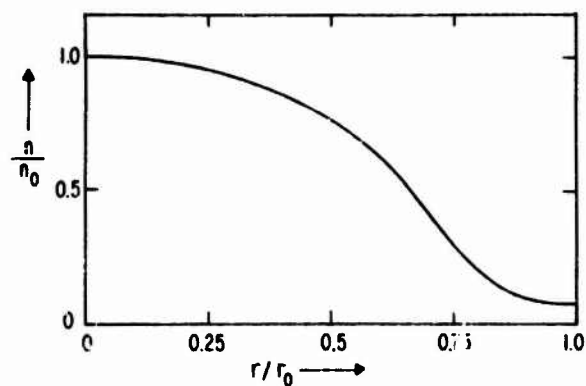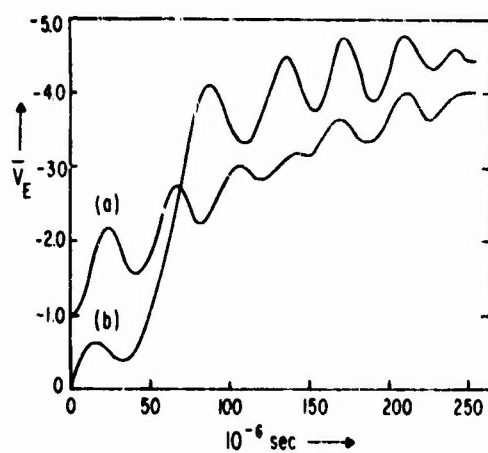
Fig. 4. Radial density profile.

Fig. 5. Growth of $\underline{E} \times \underline{B}$ drift for laboratory parameters: $n = 10^{13}$ cm^{-3}, $B = 10^4$ gauss, and classical resistivity.

633

Comparison of the two curves shows that rotation builds up at a **faster** rate for the smaller value of rotational transform (note that the initial rotation for curve (a) is nonzero because this is a continuation of a previous run). In both cases the oscillations that occur during the buildup of rotation are damped upon reaching maximum rotation. Their frequency corresponds to the geodesic acoustic mode,[12] modified by drift terms.

Stringer[6] has shown that in the absence of viscosity a singularity exists in the region where the $\underset{\sim}{E} \times \underset{\sim}{B}$ drift is of order minus the electron drift velocity. Lee, Hazeltine, and Rosenbluth,[13] neglecting the drift terms, showed that the singularity would lead to shock formation at the critical speed $f v_T$. Later theory[14,15] predicted that viscosity would lead to a stable rotational state. These results are based on an ordering that breaks down with small viscosity, as Fig. 6 demonstrates. This figure shows the azimuthal variation of density after 250 μsec, corresponding to the parameters of curve (b) in Fig. 5. The $\theta = \pi$ position is the outside of the torus. The density variation is given on surfaces out to and including $r = 3.6$ cm. The plasma has formed a shock towards the inside of the torus. The velocity on the inside exceeds the average velocity plotted in curve (b), which is of order minus the electron drift velocity, in agreement with Ref. 6. The flux out of the system is now an order of magnitude larger than the Pfirsch-Schlüter value, and corresponds to a particle loss time of the order of milliseconds. The equivalent profile corresponding with curve (a) of Fig. 5 would exhibit essentially a cosine dependence on θ, in accordance with Refs. 14 and 15. We conclude that when the effective viscosity coefficient, $\mu_{\parallel} f^2$, is small—in particular for small rotational transform—a shock is still able to develop.

Fluid Simulation of MHD Plasma

ACKNOWLEDGMENTS
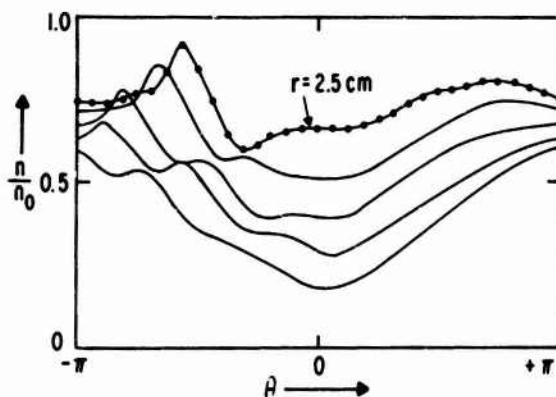
Fig. 6. Azimuthal density profile, for rotational state, $\iota = 90°$.

APPENDIX

Numerical stability of the main modes present in the difference equations will now be demonstrated. For clarity we consider limiting cases in which one mode dominates. Following Richtmyer and Morton,[9] small perturbations are assumed and the equations linearized.

1. Drift and Geodesic Acoustic Modes Without Average Flow on a Magnetic Surface.

Assuming a main mesh $2\Delta r^2 \times 2\Delta\theta \times 2\Delta t$, where, in Fig. 2, $2\Delta\theta$ is the distance between points A and C, the significant terms in the auxiliary density calculation yield (assuming $f = \iota r/2\pi R = 0$)

$$n^{t+1}(r,\theta) - \overrightarrow{n}^t(r,\theta) + \frac{nc\Delta t}{RB}\sin\theta\left(\frac{\partial\overrightarrow{\phi}^{t+1}}{\partial r} + \frac{\partial\overrightarrow{\phi}^{t-1}}{\partial r}\right)$$

$$+ \frac{\Delta t\, V_d^e}{2r\Delta\theta}[n^t(r,\theta+1) - n^t(r,\theta-1)] = 0 \qquad , \tag{A1}$$

where

$$\overrightarrow{n}^t = [n^t(r+1,\theta) + n^t(r-1,\theta) + n^t(r,\theta+1) + n^t(r,\theta-1)]/4 \quad .$$

On the main mesh,

$$n^{t+2}(r,\theta) - n^t(r,\theta) + \frac{4nc\Delta t}{RB}\sin\theta\,\frac{\partial\overrightarrow{\phi}^{t+1}}{\partial r}$$

$$+ \frac{\Delta t\, V_d^e}{r\Delta\theta}[n^{t+1}(r,\theta+1) - n^{t+1}(r,\theta-1)] = 0 \quad . \tag{A2}$$

The change conservation condition yields the average potential on a magnetic surface,

$$\frac{\partial\overrightarrow{\phi}^{t+1}}{\partial r} - \frac{\partial\overrightarrow{\phi}^{t-1}}{\partial r} - \frac{2\Delta t\, Bv_T^2}{ncR\pi}\sum_j n^t(r,\theta_j)\sin\theta_j\Delta\theta = 0 \quad . \tag{A3}$$

636

Here, v_T is the thermal velocity $(\Sigma KT/m)^{1/2}$, and the summation is taken over all values of j, representing the closed integral over a magnetic surface. If we now let $R \rightarrow \infty$ and assume $\partial\bar{\phi}/\partial r = 0$ in these equations, and substitute for the auxiliary density in Eq. (A2) from Eq. (A1), we obtain

$$n^{t+2}(r,\theta) - n^t(r,\theta) + \frac{\Delta t\, v_d^e}{r\Delta\theta} \{ [n^t(r+1, \theta+1) - n^t(r+1, \theta-1)$$

$$+ n^t(r, \theta+2) - n^t(r, \theta-2) + n^t(r-1, \theta+1)$$

$$- n^t(r-1, \theta-1)]/4$$

$$- \frac{\Delta t\, v_d^e}{2r\Delta\theta} [n^t(r, \theta+2) - 2n^t(r,\theta) + n^t(r, \theta-2)] \} = 0 \quad . \qquad \text{(A4)}$$

Taking an average over surfaces of the form

$$n^t(r+1, \theta+1) + n^t(r-1, \theta+1) \cong 2n^t(r, \theta+1) \quad ,$$

and assuming a variation of $\exp(im\theta)$, we obtain

$$n^{t+2} = n^t \left[1 - \frac{i\Delta t\, v_d^e}{2r\Delta\theta} (\sin 2m\Delta\theta + 2\sin m\Delta\theta) \right.$$

$$\left. - \left(\frac{\Delta t\, v_d^e}{r\Delta\theta}\right)^2 (1 - \cos 2m\Delta\theta) \right] \quad . \qquad \text{(A5)}$$

Writing $n^{t+2} = \lambda n^t$, numerical stability requires $|\lambda| < 1$, which is satisfied provided

$$\Delta t < \frac{r\Delta\theta}{\sqrt{2}\, v_d^e} \quad . \qquad \text{(A6)}$$

The difference equations for the geodesic acoustic mode are obtained by letting $v_d^e \rightarrow 0$ and keeping R finite in Eqs. (A2) and (A3). This reduces to the same form considered in Ref. 1, which has shown numerical stability of the mode provided

$$\Delta t < \frac{R}{\sqrt{2}\, v_T} \quad . \qquad \text{(A7)}$$

637

2. Parallel Acoustic Mode with Flow Present.

Considering the case $V_d^e = 0$, $R \to \infty$ but f finite, the auxiliary density and momentum calculations yield

$$n_\theta^{t+1} - \overrightarrow{n}_\theta^{t} + \frac{\Delta t V}{2r\Delta\theta}(n_{\theta+1}^{t} - n_{\theta-1}^{t})$$

$$+ \frac{\Delta t f}{2r\Delta\theta}(n v_{b,\theta+1}^{t} - n v_{b,\theta-1}^{t}) = 0 \quad , \tag{A8}$$

$$n v_{b,\theta}^{t+1} - \overline{n v}_{b,\theta}^{t} + \frac{\Delta t V}{2r\Delta\theta}(n v_{b,\theta+1}^{t} - n v_{b,\theta-1}^{t})$$

$$+ \frac{\Delta t v_T^2 f}{2r\Delta\theta}(n_{\theta+1}^{t} - n_{\theta-1}^{t}) = 0 \quad . \tag{A9}$$

Here, V represents the average poloidal flow on a surface and $\overrightarrow{nv}_b^{t}$ is averaged in the same manner as the density appearing in Eq. (A1). The difference equations on the main mesh are:

$$n_\theta^{t+2} - n_\theta^{t} + \frac{\Delta t V}{r\Delta\theta}(n_{\theta+1}^{t+1} - n_{\theta-1}^{t+1})$$

$$+ \frac{\Delta t f}{r\Delta\theta}(n v_{b,\theta+1}^{t+1} - n v_{b,\theta-1}^{t+1}) = 0 \quad , \tag{A10}$$

$$n v_{b,\theta}^{t+2} - n v_{b,\theta}^{t} + \frac{\Delta t V}{r\Delta\theta}(n v_{b,\theta+1}^{t+1} - n v_{b,\theta-1}^{t+1})$$

$$+ \frac{\Delta t v_T^2 f}{r\Delta\theta}(n_{\theta+1}^{t+1} - n_{\theta-1}^{t+1}) = 0 \quad . \tag{A11}$$

Eliminating the auxiliary quantities in Eqs. (A10) and (A11), by use of Eqs. (A8) and (A9), yields two equations which can be put in the form

$$\underline{x}^{t+2} = A\underline{x}^{t} ,$$

where A is a 2×2 matrix and $\underline{x}$ is the vector $\underline{x}^{t} = (n^{t}, n v_b^{t})$. The eigenvalues of the matrix are:

$$\lambda = 1 - \frac{i\Delta t}{2r\Delta\theta} (V \pm f v_\tau)(\sin 2m\Delta\theta + 2 \sin m\Delta\theta)$$

$$-\left(\frac{\Delta t}{r\Delta\theta}[V \pm f v_\tau]\right)^2 (1 - \cos 2 m\Delta\theta) \quad .$$

By analogy with (A5), we have stability provided:

$$\Delta t < \frac{r\Delta\theta}{\sqrt{2}\,(f v_\tau + |V|)} \quad . \tag{A12}$$

In practice, a time step of 0.5 μsec was sufficient to keep all the modes numerically stable for the typical stellarator parameters quoted in the text.

Finally, we give the differential equation which uses the Lax-Wendroff procedure to time-advance the parallel momentum:

$$\frac{\partial}{\partial t}(nv_b) + \frac{1}{rN^2} \frac{\partial}{\partial r} [rN^2(nv_b v_r + \tau_{rb})]$$

$$+ \frac{1}{hrN^2} \frac{\partial}{\partial\theta} [N^2(nv_b v_s + \tau_{sb})] + \frac{f}{Nhr} \frac{\partial}{\partial\theta}(Nnv_b^2)$$

$$+ \frac{\Sigma KTf}{mhr} \frac{\partial n}{\partial\theta} + \frac{f^2}{rh^2 N} (nv_r v_b + \tau_{rb})$$

$$+ \frac{f \sin\theta}{NRh} (nv_s^2 + \tau_{ss}) + \left(\frac{f}{Nr} - \frac{\partial f}{\partial r}\right) (nv_r v_s + \tau_{rs}) = 0 \quad .$$

Here, $\underset{\sim}{\tau}$ is the traceless stress tensor defined in the body of the paper, divided by the mass. Notice that the smallness of f ensures that the non-conservative terms will be unimportant compared with the conservative terms.

Bowers and Winsor

REFERENCES

[1]J. L. Johnson, N. K. Winsor, and J. M. Dawson, "A Fluid Description for Toroidal Low-β Confinement," in Proceedings of the APS Topical Conference on Numerical Simulation of Plasma, Los Alamos Report LA-3990, paper D4.

[2]R. Courant, E. Isaacson, and M. Rees, Comm. Pure and Appl. Math. 5, 243 (1952).

[3]P. D. Lax and B. Wendroff, Comm. Pure and Appl. Math. 13, 217 (1960).

[4]D. E. Potter and K. V. Roberts, Explicit Magnetohydrodynamic Calculations in the R-Z Plane, Conference on Computational Physics, July 1969, Vol. II, paper 6, published by the Institute of Physics and the Phyrical Society.

[5]D. Pfirsch and A. Schlüter, Max Planck Institute Report MPI/PA/7/62, unpublished.

[6]T. E. Stringer, Phys. Rev. Letters 22, 770 (1969).

[7]A. Simon and W. B. Thompson, J. Nuclear Energy, Pt. C. 8, 373 (1966).

[8]S. I. Braginskii, Reviews of Plasma Physics (Consultants Bureau, New York, 1965), Vol. 1, p. 205.

[9]R. D. Richtmyer and K. W. Morton, Difference Methods for Initial-Value Problems (Interscience Publishers, New York, 1967).

[10]A. Lapidus, J. Comp. Phys. 2, 154 (1967).

[11] E. Bowers, J. M. Greene, and N. K. Winsor (to be published).

[12] N. K. Winsor, J. L. Johnson, and J. M. Dawson, Phys. Fluids 11, 2448 (1968).

[13] R. D. Hazeltine, E. P. Lee, and M. N. Rosenbluth (to be published in Phys. Fluids).

[14] M. N. Rosenbluth and J. B. Taylor, Phys. Rev. Letters 23, 367 (1969).

[15] T. E. Stringer, Phys. Fluids 13, 1586 (1970).

Simulation of Infinite Space on a Finite Computer

O. Buneman*
E. E. Department
Stanford University
Stanford, California

Two new schemes are presented for imposing boundary conditions which simulate charge-current free space outside a computed field domain. The first applies to static fields (Poisson's equation), the second to radiating fields (Maxwell's equations).

I. Static Fields

When infinite, effectively charge- and current-free space surrounds the domain in which one simulates interacting charges and/or currents, appropriate boundary conditions must be imposed on the periphery of the domain, to simulate the outer void. For static fields Hockney[1] evaluated, in some of his simulations, the cylindrical harmonics of the potential created by the internal charges or gravitating masses on the periphery, while Hohl et al.[2] truncated the interaction kernel, used periodic boundary conditions and restricted charges or masses to the interior quarter (in 2D) of the computed domain.

A new scheme was developed which resembles Hockney's scheme. It assumes that a Poisson subroutine is available which returns the potentials within a domain for specified interior charges and specified peripheral potentials. These peripheral potentials are to be evaluated, prior to calling the Poisson subroutine, by applying the direct interaction kernel to the interior charges.

It might be argued that the direct interaction kernel, if used at all, could be used throughout, for calculating potentials in the interior

---

* Work done, in part, while on leave as ESRO Fellow at ESRIN, Frascati.

Simulation of Infinite Space

as well as on the periphery. This latter scheme was found uneconomical by Hockney[3] and therefore the proposed use of the direct interaction kernel on the periphery must be justified against objections on grounds of economy.

The arguments against the kernal method spply only when the number of particles is large. It is then better to solve for the potential over a grid after recording the charges (masses) in the form of s density array. We consider, therefore, the tssk of calculating the potentisls in the peripheral cells due to the array of the charges located at the centers of the internal cells. For s squsre array (in s two-dimensional simulation) of M by M cells we get $4M^3$ kernel operstions.

Since the interaction kernel is an inverse squsre root in three dimensions, a logarithm in two Csrtesian dimensions snd sn elliptic integral in R-Z geometry, pretsbulation of the kernal is essential. Even taking into account some symmetries, the storage requirements for the proposed scheme would be prohibitive in most csses. And even given a stored kernel array, the number of algebraic operations in its application would normally exceed the number of algebraic operations $(4M^2 \log_2 M)$ in the direct Poisson solving routine.

II. Cubic Interpolation

To make the scheme feasible, we propose admitting slight imperfections. In the first plsce, we only cslculate the potential st every fourth point on the boundary and fill in the remainder by cubic interpolation. If there is no charge very near the boundary, the imperfections of the boundary potentisls will not propsgate to the charges, remembering that any error pattern is attenuated by $e^{-2\pi}$ scross a distance comparable to its own period.

643

However, not only do we use cubic interpolation at the output end of the kernel, but we likewise interpolate cubically at the input, in the two (or three) dimensions of the charge array. Again, provided that there is no charge near the boundary, the errors will not be felt.

In practice, the procedure is as follows:

(1) Condense the charge array by a factor $\frac{1}{4}$ in each dimension, keeping the charge in situ at every 4th co-ordinate value and re-distributing the three intermediate charges among their nearest neighbors. This re-distribution is done in such a way as to conserve moments of the charge distribution up to, and including, cubic momenta.

(2) Propagate the effect of the contracted array of charges to every fourth point along the boundary by means of the interaction kernel.

(3) Interpolate cubically along the remainder of the boundary.

This procedure is equivalent to a rigorous full evaluation of the boundary potentials using a short table of the kernel and interpolating cubically from this table where necessary. It is inaccurate only to the extent that such cubic interpolation in each of the variables of the kernel may be inaccurate. In other words, it is sound, provided we stay away from the singularities of the kernel. These occur when cause and effect co-ordinates coincide. This means the charges must stay away from the boundaries.

Typically, we might play safe and restrict charges to only the internal three-quarters of the full domain in each dimension. In a two-dimensional square domain this means there are only $(9/16)\ M^2$ charges before contraction. Then, after contraction of the array, we now have only $(9/256)\ M^3$ kernel operations to get the short table of boundary potentials. Our original count has come down by a factor exceeding 100. The scheme is now feasible, from the points of view

644

of both operational speed and kernel storage.

The cubic interpolations and re-distributions have yet to be accounted for. These are carried out in several stages. When interpolating, one first finds the values at the mid-points between given data, using only linear interpolation: an add and a binary shift. One corrects this to cubic interpolation by adding the four nearest neighbors with weights -1/16, +1/16, +1/16, -1/16: four adds and one shift by four binary places. Having thus interpolated the mid-point values, one repeats the process to get quarter-point and three-quarter point values.

The re-distribution is carried out with exactly the same weights. Every odd-indexed charge value is re-distributed between its four nearest even-indexed neighbors, and subsequently the charges with twice-odd index are similarly re-distributed among neighbors with indices divisible by four. This is done in each dimension.

Since re-distribution and interpolation employ only adds and shifts, with no table look-ups, they are extremely fast and do not impede execution significantly.

Example

The whole scheme was put to the test in r-z geometry. An r-z Poisson solver was available for a 64 by 128 grid, the long dimension being in the axial direction. The periphery consisted of two lines of 65 grid points radially and one line of 127 points axially. This was reduced to two lines of 17 points and one line of 31 points for the interaction calculation.

Internally, an original array of 49 by 97 charge points was reduced to 13 by 25. The kernel $K(r_1, r_2, |z_1 - z_2|)$, being symmetric in r_1 and r_2, required only $29 \times 17 \times (17+1)/2 = 4437$ locations, and even some of these remained unused so as to become available for other purposes.

645

The number of multiplications in the kernel operation was 13 x 25 x (2 x 17+31) = 21125, rather less than the number of multiplications in an r-z Poisson solver over a 64 x 128 grid. This was borne out by timing of the runs. Even including the charge-array contraction and the interpolation, the subroutine for establishing the peripheral potentials took less time than solving Poisson's equation.

The precision was tested by calculating the potential due to a single ring of charge and moving this ring from positions requiring re-distribution to positions which were subjected to the kernel operation directly.

To the overall accuracy available (approximately sixteen bits) the potential pattern was insensitive to ring position - in fact it agreed with the direct kernel values everywhere.

From these tests one feels encouraged to reduce the "no mans land" between the charge and the outer boundary. Probably a zone of four meshes would give acceptable results in general.

III. Radiating Fields

Maxwell's equations,

$$\frac{1}{c} \frac{\partial E_x}{\partial t} = \frac{\partial B_z}{\partial y} - \frac{\partial B_y}{\partial z} - 4\pi J_x \tag{1}$$

$$\frac{1}{c} \frac{\partial B_x}{\partial t} = \frac{\partial E_y}{\partial z} - \frac{\partial E_z}{\partial y} \tag{2}$$

$$(x,y,z \text{ cyclic})$$

can be programmed sequentially and to central-difference precision with no sophisticated algorithms, since these equations, unlike Poisson's, are hyperbolic.[4] Fourier transforms are not needed.

Difficulties arise only over advancing field values at the boundary

646

of the domain covered by such sequential computations. The "causal" (retarded) solution is automatically built up in the interior, and we consider the case where no exterior currents are flowing, so that there should be no incoming fields. Then we must program the Sommerfeld radiation condition at the boundary: there should be outgoing waves only.

This condition is itself formulated in "wave" terminology and therefore it will be necessary to diagnose wave structure in our fields although the algorithm for calculating the interior fields makes no reference to waves. It does not seem possible to formulate the radiation condition as a purely local condition - some linear relation between field components at neighboring points.

We have studied this problem for a simple geometry, in the first place, namely the "periodic slab". The domain for computations lies between $x = -x_o$ and $x = x_o$ say, while in y and z it is infinitely extended, with a strict periodicity condition on currents and fields in both y and z. This is the problem encountered in sheet pinch simulations.[5]

The periodicity of the fields eliminates boundary problems in the y and z dimensions. In x, we have the condition that for $x \geq x_o$ the fields should travel towards $+\infty$ and for $x \leq -x_o$ towards $-\infty$. In order to formulate this as a wave condition, we must Fourier transform the fields at $x = x_o$ and $x = -x_o$ (but not in the interior) in both y and z. The periodicity comes in useful at this point.

A record must be kept of each transform for all times, but since it is only called in once each time step, external storage is satisfactory.

Without going into the details of what happens to each of the six field components, we present here only the general formula for advancing a quantity A (such as a magnetic vector potential) that solves the free-space wave equation. In the region $x \geq x_o$ beyond the computer-handled domain it can be advanced on the boundary $x = x_o$ in accordance with

$$A(t) = -c \int_{-\infty}^{t} \left(\frac{\partial A}{\partial x}\right)_{t'} J_o[\omega_o(t-t')] \, dt' \tag{3}$$

or

$$\frac{1}{c}\frac{\partial A}{\partial t} = -\frac{\partial A}{\partial x} + \omega_o \int_{-\infty}^{t} \left(\frac{\partial A}{\partial x}\right)_{t'} J_1[\omega_o(t-t')] \, dt' \tag{4}$$

where $\omega_o^2 = c^2 (k_y^2 + k_z^2)$. Proofs will be found in the litersture.[6,7]

The second of these formulas is probsbly more appropriate: since $J_1(0) = 0$, tbe "present" is separsted in the first term from the "past" in tbe second term. The formulas are plausible: by Huygens's principle, signals are reflected back into tbe slab from outside, there should be a periodicity associated with the wavelength, and a weak geometric sttenuation as indicsted by the inverse square-root asymptotic decay of the Bessel functions. Unfortunat·ly, this sttenuation is too weak for it to become practically permissible to write off the earliest information on the Fourier components.

These formulas for advancing boundary conditions are presented here for tbeir potential use: tbey have not yet been implemented in ·any actual programs. Simulations of the sheet pincb were done, hitherto, witb a more primitive approximate boundary condition[5] amounting to taking only the first term in (4).

648

Simulation of Infinite Space

References

1. R. W. Hockney, Astrophya. J. 150, 797 (1967).

2. P. Hohl and R. W. Hockney, "A Computer Model for Diaka of Stara," J. Comp. Phys. 4, 306 (1969).

3. R. W. Hockney, "The Potential Calculation and Some Applicationa," Methoda of Computational Phyaica (ed. B. Alder), 9, 135 (Acad. Presa, 1970).

4. O. Buneman, "Fast Numerical Procedurea for Computer Experimenta on Relativiatic Plaamas," Relativiatic Plasmas (eds. Buneman and Pardo), 205 (Benjamin, Inc., 1968).

5. R. D. Burn, "Computer Experimenta on Sheet Pinch Stability," Plaama Phyaics, 12, 331 (1970).

6. J. A. Stratton, "Electromagnetic Theory," ch. 5, problem 18 (McGraw Hill, 1941).

7. R. E. Collin, "Field Theory of Guided Waves," ch. 7.4 (McGraw Hill, 1960).

Coping with the Singularity at the Axis in R-Z Geometry

O. Buneman*
E. E. Department
Stanford University
Stanford, California

In r-z geometry there is a centrifugal acceleration L^2/r^3 acting on particles with angular momentum L per unit mass. The numerical problems arising from this inverse cube singularity are eased by working with $s \equiv r^2$ as a variable: Only a simple inverse singularity remains in the equation for d^2s/dt^2. A time-symmetric algorithm for advancing particles in s and z was found which gives exact orbits in a parabolic bowl ($\emptyset \propto s + z^2$). The finite-difference Poisson equation is also simplified by going to s as radial variable. The domain near the axis is weighted according to its volume and the finite-difference recurrence relation for the Fourier harmonics can be terminated on the axis in a convenient manner.

I. Canonical Angular Momentum and Effective Potential

R-Z geometry is popular for simulations, not only when axisymmetric boundaries call for it, but also when a three-dimensionally bounded system is to be simulated by means of only two space variables ("two-and-a half dimensional simulation"). This is achieved by imposing axial symmetry, but axi-symmetry does not mean that motion about the axis is ignored. All particles can possess some angular momentum about the axis. However, for every particle with given r, θ, z, $\dot{r}$, $\dot{\theta}$, $\dot{z}$ there are others with the same r, z, $\dot{r}$, $\dot{\theta}$, $\dot{z}$ but different θ, and their distribution in θ is uniform.

Singularity in R-Z Geometry

As a result, particles can be grouped into rings of charge. We trace these rings in r and z. We record $\dot{r}$, $\dot{z}$ and we keep a tag on the value of the conserved angular momentum $r^2\dot\theta$ per unit mass. Owing to the axial symmetry of the charges, there will be axial symmetry in the fields and hence the angular momentum is conserved. It can therefore be stored as the first few bits of the particle index.

In the presence of an axisymmetric magnetic field (which can be derived from a magnetic vector potential with only a θ-component, A_θ), it is the "canonical" angular momentum per unit mass,

$$\Lambda = r^2\dot\theta - (e/m)rA_\theta(r,z) ,\qquad (1)$$

which is conserved.[1] The combination of axisymmetric electric and magnetic fields, static or slowly varying, leads to the dynamical equations for electrons:

$$\ddot{r} = \partial\Phi^1/\partial r , \quad \ddot{z} = \partial\Phi^1/\partial z \qquad (2)$$

where

$$\Phi^1 = \Phi - \frac{1}{2}\left(A_\theta + \Lambda/r\right)^2 ,\qquad (3)$$

after normalizing away the mass and charge of the electrons.

Since $2\pi rA_\theta$ is the magnetic flux through a loop of radius r, and since this flux is of the form $\pi B_{axis}r^2 +$ higher even powers of r, the difference between the effective potential Φ^1 and the electric potential Φ is an even function of r, the lowest power being $\Lambda^2/2r^2$. Moreover, the charge density near the axis should be a regular power series in x and y for each z. If it is to be independent of θ, it must be developable in powers of $(x^2 + y^2)$. Thus the entire potential is an even function of r.

651

II. Use of the Square of the Radius

Equation (2) show that the radial acceleration becomes infinite like Λ^2/r^3 near the axis. This leads to no end of numerical trouble and since

$$a \equiv r^2 = x^2 + y^2 \tag{4}$$

might be a better variable against which to tabulate the potential, one is motivated to write the dynamical equations in terms of s. In a pure electric field this leads to:

$$\ddot{s} = 4s\,\frac{\partial\Phi}{\partial s} + \frac{4\Lambda^2 + \dot{s}^2}{2a}$$

and one observes with gratification that the centrifugal force, Λ^2/r^3, has been changed from an inverse cube singularity to the much milder simple inverse singularity. A time-symmetric[2] finite-difference version of the dynamical equation for a results from interpreting $\dot{s}^2$ as $\dot{s}_{new}\dot{s}_{old}$:

$$\Delta s_{new} = \Delta a_{intermediate} + \frac{\Delta s_{old}\cdot\Delta s_{intermediate} + (2\Lambda\Delta t)^2}{2s - \Delta s_{old}} \tag{6}$$

with

$$\Delta s_{intermediate} = \Delta a_{old} + 4(\Delta t)^2 s\,\partial\Phi/\partial s \tag{7}$$

and this equation has been programmed into the subroutine for advancing particles, "ADVA". (The finite difference equation for advancing z is trivial.)

Subroutine "ADVA" has been tested for a parabolic bowl potential, $\Phi = -z^2 - s$. In this potential each Cartesian coordinate performs

simple harmonic motion and hence s should be harmonic with twice the
frequency. Indeed, one checks that the finite difference version above
possesses exact sinusoidal solutions for a potential which is linear in
s. The computer reproduces these solutions to machine accuracy and so
all is well.

III. The Solution of Poisson's Equation

Since tabulation of potentials versus s is required rather than tabu-
lation versus r, one would naturally solve Poisson's equation in s,
namely:

$$4s \frac{\partial^2 \phi}{\partial s^2} + 4 \frac{\partial \phi}{\partial s} + \frac{\partial^2 \phi}{\partial z^2} = - \frac{\rho}{\epsilon_o} \quad . \tag{8}$$

If, in the display of the grid, we think of radius or s as increasing
from left to right, while z increases down the page from top to bottom,
the finite-difference version of Poisson's equation in s becomes:

$$\frac{(4s-2\Delta s)\phi_{left} - 8s\phi_{centre} + (4s+2\Delta s)\phi_{right}}{\Delta s^2}$$

$$+ \frac{\phi_{below} - 2\phi_{centre} + \phi_{above}}{\Delta z^2} = - \frac{\rho}{\epsilon_o} \tag{9}$$

For the harmonics[3] which go like $\exp(\pm ikz)$ the second term on the left
becomes

$$\frac{-2(1-\cos k\Delta z)}{\Delta z^2} \phi_{centre} \quad .$$

Multiplying the finite difference equation by $\Delta s \Delta z / 2$ one obtains the
recurrence relation

$$(2n-1)\phi_{n-1} - (4n + \frac{\Delta s}{\Delta z}(1-\cos k\Delta z))\phi_n + (2n+1)\phi_{n+1} = -q_n \qquad (10)$$

where $n = s/\Delta s$ and q_n is the (suitably normalized) charge in the nth radial cell, Fourier-transformed in z. (Notice that here is another advantage of "s" over "r", in that $\Delta s = 2r\Delta r$ contains the factor r necessary for converting point charge density to <u>ring</u> charge density!) A value $\Delta s/\Delta z = 64$ was used in tests and production runs, giving satisfactory resolution near the axis as well as away from it.

To find the conditions on the axis, $n = 0$, we postulate that the finite difference form of Poisson's equation shall give correct answers for potentials which consist of low powers of z multiplied by low powers of s. One then obtains, for the start of the recurrence relation:
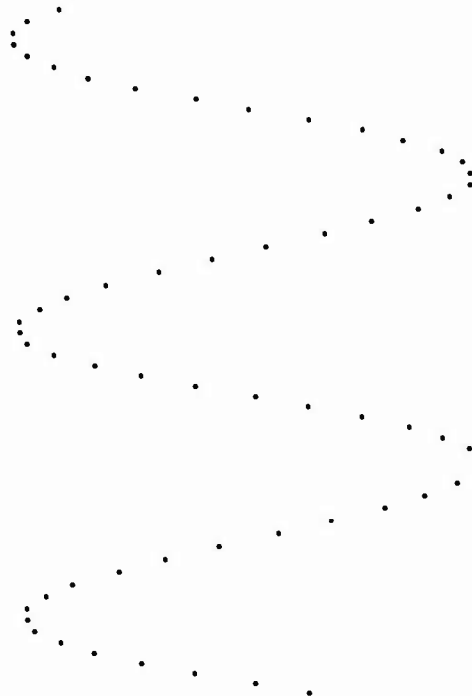
Singularity in R-Z Geometry

$$-(2 + \frac{\Delta s}{\Delta z} (1-\cos k\Delta z))\phi_0 + \phi_1 = -2q_0 \tag{11}$$

where q_0 is the charge in the interval $0 \leq s \leq \Delta s/2$.

The tridiagonal system (10), (11) should be terminated at the outer boundary in accordance with the conditions prevailing there. It can then be solved by Gauss elimination, equivalent to an outward and inward (in that order) march. Since the coefficients are variable, this is more economical than solving by "cyclic reduction", the scheme explained by Hockney.[4]

Both the particle mover "ADVA", and the s-z Poisson solver described here, were used successfully in a simulation of the photoelectron sheath which surrounds a satellite lit by the sun on one side.[5]

References

1. See H. Goldstein, Classical Mechanics , ch. 2.6 (Addison Wesley, 1959).

2. "Time-Reversible Difference Procedures" by O. Buneman, J. of Comp. Phys. 1, 517 (1967).

3. In test and production runs, we used the fast Fourier-transform algorithm of J. W. Cooley and J. W. Tukey, Math. Comp. 19, 297 (1965).

4. "The Potential Calculation and Some Application", Methods in Computational Physics, 9, Academic Press, New York and London, 1969, by R. . Hockney.

5. See ESRIN Internal Note No. 92, June 1970, ESRIN, Frascati, Italy.

Quasi Three-Dimensional Particle Code for Simulating an Anisotropic Plasma

R. N. Carlile
Department of Electrical Engineering
University of Arizona
Tucson, Arizona

ABSTRACT

This paper describes a 2-1/2 dimensional simulation code in which the coulomb force on a simulation rod is two dimensional while the lorentz force due to an external uniform magnetic field is three dimensional. A method for moving the particles is described in which new velocities and positions can, in principle, be calculated which are accurate through fourth order in the time step. Finally, the linear behavior of the code is examined in which it is found that Bernstein modes are the normal modes of the system.

A. Introduction

This paper describes a two-dimensional particle code, which is an extension of that discussed by Kruer and Dawson[1], in which particles are simulated by extended charged rods constrained to be parallel to the z axis, but otherwise free to move, so that each rod is completely described by the coordinates (x, y, w_x, w_y, w_z). This situation is depicted in Fig. 1. The force per unit length in the z direction which the i-th rod may experience consists of the self-consistent coulomb force,
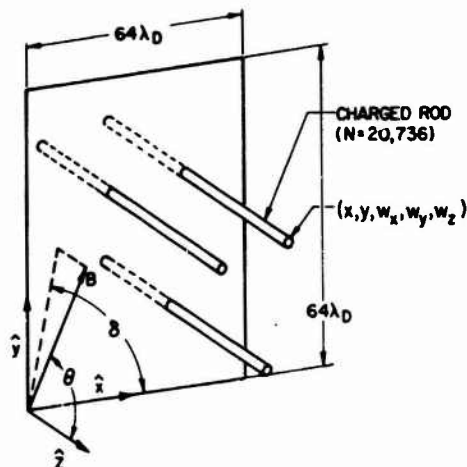
Quasi 3D Particle Code

Fig. 1. Basic cell for simulation code. N is number of rods in the basic cell.

$\epsilon_i \overline{F}_i$, $\epsilon_i = 1$ (ions) or, $- 1$ (electrons), and a lorentz force due to an externally imposed homogeneous magnetic field $\overline{B}$ of any desired three-dimensional orientation. Periodic boundary conditions are used. This code is ideally suited to simulate plasmas whose behavior can be described by electrostatic waves with coplanar wave numbers.

B. Moving the Particles

Of particular interest is the way that the particles are advanced in time. The equation of motion of the i-th rod is

$$n_o \frac{m_i}{m_e} m_e \ddot{\overline{r}}_i = \epsilon_i \overline{F}_i + n_o e \epsilon_i \overline{w}_i \times \overline{B} \qquad (1)$$

where $n_o m_i$ and $n_o e$ are the mass and absolute charge per unit length of the rod (n_o is the number of real electrons or ions associated with a unit length of the rod). In (1), m_i is the mass of the real particle associated with the i-th rod, either the electron mass m_e, or the ion mass. If we normalize all distances to the Debye length λ_D and times to the electron plasma frequency ω_p of the real plasma, then, for electrons, (1) becomes

657

$$\frac{d^2R}{d\tau^2} = \frac{dV}{d\tau} = -E + GV \qquad (2)$$

where

$$R = \begin{bmatrix} x_i/\lambda_D \\ y_i/\lambda_D \\ 0 \end{bmatrix} \quad , \quad V = \begin{bmatrix} w_{xi}/\lambda_D\omega_p \\ w_{yi}/\lambda_D\omega_p \\ w_{zi}/\lambda_D\omega_p \end{bmatrix} \quad ,$$

$$E = \begin{bmatrix} F_{xi}/n_o m_e \omega_p^2 \lambda_D \\ F_{yi}/n_o m_e \omega_p^2 \lambda_D \\ 0 \end{bmatrix} \quad , \quad G = \Omega \begin{bmatrix} 0 & -\cos\theta & \sin\theta\sin\delta \\ \cos\theta & 0 & -\sin\theta\cos\delta \\ -\sin\theta\sin\delta & \sin\theta\cos\delta & 0 \end{bmatrix} \quad ,$$

$$\Omega = \frac{eB/m_e}{\omega_p} \quad , \qquad \tau = \omega_p t \quad . \qquad (3)$$

Equation (2) is the normalized equation of motion of a particular rod; we have suppressed the subscript i. The view is now taken that all the dynamical variables vary continuously in time. One then makes a Taylor expansion of the velocity of V about the time $\tau_n = n\Delta\tau$, and of the position R about $\tau_{n+\alpha} = (n + \alpha)\Delta\tau$, where $\Delta\tau$ is a finite increment in time, the time step, and $0 \le \alpha \le 1$.

1. Stepping the rod velocity

In storage after the n-th iteration is the rod velocity $V(\tau_n)$ at τ_n and the position $R(\tau_{n+\alpha})$ and information such that the coulomb force $E(\tau_{n+\alpha})$ can be calculated on our typical rod, at $\tau_{n+\alpha}$. We now make a Taylor series expansion of V about τ_n and evaluate it at τ_{n+1}.

$$V(\tau_{n+1}) = V(\tau_n) + V'(\tau_n)\Delta\tau + V''(\tau_n) \frac{(\Delta\tau)^2}{2!} + \dots \qquad (4)$$

and

$$V^{(m)}(\tau_n) = - E^{(m-1)}(\tau_n) - GE^{(m-2)}(\tau_n) - G^2 E^{(m-3)}(\tau_n)$$

$$- \ldots - G^{m-1} E(\tau_n) + G^m V(\tau_n) \qquad (5)$$

where $V^{(m)} = d^m V/d\tau^m$; a similar convention will be used to denote derivatives of other dynamical variables. In obtaining (5), we have used (2) successively. Now, we have E in storage for $\tau_{n+\alpha}$, but not for τ_n. Therefore, we make a Taylor series expansion of E about $\tau_{n+\alpha}$ and evaluate it at τ_n:

$$E^{(m)}(\tau_n) = E^{(m)}(\tau_{n+\alpha}) + E^{(m+1)}(\tau_{n+\alpha})(-\alpha\Delta\tau) + E^{(m+2)}(\tau_{n+\alpha}) \frac{(-\alpha\Delta\tau)^2}{2!}$$

$$+ \ldots \qquad (6)$$

When (6) is substituted into (5), we obtain Taylor coefficients which are functions of $V(\tau_n)$, $E(\tau_{n+\alpha})$ and derivatives of E at $\tau_{n+\alpha}$. The latter we do not have in storage. However, if we choose $\alpha = 1/2$, we can make the derivatives disappear from all coefficients up to and including $\Delta\tau^2$. We then have, for $\alpha = 1/2$,

$$V(\tau_{n+1}) = \left[\sum_{n=o}^{\infty} (\Delta\tau G)^n / n! \right] V(\tau_n) - \Delta\tau \left[\sum_{n=1}^{\infty} (\Delta\tau G)^{n-1} / n! \right] E(\tau_{n+1/2})$$

$$+ \Delta\tau^3 \left[\frac{1}{12} GE'(\tau_{n+1/2}) - \frac{1}{24} E''(\tau_{n+1/2}) \right]$$

$$+ \Delta\tau^4 \left[\frac{1}{24} G^2 E'(\tau_{n+1/2}) - \frac{1}{48} GE''(\tau_{n+1/2}) \right] + \ldots$$

$$(7)$$

The eigenvalues of G are 0, $\pm j$, $j = \sqrt{-1}$. One can then show that the first operator in the brackets in the first line of (7), L, can be written[2] as a second order polynomial of G:

$$L = e^{\Delta\tau\,G} = I + \sin\Delta\tau\,G + (1-\cos\Delta\tau)\,G^2$$

The adjoint (transpose) of this operator is equal to its inverse, so L is unitary. If $E = 0$, this property would guarantee that the kinetic energy of a rod would be exactly conserved.

The second operator in the first line of (7) can also be written as a second order polynomial of G. We have finally,

$$
\begin{aligned}
V(\tau_{n+1}) = &\, [I + \sin\Delta\tau\,G + (1 - \cos\Delta\tau)\,G^2]\,V(\tau_n) \\
&+ [- \Delta\tau + (1-\cos\Delta\tau)\,G - (\Delta\tau - \sin\Delta\tau)\,G^2]\,E(\tau_{n+1/2}) \\
&+ \Delta\tau^3\left[\frac{1}{12}\,GE'\,(\tau_{n+1/2}) - \frac{1}{24}\,E''\,(\tau_{n+1/2})\right] \\
&+ \Delta\tau^4\left[\frac{1}{24}\,G^2E'(\tau_{n+1/2}) - \frac{1}{48}\,GE''\,(\tau_{n+1/2})\right] + \dots
\end{aligned}
$$

$$(8)$$

2. Stepping the rod position

After the velocity $V(\tau_n)$ has been transformed according to (8), the new velocity $V(\tau_{n+1})$ has replaced it in storage. We now make a Taylor expansion of R about $\tau_{n+1/2}$ and evaluate it at $\tau_{n+3/2}$. Noting that $V = R'$ and using (2), we can express the coefficients of this series in terms of $V(\tau_{n+1})$ and $E(\tau_{n+1/2})$ and derivatives of E at $\tau_{n+1/2}$ as follows:

$$
\begin{aligned}
R(\tau_{n+3/2}) = &\, R(\tau_{n+1/2}) + \Delta\tau V(\tau_{n+1}) \\
&+ \Delta\tau^3\left[\frac{1}{24}\,(G^2V(\tau_{n+1}) - GE(\tau_{n+1/2})) - \frac{13}{24}\,E'(\tau_{n+1/2})\right] \\
&- \Delta\tau^4\left[\frac{1}{16}\,GE'(\tau_{n+1/2}) + \frac{1}{24}\,E''(\tau_{n+1/2})\right] + \dots
\end{aligned}
$$

$$(9)$$

Note that R is a two element vector. In (9), V should be reduced to a two element vector by eliminating the z component, and G and G^2 should

be made into 2 by 2 matrices by abandoning the third row and column from each.

In examining (8) and (9), we see that if we do not have available derivatives of E, the error in computing $V(\tau_{n+1})$ and $R(\tau_{n+1/2})$ is of order $\Delta\tau^3$. Further, the largest error comes from E'. If we are computing E by the nearest-grid-point approximation, then if we are willing to store $E(\tau_{n-1/2})$, we can compute $E'(\tau_{n+1/2})$. If there are M grid points, this would require 2M additional words of storage. For this modest increase in storage, we can, in principle, compute the co-efficient of $\Delta\tau^3$ for R. If in addition, we also store $E(\tau_{n-3/2})$, an additional 2M words, we can compute $E''(\tau_{n+1/2})$ and thus compute the coefficients of $\Delta\tau^3$ and $\Delta\tau^4$ for both V and R! Although this additional storage is not excessive, it is doubtful if it is worthwhile to do this, because computing E from Poisson's equation at the position of the rod may cause errors much greater than those obtained by neglecting the co-efficient of $\Delta\tau^3$ and $\Delta\tau^4$.

Equations (8) and (9) are exact up to and including terms of order $\Delta\tau^4$. The role of the quantities E' and E", normally not retained in storage, in producing an error in $V(\tau_{n+1})$ and $R(\tau_{n+1/2})$ is clearly shown. If E=0, kinetic energy of the rods is conserved.

C. Linear behavior of the code

The rods in the code described in the introduction have been stepped according to (8) and (9) where all terms of higher order than $\Delta\tau^2$ have been eliminated. The size of the extended particle was chosen so that the ratio of collision frequency to ω_p is approximately .01.

The number N of simulation rods in the "basic cell" is 5184 and the number of rods per Debye square is about 5. The dipole term in the Dawson-Kruer Code[1] was retained, in dictating a precise determination from Poisson's equation of E at the rod. Ion rods were held fixed.

The total energy of the system, electric plus kinetic, is shown in Fig. 2 as a function of time for various time steps. It is seen that for $\tau = \omega_p t < 25$, energy was conserved quite precisely for time steps up to 0.20. For $\Delta\tau = \omega_p \Delta t = 0.20$, the total energy changed by one part in 1535 over 125 iterations ($\tau = 25$). For $\Delta\tau = .1$, the energy changed by less than one part in 15,000 over $0 < \tau < 25$.

The normal modes with wave vectors in the plane perpendicular to a uniform magnetic field in a homogeneous plasma are Bernstein modes[3]. Dispersion curves for these modes are shown as the solid curves in Fig. 3. These modes are not subject to Landau damping, and will only be attenuated by collisional damping. In our simulation plasma, they should be present. As in a real unperturbed plasma, they will be present at low power level, their amplitude being determined by equilibrium between the excitation process of Cerenkov radiation and collisional damping.

Because of the periodic boundary conditions, the wave vectors of waves which can propagate in the simulation plasma are discrete. Arbitrarily selecting a wave number $\bar{k}_\perp$ which is one of the discrete set, and which is perpendicular to the magnetic field, we let the code run until $\tau = T$. We sampled the spacial Fourier amplitude $A_{k_\perp}$ belonging to $\bar{k}$ every five time steps for $\Delta\tau = 0.20$. We thus have this amplitude as a function of real time $A_{k_\perp}(\tau)$. We correlated this amplitude to
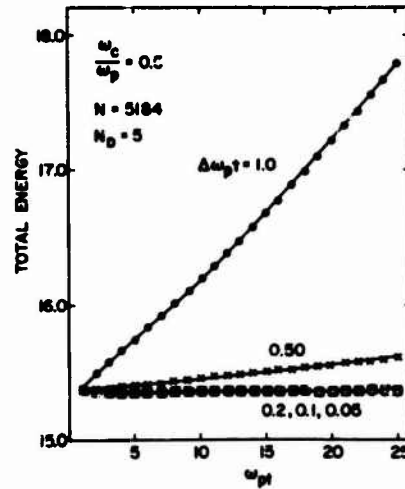
Fig. 2. Test for conservation of energy. Total energy is sum of kinetic energy or rods plus energy stored in the electric field. ω_c is the cyclotron frequency and N_D is the number of rods per Debye square. $\Delta\omega_p t = \Delta\tau$, the time step.
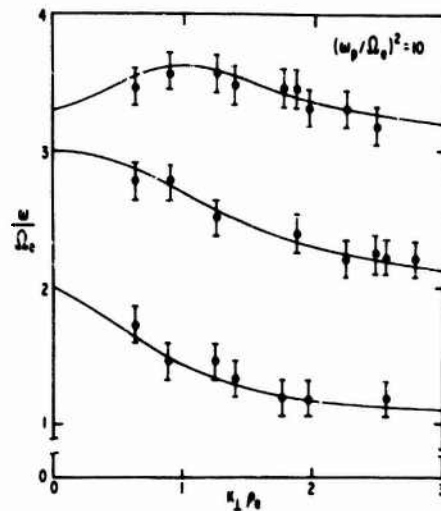

Fig. 3. Dispersion curves for Bernstein modes (solid curves) and "experimental data" obtained from the simulation code (dots). Ω_e is the cyclotron frequency. $k_\perp$ is the wave number and ρ_e is the Larmor electron radius.

663

suppress incoherent noise, then computed the frequency spectrum of the correlated $A_{k_\perp}(\tau)$, where the fundamental frequency is $1/2\ T/2\pi \equiv \omega_o/\omega_p$. One could clearly discern major peaks in the spectrum corresponding to frequency components coherent over the time T. The frequencies of these peaks are shown as the dots in Fig. 3. The error bars represent an error of $\pm\omega_o/\omega_p$.

The coherent signals evidentally are Bernstein modes because of the good fit with the dispersion curves. The data in Fig. 3 were obtained for the magnetic field along the z axis, i.e., $\theta = 0$ in Fig. 1. However, almost identical data was obtained with the magnetic field along the x axis and $\bar{k}_\perp$ chosen along the y axis.

D. Acknowledgment

REFERENCES

1. Kruer, W. L., and J. M. Dawson, Bull. Am. Phys. Soc. 14, 1025 (1969).

2. Friedman, B. Principles and Techniques of Applied Mathematics, J. Wiley, 1956, p. 121.

3. Bernstein, I. B., Phys. Rev., 109, 10 (1958).

Numerical Techniques Applied to the Computation of the Dispersion Relation for Perpendicularly Propagating Cyclotron Harmonic Waves

Jeno Gazdag
IBM Scientific Center
Palo Alto, California

Abstract

A computer simulation study of the dispersion relations for Cyclotron Harmonic Waves (CHW) is presented. A two-dimensional particle model is used to simulate CHW oscillations in an infinite uniform Maxwellian plasma in a plane perpendicular to an externally applied constant magnetic field. The resonant frequencies of the computer plasma are compared with those predicted by the linear approximation theory for small perturbations. The numerical methods used are known as the Nearest Grid Point method and the Particle in Cell method. The difference in these methods do not appear to affect the results significantly except for the ability of the computer plasma to conserve energy. The operation of smoothing the electric field is also considered as a means to better energy conservation in the computer plasma.

1. Introduction

A warm, uniform magnetoplasma can support longitudinal electron waves. The propagation of these waves is restricted to passbands associated with the harmonics of the electron cyclotron frequency. Because of this they have been called Cyclotron Harmonic Waves

(CHW). These waves are characterized by phase velocities slow
compared with the velocity of light and have parallel propagation and
electric field vectors $(k||E)$. They were studied by several investi-
gators in the 1950's. A comprehensive description of the subject was
given by Bernstein in 1958 [1]. The existence of these waves has
been confirmed by experiments [2,3]. A number of experimental results
which can be explained in terms of this type of wave motion are dis-
cussed by Crawford [4,5].

An alternative means of experimenting is offered by the simulation
of the plasma on a digital computer [6,10]. A "computer experiment"
differs from a typical computation of a theoretical result in that
instead of evaluating mathematical expressions which describe some
laws of nature, we make the computer simulate the physical system.
The plasma is modeled by a large number $(10^3 - 10^5)$ of particles.
We attribute individuality to the particles by following them in space
and time. Their dynamic behavior is governed by Newton's law of
motion and Maxwell's field equations. This approach is generally
referred to as the "Lagrangian" model. A computer model of this type
is used much the same way as a real experiment. The model gives
a time-dependent simulation and macroscopic averages are evaluated
when measurements are required. Thus, we test for instability, for
example, by observing whether or not certain disturbances grow rather
than finding analytically complex values of ι for an assumed time
dependence $\exp(i\iota t)$.

The work reported in this paper is concerned mainly with the computer
simulation study of the dispersion relations for cyclotron harmonic
waves propagating perpendicularly to the externally applied, constant
magnetic field $(k \perp B)$. We compute the dispersion relation for such
oscillations from the time responses of the computer plasma. Periodic
boundary conditions are used to simulate an infinite uniform Maxwellian
plasma for which the dispersion relations have been derived through
small-signal linear approximation theory [1,4,5]. We use these
analytic results to estimate the accuracy of the dispersion relations

obtained from the computer simulations. We find excellent agreement between the results of the computer simulation and those predicted by the small-signal theory.

The numerical simulation techniques which we use are known as the Nearest Grid Point and the Particle in Cell methods. The most significant difference between these methods is found in their energy conserving properties and the speed of computation. The idea of smoothing the electric field is considered as another means of achieving better energy conservation in the computer plasma.

The main objective of this study has been, in general, to find out the requirements for reliable plasma simulation and to learn about the limitations of the computer plasma model. The work reported here should be regarded as a prelude to an undertaking where the long-term goal is to study problems which do not lend themselves to analytical treatment. It is hoped that the simulation of linear dispersion relations will serve as a stepping stone toward more practical problems complicated by nonlinearities, inhomogeneities and finite boundaries.

The organization of the paper is as follows. Section 2 describes the computer plasma model. Section 3 deals with the numerical experiment. The discussion of the results is given in Section 4, here we make comparisons with the results of the small-signal linear theory. Section 5 is the summary of our experience using different methods. Section 6 concludes the paper.

2. Computational Models

2.1 The Purpose of Particle Models

Particle models [6-13] are attempts to simulate the behavior of a fully ionized plasma whose collisionless approximation satisfies the collisionless Boltzmann equation with the Lorentz force

$$\frac{\partial f_s}{\partial t} + \underset{\sim}{v} \cdot \frac{\partial f_s}{\partial \underset{\sim}{r}} + \frac{q_s}{m_s} \left(\underset{\sim}{E} + \frac{\underset{\sim}{v}}{c} \times \underset{\sim}{B} \right) \cdot \frac{\partial f_s}{\partial \underset{\sim}{v}} = 0 \quad . \tag{1}$$

Eq. (1) describes the rate of change of the distribution functions f_s for particles of various types s, charge q_s, mass m_s and velocity $\underset{\sim}{v}$ in the plasma. $\underset{\sim}{E}$ and $\underset{\sim}{B}$ are obtained from Maxwell's equations with the definitions of charge and current densities as

$$\rho = \sum_s q_s \int d^3 \nu\, f_s$$

$$\underset{\sim}{I} = \sum_s q_s \int d^3 \nu\, \underset{\sim}{v}\, f_s \tag{2}$$

In the commonly used models the simulation particles are assigned time-varying velocities as well as positions. The motion of the individual particle is obtained by means of the Newton–Lorentz equation,

$$\frac{d\underset{\sim}{v}}{dt} = \frac{q}{m} \left(\underset{\sim}{E} + \frac{\underset{\sim}{v}}{c} \times \underset{\sim}{B} \right) \tag{3}$$

The magnetic field B is the externally applied field. The electric field $\underset{\sim}{E}$ is obtained from the electric charge density by solving the field equation

$$\nabla \cdot \underset{\sim}{E} = 4\pi \rho \tag{4}$$

The particle velocities $\underset{\sim}{v}$ and positions $\underset{\sim}{r}$ are computed as

$$\underset{\sim}{v}_{+\frac{1}{2}} = \underset{\sim}{v}_{-\frac{1}{2}} + \left(\frac{q}{m} \right) \left\{ \underset{\sim}{E} + \frac{\underset{\sim}{v}_o}{c} \times \underset{\sim}{B} \right\} \Delta t$$

$$\underset{\sim}{v}_o = \left(\underset{\sim}{v}_{+\frac{1}{2}} + \underset{\sim}{v}_{-\frac{1}{2}} \right) / 2 \tag{5}$$

$$\underset{\sim}{r}_{+1} = \underset{\sim}{r}_o + \underset{\sim}{v}_{+\frac{1}{2}} \Delta t$$

The subscripts in Eq. (5) signify time in unit of Δt. If the particle positions used in computing the electric field $\underline{E}$ correspond to $t = 0$ values, then the velocities stored with them are those at $t = -\Delta t/2$, where Δt is the time step. The new velocity is computed at $t = +\Delta t/2$. This difference scheme has the very desirable property that it is time reversible [8,14].

2.2   Differences in Particle Models

The most commonly used variations of particle models are the "Nearest Grid Point" or NGP, the "Cloud in Cell" or CIC and the "Particle in Cell" or PIC. The difference between these models lies in the method of computing the electric field $\underline{E}$ over an Eulerian grid from the charge distribution defined by the particle positions. In the NGP model [7] the whole charge of the particle is associated with only one, the nearest grid point. Similarly the field acting on the particle is assumed to be that computed at the same grid point. In the PIC method [8] the charge of any particle is shared by the four surrounding grid points. The amount of charge associated with the grids is determined by the area weighting procedure which is bilinear interpolation. The field acting on the charge is computed from the values at the four nearest grid points by using the same bilinear interpolation. In the CIC model [9] the particle is regarded as a cloud of finite extent. The charge of the cloud assigned to several points of the spatial grid. This is done by sharing the charges in proportion to the area of the cloud overlapping the cell centered at the grid point. The total field on the cloud is found by summing up the partial fields. The size of the cloud is arbitrary. If the cloud size in the CIC scheme is equal to the size of the cell the resulting interpolation is equivalent to that of the PIC method. The relative merits of these models were studied by Hockney [11,12]. It appears that while the NGP model requires less computation than the others, it is characterized by greater fluctuations and lack of energy conservation which can be undesirable under certain circumstances.

2.3 Description of the Computer Model Used

The computer plasma simulations described in this paper were performed on a rectangular domain of size $L_x \times L_y$. The domain is divided into 64×64 uniformly spaced grids. The grid points are thought to be centered in cells whose dimensions are the same as the grid spacing. The boundary conditions are assumed to be periodic in both the x and y coordinates. Double periodic boundary conditions permit us to solve for the electrostatic field $\underline{E}$ directly by Fourier transform methods. We do this not by solving Poisson equation

$$\nabla^2 \phi = -4\pi \, c \qquad (6)$$

for the potential ϕ followed by the computation of $\underline{E}$ from

$$\underline{E} = -\mathrm{grad}\phi \qquad (7)$$

through a finite difference scheme. In our model the partial differentiation is performed in the spatial frequency domain. This is accomplished by multiplying the Fourier coefficients of ϕ by their exact differential operator whose magnitude is proportional to the spatial frequency. At this point we have the Fourier representation of both components of the electric field vector. Thus, the electric field components may be subjected to smoothing operations independently. The smoothing which we consider in this paper is a simple suppression of the high spatial frequency components of the computed electric field. A more precise definition of the spatial filtering used is given in Section 5. The NGP and PIC models in which the electric field is subjected to the spatial filtering operation are denoted as NGP-S and PIC-S, respectively.

The plasma model allows the simulation of an arbitrary number of particles. Their initial spatial distribution is uniform over the domain so that they form an evenly spaced rectangular mesh. The initial

velocity components of the particles v_x and v_y are computed independently from each other by a Gaussian random number generator. Since the intended simulation has to do with electrostatic space-charge waves restricted to interactions which involve only electrons, the model simulates only electrons, while the ions form a rigid, uniform background.

3. Description of Experiment

3.1 Definitions

Observations are limited to a few variables obtained by some averaging either over the entire domain or over the total number of particles. With respect to the electric field and current density, we are only interested in the components directed along one, say the x-axis. Moreover, we will be observing wave motions associated with the lowest (nonzero) spatial frequency or wave number. More specifically, we are approximating

$$E(t) \cong \frac{1}{L_x L_y} \int_0^{L_x} \int_0^{L_y} E_x(x,y,t) \sin(kx) \, dx \, dy \tag{8}$$

by computing

$$E(t) = \frac{1}{64 \times 64} \sum_{j=1}^{64} \sum_{i=1}^{64} E_x(x_i, y_j, t) \sin(kx_i) \tag{9}$$

where

$$k = \frac{2\pi}{L_x} \tag{10}$$

and x_i and y_j refer to the grid points, i.e.,

$$x_i = (i + 0.5) \frac{L_x}{64}$$

671

$$y_1 = (j + 0.5)\,\frac{L_x}{64}$$

E(t) , as given by Eq. (9), is one-half of the amplitude of the sin(kx) component in the Fourier expansion of $E_x(x,y,t)$. The corresponding current density is defined as

$$I(t) = \frac{1}{L_x L_y} \sum_{\eta=1}^{\mathcal{N}} q\, v_x(\eta,t)\, \sin\left(k\,x(\eta,t)\right) \qquad (12)$$

where $v_x(\eta,t)$ and $x(\eta,t)$ refer to the ηth particle and $\mathcal{N}$ is the total number of particles whose charges are q . The kinetic energy of the system is computed from the expression

$$W_{kin}(t) = \frac{m}{2} \sum_{\eta=1}^{\mathcal{N}} \left(v_x^2(\eta,t) + v_y^2(\eta,t)\right) \qquad (13)$$

The mass of the particle m is the electron mass multiplied by the appropriate magnification ratio. The potential energy is approximated by

$$W_{pot}(t) = \frac{\Delta x\,\Delta y}{8\pi} \sum_{j=1}^{64} \sum_{i=1}^{64} \left(E_x^2(x_i, y_j, t) + E_y^2(x_i, y_j, t)\right) , \qquad (14)$$

where Δx and Δy are the cell dimensions of grid spacings.

3.2   Driving the Computer Plasma

In order to observe the resonance characteristics of the plasma it is necessary to provide some external excitation. We found that a single mode of oscillation could be excited very conveniently by applying an external electric field.

$$E_x'(x,t) = E_o \sin(kx)\sin(\omega t) \qquad (15)$$

over the domain $L_x \times L_y$. This external field is applied for 5-10 periods $\left(\frac{2\pi}{\omega}\right)$. If ω is near to some natural mode of resonance ω_r of the plasma, and assuming that conditions are favorable, the plasma keeps oscillating with frequency ω_r after the driving source (15) had been set to zero.

The dispersion relations can not be established conveniently from such a time response described above. To obtain the frequency response of the plasma it is desired to drive the plasma with a source which has a broad spectrum. The most convenient method for doing this was found to be the application of an external charge at the origin of the domain, i.e., at grid point (1,1) for the duration of one time step. This is an approximation to a delta function in space and time.

3.3 Choice of Parameters for the Computer Experiment

Working with a computer plasma we face different sort of limitations than those found in real experiments. The computer experiment is characterized by coarseness which can influence the results. In this section we define the operational parameters of the computer plasma and indicate ranges where reliable results should be expected.

For the sake of definiteness the size of the principal domain has been set to 10×10 cm^2, i.e., $L_x = L_y = 10$ cm . The cyclotron frequency

$$\omega_c = \frac{qB}{mc} \tag{16}$$

was also held constant at 10^8 rad/sec. These choices do not affect the generality of the results since all the variables of interest are expressed as multiples of ω_c . As for the value of L_x , the results obtained are valid for any wave number if the same scaling is applied to the thermal velocity of the electrons.

673

We are primarily interested in the dispersion relation for perpendicular propagation of CHW in a collisionless, homogeneous Maxwellian plasma. This relation can be expressed in the following form [4,15].

$$1 = 2 \left(\frac{\omega_p}{\omega_c} \right) \sum_{m=1}^{\infty} \frac{e^{-\lambda}}{\lambda} \frac{m^2 I_m(\lambda)}{(\omega/\omega_c)^2 - m^2} \tag{17}$$

where I_m is the modified Bessel function of the first kind, ω_p is the plasma frequency and

$$\lambda = \left(\frac{k v_t}{\omega_c} \right)^2 \quad ; \quad v_t^2 = \frac{\varkappa T}{m_e} \tag{18}$$

The proper value of the time step Δt is of considerable importance. The guiding principle in determining Δt was to allow at least $14 \Delta t$ for the period for the highest working frequency of interest. In all of the experiments aimed to obtain the spectra of the electric field and current density we used

$$\Delta t = \frac{2\pi}{\omega_c} \cdot \frac{1}{102.4} \tag{19}$$

which assures somewhat better than fourteen samples/cycle even for the 7th harmonic of ω_c. Over 1024 timesteps, this choice, Eq. (19), allows ten complete periods of a signal of frequency ω_c. Furthermore, the line spectra obtained from Fourier analysis are spaced $0.1\omega_c$ apart, a convenient value.

Another aspect of Δt that must be considered is the distance s which an electron of thermal velocity v_t travels in one time step as a function of λ. By substituting Eqs. (10) and Eq. (19) into Eq. (18) we get

$$\sqrt{\lambda} = \frac{102.4 \, v_t \Delta t}{L_x} \tag{20}$$

674

which, in view of

$$I_x = 64 \Delta x \tag{21}$$

becomes

$$\sqrt{\lambda} = \frac{1.6 v_t \Delta t}{\Delta x} \quad , \tag{22}$$

or equivalently

$$s \cong 0.625 \sqrt{\lambda} \tag{23}$$

in units of Δx . The number of Debye lengths

$$\lambda_d = \frac{v_t}{\omega_p} \tag{24}$$

per total length L_x can be expressed in terms of $\sqrt{\lambda}$, ω_p and ω_c by substituting Eqs. (18) and (10) into Eq. (24). The result is

$$\frac{L_x}{\lambda_d} = \frac{2\pi}{\sqrt{\lambda}} \cdot \left(\frac{\omega_p}{\omega_c} \right) \quad . \tag{25}$$

In the numerical experiments reported in this paper the value of $\sqrt{\lambda}$ did not exceed 3. The ratio given by Eq. (25) was always less than 2.9. Since we consider only the longest wave, Eq. (25) also represents the wavelength of the oscillations in units of Debye lengths.

4.   Discussion of Results

We performed computer experiments aimed to determine the dispersion relations whose propagation vector $\underset{\sim}{k}$ is perpendicular to the externally applied, constant magnetic field $\underset{\sim}{B}$. The plasma was excited by externally applied charge restricted to one grid point for

675

the duration of one time step. At higher plasma temperatures, however, the internal fluctuations of the plasma dominated the effect of the impulse which was intended to be sufficiently small to assure linear behavior. The length of the computer experiments were $1024\Delta t$ and $2048\Delta t$, where Δt is defined by Eq. (19).

The experimental verification of the dispersion relations is equivalent to finding the resonant frequencies of the computer plasma for given values of λ which is defined by Eq. (18). This is done by means of frequency analysis of sufficiently long records, of the electric field $E(t)$ and the current density $I(t)$ which are defined by Eq. (9) and (12).

Let $E(j\Delta t)$ and $I(j\Delta t)$, $j = 0, 1, \ldots N-1$, be the sequences representing the electric field and current density records obtained in N time steps. The finite Fourier transforms of these sequences are defined as

$$E(n\Delta\omega) = \sum_{j=0}^{N-1} E(j\Delta t) \exp(-i\, n\Delta\omega\, j\, \Delta t) \qquad (26)$$

$$I(n\Delta\omega) = \sum_{j=0}^{N-1} I(j\Delta t) \exp(-i\, n\Delta\omega\, j\, \Delta t) \qquad (27)$$

where $i = \sqrt{-1}$ and $n\Delta\omega$ is the frequency. From these complex sequences $E(n\Delta\omega)$ and $I(n\Delta\omega)$, $n = 0, 1, \ldots, N-1$, we compute the electric field spectrum $|E(n\Delta\omega)|$ and the current density spectrum $|I(n\Delta\omega)|$. Examples of these spectra are shown in Figs. 1 and 2, where $n\Delta\omega$ is replaced by ω. The number of time steps N and their length Δt determine the resolution of these spectra. This relation is expressed as

$$\Delta\omega = \frac{2\pi}{N\Delta t} \qquad (28)$$

If the value of Δt is given by Eq. (19) and $N=1024$, then $\Delta\omega = 0.1\omega_c$. For twice as long experiments, such as the ones shown in Fig. 1-b and Fig. 2-b $\Delta\omega$ becomes $0.05\omega_c$. In order to estimate the maxima
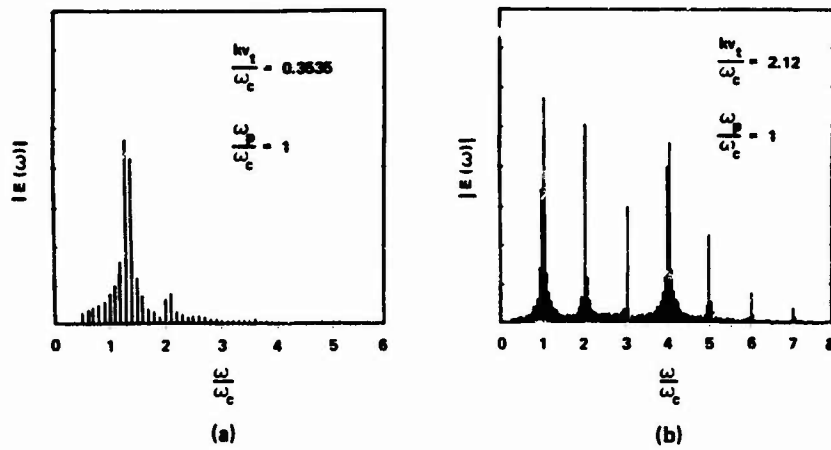
Figure 1. Examples of electric field spectra as defined by Eq. (26). The spacing between the lines is $0.1\omega_c$ in (a) and $0.05\omega_c$ in (b).
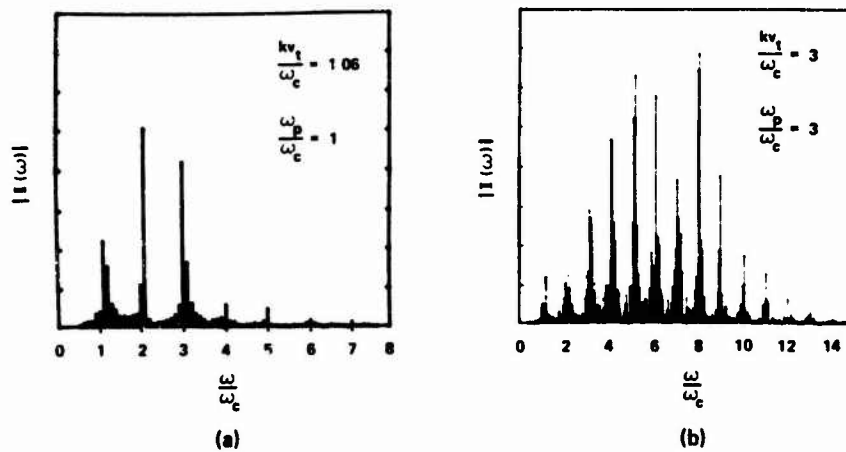

Figure 2. Examples of current density spectra as defined by Eq. (27). The spacing between the lines is $0.1\omega_c$ in (a) and $0.05\omega_c$ in (b).

677

between the lines of the spectra, we used a simple curve fitting technique. A second order parabola was fitted to the end points of three lines - the one with the maximum value and its two immediate neighbors. The frequency of the local maximum was estimated by the location of the peak of the parabola. The frequencies of these spectral peaks are given in Table I for a number of cases. These frequencies obtained from the simulation are listed under "SIM.". If no definite peaks are observed in the electric field or current spectra, the corresponding spaces in Table I were kept blank.

Table I also contains the resonant frequencies predicted from the linear theory (TH.). These were computed from the integral representation of the dispersion relation for perpendicular propagation, Eq. (17), which is

$$\sin\left(2\pi \ \frac{\omega}{\omega_c}\right) = \left(\frac{\omega_p}{\omega_c}\right)^2 \ \exp(-\lambda) \int_0^{2\pi} \sin\left(\frac{\omega}{\omega_c}\varphi\right) \ \sin\varphi \ \exp(\lambda \cos\varphi) \ d\varphi \qquad (29)$$

as given by Crawford [4].

In comparing the results of the simulation with those predicted by the theory, the greatest deviation is observed in the first mode. In shorter runs (1024 Δt) the error in the first mode was within 3% and considerable improvement is observed in the higher modes. The better agreement between the results of theory and simulation can be attributed to the smaller $\Delta\omega/\omega$ ratio in the case of the higher modes.

The simple method that we employed for estimating the resonant frequencies could not be applied to the first two modes of case 7. This spectrum is shown in Fig. 2-b. There is a lack of continuity in the spectrum which is most likely due to exceedingly high internal fluctuations of the computer plasma. We observed such "irregularities" of the spectra only in cases where the plasma frequency ω_p is greater than the electron cyclotron frequency ω_c.

Table I. Comparison of the CHW Resonant Frequencies with the Dispersion Relation.

Case	Method	$\sqrt{\lambda} = \dfrac{kv_t}{\omega_c}$	$\dfrac{\omega_p}{\omega_c}$		Mode Number						
					1	2	3	4	5	6	7
1	PIC	1.06	1	TH	1.149	2.106	3.031	4.005	5.001		
				SIM	1.125	2.094	3.008	4.00	5.00		
2*	PIC	2.12	1	TH	1.033	2.049	3.044	4.028	5.014	6.005	7.002
				SIM	1.041	2.052	3.050	4.034	5.002	6.001	7.00
3	NGP-S	0.3535	1	TH	1.357	2.038					
				SIM	1.338	2.07					
4	PIC	2.664	2	TH	1.056	2.099	3.117	4.107	5.078	6.045	7.022
				SIM	1.054	2.105	3.095	4.10	5.013	6.049	7.010
5	PIC-S	0.20	3	TH			3.210				
				SIM			3.17				
6	NGP-S	1.0	3	TH	1.475	2.676	3.571	4.113			
				SIM	1.49	2.706	3.53	4.075			
7*	NGP-S	3.0	3	TH	1.071	2.133	3.178	4.194	5.176	6.130	7.078
				SIM	-	-	3.171	4.175	5.187	6.108	7.057

* 2048 Time Steps

5. Experience with Different Methods

All computer experiments were carried out with 5776 particles. The wave number k and the electron cyclotron frequency ω_c were kept constant. Changes were introduced by varying the initial thermal velocity v_t and the plasma frequency ω_p . The latter was accomplished by assigning the proper magnification ratio to the particles.

Most of the experiments were performed by using the PIC method. We used the NGP method, which is faster [12], most frequently in trial runs preceeding the main experiment. The only significant difference that we could observe between these two methods was that with the NGP method the plasma heated up much faster. For this reason we could not rely on the NGP method except in the very low density and high temperature range.

The idea of smoothing the electric field was also considered as a means of reducing the heating up of the computer plasma. The smoothing was accomplished by suppressing the Fourier coefficients of the computed electric field associated with the higher spatial frequencies. Let $E_x(m,n)$ and $E_y(m,n)$ be the Fourier coefficients of the electric field components. The spatial frequencies m and n assume integer values with ranges

$$-31 \leq m \leq 32$$
$$-31 \leq n \leq 32$$

(30)

in the case of the 64x64 grid. In terms of these quantities, the smoothing scheme which we used can be defined by the requirement that

$$E_x(m,n) = E_y(m,n) = 0$$

(31)

for

$$|m| \geq 9 \quad \text{or} \quad |n| \geq 9$$

(32)

The particle methods PIC and NGP, in which the electric field is modified to satisfy Eqs. (31) and (32) are denoted as PIC-S and NGP-S, respectively.

The NGP-S and PIC-S methods showed considerable improvement in energy conservation if compared with NGP and PIC methods, respectively. No loss of accuracy was noticed due to the smoothing. On the contrary, in certain cases there was some improvement. For example, case 3 was also simulated by using the PIC method. The resonant frequencies estimated from the results of the NGP-S method were closer to the theoretical value than those obtained through the PIC method. Similar improvements were observed in case 5 when PIC-S was used instead of the PIC method. In this case, however, the PIC method could not be used because of lack of energy conservation. When simulating case 5 with the PIC method, the energy of the system increased by 23% over 1000 time steps. The same problem with PIC-S showed no more than 0.5% increase of the total energy over the same period. Apart from the question of energy conservation, the improvements in the results may also be connected with the reduced collisional effects in the NGP-S and PIC-S methods. This aspect of the problem was not investigated.

The examination of the results obtained from 25 computer experiments reveals that we came closest to our objective in those cases in which the plasma density is low. The best agreement between the results of simulation and theory was obtained in a case with $w_p = 0.5 v_c$. As w_p increases the internal fluctuations become more pronounced and there are indications that we are not dealing with pure linear oscillations. The spectrum of such oscillations shows lack of continuity and the maxima are less clearly defined. This is seen in Fig. 2-b in comparison with Fig. 1-b. We expect that these fluctuations can be reduced by using greater number of particles.

681

6. Conclusions

We have simulated CHW resonances whose propagation vector $\underset{\sim}{k}$ is perpendicular to the externally applied constant magnetic field $\underset{\sim}{B}$ on a digital computer using two dimensional particle models. Our aim was to obtain the dispersion relations for such oscillations in a homogeneous Maxwellian plasma. We found very good agreement between the results of the simulation and those predicted by the small signal theory. The best correspondence between theory and simulation is in plasmas of lower density, i.e., $\omega_p \leq \omega_c$. In a number of cases with $\omega_p > \omega_c$ the oscillations become less smooth and regular, suggesting some nonlinear influence. It is likely that this is caused by the excessive fluctuations of the particle model. It is expected that the problem can be remedied by using more particles.

We experimented with the NGP and PIC models. In simulating CHW phenomena, the only difference between these methods that we could observe was that the NGP model heated up much faster than the PIC model.

The effect of smoothing on the computed electric field was most noticeable in the improved energy conserving properties of the models. The elimination of the high spatial frequencies of the electric field in the NGP-S and PIC-S had no adverse effect on the accuracy of the dispersion relations obtained from the results of the simulation to say the least. This could be expected since the observed oscillations were always those of longest wavelengths.

References

1. I.B. Bernstein, Phys. Rev. 109, 1, 10 (1958).

2. F.W. Crawford, G.S. Kino, H.H. Weiss, Phys. Rev. Letters 13, 229 (1964).

3. F.W. Crawford, G.S. Kino, H.H. Weiss, Microwave Lab. Report No. 1210, Stanford University, Stanford, California (1964).

4. F.W. Crawford, J. Res. NBS 69D, 789 (1965).

5. F.W. Crawford, Nucl. Fusion 5, 73 (1965).

6. J. Dawson, Phys. Fluids 5, 4, 445 (1962).

7. R.W. Hockney, Phys. Fluids 9, 9, 1826 (1966).

8. R.L. Morse, "Methods in Computational Physics" 9, 213-239 (1970).

9. C.K. Birdsall and D. Fuss, J. Comp. Phys. 3, 4, 494 (1969).

10. R.W. Hockney, SU-IPR Report No. 202, Stanford University, Stanford, California (1967).

11. R.W. Hockney, Proceedings of Computational Physics Conference 1969, UKAEA Culham Laboratory, CLM-CP (1969), HMSO, London.

12. R.W. Hockney, Research Paper No. RC-2933, IBM Watson Research Center, Yorktown Heights (1970).

13. C.K. Birdsall, A.B. Langdon, H. Okuda, "Methods in Computational Physics" 9, 241 (1970).

14. O. Buneman, J. Comp. Phys. 1, 4, 517 (1967).

15. G. Bekefi, "Radiation Processes in Plasmas" (John Wiley and Sons, Inc., New York, 1966), p. 237.

The Numerical Solution of Multi-Species Fokker-Planck Equations

John Killeen and Arthur A. Mirin
Lawrence Radiation Laboratory
University of California
Livermore, California

Abstract

In studying the feasibility of fusion reactors based on magnetic mirror confinement of the plasma it is necessary to solve the Fokker-Planck equations in order to determine end losses and energy transfer. In any realistic system several ion species will be present including the charged reaction products. We have developed a new program, called NFP, for the purpose of solving the system of time-dependent Fokker-Planck equations for the distribution functions of several species of particle. Azimuthal symmetry is assumed so the resulting distribution functions are of the form $f(v, \theta, t)$. We assume that the distribution functions can be separated into a product of two terms -- the first term is a function of v and t and the second term is a function of θ only. The θ dependent part is given analytically and the equation for $f(v, t)$ must be solved numerically.

I. Mathematical Formulation Which Describes the Collisional Behavior of a Plasma

A. Fokker-Planck Equation

The usual transport equation for particles in a plasma is

$$\frac{\partial f_a}{\partial t} + \underline{v} \cdot \frac{\partial f_a}{\partial \underline{r}} + \frac{\underline{F}}{m} \cdot \frac{\partial f_a}{\partial \underline{v}} = \left(\frac{\partial f_a}{\partial t} \right)_c + S_a, \tag{1}$$

where $f_a(\underline{r}, \underline{v}, t)$ is the distribution function for particles of species a in a six-dimensional phase space. $(\partial f_a / \partial t)_c$ is a term describing collisional effects; $S_a(\underline{r}, \underline{v}, t)$ describes a particle source, if applicable. $\underline{F}$ is the force on a particle.

The collision operator most often applied in plasma theory is the Fokker-Planck operator. It is given by Rosenbluth et al.[1]

$$\frac{1}{\Gamma_a} \left(\frac{\partial f_a}{\partial t} \right)_c = - \frac{\partial}{\partial \underline{v}} \cdot \left(f_a \frac{\partial h_a}{\partial \underline{v}} \right) + \frac{1}{2} \frac{\partial^2}{\partial \underline{v} \partial \underline{v}} : \left(f_a \frac{\partial^2 g_a}{\partial \underline{v}} \right), \tag{2}$$

where

$$h_a(\underline{v}) = \sum_b \frac{m_a + m_b}{m_b} \left(\frac{z_b}{z_a} \right)^2 \int d\underline{v}' \, f_b(\underline{v}') / |\underline{v} - \underline{v}'|,$$

$$g_a(\underline{v}) = \sum_b \left(\frac{z_b}{z_a} \right)^2 \int d\underline{v}' \, f_b(\underline{v}') \, |\underline{v} - \underline{v}'|,$$

$$\Gamma_a = \frac{4\pi z_a^4 e^4}{m_a^2} \log_e D_a,$$

$$D_a = \frac{E_a \lambda_D}{z_a^2 e^2}.$$

T_e and N_e refer to electron temperature and density, and λ_D is the electron Debye length:

$$\lambda_D = \left(\frac{KT_e}{4\pi N_e e^2} \right)^{1/2}.$$

In reference (1), spherical polar coordinates (v, θ, ϕ) in velocity space are used, where θ is the angle between the velocity vector and the magnetic field vector. Azimuthal symmetry is assumed so the resulting distribution functions are of the form $f_a(v, \mu, t)$, where $\mu = \cos \theta$. The equation for each species is

686

then given by

$$\Gamma_a^{-1} \frac{\partial f_a}{\partial t} = -\frac{1}{v^2} \frac{\partial}{\partial v} (f_a v^2 \frac{\partial h_a}{\partial v}) - \frac{1}{v^2} \frac{\partial}{\partial \mu} \{f_a(1-\mu^2) \frac{\partial h_a}{\partial \mu}\}$$

$$+ \frac{1}{2v^2} \frac{\partial^2}{\partial v^2} (f_a v^2 \frac{\partial^2 g_a}{\partial v^2})$$

$$+ \frac{1}{2v^2} \frac{\partial^2}{\partial \mu^2} \{f_a[\frac{1}{v^2}(1-\mu^2)^2 \frac{\partial^2 g_a}{\partial \mu^2} + \frac{1}{v}(1-\mu^2)\frac{\partial g_a}{\partial v} - \frac{1}{v^2} \mu(1-\mu^2) \frac{\partial g_a}{\partial \mu}]\}$$

$$+ \frac{1}{v^2} \frac{\partial^2}{\partial \mu \partial v} \{f_a(1-\mu^2) [\frac{\partial^2 g_a}{\partial \mu \partial v} - \frac{1}{v} \frac{\partial g_a}{\partial \mu}]\} \qquad (3)$$

$$+ \frac{1}{2v^2} \frac{\partial}{\partial v} \{f_a[-\frac{1}{v} (1-\mu^2) \frac{\partial^2 g_a}{\partial \mu^2} - 2 \frac{\partial g_a}{\partial v} + \frac{2\mu}{v} \frac{\partial g_a}{\partial \mu}]\}$$

$$+ \frac{1}{2v^2} \frac{\partial}{\partial \mu} \{f_a[\frac{1}{v^2} \mu(1-\mu^2) \frac{\partial^2 g_a}{\partial \mu^2} + \frac{2\mu}{v} \frac{\partial g_a}{\partial v}$$

$$+ \frac{2}{v} (1-\mu^2) \frac{\partial^2 g_a}{\partial \mu \partial v} - \frac{2}{v^2} \frac{\partial g_a}{\partial \mu}]\}$$

B.   Separated Solutions

Calculations performed in two-dimensional velocity space for the ion distribution function indicate that approximate results can be obtained by separating the distribution function into a product of two terms (Bing and Roberts, 1961; BenDaniel and Allis, 1962). The first term is a function of v and t and the second term is a function of θ only. The equation for the function of θ is a Legendre differential equation on the domain $-\theta_c \leq \theta \leq \theta_c$, where θ_c defines the magnetic mirror loss cone. The equation for $f(v, t)$ must be solved numerically, and it is given in Eq. (6) of this paper for each species. The boundary condition on the distribution function in such a loss cone problem is $f(v, \theta_c, t)=0$ for all v and t for each species, which implies $f = 0$ at $v = 0$ in

the separated solution. In those problems where we assume that the distribution functions are isotropic we take a symmetry condition at $v = 0$, i.e., $\partial f/\partial v = 0$ for all t.

In the equations for ions and electrons we include source terms and also include the loss of each species by scattering into the velocity-space loss cone of the magnetic mirror configuration, and the hot ions can be lost by charge-exchange with the background gas.

A plasma potential is computed at each time step of the calculation by requiring charge neutrality. A critical velocity $v_c(t)$ is determined such that electrons with $v < v_c$ are not lost and those with $v > v_c$ can be lost by scattering into the loss cone. At each time step the electron charge density is compared to the total ion charge density and the velocity v_c modified accordingly. The plasma potential is obtained from $e\phi = 1/2\ mv_c^2$.

In Eq. (3) if we let g_a and h_a be isotopic, i.e. $\dfrac{\partial g_a}{\partial \mu} = \dfrac{\partial h_a}{\partial \mu} = 0$ then we have

$$\frac{1}{\Gamma_a}\frac{\partial f_a}{\partial t} = -\frac{1}{v^2}\frac{\partial}{\partial v}\left(f_a\ v^2\ \frac{\partial h_a}{\partial v}\right) + \frac{1}{2v^2}\frac{\partial^2}{\partial v^2}\left(f_a\ v^2\ \frac{\partial^2 g_a}{\partial v^2}\right)$$

$$+ \frac{1}{2v^3}\frac{\partial g_a}{\partial v}\left\{(1-\mu^2)\frac{\partial^2 f_a}{\partial \mu^2} - 4\mu\frac{\partial f_a}{\partial \mu} - 2\ f_a\right\} \qquad (4)$$

$$- \frac{1}{v^2}\frac{\partial}{\partial v}\left\{f_a\frac{\partial g_a}{\partial v}\right\} + \frac{1}{v^3}\frac{\partial g_a}{\partial v}\left\{\mu\frac{\partial f_a}{\partial \mu} + f_a\right\}$$

Let $f_a(v,\ \mu,\ t) = U_a(v,\ t)\ M_a(\mu)$ then

$$\frac{M_a}{\Gamma_a}\frac{\partial U_a}{\partial t} = -\frac{M_a}{v^2}\frac{\partial}{\partial v}\left(U_a\ v^2\ \frac{\partial h_a}{\partial v}\right) + \frac{M_a}{2v^2}\frac{\partial^2}{\partial v^2}\left(U_a\ v^2\ \frac{\partial^2 g_a}{\partial v^2}\right)$$

$$- \frac{M_a}{v^2} \frac{\partial}{\partial v} \left(U_a \frac{\partial g_a}{\partial v} \right)$$

$$+ \frac{U_a}{2v^3} \frac{\partial g_a}{\partial v} \left\{ (1-\mu^2) \frac{\partial^2 M_a}{\partial \mu^2} - 2\mu \frac{\partial M_a}{\partial \mu} \right\}$$

$M_a(\mu)$ satisfies

$$(1-\mu^2) \frac{\partial^2 M_a}{\partial \mu^2} - 2\mu \frac{\partial M_a}{\partial \mu} + \Lambda_a M_a = 0$$

Hence

$$\frac{1}{\Gamma_a} \frac{\partial U_a}{\partial t} = -\frac{1}{v^2} \frac{\partial}{\partial v} \left(U_a v^2 \frac{\partial h_a}{\partial v} \right) + \frac{1}{2v^2} \frac{\partial^2}{\partial v^2} \left(U_a v^2 \frac{\partial^2 g_a}{\partial v^2} \right)$$

$$\frac{1}{v^2} \frac{\partial}{\partial v} \left(U_a \frac{\partial g_a}{\partial v} \right) - \frac{\Lambda_a}{2v^3} \frac{\partial g_a}{\partial v} U_a \tag{5}$$

In what follows U_a will be denoted by f_a. Eq. (5) becomes

$$\frac{1}{\Gamma_a} \frac{\partial f_a}{\partial t} = \frac{\partial}{\partial v} \left[\frac{1}{2} \frac{\partial^2 g_a}{\partial v^2} \right]$$

$$+ \frac{\partial f_a}{\partial v} \left[-\frac{\partial h_a}{\partial v} - \frac{1}{v^2} \frac{\partial g_a}{\partial v} + \frac{2}{v} \frac{\partial^2 g_a}{\partial v^2} + \frac{\partial^3 g_a}{\partial v^3} \right]$$

$$+ f_a \left[-\frac{2}{v} \frac{\partial h_a}{\partial v} - \frac{\partial^2 h_a}{\partial v^2} + \frac{2}{v} \frac{\partial^3 g_a}{\partial v^3} + \frac{1}{2} \frac{\partial^4 g_a}{\partial v^4} \right]$$

$$- f_a \left[\frac{\Lambda_a}{2v^3} \frac{\partial g_a}{\partial v} \right] \tag{6}$$

The functions $h_a(v, t)$ and $g(v, t)$ are defined by the equations

$$h_a(v,t) = 4\pi \sum_b \left(\frac{z_b}{z_a} \right)^2 \frac{m_a + m_b}{m_b} \left[\int_0^v f_b(v',t) \frac{v'^2}{v} dv' \right.$$

$$\left. + \int_v^\infty f_b(v',t) v' dv' \right], \tag{7}$$

689

$$g(v,t) = 4\pi \sum_b (\frac{Z_b}{Z_a})^2 [\int_0^v f_b(v',t)v (1 + \frac{1}{3} \frac{v'^2}{v^2}) v'^2 dv'$$

$$+ \int_v^\infty f_b(v',t) (1 + \frac{1}{3} \frac{v^2}{v'^2}) v'^3 dv']. \tag{8}$$

The summations are taken over all the species of particles being considered, including type a.

The number density of particles of type a is given by

$$n_a(t) = 4\pi \int_0^\infty f_a(v,t)v^2 dv. \tag{9}$$

C. Dimensionless Equations

We wish to solve the system of equations

$$\frac{\partial f_a}{\partial t} = \alpha^{(a)} \frac{\partial^2 f_a}{\partial v^2} + \beta^{(a)} \frac{\partial f_a}{\partial v} + \gamma^{(a)} f_a + \delta^{(a)} \tag{10}$$

for an arbitrary number of species (denoted by Roman letter subscripts).

The domain is given by

$$t \geq 0 \qquad 0 \leq v \leq v_{max}$$

and the initial and boundary conditions are

$$f_a(v,0) \text{ given;} \qquad f_a(v_{max},t) = 0$$
$$f_a(0,t) = 0 \quad \text{or} \quad \frac{\partial f_a}{\partial v}\Big|_{v=0} = 0$$

The coefficients of Eq. (10) are given by

$$\alpha^{(a)} = 4\pi \Gamma_a \sum_b (\frac{Z_b}{Z_a})^2 [\frac{1}{3v^3} \int_0^v f_b(v')v'^4 dv' + \frac{1}{3} \int_v^\infty f_b(v')v' dv']$$

$$\beta^{(a)} = 4\pi \Gamma_a \frac{1}{v} \sum_b (\frac{Z_b}{Z_a})^2 [\frac{m_a}{m_b} \frac{1}{v} \int_0^v f_b(v') v'^2 dv'$$

$$- \frac{1}{3v^3} \int_0^v f_b(v') v'^4 dv' + \frac{2}{3} \int_v^\infty f_b(v')v' dv']$$

690

$$\gamma^{(a)} = 4\pi\ \Gamma_a\ \{\sum_b (\frac{Z_b}{Z_a})^2\ [\frac{m_a}{m_b}\ t_b] - \frac{P_a(v)}{v^3}\ \sum_b \lambda_{ab}\ (\frac{Z_b}{Z_a})^2\ [\ \int_o^v f_b(v',t)v'^2 dv'$$

$$- \frac{1}{3v^2}\ \int_o^v f_b(v',t)v'^4\ dv' + \frac{2v}{3}\ \int_v^\infty f_b(v',t)v'dv']\}$$

(the summations are taken over all species.)

Let $x = v/v_0$, where v_0 is a constant, and let $F_a = (\frac{4\pi v_0^3}{K_a})\ f_a$,

where

$$n_a(0) = K_a \int_o^\infty F_a(x,0)\ x^2\ dx = K_a I_2^a(0)$$

($n_a(0)$ is given and the integral I_2^a is computed from the initial distribution.)

We define the functionals

$$M(F) = \int_x^\infty F(y,t)\ y\ dy$$

$$N(F) = \int_o^x F(y,t)\ y^2\ dy$$

$$E(F) = \int_o^x F(y,t)\ y^4\ dy$$

In terms of the new variables Eq. (10) becomes

$$\frac{\partial F_a}{\partial t} = A'_a\ \frac{\partial^2 F_a}{\partial x^2} + B'_a\ \frac{\partial F_a}{\partial x} + C'_a\ F_a + D'_a \tag{11}$$

where

$$A'_a = \frac{\Gamma_a}{v_0^3}\ \sum_b (\frac{Z_b}{Z_a})^2\ [\frac{1}{3x^3}\ E(F_b) + \frac{1}{3}\ M(F_b)]\ K_b$$

$$B'_a = \frac{\Gamma_a}{v_0^3 x}\ \sum_b (\frac{Z_b}{Z_a})^2\ K_b[\frac{m_a}{m_b}\frac{1}{x}\ N(F_b) - \frac{1}{3x^3}\ E(F_b) + \frac{2}{3}\ M(F_b)]$$

$$C'_a = \frac{\Gamma_a}{v_0^3}\ \sum_b (\frac{Z_b}{Z_a})^2\ [\frac{m_a}{m_b}\ F_b - \frac{P_a(x)\lambda_{ab}}{x^3}\ \{N(F_b) - \frac{1}{3x^2}\ E(F_b) + \frac{2x}{3}\ M(F_b)\}]K_b$$

$D'_a = S_a(x,t)$ is the source term for species a.

691

Let $\Gamma_{oe} = \dfrac{4\pi e^4}{m_0^2} = .806 \times 10^{18}$

where m_0 is the electron mass.

We introduce the independent variable

$$\tau = \frac{\Gamma_{oe} K_e}{2 v_0^3} t = \frac{t}{t_N}$$

We have

$$\frac{\Gamma_a}{\Gamma_{oe}} = \frac{\dfrac{4\pi e^4 z_a^4}{m_a^2} \ln D_a}{\dfrac{4\pi e^4}{m_0^2}} = \left(\frac{m_o}{m_a}\right)^2 z_a^4 \ln D_a$$

Eq. (2) becomes

$$\frac{\partial F_a}{\partial \tau} = A_a \frac{\partial^2 F_a}{\partial x} + B_a \frac{\partial F_a}{\partial x} + C_a F_a + D_a \tag{12}$$

where

$$A_a = \frac{v_o^3}{\Gamma_{oe}} \frac{2}{K_e} A_a' = t_N A_a'$$

$$B_a = \frac{v_0^3}{\Gamma_{oe}} \frac{2}{K_e} B_a' = t_N B_a'$$

$$C_a = \frac{v_0^3}{\Gamma_{oe}} \frac{2}{K_e} C_a' = t_N C_a'$$

II. Calculation of the Ambipolar Potential

The coefficient of the scattering loss term is

$$P_a(v) \lambda_{ab} = \frac{1}{2} \Lambda_a$$

where Λ_a is the separation constant (eigenvalue of the Legendre equation corresponding to first normal mode). For Λ_a we shall use the approximate value

$$\Lambda_a = (\log_{10} R_a)^{-1}$$

where R_a is the effective mirror ratio for particles of type a
and depends on the ambipolar potential ϕ.

For electrons we have

$$R_e = R(1 - \frac{\phi}{\frac{1}{2}m_e v^2})^{-1}$$

where $R = B_{max}/B_0$, $\phi = \frac{1}{2} m_e v_{cr}^2$.

For ions we have

$$R_a = R(1 + \frac{\phi}{\frac{1}{2} m_a v^2})^{-1}$$

The procedure for determining ϕ follows. Let

$$Q^-(\tau) = n_e(\tau)$$

$$Q^+(\tau) = \sum_b Z_b n_b(\tau) \qquad\qquad (b \neq e)$$

(The sum taken over the ion species.)

At every time step Q^- and Q^+ are computed and the difference

$$\frac{Q^+ - Q^-}{Q^-}$$

compared to a specified small number. If the difference exceeds
this number, then v_{cr} is increased by an amount Δv_{cr} and the time
step is repeated. This process is repeated until the condition is
satisfied. The term $P_e(x)$ is then

$$P_e(x) = \begin{cases} [\log_{10}\{R(1 - \frac{x_{cr}^2}{x^2})^{-1}\}]^{-1} & x > x_{cr} \\ \\ 0 & x \leq x_{cr} \end{cases}$$

where $v_0 x_{cr} = v_{cr}$. (Note: let $\lambda_{ab} = 1/2$.)

In the ion equations for those values of x such that $x \leq \sqrt{\frac{m_e}{m_a}} \frac{1}{\sqrt{R-1}} x_{cr}$

set the corresponding values of the distribution function $F_a(x,\tau)$

equal to zero. For
$$x > \sqrt{\frac{m_e}{m_a}} \frac{1}{\sqrt{R-1}} \ x_{cr}$$

$$P_a(x) = [\log_{10}\{R(1 + \frac{\phi}{\frac{1}{2}m_a v_0^2 x^2})^{-1}\}]^{-1}$$

(Again set $\lambda_{ab} = 1/2$.)

An option for determining the ambipolar potential is also available in the code, and is described as follows.

The new electron density Q^- is compared to the ion density Q^+ and the change in electrons is compared to the change in ions. Since charge neutrality is to be maintained, if the electron density is less than the ion density, and the electron change is less than the ion change, the ambipolar potential is increased by a small amount, and the time step is repeated. This cycling is continued until either the condition

$$Q^- \geq Q^+$$

or the condition

$$\Delta Q^- \geq \Delta Q^+$$

is obtained.

On the other hand, if the ion density is less than the electron density, and the ion change is less than the change in electrons, the potential is decreased and the time step is repeated, this cycling continuing until either

$$Q^- \leq Q^+$$

or

$$\Delta Q^- \leq \Delta Q^+.$$

The requirement on the change in densities keeps the electron density from getting too far ahead of the ion density, and vice

694

versa. This could happen due to discrepancies in rates that might otherwise build up.

III. Difference Methods

The system of equations (12) is solved by an implicit difference scheme which is similar to that described in earlier works.[2,3] In this application the system (12) is treated as a single vector equation for the p-dimensional vector F where the elements of F are the distribution functions for each species. A variable mesh is used in velocity space with a fine spacing for small v to accurately represent the ion distribution functions.

IV. Applications

The program has been applied to three-species problems (e, D, T) and (e, D, He^3), to four-species problems (e, D, T, α), and to five-species problems (e, D, He^3, α, p). We also plan to apply it to a full six-species problem (e, D, T, He^3, α, p). Source terms suitable for neutral injection[2,3] are included and also source and loss terms of the form $<\sigma v>\, n_a n_b$ corresponding to thermonuclear reactions are included.

References

1. Rosenbluth, M. N., MacDonald, W. M., and Judd, D. L., Phys. Rev. 107, 1, (1957)

2. Killeen, J., and Futch, A. H., Jr., J. Comp. Phys. 2, 236 (1968)

3. Killeen, J., and Marx, K. D., Methods for Computational Physics, Vol. 9, p. 421, Academic Press, 1970

Plasma Generation by an Electric Field

L. E. Kline* and J. G. Siambis
Department of Electrical Engineering
Carnegie-Mellon University
Pittsburgh, Pennsylvania

ABSTRACT

We present a new method for the simulation of electrical
breakdown phenomena, and plasma phenomena where both binary electron-
neutral collisions and collective interactions are important. Binary
collisions are included using a Monte Carlo technique. Collective
interaction is included using a one dimensional plasma model. The
method is used to simulate the growth of electron avalanches and
electron streamers. Photoionization is also included in the simulations
and is an important mechanism in streamer growth. Good agreement is
obtained between calculated and experimental results for both
avalanches and streamers.

I. INTRODUCTION

When an intense electric field is applied to a gas, the gas
breaks down, chai   , from an insulator to a conductor. During the
breakdown process the electron and positive ion densities in the gas
increase over many orders of magnitude in as short a time as twenty
nanoseconds for centimeter gaps.

* Present address, Westinghouse Research Labs, Pittsburgh, Pa. 15235

Plasma Generation by Electric Field

We have carried out computer simulation studies of electron pulse experiments[1,2]. The simulation includes elementary collision process in the gas as well as collective interactions among the electrons and ions that are released in the breakdown process. In the simulation experiments a pulse of low energy electrons is released at the cathode, in a parallel plane gap with an applied electric field. (The word electron is used below to denote simulation particles that can represent one or many actual electrons). The simulation simultaneously follows the trajectories of a large number of individual electrons as they drift from the cathode to the anode. Electron velocity components parallel and normal to the electric field and electron position measured from the cathode, parallel to the electric field, are computed for each electron as a function of time, the independent variable in the simulation. Time is advanced in equal steps, Δt. At each time, t_k, ($t_k = k\Delta t$) the probability of a collision with a neutral gas molecule, between t_k and t_{k+1}, is computed for each electron and compared with a random number to decide whether that electron suffers a collision between t_k and t_{k+1}. When an electron suffers a collision the relative probabilities for elastic, vibrational, exciting and ionizing collisions are used along with another random number to decide what kind of collision the electron has suffered. The collision probabilities are based on published cross-sections[3]. Cross-section magnitudes are assumed to be proportional to the pressure, while their form is independent of pressure. Uniformly distributed scattering angle cosines are assumed in all collisions. Similar Monte Carlo calculations for electron avalanches in gases, assuming negligible space charge distortion, are described in Ref. 4.

In simulated and actual electron pulse experiments N, the number of electrons in the pulse, increases exponentially with time as a result of ionizing collisions.

$$N(t) = N(t = 0) \exp(\alpha v_d t) \qquad (1)$$

Where α is called the ionization coefficient and v_d is the electron drift velocity, given by Eq. (2), where $\bar{x}$ is the average electron position.

$$v_d = \bar{x}/t \qquad (2)$$

The growing pulse of electrons is called an electron avalanche[1,2]. When the electron density in the avalanche exceeds $10^8/cm^3$ collective electron interaction and distortion of the applied electric field begins.

We account for collective interactions by regarding the electrons as charge sheets[5]. The electric field at all points within the gap is obtained by solving Poisson's equation in one dimension at each time t_k, based on the positions of all of the charge sheets. The charge sheets are then allowed to move under the influence of the electric field until t_{k+1} when a new electric field is computed based on the new electron positions. The size of the time step, Δt, is based on the electron plasma frequency and the average frequency of collisions between electrons and neutral gas molecules.

The total number of electrons represented by the simulation particles typically varies over eight orders of magnitude during the course of the simulation. At the beginning of the simulation each simulation particle typically represents ten actual electrons. At the end of the simulation each particle represents 10^8 actual electrons, hence the simulation particles must be rescaled several times during the course of the simulation.

698

Plasma Generation by Electric Field

The exponential growth of electron avalanches, described by
Eq. (1), is due to ionizing collisions between electrons and neutral
gas molecules. Experiments[1,6] also show that gas photoionization is
an important mechanism for the release of electrons and positive ions
in gases. Photoionization is included in the simulation using recent
experimental data[6].

When electric fields well above the minimum electric field
required for breakdown are applied to parallel plane gaps, light
emitting regions called streamers develop in the gaps during the
electrical breakdown process.

Streamers are studied experimentally[7] by recording the
spatial and temporal development of the light that they emit. We
estimate the light output of the simulated streamer by recording the
spatial and temporal development of the density of excited molecules
which appear when a simulation electron undergoes an exciting collision.
The spatial density of excited molecules is printed out and reset to
zero at successive times tx_k ($tx_k = k\Delta tx$) where Δtx is comparable to
the mean lifetime of the excited molecules.

Computer simulation results are used below to calculate
electron avalanche and streamer velocities as well as the ionization
coefficient for electron avalanches. The calculated values of these
quantities are in good agreement with experimentally measured values
in all cases.

II. THE SIMULATION MODEL

Electron-Neutral Collision Calculations

The probability of a collision between an electron and a
neutral gas molecule between t_k and t_{k+1} is given by Eq. (3).

$$P(t_k) = 1 - \exp\ (-\ \nu(v(t_k))\Delta t) \tag{3}$$

In Eq. (3) ν is the total collision frequency for electron-neutral gas molecule collisions. The total collision frequency is a function of electron velocity and is the sum of the individual collision frequencies for elastic, exciting and ionizing collisions.

$$\nu_{total} = \nu_{elastic} + \nu_{exciting} + \nu_{ionizing} \tag{4}$$

$P(t_k)$ is calculated for each electron at the beginning of each time step. The calculated collision probability for each electron is compared with a pseudo-random number, drawn from a uniform distribution, to decide whether that electron suffers a collision in that time step.

When an electron suffers a collision the collision type is determined based on Eq. (4) and on the fact that the probability of a particular kind of collision, given that a collision has occurred, is equal to the collision frequency for that kind of collision divided by the total collision frequency. For example, the probability of an ionizing collision, given that a collision has occurred is:

$$P = \nu_{ionizing}/\nu_{total} \tag{5}$$

The collision frequencies in Eq. (5) must be calculated at each time step, for a particular electron, based on that electron's energy. Exciting and ionizing collisions both have threshold velocities. Electrons with velocities lower than the respective threshold velocities cannot undergo exciting and ionizing collisions, thus simplifying the collision type decision for electrons with low velocities.

When the collision type has been determined, for an electron that has suffered a collision, the total electron velocity following the collision is computed as shown in Table 1.

Plasma Generation by Electric Field

The equation for the electron velocity following an exciting collision is based on the average velocity loss in an exciting collision, $v_{\cdot}$, which is known as a function of incident electron energy.

The incident electron also loses a known amount of energy in an ionizing collision. The remaining energy in ionizing collisions is shared between the incident and secondary (newly relea ed) electrons. Since almost no experimental data is available concerning the sharing of energy between incident and secondary electrons in ionizing collisions, equal sharing has been assumed. A secondary electron is added for ionizing collisions, with the secondary electron velocity equal to the new incident electron velocity.

A new direction is chosen for the incident electron (and the secondary electron in ionizing collisions) by randomly choosing a direction cosine, $\cos\theta$, from a uniform distribution on the interval $(-1, 1)$. Then the new velocity components are computed using (6) and (7)

Table 1 Electron Ve.ocities Before and After Collisions

Collision Type	v = velocity after collision v' = velocity before collision
elastic	$v^2 = v'^2$
exciting	$v^2 = v'^2 - v_x^2$
ionizing	$v^2 = 1/2(v'^2 - v_1^2)$

701

along with the new total velocity already computed.

$$v_{\parallel}(t_k) = v(t_k) \cos \theta \qquad (6)$$

$$v_{\perp}(t_k) = v(t_k)(1-\cos \theta) \qquad (7)$$

The new parallel velocity, $v_{\parallel}$, and the square of the new normal velocity, $v_{\perp}^2$, are then stored, completing the short-range collision calculations for the particular electron under consideration.

The secondary electron (simulation particle) which is released in a particular ionizing collision always represents the same number of actual electrons as the incident electron (simulation particle) involved in that ionizing collision.

When an ionizing collision occurs in a cell the number of fixed positive ions in that cell is increased by an amount equal to the number of actual electrons represented by the simulation particle involved in the ionizing collision. The resulting fixed positive charge density corresponds to an assumption of immobile positive ions.

Electric Field and Electron Motion

During the simulation the potential difference between the electrodes in the discharge gap is assumed constant. Poisson's equation is solved in one dimension using standard sheet model techniques[5,8] to find the electric field in each cell. The total charge in each cell is the sum of the charges of the simulation particles in that cell and the fixed positive charge, due to ionizing collisions in that cell. The equations of motion for the electrons are:

$$x(t_{k+1}) = x(t_k) + v_{\parallel}(t_k) \Delta t + (\frac{q}{m}) E_k (\Delta t)^2 \qquad (8)$$

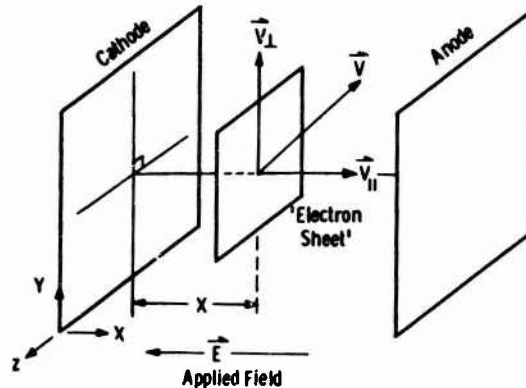$$v(t_{k+1}) = v(t_k) + (\frac{q}{m}) E_k \Delta t \qquad (9)$$

702

Fig. 1.   Position and Velocity Components for a Typical

Electron Sheet.

In Eqs. (8) and (9) $t_{k+1} = t_k + \Delta t$, and x is the position of an

electron measured from the cathode as shown in Fig. 1. Although the

positions of electron sheets are followed in only one dimension, as

shown in Fig. 1, each electron sheet has two velocity components

which are also shown in the figure. Only $v_{||}$, the parallel component

of velocity, is affected by the electric field, as shown in Eq. (8).

Both velocity components are altered in short-range collisions as

discussed above. After new positions and velocities at t_{k+1} have

been found for all electrons time is advanced and the short-range

collision calculations are begun for the next time step.

Scaling

When N(t), the total number of simulation particles exceeds

the maximum allowable number of particles, which is specified in the

program input data, then the original group of simulation particles is

replaced by an approximately equivalent group containing few   simulation

particles.   Each new particle represents several times as many actual

electrons as the old particles.   The old and new groups of particles

should be equivalent, in the sense that their distribution in phase space are approximately equivalent.

In the simulation program a new group of "larger" particles is generated to represent the old, larger group of "smaller" particles by randomly selecting some fraction, f, of the old group of particles. Each of the selected particles then represents 1/f times as much charge and mass as each of the old particles. This technique has the advantage of simplicity and the disadvantage that there is no guarantee that the distribution of the selected particles in phase space is approximately equal to the original particle distribution. This disadvantage can be minimized by careful choice of the maximum allowable number of particles and the fraction, f which is retained each time that scaling is necessary.

Gas Photoionization

Photoionization of a gas due to radiation emitted by an electrical discharge has been measured experimentally in Nitrogen and in other gases[6] The experimental results of Ref. 6 form the basis for the photoionization calculations which are described below. In the experiments a point-plane corona discharge is used as a radiation source. Radiation emitted by the discharge causes gas photoionization which is measured by the current to a photoelectron collector. The experimental results show that the photoionization rate in the collection region is proportional to the rate of ionizing electron-neutral gas molecule collisions in the discharge.

Since the short range collision calculations described above provide an estimate of the collisional ionization rate at all points in the gap, in the computer simulation, the experimental data described above can be used to estimate the rate of photoion pair production in the gap.

Plasma Generation by Electric Field

The photoionization calculations are carried out at successive times tp_k, where $tp_k = k\Delta tp$. The gap is divided into cells to carry out the photoionization calculations. N_{p_i}, the number of photoion pairs (photoelectrons and photoions) produced in the ith cell between tp_k and tp_{k+1} is calculated using Eq. (10).

$$N_{p_i} = \sum_{j=1}^{n \text{ cells}} \psi_{ij} \, pd \, \theta_{ij} \, N_{D_j} \tag{10}$$

In Eq. (10) N_{D_j} is the collisional ionization rate in the jth cell, ψ_{ij} is an experimentally measured coefficient which depends on pressure and on the distance between the ith and jth cells, p is the pressure, d is the cell width and θ_{ij} is the solid angle subtended at cell j by cell i. The radius, R_{GAP}, of the region where photoion release is calculated, is fixed in the simulations. A fixed radius allows θ_{ij} in Eq. (10) to be calculated and is equivalent to ignoring photoion pairs that are produced outside a cylindrical region with radius R_{GAP}.

III. ELECTRON AVALANCHE RESULTS

When the electric field, E, pressure, p, and gap length, d, are appropriately adjusted in the simulation experiments, so that $\alpha d \leq 4$, no scaling is required, and collective interaction does not occur in the simulations. Hence the results of simulation experiments carried out with $\alpha d \leq 4$ can be compared with the results of corresponding actual experiments to provide a check on the electron-neutral collision calculations. Figures 2 and 3 compare calculated and experimental values of v_d, the electron avalanche drift velocity (see Eq. (2)) and α/p where α is the ionization coefficient (see Eq. (1)) and p is the pressure in Torr. The pressure determines the magnitudes

of the collision frequencies used in the simulation. When space
charge distortion does not occur both actual experiments and simulation
experiments show that α/p and v_d depend on E/p, the ratio of the
applied electric field to the pressure, hence both α and v_d are
plotted vs. E/p. The good agreement shown in Figs. 2 and 3 indicates
that the short-range collision calculations accurately predict the growth
of the electron pulses into electron avalanches. When both E and p
are increased, with E/p fixed, α is increased and the maximum number
of electrons in the avalanche increases compared to the number of
electrons in an avalanche at lower E and p but the same value of E/p.
When E and p are increased at fixed E/p so that $\alpha d \gtrsim 4$, scaling must
be used in the simulation experiments. The calculated values of α/p
and v_d are approximately equal for cases with $\alpha d > 4$ and cases with
$\alpha d < 4$ as long as space charge distortion of the applied electric field
does not occur, thus validating the scaling procedure that is used.

IV. ELECTRON STREAMER RESULTS

When $\alpha d \gtrsim 14$ space charge distortion of the applied field
occurs in both simulated and actual electron pulse experiments[1], and
the electrons interact collectively. Figure 4 shows N (t) for a case
where $\alpha d \simeq 36$. In this case the electron density is large enough to
distort the applied electric field at $t \simeq 12$ ns, when the electron
avalanche is midway between the electrodes. Once space charge distortion
begins most of the electrons in the avalanche are in a region of
reduced electric field, causing the reduced growth rate shown in Fig. 4.
The coefficient $\psi_{ij} p d\theta_{ij}$ in Eq. (10) is on the order of 10^{-4} to 10^{-6}
for the pressures used in the simulation. Large values of αd give the
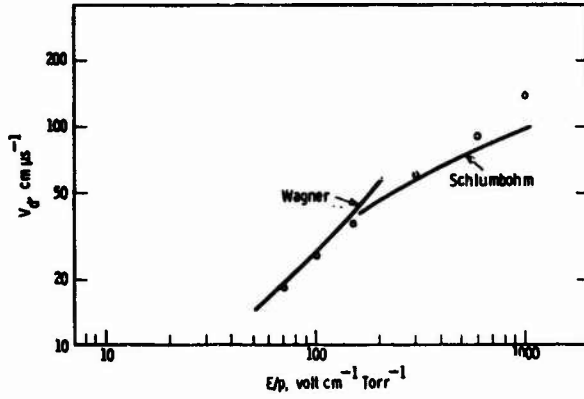high collisional ionization rates needed for the release of a large

Fig. 2   Calculated and Experimental Values of v_d, the Electron
Avalanche Drift Velocity. Calculated Results are Shown
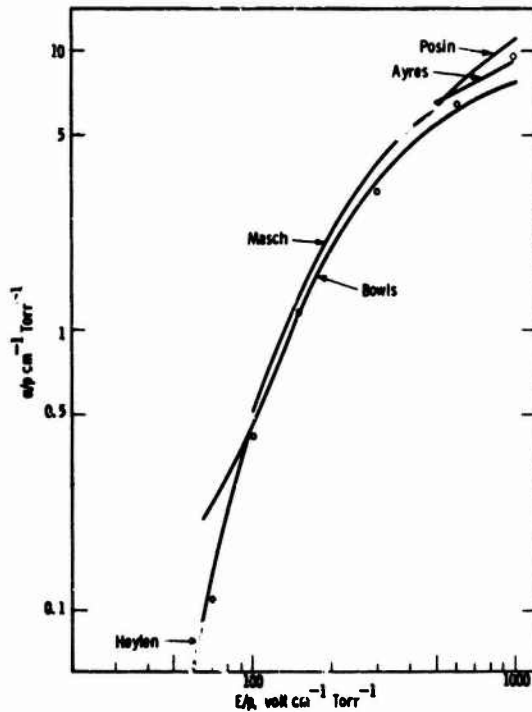as Points. The Curves Show the Experimental Results of
Wagner[9], and Schulmbohm[10].

Fig. 3   Calculated and Experimental Values of α/p. Calculated
Results are Shown as Points. The Curves Show the Experi-
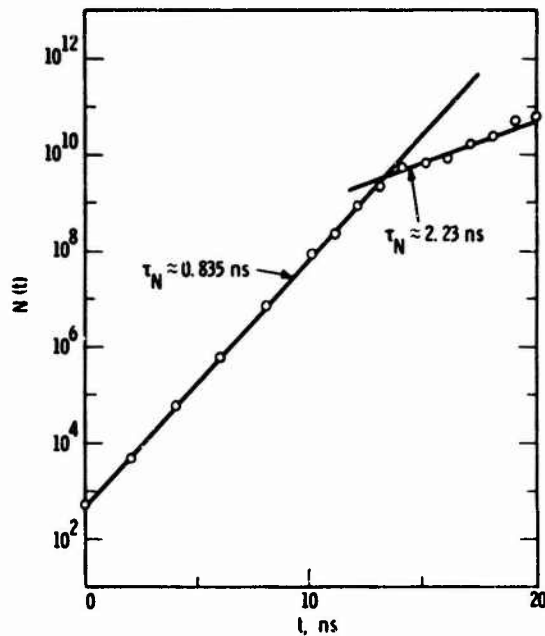mental Results of Masch, Ayres, and Posin[11], Bowls[12] and
Heylen[13].

707

Fig. 4   Calculated Total Number of Electrons in a Simulated Electron
Pulse Experiment where $\alpha d \tilde{=} 36$.

number of photoion pairs as indicated by the values of $\psi_{ij} p d\theta_{ij}$ and
Eq. (10).

The electrons released by photoionization start avalanches,
called secondary avalanches, which grow and increase the charge density
in the gap both ahead of and behind the primary avalanche. (The
primary avalanche is the avalanche which grows from the original
electron pulse). The growth of the primary and secondary avalanches
is accompanied by light emission from the region occupied by the
avalanches.

The exciting collision number density in each cell is increased
each time an exciting collision occurs in that cell. The exciting collision
number density is printed out at times tx_k ($tx_k = k\Delta tx$), and then reset

708

to zero. As a result the exciting collision number density that is
printed out at each time tx_k gives the number density of exciting collisions
which have occurred between tx_k and tx_{k+1}. Since the light emitted by
an avalanche or a streamer is due to the photons emitted by excited
molecules, when they return to a lower state, the spatial density of
exciting collisions should be a good estimate of the spatial density
of the light emitted by the simulated avalanche or streamer.

The boundaries of the light emitting region of the simulated
avalanche or streamer are assumed, at each time, to be the points
where the exciting collision density falls to two orders of magnitude
below its peak value. The boundaries of the light emitting region for
the run shown in Fig. 4 where $ad \stackrel{\sim}{=} 36$, $E/p = 1000$, $p = 1$ and $N(t=0) = 500$
are plotted in Fig. 5. The figure shows that both boundaries of the
light emitting region propagate toward the anode for $t \lesssim 12$ ns. At $t \stackrel{\sim}{=} 12$
the propagation velocity of the anode-side boundary abruptly increases,
and the cathode-side boundary reverses direction, and moves toward the
cathode.

Light fronts propagating toward the anode at velocities much
greater than the electron avalanche drift velocity and light fronts
propagating toward the cathode are also observed in experiments and
are called anode-directed and cathode-directed streamers respectively.
The anode-directed streamer velocity in this case is the increased
velocity of the anode-directed light front for $t \gtrsim 12$ ns. The cathode-
directed streamer velocity is the velocity of the cathode-directed
light front. The anode-directed streamer velocity is positive toward
the anode, while the cathode-directed streamer velocity is positive
toward the cathode. The streamer velocities are equal to the slopes of
the boundaries of the light emitting region in the distance-time plot
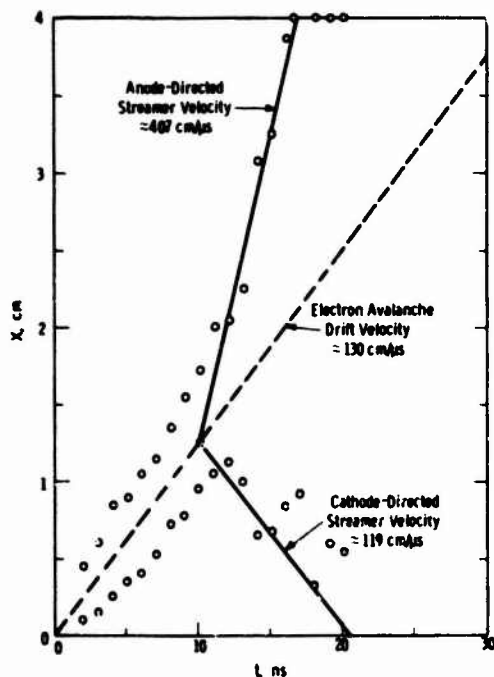of Fig. 5. The electron avalanche drift velocity is also shown in

709

Fig. 5   Avalanche and Streamer Velocities for $\alpha d \tilde{=} 36$. In this Case
         E/p = 1000 volt/cm Torr, p = 1 Torr and N(t=0) = 500.   The
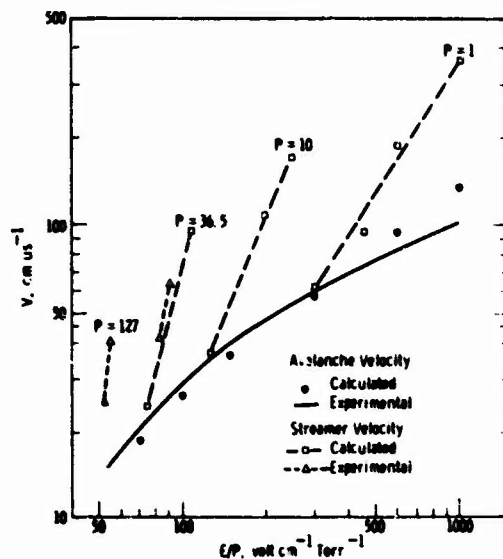   Points are the Boundaries of the Light Emitting Region.

Fig. 6   Calculated and Experimental Electron Avalanche and Electron
         Streamer Velocities. The Experimental Values are from Ref. 7.

Fig. 5. The electron avalanche drift velocity is calculated using Eq. (2) for $t \lesssim 12$ ns, the time period preceeding the increase in anode-directed streamer velocity and the development of a cathode-directed streamer.

Calculated anode-directed streamer velocities are shown in Fig. 6 along with experimentally measured streamer velocities[7]. Calculated values of the electron avalanche drift velocity are shown for $p = 1$ Torr. The measured values of the electron avalanche drift velocity are from Ref. 10. The calculated anode-directed streamer velocity for $p = 36.5$ Torr and $E/p = 81.5$ volt/cm Torr is about 10 percent lower than the measured velocity. For $p = 36.5$ Torr and $E/p = 90$ volt/cm Torr the calculated value is about 20 percent lower than the experimental value. The calculated and experimental streamer velocities depend exponentially on E/p at all pressures.

V. CONCLUSIONS

The computer simulations described are the first plasma simulations which include both realistic binary electron-neutral gas molecule collision effects and collective interactions among charged particles Binary electron-neutral gas molecule collisions are the essential mechanism in electron avalanche growth. The good agreement between calculated and measured electron avalanche drift velocities and ionization coefficients demonstrates the validity of the binary collision simulation techniques. Simulation of electron avalanches provides detailed information about electron energies that would be impossible to obtain experimentally.

The streamer simulation results show that collective interaction and photoionization are both important mechanisms in streamer development. Streamers do not develop when photoionization is omitted

from the calculations. Collective interactions (or space charge effects) increase the electric field both ahead of and behind the primary avalanche in the simulations, thus accelerating the development of the secondary avalanches which are started by photoelectrons released by gas photoionization. Streamer velocities calculated from the simulation results are in good to excellent agreement with experimentally measured streamer velocities. Computer simulation which accounts for binary collisions between electrons and neutrals, collective interaction and photoionization is the only available theoretical approach which can be used to predict the growth of electron streamers.

REFERENCES

1. H. Raether, Electron Avalanches and Breakdown in Gases (Butterworths, Washington, 1964).

2. F. Llewellyn-Jones, Ionization Avalanches and Breakdown (Methuen, London, 1967).

3. A. G. Engelhardt, A. V. Phelps and C. G. Risk, Phys. Rev. 135, A1566 (1964).

4. R. W. L. Thomas and W. R. L. Thomas, J. Phys. B, Ser. 2, 2, 562 (1969).

5. Methods in Computational Physics, vol. 9, Plasma Physics. (New York: Academic Press, 1970).

6. G. W. Penney and G. T. Hummert, J. Appl. Phys. 41, 572 (1970).

7. K. H. Wagner, Z. Physik 189, 465 (1965).

8. P. Berger, J. Appl. Phys. 35, 3048 (1964).

9. K. H. Wagner, Z. Physik 178, 64 (1964).

10. H. Schlumbohm, Z. Physik 182, 317 (1965).

11. D. Q. Posin, Phys. Rev. 50, 650 (1936).

12. W. E. Bowls, Phys. Rev. 53, 293 (1938).

13. A. E. D. Heylen, Nature 183, 1545 (1959).

Numerical Simulation of a Laboratory Neutron Tube*

J. W. Poukey and J. R. Freeman
Sandia Laboratories
Albuquerque, New Mexico

ABSTRACT

A two-dimensional cloud-in-cell simulation technique,
using recently developed fast methods of solving Poisson's
equation, has been employed in practical studies of a
laboratory neutron tube. In such a tube, tritons are
pulled from the surface of a plasma and accelerated to a
target held at large negative potential. Results of the
simulation are in reasonable agreement with experimental
observations of tube current vs. voltage and triton beam
size. The simulation code has been used to investigate
such details as the spatial distribution of the triton
current on the target. The code is expected to be a
valuable tool in the future development of such devices.

I.   INTRODUCTION

Recent advances in computer simulation techniques,
together with presently available computer memory capaci-
ties, make it possible to model certain complex laboratory
devices with a substantial degree of realism. In this

714

paper, we discuss a quantitatively successful simulation of a laboratory neutron tube in which experimental results were reproduced by the simulation to within the experimental error. The neutron tube studied is similar in design to that described by Gow and Pollock[1] and by Murguliya and Plyutto.[2] The simulation code has become a useful engineering tool in improving the efficiency of various laboratory vacuum tube devices.

The simulation consists of computing the motion of charged particles in their self-consistent and applied electric fields. A cloud-in-cell technique, developed for one and two-dimensional problems by Birdsall and Fuss,[3] was employed. This method is quite analogous to the particle-in-cell approach with area weighting, developed by Morse and Nielson.[4] Ion gun calculations somewhat similar to the present study were reported by Hockney.[5] Calculations were made in both Cartesian coordinates, using the Buneman[6] double cyclic reduction Poisson solver, and in cylindrical coordinates, using a Poisson solver based on the fast Fourier transform method of Hockney.[5] Both solvers incorporated the inverse capacity matrix method[5] for including internal electrodes.

In Section II the neutron tube behavior is described, and the approximations of our model are discussed. The simulation code is described in Section III, and the code's predictions are compared with experiment in Section IV. Section V discusses some of the studies to which the code has been and will be applied.

II. THE DEVICE AND THE MODEL

Figure 1 shows a schematic cross-sectional view of the neutron tube, with dimensions normalized to $FF' = 1.0$. An arc, located somewhere in region 1, is switched on and a plasma is produced. This plasma is assumed to consist entirely of free electrons and triton ions. Some of the ions are drawn from the plasma and accelerated onto the deuterided target DD' by the application of a large negative target voltage, typically -70 kV with respect to the shield $ABFF'B'A'$ around region 1. The ions striking the deuterided target produce neutrons by the D-T reaction. For efficiency, one would like the largest possible triton current striking the smallest possible target area. Thus, the crucial quantities are the magnitude and distribution of the triton current to the target.
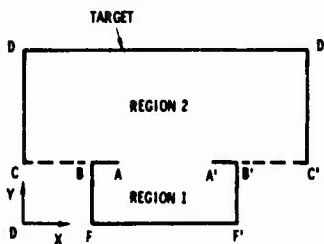

Figure 1: The laboratory neutron tube. Dimensions: $FF' = 1.0$, $AA' = .6$, $BF = .4$, $DC = .7$, $DD' = 2.0$

Simulation of Neutron Tube

The neutron tube is cylindrically symmetric (about a line through the centers of segments FF' and DD' in Figure 1) except possibly in the location of the arc source. Many arc source locations have been studied, a common configuration being a point source positioned between A' and B' at one particular azimuthal location, thereby producing a three-dimensional non-symmetric plasma distribution. Since three-dimensional calculations are not presently practical, two separate two-dimensional approaches were pursued. First, a Cartesian simulation, in which a non-symmetric arc source could be used, was performed. Second, the calculations were repeated in cylindrical coordinates, using a cylindrically symmetric arc source. It was found that the rectangular simulation produced results in better agreement with experiment.

Experiment shows that the target current rises quickly, and then remains nearly constant until the plasma producing arc is shut off. Thus, it is sufficient if we model the device in its quasi-steady state, which is done in the following way. We start with a uniform plasma, density n_o and zero temperature, filling region 1. This plasma is represented in the simulation by N electrons and an equal number of ions. Whenever an electron or ion hits any boundary, it is absorbed, and a new particle of the same kind is simultaneously injected at the postion of the arc source, so that N remains constant. It is found that the system rapidly tends toward a steady state, and we take this state to be the same as the quasi-steady state assumed by the device.

717

Magnetic forces and relativistic effects are negligible in this problem so that the simulation particles obey the simple equations of motion for charged particles in an electric field. This field is partly due to space charge and partly due to the applied target potential. The vacuum equipotentials for the rectangular calculation are shown in Figure 2. The equipotentials in cylindrical coordinates are very similar in appearance.

Finally, we must discuss some of the basic limitations of our model. We have not included neutral particles, or any type of collision except with the boundaries. We neglect all ionization, recombination, and secondary emission processes. In representing a plasma by a relatively small number of particles, statistical fluctuations in density are enhanced. Spatial variations in the plasma are calculated on the scale of the cell size, which is much larger than the Debye length in the actual device. Hence, effects depending on the plasma temperature (e.g., wall Debye sheaths) are not calculated (and do not affect our results unless the temperature is extremely high). The only properties of the arc source which we include are its location and the quasi-steady state density of the plasma it produces. In short, we do not simulate microscopic details, only certain macroscopic effects. The justification of the model must come from comparisons with experimental observations.

III. THE CODE

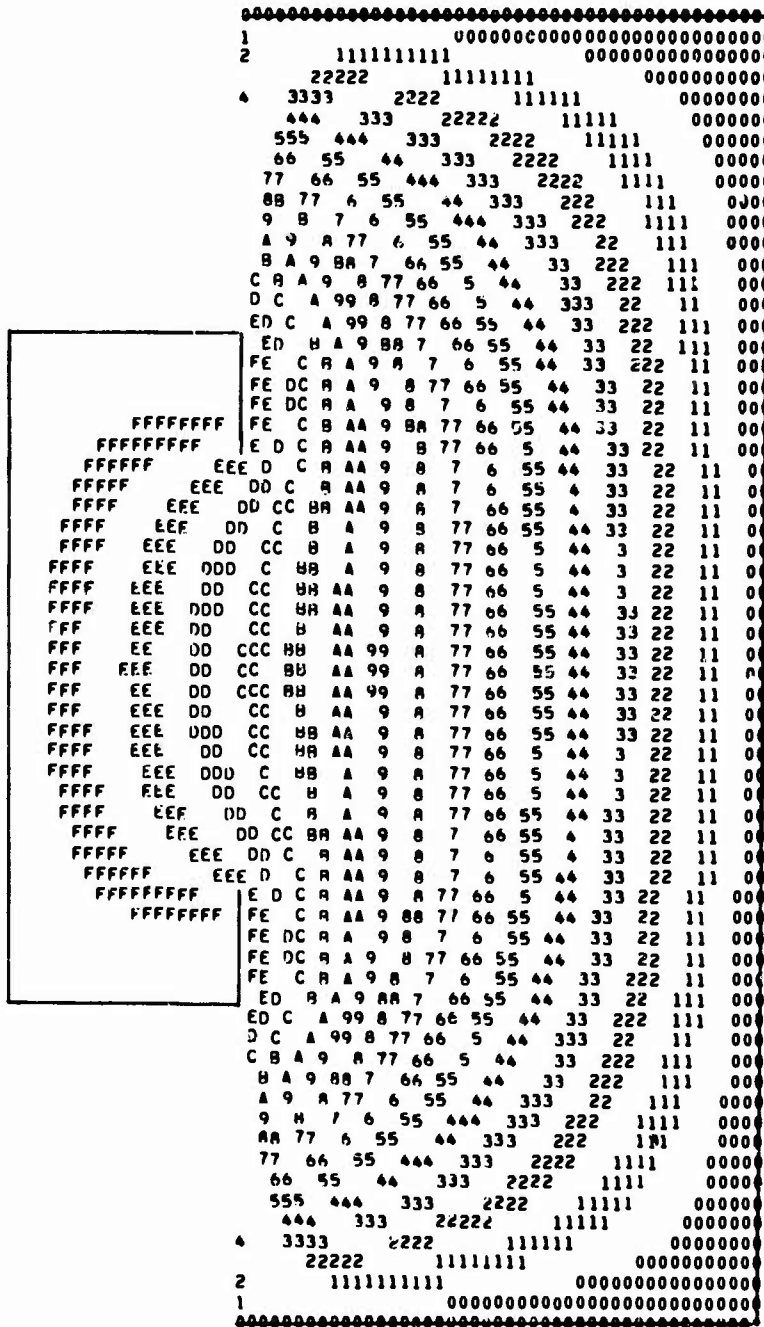In rectangular simulation, a 64 x 64 grid was superimposed over the entire cross-section in Figure 1. The

Figure 2: The vacuum equipotentials

cylindrical calculations were performed on a 32 x 62 grid,
using one-half of the cross-section.

We start with a uniform plasma filling region 1. This
plasma is represented by N equally weighted simulation ions,
and N equally weighted simulation electrons. For cylin-
drical calculations, the number of real ions or electrons
represented by a simulation particle is easily computed,
since the simulation particles are rings. In the rectangular
case, however, the simulation particles are infinitely long
rods, which creates complications in the calculation of the
current. For this reason, we define the rods as having an
effective length $L = N/n_0 A$, where A is the area of region 1.
If each simulation particle is allowed to represent $\pi b/4L$
real particles, where b is the width of the opening AA',
then the current density will be the same when calculated in
the simulation for a rectangular opening of area bL as
for the real cylindrical opening of area $\pi(b/2)^2$.

A necessary condition for practicality of the code
is that the required number of simulation particles be
not too large. By varying this number, we find that
adequate numbers are 10,000 (rectangular) and 5,000
(cylindrical) of each type of particle.

Since the time step in the simulation is determined
by the electron plasma frequency, while the ion motion is
of primary interest, it is desirable to use the largest
possible electron/ion mass ratio. Comparison of the
calculated ion current for various mass ratios indicated
that a value of 1/16 was sufficient. A one-dimensional
simulation for this problem was also constructed to permit

720

a more economical and complete investigation of the mass
ratio dependence. Mass ratios ranging from 1/4 to 1/1024
were investigated, and again a value of 1/16 was found to
be sufficient.

Having fixed the mass ratio at 1/16, one would still
like to use the largest possible time step. The optimum
value depends on the plasma density (and somewhat on the
tube voltage), but it was found that a time step of about
5% of an electron plasma period is sufficiently small.

IV. COMPARISON WITH EXPERIMENT

The two basic parameters in the simulation code are
the target potential V and the initial density n_0.
Available experimental data provided the beam diameter
at 70 kV, and ion currents for various voltages in the
range 60 - 120 kV. n_0 was adjusted until the computed
ion current compared with the experimental current for
one particular voltage, 70 kV. The value of n_0 was then
fixed for the remaining runs, and a current-voltage
relationship was obtained.

Three runs were made with each version of the code to
check the current-voltage relationship, using target voltages
of 70, 90, and 120 kV. A least squares fit provided the
following relationships:

$$I \propto V^{.53} \quad \text{(rectangular)} ;$$

$$I \propto V^{.82} \quad \text{(cylindrical)} .$$

The rectangular simulation is thus in excellent agreement with
the experimental relationship,

$$I \propto V^{.55} \quad \text{(experimental)}.$$

Using the n_o defined above, the rectangular calculations for 70 kV produced a beam diameter of .81, again in excellent agreement with the experimentally measured diameter of .80. The cylindrical simulation gave a beam diameter of .60.

The reason for the superiority of the rectangular code in predicting the experimental results is that the asymmetric nature of the plasma source is taken into account in the rectangular simulation, but completely ignored in the cylindrical version. The geometry itself is not as important in determining the behavior of the neutron tube because, as seen in Figure 2, the field which draws ions from the plasma and accelerates them is mainly in the direction perpendicular to the target, and this component of the field is nearly the same in either geometry. The main value of the cylindrical code is in the study of other neutron tubes which do have symmetric plasma sources.

V.   FURTHER STUDIES AND CONCLUSIONS

The rectangular simulation of the neutron tube operating in its quasi-steady state is shown for two values of n_o in Figures 3 and 4. Although the higher density case, Figure 3, has more space-charge spread, the total current is larger as shown in Table I. From the practical standpoint, the current/area is the most significant quantity, and this is slightly higher for the high density case. The way in which the current is actually distributed on the target is shown in Figure 5 where the current density (j) is plotted vs. distance along the target (x).
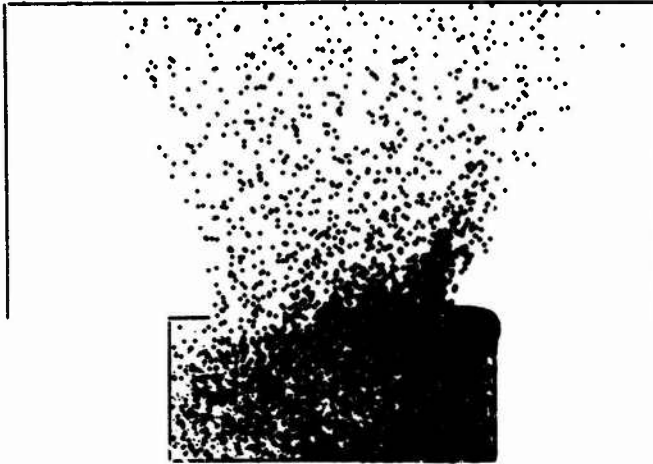
Figure 3: The device in a steady state for $V = 70$ kV, $n_o = 3.2 \times 10^{11}$ cm^{-3}. There are 9600 simulation tritons (shown as +'s) and 9600 simulation electrons (shown as dots). The plasma arc source is located along A'B' (see Fig. 1).
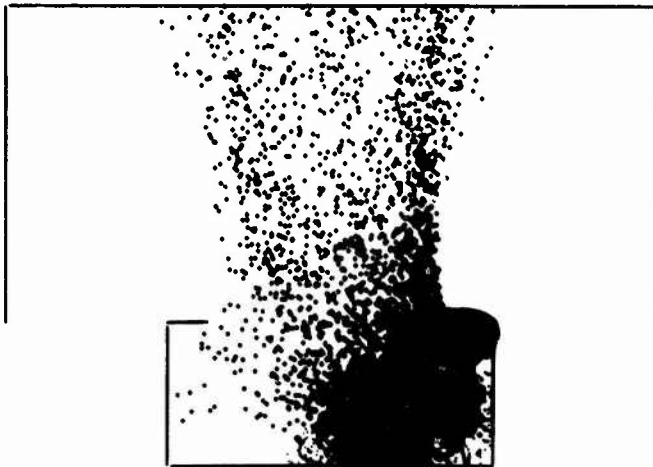

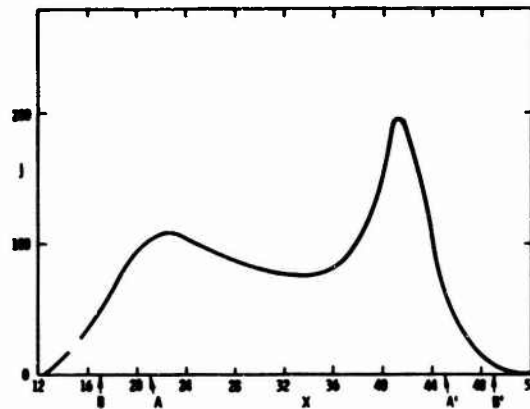Figure 4: The device in a steady state for the same conditions as in Fig. 3 except now $n_o = 10^{11}$ cm^{-3}.

Figure 5: Current distribution on target for
$V = 70$ kV, $n_0 = 10^{11}$ cm^{-3}, and arc
source located along A′B′. j is in
arbitrary units, x is in units of
the cell size. The letters B, A, A′,
B′ show how the current is located with
respect to the opening AA′ (see Fig. 1).

TABLE I

Comparison of Cases with Different Densities

n_0	I	Beam Diameter	Normalized Current/Area
10^{11} cm^{-3}	.40 amps	.92	.36
3.2×10^{11} cm^{-3}	.77 amps	1.17	.42

The codes have been used for a number of other
studies, such as the variation of beam diameter with V,
the ratio of tritons hitting the target to those being
lost on other boundaries, the effect of secondary electrons
knocked from the target by the impinging ions, and the
effect of different arc source configurations. Studies

724

which are expected to be carried out in the near future
are the inclusion of other types of ions, different tube
sizes and boundary configurations, and the inclusion of
additional internal electrodes to help focus the ion beam.

In conclusion, a cloud-in-cell simulation program has
been written to study a particular neutron tube. The model
on which the program is based is somewhat crude inacfar as
simulating the plasma region is concerned, and a complete
treatment would require a three-dimensional simulation.
Nevertheless, the code's predictions compare reasonably well
with experiment, and we conclude that the code is a
practical tool in studying the neutron tube's behavior.

Electron Stream Disruption by a Nonlinear, Infinite Ion Mass Instability

D. W. A. Whitfield
Department of Physics
University of Saskatchewan
Saskatoon, Saskatchewan

ABSTRACT

The one-dimensional behaviour of plasma electrons under the influence of an external electric field and a parallel ion density inhomogeneity was simulated on a computer. A non-linear wave, not due to the two-stream instability grew to large amplitude, causing both disruption of the electron stream and heating of the electrons by trapping.

Introduction

The following problem was studied: the ions in a plasma were considered fixed with spatial density

$$n_i = n_0 \left(1 + \Delta \sin k_i x\right).$$

The electrons had a finite temperature, and initially were given the same spatial density as the ions. At $t = 0$, an external electric field, which increased from zero with time, was applied in the direction of the density perturbation.

A one-dimensional simulation of the ensuing electron behaviour was carried out on a digital computer using the P.I.C. method developed by Morse and Nielson[1]. This model

is similar to that used by Burger, Dunn and Halsted[2], with the additional feature of linear interpolation of the electric field betweel cell ends, and to the C.I.C. procedures of Birdsall and Fuss[3]. The important model parameters were as follows: $\Delta = 0.125$, 30,000 sheets, 2 cells per Debye length, and a total of 500 cells in the length $L = 2\pi/k_i$. All quantities satisfied the condition $F(x) = F(x + L)$. The length of the time step was varied from $2\pi/10\omega_p$ to $2\pi/80\omega_p$ as required to maintain accuracy. The initial thermal velocity was 1.26 in units of cell length per time step.

Results of the Computer Experiment

Figure 1 shows the drift velocity, U, and r.m.s. velocity as functions of time. The increase of V_{rms} in the interval $\omega_p t/2\pi = 25$ to about 90 was due largely to macroscopic modulation of the electron stream velocity and did not represent more than a very little heating or trapping. The catastrophic decline of U and corresponding increase of V_{rms} after about $\omega_p t/2\pi \doteq 100$ were due to the trapping of many of the electrons in the field of a large amplitude wave. After $\omega_p t/2\pi = 110$, V_{rms} leveled off and U again increased at the rate due to free acceleration in the applied field.

The energy, ϵ, in the self electric field is plotted against time in Figure 2. Also shown are the energies in modes 2 and 3 during the times when they are most prominent. The rapid growth of ϵ near $\omega_p t/2\pi = 75$ and 95 corresponds to resonance of modes 3 and 2, respectively. That is, $U = \omega_p/mk_i$, where m = 3 and 2. The frequencies of these
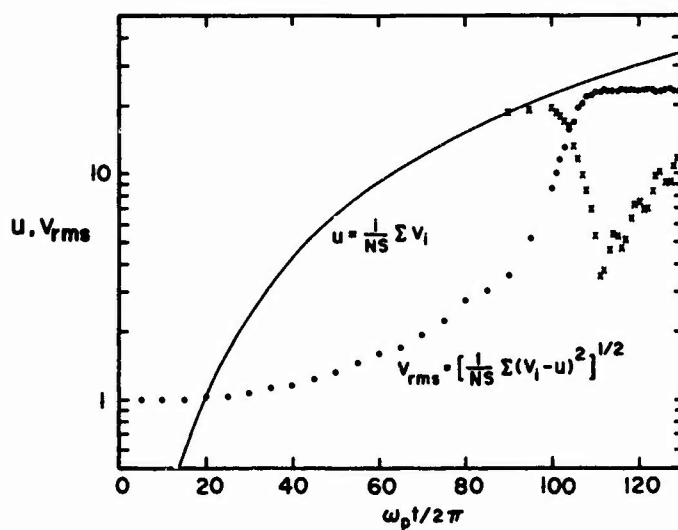
Figure 1. Drift velocity and r.m.s. velocity. The solid
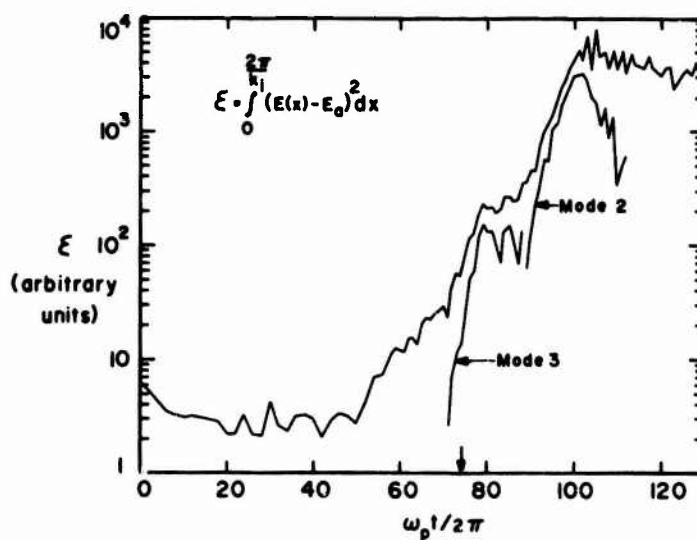curve represents the velocity of free acceleration
in the applied field.

Figure 2. Energy in the self electric field. The
vertical arrow indicates the time at which
mode 3 passed through resonance.

waves were indeed zero in the ion rest frame, as revealed in plots of the electric field or charge density versus x, for successive times.

Before mode 3 became prominent, appreciable energy was in higher modes, whereas after about $\omega_p t/2\pi = 75$, most of the field energy not in modes 2 or 3 was in mode 1.

Figures 3(a) and 3(b) are phase space scatterplots for $\omega_p t/2\pi = 80$ and 100. As the applied field was positive, most of the electrons have negative velocities. At $\omega_p t/2\pi = 80$, mode 3 has reached its greatest amplitude and three minima of the streaming velocity magnitude are visible. These correspond to maxima of the density. In Figure 3(b), mode 2 is predominant, and has grown to such a large amplitude that electron trapping is occurring. At later times most of the electrons become trapped.

In these scatterplots, the few particles separated from the main stream are remnants of an earlier, weak, electron-electron, two-stream instability which arose because some electrons remained at near zero velocity while the rest were accelerating in the applied field. The author has reported this effect previously[4].

Discussion

The observed growing wave structures are not due to the two-stream instability, as the two-stream growth rate is zero for infinitely massive ions. The uneven spacings of the velocity minima, as seen in Figures 3(a) and 3(b) indicate the presence of important higher order modes and suggest that the instability is inherently non-linear in
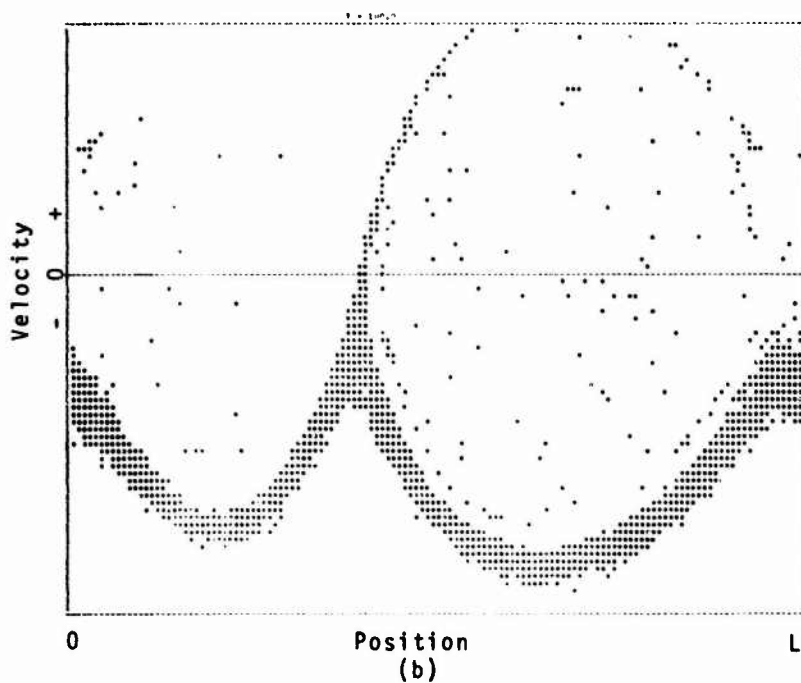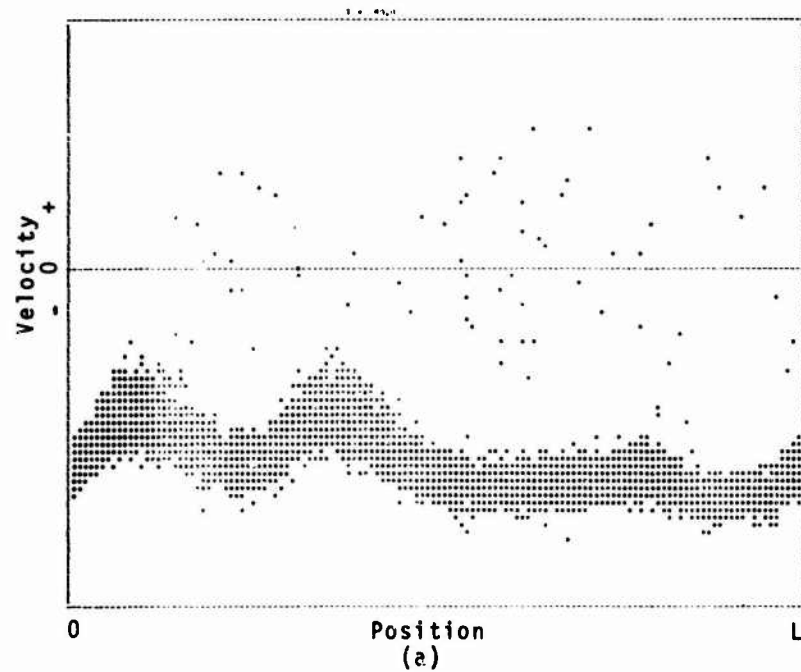
Figure 3. Phase space plots at (a) $\omega_p t/2\pi = 80$, and (b) $\omega_p t/2\pi = 100$.

character. It is possible that it is of numerical origin, but if so, it should be due to non-linear effects, as the simulation parameters (marginally) satisfy Langdon's[5] condition for the absence of linear numerical instabilities. ($\lambda_D \gg \Delta x$, where Δx is the grid spacing.) That growth occurs at resonance, as described above, suggests a real plasma effect. The sharp peaks and broad valleys in $V(x)$, Figure 3, and corresponding features in $n(x)$ strongly resemble the form found by Davidson and Schram[6] for large amplitude electron plasma oscillations.

Acknowledgements

It is a pleasure to thank Dr. H.M. Skarsgard for his valuable help in this work. Financial support came from the Atomic Energy Control Board of Canada .

References

1. Morse, R.L. and C.W. Nielson, Phys. Fluids 12, 2418 (1969).

2. Burger, P., D.A. Dunn, and A.S. Halsted, Phys. Fluids 8, 2263 (1965).

3. Birdsall, C.K. and D. Fuss, J. Comp. Phys. 3, 494 (1969).

4. Whitfield, D.W.A., Phys. in Canada 26, #4, 19 (1970).

5. Langdon, A. Bruce, "Theory of Simulation Plasmas: Grid Effects", unpublished (1969).

6. Davidson, R.W.C. and P.P.J.M. Schram, Nucl. Fusion 8, 183 (1968).

Interpretation of the Vlasov Equation
Through the Wigner Formalism

Marc. R. Feix*
Groupe Physique Théorique et Plasma
Nancy, France

INTRODUCTION

The reasons for which this work has been undertaken are a little bit unusual and some preliminary explanations are in order. The motivation is strictly "practical". We want to solve the classical Vlasov equation i.e. an equation describing the motion of a phase space fluid.

This equation describes very low density and/or high temperature plasma. The validity and justification of the Vlasov equation are now well established and, in this respect, comparison between the results of the Vlasov model and those of the numerical simulation of the N body problem (with the possibility, in this last case, of varying the graininess factor) have been very useful and interesting. Consequently a numerical scheme for the solution of the Vlasov equation would be an extremely valuable tool. Unfortunately, the difficulties are discouraging and actually, with the help of the biggest available computers (C D C 6600 IBM 360-91) only very simplified problems have been solved (one fluid, one dimension, not

too strong nonlinearity, solution valid for a short time ... plus sometimes a credibility gap).

In fact, the Lagrangian model (i.e. the simulation of the plasma by N bodies) is now the best practical scheme to study the Vlasov equation. This is a somewhat paradoxical result, the Vlasov model being the limit of the general case (when only collective motion are taken into account with a graininess parameter

$$g = (nD^3)^{-1} \quad \text{or} \quad g = (nD)^{-1}$$

(respectively for three and one dimension) going to zero.

Usually limiting cases are simpler to solve than the general ones but here this is not true and to treat smaller g we must increase the number of particles and consequently the time of calculation.

Why is an Eulerian numerical scheme for Vlasov equation so difficult ? We feel that the origins of the difficulties must be found in subtle correlations developping, as time goes on, in the phase space. To keep track of these correlations we introduce smaller and smaller wavelengths both in configuration and velocity space. To stock and treat this increasing mass of information is a process which quickly overcomes the possibilities of the computer.

In part I, we review some of schemes which partly solve this problem. Then we introduce a new scheme based on the use of the Schroedinger equation. At that point we introduce quantum mechanics and its relation with classical mechanics (since we are mainly interested in classical plasma). This is a very complex and much debated topic.

733

Interesting comments will be found in $[I]$. Very quickly
this question brings in the most famous papers, authors... and dis-
putes on interpretation of Quantum Mechanics.

Of course we are not going to settle these problems.
Let us repeat that our approach is strictly mathematical and numeri-
cal. We will find that, provided some initial conditions are ful-
filled, the solutions of the Schroedinger equation can approximate
as closely as we like those of the Vlasov equation (with equivalent
initial conditions). The mathematics involved in this projection of
the phase space upon the configuration (or the momentum)space will
bring interesting problems (independent of the exact physical
meaning). The solution of the difficulties connected to the physical
interpretation is not -let us repeat it again- the purpose of this
paper.

Nevertheless, it is reasonable to expect that the mathe-
matical works conducted on the connection between these three equa-
tions (Vlasov, Wigner, Schroedinger) will help the quantum physicists
and will provide some stimulating results. We hope that the prelimi-
nary results presented in part VII will lead in this way. It is well
known that, often, useful indications on the physical meaning of an
equation are brought by the solution of this equation. In any case
a justification of this work is already provided by the numerical
schemes which will be obtained.

II - DIFFICULTIES WITH THE NUMERICAL SOLUTION OF THE VLASOV EQUATION

The method which, up to now, has given the best results
is undoubtedly the expansion of the distribution function $f(x,v,t)$

into a Fourier Hermite series.[2]   [3]

$$f(x,v,t) = \sum_{k=-\infty}^{\infty} \sum_{n=0}^{\infty} f_{kn}(t) \, H_n\left(\frac{v}{v_0}\right) \exp\left(-\frac{v^2}{2v_0^2}\right) \exp i K \frac{2\pi}{L} x$$

Numerical and analytical studies of this model [2] [3] have shown that numerical difficulties appear for a time $T \approx (K_0 V_0 \int)^{-1} \sqrt{N}$ where K_0 is the maximum wavenumber kept in the k summation, V_0 is a characteristic (for example thermal) velocity and N is the highest order retained Hermite coefficient.

We note the slow increase of T with N and the fact that K_0 must increase when the problem becomes more non linear.

Up to now, in practical calculation, the k space has been "sacrificed" to the velocity space by taking a rather short box. For example, for the study of a two stream instability, the number of unstable modes considered is usually two or three and the others are neglected. As a consequence, the physical meaning of the results can and should be discussed.

To solve this problem we may dispose of the information stocked in the high order coefficients of the Hermite expansion. Of course, to do that, we must be sure that this information is useless, and this depends of the problem we want to treat. Moreover, we must avoid triggering numerical instabilities. The best way is to imitate nature and to introduce a Fokker Planck term.

$$\left(\frac{\partial f}{\partial t}\right)_{coll} = \gamma \frac{\partial}{\partial v}\left\{ v f + v_0^2 \frac{\partial f}{\partial v}\right\}$$

The Fourier Hermite transform of this term is $-\gamma \, n f_{kn}$ and introduces, for each component n, a damping proportional to n and to a collision frequency γ which must be kept very small. A compromise must be found between a too large γ (which may destroy the interesting results) and a too large N (with the associated nume-

rical difficulties). Analytical studies [6] lead to the interesting

$N \rightarrow \sim$ 2 or 3 compromise.

Another popular model is the "Water Bag" [4]. We deli-
neate a region of the phase spcae such that at the initial time f=A
inside and 0 outside. We know that the initial value of f is carried
over the trajectories of the particles. Consequently, we do not need
to look at the trajectories of the particles inside the contour and
we have simply to follow the evolution of the boundary. If the initial
phase space region is limited by two contours v_+ and v_- we have to
solve the two equations

$$\frac{\partial v_{\pm}}{\partial t} + v_{\pm} \frac{\partial v_{\pm}}{\partial x} = \frac{e}{m} E$$

We feel that we got rid of the difficulties of the
phase space. But we must ma   o remarks.

1) We paid a certain price for that : precisely we had
selected a special subset of all possible intitial conditions. Espe-
cially, by so doing, we have lost the important Landau damping pheno-
mena.

2) As soon as the problem is too much nonlinear the
phase space complications are reintroduced because v_+ and v_- become
multivalued functions for a given x, and the two contours become
quickly very complex. (See for example in [7] the results of the two
stream instability problems). Usually we must again neglect some of the
details of the phase space if we want to keep the computer time under
reasonable limits.

III - RESORT TO (AND HELP FROM) QUANTUM MECHANICS

These finer and finer structures in phase space remind us that, in this space, there is an elementary cell within which it is impossible to precisely specify the coordinate and the momentum of a particle. The surface of this cell is $\hbar = h/2\pi$ where h is the Planck constant. We must distinguish between two cases.

- Classical case : the characteristic wavelength and momentum involved in the problem are such that their product is much, much bigger than $\hbar$ and we cannot follow the evolution of the phase space microstructure to the point where, effectively, quantum effects become important. Then we will use artificially increased quantum effects and $\hbar$. This increase should be sufficient to kill the numerical difficulties but small enough in order that quantum effects are unimportant for the wavelengths of interest. This is exactly the same philosophy which leads in the Fourier Hermite model of the Vlasov equation to the introduction of a small collision frequency.

Also we use Lagrangian (N body) models with an increased -but still sufficiently small graininess factor- to keep down the number of particles.

As in these last models the more negligible we want to keep the undesired quantum effects the larger will be the computer time required. Finally, in this case, we see that we can be "cavalier" with the physical interpretation of the manipulated functions and the Schroedinger scheme will be a mathematical trick to solve Vlasov equations.

- Quantum case : for solid state plasmas quantum effects become important and, now, the correct interpretation of the manipulated symbols become important. Also the spin effects (and quantum

737

statistics) should be introduced. Consequently, the results found in this case with our proposed model have only an exploratory character in agreement with the often repeated philosophy of this work.

We see consequently that to study classical plasma we must introduce not quite negligible quantum effects (to decrease them being quite expensive). We should see if the scheme is worth this price. The answer is yes.

The main advantage is that we are going to get rid of the phase space or more precisely to describe it through one single function defined either in the configuration or in the momentum space with numerical resolution of the rather simple Schroedinger equation on Ψ (x, t)

The use of the Schroedinger equation is very logical since it must be realized that in this equation as in the Vlasov equation we deal with a single particle representing statistically all the particles. The motion takes place in a self consistent field obtained by integration of the Poisson equation where the electrical density is obtained respectively from f(x, v, t) and Ψ (x, t).

IV - SCHROEDINGER - WIGNER - VLASOV

Now we must deal with the exact mathematical formulation of the above mentioned ideas. Especially we must clearly understand how, with a function of one independent variable Ψ (x) we can represent the behaviour of a function of two independent variables f(x, v). The crucial point is the use of the Wigner distribution function usually introduced through the density matrix and ensemble average. Here we will make a simpler demonstration, building directly the Wigner func-

tion from Ψ and exhibiting the equation governing this function. Let us specify the problem and the notations.

We will suppose from now a one dimensional, non relativistic motion, taking into account only electrostatic forces described by a potential ϕ. Moreover to simplify, we will suppose $e = m = \hbar = 1$.

We have inside a box of length L a population of N electrons embedded in an uniform motionless distribution of N ions. Ψ is supposed normalized and obeys the Schroedinger-Poisson-equations system. Consequently

(1) $$i \frac{\partial \Psi}{\partial t} = (p^2/2 + \Phi) \Psi = -\frac{1}{2} \frac{\partial^2 \Psi}{\partial x^2} + \phi \Psi$$

(2) $$\frac{\partial^2 \phi}{\partial x^2} + N \left[\Psi \Psi^* - \frac{1}{L} \right] = 0$$
$$\int_0^L \Psi \Psi^* \, dx = 1$$

(1) and (2) describe the evolution of the information in the configuration space. But it is well known that Ψ includes also information on momentum space. We define Θ (k, t) the Fourier transform of Ψ (x, t)

$$\Theta(k,t) = (2\pi)^{-\frac{1}{2}} \int \Psi(x,t) \exp{-ikx} \, dx$$

The density in velocity (momentum) space is $\Theta \Theta^*$ while the density in configuration space is $\Psi \Psi^*$ (Note that with our notations $k = m v/\hbar = v$).

As it is well known there is quite satisfactory reciprocity between the two spaces. For example, the operator connected to the average position is $\hat{x} = x$ in configuration space and $\hat{x} = i \partial/\partial k$

739

in momentum space while the average momentum is given by the operator $\hat{p} = k$ in momentum space and $\hat{p} = -i \partial/\partial x$ in configuration space. Consequently

$$\langle x \rangle = \int \psi^* \, x \, \psi \, dx = \int \theta^* \, i \, \frac{\partial \theta}{\partial k} \, dk$$

(3)

$$\langle p \rangle = \int \psi^* (-i) \frac{\partial \psi}{\partial x} \, dx = \int \theta^* \, k \, \theta \, dk$$

We see that the Schroedinger equation gives consequently information on the properties of the particle in both spaces. Can we get simultaneously information on both spaces with of course an uncertainty margin ? At that point —and within our utilitarian philosophy— the introduction of the Wigner function allows us to answer yes. (See [1] for a more physical discussion on the statistical interpretation of quantum mechanics).

Wigner introduces a function $f(x, v)$ from the Schroedinger function $\psi(x)$. We like to consider this process as an induction of information.

We have

(4)
$$f(x, v) = (2\pi)^{-1} \int_{-\infty}^{\infty} d\Delta \, \psi \left(x + \frac{\Delta}{2} \right) \psi^* \left(x - \frac{\Delta}{2} \right) exp\, {-iv\Delta}$$

We like to point out that radar theoreticians introduce, from a signal $S(t)$ the so called ambiguity function through a quasi identical relation. See [5].

(5)
$$f(t, \Omega) = \frac{1}{E} \int_{-\infty}^{\infty} S\left(\tau + \frac{t}{2} \right) S^* \left(\tau - \frac{t}{2} \right) exp\, i\Omega\tau \, d\tau$$

$$E = \int_{-\infty}^{\infty} |S(\tau)|^2 \, d\tau$$

If in (4) we change Δ to $-\Delta$, the element under the sign is changed to its complex conjugate. Consequently, f is real ;

unfortunately f is not necessarily positive and this is probably the biggest difficulty for a physical interpretation of the Wigner function.

Nevertheless, f can be used as if it was a "bona fide" distribution function. For example, to compute the density n(x) we will write

$$n(x) = \int f(x,v)\,dv = \int_{-\infty}^{\infty} d\Delta \; \Psi\left(x + \frac{\Delta}{2}\right) \Psi^*\left(x - \frac{\Delta}{2}\right) \frac{1}{2\pi} \int_{-\infty}^{\infty} \exp -iv\Delta \, dv$$

The last integral is trivial and gives $\delta(\Delta)$. Consequently

$$n(x) = \int f(x,v)\,dv = \Psi(x)\,\Psi^*(x)$$

Then we compute the Fourier transform with regard to the x variable of $f(x, v)$

$$(6) \qquad F(v, \xi) = \int_{-\infty}^{\infty} f(x,v)\left[\exp -i\,\xi\,x\right] dx$$

Combining (4) and (6) we find

$$(7) \qquad F(v, \xi) = \iint_{-\infty}^{\infty} \frac{1}{2\pi} \; \Psi\left(x + \frac{\Delta}{2}\right) \Psi^*\left(x - \frac{\Delta}{2}\right) \cdot$$
$$\cdot \left[\exp -iv\Delta\right]\left[\exp -i\,\xi\,x\right] d\Delta\,dx$$

Taking into account

$$(8) \qquad \Psi\left(x + \frac{\Delta}{2}\right) = (2\pi)^{-\frac{1}{2}} \int \Theta(v') \exp i v'\left(x + \frac{\Delta}{2}\right) dv'$$
$$\Psi^*\left(x - \frac{\Delta}{2}\right) = (2\pi)^{-\frac{1}{2}} \int \Theta^*(v'') \exp -i v''\left(x - \frac{\Delta}{2}\right) dv''$$

We carry over (8) into (7)

$$F(v, \xi) = \iiiint (2\pi)^{-2} \, \Theta(v') \, \Theta^*(v'') \exp i\Delta\left(\frac{v'+v''}{2} - v\right) \cdot$$
$$\cdot \left[\exp i(v'-v''-\xi)x\right] d\Delta\,dx\,dv'dv''$$

The two integrals on Δ and x give :

$$(2\pi)^2 \, \delta(v' - v'' - \xi) \, \delta\left(\frac{v' + v''}{2} - v\right)$$

and we obtain

$$(9) \quad F(v, \xi) = \theta\left(v + \frac{\xi}{2}\right) \theta^*\left(v - \frac{\xi}{2}\right)$$

(9) is for the momentum space the equivalent of (4) for the configuration space. If $\xi = 0$

$$F(v, \xi = 0) = \int f(x, v)\, dx = \theta(v)\, \theta^*(v)$$

and we obtain the density in the velocity space.

V – EQUATION OF EVOLUTION OF f. THE POTENTIAL ∅ IS ZERO

Starting from (4) we get

$$(10) \quad \frac{\partial f}{\partial t} = \frac{1}{2\pi} \int_{-\infty}^{\infty} \left[\frac{\partial \psi\left(x + \frac{\Delta}{2}\right)}{\partial t} \psi^*\left(x - \frac{\Delta}{2}\right) + \psi\left(x + \frac{\Delta}{2}\right) \frac{\partial \psi^*\left(x - \frac{\Delta}{2}\right)}{\partial t} \right] \left[\exp - iv\Delta\right] d\Delta$$

But ψ satisfies the Schroedinger equation. Consequently

$$(11) \quad i\, \frac{\partial \psi}{\partial t} = -\frac{1}{2}\, \frac{\partial^2 \psi}{\partial x^2} \qquad \begin{cases} \dfrac{\partial \psi}{\partial t} = \dfrac{i}{2}\, \dfrac{\partial^2 \psi}{\partial x^2} \\[2mm] \dfrac{\partial \psi^*}{\partial t} = -\dfrac{i}{2}\, \dfrac{\partial^2 \psi^*}{\partial x^2} \end{cases}$$

Combining (11) and (10)

$$(12) \quad \frac{\partial f}{\partial t} = \frac{1}{2\pi} \int_{-\infty}^{\infty} \frac{i}{2} \left[\frac{\partial^2 \psi\left(x + \frac{\Delta}{2}\right)}{\partial x^2} \psi^*\left(x - \frac{\Delta}{2}\right) - \frac{\partial^2 \psi^*\left(x - \frac{\Delta}{2}\right)}{\partial x^2} \psi\left(x + \frac{\Delta}{2}\right) \right] \exp - iv\Delta \; d\Delta$$

We take into account the definition of f.

$$
(13) \quad v\frac{\partial f}{\partial x} = \frac{1}{2\pi}\int_{-\infty}^{\infty}\left[\frac{\partial \psi(x+\frac{\Delta}{2})}{\partial x}\psi^*(x-\frac{\Delta}{2}) + \psi(x+\frac{\Delta}{2})\frac{\partial \psi^*(x-\frac{\Delta}{2})}{\partial x}\right]v\,\exp-iv\Delta\,d\Delta
$$

We integrate (13) by parts

$$
v\,\exp-iv\Delta\,d\Delta = d\alpha \implies \alpha = i\,\exp-iv\Delta
$$

$$
(14) \quad \frac{\partial \psi(x+\frac{\Delta}{2})}{\partial x}\psi^*(x-\frac{\Delta}{2}) + \psi(x+\frac{\Delta}{2})\frac{\partial \psi^*(x-\frac{\Delta}{2})}{\partial x} = \beta
$$

$$
\implies d\beta = \frac{1}{2}\left[\frac{\partial^2\psi(x+\frac{\Delta}{2})}{\partial x^2}\psi^*(x-\frac{\Delta}{2}) - \frac{\partial^2\psi^*(x-\frac{\Delta}{2})}{\partial x^2}\psi(x+\frac{\Delta}{2})\right]d\Delta
$$

Consequently

$$
(15) \quad v\frac{\partial f}{\partial x} = \frac{1}{2\pi}\int\left(-\frac{i}{2}\right)\left[\frac{\partial^2\psi(x+\frac{\Delta}{2})}{\partial x^2}\psi^*(x-\frac{\Delta}{2}) - \frac{\partial^2\psi^*(x-\frac{\Delta}{2})}{\partial x^2}\psi(x+\frac{\Delta}{2})\right]\exp-iv\Delta\,d\Delta
$$

(15) and (12) show that

$$
(16) \quad \frac{\partial f}{\partial t} + v\frac{\partial f}{\partial x} = 0
$$

This is the Liouville equation for free particles.

VI - EQUATION OF EVOLUTION : $\phi \ne 0$

The computation of $v\frac{\partial f}{\partial x}$ is the same. But the computation of $\frac{\partial f}{\partial t}$ is different. Instead of (17) we get

$$
(17) \quad \frac{\partial \psi}{\partial t} = \frac{i}{2}\frac{\partial^2\psi}{\partial x^2} - i\phi\psi
$$
$$
\frac{\partial \psi^*}{\partial t} = -\frac{i}{2}\frac{\partial^2\psi^*}{\partial x^2} + i\phi\psi^*
$$

We plug (17) in $\frac{\partial f}{\partial t}$ and compute $\frac{\partial f}{\partial t} + v\frac{\partial f}{\partial x}$

We get instead of (14)

$$\frac{\partial f}{\partial t} + v\frac{\partial f}{\partial x} + \frac{i}{2\pi}\int_{-\infty}^{\infty}\left[\phi\left(x+\frac{\Delta}{2}\right)-\phi\left(x-\frac{\Delta}{2}\right)\right]\cdot$$

$$\cdot\,\Psi\left(x+\frac{\Delta}{2}\right)\Psi^*\left(x-\frac{\Delta}{2}\right)\exp{-iv\Delta}\;d\Delta = 0 \tag{18}$$

We introduce the operator A defined in the following way

$$Af = \frac{i}{2\pi}\iint \exp i(v-v')\Delta\left[\phi\left(x-\frac{\Delta}{2}\right)-\phi\left(x+\frac{\Delta}{2}\right)\right]\cdot$$

$$\cdot\,f(x\,v'\,t)\;dv'\,d\Delta \tag{19}$$

Introducing in (19) the f definition (See (4))

$$Af = \frac{i}{(2\pi)^2}\iiint \exp i(v-v')\Delta\left[\phi\left(x-\frac{\Delta}{2}\right)-\phi\left(x+\frac{\Delta}{2}\right)\right]\cdot$$

$$\Psi\left(x+\frac{\Delta}{2}\right)\Psi^*\left(x-\frac{\Delta}{2}\right)\exp{-iv'\Lambda}\;d\Lambda\,d\Delta\,dv'$$

We first integrate on v'. We get $2\pi\,\delta(\Delta+\Lambda)$. Then we integrate on Δ and obtain

$$Af = \frac{i}{2\pi}\int \exp{-iv\Lambda}\left[\phi\left(x+\frac{\Lambda}{2}\right)-\phi\left(x-\frac{\Lambda}{2}\right)\right]\cdot$$

$$\cdot\,\Psi\left(x+\frac{\Lambda}{2}\right)\Psi^*\left(x-\frac{\Lambda}{2}\right)\;d\Lambda \tag{20}$$

Except the change of notation $\Delta\rightarrow\Lambda$ (20) is strictly identical to the last term of (18). Finally we obtain the Wigner equation.

$$\frac{\partial f}{\partial t} + v\frac{\partial f}{\partial x} + \frac{i}{2\pi}\iint \exp i(v-v')\Delta\left[\phi\left(x-\frac{\Delta}{2}\right)-\phi\left(x+\frac{\Delta}{2}\right)\right]\cdot$$

$$\cdot\,f(x,v',t)\;dv'\,d\Delta = 0 \tag{21}$$

Classical limits and quantum corrections

We want to obtain the classical limit of (21). We must remember that we have taken $\hbar = 1$ and consequently the term exp$-iv\Delta$ of (18) should be written exp$-imv\Delta/\hbar$. If $\hbar\rightarrow 0$ (classical limit) this term is violently oscillating and only the region in the neigh-

bourhood of $\Delta = 0$ gives a non negligible contribution. Consequently we may developp $\phi\left(x + \frac{\Delta}{2}\right)$ and $\phi\left(x - \frac{\Delta}{2}\right)$ around the value x, keeping only the four first terms.

$$\phi\left(x \pm \frac{\Delta}{2}\right) = \phi(x) \pm \frac{\Delta}{2} \frac{\partial\phi}{\partial x} + \frac{\Delta^2}{8} \frac{\partial^2\phi}{\partial x^2} \pm \frac{\Delta^3}{48} \frac{\partial^3\phi}{\partial x^3}$$

(18) is written

(22)
$$\frac{\partial f}{\partial t} + v \frac{\partial f}{\partial x} + \frac{i}{2\pi} \iint \left[\Delta \frac{\partial\phi}{\partial x} + \frac{\Delta^3}{24} \frac{\partial^3\phi}{\partial x^3} \right] \cdot$$
$$\psi\left(x + \frac{\Delta}{2}\right) \psi^*\left(x - \frac{\Delta}{2}\right) \exp{-iv\Delta}\, d\Delta = 0$$

We easily check

(23)
$$\frac{1}{2\pi} \int \Delta\, \psi\left(x + \frac{\Delta}{2}\right) \psi^*\left(x - \frac{\Delta}{2}\right) [\exp{-iv\Delta}]\, d\Delta = i \frac{\partial f}{\partial v}$$
$$\frac{1}{2\pi} \int \Delta^3\, \psi\left(x + \frac{\Delta}{2}\right) \psi^*\left(x - \frac{\Delta}{2}\right) [\exp{-iv\Delta}]\, d\Delta = -i \frac{\partial^3 f}{\partial v^3}$$

Introducing the field $E = -\partial\phi/\partial x$ we obtain for (22)

(24)
$$\frac{\partial f}{\partial t} + v \frac{\partial f}{\partial x} + E \frac{\partial f}{\partial v} = \frac{1}{24} \frac{\partial^2 E}{\partial x^2} \frac{\partial^3 f}{\partial v^3}$$

We introduce e, m and $\hbar$ in (24) which becomes :

(25)
$$\frac{\partial f}{\partial t} + v \frac{\partial f}{\partial x} + \frac{e}{m} E \frac{\partial f}{\partial v} = \frac{e}{m^3} \frac{\hbar^2}{24} \frac{\partial^2 E}{\partial x^2} \frac{\partial^3 f}{\partial v^3}$$

(25) is just the Vlasov equation provided with a second member, vanishing with $\hbar$. It is interesting to compare the orders of magnitude of this term and the Vlasov term. The ratio is

$$(1/24)\, \hbar^2 k^2 / m^2 v_T^2$$

where v_T is the characteristic velocity of the distribution. Consequently the order of the correction is $(1/24) k^2 \lambdabar^2$ where $\lambdabar$ is the De Broglie wavelength.

VII – INITIAL CONDITIONS : A SYNTHESIS PROBLEM

We have, in the preceeding paragraphs, found an interesting connection between the Schroedinger equations on one side and the Wigner and Vlasov equations on the other. To solve Vlasov, we replace it by the Wigner equation (keeping small the quantum correction) and go to the Schroedinger formalism. Consequently, we must use a wave function which will represent through its variation in x both the variation in configuration space and velocity space of $f(x, v)$. Probably this will require quite a few modes. To get a more precise idea let us consider the momentum space (See Figure 1).

$$O \qquad k_o \qquad\qquad k_M \qquad k \qquad Fig\ 1$$
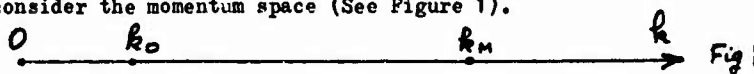
If V_M is the maximum velocity above which the number of particles is negligible, we must keep all the wavenumbers up to $k_M = m V_M / \hbar$. On the other hand we know that the Fourier components of the electric field are damped above a certain wavenumber k_o (k_o is the inverse of the Debye distance for a Maxwellian Plasma). Consequently the ratio of the corrective term to the Vlasov term is given by

$$\frac{1}{24} k_o^2 / k_M^2$$

and if $k_M / k_o = 10$ the corrective term will be of the order of 4×10^{-4}. Finally if we use a box of length L we can hope that 10 wavenumbers will give already a good picture of nonlinear interactions. Altogether this gives 100 modes. Of course, this guess must be submitted to a numerical test. Finally we may find some comfort in the fact that quantum effects are also interesting by themselves.

One important advantage is that we do not have to decide how we will divide our effort between the configuration and momentum space. This is automatically solved. Also solved is the problem of the

convection term $v \dfrac{\partial f}{\partial x}$ which in the Fourier Hermite model was responsible of the appearance of higher and higher Hermite coefficient.

A difficulty appears on the time behaviour of the small wavelengths components which oscillate with the very high frequency $\omega_k \approx \hbar k^2/2m$. But this difficulty appears also in a classical frame as this has been recently recognized on the Fourier Hermite model. Numerical multiple-time-scale treatment would help.

Finally the Schroedinger equation must be considered as a new numerical model in plasma physics. Practical results are now needed in order to test the exact value of this method.

However, there is a fundamental problem that we have still to solve. The resolution of Vlasov can be replaced by the resolution of the Schroedinger provided there is the possibility of introducing correct initial conditions.

From (4) we see that $\Psi(x)$ gives $f(x, v)$. But the inverse is not true. Finally we face again the problem of doing with the independent variable x the job of the two independent variables x and v.

In a certain way the situation reminds us of the Water Bag model where the initial situation has a very special form. However, we think that as soon as we go to the classical case we may synthesize any initial conditions, at least in average. Let us take an example.

We want to represent the initial situation corresponding to an homogeneous two stream plasma with velocities $\pm V$. We feel that we should take

$$(26) \quad \Psi(x) = \frac{1}{\sqrt{2}} \left[\exp - i V x + \exp i V x \right] = \sqrt{2} \cos V x$$

Plugging (26) in (4) we obtain

$$(27) \quad f(x,v) = \frac{1}{2} \delta(v - V) + \frac{1}{2} \delta(v + V) + \cos 2 \dot{V} x \, \delta(v)$$

The two first terms of (27) correspond to the situation
we wanted to realize but we get an extra third term which in fact
oscillates in space with the very small wavelength $2 m V \hbar$. If $\hbar \rightarrow 0$
as soon as we average on a small but finite distance this distribution
of particles alternatively "existing" and "antiexisting" we get zero.
But we see that the disappearance of the unwanted term is not trivial
and we forecast difficulty in the synthesis problem.

As we point out already the Radar theoreticians have stu-
died this problem for the ambiguity function (as given by (5)). They
introduce what they call sophisticated signals, obtained by repeating
a large number of times the same elementary signal. We study the distri-
bution function corresponding to

$$(28) \quad \phi(x) = \sum_{n=-\infty}^{\infty} \psi(x - n\ell)$$

Let us call $\Theta(k)$ the Fourior transform of $\psi(x)$. We intro-
duce (28) in (4) and obtain after a little algebra :

$$(29) \quad f(x,v) = \ell^{-2} \sum_{s=-\infty}^{\infty} \delta\left(v - V \frac{s}{2}\right) \exp -ix V s \sum_{q=-\infty}^{\infty} \Theta(q V) \cdot$$

$$\Theta^*(s-q)V \, \exp 2ixq V$$

V is a velocity $V = 2\pi \hbar / m\ell = 2\pi/\ell$

We see that $f(x, v)$ corrosponds to a set of beams of velo-
city $s V/2$. The stratification of the velocity field is not surprising,
$\phi(x)$ being a periodic function of spatial period L. In fact we would

expect a stratification with a jump equal to V and not $V/2$. (The Fourier transform of $\phi(x)$ being different from zero only for integer multiples of V). This is at this point that we see that the Wigner function has been obtained by introduction from $\phi(x)$ of a more detailed information (with a controversial physical meaning).

On the other hand if we integrate $f(x, v)$ as given by (29) on x to get the velocity distribution we obtain

$$(30) \quad \frac{1}{\ell} \int_0^\ell f(x,v)\,dx = 2\pi\, \ell^{-2} \sum_{s=-\infty}^{\infty} \delta\left(v - V\frac{s}{2}\right)$$
$$\sum_{q=-\infty}^{\infty} \Theta(qV)\, \Theta^*(s-q)\, V\, \frac{1}{\ell} \int_0^\ell \left[\exp i x V (2q-s)\right] dx$$

We see (on 30) that if $s \neq 2q$ the last integral is zero. On the other hand if s is even we get ($s= 2q$)

$$(31) \quad \frac{1}{\ell} \int_0^\ell f(x,v)\,dx = 2\pi\, \ell^{-2} \sum_{q=-\infty}^{\infty} \delta(v - Vq)\, \Theta(qV)\, \Theta^*(qV)$$

which is nothing else but the usual results of the theory of velocity measurement in quantum mechanics. Finally, if we take $\Psi(x) = \delta(x)$ we have

$$\Theta = \Theta^* = 1$$
$$(32) \quad \sum_{q=-\infty}^{\infty} \exp 2 i x V q = 2\pi \sum_{n=-\infty}^{\infty} \delta(2xV - 2\pi n) = \frac{\ell}{2} \sum_{n=-\infty}^{\infty} \delta\left(x - n\frac{\ell}{2}\right)$$

We see that particles will be located at points $x = n\frac{\ell}{2}$; we take into account this result to replace in (29) x by $n\ell/2$ and compute

$$\exp - i x V s = \exp - i\, n s\, V\frac{\ell}{2} = \exp - i\pi n s = (-1)^{ns}$$

Consequently

$$(33) \quad f(x,v) = \frac{\ell^{-1}}{2} \sum_{s=-\infty}^{\infty} \sum_{n=-\infty}^{\infty} (-1)^{ns} \delta\left(v - s\frac{V}{2}\right) \delta\left(x - n\frac{\ell}{2}\right)$$

749

Eq. (33) (See figure 2) shows a distribution of particles "existing" and "antiexisting" with well precised velocities $v = s\sqrt{V}/2$ and locations $x = \lambda \ell/2$. The uncertainty principle appears in a curious form. It would be interesting to try to synthesize distribution functions with no "antiexisting" particles and also to try to concentrate on one of the "existing" particles an important probability.

Sophisticated signals as given by (28) show how we will build a plasma homogeneous in average with a given velocity distribution. An often used trick will allow us to build from this situation an initial wave. Let us suppose that we apply to this plasma a large potential ϕ (x) during a very short time τ such that $\phi(x)\tau$ is finite and τ can be considered as arbitrarily small.

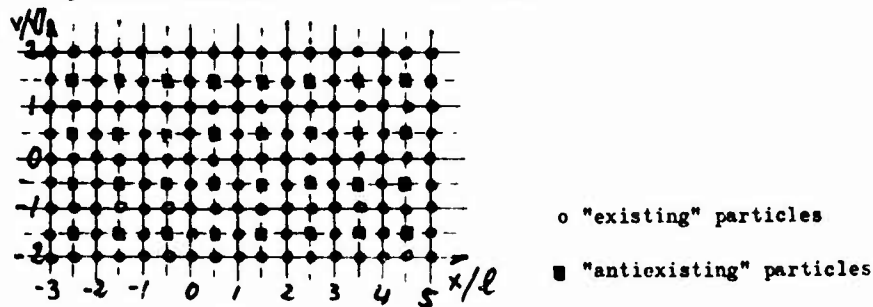o "existing" particles

■ "antiexisting" particles

Figure 2

If $\psi_0(x)$ was the Schroedinger function before the application of the pulse, due to the smallness of τ one can easily obtain for $\psi(x)$ (the function after the pulse)

$$(34) \quad \psi(x) = \psi_0(x) \exp{-i\,\phi(x)\tau/\hbar} = \psi_0(x)\exp{-i\phi(x)\tau}$$

This last expression corresponds to a f(x, v) given by

$$(35) \quad f(x,v) = (2\pi)^{-1} \int_{-\infty}^{\infty} \Psi_0\left(x+\frac{\Delta}{2}\right) \Psi_0^*\left(x-\frac{\Delta}{2}\right) \exp -i\tau\left[\Phi\left(x+\frac{\Delta}{2}\right) - \Phi\left(x-\frac{\Delta}{2}\right)\right] \cdot$$
$$\cdot \exp -iv\Delta \; d\Delta$$

in the classical limit we have already pointed out that $\Phi\left(x\pm\frac{\Delta}{2}\right)$ should be expanded around x

$$(36) \quad \Phi\left(x+\frac{\Delta}{2}\right) - \Phi\left(x-\frac{\Delta}{2}\right) = \Delta \frac{\partial \Phi}{\partial x} = -E(x)\Delta$$

Combining (35) and (36) we get for the classical limit

$$f(x,v) = f_0\left[x, v - E(x)\tau\right]$$

as it should be.

The applied potential can be as strong as we like : provided its duration is arbitrarily short, (34) is always valid.

VIII - LINEARIZED FORM OF THE WIGNER EQUATION - QUANTUM DIELECTRIC CONSTANT

In the linear treatment of the Wigner equation we suppose that the distribution function $f(x, v, t) = \mathcal{F}(v) + f_1(x, v, t)$ where f_1 (and also the self consistent potential ϕ associated to f_1) are considered as small perturbations. It must be pointed out that because of the nonlinear relation connecting Ψ and f, it is impossible to consider the strictly equivalent problem in the Schroedinger formalism where the interaction between thermal and collective effects is taken into account through interactions between the different Ψ_Q (The only exception is the cold plasma case with $\Psi = 1 + \Psi_1$ and $F(v) = \delta(v)$

The linearized form of the Wigner equation is now written

$$(37)\ \frac{\partial f_1}{\partial t} + v\frac{\partial f_1}{\partial x} + \frac{i}{2\pi}\iint \exp i(v-v')\Delta\left[\Phi\left(x-\frac{\Delta}{2}\right) - \Phi\left(x+\frac{\Delta}{2}\right)\right]\cdot$$
$$\cdot F(v')\,d\Delta\,dv' = 0$$

We take into account

$$(38)\quad \Phi(x) = \int \Phi(k)\,\exp -ikx\,\,dk$$

We Fourier analyse (37). We get

$$(39)\ \frac{\partial f_1}{\partial t} - ikv\,f_1 + \frac{i}{2\pi}\iint \exp i(v-v')\Delta\left[\left(\exp ik\frac{\Delta}{2}\right) - \left(\exp -ik\frac{\Delta}{2}\right)\right]\Phi(k)\,F(v')\,d\Delta\,dv' = 0$$

(39) is integrated first on Δ which brings the Dirac

functions $\delta\left(v-v'+\frac{k}{2}\right)$ and $\delta\left(v-v'.\frac{k}{2}\right)$

The v integration becomes trivial. Taking into account

$E(k) = ik\Phi(k)$, (39) becomes :

$$(40)\ \frac{\partial f_1}{\partial t} - ikv\,f_1 + E(k,t)\frac{F(v+k/2) - F(v-k/2)}{k} = 0$$

To obtain the classical limit we take the first term of the k expansion

of $F\left(v\pm\frac{k}{2}\right)$

$$k^{-1}\left\{F\left(v+\frac{k}{2}\right) - F\left(v-\frac{k}{2}\right)\right\} \longrightarrow dF/dv$$

The Laplace transform on time is introduced in (40) and

f_1 and the density are computed. Completing with the Poisson equation

the dielectric constant is easily obtained. The dispersion equation

takes the form (we call $s = i\omega$ the Laplace variable)

$$(41)\ \mathcal{E}(k,s) = 1 + \frac{4\pi i}{k}\int_{-\infty}^{\infty} \frac{F(v+k/2) - F(v-k/2)}{k\,(s-ikv)}\,dv = 0$$

If e, m, $\hbar$ are reintroduced and if $\omega_p^2 = 4\pi Ne^2/m$

(41) takes the form

$$(42)\ \epsilon(k,s) = 1 + \frac{i\omega_p^2}{k} \int_{-\infty}^{\infty} \frac{F(p+\frac{\hbar k}{2}) - F(p-\frac{\hbar k}{2})}{(\hbar k/m)(s - ik\,p/m)}\, dp = 0$$

IX – STATIONARY SOLUTIONS OF THE WIGNER EQUATION

Taking $\partial/\partial t = 0$ gives the stationary solutions of the Wigner equation (21). Let us show that these solutions correspond to the stationary solution of the Schroedinger equation defined by

$$(43)\qquad H\Psi = E\Psi$$

(43) can be written

$$\phi\Psi = E\Psi + \frac{1}{2}\frac{\partial^2\Psi}{\partial x^2}$$

$$(44)\qquad \phi\Psi^* = E\Psi^* + \frac{1}{2}\frac{\partial^2\Psi^*}{\partial x^2}$$

Introducing (44) in (20) we compute the term $A\,f$ in the Wigner equation

$$A f = \frac{i}{2\pi}\int\Big\{\Big(E\,\Psi(x+\tfrac{\Delta}{2})\Psi^*(x-\tfrac{\Delta}{2}) + \frac{1}{2}\frac{\partial^2\Psi(x+\tfrac{\Delta}{2})}{\partial x^2}\Psi^*(x-\tfrac{\Delta}{2})$$

$$(45)$$

$$-E\,\Psi^*(x-\tfrac{\Delta}{2})\Psi(x+\tfrac{\Delta}{2}) - \frac{1}{2}\frac{\partial^2\Psi^*(x-\tfrac{\Delta}{2})}{\partial x^2}\Psi(x+\tfrac{\Delta}{2})\Big)\Big\}\exp{-iv\Delta}\,d\Delta$$

In (45) the first and third term in $\{\ \}$ cancel. We compare with (15). If Ψ is solution of (43) then, indeed :

$$v\frac{\partial f}{\partial x} + A f = 0$$

Finally we notice the interesting case of the harmonic oscillator with $\phi = (1/2)\,Kx^2$

$$E = -\frac{d\phi}{dx} = -Kx$$

$$(46)\qquad \phi(x+\tfrac{\Delta}{2}) - \phi(x-\tfrac{\Delta}{2}) = Kx\Delta = -\Delta E$$

Consequently for the harmonic oscillator the Wigner equation is strictly identical to the classical equation. This is also true for uniform and uniformly accelerated motions.

Consequently for the harmonic oscillator the solutions are function only of the energy $E = (1/2) \, v^2 + (K/2) \, x^2$

$$f(x, \, v) = F(1/2 \, v^2 + K/2 x^2)$$

We compute the distribution $f(x, \, v)$ for the two first eigen functions of the Schroedinger equations for the harmonic oscillator. We take the energy $\hbar \omega = \hbar \sqrt{\dfrac{K}{m}}$ equal to unity. We get for the first eigenfunction

$$n = 0 \qquad \langle E \rangle = 1/2$$

(47)
$$f(x, v) = \pi^{-1} \exp - 2E$$

In this case f is positive for all value of x and v. For the second eigenfunction

$$n = 1 \qquad \langle E \rangle = 3/2$$

(48)
$$f(x, v) = (2/\pi) \exp - 2E \left(2E - \frac{1}{2} \right)$$

It should be noticed that the element dx dv of the phase space can be written $2\pi \, \rho \, d\rho$ where $\rho = (x^2 + v^2)^{1/2}$

Taking into account $E = (1/2) \, (v^2 + x^2)$ we see that $\rho \, d\rho = dE$ and dx dv $\longrightarrow 2\pi dE$ (the integration on E being carried from 0 to infinity).

It can be checked that (47) and (48) fulfill the two relations.

$$\iint f(x, v) \, dx \, dv = \int_0^\infty f(x, v) \, 2\pi \, dE = 1$$

$$\iint f(x, v) \, E \, dx \, dv = \int_0^\infty f(x, v) \, 2\pi \, E \, dE = \langle E \rangle$$

BIBLIOGRAPHY

1   J. E. MOYAL
Proceeding Cambridge Philosophical Society $\underline{45}$ 99   1949

2   G. KALMAN and M. R. FEIX Editors
Nonlinear effects in Plasma – Gordon and Breach –
Chapter 6

3   T. P. ARMSTRONG
Physics of Fluids $\underline{10}$ 1269   1967
T. P. ARMSTRONG and D. C. MONTGOMERY
Plasma Physics $\underline{1}$ 425   1967

4   P. BERTRAND and M. R. FEIX
Physics Letters $\underline{28}$ A   68   1968
P. BERNARD and M. R. FEIX and G. BAUMANN
Physics Letters $\underline{29}$ A   489   1969

5   D. E. VAKMAN
Sophisticated signals and the uncertainty principle
in Radar.
Springer Verlag   1968

6   F. C. GRANT and M. R. FEIX
Physics of Fluids $\underline{10}$ 1356   1967

7   K. V. ROBERTS – H. L. BERK
Physical Review Letters $\underline{101}$ 297   1967
H. L. BERK and K. V. ROBERTS
Physics of Fluids $\underline{10}$ 1595   1967

AUTHOR INDEX